STRONG MICROWAVES IN PLASMAS

2003

Volume *1*

STRONG MICROWAVES IN PLASMAS

PROCEEDINGS
OF THE INTERNATIONAL WORKSHOP

Nizhny Novgorod,
1 – 9 August 2002

Edited by
A.G. Litvak

In two volumes
Volume 1

Editor's Preface

The 5th International Workshop "Strong Microwaves in Plasmas" took place from the first till the eighth of August, 2002 on board the "Mikhail Frunze" river boat, which cruised the Volga and Kama rivers from Nizhny Novgorod to Perm and back.

It is a rather natural idea to congregate developers of a new type of microwave sources and scientists using such sources in fundamental and applied researches, and it was first realized in 1990, in Suzdal. The twelve years that passed saw three consequent SMP Workshops, and have become a demonstrative proof of how fruitful this idea was. This is the fifth time the Workshop participants meet, and one should, evidently, look backward and make an attempt to estimate its role. Along with the task of providing an efficient information exchange, which is traditional for meetings of scientists, the SMP Workshops were also very important for the Russian scientists working in the fields of plasma and microwave physics: the Workshops provided them with the possibility to come in close contact and initiate actual scientific collaborations with their colleagues from leading laboratories of the world. It is appropriate to remember here that the SMP Workshops started right after the iron curtain was raised, when the deficit of such collaboration and interest in it on both sides were huge.

Now we can make up a long list of what Russian and foreign scientists achieved in the recent decade owing much to the collaboration that arose from the progress of SMP Workshops. This list includes but by far is not limited to development of quasi-continuous megawatt gyrotrons; successful experiments with EC heating and current drive in tokamaks and stellarators; diagnostics of fusion plasma using collective Thomson scattering; development of the basics of electrodynamics for oversized multi-mode systems and a wide range of devices to convert and transport high-power radiation; creation of relativistic microwave generators based on the phenomenon of superradiation; development of quasi-optical elements (pulse compressors, accelerating structures) for the next-generation supercolliders; realization of sources of multi-charge ions with gyrotron pumping that provide record-breaking parameters of ion beams injected into heavy-nuclei accelerators; demonstration of the prospects of using mm-wave

3

radiation in material processing (nanoceramic sintering, fast annealing of semiconductors, etc.). It is the interdisciplinary nature of the Workshops that provides such a wide range of scientific interactions.

The 2002 SMP Workshop followed the traditional scheme and combined strenuous work in scientific sections with an interesting social programme, which included interesting tours in historical Russian cities and night concerts of classical and modern music performed by specially invited young world-class musicians. 148 participants from 13 countries took part in the Workshop and submitted 128 presentations, of which 25 were plenary invited talks, 31 topical invited talks, and 72 oral contributed talks. The scientific programme, along with plenary talks, included sessions and discussions in four traditional sections: Development of High-Power Microwave Sources, Current Drive and Microwave Plasma Heating in Fusion Installations, Gas Discharges in Electromagnetic Wave Fields and Other Applications of High-Power Microwaves, and Nonlinear Processes in Plasmas (Theory and Microwave Experiments).

This book is an almost complete collection of the invited and original contributions presented at the 5th International Workshop on Strong Microwaves in Plasmas. The texts of a few papers have not been submitted by the authors mainly since they have been already published as original papers. The materials of this book provide a sufficiently comprehensive information about the state-of-the-art in the field of creating high-power microwave sources and their applications. With no doubt, this publication will be useful for the professional working in these fields.

Alexander Litvak

DEVELOPMENT OF HIGH-POWER MICROWAVE SOURCES

DEVELOPMENT AND DEMONSTRATION
OF GYROTRON OSCILLATORS AND AMPLIFIERS AT CPI

M. Blank, P. Borchard, P. Cahalan, S. Cauffman,
T. S. Chu, K. Felch, H. Jory

CPI, Palo Alto, CA, USA

Several gyrotron oscillators and amplifiers are currently under development at CPI. Three oscillators, each developed for fusion applications, were recently demonstrated. The oscillators, operating at 84 GHz, 110 GHz, and 140 GHz, have several common features including diode magnetron injection guns, internal mode converters to produce a Gaussian output mode, and edge cooled chemical-vapor deposition (CVD) diamond windows.

Three 110 GHz, 10-second pulse, 1 MW gyrotrons operating in the $TE_{22,6,1}$ cavity mode have been built. The 110 GHz gyrotrons do not include depressed collectors. All three gyrotrons have been tested to 600 kW for 10-second pulses and 1 MW for short pulses at CPI. Two of the three demonstrated 5-second pulses at the 1 MW power level at General Atomics.

A 1 MW power level, 140 GHz prototype gyrotron has been built and tested. The gyrotron, which operates in the $TE_{27,7,1}$ cavity mode, includes a single-stage depressed collector for efficiency enhancement. Power levels of about 900 kW, corresponding to 27% interaction efficiency, were reached during short-pulse operation. With collector depression, overall efficiencies of 37% were achieved. Long-pulse testing is currently in progress.

An 84 GHz, 2-second pulse, 500 kW gyrotron oscillator was successfully demonstrated in the Spring of 2002. The gyrotron operates in the $TE_{15,4,1}$ cavity mode and, like the 140 GHz device, makes use of a single-stage depressed collector. Power levels of 600 kW were achieved with 44% overall efficiencies at 2-second pulse widths.

In addition, gyrotron amplifiers for radar applications are also under development at CPI. Previously, a five-cavity gyroklystron amplifier achieved 10 kW average power at 700 MHz full-width half-maximum bandwidth. A five-section gyrotwystron amplifier, designed for greater bandwidth, has been constructed and tested. The amplifier achieved 1500 MHz bandwidth at 58 kW peak output power.

110 GHz, 1 MW gyrotron oscillators

Three 110 GHz, 10 second-pulse, 1 MW gyrotrons for the Doublet III-D experiments at General Atomics have been constructed and demonstrated. A sche-

matic diagram of the 110 GHz gyrotron is shown if Figure 1. The single-anode magnetron injection gun operates at 80 kV and up to 40 A. An internal converter is used to transform the $TE_{22,6,1}$ operating mode to a nearly Gaussian beam. The Gaussian-like beam exits the vacuum system via a CVD diamond window with a 50.8 mm diameter clear aperture.
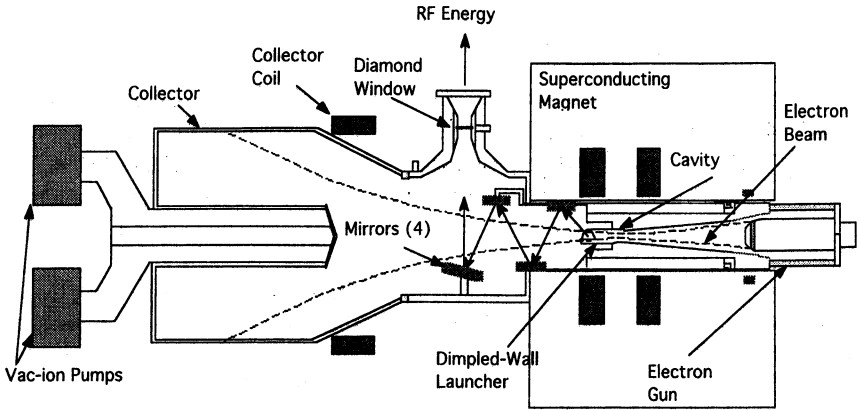

Fig. 1. Schematic of the 110 GHz, 1 MW gyrotron oscillator

All three 110 GHz gyrotrons were tested to 1 MW output power at millisecond-pulse lengths and to 600 kW for 10-second pulses. Two of the three gyrotrons were also tested to 1 MW power levels for 5-second pulses at General Atomics. A plot of the measured peak output power versus beam voltage is shown in Figure 2.
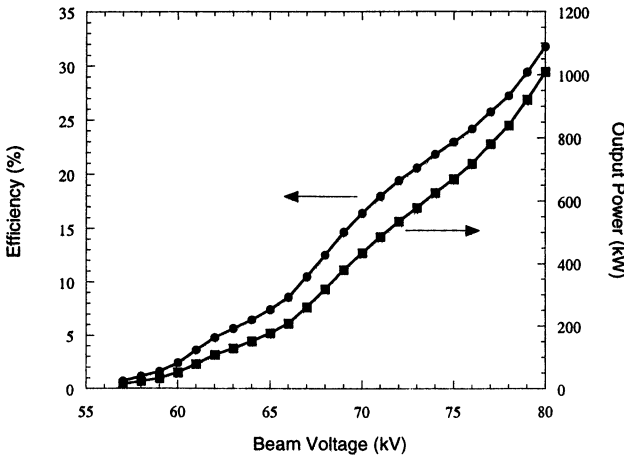

Fig. 2. Measured peak output power (filled squares) and efficiency (filled circles) versus beam voltage for the 110 GHz, 1 MW gyrotron oscillator.

8

140 GHz, 1 MW gyrotron oscillator

The 140 GHz gyrotron is being developed for the Wendelstein 7X experiments in Germany. A photograph of the completed 140 GHz gyrotron is shown in Figure 3. The main design difference between the 140 GHz, 1 MW gyrotron and the 110 GHz gyrotron is the use of a depressed-collector configuration in the 140 GHz tube. As with the 110 GHz gyrotron, the 140 GHz device uses a single-anode magnetron injection gun designed to operate at 80 kV accelerating voltage and 40 A beam current. The $TE_{28,7,1}$ mode is employed in the interaction cavity and the TEM_{00} microwave output beam exits the gyrotron through a CVD diamond window that has a clear aperture of 88 mm. Initial tests of the 140 GHz tube were completed in the Fall of 2001. Power levels of around 700 kW were obtained during short-pulse operation but interaction efficiencies were less than 20%. Through the use of the depressed collector, overall efficiencies of over 25% were observed. The cause of the low efficiency was attributed to mode competition with the nearby $TE_{25,8,1}$ mode. As the result of the low efficiency, long-pulse tests were not performed on the tube during the initial testing phase.
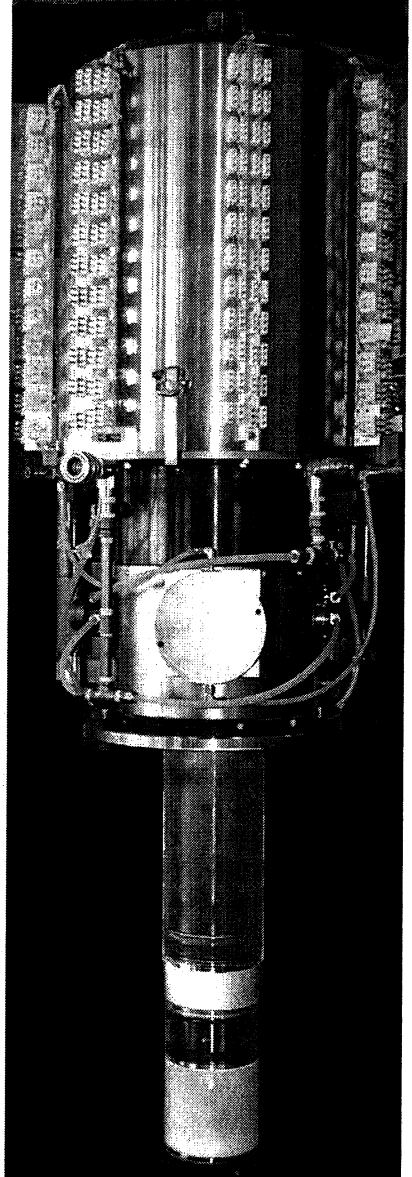

Fig. 3. Photograph of the 140 GHz, 1 MW gyrotron oscillator.

9

The gyrotron was rebuilt with a new cathode and a modified interaction cavity to reduce the mode competition with the $TE_{25,8,1}$ mode. The second series of tests, which began in September, 2002, showed greatly improved the gyrotron performance. Power levels of about 900 kW, corresponding to 27% interaction efficiency, were reached during short-pulse operation. With collector depression, overall efficiencies of 37% were achieved. In addition, pulse lengths of up to 500 ms were achieved at the 500 kW output power level. Long-pulse testing is proceeding.

84 GHz, 500 kW gyrotron oscillator

The 84 GHz, 500 kW, 2-second pulse gyrotron was developed for the KSTAR Tokamak in Korea. A photograph of the 84 GHz gyrotron is shown in Figure 4.

The overall design of the 84 GHz gyrotron, including the single-stage-depressed-collector, is quite similar to that of the 140 GHz gyrotron except that it operatesin the $TE_{15,4,1}$ cavity mode. In tests on the 84 GHz gyrotron, an output power of 560 kW was achieved for the specified pulse duration of 2 seconds. With the collector depressed by a voltage of 25 kV, the resulting output efficiency was 44% for a cathode-to-collector voltage of 55 kV (80 kV cathode-to-body voltage).
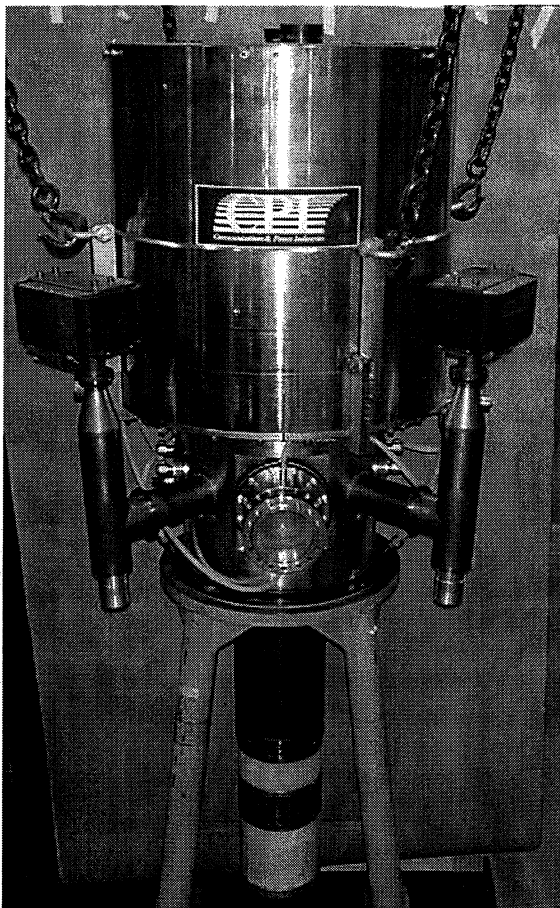

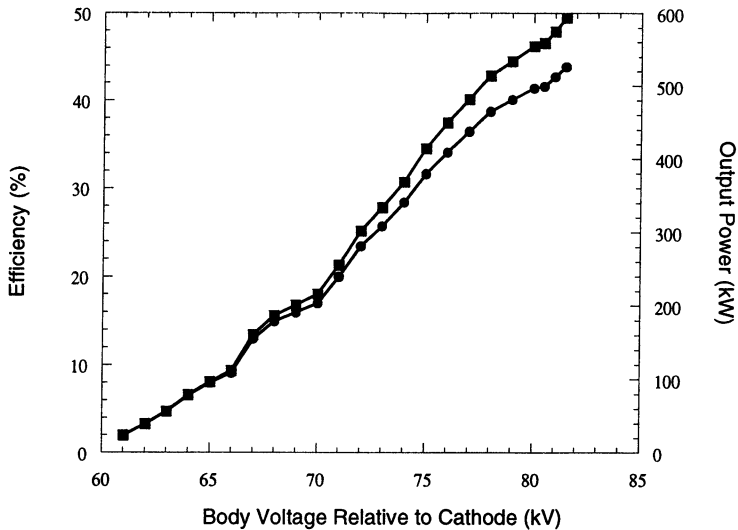**Fig. 4.** Photograph of the 84 GHz, 500 kW gyrotron oscillator.

10

Fig. 5. Measured peak output power (filled squares) and efficiency (filled circles) versus beam voltage for the 84 GHz, 500 kW gyrotron oscillator.

During short-pulse testing, the tube was characterized up to power levels of 600 kW. A plot of output power and efficiency versus cathode-to-body voltage, for a cathode-to-collector voltage of 56 kV, is shown in Figure 5. As shown in the plot, the output power level varies smoothly from 600 kW down to nearly 20 kW as the cathode-to-body voltage is decreased. This feature enables deep modulation of the output power during electron-cyclotron-heating experiments.

W-band gyroklystron amplifiers

W-band gyrotron amplifiers for radar applications are also under development at CPI. Two W-band gyroklystron amplifiers were previously demonstrated at the 10 kW average power level. The first, a four-cavity gyroklystron amplifier, achieved 10.1 kW average power at 11% rf duty factor and 33% electronic efficiency. At the 10.1 kW average power operating point, the FWHM bandwidth was 420 MHz and the saturated gain was 32 dB. The second, a five-cavity gyroklystron amplifier, achieved 10 kW average power at 700 MHz full-width half-maximum bandwidth. More recently, a five-section gyrotwystron amplifier, designed for greater bandwidth, has been constructed and demonstrated.

The gyrotwystron is comprised of an input cavity, three stagger-tuned buncher cavities, and a traveling-wave output section, all operating in the TE_{01} mode near the fundamental cyclotron frequency. Two non-linear simulation codes, MAGY and MAGYKL, were used to determine the optimal circuit pa-

11

rameters. An extensive study of performance versus variations in circuit and beam parameters was made using the non-linear simulation tools and linear stability codes. The optimized cavity parameters are shown in Table.

Optimized circuit parameters for the five-section gyrotwystron amplifier

	L (cm)	f_0 (GHz)	Q_L
cavity 1	0.40	93.10	150
cavity 2	0.48	93.10	160
cavity 3	0.48	94.30	160
cavity 4	0.48	92.80	160
section 5	0.87	93.28	70

The gyrotwystron was constructed and testing began in the Summer of 2002. A photograph and schematic diagram of the device are shown in Figure 6.
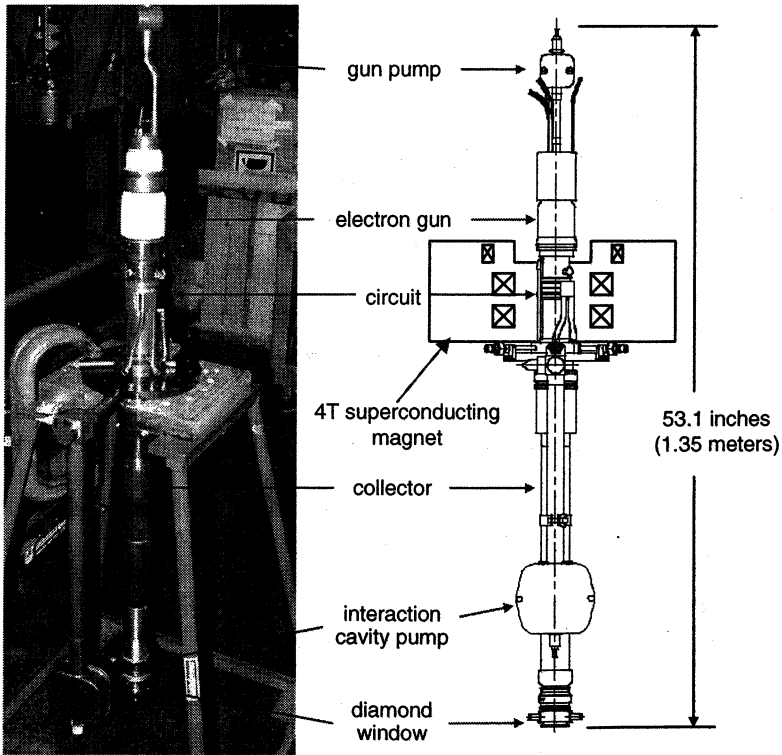

gun pump

electron gun

circuit

4T superconducting magnet

collector

interaction cavity pump

diamond window

53.1 inches (1.35 meters)

Fig. 6. Photograph and schematic diagram of the five-section W-band gyrotywstron amplifier

12

Peak output power, gain, and bandwidth were measured as a function of operating parameters at 400 Hz pulse repetition frequency, 28 µs beam pulse width (1.12% beam duty factor), and 10 µs RF drive pulse width (0.4% RF duty factor). Beam parameters and magnetic fields were varied in order to experimentally explore the operating space and demonstrate the theoretically predicted trade-offs in peak output power and bandwidth.

The measured peak output power as a function of drive frequency for the operating point at 65 kV beam voltage, 6 A beam current, and 37.1 kG interaction magnetic field is shown in Fig. 7. A peak output power of 64 kW was measured at a drive freuqency of 93.9 GHz. As shown in the figure, the measured full-width-half-maximum (FWHM) bandwidth at this operating point is 1300 MHz. The peak input power at the gyrotron flange was held constant at 14.8 W for all points on the curve.
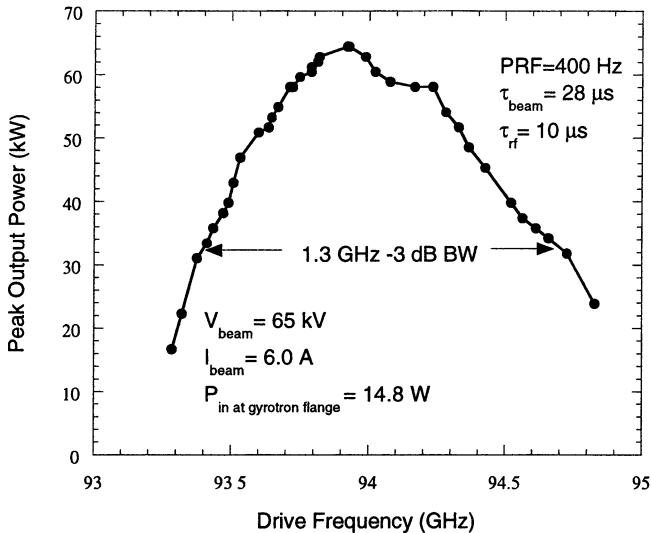

Fig. 7. Measured peak output power versus drive frequency for the operating point 65 kV, 6 A, and 37.1 kG.

Operating points with larger bandwidths and lower output powers were explored at higher interaction magnetic fields. Figure 8 shows the measured peak output power as a function of drive frequency for the 65 kV, 6 A, 37.2 kG operating point. A peak output power of 58 kW was measured at 93.9 GHz drive frequency. The measured FWHM bandwidth is 1500 MHz.

At 37.5 kG, 65 kV, and 6 A, 43 kW peak output power and 1900 MHz FWHM bandwidth were achieved, as shown in Figure 9. Further increases in the interaction magnetic field resulted in reduced bandwidths and reduced output powers.
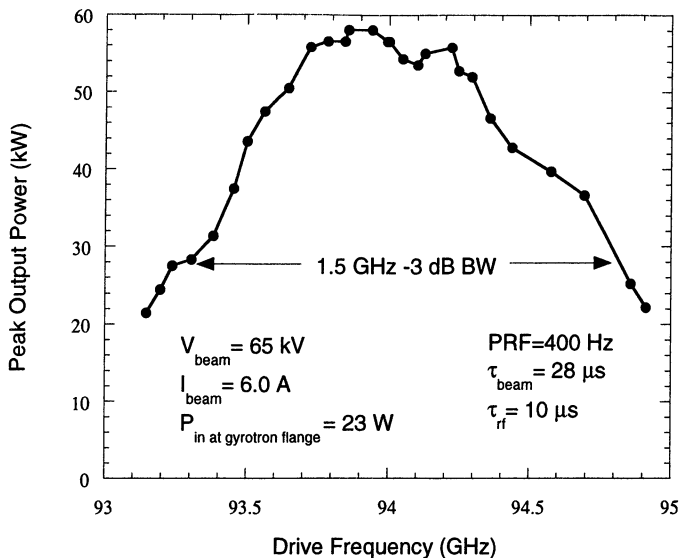
13

Fig. 8. Measured peak output power versus drive frequency for the operating point at 65 kV, 6 A, and 37.2 kG.
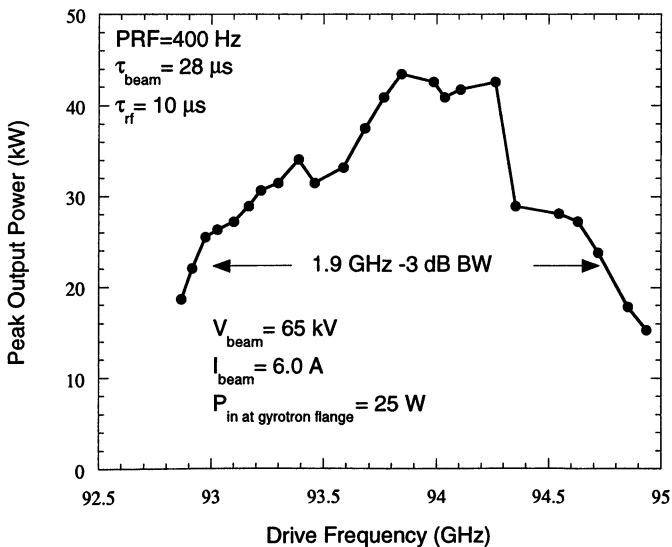

Fig. 9. Measured peak output power versus drive frequency for the operating point at 65 kV, 6 A, and 37.5 kG.

14

Operating points at beam voltages above and below the nominal 65 kV value were also investigated. At 70 kV and 6 A, a maximum output power of 80 kW was achieved at 1200 MHz FWHM bandwidth. As was demonstrated at 65 kV beam voltage, larger bandwidths can be achieved at the expense of peak output power by operating at higher interaction magnetic fields. At 70 kV beam voltage, 6 A beam current, and higher magnetic fields, 52 kW peak output power and 1500 MHz FWHM bandwidth were achieved.

Summary

Several millimeter wave gyrotron oscillators and amplifiers currently under development at CPI were described. Three oscillators, each developed for fusion applications, were recently demonstrated at 110 GHz, 140 GHz, and 84 GHz.

Three 110 GHz, 10-second pulse, 1 MW gyrotrons operating in the $TE_{22,6,1}$ cavity mode have been built. All three gyrotrons have been tested to 600 kW for 10-second pulses and 1 MW for short pulses at CPI. Two of the three demonstrated 5-second pulses at the 1 MW power level at General Atomics.

A 1 MW power level, 140 GHz prototype gyrotron with a single-stage-depressed-collector has been built and tested. Power levels of about 900 kW, corresponding to 27% interaction efficiency, were reached during short-pulse operation. With collector depression, overall efficiencies of 37% were achieved. Long-pulse testing is currently in progress.

An 84 GHz, 500 kW gyrotron oscillator was successfully demonstrated in the Spring of 2002. The 84 GHz gyrotron, which includes a single-stage-depressed-collector, is similar in design to the 140 GHz oscillator. Power levels of 600 kW were achieved with 44% overall efficiencies at 2-second pulse widths.

In addition, the experimental demonstration of a five-cavity gyroklystron amplifier was described. The amplifier achieved 1500 MHz bandwidth at 58 kW peak output power, and larger bandwidths were demonstrated at the expense of peak power.

TATUS OF THE 1 MW, 140 GHZ, CW GYROTRON FOR W7-X

G. Dammertz[1a], S. Alberti[2], A. Arnold[1a, 3], E. Borie[1a], V. Erckmann[4],
G. Gantenbein[5], E. Giguet[7], R. Heidinger[1b], J. P. Hogge[2], S. Illy[1a],
W. Kasparek[5], K. Koppenburg[1a], M. Kuntze[1a], H. P. Laqua[4],
G. Lecloarec[7], Y. Legoff[7], W. Leonhardt[1a], C. Lievin[7], R. Magne[6],
G. Michel[4], G. Müller[5], G. Neffe[1a], B. Piosczyk[1a], M. Schmid[1a],
M. Thumm[1a, 3], M. Q. Tran[2]

[1]Forschungszentrum Karlsruhe, Association EURATOM-FZK, [a]IHM, [b]IMF I, Postfach
3640, D-76021 Karlsruhe, Germany
[2]Centre de Recherche en Physique des Plasmas, Association Euratom-Confédération
Suisse, EPFL Ecublens, CH-1015 Lausanne, Suisse
[3]Universität Karlsruhe, Institut fuer Hoechstfrequenztechnik und Elektronik,
Kaiserstr. 12, D-76128 Karlsruhe, Germany
[4]Max-Planck-Institut fuer Plasmaphysik, Teilinstitut Greifswald, Association EURATOM,
Wendelsteinstr. 1, D-17491 Greifswald, Germany
[5]Institut fuer Plasmaforschung, Universitaet Stuttgart, Pfaffenwaldring 31, D-70569
Stuttgart, Germany
[6]CEA/Cadarache, 13108 Saint Paul-lez-Durance Cédex, France
[7]Thales Electron Devices, 2 Rue de Latécoère, F-78141 Vélizy-Villacoublay, France

The development of high power gyrotrons in continuous wave operation for heating
nuclear fusion plasmas has been in progress for several years in a joint collaboration
between different European research institutes and industrial partners. The development of
a 140 GHz gyrotron which will be installed at the powerful ECRH system (10 MW) of the
new stellarator facility W7-X at the Max-Planck-Institute of Plasma Physics (IPP) in
Greifswald, Germany, aims at an output power of 1 MW for each tube in continuous wave
operation. The gyrotrons operate in the $TE_{28,8}$ mode and are equipped with a diode type
magnetron injection electron gun, an improved beam tunnel, a high-mode purity low-
Ohmic-loss cavity, an optimized non-linear up-taper, a highly efficient internal quasi-
optical mode converter, a single-stage depressed collector and an edge-cooled, single-disk
CVD-diamond window. After the tests of the first tube, a pre-prototype tube, an improved
version was built and tested at the Forschungszentrum Karlsruhe. Long pulse operation
(180 s at 0.89 MW) was possible without any signs of a limitation caused by the tube. For
this output power the efficiency of the tube was 44% at a depression voltage of about
29 kV. The improvements for this tube and the experimental results are described. The
modulation of the power launched into a plasma presents a very versatile experimental tool
for plasma stabilization and diagnostics. Therefore, modulation capabilities of the output
power of gyrotrons with a frequency up to about 1 kHz (rectangular) should be possible.
For tokamaks, the modulation is essential for achieving high performance in terms of the
beta-limit, as it provides a tool for control of instabilities, so-called neoclassical tearing
modes. The capability of modulating the power of a gyrotron has been investigated with
the pre-prototype tube and are reported. In RF pulses of 1 s length, RF power modulation
depths higher than 80% have been obtained either by modulating the cathode or the
depression voltage. Frequency modulation as high as 50 kHz (sinusoidally) has been
obtained with cathode voltage modulation and 1.5 kHz with depression voltage modulation
(limited by the slew rate of the power supply).

Introduction

Electron-Cyclotron-Resonance-Heating (ECRH) and Electron-Cyclotron-Current-Drive (ECCD) require gyrotrons operating at a frequency of 110–170 GHz with an output power in the megawatt range and an efficiency of about 50%. These gyrotrons have been subject of intense investigation world-wide for a number of years. Powers of 2 MW and more have been achieved in short pulse operation [1–3] and great progress has been made in the development of 1 MW long pulse gyrotrons [4–6].

ECRH and ECCD have proven to be important tools for plasma devices especially for stellarators, as they provide both net current free plasma start up from the neutral filling gas and efficient heating of the plasma [7].

The development of ECRH is closely linked to the development of stellarators, and one of the key issues for stellarators is the development and demonstration of high power gyrotrons with CW capability. For the stellarator Wendelstein 7-X now under construction at IPP Greifswald, Germany, a 10 MW ECRH system is foreseen.

The Forschungszentrum Karlsruhe has signed a contract to build up the 10 MW ECRH system at Greifswald, and a European collaboration has been established between Forschungszentrum Karlsruhe, CRPP Lausanne, IPF Stuttgart, CEA Cadarache and TED Vélizy, to develop and build the 10 gyrotrons each with an output power of 1 MW for continuous wave operation (30 min).

The major problems of high power, high frequency gyrotrons are given by the Ohmic heating of the cavity surface, by the stray radiation due to non-perfect quasi-optical mode conversion, by the dielectric losses in the output window and by the power capability of the collector. The technical limit of the power density at the resonator surface is assumed to be 2 kW/cm^2 for CW operation. For this reason high power gyrotrons are operated in high order volume modes with a large cavity.

A major break through for a CW source is the use of a diamond window fabricated by microwave plasma assisted chemical vapor deposition (MPACVD), which allows the design and the operation of a CW tube at the 1 MW power level [6, 8–10]. The single-stage depressed collector brings the overall efficiency of the gyrotron in the 50% range and at the same time significantly decreases the thermal loading on the collector [11, 12].

Gyrotron design

The superconducting (SC) magnet configuration is composed of two main coils generating a constant magnetic field B_c in the interaction region and, for minimizing the cathode-cavity distance, a third SC magnet generating a reverse field in the gun region. This configuration allows the control of the magnetic field at the cathode independent from that of the gun. The compression ratio between the cavity field and the cathode field $B_c/B_g = 23.5$.

The design specifications and parameters are summarized in Table 1.

Table 1. Gyrotron design parameters

Cavity mode	TE $_{28.8}$
RF output power	1 MW
Frequency	140.3 GHz
Accelerating voltage	81 kV
Beam current	40 A
Mode purity of cavity	98.8 %
Retarding collector voltage	> 25 kV
Modulation depth	0.3–1 MW
Modulation frequency	up to 10 kHz
Average velocity ratio	1.3
Cathode-cavity distance	350 mm
Cathode half angle	21.8°
Beam radius at cavity	10.1 mm
Cavity radius	20.48 mm
Cavity length	14.5 mm

A schematic view of the gyrotron is shown in Fig. 1. The gyrotron uses a diode-type magnetron injection gun with a thermionic annular emitter which consists of an impregnated tungsten matrix. The conical beam tunnel between gun and resonator is equipped with alternating rings of copper and strongly absorbing ceramics (AlN/SiC in a mixture of 60/40, respectively) in order to suppress the spurious oscillations in that region [13]. The temperature limited magnetron injection electron gun (MIG) without intermediate anode is designed to operate at voltages V_{acc}= 81 kV with respect to the body (beam tunnel, cavity, quasi-optical launcher and the first two mirrors) and at cathode currents of I_b = 40 A, corresponding to a current density j_c = 2.5 A/cm.

The cylindrical cavity is designed for operating in the TE$_{28,8}$ mode with a diffractive quality factor of 855 in cold cavity approximation and of 1100 in a self-consistent calculation. It is a standard tapered cavity with linear input downtaper of
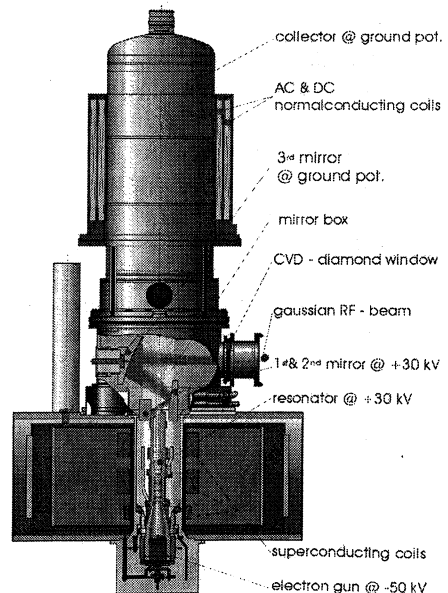

collector @ ground pot.

AC & DC normalconducting coils

3rd mirror @ ground pot.

mirror box

CVD - diamond window

gaussian RF - beam

1st & 2nd mirror @ +30 kV

resonator @ +30 kV

superconducting coils

electron gun @ -50 kV

Fig. 1. Schematic view of gyrotron

2.5° and a non-linear uptaper with the initial angle of 3°. The length of the cylindrical part is 14.5 mm, its diameter 40.96 mm. The transitions from the tapers to the cylindrical parts are smoothly rounded over a length of 4 mm at the input taper and 6 mm at the output taper in order to reduce mode conver-sion. The (cold-cavity) frequency is designed to operate at 140.3 GHz. The magnetic field at the cavity is 5.56 T, at the gun 0.22 T. The start-up behavior is determined by space-charge neutra-lization with a time con-stant of about 100 ms (at a pressure of 10^{-8} mbar). The cavity is made of dispersion strengthened copper (Glidcop), and at 1 MW output power, the peak wall losses are below 2 kW/cm^2. For this value, the conduct-ivity of Glidcop, the temperature (T_{peak} = = 270 °C), the surface roughness and frequency effects were taken into account.

The RF-beam is separated from the electron beam through a highly efficient quasi-optical mode converter consisting of a rippled-wall, helically cut waveguide launcher [14] followed by a mirror of quasi-elliptical shape and two toroidal-focussing mirrors which match the beam to the output-window size. The launcher profits from an improved perturbation structure with linearly uptapered diameter leading to optimum phasing of the mode mixture and suppression of spurious oscillations. The output window vacuum unit uses a single, edge-cooled CVD-diamond disk with an outer diameter of 106 mm, a window aperture of 88 mm and a thickness of 1.8 mm corresponding to four half wavelengths. The calculated absorbed power for tanδ = $2 \cdot 10^{-5}$ is 360 W and the window temperature stabilization time is of the order of 5 s.

The diameter and the length of the collector are 450 mm and 1300 mm respectively. The collector, the mirror box with the output window and the third mirror of the quasi-optical mode converter are on ground potential. At the nominal depress-sion voltage (voltage between cavity and collector), the cathode is at −50 kV, the beam tunnel, cavity, the quasi-optical launcher and the first two mirrors on the depression voltage of +30 kV (Fig. 2). Very fast RF modulation can be achieved by modulating the accelerating voltage. Calculation of the be-havior of the electron beam shows that such a modulation is possible without changing the depression voltage up to at least 25 kV. For heat wave experiments, the gyrotrons
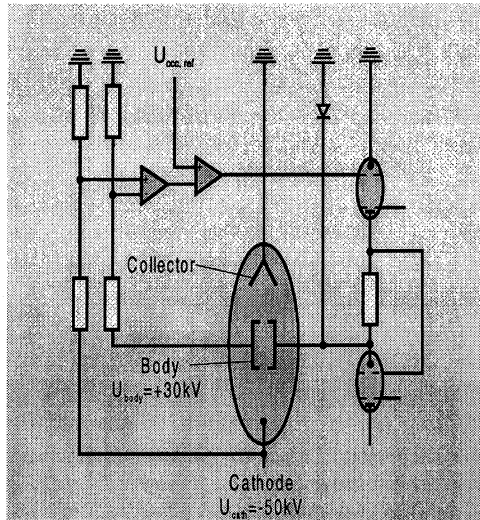

Fig. 2. Schematic HV-circuits

19

are specified to be able to be modulated with an output power of 0.3 to 1 MW with a sinusoidal frequency of up to 10 kHz.

Without sweeping the electron beam over the surface of the collector, the loss density at the collector cannot be handled technically. Additional DC- and AC-normal-conducting coils are employed, which produce an axial magnetic field. The DC-coil is necessary for adjusting the electron beam to the mid-plane of the collector. The field from the AC-coil is operated at a frequency of 7 Hz.

Experimental arrangement

The RF beam from the gyrotron is injected into an RF-tight microwave chamber which is equipped with two water-cooled deflecting mirrors (directing the beam towards the 1 MW water load [15]) and two water-cooled polarization mirrors. (The polarization mirrors are placed between the two deflecting mirrors shown in Fig. 3). The surface of the first deflecting mirror contains a grating, which reflects a small power fraction towards a horn antenna and a waveguide. This RF is transmitted to an RF detecting diode and to a frequency analyzer, which consists of a filterbank receiver with a spectral resolution of 100 MHz and a frequency time analyzer for better time dependent frequency measurements.
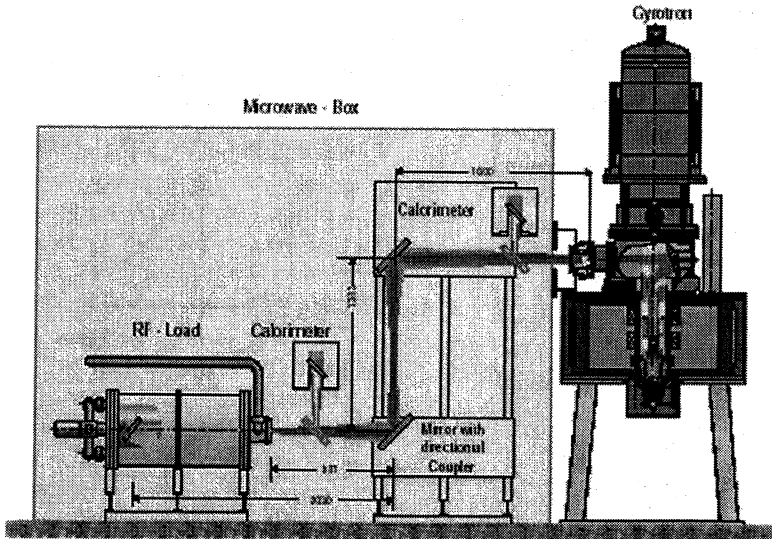

Fig. 3. Schematic layout of microwave chamber and RF-diagnostic. The polarization mirrors are not shown.

The power in short pulse operation can be measured by inserting a mirror into the RF beam which deflects the beam into a calorimeter (see Fig. 3). The

20

position of this calorimeter is about 70 cm away from the window. The power in long pulse operation is usually measured by the calorimetric RF load.

The second deflecting mirror contains a directional output coupler formed by a row of holes in the mirror surface. The connecting waveguides at the back of the mirror are terminated each with an RF detector diode on one side and a matched load on the other side. This signal could be used for long-pulse power measurements, however, it has to be calibrated in short pulse experiments, and it is difficult to extrapolate from short pulse calibration to long pulse operation. This signal is only used for fast detection of the RF power, as for example during real modulation measurements described below.

In comparison to the measurements of the first tube, the pre-prototype "Maquette", the calorimetric equipment has been improved strongly. All the components of the microwave chamber were cooled by water, and this cooling circuits have been equipped with thermocouples and flow meters. In front of the RF-load a further load has been installed (not shown in Fig. 3). With this preload – consisting of a cylindrical stainless steel vessel with Teflon water pipes on the inner surface – it was possible also to measure the power reflected from the RF absorber load. The sum of all calorimetric measurements in the microwave chamber yields the total output power (undirected beam power), whereas the sum of the preload and the main load yields the directed power.

Modulation experiment

The generation of the RF output power is determined by the accelerating voltage U_{acc} which is given by the difference between the cathode voltage U_{cat} and the depression voltage U_{dep}. According to Fig. 2, the difference of these values $U_{acc} = U_{cat} - U_{dep}$ is compared to a reference signal and is kept constant by a feedback system which acts on the power supply of the retarding collector voltage (depression voltage U_{dep}). The advantage of this system is given by the fact that in normal operation the feedback control is performed at low high-voltage levels (~30 kV) with a small power supply compared to the cathode power supply. This big power supply with high current can operate at rather moderate stabilization.

One way of performing an output power modulation is the modulation of the reference signal at constant cathode voltage: Fig. 4 shows the output power and the collector loading for 1 s pulses with constant magnetic field values and with constant beam current of 41 A. The collector loading is expressed by the temperature difference between inlet and outlet of the water in the collector cooling circuit. The output power varies almost linearly with the accelerating voltage, and between 69–82 kV the output power is changed from 100 kW to 800 kW, respect-ively. For this range, the loading of the collector decreases by about 30%, from a temperature increase of 1.6 °C at high output power of about 800 kW to 2.1 °C at low output power of 100 kW. In case, the loss density of the

21

collector is at its technical limits (which is still true, nowadays), this would mean a rather big disadvantage. Assuming an output power of 1 MW and a gyrotron efficiency (with depressed collector) of 45%, the power on the collector will be 1.2 MW. At a decreased output power of 100 kW, this value would increase to 2.1 MW. However, this value only will be achieved for very low modulation frequencies (small compared to the collector

Fig. 4. Output power and collector loading versus accelerating voltage at a cathode voltage of 58 kV. Magnetic field and beam current were kept constant.

sweeping frequency of 7 Hz). For higher frequencies, an average loading of the collector of about 1.7 MW has to be handled. But also for this value, new collector concepts have to be developed [16].

Cathode modulation (constant depression voltage) is not possible with the scheme shown in Fig. 2. The reason is the feedback system which regulates the accelerating voltage to the reference signal. The feedback system has to be switched off or has to be disconnected. In order to achieve an accelerating voltage which follows the modulation signal, both a regulated (constant) depression power supply and a regulated cathode voltage power supply are necessary. In order to avoid such an expensive system, the modulation of the depression voltage would be preferable.

Fig. 5 shows that the same amplitude modulation can be achieved with modulation at constant depression voltage, the collector loading problem, however, is strongly reduced. The loading is almost constant over the whole output power range. The increase is less than 6% at a low output power of 100 kW, and the power at the collector is kept below 1.3 MW. It has to be pointed out here, that – according to Fig. 5 – cathode modulation at constant dep-
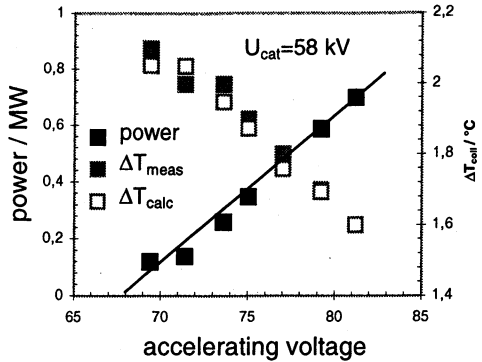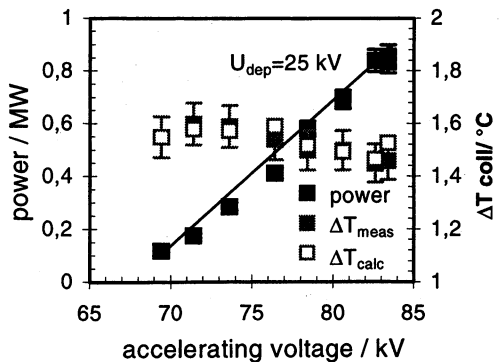

Fig. 5. Output power and collector loading versus accelerating voltage at a depression voltage of 25 kV. Magnetic field and beam current were kept constant.

ression voltage indeed is possible at least up to depression voltages of 25 kV as predicted by theory.

From the physical point of view, both systems are comparable. The output power for different accelerating voltages agrees very well within the measuring tolerances.

Due to Ohmic heating of the cavity, an expansion of the cavity and thus a frequency shift of the oscillation will take place which should be proportional to the generated power and thus to the output power. Fig. 6 shows the frequency shift as function of the output power. The frequency indeed varies linearly with varying output power, however, a constant frequency shift is super-imposed during the 1 s pulse. This effect can be explained by neutralization of the electron beam. The time constant for neutralization is about 100 ms (at about 10^{-8} mbar). This is comparable to the time constant for the expansion of the cavity which occurs within about 150 ms. For the neutralization, a

Fig. 6. Frequency shift of the resonator versus output power.

frequency shift of about 50 MHz is expected from theory, a value which agrees very well with the measured value.

Fig. 7 shows traces of an oscilloscope screen for a real modulation experiment. The cathode voltage has been modulated at constant depression voltage of 25 kV in a range between 70 kV to 82 kV. Due to the Schottky-effect, a modulation of the beam current is correlated. (The phase shifts between the signals are assumed to be produced by the external measurement circuits). The power P_{out} is measured by an RF detector diode which is coupled from the directional coupler at the second reflecting mirror in the microwave chamber. The zero line is marked with the light arrow, the third arrow from above. As can be seen, the output power varies between values corresponding to 4 V and 0.4 V of the RF detector signal, which gives a modulation depth of about a factor of 10. The output power follows the sinusoidal excitation very well.

The horizontal time scale is 20 µs/div. This means, an amplitude modulation has been possible with a frequency of 50 kHz. At higher frequencies, the modulation depth started to decrease.

For depression voltage modulation, the behavior was similar, however, due to a slew rate limitation of the power supply only a frequency of 1.5 kHz could be achieved. It is assumed, that the slew rate of the body power supply could be lowered and thus a faster modulation than 1.5 kHz could be possible.
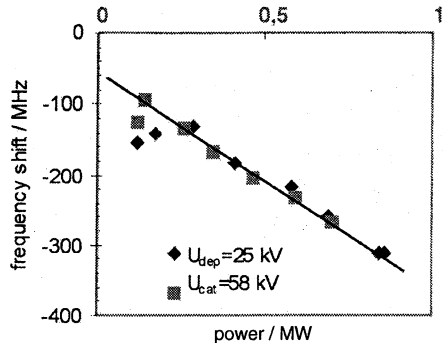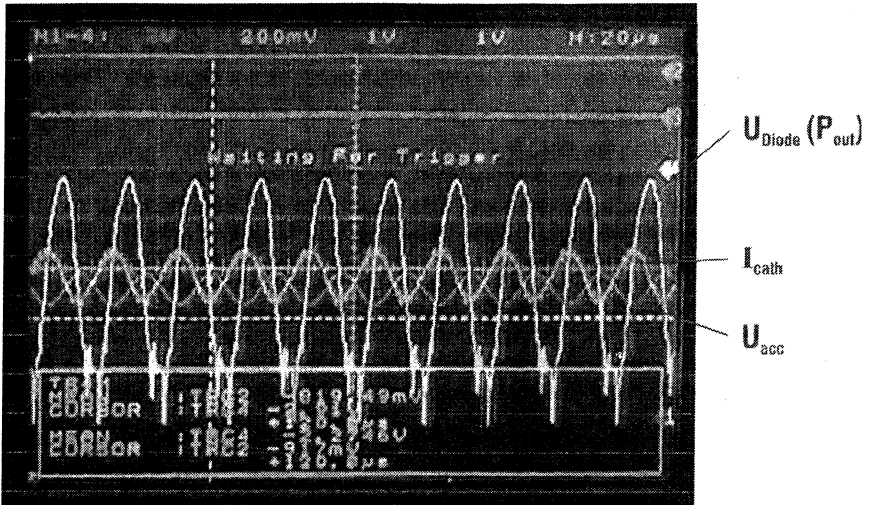
Fig. 7. Traces of accelerating voltage, beam current and output power. The power has been taken by an RF detector signal.

Gyrotron improvements

Fig. 8 shows the short- and long-pulse output power obtained with the pre-prototype tube "Maquette". The limitations in power and pulse length were partly given by the pressure increase inside the tube during operation and partly by limitation due to the RF-absorber load. Most of the gyrotron cooling circuits showed constant temperature, but the temperature at the water outlet of the mirror box (Fig. 1) increased steadily during a 180 s pulse. This gave clear evidence that the cooling of the mirror box was by far not sufficient. This also could be seen by a visual inspection of the interior of the gyrotron. The mirror box showed some melted spots mainly between the second mirror (at body potential) and the bottom plate of the mirror box. To improve this, the following modifications of the mirror box were performed:
– an additional relief window has been added,
– the cooling channels for the cylindrical part have been improved,
– a cooling circuit for the bottom plate has been added,
– the lower part of the collector (which is not hit by electrons) has been fabricated of stainless steel in order to increase the RF-absorption area,
– most inner parts which are difficult to be cooled have been made from copper.

With the assumption, that the stray radiation is distributed homogeneously [17], the relief window allows to make calorimetric measurements of the stray radiation inside the mirror box.

24

The limitation of the RF load could be overcome by adding polarizers between the two deflecting mirrors in the microwave measurement chambers. They converted the horizontally polarized RF output beam into a circularly polarized one resulting in a more homogeneously distributed power absorption on the TiO_2 surface of the load.

Apart from the improved cooling, some other modifications had been installed:

– the quasi-optical launcher system has been corrected,
– the window had been given a tilt of 1.5° with respect to the RF beam axis,
– a high temperature braze (about 850 °C) for the window has been used,
– a polished transparent CVD-diamond disk from the Institute of Applied Solid State Physics (Fraunhofer-Gesellschaft in Freiburg, Germany) has been employed.

The correction of the mirror system was necessary in order to eliminate the launcher design error of the pre-prototype tube. With this correction and without a tilt of the window, the RF beam would have been perpendicular to the window disk. It is well known that even very small reflections (matched window) going back to the cavity will decrease the generated power significantly [18].

Long pulse experiments

The long-pulse results of the prototype together with those of the pre-prototype tube "Maquette" are shown in Fig. 8. An output power of 890 kW has been measured at pulse lengths of 180 s. The efficiency has been calculated to 41%
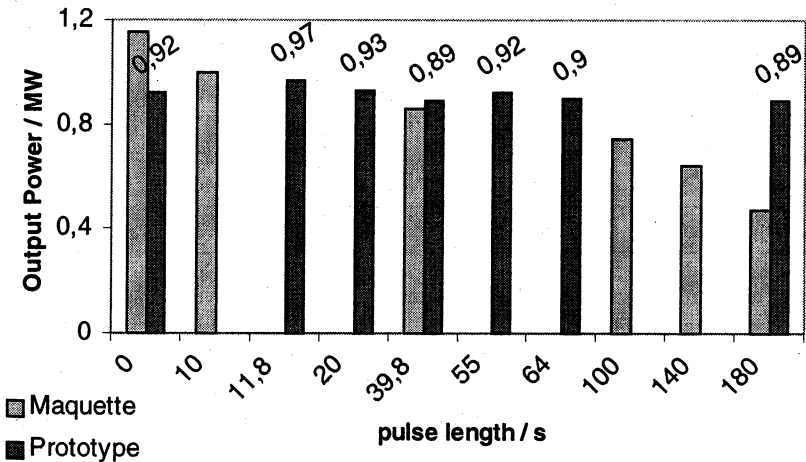
Fig. 8. Output power of the prototype gyrotron for different pulse lengths. Those for the pre-prototype tube "Maquette" are given for comparison.

with a depression voltage of about 29 kV. This gives an energy content of 160 MJ. For shorter pulse lengths, the output power increased slightly to 970 kW at a pulse length of about 12 s with an efficiency of 44%. In short pulse operation, only an output power of 920 kW was measured. The reason for the reduced power might be twofold: it was not tried very carefully to optimize the output power in short pulse operation and further the calorimeters for short and long pulse operation are different. Nevertheless, the values agree within the tolerances which are assumed to be about ±5% for long pulse measurements and about ±10% for the short pulse calorimeter.

It is interesting to consider the power balance for this gyrotron. In table 2, this is shown for two different pulses: for the 55 s pulse (output power: 922 kW) and for an 180 s pulse (output power: 890 kW). The 55 s pulse has been chosen as it fulfils already the specifications of at least 900 kW of Gaussian beam power, the second one has been chosen as it is the longest one.

Table 2. Power balance for gyrotron pulses

	922 kW; 55 s		892 kW; 180 s	
	efficiency (SDC)	42.2%	efficiency (SDC)	40.9%
	Power / kW	Power / %	Power / kW	Power / %
Generated Power	972 ± 48	100	941 ± 47	100
Internal Losses	50 ± 6	5.1	49 ± 6	5.2
Ohmic Losses	37 ± 5	3.8	37 ± 5	3.9
Stray Radiation	13 ± 4	1.3	12 ± 4	1.3
Window Losses	0.4	0.04	0.4	0.04
Output Power	922 ± 46	94.9	892 ± 45	94.8
Undirected Power	16 ± 4	1.6	16 ± 4	1.7
Directed Power	907 ± 45	93.3	876 ± 44	93.1
Total Stray Radiation	29 ± 6.0	3.0	28 ± 6.0	3.0

The Table 2 shows the calorimetrically measured power absorption for different components. The internal losses – those are both the Ohmic losses and the internal stray radiation – are measured to be only about 50 kW. The generated power thus can be calculated to 972 kW and 941 kW, respectively, for the two pulses. The relative values given in column two for each pulse are related to this value. Both, the internal and external stray radiation is measured to only 3.0 and 2.8%, respectively. This indicates the quality of the mode purity of both the cavity and the quasi-optical mode converter system. The theoretical value is given to 1.2%.

The directed power is about 93.5% that of the total output power about 95%. One should mention here, that the loss inside the CVD-window is only 400 W in good agreement with the expectations.

The reason for the limitations in power and pulse lengths are mostly of statistical nature: the main reasons were either increase of body current to two high values (assumed to be caused by arcing inside the tube) or mode loss. As one operates during these power measurements at high accelerating voltages, the limit of operation due to mode loss is very near.

Sometimes the gyrotron operation also was terminated by an interlock signaling a cathode overcurrent. A corresponding current to the body could not be observed, however, a corresponding increase in collector current. Whether this effect is caused or connected with spurious parasitic oscillation, or whether it corresponds to arcing inside the tube, is not yet understood. In any case, it is strongly correlated to the magnetic field at which the gyrotron is operated. This effect seems to have disappeared with time. This seems to indicate that the interlock was caused by internal arcing, and has been conditioned during operation.

Conclusions

An output power of 1 MW and an efficiency of 44% in depressed collector operation has been obtained with the prototype of the European 140 GHz gyrotron R&D program. The gyrotron almost meets the specified design values and combines advanced features such as single-stage depressed collector, high efficiency dimpled wall mode converter and a large diameter diamond window. Within the measurement accuracy, a low level of internal stray radiation was obtained. Long pulse operation was performed with output powers of 0.89 MW for 180 s pulse lengths with an efficiency of more than 40%, and 0.97 MW with a pulse length of about 12 s (efficiency: 44%). The best performance reached so far has produced an energy per pulse as high as 160 MJ which is the highest achieved value in gyrotrons operating at this frequency and power level.

References

1. *Piosczyk B.* et al., Development of Advanced High Power Gyrotrons at Forschungszentrum Karlsruhe, Frequenz **55** (9–10), 242–246 (2001).
2. *Dammerz G.* et al., 140 GHz Gyrotron with Multimegawatt Output Power, IEEE Trans. on Plasma Science **PS-28** (3), 561–566 (2000).
3. *Kreischer K. E.* et al., High frequency, megawatt gyrotron experiments at MIT, Conf. Dig. 18th Int. Conf. on Infrared and Millimeter Waves (Colchester, UK, 1993), 515–516.

4. *Chu T. S.* et al., Recent Progress in Producing Megawatt Gyrotrons for ECH-Applications, Conf. Digest 25th Int. Conf. on Infrared and Millimeter Waves (Beijing, P. R. China, 2000), 13–14.
5. *Zapevalov V. E.* et al., Development of a 170 GHz / 1 MW Russian gyrotron for ITER, Fusion Engineering Design **53,** 377–385 (2001).
6. *Sakamoto K.* et al., Development of 100 GHz band gyrotron and its application for JT-60U and ITER, Conf. Digest 25th Int. Conf. on Infrared and Millimeter Waves (Beijing, P. R. China, 2000), 11–12.
7. *Erckmann V.* et al., ECRH and ECCD with high power gyrotrons at the stellarators W7-AS and W7-X, IEEE Trans. on Plasma Science **PS-27,** 538–546 (1999).
8. *Thumm M.* MPACVD-diamond windows for high-power and long-pulse millimeter wave transmission, Diamond and Related Materials **10,** 1692–1699 (2001).
9. *Heidinger R.* Dielectric property measurements on CVD diamond grades for advanced gyrotron windows, Conf. Digest 19th Int. Conf. on Infrared and Millimeter Waves (Sendai, Japan, 1994), 277–278.
10. *Felch K.* et al., Status report on a 110 GHz, 1 MW CW gyrotron with a CVD diamond window, Conf. Digest 23rd Int. Conf. on Infrared and Millimeter Waves (Colchester, UK, 1998), 367–368.
11. *Piosczyk B.* et al., Single-stage depressed collectors for gyrotrons, IEEE Trans. on Plasma Science **PS-24,** 579–585 (1996).
12. *Sakamoto K.* et al., Major improvements of gyrotron efficiency with beam energy recovery, Phys. Rev. Letters **73,** 3532–3535 (1994).
13. *Pedrozzi M.* et al., Electron beam instabilities in gyrotron beam tunnels, Phys. Plasmas **5,** 2421–2430 (1998).
14. *Denisov G. G.* et al., 110 GHz gyrotron with a built-in high-efficiency converter, Int. J. Electronics **72,** 1071–1091 (1992).
15. *Ives R. L.* et al., 1.25 MW CW Waterload Development, Conf. Digest 26th Int. Conf. on Infrared and Millimeterwaves (Toulouse, France, 2001, to be published).
16. *Piosczyk B.*, A New Collector for a coaxial cavity gyrotron, Conf. Digest 26th Int. Conf. on Infrared and Millimeterwaves (Toulouse, France, 2001, to be published).
17. *Piosczyk B.* et al., Coaxial Cavity Gyrotron: Recent Experimental Results, IEEE Trans. on Plasma Science (to be published).
18. *Dammertz G.* et al., Recent Results of the 1 MW, 140-GHz, TE 22,6-Mode Gyrotron, IEEE Trans. on Plasma Science **PS-27** (2), 330–339 (1999).

MEGAWATT GYROTRONS FOR FUSION RESEARCH. STATE OF THE ART AND TRENDS OF DEVELOPMENT

G. G. Denisov

Institute of Applied Physics Russian Academy of Sciences,
GYCOM Ltd, Nizhny Novgorod, Russia

The paper analyzes tendencies of development of 1 MW power level gyrotrons for future fusion installations. These applications require a very long pulse of microwaves (10...1000 s) or CW tube operation at frequencies 110...170 GHz. The features of modern gyrotrons, highlights of gyrotron development in the last 3–4 years and future perspectives are discussed.

Introduction

Gyrotrons are the most advanced high-power sources of millimeter wavelength radiation [1–5]. They are used for many years in electron-cyclotron-wave (ECW) systems of many existing fusion installations. For the next generation of fusion installations, such as ITER or W7-X the ECW systems based on gyrotrons capable to produce 1MW/CW radiation are considered.

In the revue paper of the previous conference [5] we noticed that during the period of 1995–1999 several principal steps were made in the development of megawatt power gyrotrons:

– Efficient and stable gyrotron operation was demonstrated at very high order volume modes (e.g. $TE_{25.10}$). Operation at such modes allows one to solve the problem of thermal cavity loading.

– Demonstration of a depressed collector in high power gyrotrons. This gave a great move in solving collector and power supply problems.

– Gyrotron windows made of artificial diamond discs were developed. They are very expensive, but solve the very old and painful problem of barrier windows.

– Successful use of megawatt power level gyrotrons in plasma experiments.

The present paper discusses the main steps of gyrotron development in the period 1999–2002 between two last SMP conferences. The highlights of the work are also very bright and important:

• Demonstration of quasi-CW operation of MW gyrotrons equipped with diamond windows and depressed collectors.

• Tests of prototypes for frequency tunable MW gyrotrons.

• Tests of prototypes for 1.5–2 MW gyrotrons.

• Integration and use of MW gyrotron complexes at major fusion installations (see, for example, [8, 12, 38, 43, 45]).

Main features of modern gyrotrons

Gyrotrons for fusion systems are developed by several companies and institutions [1–5, 6–12]. The schemes of the most advanced gyrotrons are similar for all companies and illustrated by Fig. 1, 2.

There are the following main sub-assemblies in the gyrotrons.

Electron gun and beam tunnel is used to form an intense electron beam with optimal parameters. The goals of optimization are maximal transverse energy $(V_\perp/V)^2$, small velocity spread $(\Delta V_\perp/V_\perp)$ and prevention of instabilities in the beam tunnel. This component is usually optimized thoroughly on the base of special codes [13, 14].
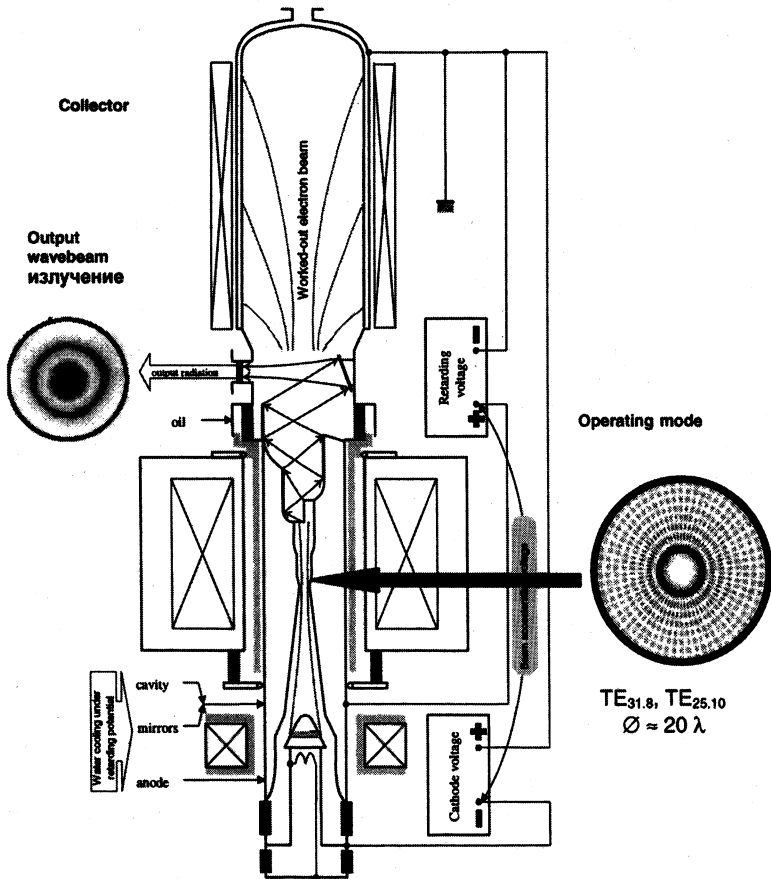
Fig. 1. Scheme of the 170 GHz gyrotron developed by IAP/GYCOM. In particular the figure shows structure of the operating mode and of the output wavebeam, scheme of power supply connection.
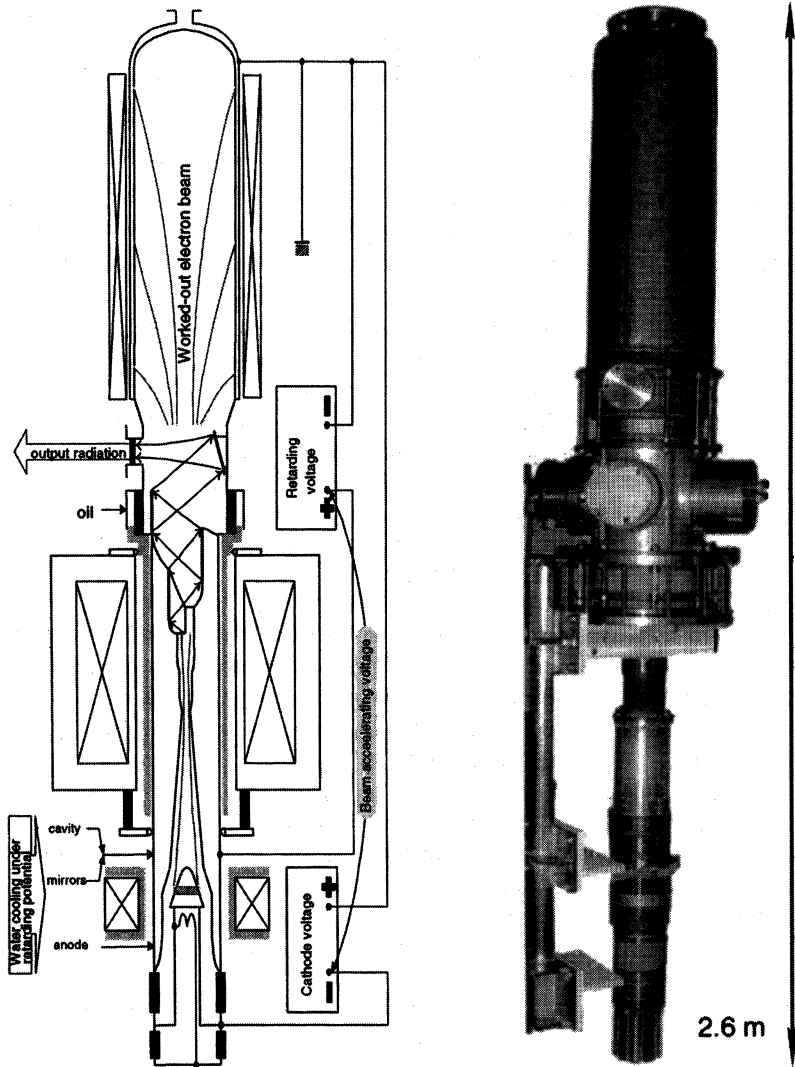
Fig. 2. Scheme and photo of Russian 170 GHz gyrotron for ITER

Cavity size and its quality factor depend on electron beam parameters. A very critical point is the thermal loading of the cavity. There are some contradictions in providing simultaneously high gyrotron efficiency and acceptable specific Ohmic losses. The compromise is achieved in numerical optimization of cavity/beam parameters.

Quasi-optical mode converter transforms a high-order operating mode into a paraxial wave beam with linear polarization and separates electron and wave beams. The electron beam goes to the collector and the wave beam usually comes out of the tube in the direction perpendicular to the magnet axis. This separation gives the possibility to solve collector and window problems practically independently.

In fact, the mode converter ends outside the tube. The output wave beam practically in all cases passes through a so-called *matching optics* which adjusts the beam to the following transmission line. To do this accurate wavebeam measurements are needed [39, 20].

Electrons after separation from the wave beam come to a *collector*, which is the biggest part of a megawatt gyrotron (Fig. 1, 2). A tremendous power (1–2 MW) is to be dissipated on the collector surface. This results in the huge water consumption of 20–30 l/s. For some gyrotrons electron beam sweeping is applied to distribute it over the collector surface. Magnetic field guiding the electrons is weak at the collector area and consequently it is rather sensitive to a stray magnetic field (from neighboring gyrotrons, tokamak or stellarators). A principal step in gyrotron development was demonstration of possibility of electron energy recovery in collectors with potential depression.

Microwaves leave the tube through a *barrier window*. For a pulse gyroton operation up to several second pulse duration the windows are made of ceramics as BN or SiN. The ceramics windows are very reliable and convenient in use, however, because of low thermal conductivity, the pulse duration of such gyrotrons is limited (1 MW / 140 GHz / 3 s) and average transmitted power does not exceed 100–200 kW. Ceramics windows at extreme parameters of operation withstand temperatures higher than 1000 °C [6, 7].

The gyrotron consists of many large, complicated and precise sub-assemblies and their joining and finally baking out the tube are very serious operations on the way of tube fabrication. In this paper we shall not discuss these issues as well as development problems of external gyrotron sub-assemblies such as gyrotron magnets, power supply and protection systems though they are very important.

There are principal gyrotron features which make the tubes capable to produce megawatt power at millimeter waves. Further we shall mention them in spite of the fact that they have been discussed many times.

High-order operating modes in gyrotrons. Gyrotrons are capable to produce a very high average power because they operate at very high volume modes of oversized cavities formed by sections of slightly irregular waveguides. Practically every year gyrotron developers show higher and higher gyrotron operating modes. Twelve years ago $TE_{15.4}$ (fifteen azimuth and four radial variations) seemed to be a very high gyrotron mode. Several years ago $TE_{22.6}$ mode was a favorite mode for gyrotron developers. In the last years extremely high-order modes $TE_{25.10}$, $TE_{28.8}$, $TE_{31.8}$ were successfully used in gyrotrons [6–9, 40]. Cavities for the latter modes are approximately twenty wavelengths in diameter.

32

Nowadays even higher modes are used in advanced gyrotron designs. Fig. 3 gives an idea about the field structure of such a high modes.
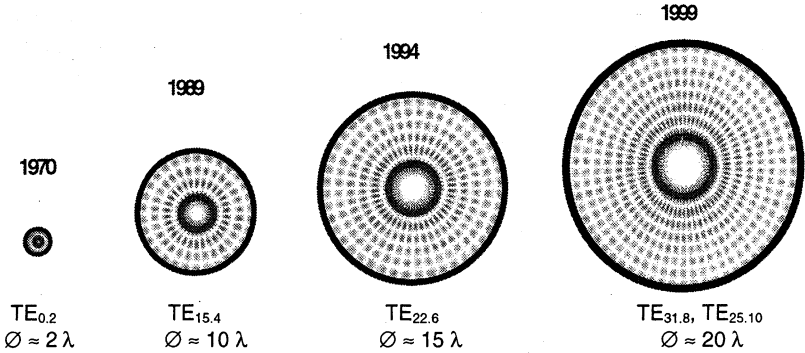

Fig. 3. Picture showing scaled size of cavities and number of radial and azimuth variations for various gyrotron operating modes. Inner circles correspond to the position of the electron beam.

Specific power absorbed in the cavity with radius R_C, length L_C, Ohmic and diffraction Q factors is:

$$\Delta P/\Delta S = P_{out} \cdot (Q_{diff}/Q_{ohm}) \cdot (R_C \cdot L_C)^{-1}, \quad Q_{ohm} = (R_C/\delta)(1 - m^2/v^2),$$

where $k \cdot R_C = v_{mp}$, $k = \omega/c = 2\pi/\lambda$, v_{mp} is corresponding Bessel function root, m is azimuth index, and δ is skin depth.

The specific power is limited for gyrotron cavity configuration and cooling technology as $\Delta P/\Delta S < (\Delta P/\Delta S)_{crit} = 2$–$3$ kW/cm^2 and power enhancement is strictly linked with the cavity size increase. Typical diffraction Q-factor is 1000–1500, Ohmic quality depending on the cavity size and wavelength is about of 50000, so several per cent of power (tens kilowatt) is dissipated in the cavity. This power and its density require very advanced cooling systems for gyrotron cavities.

The use of very high-order modes in gyrotrons brings some principal problems. The main problem is stable and efficient gyrotron operation. Recent calculations and experiments give a feeling that operating modes with indexes 60–70 are near the limit for gyrotron operation with acceptable efficiency (not less than 30% without collector energy recovery) in sufficient (not extremely small) area of the magnetic field and voltage.

Fig. 4 illustrates a part of complex processes happening, for example, during switching on a gyrotron with a high-order operating mode [15]. When the energy of electrons (horizontal axis) and electron beam current of the electron gun increase, then the excitation of several modes (TE$_{26\ 10}$, TE$_{23\ 11}$) occurs. Near design voltage only (80 kV) oscillations at the proper mode with acceptable efficiency

take place. Note that the oscillations happen in the "hard" regime when the current is lower than the starting one. Rather small changes of voltage, current and magnetic field may switch the gyrotron to a wrong mode with another frequency and low efficiency [15]. We also may note that the spectrum of possible exciting modes is not homogeneous versus their indexes (the cavity radius) and such kind of analysis allow one to find more or less "isolated" operating modes among dense mode spectrum.
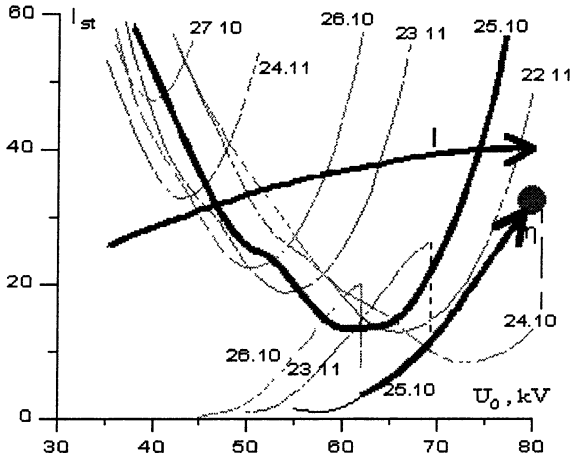

Fig. 4. Scenario of switching on for 170 GHz gyrotron with TE$_{25\ 10}$ operating mode. Thick curves (starting currents and efficiencies of interaction) correspond to the operating TE$_{25\ 10}$ mode, the thin ones – to other modes interacting with the electron beam.

A further significant increase of the cavity size requires additional ways of mode discrimination. One of the tested ways is the use of a coaxial insert into the cavity (Fig. 5). Such an insert of a proper diameter and shape makes a diffraction quality of some parasitic modes lower. The insert has diameter a bit less than the caustic diameter of the chosen operating mode and does not disturb it but makes less diffraction quality of modes with smaller caustics. Sophisticated methods [31–33, 42] based on optimization of the insert profile and its surface impedance resulted already in successful gyrotron operation at modes with extremely high transverse indexes as TE$_{28.16}$ and TE$_{31.17}$, (cavity diameter about 30 λ).

Calculations and experiments show that this way is promising and for further steps in the cavity size. In particular, the calculations performed in Zapevalov's group give hopes to design in future a gyrotron with extreme parameters if other problems (besides the cavity cooling) are solved (see Table 1).
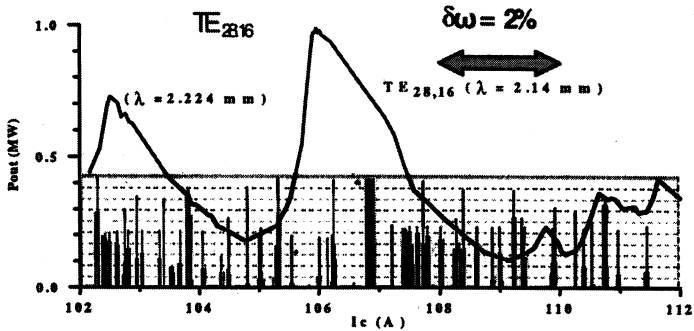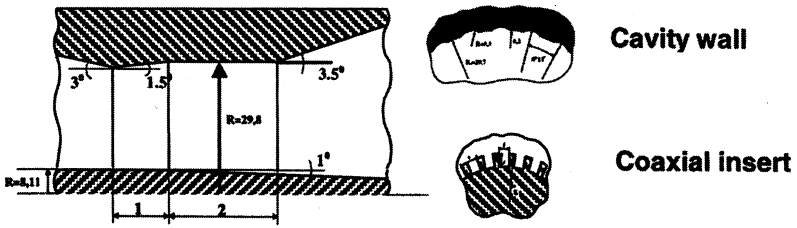
Fig. 5. Coaxial cavity view. Spectrum of cavity modes

Table 1. "Far-future" gyrotron operating mode

Operating frequency	170 GHz
Operating mode	$TE_{44.44}$
Accelerating voltage	150 kV
Electron beam current	100 A
Pitch-factor	1.3
Cavity radius	56.2 mm
Cavity quality	3000
RF output power	5 MW
Efficiency (without depress collector)	33%
Thermal wall loading (real copper)	1.7 kW/cm^2

The use of high-order operating modes assumes their efficient conversion into paraxial wavebeams with a simple spatial structure (e.g. Gaussian wave beam). The mode converter [17–20] consists of a special irregular cut ending

waveguide up-taper from the cavity, quasi-parabolic reflector and one or two specially shaped mirrors. The mode converter is an open mirror line with intrinsic diffraction losses. For a megawatt tube the acceptable level of these losses is below 3...5 %. There are methods to provide so low diffraction losses: pre-shaping of the wavebeam before its launching from the guide cut [17], and synthesis of the quasi-optical reflectors [18, 19]. In the first method the field of the operating wave is shaped due to irregularities of the up-taper. The shaped beam has weak fields at the cut edges and a nearly Gaussian angle spectrum. The second method implies the use of shaped mirrors (see Fig. 6).

a) Pre-shaping waveguide section + Conventional quasi-optical converter.
Efficiency 96–98%
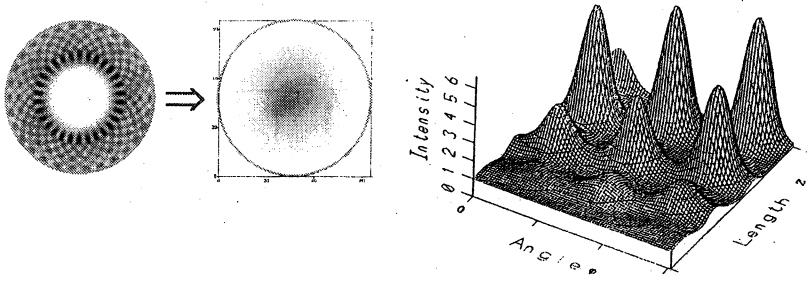
Field intensity on the wall of pre-shaping waveguide section

b) Conventional quasi-optical converter + Synthesized shaped mirrors.
Efficiency 90–95%
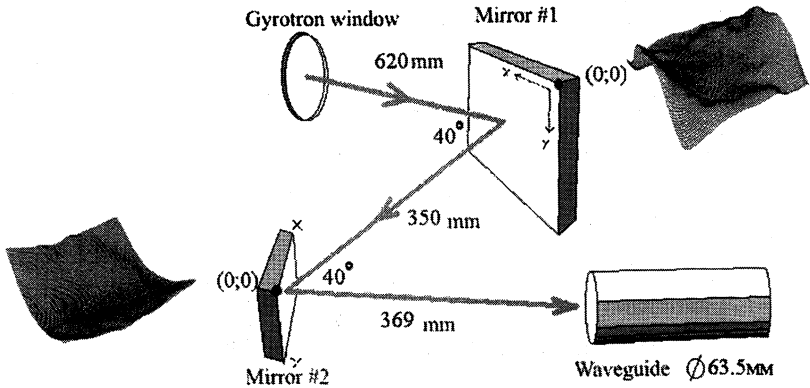
Fig. 6. Main principles of quasi-optical converters efficiency enhancement: the use of a wavegude section which provides a pre-shaping of the wavebeam before its radiation through the waveguide end (*a*); the use of shaped mirrors (*b*).

36

Depressed collectors in high power gyrotrons. The possibility of energy recovery of electrons in gyrotrons was discussed for the first time many years ago [21]. The problem was not very acute for short pulse gyrotrons and showed up itself when the development of megawatt power, CW gyrotrons for ITER began. Extraordinary power dissipated at the collector and the requirement of 50% efficiency of the tube brought back depressed collectors to consideration.

Along with the efficiency enhancement (for real tubes efficiency increase is about 1.5 times) there is obvious but very impressive drop in the power dissipated on the collector. So the efficiency increase from 33% to 50% makes the dissipated power two times lower: 1 MW instead 2 MW for 1 MW output power. Very important points which also come with depressed collectors are: simplifications in the main power supply and protection systems, significant drop of X-rays level at the collector, possibility to use electron beams with a higher operating energy and lower electron current and, hence, better quality.

The return of depressed collectors for megawatt power gyrotrons in the experiment was very impressive. Practically simultaneously several groups demonstrated significant efficiency enhancement [34–36]. Nowadays gyrotron efficiency of 50% seems to be more a routine than a record [22, 40]. We can illustrate the situation by the results of "low" frequency gyrotrons (see Fig. 7) developed and delivered by GYCOM for different plasma installations. More results will be presented in the next chapter.
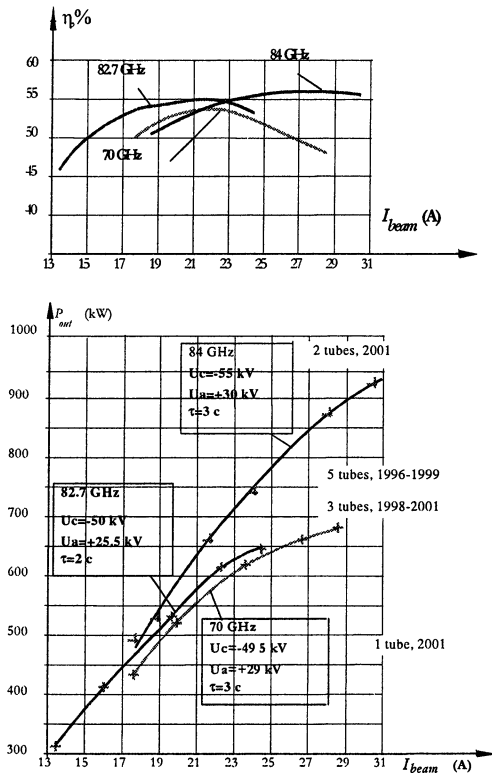

Fig. 7. Efficiency and power of 70–84 GHz GYCOM's tubes depending on electron current.

CVD diamond windows for gyrotrons. A CVD diamond disc has the outstanding combination of features.
- High thermal conductivity. It is close to the conductivity of natural diamonds and very high (about four times higher than for copper) for a very wide temperature range.
- Low losses of microwaves. Loss tangent less than 10^{-5} at millimeter waves was demonstrated for many discs of the proper size.
- High mechanical strength. For example, the disc of 1.5 mm thickness and 100 mm diameter withstands several bars of gas pressure.

The windows based on a CVD diamond are very expensive but today they are the only option for a megawatt CW window [23–30]. Calculations show that the windows based on the best discs are capable to transmit even 2–3 MW power.

Diamond windows allow edge cooling of discs by water at room temperature. This makes their use much more comfortable as compared with previous window schemes [e. g. 27, 37] operating at cryogenic temperatures or using some sophisticated coolants.

The microwave losses occur in the "body" of the discs and at their surface [29–30]. The latter depends on the surface cleaning and treatment.

Table 2 gives an idea about microwave properties of the discs.

It is necessary to note that a very extensive study of electrical, mechanical and heat properties of CVD discs is carried out at FZK and their papers content a lot of information [23–24, 28–29].

Table 2. Parameters of some recently tested CVD diamond discs

	Resonance frequency, MHz	Surface absorption P_{abs}/P_0 [10–6]	Absorption in diamond "body" P_{abs}/P_0 [10–6]	tgδ [10–5]
Gyrotron window "TEXTOR" thickness 1.798 mm	105257	530	130	1.0
	140332	590	140	0.79
	175407	660	140	0.64
Gyrotron Window "India" thickness 1.525 mm	82622	860	170	1.84
	123920	1000	240	1.71
	165220	1200	300	1.65
Gyrotron window ITER2 thickness 1.489 mm	126958	1300	95	0.72
	169261	1500	97	0.55
Barrier window "Ind" thickness 1.523 mm	164080	410	57	0.33

Diamond discs for gyrotron windows must be brazed to metal constructions with a high temperature alloy in order the tube can pass the process of baking out. This is a difficult problem because diamond and metal parts have very different thermal expansion. There is a way to braze the diamond discs on the base of Aluminum. This kind of brazing limits the maximal temperature of baking out as 400–450 °C, however the main part of the brazed discs made in such a way. High temperature brazing is now also under development in several groups.

More then ten tubes with diamond windows have been fabricated and tested by different institutions and companies [8, 10–12, 40, 45]. Some gyrotrons with diamond windows are already used at plasma installations: DIII-D, JT-60, TEXTOR.

The reliability of the CVD diamond windows is still an open question. Rather high percentage (~ 20%) of the windows used in gyrotrons failed (cracked with lose of vacuum tightness) after relatively short time of commissioning (e. g. Fig. 8). The failures happened during operation of the tubes. The reasons of some window cracks failures are not still clear.
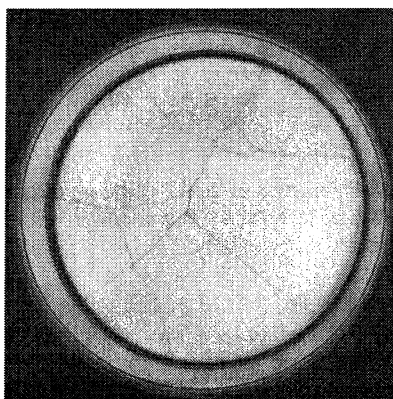
Fig. 8. Photo of CVD diamond disc before mounting in gyrotron (*a*) and after its falure (*b*).

Recent results of megawatt gyrotron test

Impressive parameters of long pulse tubes were demonstrated by all gyrotron developers during last years [40, 8, 45, 12]. The most impressive achievement was done by European team which tested 140 GHz gyrotron output power level near 1 MW in pulses of hundreds seconds. JAERI/Toshiba showed long pulse

gyrotron operation 0.9 MW / 9 s at 170 GHz and 1.2 MW / 4 s at 110 GHz, CPI produced several 110 GHz gyrotrons generating 0.6 MW power in 10 second pulses. IAP/GYCOM achieved new results with 140 GHz (0.7 MW / 10 s, delivered to TEXTOR) and 170 GHz (0.5 MW / 80 s) gyrotrons.

Practically for all cases efficiencies of the tubes were in the range of 40–50%. Typical behavior of the main gyrotron parameters and characteristics are illustrated by Fig. 9–11.
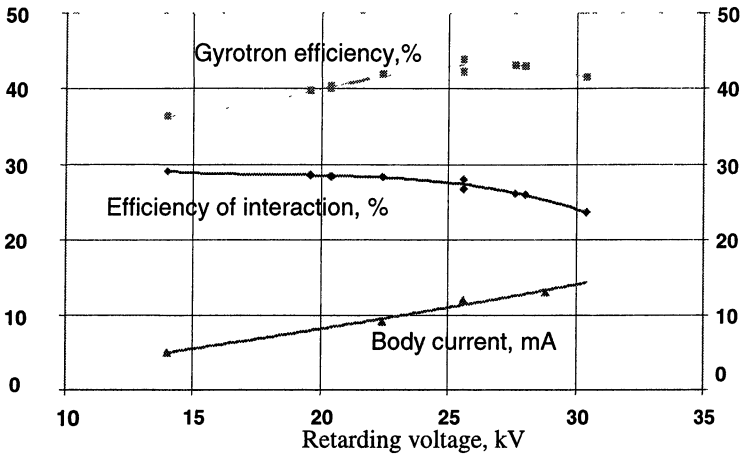

Fig. 9. Parameters of the 170 GHz gyrotron at 70-keV energy of electrons and 38–40 A beam current. Output power is 0.7 MW.
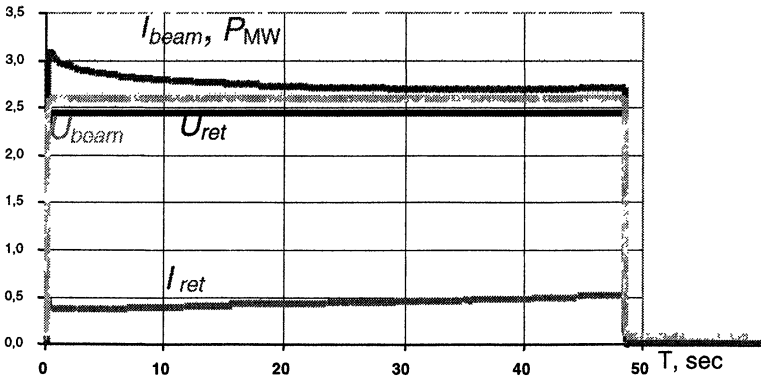
Fig. 10. Behavior of some important parameters of the 170 GHz gyrotron during 50 second pulse. Output power is 0.5 MW.
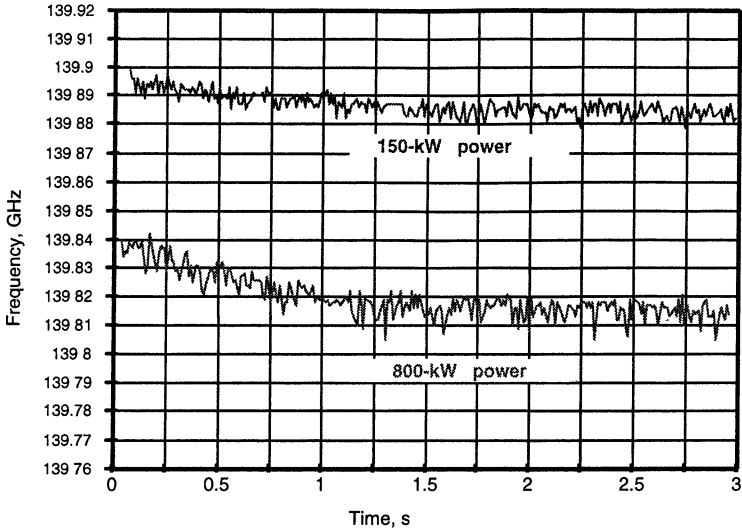
Fig. 11. Drift of oscillation frequency during first 3 seconds of the 140 GHz operation. Small frequency drift confirms a proper cooling system design.

Tendencies of gyrotron development

Megawatt power CW gyrotron at millimeter wavelengths is feasible. Definitely such gyrotrons will be and integrated in ECW systems of advanced fusion installations in a few years.

For the next round of gyrotron development there are two more demands and two directions: development of multi-megawatt microwave power source and frequency tunable megawatt gyrotrons. The work on these extremely ambitious and difficult problems is carrying out. Projects of multi-megawatt coaxial gyrotrons and step-frequency-tunable gyrotrons are now at the stage of studying short pulse prototypes.

High power 2.2 MW at 165 GHz was demonstrated in millisecond pulses in coaxial gyrotron at FZK. There are plans for next year to test at GYCOM an industrial version of long pulse 1.5 MW coaxial gyrotron with a depressed collector. The cost of the higher power in coaxial gyrotron includes complications in the cavity, electron gun, mode converter and bigger required magnet bore.

Last achievements with CVD diamond output windows and model experiments with coaxial gyrotrons, in principal, make it possible to consider the 5 MW coaxial gyrotrons at the frequencies up to 170 GHz. Now discussions on such a gyrotron look similar to the discussion on 1 MW / CW gyrotron ten-fifteen years ago.

41

The second direction aims the development of frequency tunable megawatt gyrotrons [41–42, 44]. Change of the main magnetic field give a possibility to make a step frequency tuning with a typical step of 2–3% depending on the gyrotron cavity size. Development of such tubes includes the following tasks: design of an electron gun operating in wide range (30–40%) of magnetic fields; a proper choice of the set of operating modes with the same direction of rotation, design of a depressed collector capable to operate at various magnetic fields and a mode converter transforming all operating modes into Gaussian wavebeam, choice of a broad band or tunable window.

For example, two gyrotron designs have been completed by IAP/GYCOM. In the first one the mode $TE_{22.8}$ has the resonant frequency 140 GHz and the second gyrotron has this frequency at $TE_{22\,10}$ mode. Number of operation modes with high efficiency in the range of interest between 100 GHz and 160 GHz is about 10 for each design (Fig. 12). The gyrotrons are based on a diode type of electron gun. This resulted in the change of optimal electron beam radius (approximately as $f^{1/3}$, f is frequency) and consequently in the necessity of an additional collector coil correcting position of the beam on the collector surface.
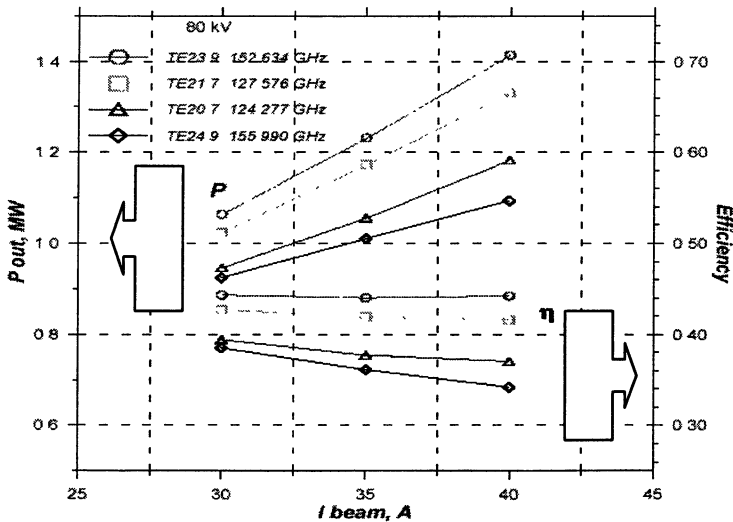

Fig. 12. Short-pulse tests of multi-frequency gyrotron. Powers and efficiencies of different operating modes.

The shapes for reflectors of the mode converter were found which provide a rather high (94–96%) Gaussian mode content in the output wave beams for all operating modes. Two window concepts were considered: Brewster window and two-disc adjustable window. Both concepts imply the use of CVD diamond discs

with 88 mm diameter of brazed cuffs. The Brewster window is very attractive because of very wide instant frequency band, however the converter design in this case is more complicated and it was decided that in initial tests the frequency tunable gyrotron will be equipped with the two-disc windows.

Table 3. Parameters of two-frequency gyrotron prototype

Operation frequency	104 GHz	140 GHz
Operating mode	$TE_{18.7}$	$TE_{22\,10}$
Output power	0.98 MW	1.0 MW
Pulse duration	0.5 s	
Cathod votage	– 62 kV	– 61 kV
Anode voltage	29 kV	30 kV
Beam current	34 A	34.5 A
Efficiency	46.5%	47%

The prototypes of frequency tunable gyrotrons were tested recently. At this stage BN ceramics windows were used in the gyrotron constructions. High power (over 1 MW) and high efficiencies (about 50%) at several frequencies in microwave pulses about 0.5 s were demonstrated in the experiments (see Table 3).

The pulse duration was limited by overheating of the ceramics windows used in the prototypes. Tests of the multi-frequency gyrotron with a diamond window are planned for 2003. The goal of these near-time tests is to demonstrate 0.8–1 MW power in microwave pulses of 10 seconds at lest at two frequencies 105 GHz and 140 GHz, corresponding to pass bands of the single diamond disc.

References

1. *Felch K. L., Danly B. G., Jory H. R.* et al., Characteristics and Applications of Fast-Wave Gyro-devices. Proceedings of IEEE, **87** (5), 752–781 (1999).
2. *Thumm M.* State-of-the-Art of High power Gyro-Devices and Free Electron Masers. Update 2000 (Forschungcentrum Karlsruhe, Germany, 2001).
3. *Litvak A. G., Alikaev V. V., Denisov G. G., Zapevalov V. E., Kurbatov V. I., Myasnikov V. E., Flyagin V. A.* Development of 1 MW output power level gyrotron for ITER ECRH system. 17th IAEA Fusion Energy Conference (Yokohama, Japan, 19–24 October 1998), IAEA-F1-CN-69/FTP/24.
4. *Goldenberg A. L., Denisov G. G., Zapevalov V. E.* et al., Cyclotron Resonance Masers: State of the Art. Radiophys. and Quantum Electronics, **39**, 423–446 (1996).
5. *Denisov G. G.* Development of 1 MW output power level gyrotrons for fusion systems. Proc of 4th Int. Workshop "Strong Microwaves in Plasmas" (Nizhny Novgorod, 2000), 967–986.

6. *Denisov G. G., Flyagin V. A., Kuftin V. A.* et al., Development of the prototype170 GHz, 1 MW gyrotron for ITER at IAP. Proc, 3rd Int Workshop on Strong Microwaves in Plasmas, Nizhny Novgorod, **2**, 717–722 (1996).

7. *Zapevalov V. E., Denisov G. G., Flyagin V. A.* et al., Development of 170 GHz / 1 MW Russian Gyrotron for ITER. Fusion Ingineering and Design, **53**, 377–385 (2001).

8. *Litvak A. G., Agapova M. V., Denisov G. G.* et al., New Results in Development of MW Output Power Gyrotrons for Fusion Systems. 27th Conf. on Infrared and MM Waves (San-Diego, USA, 2002), 295–296.

9. *Sakamoto K., Kasugai A., Takashi K.* et al., Stable single-mode oscillation with high-order mode at 1 MW, 170 GHz Gyrotron. J. of Physical Society of Japan, **65**, 1888–1890 (1996).

10. *Sakamoto K., Kasugai A., Tsuneoka M.* et al., Development of high-power gyrotron with a dia-mond window. Proc. 23rd Int. Conf. Infrared and MM Waves (Sept., 1998, Colchester, UK), 363–364.

11. *Felch K., Borchard P., Caufman S.* et al., Status report on a 110 GHz, 1 MW gyrotron with a diamond window. Proc. 23rd Int. Conf. Infrared and MM Waves (Sept., 1998, Colchester, UK), 367–368.

12. *Chu T. S., Blank M., Borchard P.* et al., Recent progress in producing megawatt gyrotrons or ECH applications. Conf. Digest 25th Conf. on Infrared and MM Waves (China, Beiging, 13–14, 2000).

13. *Kuftin A. N., Lygin V. K., Tsimring Sh. E., and Zapevalov V. E.* Int. J. Electronics, **72** (5–6), 1145–1151 (1992).

14. *Kuftin A. N., Lygin V. K., Manuilov V. N.* et al., Advanced numerical and experimental investi-gation for gyrotron helical electron beams. Int. J. Infrared and Millimeter Waves, **20** (3), 361–282 (1999).

15. *Moiseev M. A., Nemirovskaya L. L., Zapevalov V. E., Zavolsky N. A.* Int. J. IR&MM Waves, **18** (11), 2177 (1997).

16. *Vlasov S. N., Zagryadskaya L. I., Petelin M. I.* Transformation of a whispering gallery mode, propagating in a circular waveguide, into a wavebeam. Radio Eng. Electron. Phys, **20** (10), 14–17 (1975).

17. *Denisov G. G., Kuftin A. N., Malygin V. I.* et al., 110 GHz gyrotron with a built-in high-efficiency converter. Int. J. Electronics, **72** (5–6), 1079–1091 (1992).

18. *Katsenelenbaum B. Z. and Semenov V. V.* Synthesis of the phase correctors forming arequired field. J. Radiotechnics and Electronics, **12**, 244–252 (1967).

19. *Bogdashov A. A., Chirkov A. V., Denisov G. G.* et al., Mirror synthesis for gyrotron quasi-optical mode converters, Int. Journal of Infrared and Millimeter Waves, **16** (4), 735–744 (1995).

20. *Aleksandrov N. L., Denisov G. G., Chirkov A. V.* 3D wavebeam field reconstruction from inte-sity measurements in a few cross-sections, Optics Communication, **115**, 449–452 (1995).

21. *Fix A. Sh., Flyagin V. A., Goldenberg A. L.* et al., Int. J. Electronics, The problems of increase in power, efficiency and frequency of gyrotrons for plasma investigations, **57** (6), 821–826 (1984).

22. *Kurbatov V. I., Malygin S. A., Orlov V. B., Solujanova E. A., Tai E. M.* 70–140 GHz 1 MW gyrotrons on their way to CW operation, Proc. of 4th Int. Workshop "Strong Microwaves in Plas-mas" (Nizhny Novgorod, 2000), 641–650.

23. *Hiedinger R., Sporl R., Thumm M.* el al., CVD diamond windows for High power gyrotrons. Procedings of 23rd Int. Conf. Infrared and Millimeter Waves (Sept., 1998), 223–224.

24. *Thumm M.* Development of output windows for high-power long-pulse gyrotrons and EC wave applications. Int. J. Infrared and Millimeter Waves, **19**, 3–14 (1998).

25. *Kasugai A., Sakamoto K., Takashi K.* et al., Chemical vapor deposition diamond for high-power and long-pulse millimeter wave transmission. Rev. Scientific Instruments, **69**, 2160–2165 (1998).

26. *Alikaev V. V., Khmara D. V., Khmara V. A.* et al., Output Power Windows of GYCOM Gyro-trons and their Prospectiv. ITG Conf. Displays and Vacuum Electronics (Garmisch-Patenkirchen, Germany, 1998), 357–362.

27. *Moeller C P., Doane J. L., DiMartino M.* A vacuum window for 1MW CW 110 GHz gyrotron. Conf. Digest 19th Int. Conf. on Infrared and MM Waves (1994, Sendai), 279–280

44

28. *Sporl R., Schwab R, Heidinger R., Parshin V. V.* CVD Diamond for High Power Gyrotrons: Characterisation of Dielectric Properties. ITG Conf. Displays and Vacuum Electronics (Garmisch-Patenkirchen, Germany, 1998), 369–374.

29. *Heidinger R, Meier A., Rohde M.* et al., Millimeter wave characteriza-tion of large area MPACVD diamond windows. 25th Conf. on Infrared and MM Waves (China, Beiging, 2000), 389–390.

30. *Parshin V., Ralchenko V. and Konov V.* Diamond for High-Power Gyrotron Window. The 23th Int. Conf. on IR & MM Waves (Colchester, England, 1998).

31. *Vlasov S. N., Zagryadskya L. I., Orlova I. M.* Open coaxial resonators for gyrotrons. Radio Eng. Electron. Phys, **21**, 96–102 (1976).

32. *Flyagin V A., Khizhnyak V. I., Kuftin A. N.* et al., Investigation of coaxial gyrotrons at IAP RAS. Conf. Digest 22nd Int. Conf on Infrared and MM Waves (Wintergreen, USA, 1997), 112–113.

·33. *Thumm M., Braz O., Dammertz G.* et al., Experimental results of 1.5MW coaxial cavity gyro-
.   trons in the frequency range 115–170 GHz. Proc.3rd Int. Workshop on strong Microwaves in Plasmas (Nizhny Novgorod, 1997), **2**, 614–633.

34. *Sakamoto K., Tsuneoka M., Kasugai A.* et al. Major improvement of gyrotron efficiency with beam energy recovery. Phys. Rev. Lett., **73**, 3532–3535 (1994).

35. *Piosczyk B., Iatrou C. T., Dammertz G., Thumm M.* Operation of gyrotrons with single-stage depressed collector. Conf. Digest 20th Int. Conf. on Infared and Millimeter Waves (Orlando, 1995), 491–492.

36. *Glyavin M. Yu., Kuftin A. N., Venediktov N. P., Zapevalov V. E.* Experimental investigation of a 110 GHz / 1 MW gyrotron with one-step depressed collector. Int. J. Infrared and Millimeter Waves, **18**, 2129–2136 (1997).

37. *Alberti S., Braz O, Garin P.* et al., Long-pulse operation of a 0.5 MW – 118 GHz gyrotron with cryogenic window. Proc. 21st Conf. on Infrared and Millimeter Waves (Berlin, 1996), AF1.

38. *Darbos C., Magne R., Alberti S.* et al., The 118 GHz ECRH experiment on Tore Supra. 21st Symposium on Fusion Technology (Madrid, Spain, 2000).

39. *Kuznetsov S. O., Malygin V. I.* Determination of gyrotron wave beam parameters. Int. J. of Infrared and Millimeter Waves, **12** (11), 1241–1252 (1991).

40. *Dammertz G., Alberti S., Arnold A.* et al., 140 GHz, 1 MW, CW Gyrotron for Fusion Plasma Heating. Proc. Third IEEE International Vacuum Electronics Conf. (Monterey, USA, 2002), 330–331.

41. *Thumm M., Arnold A., Borie E.* et al., Frequency step-tunable (114–170 GHz) megawatt gyrotrons for plasma physics applications. Fusion Engineering and Design, **53**, 407–421 (2001).

42. *Piosczyk B., Arnold A., Dammertz G.* et al., Step-Frequency Operation of a Coaxial Cavity Gyrotron from 134 to 169.5 GHz. IEEE Transaction on plasma Science (June 2000), **28** (3).

43. *Zohm H., Gantenbein G., Giruzzi G.* et al., Experiments on neoclassical tearing mode stabilization by ECCD in ASDEX Upgrade. Nuclear Fusion, **39**, 577–580, (1999).

44. *Zapevalov V. E., Bogdashov A. A., Chirkov A. V.* et al., Optimization of the frequency step-tunable 105–170 GHz 1 MW gyrotron prototype. 27th Conf. on Infrared and MM Waves (San-Diego, USA, 2002), 1–2.

45. *Okubo K., Kubo S., Shimozuma T.* et al., Electron Cyclotron plasma production on LHD: system and its application. Proc. of 4th Int. Workshop "Strong Microwaves in Plasmas" (Nizhny Novgorod, 2000), 27–40.

BROADBAND GYRO-TWTs AND GYRO-BWOs
WITH HELICALLY RIPPLED WAVEGUIDES

V. L. Bratman, A. W. Cross[1], G. G. Denisov, M. Yu. Glyavin, W. He[1],
A. G. Luchinin, V. K. Lygin, V. N. Manuilov, A. D. R. Phelps[1],
S. V. Samsonov, M. Thumm[2], A. B. Volkov

Institute of Applied Physics, Nizhny Novgorod, Russia
[1]University of Strathclyde, Glasgow, UK
[2]Forschungszentrum Karlsruhe, Karlsruhe, Germany

Recent results on low-relativistic second-harmonic gyro-devices based on a microwave system in the form of a helically rippled waveguide are presented. A gyro-TWT provides stable amplification with a maximum electronic efficiency of 27 %, maximum output power of 180 kW, saturated gain of 25 dB and instantaneous −3 dB bandwidth of nearly 10 %. A frequency-tunable gyro-BWO, attractive for some technological applications, is also under investigation. In the experiment a pulsed prototype of a 20-kV CW oscillator was developed which generated an output power of about 5 kW with smooth frequency tuning within a frequency range of 23.5–25 GHz.

Introduction

The gyrotron traveling wave tubes (gyro-TWTs) and gyrotron backward wave oscillators (gyro-BWOs) are known as wide-frequency-band varieties of gyrodevices [1–10]. Due to operation with electromagnetic waves possessing large group velocities, a gyro-TWT amplifier may have a wide instantaneous bandwidth while a gyro-BWO permits smooth frequency tuning by varying the axial magnetic field or electron beam voltage. However, for the simplest microwave system in the form of a smooth cylindrical waveguide, a large wave group velocity inevitably leads to a large axial wavenumber, which makes these devices significantly more sensitive to particle velocity spread in comparison with a gyrotron. The most favorable wave dispersion for a gyro-TWT and gyro-BWO is when the wave group velocity is sufficiently large and constant in the region of close-to-zero axial wavenumber. A similar dispersion can be realized in an over-sized circular waveguide with a helical corrugation of its inner surface (Fig. 1) [11, 12].

Theoretical analysis and proof-of-principle experiments have demonstrated important advantages of "helical" gyro-TWTs and gyro-BWOs as compared to analogous gyro-devices based on "smooth bore" interaction regions, such as reduced sensitivity to electron velocity spread, an in-crease in the frequency bandwidth and improved stability to parasitic self-oscillations [12–14]. The most selective configuration for gyro-devices with helically rippled waveguides is when an axis-encircling electron beam resonantly interacts at the second cyclotron

harmonic with the $TE_{2,1}$ mode, which is scattered on the 3-fold helical corrugation into counter-rotating forward (for TWT) or backward (for BWO) propagating $TE_{1,1}$ mode (Fig. 2).
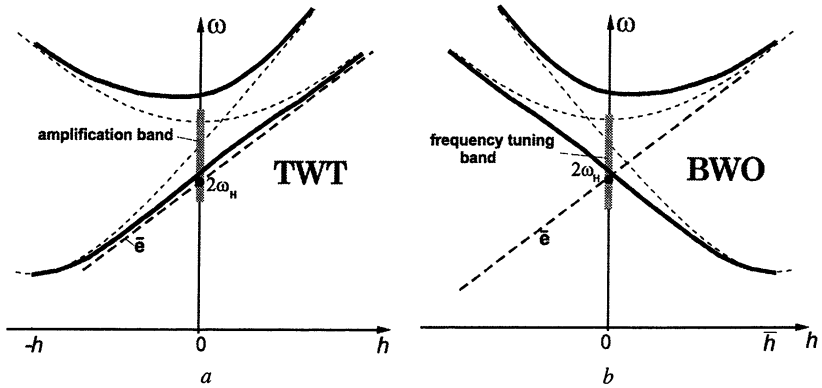

Fig. 1. Wave dispersion diagram for a gyro-TWT (*a*) and a gyro-BWO (*b*) with a helically rippled waveguide.
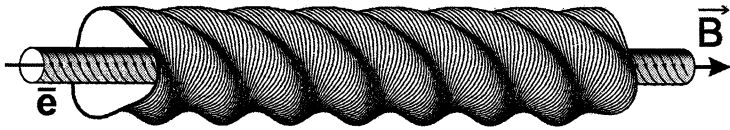

Fig. 2. Schematic view of principal elements of the helical-waveguide gyro-TWT/BWO

An additional advantage of using the second cyclotron harmonic interaction is the reduction in the required magnetic field by a factor two, as compared to equivalent sources operating at the fundamental cyclotron frequency. In addition, the gyro-TWT and gyro-BWO configuration was such that a relatively simple technique could be used to couple radiation into and out from the microwave source. The main goal of the experiments discussed below was the realization of high power microwave devices, which are attractive for a number of important applications.

Highly efficient broadband gyro-TWT

The operating waveguide for the gyro-TWT has been designed to provide a wave dispersion, which is matched within the maximum frequency band to an 80-keV electron beam having a pitch ratio of 1.2 (Fig. 3) [16, 17].

47
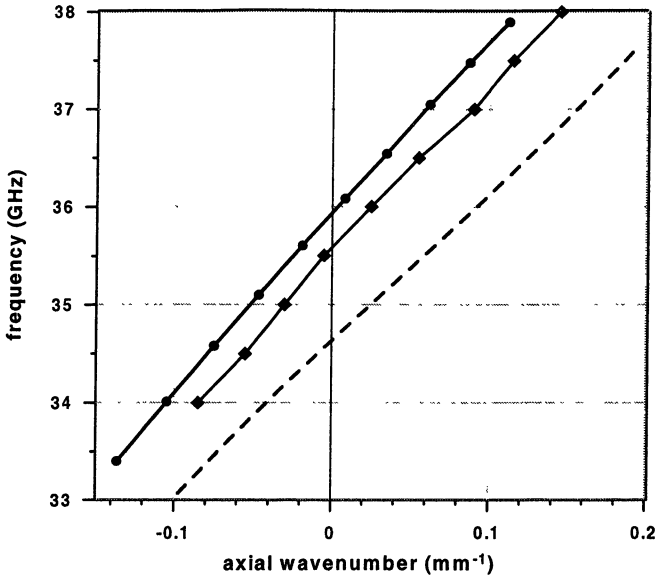
Fig. 3. Dispersion of the gyro-TWT operating wave: circles correspond to measured dispersion, squares – dispersion computed by ISFEL3D code, dashed line – dispersion found with method of perturbation.

An axis-encircling electron beam was formed in a thermionic gun with a reversed magnetic field near the cathode (cusp) [18, 19, 17]. In the gun, an annular beam was produced from a relatively narrow emitting ring at the cathode, with the electrons acquiring azimuthal velocity when passing through a region where the guiding magnetic field changes direction. After this point the azimuthal particle velocity was further enhanced as the electrons propagated in a region of increasing magnetic field (Fig. 4). A magnetic field of up to 0.7 T at the interaction region was produced by a pulsed (3 ms) solenoid. A high-voltage power supply produced pulses of voltage up to 80 kV and current up to 20 A with a flat-top duration of up to 10 μs. The high-voltage and magnetic systems were capable of operation at a pulse repetition rate of 1 Hz.

Advanced designs of an input RF launcher and an output window allow operation at sufficiently high electron pitch-ratio and, correspondingly, with high amplifier efficiency without parasitic oscillations. The input coupler provides effective transformation (>70 %) of a fundamental mode of a rectangular Ka-band waveguide into $TE_{1,1}$ mode of a circular tube whose axis was perpendicular to the waveguide with relatively low (<10 %) reflection within frequency band from 32.5 to 37 GHz.

48
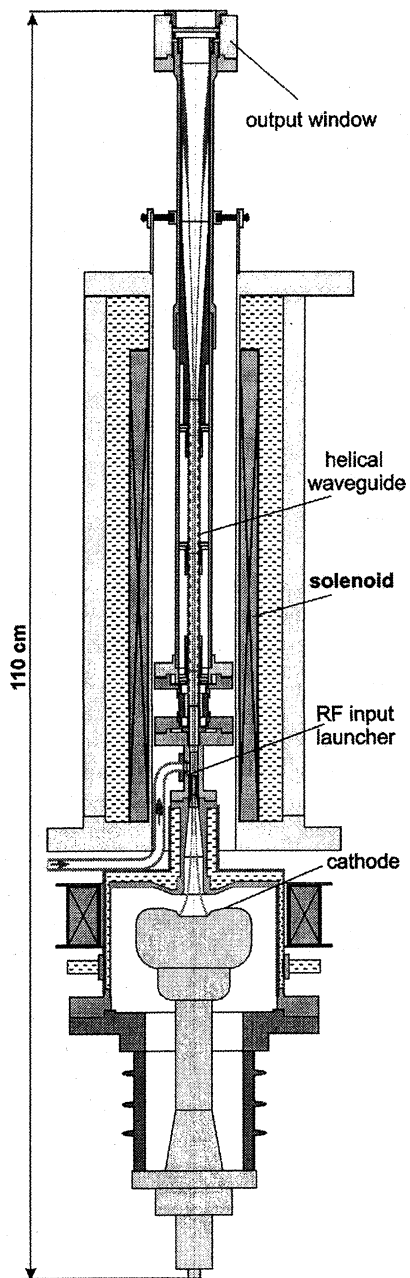
Fig. 4. Gyro-TWT experimental setup

49

The output window was in the form of a 3.5-mm thick and 40 mm in diameter quartz disc with two thin "antireflection" discs separated by vacuum/air gap from the thick inner disc. This window provided power reflection coefficient of less than 10^{-3} within a frequency range from 32 to 37 GHz (Fig. 5) that was about one order of magnitude wider than that for a single "one-wavelength" quartz disc [16].
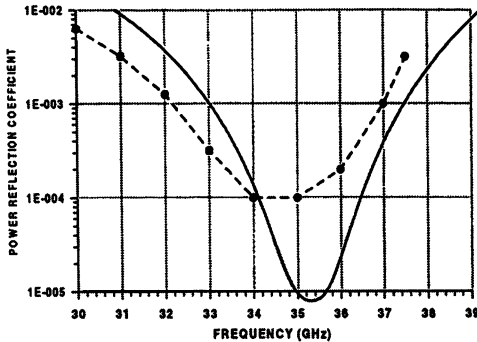

Fig. 5. Reflection of the output window: simulation (solid line) and measurement (dots and dashed line) results.

A driving microwave pulse of duration up to 3 μs was produced by one of two magnetrons with mechanical tuning of the radiation frequency within a 33.4–35.6 GHz frequency band at a power of 7–9 kW and 35.1–36.8 GHz at power of 11–14 kW respectively. This pulse was usually shorter than the electron beam pulse, which allowed clear identification of the regimes of self-oscillations, zero-drive stability and amplification of the gyro-TWT (Fig. 6). The parasitic oscillations arise at the leading and falling edge of the voltage pulse because the electron pitch-factor was higher at a lower voltage when a cusp gun was used for beam formation. Some special experiments and measurements have shown that the oscillations are caused by parasitic reflections from parts of the microwave system and their frequency lies within an amplification band of the gyro-TWT. At slightly higher electron pitch-factor these oscillations occur at the top of the voltage pulse also. In this case they are suppressed in the presence of a driving RF signal with a power of a few tens of watts and practically do not influence the gyro-TWT operation. The best results were obtained with no

Fig. 6. Oscilloscope traces of voltage, beam current and microwave signal.

50

additional microwave absorbers inside the operating waveguide. The output power was measured using a precise attenuator and a microwave detector. The detecting system was calibrated using known input power. Accuracy of the microwave power measurements was within 20 %. Reproducibility of the microwave pulses from shot to shot was usually within 5 %.

The maximum electron efficiency was measured to be 27–28 % for beam voltages from 50 to 80 kV and beam current in the range of 4–8 A (Fig. 7). The saturated gain of 23–25 dB was measured at an input power of about 0.5 kW. The linear gain of 30–35 dB was obtained when the input power was less than 0.1–0.3 kW (Fig. 8). The maximum output power amounted to 180 kW when the voltage was 80 kV and beam current was 8.5–9 A. The most broadband operation of the gyro-TWT was demonstrated at a beam voltage of 80 kV, which agreed well with the theoretical predictions (Fig. 9). As was clear from the measurements, the maximum −3 dB bandwidth of the gyro-TWT exceeds 3.2 GHz, or 9 % (upper fre-

Fig. 7. Electron efficiency (filled circles) and output power (unfilled circles) as functions of beam current at voltage of 70 kV, magnetic field of 0.67 T and driving frequency of 36.1 GHz.

quency boundary of the amplification lies beyond the frequency band-width provided by the RF driving sources which were available). The simulated bandwidth at an electron pitch-factor of 1.2 and perpendicular velocity spread of 30 % amounted to 14 %.
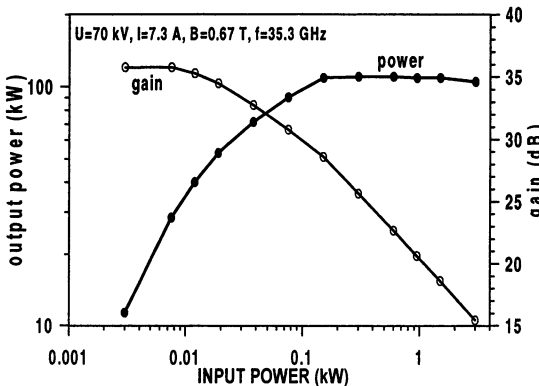

Fig. 8. Output power (filled circles) and gain (unfilled circles) as functions of input power.
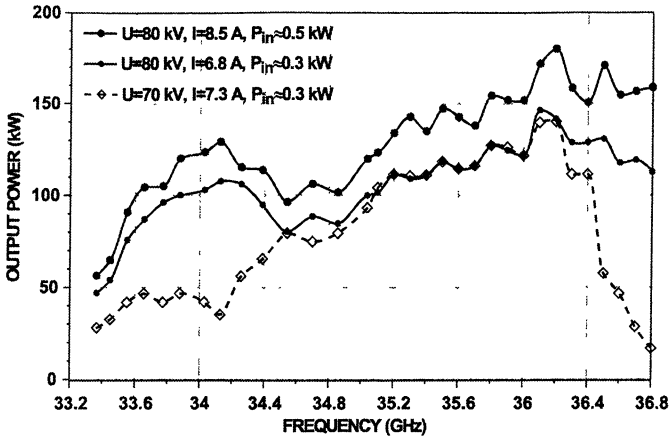
51

Fig. 9. Instantaneous gyro-TWT bandwidth at various parameters

In the near future it is planned to test helical waveguides with slightly different parameters of corrugation in order to experimentally optimize gyro-TWT operation. A project on a realization of a Ka-band helical-waveguide gyro-TWT with an average power of about 10 kW based on a permanent or superconducting magnet is also under consideration.

Frequency tunable gyro-BWO

Using the experimental setup discussed above (Fig. 4) the mode of operation can be switched from a gyro-TWT to a gyro-BWO regime by changing the direction of the magnetic field. In this case electrons excite the $TE_{2,1}$ mode having another direction of rotation, which is scattered by the same helical corrugation not into a forward propagating wave but into a backward traveling wave that provides internal feedback and BWO oscillations. The equivalent change in the wave dispersion (Fig. 1, *b*) shows a good opportunity for smooth frequency tuning by varying the cyclotron frequency. When using the gyro-TWT setup and switching to the gyro-BWO regime, the output power can be extracted from the rectangular waveguide port. Alternatively experiments using a cutoff reflector and extracting radiation from the output window were performed. The gyro-BWO worked very reliably and generated reproducible pulses of 10 μs duration over a very wide range of accelerating voltages and beam currents (Fig. 10) [20]. At the leading and falling edges of the voltage pulse a so-called fast frequency sweep was observed. For example, when the voltage increased from 20 kV to 42 kV (during about 1 μs) the radiation frequency dropped by 0.65 GHz. A much wider frequency tuning band can be achieved by variation of the magnetic field (Fig. 11).
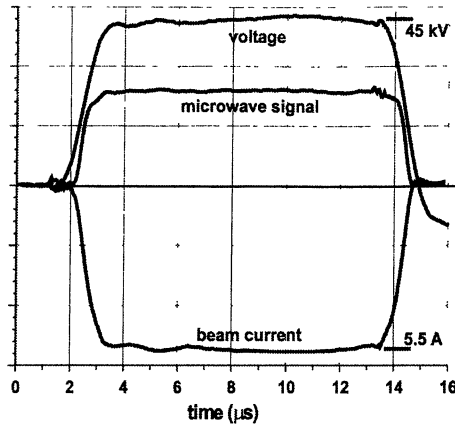
52

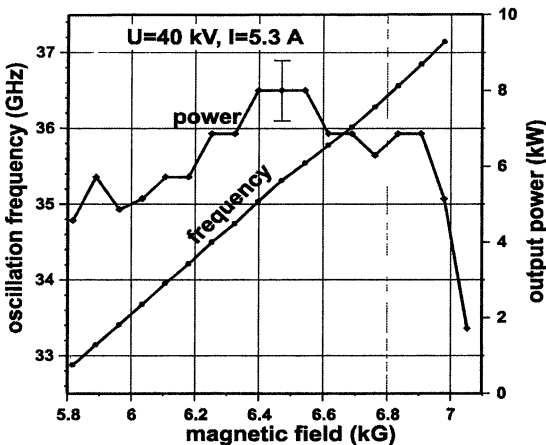**Fig. 10.** Oscilloscope traces for a gyro-BWO operation

Fig. 11. Output power and radiation frequency versus magnetic field for a gyro-BWO operation.

High power frequency tunable oscillators are attractive for some technological applications, for example, for material processing in an RF oven. For this application frequency tuning would allow the movement of standing wave maximums inside the oven and therefore provide more uniform microwave action on the samples. This was the motivation to start a project to realize a CW gyro-BWO with a power of several kilowatts at a frequency of 24 GHz with a tuning band of 5–10 % [20].

53

A specific feature of developing helical-waveguide gyro-BWO as compared to our previous experiments was the use of a low-voltage (20 kV) magnetron-injection gun typical for conventional gyrotrons. An electron beam produced by this gun is not an axis-encircling beam, but the electron guiding center radius is sufficiently small for selective BWO operation at the second cyclotron harmonic (Fig. 12, *a*). The helically rippled waveguides were made at the Forschungszen-trum Karlsruhe, Ger-many. The measured wave dispersion was in a good agreement with a theoretically predicted curve (Fig. 12, *b*). The simulations showed a possibility to achieve a maximum efficiency of 7–15 % for an electron pitch-factor of 1.2–1.7, respectively, for a frequency tuning band of up to 8 %. The computation also predicted the possibility of two times efficiency enhancement due to energy recovery by a single-stage depressed collector.
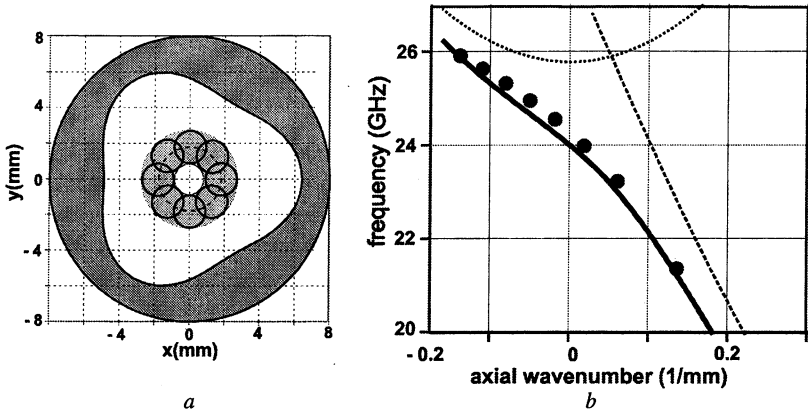

a   b

Fig. 12. Details of 20-kV CW gyro-BWO: *a* – waveguide and electron beam cross-sections; *b* – calculated (solid line) and measured (dots) dispersion of the operating mode.

Similar to previous experiments the helical waveguide had tapers at both ends where the amplitude of the corrugations linearly decreased to meet the mean diameter of the circular waveguide. At these tapers the operating eigenmode converted into a circularly polarized $TE_{1,1}$ mode and vice versa. In the experimental setup the generated $TE_{1,1}$ mode propagated toward the cathode, and was reflected by a so-called resonant reflector [21], and then traveled along the waveguide without resonant interaction with the electron beam before being radiated through a half-wavelength output window (Fig. 13).

The "hot" experiments have demonstrated selective operation of the gyro-BWO at the designed values of the magnetic field and beam voltage with smooth and sufficiently broad frequency tuning. The threshold current of the oscillations (above 1 A) was considerably higher than the expected value, which did not al-low the gyro-BWO operation in the CW regime because the collector could accept only 15 kW of average power. Using this setup all the results were obtained

in pulse-repetitive operation with a pulse width of about 50 µs and PRF of 20 Hz (Fig. 14). The maximum output power of about 7.5 kW and frequency tuning band of nearly 7 % were measured at quite a large beam current of 7.5 A.
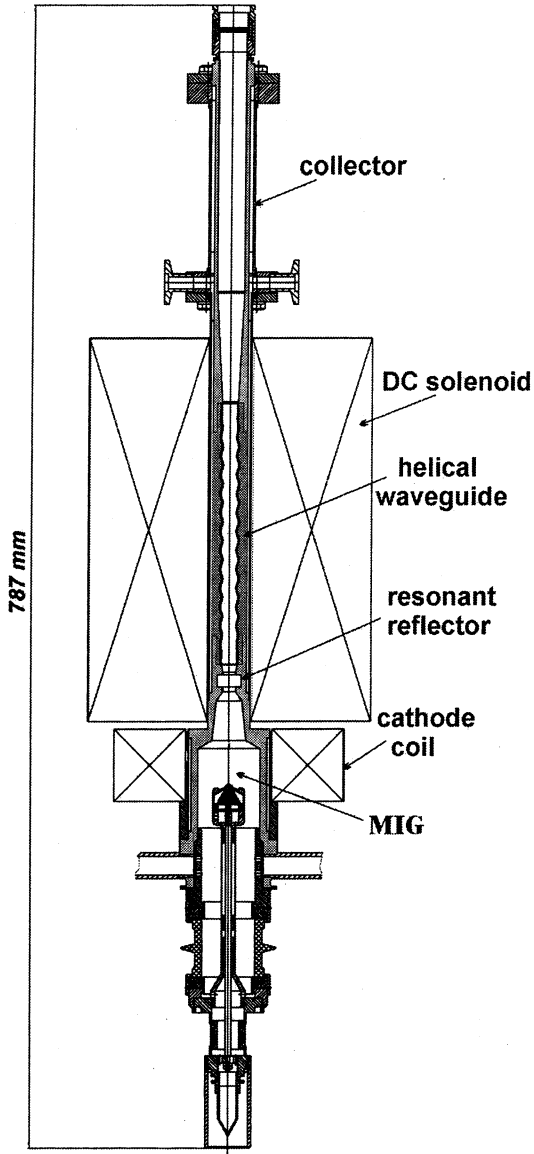

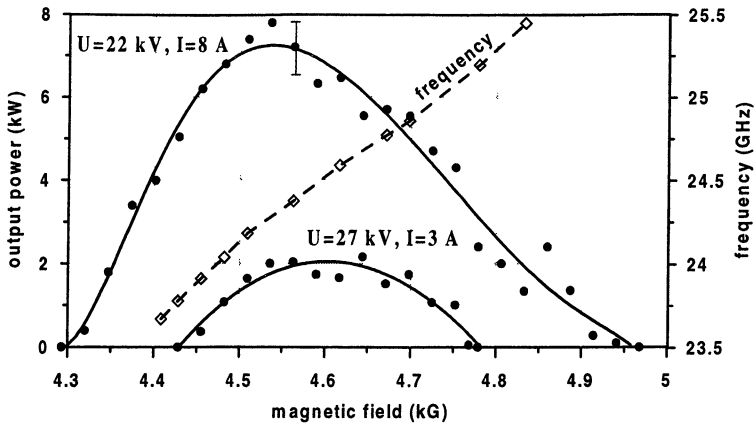**Fig. 13.** Setup of a CW gyro-BWO prototype

55

Fig. 14. Experimental results from a pulsed prototype of CW gyro-BWO

At the next stage of this project we plan to use a larger diameter DC sole-noid, which allows a collector diameter to be increased to be able to collect up to a 50–70 kW electron beam. The new solenoid will also have a 1.5 times longer uniform magnetic field region, into which a 1.5 longer helical waveguide will be immersed. This will considerably decrease the starting current of the gyro-BWO and enhance its efficiency in real CW operation. In addition, an insulator between the operating part of the microwave system and the collector has been designed, which will allow the measurements of the collector current and beam transport as well as the possibility of efficiency enhancement through the use of a single-stage beam energy recovery system.

Conclusions

Investigations performed demonstrate the attractive capabilities of the heli-cal-waveguide gyro-devices as broadband and powerful microwave sources. The components developed for the gyro-TWT permit its operation with a peak power of hundreds of kilowatts and average power of tens of kilowatts at an efficiency of 20–30 % over a frequency bandwidth of about 10–15 %. The second cyclotron harmonic interaction used reduced the magnetic field required by a factor of two and, therefore, the possibility exists of using permanent or DC water-cooled magnets for Ka-band devices. The experiments on a prototype of the CW gyro-BWO give a good basis for creation of a frequency tunable oscillator, which is attractive for technological applications.

References

1. *Gaponov A. V.,* Izv. Vyssh. Uchebn. Zaved. Radiofiz., **2**, 450 (1959).
2. *Pantell R. H.,* Proc. IRE, **47**, 1146 (1959).
3. *Gaponov A. V., Petelin M. I., Yulpatov V. K.,* Radiophys Quantum Electron., **10**, 794 (1967).
4. *Hirshfield J. L., Granatstein V. L.,* IEEE Trans. Microwave Theory Tech., **MTT-25**, 522 (1977).
5. *Chu K. R., Drobot A. T., Granatstein V. L. and Seftor J. L.,* IEEE Trans. Electron Devices, **MTT-27**, 178 (1979).
6. *Menninger W. L., Danly B. G., Temkin R. J.,* IEEE Trans. Plasma Sci., **24**, 687 (1996).
7. *Wang Q. S., McDermott D. B., Luhmann N. C.,* IEEE Trans. Plasma Sci., **24**, 700 (1996).
8. *Chu K. R., Chen H. Y., Hung C. L., Chang T. H., Barnett L. R., Chen S. H. and Yang T. T.,* Phys. Rev. Lett., **81**, 4760 (1998).
9. *Park S. Y., Kyser R. H., Armstrong C. M., Parker R. K., Granatstein V. L.,* IEEE Trans. Plasma Sci., **18**, 3 (1990).
10. *Pershing D. E., Nguyen K. T., Calame J. P., Danly B. G., Levush B.,* Digest 27th Int. Conf. IR and MM Waves. R. J. Temkin, Ed. (San Diego, USA, 2002), 199–200.
11. *Denisov G. G. and Cooke S. J.,* Digest 21st Int. Conf. IR&MM Waves (Berlin, Germany, 1996), AT2.
12. *Denisov G. G., Bratman V. L., Phelps A. D. R. and Samsonov S. V.,* IEEE Trans on Plasma Science, **26**, 508 (1998).
13. *Denisov G. G., Bratman V. L., Cross A. W., He W., Phelps A. D. R., Ronald K., Samsonov S. V. and Whyte C. G.,* Phys. Rev. Lett., **81**, 5680 (1998).
14. *Bratman V. L., Cross A. W., Denisov G. G., He W., Phelps A. D. R., Ronald K., Samsonov S. V., Whyte C. G. and Young A. R.,* Phys. Rev. Lett., **84**, 2746 (2000).
15. *Bratman V. L., Cross A. W, Denisov G. G., Kalynov Yu. K., He W., Phelps A. D. R., Ronald K., Samsonov S. V., Savilov A. V., Whyte C. G. and Young A. R.,* Proc. IV Int. Workshop "Strong Microwaves in Plasmas" (Nizhny Novgorod, Russia, 1999), 683.
16. *Bratman V. L., Denisov G. G., Manuilov V. N., Samsonov S. V., Volkov A. B.,* Digest 26th Int. Conf. IR and MM Waves (Toulouse, France, 2001, to be published).
17. *Bratman V. L., Denisov G. G., Manuilov V. N., Kalynova G. I., Ofitserov M. M., Samsonov S. V., Volkov A. B.,* Proc. 3rd Int. Conf. on Microwave and MMW Technology (Beijing, China, 2002), 90–93.
18. *Rhee M. J., Destler W. W.,* Phys. Fluids, **17**, 1574 (1974).
19. *Gallagher D., Barsanti M., Scafuri F. and Armstrong C.,* Digest 24th Int.Conf. IR and MM Waves (Monterey, USA, 1999), W-D1.
20. *Bratman V. L., Denisov G. G., Manuilov V. N., Kalynova G. I., Ofitserov M. M., Samsonov S. V., Volkov A. B.,* Digest 27th Int. Conf. IR and MM Waves. R. J. Temkin, Ed. (San Diego, USA, 2002), 197–198.
21. *Denisov G. G., Lukovnikov D. A., Samsonov S. V.,* Int. J. of Infrared and Millimeter Waves, **16**, 745 (1995).

REVIEW OF A HIGH-POWER COAXIAL FEM EXPERIMENT BASED ON TWO-DIMENSIONAL DISTRIBUTED FEEDBACK

A. D. R. Phelps[1], A. W. Cross[1], N. S. Ginzburg[2], W. He[1], I. V. Konoplev[1], N. Y. Peskov[2], K. Ronald[1], A. S. Sergeev[2], D. C. Speirs[1] and C. G. Whyte[1]

[1]Department of Physics, University of Strathclyde, Glasgow, G4 0NG, UK
[2]Institute of Applied Physics, Russian Academy of Sciences, Nizhny Novgorod, 603950, Russia

A FEM using two-dimensional (2D) distributed feedback driven by an annular, oversized electron beam is under investigation at the University of Strathclyde, in collaboration with IAP RAS (Nizhny Novgorod) [1]. It aims to demonstrate operation of a coaxial Free Electron Maser (FEM) based on two-dimensional distributed feedback and to generate sub-GW power microwave radiation at a frequency of ~37.5 GHz [2]. Recent progress achieved in the high power coaxial FEM experiment includes the development of a high-current accelerator, electron beam measurements which show successful beam production and transportation through the magnetic field system, calibration of the electron-optical system and study of two-dimensional Bragg structures of coaxial geometry with a variety of different patterns [3].

Introduction

The study of the influence of two-dimensional (2D) distributed feedback on the operation of a FEM driven by an oversized annular electron beam began in 1997 [1] in collaboration with IAP RAS. The use of such a feedback has been proposed as a method to produce spatially coherent radiation of a gigawatt power level from a large size relativistic electron beam of either annular or sheet geometry [2]. The 2D-feedback mechanism can be realised in a structure in which two-dimensional Bragg scattering takes place. In particular such scattering can be obtained on a 2D periodic shallow corrugation. The structures that have such a corrugation are considered for use in high power FEM experiments and are currently under investigation [3, 4]. To drive the FEM with an oversized annular electron beam a new high current accelerator and surrounding facilities have been designed and constructed.

We report on the results of the study of 2D Bragg structures and preliminary investigation of the high-current accelerator. In the Section II an overview of the design of the accelerator and surrounding facilities and results of the first experiments on beam transportation are presented. In the Section III the magnetic system for the FEM experiment, which consists of guide solenoid and undulator is discussed. The results of measurements of the undulator and solenoid field are presented. A brief model description and results of experimental study of the 2D Bragg structures are described in Section IV. In this section the experimental set

up used to study the 2D Bragg structures will also be presented. Good agreement between experimental data and theoretical predictions was demonstrated. In Section V an outline of some future experiments based on the new high current accelerator are presented.

The high-current electron accelerator

For high power microwave devices operating in the range from submillimetre to centimetre wavelengths it is usual to use a mildly relativistic high current electron beam. A high current accelerator (HCA) built at the University of Strathclyde can produce an electron beam of energy of up to 750 keV and current of up to 1.5 kA. It is aimed to study different microwave sources operating from centimetre to millimetre wavelengths. In Fig. 1 a schematic diagram shows the 1.5 MV Marx pulsed power (MPP) supply (I), which is connected via a transmission line (II) to the plasma flare emission electron gun (III). The power supply allows the intermediate electrode of the transmission line to be charged up to 1 MV and generates an output pulse of duration 300 ns. The transmission line is a coaxial line, filled with high purity deionised water (15 MΩ/cm) and has an impedance of 4.7 Ω and a total capacitance of 25 nF. The length of the line is 2 m and has an outer diameter of 1 m with the ratio between the diameters of the inner and outer conductors equal to 2. Taking into account that the diode has impedance of 200 Ω copper-sulphate matching resistors are used to match the two impedances. The transmission line is switched into the load using a high-pressure (10 bar) nitrogen-filled spark-gap. At the input of the load a rectangular voltage pulse with a flat top of length of up to 300 ns is formed. The voltage traces which were measured at the load end and transmission line inputs are presented in Fig. 2. The load, which is connected to the transmission line system, is a vacuum diode, which uses a plasma flare emission graphite cathode. The HCA is able to produce either an annular electron beam of diameter 7 cm. The design, i.e. optimization of the anode and the cathode geometry of the HCA, was undertaken
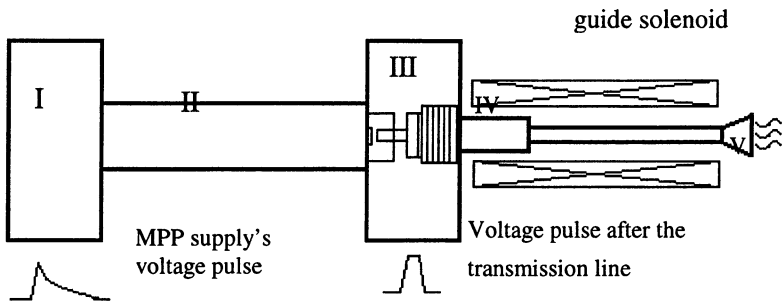

Fig. 1. Schematic diagram of the experimental set up which consists of: I – marx pulsed power supply; II – coaxial transmission line; III – high pressure spark gap; IV – high current accelerator; V – guide solenoid and drift tube.
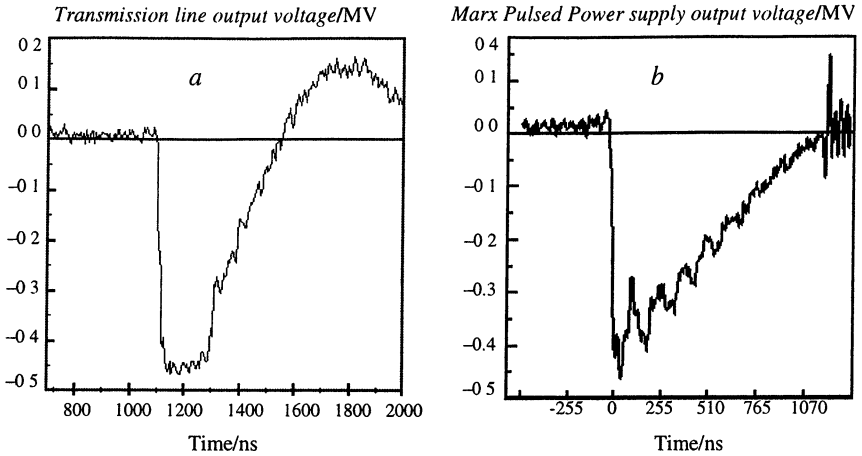
59

Fig. 2. Traces of output voltage from: *a* – transmission line; *b* – Marx pulsed power supply.

using the numerical particle-in-cell code KARAT. Simulations demonstrated that transverse velocity spread when a plasma flare emission cathode is used does not exceed 7 %. The total energy storage in the electron beam pulse in the experiments is between 80 to 140 J depending upon the applied anode cathode accelerating voltage.

Guide field solenoid and undulator

To obtain an electron beam and to propagate it through the interaction space of the microwave source with minimum losses the HCA was immersed in a uniform magnetic field (Fig. 1). The guide magnetic field was produced by a single layer guide solenoid of 0.33 m diameter and 2.5 m of length. To obtain the required amplitude of the magnetic field (up to 0.8 T) the solenoid pulsed power system, consisting of 10×250 µF capacitors giving a capacitance of total 2.5 mF was used. The capacitors were charged and discharged in parallel at a voltage up to 18 kV to provide a current through the solenoid of up to 3 kA. A schematic diagram of the power supply connection for the guide solenoid is presented in Fig. 3, *a*. The capacitors are connected to the solenoid via matching resistors to slightly over damp the RLC circuit. The current limiting charging resistors and high voltage diode ensures the absence of current back into the DC power supply during the capacitors discharge. The time dependence of the guide magnetic field when the capacitors had been charged to 12 kV is presented in Fig. 3, *b*. The flat top of the magnetic field pulse is expected to be longer than 1 ms which significantly exceeds the electron beam current pulse duration.
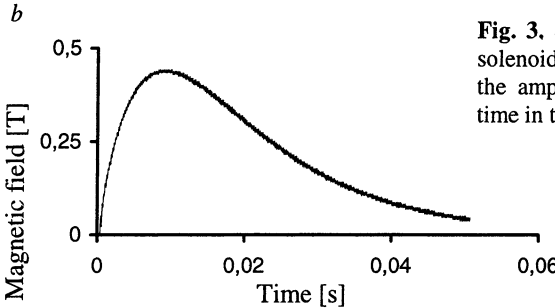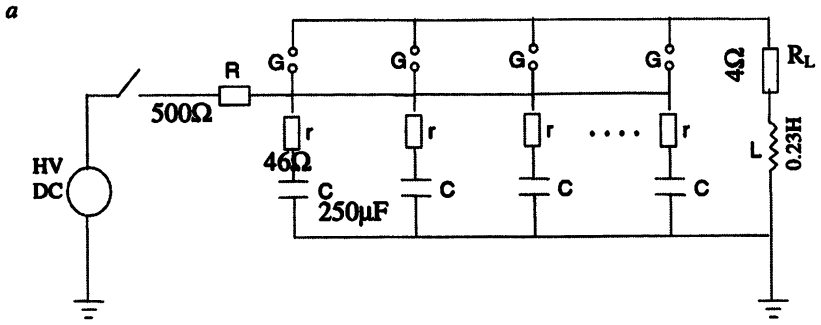
60

a

b

Fig. 3. Schematic diagram of the guide solenoid pulsed power supply (*a*) and the amplitude of magnetic field versus time in the centre of the solenoid (*b*).

To conduct the FEM experiment when the interaction space is in the form of an oversized (in comparison with operating wavelength) coaxial waveguide with diameters of the outer and inner conductors of 8 and 6 cm respectively an azimuthally symmetric undulator was designed and constructed. The period and length of the undulator are 4 cm and 120 cm respectively. The undulator has a five period input section, which should ensure a gradual increase in the amplitude of the undulator field. An undulator field amplitude of between 0.05 T and 0.06 T is required in order to obtain an efficient interaction between the electron beam and the electro-magnetic wave when a guide magnetic field of 0.6 T is used. To obtain an undulator field amplitude of 0.06 T a driving current of up to 1.7 kA was generated using a 4×300 μF, 4 kV capacitor bank. Study of the undulator field was conducted using a pick-up probe. The probe sensitivity was estimated to be 53.1 mT/V. The result of the measurement of the undulator's radial component of magnetic field is presented in Fig. 4, *a*. The presence of the azimuthal component of the field, which is due to imperfections of the undulator, was observed. However the amplitude of the azimuthal (parasitic) component of the field does not exceed 10 % of the amplitude of the operating field, Fig. 4, *b*.
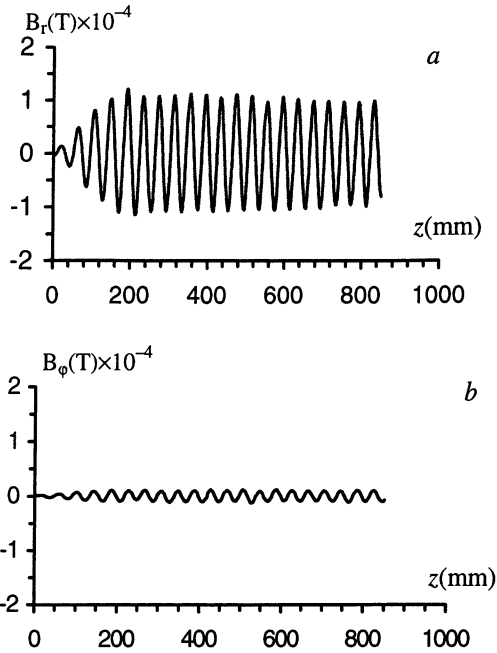
61

Fig. 4. Results of measurements of the azimuthal-symmetric undulator magnetic field components: *a* – radial and *b* – azimuthal.

Experimental study of 2D coaxial Bragg structures

Two-dimensional (2D) coaxial Bragg structures can be obtained by providing a shallow corrugation of the inner surface of a waveguide wall. The 2D feedback can be realised in such structures due to 2D Bragg scattering on the corrugated surface and can be used to synchronise radiation from different parts of the electron beam due to the presence of the transverse (azimuthal) electromagnetic energy fluxes, which arise on the 2D corrugation [2–5]. The forward and backward waves should ensure the completion of the feedback loop. The 2D Bragg structures are compatible with high-current electron beam transportation and can be used as a selective cavity or mirror for an FEM-oscillator. In particular, the structures studied below will be used to investigate operation of an FEM based on a coaxial 2D Bragg cavity when driven by an oversized annular electron beam of diameter ten times greater than the radiation wavelength (λ). Computer simulations predict that single-frequency, single-mode operation in an FEM using 2D distributed structure is possible even when driven by an electron beam with transverse size up to 103 wavelengths [6–7].

An "ideal" sinusoidal coaxial 2D Bragg structure consists of two conductors of radii $r_{in,out}$, and length l_z with a sinusoidal doubleperiodical corrugation.

62

The RF-field inside the 2D Bragg structure can be presented as a superposition of four partial waves which propagate in the $\pm z$ and $\pm \varphi$ directions:

$$\vec{E} = Re\left\{\left[\vec{E}_a\left(A_+ e^{-ihz} + A_- e^{ihz}\right) + \vec{E}_b\left(B_+ e^{-im\varphi} + B_- e^{im\varphi}\right)\right]e^{i\omega t}\right\}, \qquad (1)$$

where h and m are the longitudinal wavenumbers and azimuthal indexes of the partial waves respectively, $\vec{E}_j$ describes the wave amplitude as a function of radius and coincides with the structures of the modes of a coaxial waveguide and $A_\pm(\varphi, z)$, $B_\pm(\varphi, z)$ are slow functions of the φ and z coordinates. Effective partial wave scattering (coupling) takes place if the following resonance conditions are satisfied:

$$h \approx \overline{h}, \quad m \approx \overline{m}, \qquad (2)$$

where $\overline{h} = 2\pi/d_z$, d_z is the period of the structures over the z-coordinate and $\overline{m}$ is the number of corrugation variations over the azimuthal coordinate. The 2D Bragg structure suggested can be used in an FEM either as a single section cavity or a two-mirror (Fabry – Perot) cavity when the two corrugated structures are separated by a regular section of waveguide. The 2D Bragg corrugation may be produced in different ways. In previous work such 2D Bragg corrugations were obtained by machining $\overline{m}$ fold grooves of the regular section in both clockwise and counter clockwise direction [3]. However such a corrugation provides both 1D and 2D Bragg scattering and the presence of the 1D Bragg scattering may significantly affect the FEM performance. As a result the 2D Bragg structure with a "chessboard" corrugation has been suggested [8–10]. The corrugation machined on the outer surface of the inner conductor of a coaxial waveguide is shown in Fig. 5. Such a corrugation surface can be considered as a multiplication of two periodic functions:

$$a(\varphi, z) = a_1 g(\overline{m}\varphi)g(\overline{h}z), \qquad (3)$$

$$g(\xi) = \begin{cases} -1 & 0 < \xi < d_\xi/2 \\ 1 & d_\xi/2 < \xi < d_\xi \end{cases}, \qquad g(\xi + d_\xi) = g(\xi)$$

and can be described by a Fourier expansion. Taking into account that the amplitude of the fundamental term of the Fourier expansion is much larger than higher order terms this allows the corrugation to be approximated by the following expression:

$$a(\varphi, z) \approx \frac{8a_1}{\pi^2}\left[\cos(\overline{m}\varphi - \overline{h}z) + \cos(\overline{m}\varphi + \overline{h}z)\right], \qquad (4)$$

where a_1 is the corrugation depth. The expression (4) corresponds to a sinusoidal 2D Bragg structure and should provide 2D coupling of four partial waves (i. e. $A_+ \leftrightarrow B_\pm \leftrightarrow A_-$) without a direct 1D scattering.
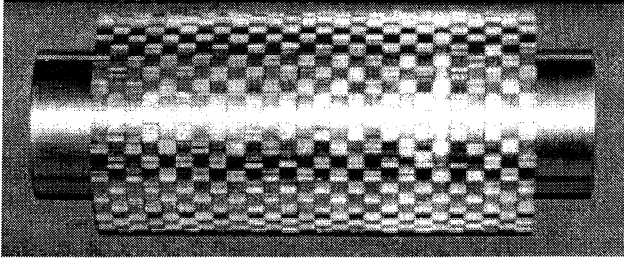
Fig. 5. Photograph of the corrugated inner conductor of the coaxial 2D Bragg structure.

Scattering of the partial waves on the corrugations of depth such that $\bar{h}a_1 \ll 1$ in the approximation that the curvature of the conductors are small can be described by the following coupled wave equations for the amplitudes of the partial waves:

$$\pm \frac{\partial A_\pm}{\partial z} + i\delta A_\pm + i\alpha(B_+ + B_-) = 0, \tag{5a}$$

$$\pm \frac{\partial B_\pm}{\partial x} + i\delta B_\pm + i\alpha(A_- + A_+) = 0, \tag{5b}$$

where $x = \varphi r_0$, r_0 is the mean radius of the coaxial waveguide, α is the wave coupling coefficient on the 2D Bragg structure, which is proportional to the corrugation depth a_1, and δ is the detuning from the Bragg resonance condition. Due to the coaxial geometry of the structure it is possible to use Fourier expansion to present the partial waves amplitudes in the following form

$$A_\pm(x,z) = \sum_{m=-\infty}^{\infty} A_\pm^m(z)e^{imsx}, \qquad B_\pm(x,z) = \sum_{m=-\infty}^{\infty} B_\pm^m(z)e^{imsx}. \tag{6}$$

Using boundary conditions: $A_+^m(z=0) = A_0^m$, $A_-^m(z=l_z) = 0$ from Eqs. (5) the transmission coefficients can be found:

$$T_m = \frac{-i\lambda_m}{\sin(\lambda_m l_z)(p_m - i\lambda_m \cot(\lambda_m l_z))}, \tag{7}$$

where

$$\lambda_m = \delta\left[4\alpha^2 \big/ \left(s^2m^2 - \delta^2\right) + 1\right]^{1/2}, \qquad p_m = i\delta\left(2\alpha^2 \big/ \left(s^2m^2 - \delta^2\right) + 1\right)$$

and $s = 1/\bar{a}$. Taking into account the distributed RF power losses σ the expression for the reflection coefficient when $m = 0$ which corresponds to the incident TEM can be presented as:

$$R_0 = \frac{-2\hat{\alpha}^2}{2\hat{\alpha}^2 - \hat{\delta}^2 - i\left(\hat{\delta}(4\hat{\alpha}^2 - \hat{\delta}^2)^{1/2}\right)cth\left(\hat{l}_z(4\hat{\alpha}^2 - \hat{\delta}^2)^{1/2}\right)},$$ (8)

where new normalised parameters were introduced $\hat{\delta} = (\delta_0/\sigma) - i$, δ_0 is the real value of detuning from the resonance condition, $\hat{\alpha} = \alpha/\sigma$, $\hat{l}_z = l_z\sigma$ is the length of the structure and σ is the distributed RF power losses. It is important to note that the distributed RF power losses are always present and their consideration is rather important as it was shown in the previous work. If the distributed losses are small in comparison with the value of the coupling coefficient then the maximum of the reflection index $(|R_0| \cong 1 - (\sigma/\alpha)^2)$ is achieved at the exact Bragg frequency $\delta_0 = 0$ and the width of the reflection zone is ~4α. However when $\alpha/\sigma \ll 1$ the reflection coefficient R_0 at the exact Bragg resonance is $0(\alpha^2/\sigma^2)$ and the reflection zone is difficult to distinguish from the background noise, via measurement of the reflection/transmission coefficients. It is important to note that this effect also exists for an incident on the structure wave with an arbitrary azimuthal index $m \neq 0$ [10].

To study the reflection and transmission coefficients several structures of lengths 4 cm and 10 cm with the inner and outer radii r_{in} = 2.95 cm, r_{out} = 3.9 cm respectively were investigated. The parameters of the corrugations manufactured on the outer surface of the inner conductor were a_1 = 0.08 cm, $\bar{m}$ = 24 and d_z = 0.8 cm for the structure of length 10 cm and d_z = 0.801 cm for the structure of length 4 cm which corresponds to a Bragg frequency of 37.5 GHz and 37.3 GHz respectively. To excite the Bragg structures with a TEM-mode of a co-axial waveguide a special transmission line which included two mode converters was constructed to provide the required mode transformation in the operating frequency band from a launched $TE_{1,1}$ wave of a single-mode circular waveguide. The first converter transformed the $TE_{1,1}$ wave into a $TM_{0,1}$ wave of circular waveguide and the second converter transformed the $TM_{0,1}$ wave into a TEM wave of a co-axial waveguide. An additional coaxial slowly up-tapered waveguide horn of length ~ 60 cm and an opening angle of 3° was used to connect the last converter with the oversized coaxial structure.

The microwave parameters of the structures were measured using a scalar network analyzer in the frequency range 25–40 GHz. In accordance with calculations the single effective zone of the Bragg scattering was observed in the designed frequency region with a maximum of the scattering at the exact Bragg frequency of 37.3 GHz. This zone is associated with the 2D Bragg scattering with participation of the four partial waves: forward and backward waves of TEM-type and two counter-propagating near cut-off waves of $TE_{24,0}$-type. Results of the measurements of the transmission coefficients from the 2D Bragg structures of different lengths are presented in Fig. 6, a, b. It is clearly seen from Fig. 6, a and Fig. 6, b that the length of the structure impacts on the effective

width of the reflection zone while approximately the same minimal value of the transmission ($T \approx -20$ dB) at the Bragg frequency was maintained. The experimental results corresponded well to predictions given by Eqs. (7), (8) which are plotted in Fig. 6 by a bold line. In the following experiments the influence of RF power losses on the wave transmission through the 2D Bragg structure has been studied. The variation of the distributed RF power losses y was obtained by putting a different number of layers of absorbing material (absorbing paint) on the surface of the outer conductor. The maximum thickness of the absorbing material was less than 1 mm and much less than the distance between the outer and inner conductors of the coaxial waveguide. To calibrate the RF power losses a smooth brass inner conductor of radius $a = 3$ cm was used. In this case the power losses inside which are due to the skin effect were estimated to be around $6 \cdot 10^{-4}$ cm. The attenuation of the wave passing through the part of the coaxial waveguide, when medium and high power losses were introduced, was compared with the power transmitted through the coaxial waveguide when no absorbing material was present. It was found that in the frequency region of the expected band gap (37–38 GHz) the attenuation was approximately 2.5 dB (≈ 0.6 dB/cm or $\sigma \approx 0.07$ cm^{-1}) for the medium loss absorbing coating and approximately 5 dB (≈ 1.25 dB/cm or $\sigma \approx 0.14$ cm^{-1}) for a high loss absorbing coating.
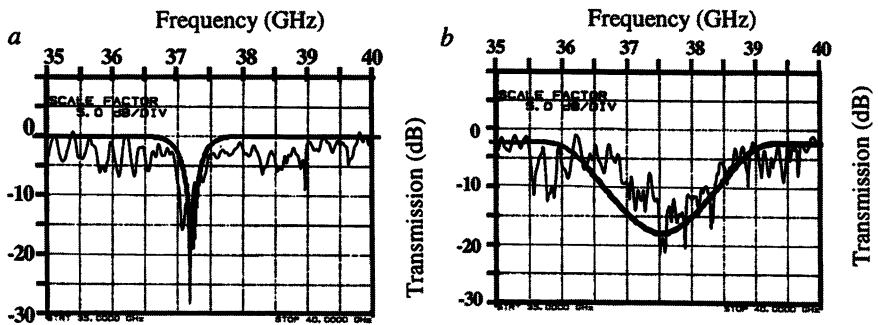

Fig. 6. Experimental data (thin line) and theoretical predictions (bold line) of RF power transmission through 2D Bragg structure with "chessboard" pattern of length (*a*) 4.8 cm and (*b*) 10 cm.

The results of the computer simulations of the power transmitted through the structures with the wave-coupling coefficient $\alpha \approx 0.12$ cm^{-1} and different values of distributed losses are presented in Fig. 7. When low absorption material was used ($\alpha/\sigma \ll 1$) a forbidden band gap is clearly evident. When medium loss absorbing material was used $\alpha/\sigma \geq 1$ the shape and amplitude of the transmission band was significantly changed (middle line, Fig. 7). However, if the power losses are further increased $\alpha/\sigma \leq 1$ this resulted in a "disappearance" of the transmission forbidden gap (Fig. 7, bottom line). In Fig. 8 comparison of the ex-

perimental results obtained for different values of ohmic losses was demonstrated. The transmission forbidden gap is clearly visible when ohmic losses are low and are less visible when medium level losses are introduced Fig. 8 with the system becoming "transparent" when high level ohmic losses were introduced Fig. 8, *b*. It is important to note that in the frequency regions far from resonance the features of transmission are reproducible as the experiment is changed.
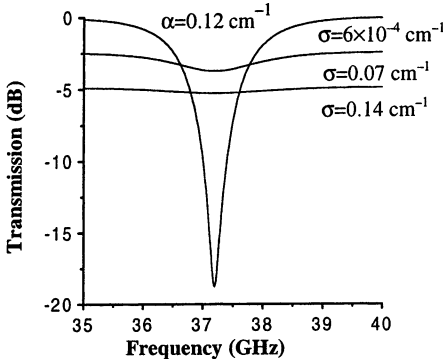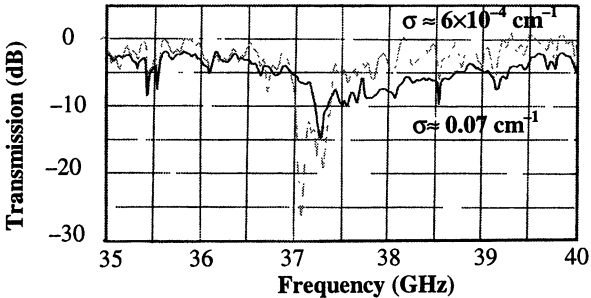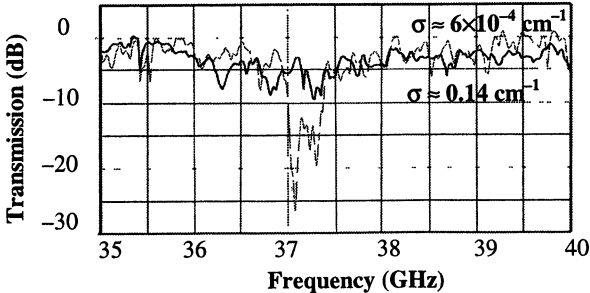

Fig. 7. Theoretical prediction of RF power transmission through the 2D Bragg structure when high, medium and low distributed power losses σ are introduced.

a

b

Fig. 8. Results of the experimental measurements of RF power transmission through the 2D Bragg structure of length 6 cm with "natural" ohmic losses (thin line) and when (*a*) medium and (*b*) high ohmic losses are introduced (bold) line.

For direct demonstration that four partial waves (including transversely propagating partial waves $B_\pm$) are involved in the scattering process, the transverse electromagnetic energy fluxes were also measured (Fig. 9) using a slit in the outer conductor wall. This slit allowed a standard WG-22 waveguide to be attached to the cavity without severely disturbing the field structure. In accordance with simulations (bold line) in the Bragg frequency band the transverse energy fluxes were measured (Fig. 9) when the waveguide probe was positioned tangentially to the waveguide.
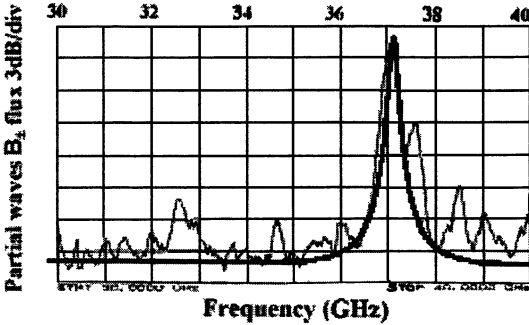
Fig. 9. Result of measurements of transverse fluxes inside the 2D Bragg structure of length 4.8 cm.

Conclusions

Taking into account the experimental data obtained from the high current accelerator let us estimate the parameters of the future FEM experiments. The experiments are aimed to demonstrate the operation of the novel 2D feedback mechanism in a FEM driven by an annular oversized electron beam where $D_{beam} / \lambda \sim 10$ (D_{beam} is the beam diameter and λ is the operating wavelength). The experiments will employ the HCA set up with the plasma flare emission cathode which will generate an annular electron beam of diameter 7 cm and a thickness of 0.2 cm with energy of up to 0.6 MeV, with the current of ~ 1.0 kA and pulse duration of 250 ns. An azimuthally symmetric wiggler of length 120 cm and period of 4 cm will produce a transverse magnetic field component of up to 0.06 T, to pump the transverse velocity of the electrons to $\beta_\perp \approx 0.2$–0.3. Transportation of the electron beam is achieved using an axial guide magnetic field of amplitude up to 0.6 T produced by a pulsed solenoid. For the beam parameters presented and taking into account the operating wavelength of ~ 8 mm the gain parameter $C \sim 7 \cdot 10^{-3}$ is calculated. Computer simulations show that in a 2D Bragg cavity (twomirror or single section) of length of 100 cm spatially-coherent singlemode oscillation with an efficiency of ~ 10–15 % can be realised (Fig. 10). The output power will amount to 70–100 MW and the transient times for both cavity schemes is expected to be less than 150 ns.
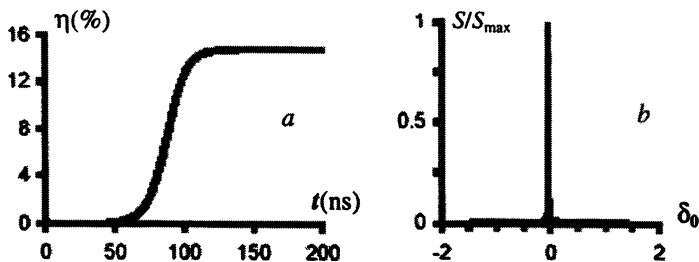
68

Fig. 10. Expected (*a*) time dependence of the efficiency and (*b*) spectrum of the output radiation of the high power FEM driven by an annular electron beam and using a 2D Bragg structure.

References

1. *Ginzburg N. S., Peskov N. Yu., Konoplev I. V., Sergeev A. S., Robb G. R. M., Phelps A. D. R., Cross A. W.,* IEEE 22nd International Conference on Infrared and Millimetre Waves (Wintergreen, Virginia, USA,1997).
2. *Ginzburg N. S., Peskov N. Yu., Sergeev A. S.,* Technical Physics Letters, **18**(9), 23 (1992).
3. *Konoplev Iv. V., Cross A. W., He W., Phelps A. D. R., Ronald K., Robb G. R. M., White C. G., Ginzburg N. S., Peskov N. Yu., Sergeev A. S.,* Nuclear Inst. And Meth. in Phys Res. A, **445**, 236 (2000).
4. *Cross A. W., Konoplev I. V., Ronald K., Phelps A. D. R., He W., Whyte C. G., Ginzburg N. S., Peskov N. Yu., Sergeev A. S.,* **80**, 1517 (2002).
5. *Ginzburg N. S., Peskov N. Yu., Sergeev A. S., Phelps A. D. R., Konoplev I. V., Robb G. R. M., Cross A. W., Arzhannikov A. V., Sinitsky S. L.,* Phys. Rev. E, **60**, 935 (1999).
6. *Ginzburg N. S., Konoplev I. V., Sergeev A. S.,* Technical Physics, **66**, 108 (1996).
7. *Ginzburg N. S., Peskov N. Yu., Sergeev A. S., Robb G. R. M., Phelps A. D. R.,* IEEE Transaction on Plasma Science, **24**, 770 (1996).
8. *Konoplev I. V., Cross A. W., Ginzburg N. S., He W., Peskov N. Yu., Phelps A. D. R., Robb G. R. M., Ronald K., Sergeev A. S., Whyte C. G.,* IEE Pulsed Power Symposium (London, UK, 2000).
9. *Agarin N. V., Arzhannikov A. V., Bobylev V. B., Ginzburg N. S., Ivanenko V. G., Kalinin P. V., Kyznetsov S. A., Peskov N. Yu., Sergeev A. S., Sinitsky S. L., Stepanov V. D.,* Nucl. Instr. and Methods in Phys. Research A, **445**, 222 (2000).
10. *Cross A. W., He W., Konoplev I. V., Phelps A. D. R., Ronald K., Robb G. R. M., Whyte C. G., Ginzburg N. S., Peskov N. Yu., Sergeev A. S.,* Nuclear Instr. and Methods in Phys. Res. A, **475**, 164 (2001).

GIGAWATT S-BAND FREQUENCY-TUNABLE SOURCES OF HIGH-POWER MICROWAVE PULSES

S. D. Korovin, I. K. Kurkan, I. V. Pegel, S. D. Polevin

Institute of High Current Electronics SD RAS, Tomsk, Russia

The paper describes S-band HPM sources recently developed at IHCE: the resonant BWO producing ~5 GW, 100 J pulses, based on the SINUS-7 electron accelerator, and a double-section vircator with peak power of ~1 GW and pulse width of 20 – 50 ns, fed from either SINUS-7 accelerator or MARINA inductive-store pulse driver with fuse opening switch.

The last five years have been marked with higher interest in the HPM community to microwave production in the decimeter wavelength range (L- and S-bands). At the Institute of High Current Electronics SD RAS, studies in this field were basically focused on two directions: the traveling-wave devices with strong guide magnetic field were represented by relativistic BWOs (studied earlier in the X-band) and the double-section vircator demonstrated successful operation with no external magnetic field.

Mastering the gigawatt level of microwave power requires employment of powerful pulse modulators providing stable electron beam parameters throughout the pulse. For this purpose, the SINUS-7 electron accelerator was used. This is a repetitively-pulsed machine (electron energy up to 2 MeV, beam current up to 20 kA, pulse width 50 ns, pulse repetition rate up to 100 pps) based on coaxial pulse forming line with built-in high-coupling Tesla transformer.

Another class of modulators also used to drive HPM sources is represented by the MARINA compact pulsed current generator with inductive energy store and fuse opening switch (beam current up to 25 kA in 50-Ω load, pulse width over 100 ns). This pulser was developed at the Pulsed Power Department (B. Kovalchuk, Head).

All the HPM sources were tested numerically before putting into real experiment. For this purpose, a series of time-dependent PIC-codes was used, including the fully electromagnetic 2.5&3D code KARAT.

Resonant relativistic BWO

The basic distinctive feature of the resonant BWO [1, 2] comparing with the conventional relativistic BWO [3] is the increased Q-factor of the electrodynamic system achieved by reflection of the TM_{01} operating wave from waveguide narrowing at the collector edge of the slow-wave structure. The resulting improvement in the longitudinal distribution of the RF field (both the (-1st) and the fundamental harmonics are important) allowed an increase in the microwave efficiency up to 30 %, which is twofold comparing to conventional BWOs. An im-

portant merit of the device is the reduced interaction length (~3 λ) allowing lower energy in the guide magnetic field (which makes 2–3 T).

Configuration of the resonant BWO is represented in Fig. 1. The electron beam is produced in a vacuum diode with edge-type cathode in strong magnetic field and is delivered to the tube via beyond cutoff-neck, which serves as a reflector for the backward wave. Slight narrowing of the slow-wave structure at its collector edge provides partial reflection of the wave and increased Q-factor of the tube. A piece of smooth cylindrical waveguide between the beyond cutoff-neck and the beginning of corrugation is used to adjust integer number of oscillations of the fundamental standing wave along the tube. The ratio between amplitudes of fundamental harmonic of the forward wave and (-1st) harmonic of the backward wave in the beam trajectory is determined by the corrugation depth of the SWS. The impedance of the diode was adjusted by varying the anode-cathode gap spacing. The guide magnetic field was produced by pulsed solenoid of rectangular cross section.
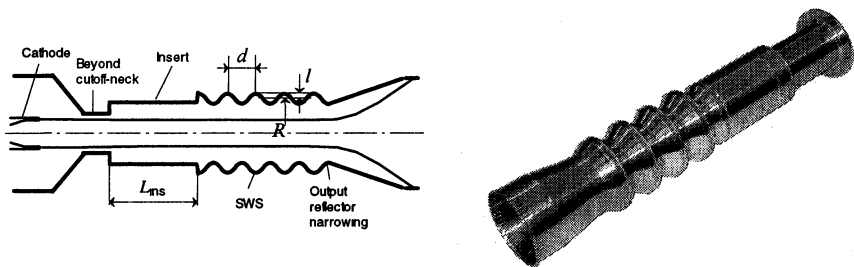

Fig. 1. Schematic and external view of the resonant BWO

Simulations using KARAT code [4] evidenced that, with optimum geometry of the electrodynamic system ($l \approx \lambda/8$, $R \approx \lambda/2$, $L_{sws} \approx 2.5\lambda$, $L_{ins} \approx \lambda$, $Q \sim 100$ (where L_{sws} and L_{ins} are lengths of the SWS and the insert, respectively and λ is the wavelength), the microwave power efficiency makes ~30 % changing only slightly through wide range of electron beam powers (from 5 up to 20 GW). The optimum vacuum diode impedance was about 100 Ω. The time for onset of microwave oscillation was ~20 ns (Fig. 2).

The experimental study of S-band resonant BWO was made using the SINUS-7 electron accelerator [5] (Fig. 3).

Optimization of fundamental-harmonic interaction was made by adjusting the length of the cylindrical insert (Fig. 4). Variation of the insert length resulted on variation of frequency within 3 %. Multifrequency generation with substantial drop of microwave power was observed with insert length of 60 mm. In the optimum regime, microwave generation at 3.6 GHz frequency with ~30% efficiency
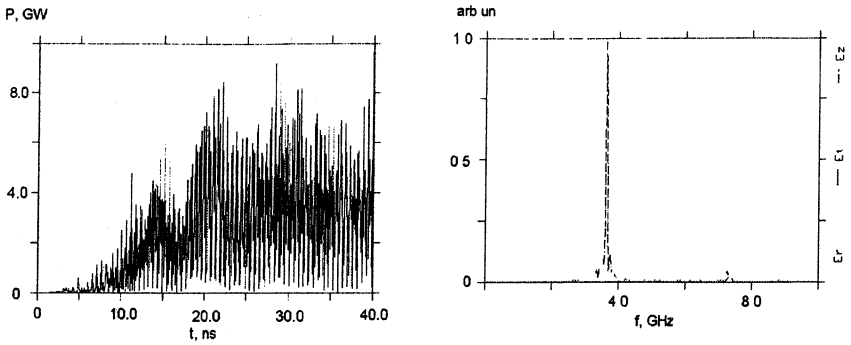
Fig. 2. Microwave power and spectrum of the resonant BWO (KARAT simulation): electron energy 1.2 MeV, beam current 12 kA, magnetic field strength 25 kOe.

was obtained. At 1.2 MeV electron energy and 15 kA beam current, the peak microwave power was 5.3 GW with 25 ns pulse width (at half power level). The typical waveforms of diode voltage, beam current, and microwave detector signal are depicted in Fig. 5. The microwave pulse energy was ~100 J as measured with a calorimeter. In experiment, like in the simulations, the microwave efficiency demonstrated minor changes in the range of electron beam power from 5 up to 19 GW (Fig. 6). The guide magnetic field strength was about 25 kOe. The pattern of radiation from horn antenna corresponded to the TM_{01} mode.
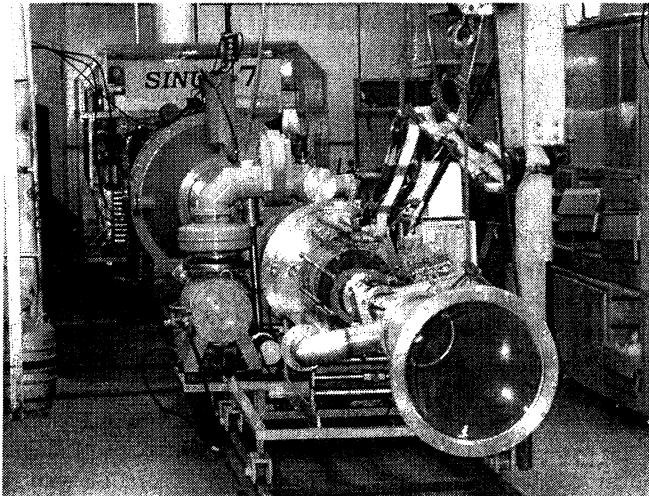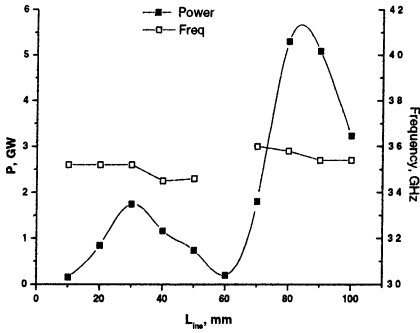

Fig. 3. SINUS-7 resonant BWO experiment

Fig. 4. Microwave peak power and frequency vs insert length, SWS corrugation period 45 mm, diode voltage 1.2 MV, beam current 15 kA, magnetic field strength 25 kOe.
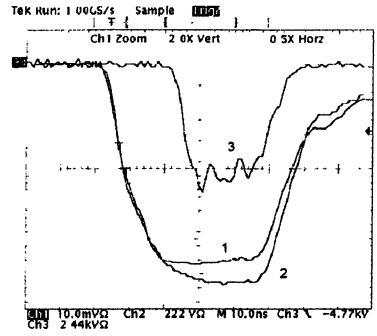
Fig 5. Waveforms of (*1*) diode voltage, (*2*) electron beam current, and (*3*) microwave detector signal, diode voltage 1.2 MV, beam current 15 kA, magnetic field strength 25 kOe.

The magnetic field dependence of the microwave power is depicted in Fig. 7. As found in simulation, the power drop below 15 kOe was caused by partial dumping of beam electrons onto SWS surface under the action of the intense RF field. The drop boundary moved to lower magnetic fields as the microwave power decreased.
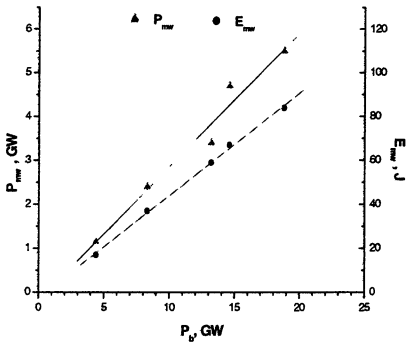

Fig. 6. Microwave pulse peak power and energy vs electron beam power (diode impedance ~ 80 Ω, magnetic field strength 25 kOe).
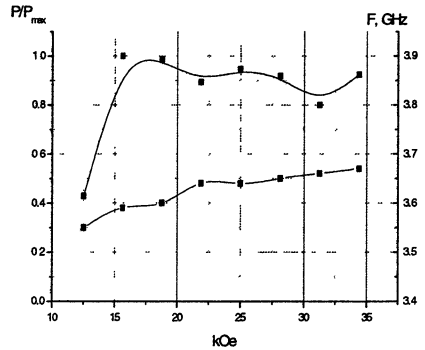
Fig. 7. Magnetic field dependence of output power and frequency (diode voltage 1.2 MV, beam current 15 kA).

73

The lower limit for the guide magnetic field may be also caused by cyclotron absorption of the backward electromagnetic wave by beam electrons:

$$H > H_r = \frac{mc^2}{e}\beta_e\gamma\bar{h},$$

where $\bar{h} = 2\pi/d$ and e, m and $c\beta_e$ are electron charge, mass and velocity. For the 3.6-GHz resonant BWO with 1.2 MeV electron energy, $H_r \approx 7$ kOe.

The operation frequency of the resonant BWO is variable by shifting the point of Cherenkov synchronism between the (-1st) spatial harmonics of the backward wave and electron beam by changing the SWS period (keeping the corrugation depth l and the electron beam parameters constant). For a relatively shallow corrugation ($l<<R$, where R is the mean radius of SWS) the condition of Cherenkov synchronism yields

$$\frac{\Delta\lambda}{\lambda} \approx \frac{\lambda}{d}\frac{\beta_e}{(1+\beta_e\beta_{ph})}\frac{\Delta d}{d},$$

where $c\beta_e$ is the electron velocity and $c\beta_{ph}$ is the phase velocity of the fundamental harmonic of the forward wave, d is the SWS period, and λ is the open-space wave length.

The simulation using KARAT code evidenced that, using this method, it is possible to vary the frequency from the critical frequency of the SWS up to the critical frequency of the beyond cutoff-neck, which can exceed 25% at half power level. It was found however that the frequency tuning is accompanied by periodic jump-wise changes in the longitudinal index of the fundamental standing wave in the tube (from 2 up to 6–7 variations) – Fig. 8. At the jump points, multi-frequency operation with substantial drop of power was observed. Within the same standing wave index, the frequency tuning may not be over 5–6%. For each SWS period, optimization of fundamental harmonic interaction is needed by means of adjusting the length of the cylindrical insert situated between the beyond cutoff-neck and the SWS.
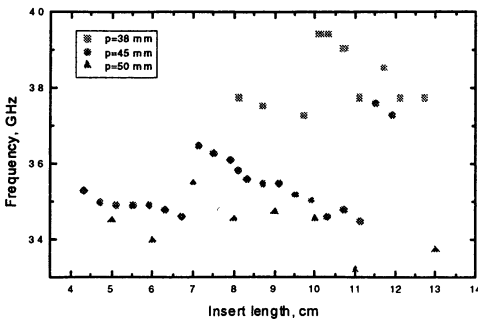

Fig. 8. Simulated microwave frequency vs length of the insert for a series of SWS corrugation periods. Beam power ~15 GW, magnetic field 20 kOe.

The frequency tuning was tested in experiment. Since consistent nonlinear variation of two SWS parameters – the period and the insert length – is a sophisticated mechanical problem, it should be pointed out that the frequency can be tuned, within some narrower band, by changing only one of the parameters, namely, the SWS period. In experiment, the insert length was fixed and the corrugation period was discretely changed from 38 up to 48 mm. The electron beam parameters (diode voltage, beam current) and guide

Fig. 9. Microwave peak power and frequency vs SWS corrugation period at invariant insert length (10 cm).

magnetic field strength were unchanged. The frequency tuning range obtained in that way was about 10% with 3.9 GW peak power and 22% efficiency (Fig. 9).
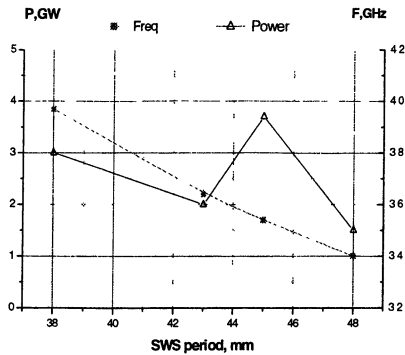
Double-section vircator

Vircators attract attention primarily as high-power microwave sources capable of operation without an external magnetic field. On the other hand, since the region of interaction between the electron beam and the electromagnetic field in vircator can be quite short (of the order of wavelength), these devices turn out to be compact, which is of considerable importance for the production of long-wavelength microwaves.

Recent theoretical and experimental studies performed at IHCE have demonstrated the capability of efficient operation of vircator system with electron beam premodulation. Energy premodulation of the electron beam, in conjunction with the fundamental property of the virtual cathode – electron energy dependence of current transmission – provide the necessary phase separation of electrons relative to the RF (radio frequency) field. It was shown that the use of a two-section single-mode electrodynamic system (resonant cavity) with proper phasing between the sections provides a more favorable RF field distribution for the electron beam versus a single-section one, resulting in improved microwave efficiency. Using a resonant cavity permits operation at small (30–50%) supercriticality of electron current. The latter circumstance allows, in turn, substantial (up to 20%) tuning of microwave frequency around the unperturbed virtual cathode relaxation frequency by adjusting the cavity parameters.

SINUS-7 experiment. Based on numerical simulations made with a 3-D version of the KARAT fully electromagnetic PIC code, an experimental mockup of two-gap vircator with in-phase RF fields was developed [6, 7]. The system

(Fig. 10, 11) includes two coupled rectangular cavities penetrated by round electron beam, which is produced in a quasi planar-gap vacuum diode (Fig. 12). Premodulation of the beam occurs in the first section, while the virtual cathode is formed in the second section. The RF fields in the two sections are co-phased. The source does not require external magnetic field.
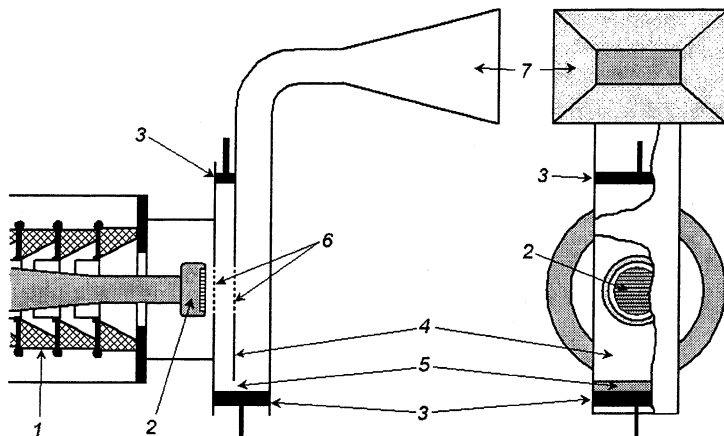

Fig. 10. Schematic of the vircator: *1* – insulator, *2* – cold cathode, *3* – tuning plungers, *4* – partition wall, *5* – coupling slot, *6* – foil or mesh windows, *7* – vacuum horn.
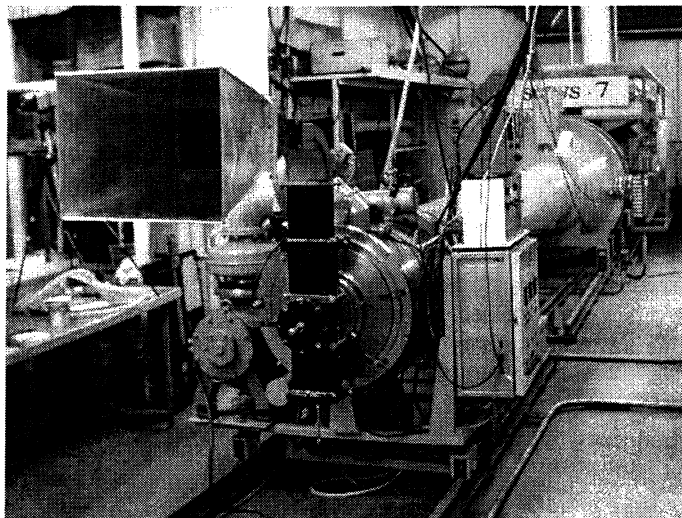

Fig. 11. Vircator installed at the SINUS-7 accelerator

76

In experiments using SUNUS-7 high-current repetitively pulsed electron accelerator, single-mode microwave oscillation in the S-band with a peak power of ~1 GW, a pulse width of ~25 ns FWHM, and ~5% power efficiency was obtained. The microwave efficiency was only slightly sensitive to beam power (Fig. 13). The factors limiting the efficiency were the substantial losses of current in the vacuum diode and the considerable drift of the electron beam parameters during the pulse inherent in high-current diodes with no magnetic field. The net microwave efficiency (accounting current losses in the vacuum diode) made 8–10%. The microwave frequency (2.6 GHz) was constant from pulse to pulse as well as during each pulse (Fig. 14).
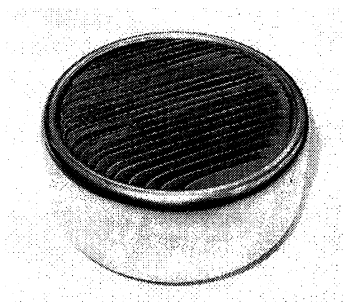

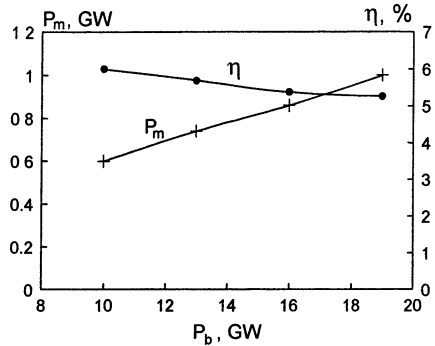**Fig. 12.** Cold bladed explosive-emission cathode.

Fig. 13. SINUS-7 vircator experiment: microwave power and efficiency vs feeding electron beam power.

The vircator frequency was varied by moving the plunger in the modulating section and the coupling window (conjointly with the upper plunger, Fig. 10). Fig. 15 illustrates the case where only one plunger was moved (curve (a)). This dependence correlates well with the dependence obtained in the "cold" measurement (curve (b)). The frequency tuning range in this case was about 7% at half power. Moving the plunger and the coupling window (keeping its width constant) in such a way that the beam axis always remained in the loop of the RF field ($A_1 \approx A_2 \approx 3\lambda_e/4$) allowed us to widen the frequency range up to 15%. The achievement of frequency tuning is supporting evidence to the fact that, at small current supercriticality, the vircator frequency is determined by the electrodynamic system.

Using the SINUS-7 electron accelerator, batch repetitively-pulsed operation of L-band vircator was demonstrated. The peak power in the pulses was about 100 MW and their width was 20–25 ns. The number of pulses in a batch was limited by the destruction of the intersectional grid and was about 50 at a pulse repetition rate of 50 pps and about 400 at 20 pps. For S-band vircator equipped
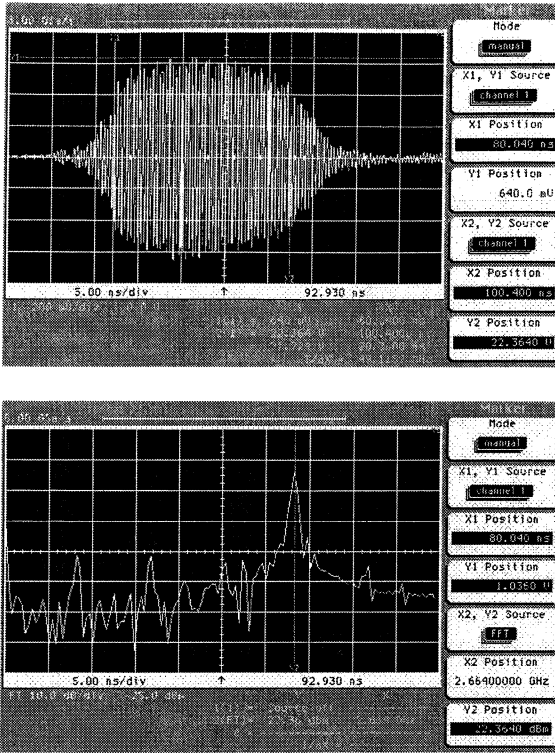
Fig. 14. SINUS-7 vircator experiment: waveform of microwave pulse (above) and its spectrum (below).
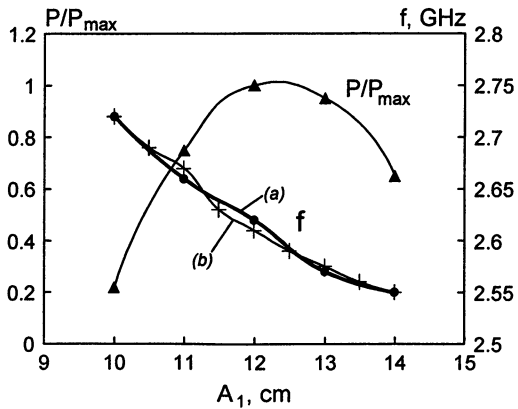

Fig. 15. Microwave power and frequency vs position of tuning plunger (*a* – experiment, *b* – "cold" electrodynamic measurements).

78

with Tungsten partition meshes and operating at 10 pps production of either 1000 pulses (200 MW) or 200 pulses (350 MW) was demonstrated, depending on feeding beam power.

Long pulse fuse driver experiment. The 2.65-GHz vircator successfully operated in an HPM source based on a compact high-voltage pulser with inductive energy store and a fuse opening switch (Fig. 16). Microwave pulses with ~300 MW peak power and ~50 ns width were produced with ~5% power efficiency [8].
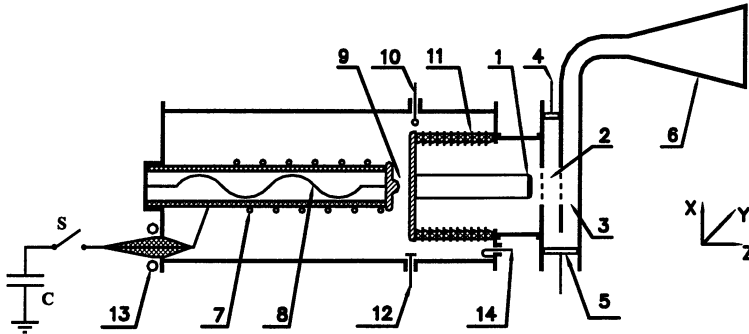

Fig. 16. Schematic of fuse driver vircator experiment: *1* – cathode, *2*, *3* – meshes, *4*, *5* – tuning plungers, *6* – microwave horn, *7* – inductance, *8* – fuse, *9* – spark gap, *10*, *12*, *14* – current and voltage probes, *11* – insulator stack, *13* – HV feeder.

This work was continued with a 2.1 GHz vircator system, with the aim of increasing the microwave pulse power and energy [9]. The MARINA compact high voltage pulse generator used in these experiments was assembled in a chamber filled with a gas mixture (N_2+SF_6) and consisted of a storage inductor, fuse, peaking switch, crowbar switch, and a sectioned vacuum insulator. As the primary energy storage, a six-stage Marx bank was used. The output voltage of the generator was 300 kV. The generator was discharged into the inductor ($L \approx$ ≈ 10 μH) and the fuse connected in series. Once the threshold current had been reached and the fuse had opened, a high voltage pulse (~1 MV) was induced across the storage inductor and applied to the peaking switch. After breakdown of the switch, the storage inductor was switched to the vacuum electron diode.

For a maximum diode voltage of ~1 MV, a beam current of ~20 kA, and a beam power of ~20 GW (beam pulse width ~150 ns) the peak microwave power was ~1 GW with ~5% efficiency. The RF signal gradually decreased during the pulse (Fig. 17), so that the pulse shape of the resulting power (which is quadratic of the electric field) was close to triangular with a ~10 ns rise time and a much slower fall (~100 ns) – see Fig. 18. The microwave pulse width was ~50 ns at

half power and the pulse energy was ~55 J. The output frequency did not change during the pulse and was determined by the adjusted parameters of the resonant cavity.
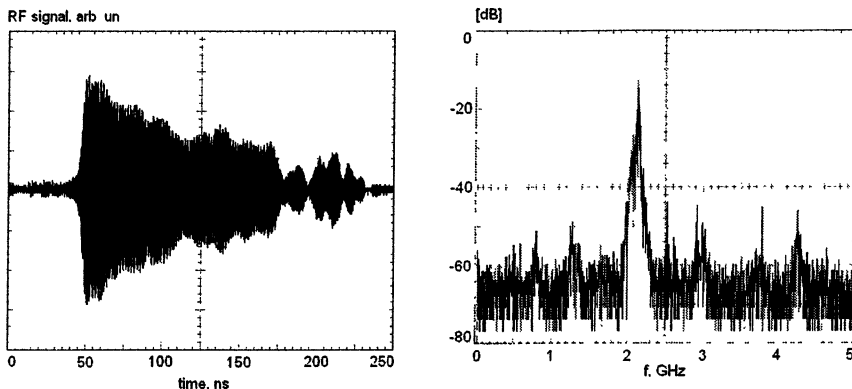

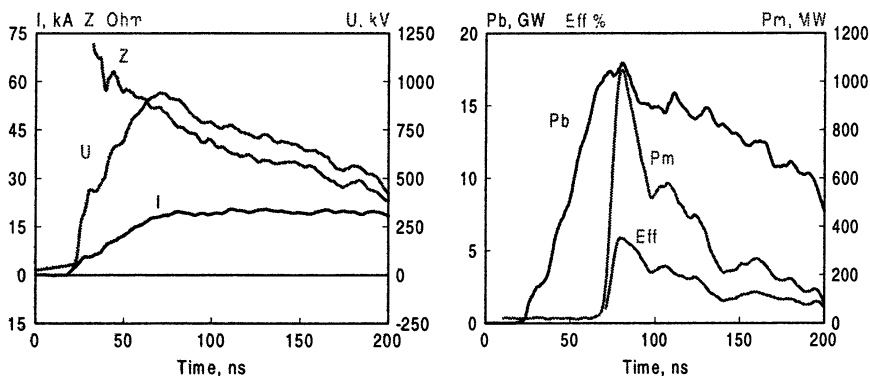**Fig. 17.** Waveform of an RF signal and its spectrum in fuse driver vircator experiment

Fig. 18. MARINA vircator experiment: waveforms of diode current I, voltage U, and impedance Z and full beam power P_b, and microwave power P_m and efficiency Eff.

An important phenomenon observed in these experiments (in contrast with previous SINUS-7 experiments) was the gradual decay of the microwave pulses produced by the vircator. It was found that this was partially caused by the explosive emission from the surface of the hemi-toroid focusing guard electrode surrounding the emitting circle on the cathode. This caused the vacuum diode impedance to decrease in time. However, since the MARINA pulser is a "generator of current", this effect resulted in a redistribution of the cathode current with its magnitude changed only slightly. The diode voltage decreased proportionally with the diode impedance. At the same time, the voltage to current ratio for the "core" part of the beam (which was emitted from the bladed area of the cathode

80

and injected in the vircator, while the "parasitic" peripheral current was cut off by a diaphragm) was almost constant. Thus, the power in the beam "core" dropped to more than a half within 100 ns. The microwave efficiency, calculated taking into account the "core" beam power only, was therefore approximately 8–10%, which is close to that predicted by simulations.

However, the experimental pulse decay was still stronger than that explained by the drop of the driving beam power. A possible additional factor to be considered is the emission of dense electron and ion flows from the plasma appearing at the surface of the electrodynamic system either under the action of the intense RF field (explosive-emission plasma) or due to the driving beam bombardment (anode and collector plasmas). As it was demonstrated in simulation, the combined emission of electrons and ions from the surface plasma and their consistent motion inwards the resonator gaps result in the formation of a quasi-neutral "synthetic" collisionless plasma and an effective microwave absorber (the microwave energy is carried away to the resonator walls by the electron fraction). In the double-section vircator, the emission in the modulating gap is most critical, causing the vircator Q-factor to drop and disturbing the operating ratio between the RF field amplitudes in the sections. The key role of the ions is to neutralize the space charge of the electron emission and to do away with the limitation on the electron emission current. Assuming the combined emission to start simultaneously with the microwave oscillation, the microwave pulse length limited by this mechanism is determined by the time its takes for the ions to accumulate in the gap of the resonator. For protons, it is a few tens of nanoseconds.

Conclusions

The relativistic BWO (studied earlier in X-band) was demonstrated to efficiently produce HPM sources in S-band. With that, the interaction length of the tube was reduced to ~3 λ. In experiment, ~5 GW, ~100 J microwave pulses were produced. Variation of slow-wave structure corrugation period enabled frequency tuning within 10% band.

Driving a double-sectioned vircator with compact high-voltage generator with inductive energy store and fuse opening switch allowed production of single-mode HPM pulses with ~1 GW peak power and ~50 J energy.

References

1. *Kitsanov S. A.* et al., Proc. BEAMS-2002.
2. *Kitsanov S. A.* et al., Lett. J. Tech. Phys. (2003).
3. *Bratman V. L.* et al., Relativistic High Frequency Electronics (Gorky, 1979, in Russian), **1**, 249–274.
4. *Tarakanov V. P.*, User's Manual for Code KARAT (Springfield, VA: BRA, 1992).
5. *Korovin S. D. and Rostov V. V.*, Russ. Phys. J., **39**, 12, 21–30 (1996).
6. *Kitsanov S. A.* et al., IEEE Trans. Plasma Sci., **30**, 1, part 2, 274–285 (2002).
7. *Kitsanov S. A.* et al., J. Tech. Phys., **72**, 5, 82–90 (2002, in Russian).
8. *Efremov A. M.* et al., Lett. J. Tech. Phys., **27**, 7, 57–63 (2001, in Russian).
9. *Kitsanov S A* et al., IEEE Trans Plasma Sci., **30**, 2 (2002).

A QUASI-OPTICAL ELECTRON-POSITRON COLLIDER?[1]

M. I. Petelin

Institute of Applied Physics, Nizhny Novgorod, Russia

Next-to-the-next linear colliders are planned to be driven with millimeter waves. To avoid the RF breakdown and the RF heating fatigue of metallic surfaces, each cell of the accelerating structure seems attractive to be fed individually through a sufficiently broad coupler. A proper structure might represent a coaxial composition of radial-corrugated disks. The delay-line-distribution pulse-compression and wave-flow-focusing feeder to the structure might be composed of mirrors, a part of them being corrugated.

Motivations and limitations

In linear electron accelerators, to avoid the dark current trapping, the accelerating gradient may be increased only proportionally to the drive frequency [2]. On the other hand, the RF electromagnetic field does not disrupt metallic surfaces of the accelerator under limitations [equivalent to (A1.1) and (A1.2) of Appendix 1]:

$$\vec{E}_s^2 T_e < M_\perp , \tag{1}$$

$$\vec{H}_s^2 T_e < M_\tau , \tag{2}$$

where $\vec{E}_s$ and $\vec{H}_s$ are electric and magnetic fields at the wall surface, T_e is the time of exposure of the surface to the RF field, $M_\perp$ and $M_\perp$ are parameters related to characteristics of the metal. The limitations (1), (2) similar to those presented in [3] must be satisfied *in every point* of the accelerating structure, of the RF feeder and of high power RF sources.

Deduction of quasi-optical accelerator [4]

Having fixed the accelerating gradient, the drive frequency and the accelerating channel inner diameter, let us synthesize a structure where minimum RF energy would be accumulated within the channel during maximum period of time allowed by limitations (1) and (2).

The latter specification might be met, first of all, with an accelerating channel profile which would provide the highest wave-electron coupling impedance and, for preventing menaces (1), (2), represent the smoothest surface. Further,

---

[1] The review represents a briefed upgrade to a talk [1] given at the AAC-2002 workshop.

again with account of limitations (1), (2), the fill time for all cells should be common, that is each cell should be fed through its individual channel. This channel should be sufficiently broad; irises and sharp ridges concentrating electric and/or magnetic RF fields should be excluded. Though broad, the feed channel should 1) provide quick fading of the RF field in the radial direction from the channel and 2) adapt the structure to the maximum fill time allowed by the limitations (1), (2). Such a performance can be realized with a sequence of mutually phased chokes representing a radial-Bragg-reflection cavity (Fig. 1).
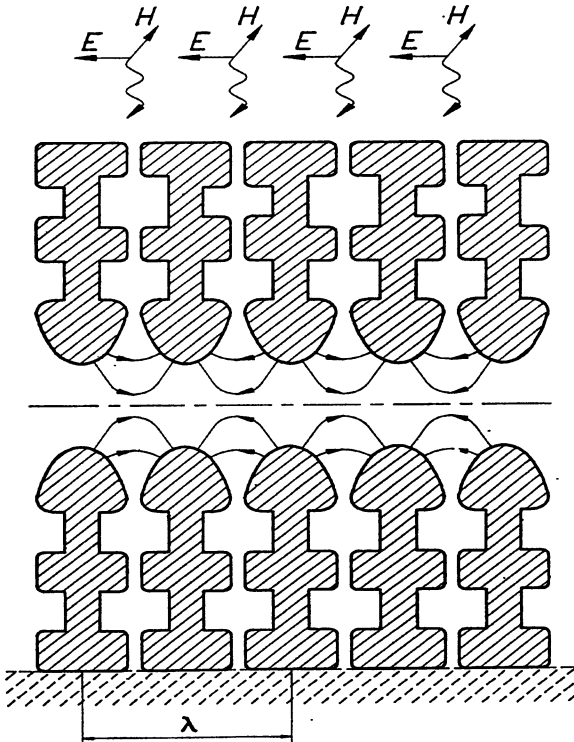

Fig. 1. Accelerating channel = RF energy accumulation cavity

The cavity is attractive to be fed with a wave flow converging onto the structure axis (Fig. 2). At a distance from the accelerating structure the wave flow is relatively broad, accordingly the RF field being relatively weak. This, with account of limitations (1), (2), gives a freedom for pulse compression in a feeder (Fig. 3) composed of a delay line distribution system and, near to any accelerating section, a passive or active pulse compressor.
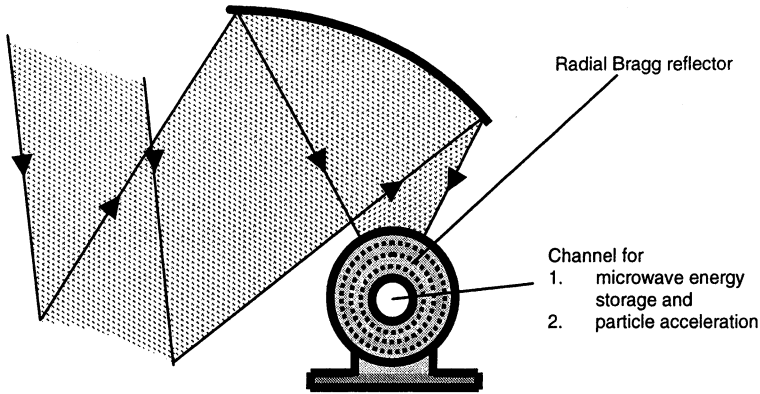
83

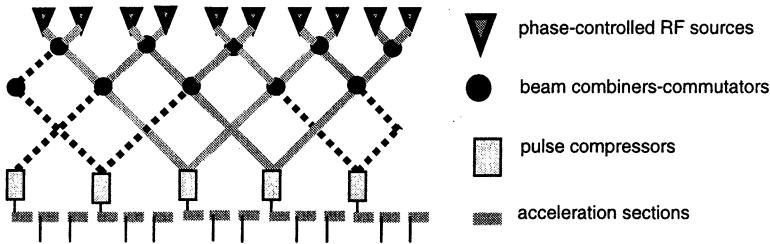**Fig. 2.** Feeding the accelerating section with converging wave flow

Fig. 3. Feeding accelerator with array of phase controlled RF sources

RF-energy-accumulation particle-acceleration cavity [4, 1]

The accelerating gradient assumed being fixed, the RF energy accumulated within the channel is minimized, if the RF field is composed of only the electron-synchronous space harmonic and counter-propagating harmonic of the same amplitude. So the field represents the transverse-magnetic π-mode

$$E_\varsigma = 2\cos\varsigma, \qquad E_\rho = \rho\sin\varsigma, \qquad H_\varphi = i\rho\cos\varsigma,$$

where $\rho = kr$ and $\varsigma = kz$ are dimensionless radial and axial coordinates, $k = \omega/c$. This field is kept by the metallic surface

$$\rho^2 = \rho_0^2 - 2\ln\sin^2\varsigma.$$

At a certain radius exceeding ρ_0, this surface continuously conjugates with an asymmetric peripheral part of the structure synthesized to

• match the accelerating channel with the converging wave flow within the feed sector,

- provide steep fading of the RF field in all radial direction outside the feed sector.

Such a performance can be realized by a disc corrugation converting the structure into a radial Bragg reflection cavity with Q-factor fit to the feed pulse duration (Figs. 1, 2).

RF feeder [4, 1]

The accelerator is assumed to be driven with an array of phase controlled microwave sources (Fig. 3), the high power being transmitted through a delay line distribution system (DLDS), RF pulse compressors and isolators protecting the microwave sources of reflection from accelerating sections.

To satisfy limitations (1) and (2), all components must be oversized. The transmission efficiency should be maximum, which, in particular, implies efficient wave filtration. The simplest system able to meet these specifications is the sequence of mirrors operating at the through Gaussian wave beam (another option is the corrugated waveguide operating at the quasi-Gaussian HE11 mode).

The **DLDS** (Fig. 3) might be composed of phase controlled binary combiners-commutators based on wave diffraction by a grating (Fig. 4). Such a grating [4] functions as a 3dB hybrid: the combined wave beam direction is changed by means of ±90° mutual phase shift between the input beams.

$$\varphi_1 - \varphi_2 = \pi/2 \qquad \varphi_2 - \varphi_1 = \pi/2$$

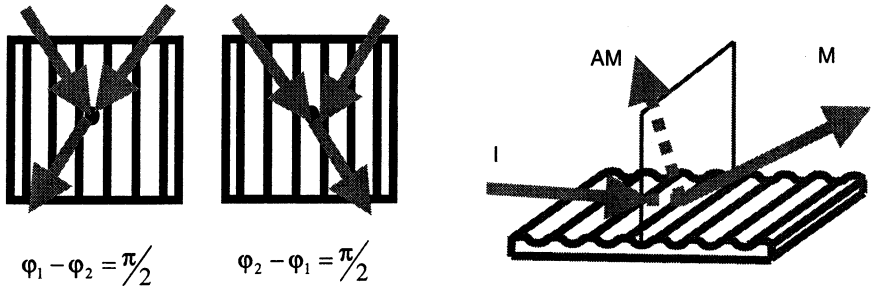**Fig. 4.** Magic Y: quasi-optical 3dB hybrid

The simplest quasi-optical RF *pulse compressor* represents an open resonator coupled with input and output wave beams by corrugation of a mirror (Fig. 5). Characteristics [5] of the compressor are identical to those of the SLED [2]. The compressor can be upgraded with using additional resonators fed with chirped (linear frequency modulated pulses) [5].

85
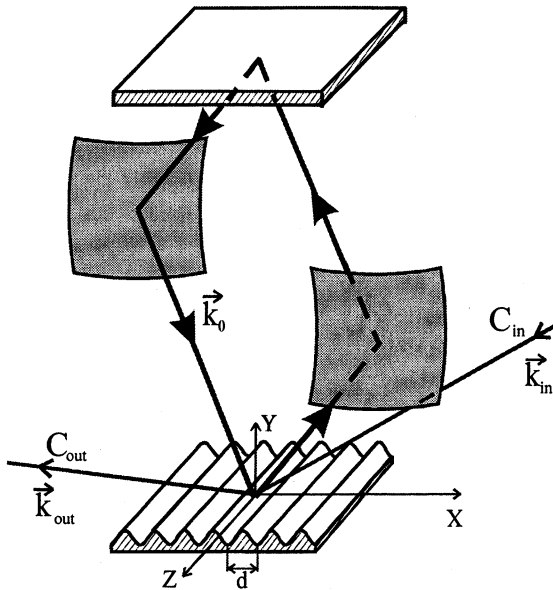
Fig. 5. RF pulse compressor: quasi-optical SLED[1]

To **protect** high power microwave **amplifiers** of reflections from accelerating sections, a scheme based on the quasi-optical 3dB hybrid (Fig. 6) can be used (this design similar to the SLED appeared when Jay Hirshfield and the author of this paper traveled to the AAC-2002, Oxnard, CA).

Fig. 6. Magic Y isolator: non-reflection feed to accelerating sections

---

[1] The cavity may be used also in a non-reflection traveling-wave resonant ring able to function as a gas-discharge (plasma) reactor.

86

Summary

At millimeter waves, the quasi-optical accelerator seems most efficient to provide durable operation: safe of RF breakdown and fatigue. Efficient out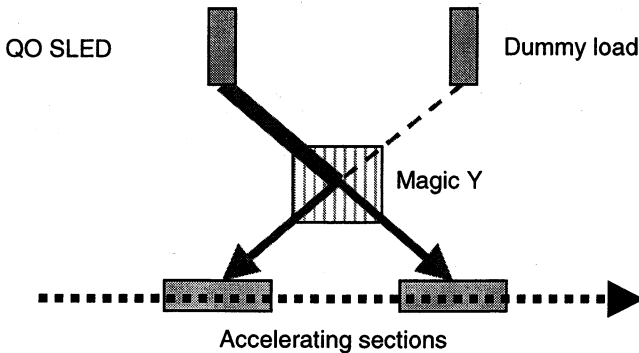-filtering of spurious modes from the accelerating structure can be used to align the particle focusing system. The reasonably compact and robust design admits the simplest manufacturing technology.

For example, a 34 GHz structure could safely operate with accelerating gradient 150 MV/m and RF fill time 10–20 ns. A 3-stage DLDS (8 amplifiers feeding simultaneously one accelerating section) with successive quasi-optical SLED could provide the total pulse compression ratio over 30. The relevant pulse repetition frequency might be $\sim 10^3$ pps.

Appendix 1. **Speculations on microwave breakdown and fatigue of metal surfaces**

(Summary of discussion with J. Haimson, S. Tantawi,
W. Wuensch and V. Yakovlev at AAC-2002)

Seen microscopically, any practical metal surface is uneven, and, so, the electron emission $\vec{j}_\perp$ induced by the electric field is peaked at microjuts. On the contrary, the tangential current $\vec{j}_\tau$ driven by the RF magnetic field in the skin layer can be regarded as uniform. Accordingly, these two effects might be treated more or less independently: during a sufficiently long RF pulse 1) the electron emission $\vec{j}_\perp$ causes the *RF breakdown* and 2) the tangential current $\vec{j}_\tau$ causes the *irreversible mechanical fatigue* of the metallic surface:

RF breakdown [6–8]. At the primary stage, the RF electric field makes electrons to tunnel from microjuts, the Fowler – Nordheim effect being accompanied with the secondary emission electrons. However the space charge interaction between electrons saturates their density at a level keeping the effective plasma frequency ω_p much less than the field frequency ω. The metal surface temperature grows proportionally to $\int_0^t \vec{j}_\perp^2 dt'$, but if the local surface temperature stays within a certain limit

87

$$\int_0^{T_e} \bar{j}_\perp^2 dt' < K_\perp ,$$ (A1.1)

no adverse effect happens.

At the second (avalanche) stage, the microjuts are melted and evaporated. The freed molecules are ionized by oscillating electrons. The resulting plasma being quasi-neutral, the electron density is not space charge limited and grows exponentially. The temperature of ions lags behind that of electrons, nevertheless the ion energy may grow sufficient to tear new molecules from the surface and even dig caverns. The plasma undergoes ambipolar diffusion, and, when in a considerable part of the structure the plasma frequency approaches the field frequency ($\omega_P \to \omega$), the RF field turns totally distorted (note that in structures of travelling wave type the plasma formation may not cause the wave reflection, because the plasma periphery may provide adiabatic matching and absorption of the wave).

Such a scenario of the RF breakdown [8] is much similar to that of the "explosion" emission of electrons from metal surfaces subjected to DC fields [9].

Fatigue of metal surface [10–12]. The near-surface RF magnetic field drives the RF electric current in the skin layer and causes its Ohmic heating. If the absorbed RF energy is kept within a certain limit

$$\int_0^{T_e} \bar{j}_\tau^2 dt < K_\tau ,$$ (A1.2)

the mechanical stress of the metal surface layer is reversible. However, if this limitation is violated, the metal deformation becomes non-elastic and, progressing from pulse to pulse, results in a degradation of the metal surface.

Appendix 2. Efficiency and bandwidth of quasi-optical 3dB hybrid

(Analysis and calculations by D. Schegolkov)

In the magic Y configuration (Fig. 4), the infinite grating combines two plane waves of equal power densities into one wave so that the resulting wave direction can be switched by means of ±90° shifting the mutual phase of the primary waves. The grating parameters being fixed, a small change of parameters of the primary waves can result in 1) scan of the resulting wave propagation direction and 2) appearance of radiation in the alternative direction. The both effects result in limitations on performance of the device combining wave beams of limited cross section, because each of them can be represented as a continuous set (Fourier integral) of plane waves; accordingly, the radiation scattered by the grating can also be calculated as a set of plane waves, and the inverse Fourier transform gives structures of the resulting beams.

For example, let two E-polarized Gaussian beams be incident to a sinusoidal corrugated metal surface so that the illuminated area is round, relevant beam cross sections being ellipsoidal. Let the propagation directions of every beam have equal angles with main axes of grating symmetry. In this case the commutation is performed within the frequency band $\Delta\omega/\omega = 0.26\lambda/a$, the power loss being $\Delta P/P_0 = 0.14\lambda^2/a^2$ where a is the greater half-width of the wave beam.

References

1. *Petelin M. I.*, Quasi-Optical Collider Concept, Proceedings of AAC-2002 (to be published).
2. *Wilson P. B.*, Application of High Power Microwave Sources to TeV Linear Colliders, in Applications of High Power Microwaves, edited by A. V. Gaponov-Grekhov, V. L. Granatstein (Boston, London: Artech House, 1994), 229–317.
3. *Wilson P. B.*, in Proccedings of the ITP Conference on Future High Energy Colliders (University of California, Santa Barbara, 1996).
4. *Petelin M. I., Caryotakis G., Tolkachev A. A.* et al., Quasi-Optical Components for MMW Fed Radars and Particle Accelerators, in High Energy Density Microwaves, edited by Robert M. Phillips, AIP Conference Proceeding. 474 (New York, American Institute of Physics, 1998), 304–315.
5. *Petelin M. I., Tai M. L.*, Compression of phase-modulated microwave pulse by chain of ring cavities, in Pulsed RF Sources for Linear Colliders, Montauk, N-Y, AIP Conf. Proc. 337, Ed. R. Fernow, 303–310 (1994).
6. *Laurent L., Scheitrum G., Vlieks A.* et al., RF Breakdown Experiments at SLAC, in High Energy Density Microwaves, edited by Robert M. Phillips, AIP Conference Proceeding 474 (New York, American Institute of Physics, 1998), 261–278.
7. *Braun H., Dobert S., Syrachev I., Taborelli M., Wilson I., Wuensch W.*, Technical Report CLIC Note No. 535, CERN, PS Givision (2002).
8. *Kovalev N. F., Nechaev V. E., Petelin M. I., Zaitsev N. I.*, A Scenario for Output Pulse Shortening in Microwave Generators Driven by Relativistic Electron Beams, IEEE Trans. on Plasma Science, **26** (3), 246–251 (1998).
9. *Mesyats G. A., Proskurovsky D. I.*, Pulsed Electrical Discharge in Vacuum (Springer, Heidelberg, 1989).
10. *Pritzkau D. P., Siemann R. H.*, Experimental study of rf pulsed heating on oxygen free electronic copper, Phys. Rev. Special Topics – Accelerators and Beams, **5**, 112002 (2002).
11. *Nezhevenko O.*, in Proc. of 1997 Particle Accelerator Conference, Vancouver, Canada, (IEEE, Piscataway, NJ, 1997), 3013–3014.
12. *Kovalenko V. F.*, Physics of Heat Transfer in Vacuum Electronic Devices (Soviet Radio, Moscow, 1975).

MICROWAVE ACTIVE PULSE COMPRESSION
USING PLASMA SWITCHES

A. L. Vikharev[1], *A. M. Gorbachev*[1], *O. A. Ivanov*[1], *V. A. Isaev*[1],
S. V. Kuzikov[1], *V. A. Koldanov*[1], *J. L. Hirshfield*[3,4], *O. A. Nezhevenko*[4],
S. H. Gold[2] *and A. K. Kinkead*[2]

[1]Institute of Applied Physics RAS, Nizhny Novgorod, Russia
[2]US Naval Research Laboratory, Washington DC, USA
[3]Department of Physics, Yale University, New Haven, USA
[4]Omega-P, Inc., New Haven, USA

The results in investigation of single- and dual-channel RF pulse compressors at 11.424 GHz using plasma switching of a high-Q TE_{01}-mode energy storage cavities are presented. Designs, low- and high-power tests of these active compressors are described. Low-power tests of single-channel compressor show 12:1 power gain, while tests of dual-channel compressor show good constructive phase interference. High-power tests of single-channel compressor using the Omega-P/NRL 11.424 GHz magnicon show compressed pulses with 24 MW peak power and 8:1 power gain. The application of developed plasma switches with an existing passive pulse compressor SLED-II for increasing its efficiency is discussed.

Introduction

Currently the high-energy physics community develops the projects of creation the next generation of electron-positron linear collider able to reach center-of-mass energies of 1 TeV and above. One of these projects is the Next Linear Collider (NLC) project at the Stanford Linear Accelerator Center (SLAC) [1]. According to the project the NLC consists of two linacs for electrons and positrons. It is supposed to use 11.424 GHz microwaves from 75 MW klystrons for accelerating of charge particles. For delivering the microwave power from klystrons to accelerator structures the Delay Line Distribution System (DLDS) is developed [1]. Each linac consists of 117 RF units. In each unit the DLDS combines the power from eight klystrons and routes it up-beam sequentially to eight sets of accelerator structures, and finally, the six structures in each set convert the RF energy to beam power. To each set with the six accelerator structures 510 MW pulses of 400 ns duration will be fed. Because the power required to drive the accelerator structures is high, it is important that the conversion and transmission of energy at every stage of the RF system be efficient. Application of the DLDS system at the NLC will require the use of multi-kilometer circular waveguides. Performed tests of the developed DLDS components show that different losses are still higher than required. Therefore the application of DLDS at the NLC is not finally approved and physics community continues to develop other RF systems for NLC. One of the candidates for RF system could be the microwave active pulse

compressor. Active compressor could provide 500 MW pulses of 100 ns duration from each klystron due to high power gain.

Our team has managed to develop an active Bragg compressor (ABC) with characteristics suitable for accelerator use. In this paper the results in investigation of ABC at 11.424 GHz are presented.

Active Bragg compressor (ABC) operating in the TE_{01} mode

The basic idea of ABC is to use Bragg reflectors in an oversized cylindrical resonator to create a cavity for storing microwave energy [2–6]. The schematic diagram in Fig. 1 shows the ABC operating in the low-loss TE_{01} waveguide mode. This is an evacuated version made of copper. The compressor consists of mode converters ($TE_{01} \rightarrow TE_{11}^{0}$, $TE_{11}^{0} \rightarrow TE_{01}^{0}$) connected with smooth tapered transitions and a resonator formed by a Bragg reflector, a section of a cylindrical oversized waveguide and an output reflector. The central part of the resonator is a section of an oversized 1m long waveguide 80 mm in diameter, which is equipped with a tapered 400 mm long transition to a narrower waveguide. The diameter of the latter waveguide was 55 mm, and the TE_{01}^{0} mode is the only propagating mode of all the axially symmetric ones.
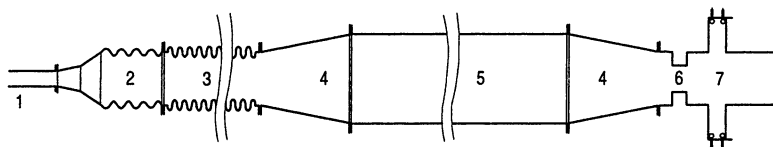

Fig. 1. Schematic diagram of the active Bragg compressor operating at the TE_{01} mode: *1* – input waveguide, *2* – TE_{01}-mode converter, *3* – input Bragg reflector, *4* – smooth tapered transition, *5* – storage cavity, *6* – over-critical narrowing of the waveguide, *7* – output reflector with electrically controlled gas discharge switch.

The output reflector has been developed with both active and passive sections. The scheme of the combined output reflector is shown in Fig. 2.
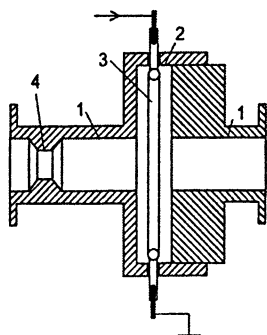

Fig. 2. Electrically controlled output reflector with active and passive sections: *1* – circular waveguide, *2* – stepped widening, *3* – gas-discharge tube, *4* – diaphragm.

91

The active section is based on step-wise widening of circular waveguide. This stepped widening section comprises a cylindrical resonator containing a quartz ring-shaped gas-discharge tube. The passive section is a waveguide section with an over-critical narrowing, referred to below as the "diaphragm". This combined output reflector makes it possible to reduce the intensity of the electric field in the region of the gas discharge tube in the active section. Frequency characteristic of such a combined output reflector are shown in Fig. 3.
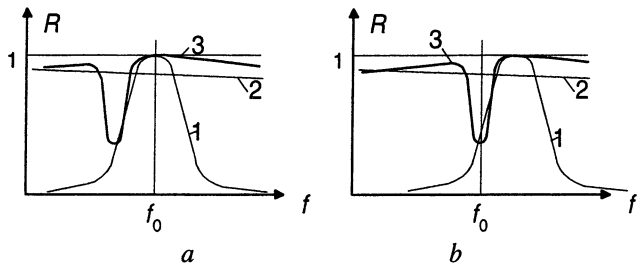

Fig. 3. Frequency characteristics of the output reflector at the regime of energy storage (*a*) and at the regime of energy extraction (*b*). Here frequency characteristics of the active section (*1*), the diaphragm (*2*) and total characteristics (*3*).

When the plasma is formed in gas-discharge tube situated in the region of waveguide widening, the maximum of the resonance curve shifts to the region of the operating frequency. This provides ejection of the power accumulated in the resonator to the load. It is evident that parameters of the compressed pulse are significantly depending on the value of the transmission coefficient, T, of the switch. By changing dimensions of the over-critical waveguide narrowing in the passive reflector section one can change the transmission coefficient and, thus, control the amplitude and duration of the compressed pulse. In our experiments the coefficient of reflection from the whole reflector including the passive and active sections was 70% in regime of energy output.

Operation of ABC as described above was tested experimentally using low-power microwave radiation. The compressor was tuned in two stages. Initially the output reflector was adjusted in such a way as to provide the match of the maximum of its non-transmission and the operating frequency of the compressor. Then, by changing the length of the cylindrical waveguide the resonator was tuned precisely to the frequency $f_0 = 11.424$ GHz by observing the minimum of the compressor-reflected signal. When a high-voltage, short-rise time pulse was fed to the discharge tube, the microwave power stored in the resonator was discharged into the TE_{01} operating mode and thence to a load.

The efficiency of microwave pulse compression was regulated by changing the length of the step-wise widening of the waveguide. The compression coefficient k was determined by the ratio of the power of the compressed pulse, P_p to power P_0 at the compressor input. The compression coefficients obtained in

92

the low-power experiment amounted to $k = 11-12$ at half-width pulse duration $\tau_p = 45-55$ ns. Experimental results are presented in Table 1.

Table 1. Experimental results of low-power test

Frequency	11.424 GHz
Operating mode	TE_{01}
Resonator Q-factor	$2.5 \cdot 10^4$
Input pulse duration	1 μs
Power gain	11–12
Output pulse duration	55 ns
Efficiency	50%

High-power tests of one-channel 11.424 GHz ABC

An active Bragg compressor has been developed that is able to provide output pulses of at least 100 MW power with pulse duration of 100 ns. In order to obtain compressed pulse with a power of 100 MW, a series of experiment was carried out using the Omega-P/NRL 11.424 GHz high-power magnicon. A schematic of the active pulse compressor experiment is shown in Fig. 4.
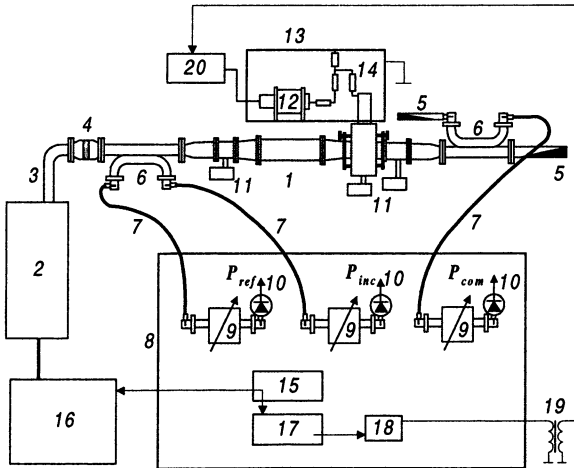
Fig. 4. Schematic of the active microwave pulse compressor experiment: *1* – compressor, *2* – magnicon, *3* – waveguide line, *4* – output window, *5* – matched load, *6* – directional coupler, *7* – coaxial waveguide, *8* – screen room, *9* – attenuator, *10* – detector, *11* – ion pump, *12* – high-voltage pulse generator, *13* – shielding box, *14* – divider, *15* – trigger generator, *16* – modulator, *17* – delay generator, *18* – trigger amplifier, *19* – pulse transformer, *20* – high-voltage power supply.

The compressor is connected to the magnicon by means of a waveguide line equipped with an output window to separate the vacuum chambers of the magnicon and the compressor. The output pulse of the compressor enters a high-power matched waveguide load. Signals proportional to the power incident on the compressor (P_{inc}), the power reflected from the compressor (P_{ref}), and the output power (P_{com}) are measured by 55.5-dB directional couplers, with the signals attenuated and measured by crystal detectors located in a screen room. A trigger generator and a set of digital delay generators trigger the magnicon modulator, then trigger the TWT amplifier to provide the magnicon input pulse, and finally trigger a high voltage pulse generator that creates an electrical discharge in a gas-filled quartz tube in the switch cavity of the pulse compressor near the end of the magnicon output pulse. This shifts the center frequency of the switch cavity, reducing the reflection coefficient at the end of the cavity, and permits the stored energy to discharge rapidly to produce the compressed output pulse. Three ion pumps are used to maintain a pressure of $10^{-6} - 10^{-7}$ Torr in the switch.

The compressor is tuned to the magnicon output frequency by changing the resonator length. The output reflector is then tuned relative to the minimum of the power transmitted through the compre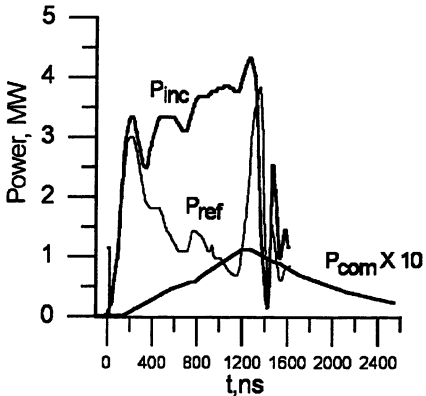ssor, P_{com}, under the condition that the difference between the incident and the reflected power, $P_{inc} - P_{ref}$, is maximized. This setting corresponds to the maximum Q-factor of the resonator. In a first experiment, the maximum stored energy was limited by multipactor discharge on the exterior of the gas-filled quartz switch tube. In the second experiment, the use of larger diameters discharge tubes and heating the tubes prior to RF conditioning made it possible to increase the incident power up to the level of 5–6 MW with no sign of multipactor discharge. A typical set of oscilloscope traces of the incident, reflected and transmitted signals is

Fig. 5. Pulse compressor waveforms, showing energy storage and decay without discharge.

shown in Fig. 5, for a case in which the output switch was not discharged. After the magnicon pulse is over, P_{com} decreased exponentially, permitting one to calculate the Q-factor: $P_{com} \propto \exp(-t/\tau)$, where $\tau = Q/\omega$. When the output reflector was tuned to the maximum of the reflection coefficient, the Q-factor of the resonator was $Q = (4-7) \cdot 10^4$.

The pressure in the quartz switch tube was externally regulated. At high levels of incident power, when the value of the electric field in the gas tube exceeded the breakdown threshold level for this pressure, a microwave discharge occurred that caused non-triggered switching of the pulse compressor. In this self-breakdown mode of operation, experiments investigated the production of compressed pulses at various pressures of nitrogen, SF_6, and their mixtures in the gas discharge tubes. Oscilloscope traces corresponding to the generation of compressed pulses at 100 Torr and 1 Torr of N_2, respectively, are shown in Fig. 6. The peak power in the compressed output pulses was 14 MW and 24 MW, in these two cases, with pulse durations of 55 ns and 45 ns. The compression factor in the latter case was ~6x. These experiments showed that at higher gas pressures in the tubes, self-breakdown occurs at a higher incident power level, which makes it possible to store higher energy in the resonator. At the same time, when the pressure is lower, and the switch is operated substantially above its self-breakdown threshold, the efficiency of energy output from the resonator and the power in the compressed pulse both increase.
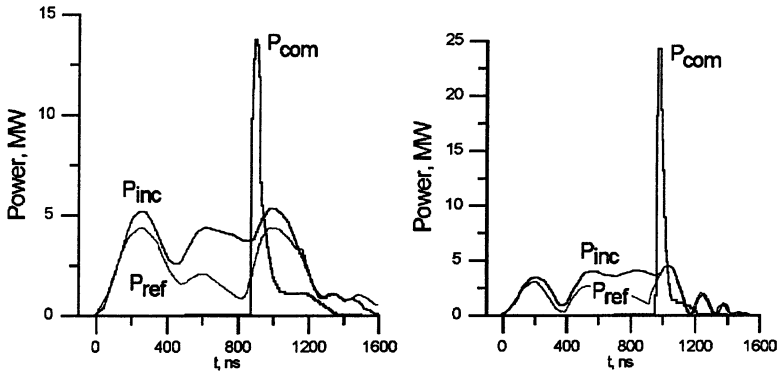

Fig. 6. Pulse compressor waveforms, showing the compressed pulse in the self-breakdown regime.

Next, we studied operation of the compressor with the discharge initiated by a high voltage pulse generator (HVPG). A high-voltage pulse (90 kV, 100 ns) was fed to the tube electrodes via a limiting resistor (100 Ω) and an inductance free divider. In these experiments, the incident microwave power was decreased below the level at which self-breakdown occurred at a particular pressure in the switch tubes. High power compressed pulses, with efficient energy output, could be obtained at low gas pressures with an N_2:SF_6 mixture in the tubes. Figure 7 shows experimental traces obtained in the case of triggered discharges. In the left-hand case, 100 Torr N_2 + 5 Torr SF_6 was used. For a stored energy of 1.85 J,

a 90-ns compressed pulse was produced with a peak power of 10 MW. In the right-hand case, using 10 Torr N_2 + 1 Torr SF_6, for a stored energy of 0.72 J, a compressed pulse with a peak power of 11 MW was produced. The compression factor in the latter case was ~8x. These traces demonstrate that, at lower pressures, when the HVPG generated plasma quickly fills the entire volume of the switch tube, the efficiency (as well as the stability) of energy output from the storage resonator improves significantly.
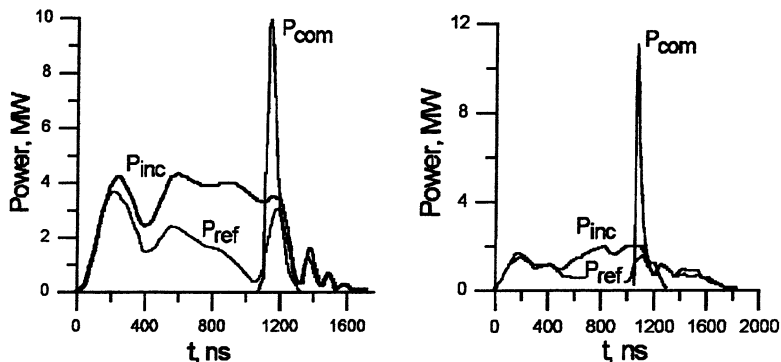

Fig. 7. Pulse compressor waveforms, showing the compressed pulse in the triggered regime.

Two-channel active Bragg compressor (ABC)

Two-channel ABC makes it possible to isolate the generator from the reflected microwave power at the initial stage of energy storage, to improve ABC efficiency, and to make the ABC design simpler [7]. The scheme of the compressor is shown in Fig. 8.
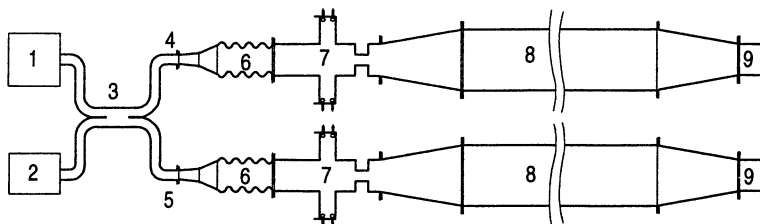

Fig. 8. Schematic diagram of the two-channel active Bragg compressor operating in the TE_{01} mode: 1 – driving generator, 2 – load, 3 – 3-dB directional coupler, 4 – first channel of ABC, 5 – second channel of ABC, 6 – TE_{01}-mode converter, 7 – input and output electrically controlled reflector, 8 – storage cavity, 9 – reflector.

Two-channel active Bragg compressor has combined input-output reflector. The compressor consists of two identical channels. Each channel of the compressor is connected to the driving generator and the load via a novel 3-dB quasi-optical coupler. The basic idea of the novel quasi-optical coupler is to use the effect of image multiplication in oversized rectangular waveguide [8]. In such waveguide an asymmetrically injected wave beam is divided, at a certain distance, into two beams of equal amplitudes, but phase shifted at 90°, Fig. 9. On the basis of this phenomena we developed a novel 3-dB quasi-optical coupler for operation of vacuum ABC prototype with at least 100 MW peak power.
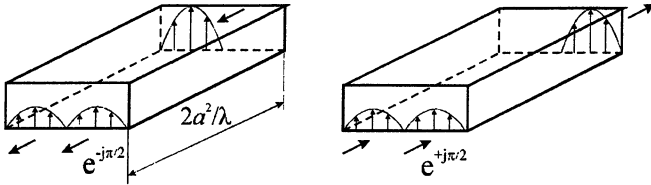

Fig. 9. Quasi-optical 3-dB directional coupler

In two-channel ABC configuration each compressor channel is excited via a reflector, which is both the input reflector and the electrically controlled output one. At the other end of the storage resonator the Bragg reflector is replaced with a simple stopper as a cone. However realization of the proposed scheme requires phase stability between the initial and compressed pulses and between pulses from each channels.

The testing of non-vacuum two-channel ABC prototype using 100kW-level microwaves was performed at 9.4 GHz. In this experiment we used the same scheme shown in Fig. 8 and 160 kW magnetron as the driving generator. It was found out that two-channel ABC is able to provide power gain up to 20. The oscillograms of the input and compressed pulses are shown in Fig. 10. Experimental results are listed in Table 2.
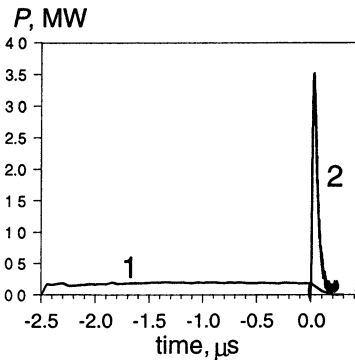

Fig. 10. Oscillograms of input (*1*) pulse with 160 kW peak power and compressed (*2*) pulse with 3.4 MW peak power.

Table 2. Experimental results of 100 kW-power test

Frequency	9.4 GHz
Operating mode	TE_{01}
Resonator Q-factor	$5 \cdot 10^4$
Input pulse duration	2.5 µs
Power gain	21
Output pulse duration	52 ns
Input power	160 kW
Output power	3.4 MW
Efficiency	44%

Novel plasma switch for next generation of 11.424 GHz ABC

The input-output reflector of existing ABC has a number of unique features. It makes it possible to control the power gain of the compressor, as well as the shape and duration of the compressed pulses. Besides, it allows for obtaining good phase characteristics of the compressed pulse. Experiments performed demonstrated that ABC with such an output reflector makes it possible to obtain output pulses with only a slight variation of phase with time.

However, it must be noted that compressed microwave pulses at levels well above 100 MW are required for the Next Linear Collider (NLC). At a power gain 11–12, ABC (as now configured) cannot handle output pulses of 500 MW. The principal limitations to output power above a level of about 100 MW in the existing ABC arise from strong electromagnetic fields in the output reflector that lead to self-breakdown in the plasma switch.

Operation of the existing ABC in the TE_{01} mode was modeled numerically by the FDTD method [9]. In numerical calculations, parameters and dimensions of the compressor were chosen to be close to those of the manufactured compressor. Calculations showed that at the 100 MW power of the output pulse the maximum electric field at the discharge tube in the combined output reflector will be 25 kV/cm. Thus, the studies performed showed that it is necessary to develop an output reflector for the ABC possessing significantly weaker fields in the region of the tubes while retaining the other positive features of combined output reflector.

To obtain high-power pulses using ABC we suggest a modified output reflector. Schematic diagram of ABC with modified plasma switch is shown in Fig. 11. In the regime of energy storage the plasma switch has the reflection coefficient close to unity in a wide frequency band. When the gas-discharge tubes are broken down the total reflection coefficient decreases resonance-wise, as in Fig. 12.
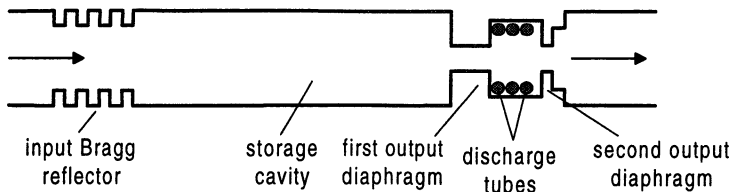
Fig. 11. Schematic diagrams of the active Bragg compressors (ABC) with modified plasma switch.
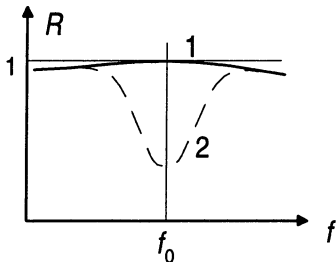

Fig. 12. Frequency characteristics of modified plasma switch at the regime of energy storage (*1*) and at the regime of energy extraction (*2*).

Operation of the modified switch was modeled numerically. The calculations were performed for a storage cavity 1 m long with a loaded Q-factor of $Q = 2.5 \cdot 10^4$. Figure 13 shows the computed time dependence of the power of the compressed pulse (1) normalized to the input power, and phase mismatch (2) between the input and output radiation. Numerical calculations showed that at the 100 MW pulsed power output level, the maximum electric field at the tubes in the compressor will be 8 kV/cm.

Thus the calculation performed showed principal possibility of building a plasma switch that would provide a high power gain of the compressor combined with high stability of phase of the compressed pulse. Intensity of the electric field in the vicinity of gas-discharge tubes in such a switch is three times lower, as compared to the fields in the combined output reflector of the existing ABC.

Fig. 13. Computed time dependence of the power of the compressed pulse (*1*) normalized to the input power and phase mismatch (*2*) between the input and output radiation.

The numerical calculations were performed with the assumption that the loaded Q-factor of the storage cavity of ABC with a modified plasma switch
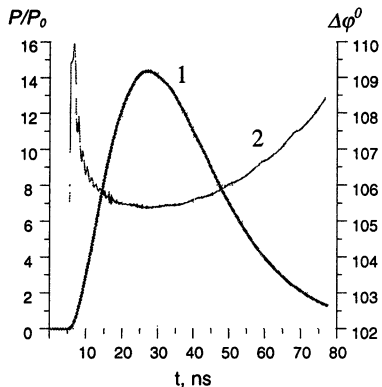
4*

99

equals the Q-factor of the cavity in the existing ABC. Calculations and measurements have shown the efficiency of pulse compression in the existing ABC is 50–60% [5]. The loaded Q-factor, namely $Q = 2.5 \cdot 10^4$, is determined by coupling losses and is optimal when pumping pulses with their duration of 1 μs are used. In the existing ABC the efficiency of pulse compression is limited due to energy losses in the

Table 3. Parameters of ABC
with modified plasma switch

Ohmic cavity Q	110,000
Loaded cavity Q	25,000
Input pulse width	1–1.5 μs
Output pulse width	0.1 μs
Power gain	10–15
Input power	50 MW
Output power	400–500 MW
Efficiency	60–65%

dielectric tube in the active section of the combined output reflector. These losses reduce the ohmic Q-factor, thus affecting efficiency of the device [5]. In ABC with the modified plasma switch the tubes have less influence on the Q-factor (and efficiency) since the field at the tubes is much less intense. That is why for the ABC with a modified plasma switch (as shown by estimates) the efficiency of pulse compression will be 60–65%. Thus, design parameters for the active Bragg compressor (ABC) with a modified plasma switch could be as listed in Table 3.

Active SLED II with plasma switches

As is known, the SLED II (SLAC Energy Development) compression system makes it possible to increase the peak microwave power by several times by means of shortening the duration of the klystron pulse. This system is fully passive. The microwave energy in such a system is stored in the low-loss delay line. The system is transferred from the energy storage regime into the power output regime by changing the phase of the microwave power source. Such a system is successfully applied in operation of the existing SLC collider at the frequency of 2.856 GHz and has the following parameters: compression ratio $C = 6$, power gain $M = 4.1$, and efficiency $\eta = 68\%$.

The schematic diagram of the SLED II system used in operation of the existing SLC collider is shown in Fig. 14. SLED II consists of a phase shifter, a klystron, two identical resonant delay lines, a 3-dB coupler, and accelerating structures. The phase shifter is situated at the klystron input and provides fast switching of the output signal to 180°. The microwave energy is stored in the delay lines at the low-loss oscillation type of the circular waveguide, TE_{01}. The each delay line has an iris at its entrance. The iris has the reflection coefficient equal to R, which less than unity. The length of each of the delay lines is chosen such as make the time of the round-trip propagation of the wave along the line, τ, equal to the time of filling the accelerating structure, and to make the length a multiple of a half of the wavelength in the line at the operating frequency. The 3-dB coupler provides decoupling of the accelerating structures and the klystron.
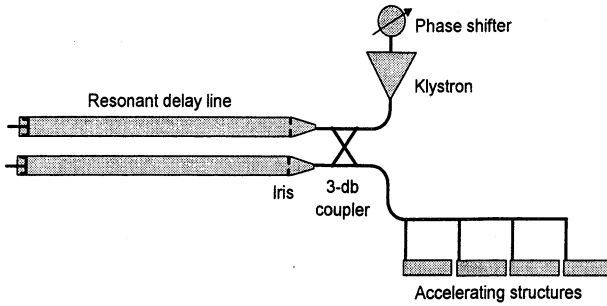
Fig. 14. SLED II RF pulse compression system

However, SLED II system cannot be proposed for use in the 11.4 GHz Next Linear Collider. The thing is that NLC requires a significantly higher quantity of the power gain than 4. The efficiency of the SLED system, though, becomes appreciably lower when the compression ratio grows.

S. G. Tantawi [10] proposed a solution to this problem, which changes opportunities of SLED system radically. The authors developed an active SLED II system. They proposed to transfer the system from the regime of energy storage to that of power output by changing the phase of the microwave source and the coupling coefficient simultaneously. This makes it possible to achieve the following parameters of the RF pulse-compression system: compression ratio $C = 8\text{--}16$, power gain $M = 7\text{--}12$, and efficiency $\eta = 82\text{--}84\%$.

Our preliminary investigations showed that the plasma switch with its configuration shown in Fig. 2 could be used to create the active SLED II and provide the required variation of the reflection coefficient just before the last time bin. Numerical calculations showed that conceptually it is possible to create plasma switches that would provide variation of the reflection coefficient in the range from $R_0 = 0.8\text{--}0.96$ to $R_d = 0.4\text{--}0.2$ using the plasma produced in the active section of this plasma switch. Such plasma switches can be of two types: the first one with low-pressure gas-discharge tubes ($p = 0.1\text{--}0.01$), and the second one with high-pressure tubes. Though the both types of the switch have similar design, they have different parameters of active and passive sections and different functioning mechanisms.

Figure 15 shows the total coefficient of reflection from the first type of the plasma switch as a function of the length of the "diaphragm-reflector" waveguide section for the tube without and with plasma. As seen from the Figure, when the length of the "diaphragm-reflector" section was 38 mm, the total coefficient of reflection from the plasma switch was changing from 0.9 to 0.3, when the plasma was produced in the tube.

Similar calculations were performed for the second type of the plasma switch. Figure 16 presents the total coefficient of reflection from the plasma switch

depending on the length of the "diaphragm-reflector" waveguide section for the tube without and with plasma. As seen from the Figure, when the "diaphragm-reflector" length is 49.5 mm, the total coefficient of reflection from the plasma switch was changing from 0.9 to 0.44 when the plasma was produced in the tube.
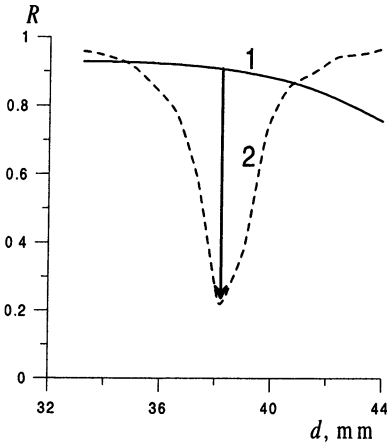

Fig. 15. Total reflection coefficient of TE_{01} mode from switch with 152 mm diameter of the stepped widening vs the length of the diaphragm-reflector waveguide section without (*1*) and with (*2*) plasma in the tube.
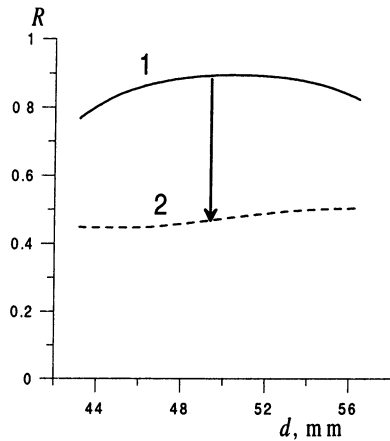
Fig. 16. Total reflection coefficient of TE_{01} mode from switch with 160 mm diameter of the stepped widening vs the length of the diaphragm-reflector waveguide section without (*1*) and with (*2*) plasma in the tube.

Preliminary calculations of the threshold electric field for microwave breakdown in the tube and of the values of electric fields near the tube in the active section yielded the following:

- The maximum output power in one delay line with the first-type plasma switch can reach 200 MW;
- The maximum output power in one delay line with the second-type plasma switch can reach 110 MW.

Thus, active SLED II can have the output power of 400 MW and 220 MW for the first-type and second-type switches, respectively, and efficiency of the order of 80% in the both cases.

Conclusions

1. Single and double-channel TE_{01} mode energy storage resonators with plasma switches have been shown, in low- and high-power tests, to be promising candidates for high-power RF pulse compressors of next linear colliders.

102

2. In self-breakdown regime, 25 MW, 40–50 ns output pulses, with energy extraction efficiency ~ 70–80% were obtained; overall energy efficiency limited by effect of reflection on magnicon output waveform.

3. In triggered regime, 10 MW, 50 ns output pulses, with maximum energy extraction efficiency > 90% were obtained.

4. Two-channel pulse compressor experiment scheduled for this fall, with 3-dB hybrid to provide a matched load to the magnicon and to obtain 100 MW, 50 ns output pulses.

5. The novel plasma switch for active pulse compressor has been developed. Compressor with the new plasma switch will be able to provide 400–500 MW, 100 ns output pulses at 11.4 GHz band and to obtain output pulses with only a slight variation of phase with time (~ 0.5 degree).

6. Plasma switch has been developed for testing with X-band SLED II for production of flat-top compressed pulses and for increasing the efficiency of SLED-II system.

References

1. 2001 Report on the Next Linear Collider, SLAC-R-571 (Snowmass, June 2001).
2. *Vikharev A. L., Kovalev N. F., Petelin M. I.*, JTP Letters, **22** (19), 41 (1996).
3. *Petelin M. I., Vikharev A. L., Hirshfield J. L.*, in Proc of 7th Advanced Accelerator Concepts Workshop, Lake Tahoe, CA, **398**, 822 (1997).
4. *Vikharev A. L., Gorbachev A. M., Ivanov O. A.* et al., in Proc. of 8th Advanced Accelerator Concepts Workshop, edited by W. Lawson, C. Bellamy and D. F. Brosius, AIP Conf. Proc., **472**, 975 (1998).
5. *Vikharev A. L., Gorbachev A. M., Ivanov O. A.* et al., in Proc. of the 1999 Particle Accelerator Conference, edited by A. Luccio and W. MacKay (Piscataway, NJ, 1999), **2**, 1474.
6. *Vikharev A. L., Gorbachev A. M., Ivanov O. A.* et al., in Proc. of the Intern. Workshop "Strong Microwaves in plasmas", edited by A. G. Litvak (IAP, Nizhny Novgorod, 2000), **2**, 896.
7. *Vikharev A. L., Gorbachev A. M., Ivanov O. A.* et al., in Proc. of 9th Advanced Accelerator Concepts Workshop, edited by P. L. Colestock and S. Kelley, AIP Conf. Proc., **569**, 741 (2001).
8. *Denisov G. G., Kuzikov S. V.*, in Proc. of the Intern. Workshop "Strong Microwaves in Plasmas", edited by A. G. Litvak (IAP, Nizhny Novgorod, 2000), **2**, 960.
9. *Yee K. S.*, IEEE Trans. Antennas Propagat., **AP-14**, 302 (1966).
10. *Tantawi S. G., Ruth R. D., Vlieks A. E.*, Nuclear Instruments and Methods in Physics Research A, **370**, 297 (1996).

A 2 MW, CW COAXIAL CAVITY GYROTRON. EXPERIMENTAL AND TECHNICAL CONDITIONS

B. Piosczyk, A. Arnold[1], H. Budig, G. Dammertz, O. Dumbrajs[2], O. Drumm[1], M. V. Kartikeyan, M. Kuntze, M. Thumm[1] and X. Yang

Forschungszentrum Karlsruhe, Association EURATOM-FZK,
Institut für Hochleistungsimpuls- und Mikrowellentechnik, D-76021 Karlsruhe, Germany
[1] also Universität Karlsruhe, Institut für Höchstfrequenztechnik und Elektronik (IHE)
[2] Department of Engineering Physics and Mathematics, Helsinki University
of Technology, Association EURATOM-TEKES, FIN-02150 Espoo, Finland

The development work on coaxial cavity gyrotrons has demonstrated the feasibility of manufacturing of a 2 MW, CW 170 GHz tube that could be used for ITER. The problems specific to the coaxial arrangement have been investigated and all relevant information needed for an industrial realization of a coaxial gyrotron have been obtained in short pulse experiments (up to 17 ms). The suitability of critical components for a 2 MW, CW coaxial gyrotron has been proved and a first integrated design has been done.

Introduction

The final goal of the development work performed at the Forschungszentrum Karlsruhe (FZK) on advanced powerful microwave sources was to provide a basis for manufacturing a 2 MW, 170 GHz coaxial cavity gyrotron for operation at long pulses up to CW as needed for ITER. Within this framework first the basic operating problems of coaxial gyrotrons were investigated before the specific problems related to the coaxial arrangement have been studied in detail [1, 2]. As a result all relevant data necessary for a technical realization of a 2 MW, CW coaxial gyrotron have been obtained.

The experimental investigations have been performed on a gyrotron operated in the $TE_{31,17}$ mode at 165 GHz and optimized for an RF output power of 1.5 MW. The frequency is limited by the maximum magnetic field obtainable with a superconducting (SC) magnet existing at FZK. The gyrotron is of modular type and enables an easy replacement of the components. Its cooling performance allows only operation at short pulses with a low duty factor.

As electron gun a coaxial magnetron injection gun (CMIG) is used [3]. The coaxial insert is supported from the bottom of the gun and is in total approximately 1 m long. The insert can be aligned with respect to the electron beam under operating conditions with high accuracy (better than ± 0.05 mm). The cooling of the insert is provided by a water flow of about 10 L/min which is sufficient even for CW operation.

The quasi-optical (q.o.) RF-output system consists of a smooth-wall launcher with a single cut and two mirrors – one quasi elliptical and one non-quadratic phase correcting mirror. The cavity mode is directly converted into a paraxial

output beam with approximately a Gaussian power distribution in the window plane. The mirrors have been optimized for minimum diffraction losses inside the tube [4].

The collector is insulated with respect to the tube body and in addition, the body is insulated from the ground allowing operation in depressed mode either by positive biasing of the body and the insert or by negative biasing of the collector with respect to the ground.

Based on the results obtained, a draft integrated design of a 2 MW, CW 170 GHz coaxial gyrotron has been performed, the suitability of the individual components for use in such a tube has been investigated and the basic parameters and requirements have been specified.

Experimental results

RF generation. The RF-measurements were performed in short pulse operation with a typical pulse length of 1 ms and a repetition rate of 1 Hz. Single-mode oscillation has been found over a reasonably large parameter range. A maximum RF output power as high as $P_{out} = 2.2$ MW was achieved at a beam current $I_b = 84$ A with an efficiency $\eta_{out} = 28$ %. A maximum output efficiency of 30% (without depressed collector) was measured at the nominal RF output power $P_{out} = 1.5$ MW. In operation with a single-stage depressed collector the overall efficiency has been increased from 30 % up to 48 % by applying a negative retarding voltage $U_{coll} = -34$ kV. The experimental values are in good agreement with numerical results obtained with a self-consistent, multi-mode code [5] using the experimental operating parameters as input.

The maximum pulse length of about 17 ms was limited by a strong and sudden rise of the current I_{ins} to the coaxial insert which could reach large values (many Amperes) independent of the value of the beam current I_b. Detailed investigations indicated that the observed phenomenon is caused by a Penning type discharge in the region between the cathode and the coaxial insert. Numerical simulations prove that the nearly cylindrical symmetric electric and magnetic fields in that region provide an efficient trap for electrons which cause the buildup of the Penning discharge. The trapping condition for electrons can be avoided by a suitable design of the gun and thus a degradation of the high voltage performance due to the occurrence of the Penning discharge can be excluded.

Coaxial insert. The mechanical stability of the coaxial insert is a crucial issue for stable long pulse and CW operation of coaxial gyrotrons. Therefore, the mechanical properties of the coaxial insert have been investigated under operating conditions. The flow of the cooling water has been identified as a main source of mechanical vibrations. Under representative operating conditions the amplitude of the vibrations has been measured to be less than 0.03 mm. This value is compatible with the requirements for a stable long pulse operation.

Calorimetric measurements of the losses at the insert have been performed. Under stationary conditions a constant heat flow of about 70 W from the hot cathode to the cooled coaxial insert was observed. The additional losses P_{ins} at the insert during RF operation have been measured for different operating parameters. The experimental value of $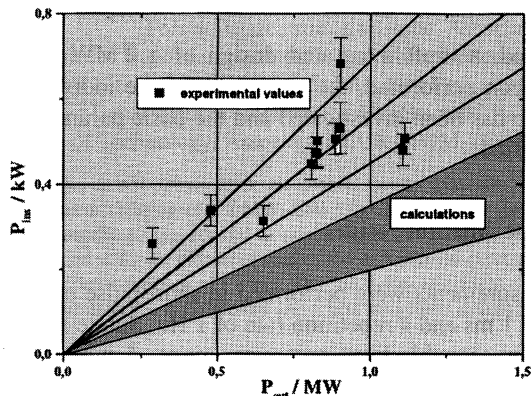P_{ins}$ has been found to be about twice the theoretical value calculated for ideal copper at room temperature (Fig. 1). This means that the total losses at the insert are expected to be less than 0.1 % of the RF output power, $P_{ins} \leq 0.001 \cdot P_{out}$, even if some increase of the RF losses due to an enhanced temperature of the insert under CW conditions is taken into account. The corresponding peak surface losses do not exceed 10 % of the peak loading at the outer cavity wall. Thus the power dissipated at the insert should not cause any technical problems even for CW operation with $P_{out} = 2$ MW.

Fig. 1. Measured and calculated losses at the coaxial insert in dependence of the RF output power for the TE$_{31,17}$ mode.

The influence of the alignment accuracy of the insert on the operating conditions of the coaxial gyrotron has been investigated experimentally (Fig. 2). The concentricity of the outer cavity with respect to the electron beam has been measured to be within 0.1 mm. A radial misalignment δR_{ins} of the insert results both in an increase of the insert losses and in enhanced problem of mode competition which leads to a reduction of the parameter range for single mode operation. In order to avoid this unfavorable effects, the alignment accuracy of the insert should be within $\delta R_{ins} \leq 0.15$ mm. This accuracy was easily achieved in the experimental coaxial gyrotron.
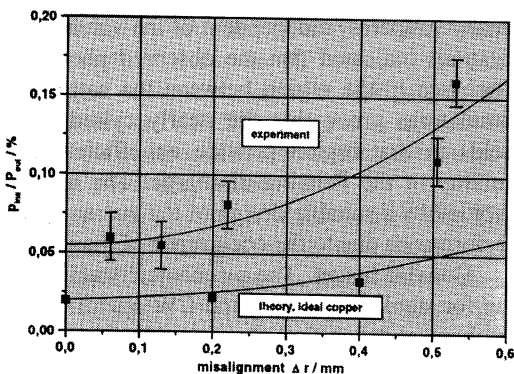

Fig. 2. The losses at the insert relative to the RF output power in dependence of the radial displacement of the coaxial insert.

Microwave stray radiation. Diffraction losses in the quasi-optical (q.o.) RF-output system lead to microwave stray radiation which is captured in the gyrotron tube. The stray radiation is partly dissipated in the gyrotron walls and may thus cause technical problems in CW operation. Therefore, the captured radiation has been investigated by using two relief windows of 100 mm diameter which are placed not symmetrically with respect to the mirrors and the main RF output window. The fact that the microwave power radiated through both relief windows was nearly the same indicates that the captured stray radiation is distributed approximately uniformly inside the mirror box. The total amount of stray radiation P_{stray} was measured to be as large as: $P_{stray} = (0.09 \pm 0.01) \cdot P_{out}$. In the investigated geometry with a stainless steel mirror box about 8 % of P_{stray} is radiated out of each relief window. The relatively large value of P_{stray} is assumed to be related to the use of a smooth-wall launcher with a single cut which has relatively large diffraction losses. However, the uniform distribution of the captured radiation inside the mirror box keeps the technical problems related to dissipation of P_{stray} inside the tube in acceptable limits, even for a 2 MW gyrotron.

2 MW, 170 GHz coaxial cavity gyrotron

A draft integrated design of a 2 MW, CW, 170 GHz coaxial cavity gyrotron is shown in Fig. 3. The overall dimensions are comparable with the dimensions of a conventional 1 MW, CW gyrotron. The collector is at ground potential, insulated from the body with a ceramic ring placed at the top of the mirror box. The positive potential of the gyrotron body including the mirror box provides the retarding voltage for energy recovery. In Table 1 the design specifications and parameters are summarized. The individual components have been checked for their suitability for a use in a 2 MW coaxial gyrotron.

The CMIG gun [3] used in the short pulse experiments is suitable for CW application. According to recent experience the technical parts of the gun have to be designed such that a built-up of a Penning discharge does not occur. For an RF-output power of 2 MW a beam current of about 75 A is needed. The corresponding emitter current density is around 4.2 A/cm^2. The radial dimension of the gun is compatible with a bore hole of 220 mm diameter for the SC-magnet.

As the operating cavity mode, the TE$_{-34,19}$ mode has been selected [6]. The geometry of the cavity is shown in Fig. 4. A beam radius $R_b = 10.2$ mm is required. For an RF output power of 2 MW, corresponding to a generated RF power of about 2.2 MW, the peak loading (ideal copper at room temperature) at the outer cavity wall and coaxial insert has been calculated to be 0.96 kW/cm^2 and 0.05 kW/cm^2, respectively. The total power dissipated at the insert is expected not to exceed a value of 2 kW.
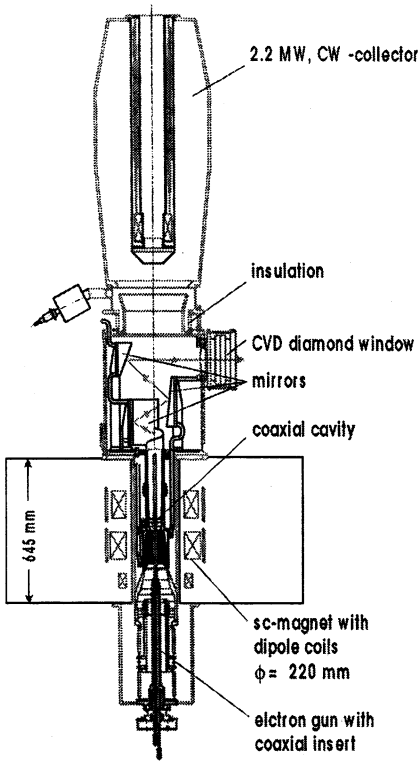
Fig. 3. A draft integrated draft design of the 2 MW, CW, 170 GHz coaxial gyrotron.

Table 1. Design specifications and parameters

| operating mode	$TE_{-34,19}$
RF output power	2 MW
beam current	75 A
accelerating beam voltage	90 kV
retarding collector voltage	$\geq$ 32 kV
output efficiency	$\geq$ 45 %
cavity magnetic field	6.87 T
velocity ratio	1.3
emitter current density	$\cong$ 4.2 A/cm²
beam radius in the cavity	10.2 mm
beam width (guiding centers)	0.25 mm
insert alignment accuracy	$\leq$ 0.15 mm
Q-value (cold)	1660
cavity losses (ideal copper, 20 ^{0}C) at P_{out}=2 MW:	
peak wall losses	0.96 kW/cm²
total losses at the outer wall	56 kW
peak losses at the coaxial insert	$\leq$ 0.1 kW/cm²
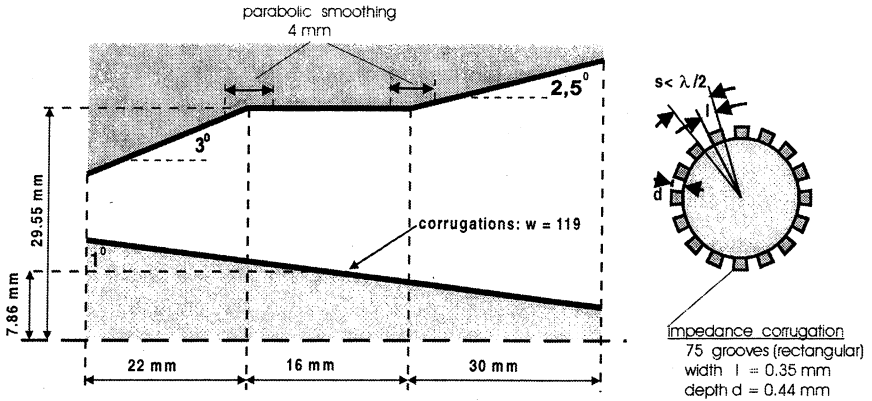
Fig. 4. Geometry of the $TE_{34,19}$ coaxial cavity

The q.o. RF-output system used in the experimental investigations consisted of a smooth launcher which resulted in the above given value of microwave stray radiation. In order to reduce the amount of stray radiation, an advanced dimple wall launcher, as used in the conventional 140 GHz gyrotron [7] which is under development for the W7-X stellarator, is under consideration together with three mirrors, a quasi-elliptical mirror and two non-quadratic phase correcting mirrors.

A single-disk CVD-diamond window can be used for transmission of 2 MW microwave power at 170 GHz. With a the loss tangent $\tan \delta \cong 2 \cdot 10^{-5}$ (state of the art) and a thickness of 1.85 mm the RF losses in the disk have been calculated to be about 0.6 kW. Because of the excellent heat conductivity of CVD-diamond, removing of the power is not seen to be a technical problem.

For an RF-output power of 2 MW generated with an output efficiency of $\geq 45 \%$ the remaining beam power which has to be dissipated in the collector can be as large as 2.4 MW. In order to handle this amount of power in CW operation a new collector with an improved power distribution along the collector surface has been designed [8]. The size of the collector is similar to the one used in the 1 MW, 140 GHz gyrotron for W7-X. Although the total dissipated power is about twice as high as for the 1 MW gyrotron, the peak surface loading is not higher and stays well within accepted technical limits. The feasibility for manufacturing of the collector has been examined and an industrial design has been done.

A SC-magnet has to provide a peak magnetic field of about 6.87 T at the axis. A warm bore hole of 220 mm diameter as needed e.g. for the W7-X gyrotron is sufficient. Rough considerations show that NbTi-technology should be applicable. In addition to the solenoidal coils, the SC-magnet has to be equipped with a set of dipole coils, which are needed to perform in particular the alignment of the insert under operating conditions.

109

Conclusions

The physical feasibility for fabrication of a 2 MW, CW 170 GHz coaxial cavity gyrotron has been demonstrated. All necessary data for an industrial realization of a 2 MW, CW 170 GHz coaxial cavity gyrotron have been provided. A draft integrated design does not show any principle limitations for a technical realization of such a gyrotron.

References

1. *Piosczyk B.* et al., Coaxial cavity gyrotrons – recent experimental results. IEEE Trans. Plasma Sci., 2002 (in press).
2. *Piosczyk B.* et al., ITER ECRF advanced source development – coaxial cavity gyrotron final report, FZKA 6701, ISSN 0947-8620 (Forschungszentrum Karlsruhe, Februar 2002).
3. *Piosczyk B.*, A novel 4.5 MW electron gun for a coaxial gyrotron. IEEE Trans. Electron Devices, **48** (12), 2938–2944 (2001).
4. *Michel G.* et al., Considerations on multimode quasi-optical converters, 24th Int. Conf. on Infrared and Millimeter Waves (Monterey, California, USA, 1999), PS-8.
5. *Kern S.*, Numerische Simulation der Gyrotron-Wechselwirkung in koaxialen Resonatoren, FZKA 5837, ISSN 0947-8620 (Forschungszentrum Karlsruhe, Nov. 1996).
6. *Dumbrajs O.* et al., Mode selection for a 2 MW, CW 170 GHz coaxial cavity gyrotron, 26th Inter. Conf. on Infrared and Millimeter Waves (Toulouse, France, September 10–14, 2001).
7. *Dammertz G.* et al., Development of a 140 GHz, 1 MW, CW gyrotron for the W7-X stellarator, Frequenz, 9–10 (2001), ISSN 0016-1136.
8. *Piosczyk B.*, A 2.2 MW, CW collector for a coaxial cavity gyrotron, 26th Inter. Conf. on Infrared and Millimeter Waves (Toulouse, France, September 10–14, 2001).

ADVANTAGES OF COAXIAL CAVITY GYROTRONS

V. E. Zapevalov, V. I. Khizhnyak, M. A. Moiseev,
A. B. Pavelyev, N. A. Zavolsky

Institute of Applied Physics, Russian Academy of Sciences,
Nizhny Novgorod, Russia

Main results of experimental study of the 140 GHz/1,5 MW coaxial gyrotron are summarized. High selective properties of the coaxial cavities and a principal possibility to control the electron beam parameters by means of the inner rod potential changing have been confirmed.

Introduction

Conventional cavity CW gyrotrons are limited in an output power because of ohmic losses, mode competition and limiting electron beam current. All these problems can be essentially reduced by the use of coaxial cavities [1] whose advantages (as compared with ordinary gyrotron resonators) are characterized by two main factors:

1. The special profiling of the inner rod and outer wall surface allows one to provide effective electrodynamic mode selection as well as in the radial and azimuthal indices.

2. The presence of the inner rod allows one to eliminate the problem of beam voltage depression and opens a principal possibility to control the parameters of electron beam by applying independently an appropriate potential on the inner rod. In particular, it becomes possible to use the inner conductor for electron beam energy recovery (without special insulation of the collector) and for the fast discrete tuning of the gyrotron frequency.

These properties of the coaxial cavities were confirmed experimentally with the 140 GHz/1.5 MW coaxial gyrotron operating on the high-order volume mode $TE_{28,16}$.

Design parameters of 140 GHz/1.5 MW coaxial gyrotron

The design of Russian version of the 140 GHz/1.5 MW coaxial gyrotron is very close to the German tube described in [2, 3]. In this gyrotron the diode type inverse electron gun with a system of alignment of the inner rod [4] and the coaxial cavity with a radially tapered and corrugated insert [5] were used. The main design parameters of the tube are summarized in Table 1.

At the first stage the electron gun operation and selective properties of two types of coaxial cavities (with the smooth cylindrical and periodically corrugated outer wall) were studied in the gyrotron with an axial RF output. Then the output

Table 1. Design parameters of the coaxial gyrotron

Operating mode	TE$_{28,16}$
Operating frequency f (GHz)	140
Accelerating voltage U_0 (kV)	90
Operating beam current I_b (A)	50
Beam radius R_b in the cavity (mm)	10
Operating magnetic field B_0 (T)	≈ 5.6
Pitch-factor α	1.3
RF output power P_{out} (MW)	1.5
Efficiency without recuperation η_0, %	> 30
Peak wall loading (for real copper) p_Ω (kW/cm^2) (calculated peak ohmic losses at the inner rod are less than 15% of the peak cavity wall losses)	≤1.3

section was replaced by the quasi-optical (q.o.) RF output system based on a two-step mode conversion scheme TE$_{28,16}$$^{(-)}$ $\Rightarrow$ TE$_{76,2}$$^{(+)}$ $\Rightarrow$ 2×TEM$_{00}$. Such system allows one to transmit the output radiation through two windows when the total power exceeds a capability of each window. At the final stage the possibilities of the electron beam energy recovery and step frequency tuning were also checked in the gyrotron with an axial RF output.

Experimental results

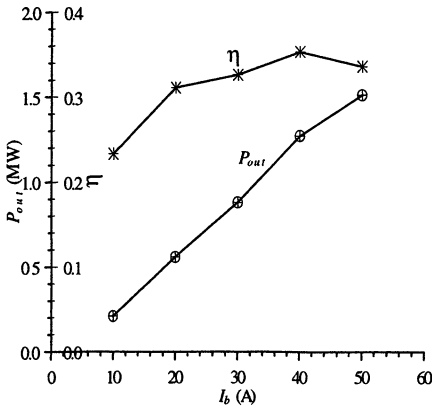**Gyrotron with an axial RF output.** The measurements were performed with pulses around 50 µs. At first the cavity with a smooth cylindrical outer wall and the conical impedance inner rod was tested. Obtained experimental results (Fig. 1) are in a good agreement with theoretically expected values. The output power P_{out} ≈ 1.5 MW at the efficiency over 33% was reached at the design values U_0 = 90 kV and I_b ≈ 50 A. The maximum efficiency η_0 exceeded 35% (at the beam current I_b = 40 A). The stable oscillations of the operating mode have been observed over wide range of the magnetic field that testified about the high efficient mode selection.

Fig. 1. RF output power and efficiency versus electron beam current (U_0 = 90 kV).

In order to extend still more the range of a single-mode operation and to enhance the efficiency of the gyrotron, at the second step the cavity with a cylindrical outer wall was replaced by the resonator with corrugated wall. In such systems the suppression of parasitic modes with neighbouring (as compared with operating mode) azimuthal indices can be achieved due to effective transformation of these modes to strongly disturbed low-Q ones. Experimental measurements have confirmed that in this way it becomes possible to thin out the eigenfrequency spectrum of high-Q oscillations at least twice (see, for example, [6]).

Gyrotron with a doublel-beam RF output. A combined two-step mode converter included the corrugated waveguide mode transformer ($TE_{28,16} \Rightarrow$ $\Rightarrow TE_{76,2}$), the double-cut launcher and set of the mirrors ($TE_{76,2} \Rightarrow 2 \times TEM_{00}$). For the resonator a cavity with a cylindrical outer wall was chosen. Taking into account the differences in the Q-factors and oscillation regimes (caused by the differences in the cavity output angles) a comparison of the experimental curves of output power for double-beam and axial gyrotrons (solid and dotted lines in Fig. 2) gives a rather good value of conversion coefficient equal approximately 90%.
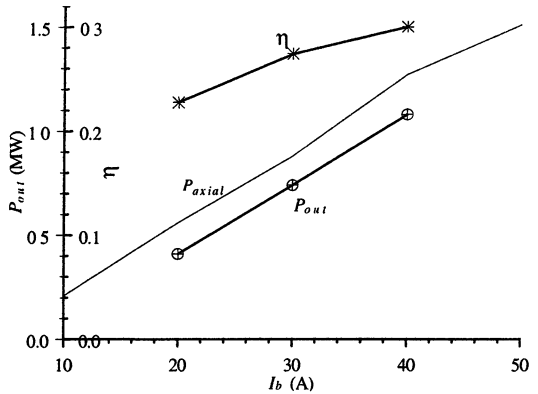

Fig. 2. RF output power and efficiency in the gyrotron with double-beam output ($U_o = 90$ kV; two-step mode converter).

Electron beam energy recovery and frequency tuning. A specificity of the coaxial gyrotron design allows carrying out a natural single-step energy recovery without any additional modifications of the tube. As the most effective mode selection in the coaxial cavities is realized at the closed electron beam and inner conductor radii then an electron beam potential in the interaction space is defined practically by the potential of the inner rod. In this case grounding the collector and gyrotron body (including the cavity outer wall) and choosing an appropriate voltages on the cathode $-U_c$ and on the inner rod $U_{in} \approx U_0 - U_c$ (where U_0 is the design electron beam voltage, $U_c < U_0$) it becomes possible to increase considerably the total efficiency of a gyrotron $\eta \approx \eta_0(U_0/U_c)$ (here η_0 is the efficiency without recuperation). It is limited by the reflection of electrons on the potential barrier after the cavity. Similar scheme can be used also for the step

113

frequency tuning and output power modulation of a coaxial gyrotron. This scheme was checked on the gyrotron with an axial RF output. Corresponding experimental results are presented in Fig. 3, 4.
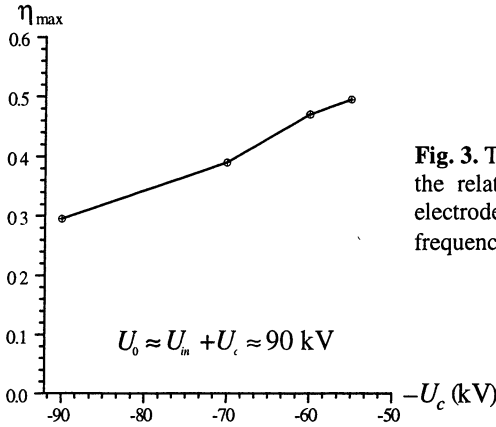

η_{max}

$U_0 \approx U_{in} + U_c \approx 90$ kV

$-U_c$ (kV)

Fig. 3. The total efficiency in dependence on the relation of potentials on the gyrotron electrodes (at the optimum cyclotron frequency mismatch and $I_b \approx 42$ A).
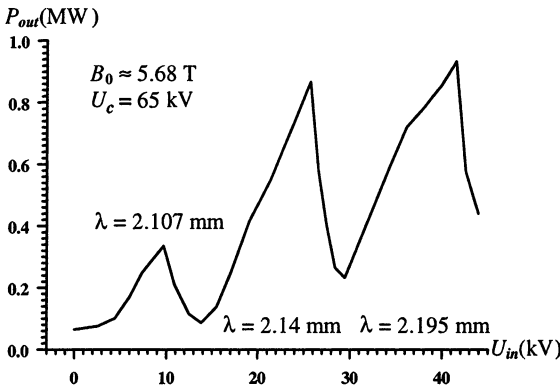

P_{out}(MW)

$B_0 \approx 5.68$ T
$U_c = 65$ kV

$\lambda = 2.107$ mm

$\lambda = 2.14$ mm $\lambda = 2.195$ mm

U_{in}(kV)

Fig. 4. An output power versus the inner conductor voltage (the cathode voltage and external magnetic field are fixed).

Conclusions

The experiments, which already have been performed, give every reason to suppose that rather effective selection of the volume modes can be provided in the coaxial cavities with relative diameters D/$\lambda \approx$ 60 – 70. Taking into account the achievements in the development of CVD diamond output windows and also the parameters of existing cryomagnets, in such situation it becomes possible, in principal, to build the 5 MW coaxial gyrotrons with an acceptable level of heat load density in the cavity on the frequencies up to 170 GHz. Moreover, the use of a two-

potential connection scheme will allow one to approach their efficiency to the efficiency of the conventional tubes with a single-stage depressed collector (without any design complication). Besides that the coaxial cavities gives an additional possibility for the building of the powerful gyrotrons with the frequency step tuning and the deep output power modulation. Now some previous versions of the supermegawatt coaxial gyrotrons are under design at IAP. Their main design parameters are shown in the Table 2 (the choice of frequencies is conditioned by requirements of the ITER program). It should be noted that one of the presented gyrotrons has two operating regimes (95 and 130 GHz). An appropriate regime can be set only by the change of magnetic field and the use of additional cathode coil.

Table 2. Design parameters of the 5 MW coaxial gyrotrons

Operating frequency f (GHz)	95/130	170
Operating mode	$TE_{31,21}/TE_{39,30}$	$TE_{44,44}$
Accelerating voltage U_0 (kV)	150	150
Operating beam current I_b (A)	100	100
Operating magnetic field B_0 (T)	4.4/6	7.9
Pitch-factor α	1.3	1.3
Radius of the cavity R_c (mm)	54.15	56.2
Q_{dif}	1350/2600	3100
Beam radius R_b in the cavity (mm)	16.35/14.7	12.85
RF output power P_{out} (MW)	5	5
Efficiency without recuperation η_0 (%)	≥ 30	≥ 30
Efficiency with recuperation η (%)	≥ 50	≥ 50
Peak wall loading (for real copper) p_Ω (kW/cm^2)	$\approx 0.9/1.5$	≈ 1.7

References

1. *Vlasov S. N., Zagryadskaya L. I., Orlova I. M.* Open coaxial resonators for gyrotrons, Radio Eng. Electron. Physics, vol. 21, p. 96–102 (1976).
2. *Piosczyk B.* et al., A 1.5-MW, 140-GHz, $TE_{28,16}$-Coaxial Cavity Gyrotron, IEEE Trans. Plasma Sci., vol. 25, № 3, p. 460–469 (1997).
3. *Piosczyk B.* et al., Coaxial Cavity Gyrotron with Dual RF Beam Output, IEEE Trans. Plasma Sci., vol. 26, № 3, p. 393–401 (1998).
4. *Lygin V. K., Manuilov V. N., Kuftin A. N., Pavelyev A. B. and Piosczyk B.* Inverse magnetron injection gun for a 1.5-MW, 140-GHz gyrotron, Int. J. Electron., vol. 79, p. 227–235 (1995).
5. *Iatrou C. T., Kern S., Pavelyev A. B.* Coaxial cavities with corrugated inner conductor for gyrotrons, IEEE Trans. Microwave Theory Tech., vol. 44, № 1, p. 56–64 (1996).
6. *Pavelyev A. B., Flyagin V. A., Khizhnyak V. I., Manuilov V. N., Zapevalov V. E.* Investigations of advanced coaxial gyrotrons at IAP RAS, Int. University Conf. "Electronics and Radiophysics of Ultra-High Frequencies" (Russia, St. Petersburg, 1999), p. 142–145.

DEVELOPMENT OF SUBMILLIMETER WAVE GYROTRON FU SERIES

T. Idehara, S. Mitsudo, R. Pavlichenko, I. Ogawa[1],
D. Wagner[2], M. Thumm[3]

Research Center for Development of Far-Infrared Region,
Fukui University, Fukui, Japan
[1]Cryogenic Laboratory, Faculty of Engineering, Fukui University, Fukui, Japan
[2]Institut für Plasmaforchung, Universität Stuttgart, Stuttgart, Germany
[3]Institut für Hochleistungsimpulse- und Mikrowellentechnik,
Forschungszentrum, Karlsruhe, Germany

High frequency, frequency tunable, medium power gyrotrons (Gyrotron FU series) are being developed in Fukui University as millimeter to submillimeter wave sources. The gyrotron series has achieved frequency tunability in a wide range from 38 to 889 GHz and medium output power from 0.1 kW to several kW. For the application to many fields, modulations and stabilizations of both amplitude and frequency of their outputs and high purity mode operation have been achieved. In this paper, the advances in recent three years are summarized.

Introduction

Submillimeter wave gyrotron FU series in Research Center for Development of Far-Infrared Region, Fukui University (FIR FU) has been developed [1] as short millimeter to submillimeter wave radiation source and applied successfully to plasma scattering measurement [2], ESR experiment [3] and a new medical technology [4]. The gyrotron FU series is frequency step-tunable source from 38 to 889 GHz and has many advantages, for example, cw operation in long time [5], modulations of amplitude [6] and frequency [7] and fast switching of frequency [8]. These advantages are useful and convenient for application of the submillimeter wave gyrotron series to many fields.

The advances in recent three years are:
1. Stabilization of the frequency by the phase lock control of beam energy;
2. Accurate frequency measurement of a submillimeter wave gyrotron output using a FIR laser as a reference;
3. High purity mode operation by installation of a carefully designed cavity.

The output frequency of Gyrotron FU IV is stabilized by stabilizing high voltage power supplies for gun anode and cathode. In addition, we apply the phase lock control of beam energy to achieve higher stabilization of the frequency. Both a half width of the frequency spectrum Δf and the frequency fluctuation δf is decreased smaller than 0.3 kHz and 0.1 kHz, respectively. This means that both $\Delta f/f$ and $\delta f/f$ are lower than $1.0 \cdot 10^{-9}$ and $0.3 \cdot 10^{-10}$.

Accurate measurement of gyrotron frequency has been carried out by using a far-infrared (FIR) molecular laser as a reference. Highly stable operation of a FIR laser enables us to make the resolution of frequency measurement so precisely that both the frequency width Δf and the frequency fluctuation level δf can be studied within the accuracy of 1 kHz or less. When our submillimeter wave gyrotron operates in a free-running cw mode, the observed frequency width Δf is around 2 kHz and the fluctuation level δf 10 kHz.

For high purity mode operations, a cavity is designed under collaboration with University of Stuttgart and FZK in Germany and installed in Gyrotron FU VA. The gyrotron emits many modes with high purities. For almost all modes, the purity is higher than 90 percent.

In this paper, such recent advances are described in detail.

First experiment on high stabilization of a frequency by a phase lock control of electron beam energy

We have already achieved the frequency modulation using Gyrotron FU IV [7]. First, the beam electron energy is modulated by the modulation of cathode or body potential. Then, this results in the modulation of cyclotron frequency following the formula $f_c = eB/2\pi m_0\gamma$, where e and m_0 are an electric charge and a rest mass of electron, γ a relativistic factor and B applied magnetic field.

Gyrotrons operate at the electron cyclotron frequency and its harmonics. So, finally, the output frequency of gyrotron can be modulated.

The frequency modulation was recently succeeded under the following conditions, the gyrotron frequency is 301.98 GHz, the operation cavity mode TE_{031}, the maximum amplitude of the frequency modulation 30 MHz. The modulation frequency can be varied up to 40 kHz. This may be useful to apply for communication in submillimeter wavelength region and for scientific applications.

The success of the frequency modulation suggests the possibility of high stabilization of the output frequency by the phase lock control of beam electron energy. We tried an experimental work on this subject. Figure 1 shows a block diagram of the experimental setup. The Gyrotron FU IV operates in a continuous wave (cw) mode using stabilized high voltage power supplies for gun anode and cathode. The output frequency f_0 and power P_0 are 301.128 GHz and around 20 W, respectively. The stabilizations of frequency $\delta f/f$ and output power $\delta P/P_0$ are around 10^{-7} and 10^{-4}. The output power from the Gyrotron FU IV is transmitted through the waveguide system and fed on a harmonic mixer. In the mixer, the gyrotron output signal is mixed with the signal from a synthesizer. The IF signal with a frequency of around 40 MHz is fed on the phase lock loop circuit (PLL) and compared with the signal from a reference oscillator (a crystal oscillator) with a frequency of 40 MHz. The output voltage from PLL is amplified and then applied to the gyrotron body.
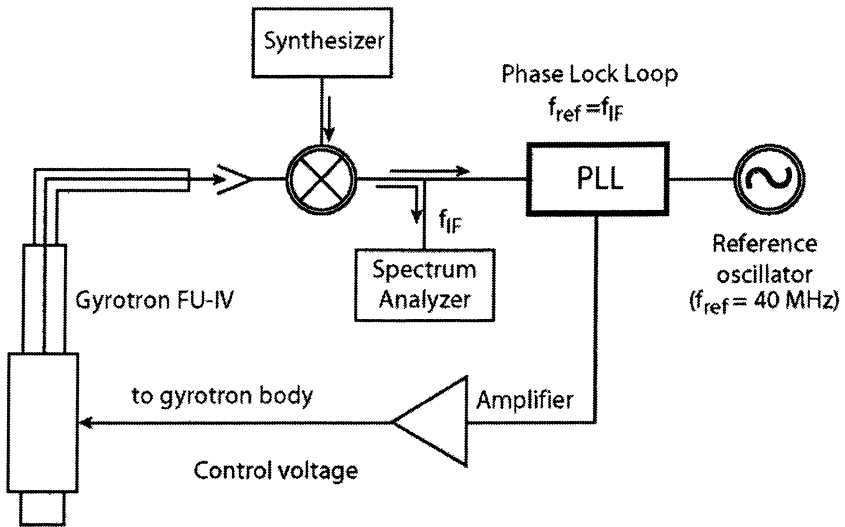
Fig. 1. Block diagram of phase lock stabilization system for a gyrotron frequency. The modulation sensitivity is 16 kHz/V.

A gyrotron cavity is included in the body. Therefore, the energy of beam electron injected into the cavity is modulated by the feedback control voltage, which is generated in PLL. The modulation sensitivity is adjusted at $1.6 \cdot 10^4$ Hz/V, by controlling the amplification factor. This value is much smaller than those of other conventional oscillators, for example, gun diodes, backward oscillators and so on, because gyrotrons are essentially frequency constant oscillators.

Figure 2 shows typically observed frequency spectra with phase lock control (an upper figure) and without phase lock control (a lower figure). During the phase lock control, a half value width of the frequency spectrum Δf and frequency fluctuation width δf are both smaller than 0.3 kHz and 0.1 kHz, respectively. This means that both $\Delta f/f$ and $\delta f/f$ are smaller than $1.0 \cdot 10^{-9}$ and $3 \cdot 10^{-10}$, respectively. On the other hand, without phase lock control, the half value width Δf is around 5 kHz.A phase lock control of the beam electron energy permit a gyrotron operate with much higher stability. This is the first experimental result on phase lock stabilization of frequency in a gyrotron.

Figure 3, *b* shows modulation voltage ΔV_b applied on a gyrotron body as a function of time, while Fig. 3, *a* corresponding observed frequency spectrum. It is seen that the output frequency is being locked by the modulation of the body potential. The amplitude of the modulation is only a few volts.
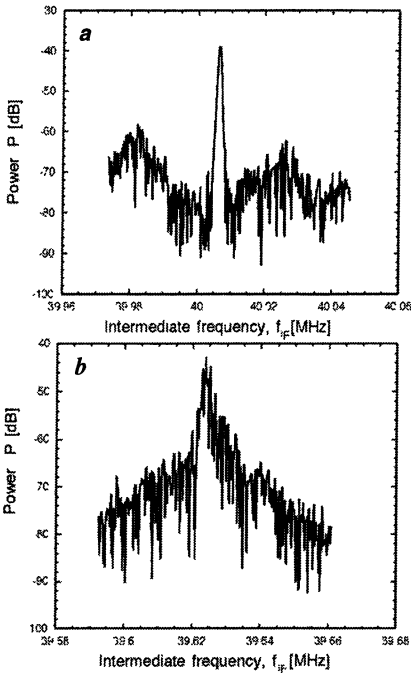
Fig. 2. Observed frequency spectra of Gyrotron FU IV output with phase lock control (*a*) and without phase lock control (*b*). Output frequency of the gyrotron f_g=301.128 GHz. Full sweep time 600 ms; 5 kHz/div.
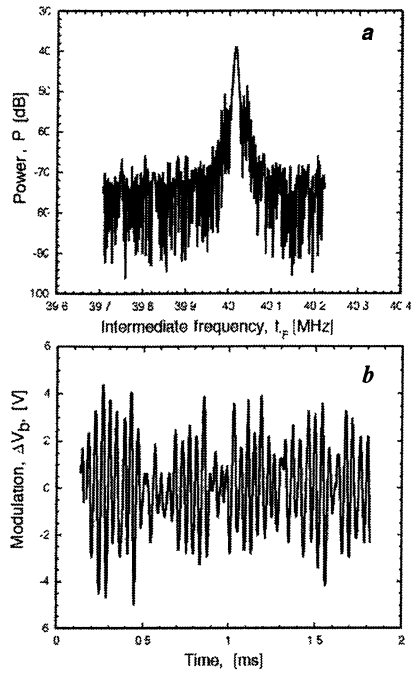
Fig. 3. Frequency spectrum during phase lock control of the body potential. Output frequency of the gyrotron f_g=301.128 GHz. Full sweep time 10 ms; 20 kHz/div (*a*); and corresponding modulation voltage ΔV_b fed on the body as a function of time (*b*).

High stabilization of output frequency enables us to use the gyrotron as a radiation source of spectroscopy in many fields. In addition, Gyrotron FU series in FIR FU is a frequency step-tunable radiation source. The frequency can be changed in the wide range from 38 GHz to 889 GHz. The output power is several ten watts, when it operates in cw mode. Therefore, a high power, high stable submillimeter wave source will be realized.

Accurate frequency measurement
of a submillimeter wave gyrotron output using a FIR laser as a reference

Figure 4 shows the experimental apparatus for accurate measurement of gyrotron frequency using a FIR laser as a reference. Gyrotron FU IV operates in cw mode. The operation frequency is about 295 GHz. The output power is about

119

20 W. It is transmitted through an oversized circular waveguide and fed on a Shottky barrier diode. The real power fed on the diode is 70 mW. The diode operates as a harmonic mixer.
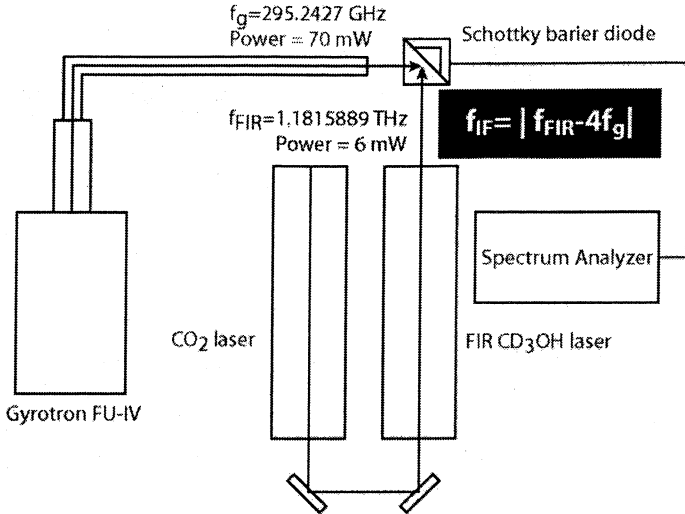

Fig. 4. Block diagram of frequency measurement system using a FIR laser as a reference.

After mixing with the signal from a FIR laser, an intermediate (IF) signal is observed on a spectrum analyzer. The IF signal includes a frequency component of four times of gyrotron frequency $4f_g$. Here, we use CD_3OH laser excited by a CO_2 laser. The frequency f_{FIR} is 1.1815889 THz. And the incident power fed onto the diode is 6 mW.

Before measurement of gyrotron frequency using a FIR laser, we tried it by the use of a synthesizer as a reference. Figure 5 shows a result of the measurement. This frequency spectrum is one of the IF signal, which is obtained by the mixing of gyrotron output with 17-th harmonic of the synthesizer output. Therefore, the signal with the frequency $f = |f_g - 17 f_{tyn}|$ is analyzed. On the frequency spectrum, the half value width Δf can be observed. It is seen that Δf around 20 kHz or wider. This frequency width of IF signal comes mainly from the frequency width of the synthesizer. In this measurement, both the feature of frequency width and frequency fluctuation of the gyrotron can not be resolved so accurately.

Figure 6 shows frequency spectra of IF signal, which are observed by the use of a FIR laser as a reference. In the Figure 6, *a*, the total sweep time is 10 ms. In this case, the observed frequency width is smaller than 10 kHz. A real frequency width of gyrotron output Δf is one fourth of it. Therefore, Δf is around 2 kHz.
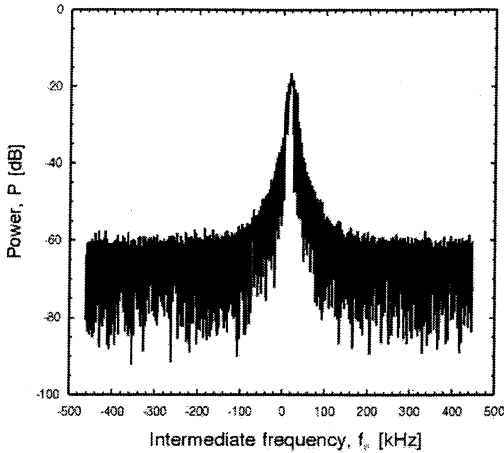
120

Fig. 5. Frequency spectrum of Gyrotron FU IV output measured by using a synthesizer as a reference. Output frequency of the gyrotron $f_g = 295.2427$ GHz.
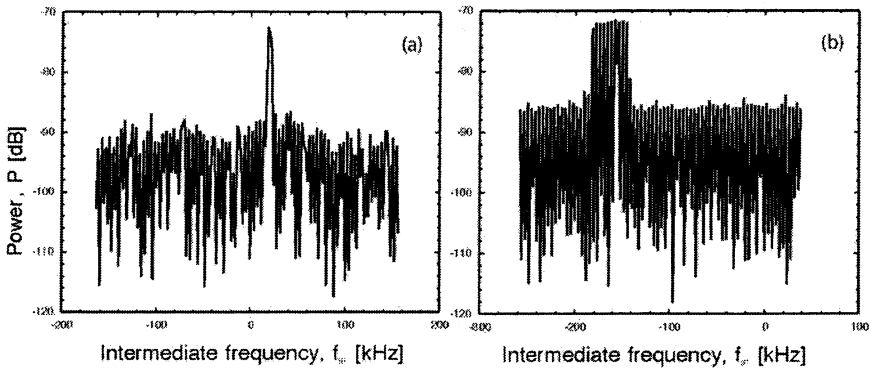

Fig. 6. Frequency spectrum of Gyrotron FU IV output measured by using a FIR laser as a reference. Full sweep time 10 ms (*a*) and 10 s (*b*).

In the Fig. 6, *b*, the total sweep time is 10 s. In the figure, some frequency fluctuations are observed. The width of frequency fluctuation is around 40 kHz. So, the real frequency fluctuation of the gyrotron output is around 10 kHz. Such a frequency fluctuation comes mainly from the fluctuation of high voltage power supplies for an anode and a cathode of electron gun. We should stabilize the power supplies for removing the frequency fluctuation. Highly stable operation of a FIR laser enables us to make such an accurate measurement of gyrotron frequency. The frequency resolution of the measurement is much higher than 1 kHz. This is a convenient and useful tool for development of high quality gyrotrons with stable frequency.

121

High purity mode operation by installation of carefully designed cavity

As can be seen in Fig. 7, Gyrotron FU VA consists of an 8 T liquid-helium free, superconducting magnet and a demountable tube. In the tube, every component, such as the triode magnetron injection gun, the resonant cavity, the transmission waveguide and the vacuum window can be replaced easily. For the work described here, a cavity designed to suppress mode conversion into parasitic modes and to get high-purity mode operation was installed. The profile of the cavity is shown in Fig. 8. At the output end of the cavity, there was a small iris for increasing the quality factor in order to allow low starting currents and a nonlinear up-taper for the suppression of any conversion to parasitic modes. The high frequency electromagnetic wave then travels along a waveguide of diameter 18 mm towards the vacuum window. The whole tube is pumped out first by a turbo-molecular pump and then by an ion pump.

The patterns of the output power radiated from the window are measured by a pyroelectric detector array moving in a plane (the x–y plane in the figure) some distance above the gyrotron window. A fixed pyroelectric detector set outside the scanned area provided a signal to normalize the signal from the array. These signals are fed into a computer, which converts the data into a 3-dimensional plot of the radiation patterns and a lot of equi-power contours in the x–y plane.
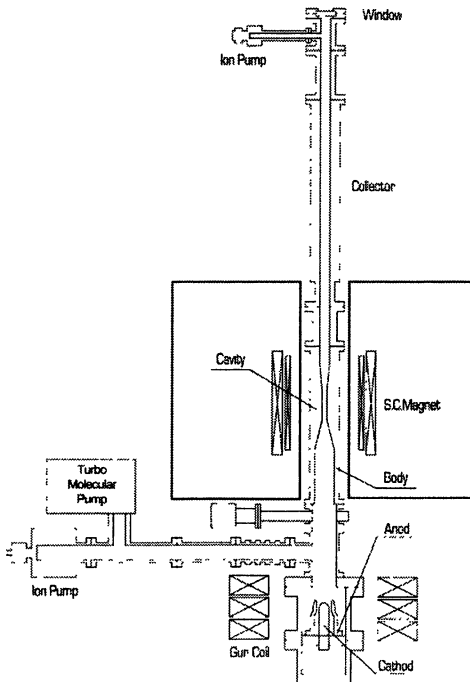

Fig. 7. A schematic drawing of Gyrotron FU VA consisting of a demountable gyrotron tube and a 8 T liquid-helium free superconducting magnet.
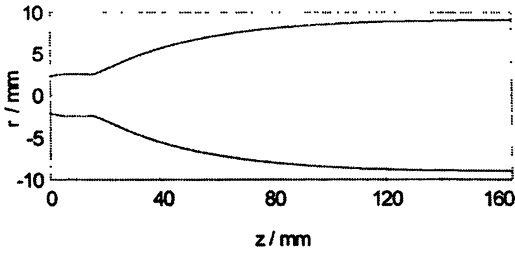
122

Fig. 8. Profile of the resonant cavity installed in Gyrotron FU VA.

Figure 9 shows radiation spectrum of Gyrotron FU VA observed by a pyroelectric detector. The detected power is demonstrated as a function of the magnetic field intensity B_0 applied at the cavity region. Several peaks of detected power are seen in the figure. The operating cavity mode corresponding respective peak is indicated as TE_{mn}.
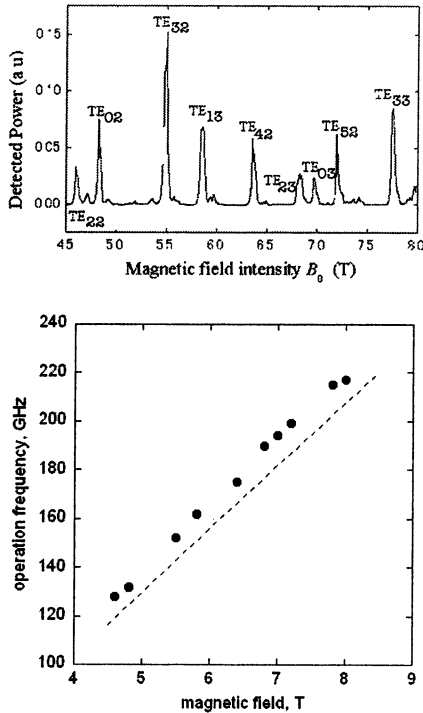

Fig. 9. Radiation spectrum of Gyrotron FU VA as a function of magnetic field intensity B_0 (upper); corresponding operational frequencies as function of magnetic field B_0 (lower). The doted line is first harmonic cyclotron frequency.

123

Table 1 summarizes all of modes observed in Fig. 9, together with corresponding field intensity B_0 and frequency f, which is measured by a Fabry – Perot interferometer. Measured frequencies indicate all of radiations come from the fundamental operations at electron cyclotron resonances.

Figure 10 shows the experimental arrangement. The output waveguide of Gyrotron FU VA can be seen coming out of the bore of its 8T liquid-helium free superconducting magnet. The array of pyroelectric detectors (at the top of the photo) is installed 300 mm above the output window of gyrotron. The distance z between the array and the window can be varried.

Table 1. All of the modes observed in Fig. 3, together with corresponding field intensity B_0 and frequency f

Magnetic field intensity B_0 (T)	Frequency f (GHz)	Cavity mode m, n (TE$_{mn}$)
4.6	128	2, 2
4.8	132	0, 2
5.5	152	3, 2
5.8	162	1, 3
6.4	175	4, 2
6.8	190	2, 3
7.0	194	0, 3
7.2	199	5, 2
7.8	215	3, 3
8.0	217	3, 3

In Figure 11, radiation patterns obtained by the array of pyroelectric detectors are shown for several cavity modes, TE$_{221}$(128 GHz), TE$_{021}$(132 GHz), TE$_{321}$(152 GHz), TE$_{131}$(162 GHz), TE$_{421}$(175 GHz), TE$_{231}$(190 GHz), TE$_{031}$(194.6 GHz), TE$_{521}$(199 GHz) and TE$_{331}$(215 GHz). Each pattern looks pure, in a single mode.

The emission patterns for TE$_{221}$, TE$_{321}$, TE$_{131}$, TE$_{421}$, TE$_{231}$, TE$_{521}$ and TE$_{331}$ modes appear as standing waves in the azimuthal direction. This has been observed previously [3, 4]. The actual ratio of the two oppositely-rotating modes can be determined by a voltage standing wave ratio (VSWR) r measurement following the azimuthal direction θ. As well-known, r is defined as,

$$r = P_{max}/P_{min} = (A_1+A_2)^2/(A_1-A_2)^2, \qquad (1)$$

where P_{max} and P_{min} are maximum and minimum power measured following θ direction for the outside peaks and A_1 and A_2 are amplitudes of rotating and counter-rotating modes.
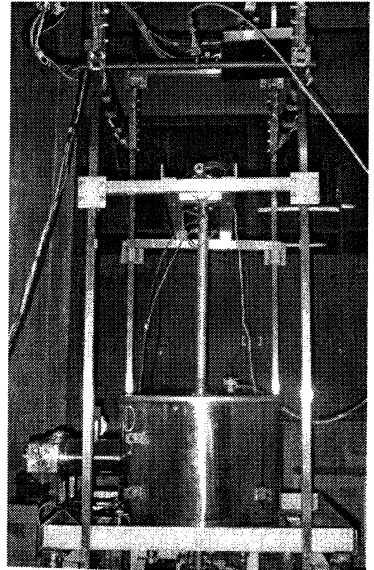

Fig. 10. Experimental arrangement for the measurement of radiation patterns above Gyrotron FU VA.
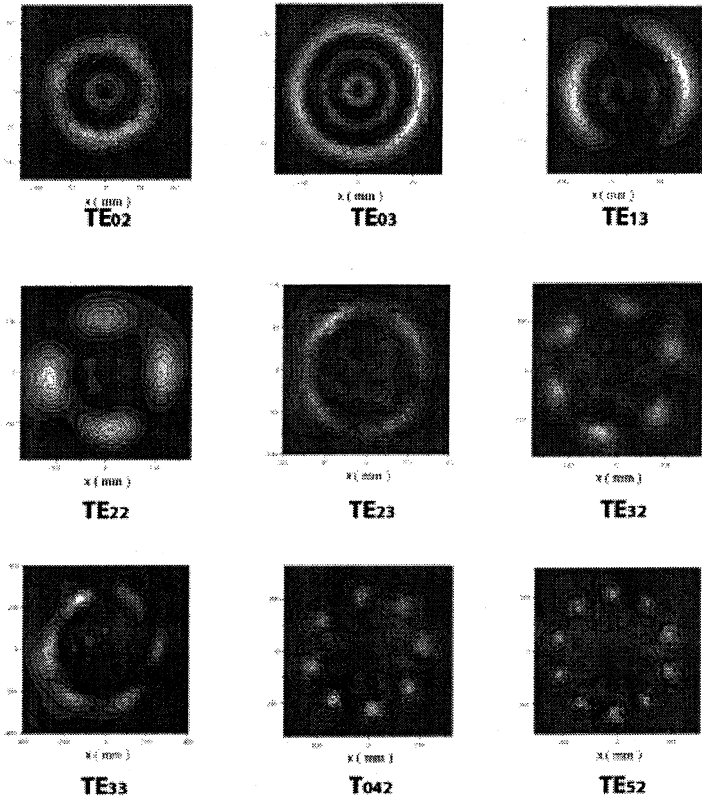
Fig. 11. Emission patterns for the TE_{221}, TE_{131} and TE_{031} cavity modes, obtained by an array of pyroelectric detectors moving in the x–y plane located a distance z above the output window.

Table 2 shows VSWRs estimated from the observed emission patterns and the ratios determined from VSWRs. We are studying the reason why the ratio is so close to one that the mode appears stationary in the azimuthal direction.

Calculations of the resonant frequency and quality factor have been carried out using a scattering matrix formalism. These calculations took into account the complete gyrotron geometry including the slots on the output waveguide for pumping, the connection between the cavity and the collector and the vacuum window [5]. Table 3 summarizes the results of radiation pattern measurements for several main cavity modes TE_{0m1} and TE_{1m1}. As can be seen, in almost all cases, more than 90 percent of the power reaching the window remains in the main cavity mode.

**Table 2. The voltage standing wave ratio (VSWR)
in the azimuthal direction, which is estimated
from the observed emission patterns, and the ratio
of the two oppositely-rotating modes determined from the VSWR**

Main cavity mode	VSWR, ρ	Ratio of rotating mode, percent (in power), A_1	Ratio of counter-rotating mode, per-cent (in power), A_2
TE_{221}	6.25	70	30
TE_{321}	20.66	61	39
TE_{131}	5.17	72	28
TE_{421}	7.72	68	32
TE_{231}	4.73	73	27
TE_{521}	12.76	64	36
TE_{331}	2.30	83	17

**Table 3. The frequencies f, quality factors Q
and mode purity factors η
from the scattering matrix calculations**

Cavity mode	Frequency f (GHz)	Quality factor Q	Mode purity η (percent)
TE_{01}	73.85	251	97.99
TE_{12}	102.36	1020	98.54
TE_{02}	134.40	2910	97.26
TE_{13}	163.37	3109	99.42
TE_{03}	194.57	2603	98.02
TE_{04}	254.63	11569	98.49
TE_{16}	344.13	27712	87.65
TE_{06}	374.63	101064	93.85

Figure 12 shows the calculated results of emission patterns for TE_{221}, TE_{021}, TE_{321}, TE_{131}, TE_{421}, TE_{231}, and TE_{031} cavity modes including the parasitic modes, in the small amounts predicted by the scattering matrix calculations. In the cases of TE_{221}, TE_{321}, TE_{131}, TE_{421} and TE_{231} modes, the counter-rotating modes are also included with the same ratios as determined from the observed patterns. These calculated patterns are in good agreement with the observed patterns. High purity mode outputs like these are desirable for conversion to Gaussian-like beams. In particular, TE_{0n} and TE_{1n} waveguide modes can be converted easily to Gaussian-like beams by a quasi-optical system including a Vlasov antenna and focusing mirrors [6].
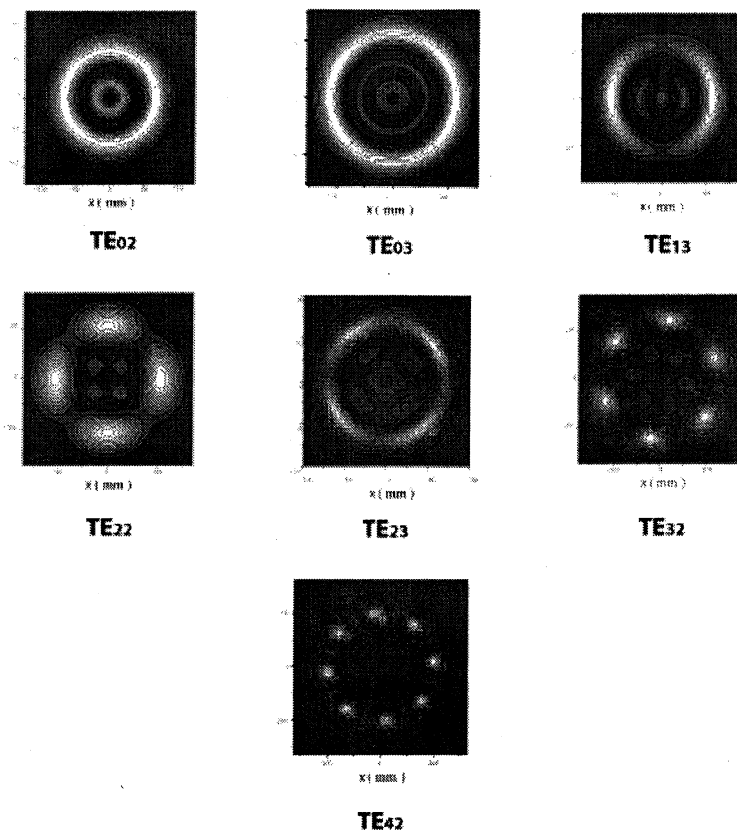
Fig. 12. Calculated emission patterns for the TE_{221}, TE_{131} and TE_{031} cavity modes, including parasitic modes and counter-rotating modes (see text).

Conclusions

For many applications of submillimeter wave gyrotron FU series, output frequency of Gyrotron FU IV is highly stabilized by a phase lock control of electron beam energy. The half value width of the frequency spectrum $\Delta f/f$ and the fluctuation level of the frequency $\delta f/f$ are smaller than $1.5 \cdot 10^{-9}$ and $3 \cdot 10^{-10}$, respectively. First experiment on the phase lock control of electron beam energy for high stabilization of the gyrotron have been made.

By the use of a FIR laser as a reference, we have succeeded the highly accurate measurement of gyrotron frequency. The frequency resolution of the measurement is higher than 1 kHz. During free-running cw operation, real frequency

width Δf and the frequency fluctuation δf of the gyrotron are around 2 kHz and 10 kHz, respectively. Such an accurate measurement of frequency will be a powerful tool for supporting our future development of high quality gyrotron with stable frequency, which is useful for spectroscopy in many fields.

Gyrotron FU VA with its carefully-designed cavity has achieved high purity mode operation in several cavity modes. In the case of the TE_{221}, TE_{021}, TE_{321}, TE_{131}, TE_{421}, TE_{231}, and TE_{031} cavity modes. The calculations based on a scattering matrix formalism are in good agreement with the observed patterns. The next step, now underway, is to employ a quasi-optical system for conversion from the high purity mode to a Gaussian-like beam.

References

1. *Idehara T., Ogawa I., Mitsudo S., Pereyaslavets M., Nishida N. and Yoshida K.*, IEEE Trans. Plasma Sci., **27**, 340 (1999).
2. *Ogawa I., Yoshisue K., Ibe H., Idehara T. and Kawahata K.*, Rev. Sci. Instrum., **65**, 1788 (1994).
3. *Mitsudo S., Aripin, Shirai T., Matsuda T., Kanemaki T. and Idehara T.*, Int. J. Infrared and Millimeter Waves, **21**, 661 (2000).
4. *Tatsukawa T., Doi A., Teranaka M., Takashima H., Goda F., Idehara T., Ogawa I., Mitsudo S. and Kanemaki T.*, Int. J. Infrared and Millimeter Waves, **21**, 1155 (2000).
5. *Idehara T., Yoshida K., Nishida N., Ogawa I., Pereyaslavets M. and Tatsukawa T.*, Int. J. Infrared and Millimeter Waves, **19**, 793 (1998).
6. *Idehara I., Shimizu Y., Makino S., Ichikawa K., Tatsukawa T., Ogawa I. and Brand G. F.*, Int. J. Infrared and Millimeter Waves, **18**, 391 (1997).
7. *Idehara I., Pereyaslavets M., Nishida N., Yoshida K. and Ogawa I.*, Phys. Rev. Lett., **81**, 1973 (1998).
8. *Idehara T., Shimizu Y., Ogawa I., Tatsukawa T. and Brand G. F.*, Phys. Plasmas, 6, 2612 (1999).

SIMULATIONS AND DESIGN
OF A HIGH HARMONIC GYROTRON
WITH A PERMANENT MAGNET SYSTEM

V. Zapevalov[1], T. Idehara[2], S. Sabchevski[3], K. Ohashi[4], V. Manuilov[5], M. Glyavin[1], S. Kornishin[1], A. Kuftin[1], V. Lygin[1], O. Malygin[1], M. Moiseev[1], A. Pavel'ev[1], V. Tsalolikhin[1], N. Zavolsky[1], H. Kobayashi[4], T. Yokoyama[4], I. Ogawa[6], S. Mitsudo[2], T. Kanemaki[2], Y. Iwata[2], H. Hoshizuki[2]

[1]Institute of Applied Physics, Russian Academy of Sciences,
GYCOM Ltd., Nizhny Novgorod, Russia
[2]Research Center for Development of Far-Infrared Region,
Fukui University, Fukui, Japan
[3]Institute of Electronics of the Bulgarian Academy of Sciences, Sofia, Bulgaria
[4]Magnetic Materials R&D Center,
Shin-Etsu Chemical Co., LTD, Takefu-shi, Fukui, Japan
[5]Nizhny Novgorod State University, N. Novgorod, Russia
[6]Faculty of Engineering, Fukui University, Fukui, Japan

The paper presents results of a numerical analysis and design of a gyro-device with the beam of electrons moving along the axis-encircling trajectories. The electron beam is formed by the low potential CUSP type electron gun with a thermocathode. The results of a numerical simulation predict satisfactory performance of this gun producing a high quality electron beam. Tube design allows one to install different cavities optimized for excitation of $TE_{4,1}$ mode at the fourth harmonic of the cyclotron frequency or $TE_{3,1}$ mode at the third one. The target parameters of the device are the frequency about 107 GHz, the output power near 1 kW and the efficiency of several percent.

Introduction

Powerful sources of high-frequency microwave radiation are in demand for great and continuously expanding number of applications in the basic research and technology. In many respects the gyrotrons are superior to other devices due to high output power level and efficiency in millimeter and submillimeter wavelength ranges. Medium power CW and quasi-CW gyrotrons can be used for high-temperature processing of a number of materials, super-high-resolution spectroscopy, medical radiology and other applications. Most of the applications require the radiation sources to be compact and simple in operation. Therefore, creation of systems is of interest on the basis of permanent magnets to lower setup dimensions and weight, to simplify and economies service. However, due to limit of magnetic field of present permanent magnets, for millimeter wave generation such device needs high harmonic operation that aggravates the mode selection problem. A relatively new scheme known as large orbit gyrotron (LOG) [1–3], allows this problem to be overcome. The group of similar microwave

129

sources is represented by devices where electron beam is composed of axis-encircling individual particle orbits with Larmor radius comparable to the cavity radius. Such a beam couples only with co-rotating modes having azimuthal indices equal to the resonant harmonic number. These modes also are attractive in that they suffer less mode competition. It leads to greater mode selectivity. As the harmonic number for such scheme of operation can be significantly greater as compared with traditional gyrotrons, the magnetic field requirements for millimeter wave range gyro-devices with an axis-encircling beam is greatly reduced. Moreover, required fields may be obtained using compact permanent magnets, allowing smaller, lightweight and portable systems.

As against the majority of known devices, in given paper it is described LOG with rather low accelerating voltage and current (less than 40 kV, 2 A) and magnetic system based on permanent magnet (about 1 T field), that as promotes depreciation, dimensions, simplicity in operation etc. [4].

Permanent magnet system

A magnet system is based on recently designed and fabricated permanent magnets (PM) using NdFeB magnetic material. This system has 60 mm operating hole diameter and creates 1 T magnetic field with the homogeneous length of about 45 mm in the cavity region.

Several magnetic circuits was investigated and finely tuned in order to manufacture the magnet circuit in practice. Also, the magnet circuit was tested at 30 °C using rubber heater to keep an invariable magnetic field distribution in spite of temperature fluctuations. Parameters of the system were adjusted so that to provide the calculated magnetic field structure in the area of an electron gun, answering the purpose of optimum formation of an electron beam and extended enough homogeneous length of the field in the cavity region. For numerical simulation the finite integral method was used. Magnetic field generated from a ring magnet with an axial magnetization in an inner bore is not so strong, while its distribution has a long enough flat region. Magnetic field generated from a ring magnet with a radial magnetization is high and its distribution has a sharp peak. Magnetic field in a PM type gyrotron has to be both a high peak value and a flat top with a moderate width. So, the hybrid type consisted of radially oriented and axially oriented rings seems to be the most favorable structure for this use. A good electron beam orbits were obtained in the improved model (C13) by simulation. So, the magnet circuit based on this model was manufactured. The obtained magnetic field strength and its distribution were well coincided to the calculated ones after field adjustment. The electron beam orbits modeling based on the measured parameters shows good results. The photo of permanent magnet and its general scheme are given on Fig. 1. Total weight of magnetic system is 405 kg.
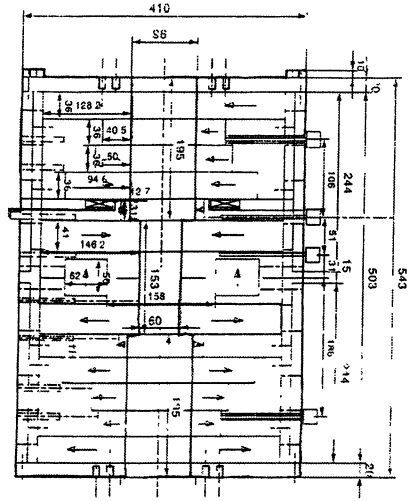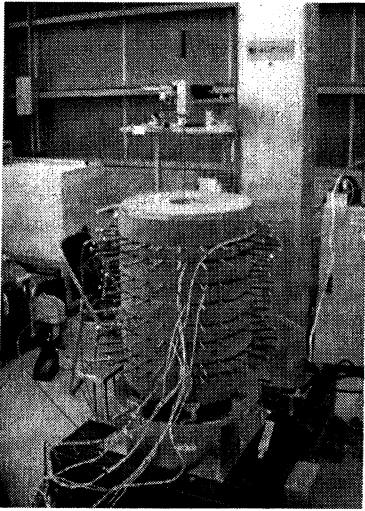
Fig. 1. General view of permanent magnet

Electron gun design

Efficient operation of gyro-devices depends critically on the helical electron beam quality. Therefore, the electron gun performance is of paramount importance for the overall efficiency of the entire system. Basic requirements, which should be satisfied by the design of the gun, are: formation of high quality electron beam with small velocity spread, optimum value of pitch-factor and geometrical parameters ensuring an effective interaction with operating mode; simple electrode configuration, which is not very sensitive to the fabrication tolerances and allows rather easy adjustment.

The choice of the configuration of the gun and magnetic field distribution is as a rule a compromise between some contradictory requirements. The final geometry of the electrodes for real magnetic field distribution that satisfies design requirements is shown in Fig. 2. As the cathode operates in a temperature limited mode the beam current can be increased by augmenting the emitter temperature. The required magnetic field was found after numerous trials with different profiles of the axial magnetic field. Detail analysis of electron beam taking into account the influence of own beam space charge forces and the real (non-paraxial) magnetic field distribution shows important role of these effects.

Another important problem is the high sensitivity of electron beam parameters to gun position along longitudinal axis. The analysis of effects of electrodes position change (both the breakage of their position relatively each other because of the thermal drift and the shift of a gun as a whole concerning the center of the magnet by virtue of tube installation errors) shows rather high

requirements to the accuracy of gun components axial position – about of 0.2 mm from calculated one. Additional coil allows to compensate discrepancy in position up to 1 mm.

GEOMETRY OF THE ELECTRON-OPTICAL SYSTEM
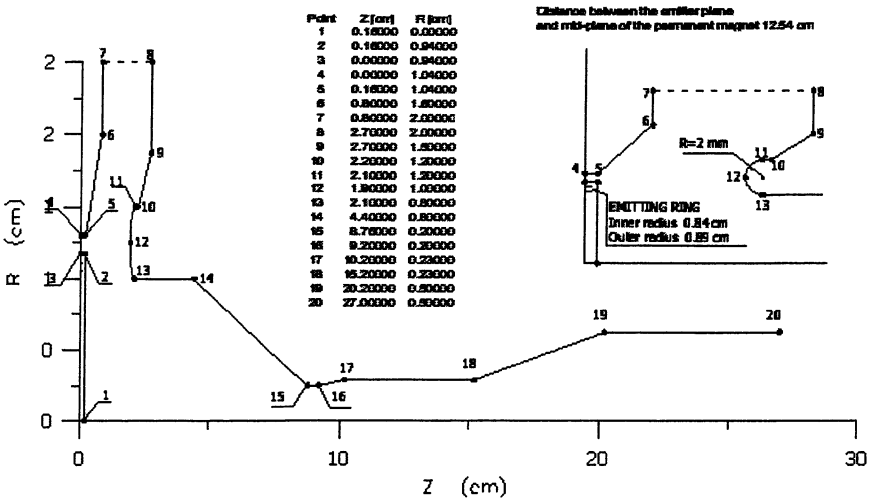(optimized for the measured distribution of the magnetic field)

Point	Z[cm]	R[cm]
1	0.16000	0.00000
2	0.16000	0.94000
3	0.00000	0.94000
4	0.00000	1.04000
5	0.16000	1.04000
6	0.80000	1.60000
7	0.80000	2.00000
8	2.70000	2.00000
9	2.70000	1.50000
10	2.20000	1.20000
11	2.10000	1.20000
12	1.90000	1.00000
13	2.10000	0.80000
14	4.40000	0.80000
15	8.70000	0.20000
16	9.20000	0.20000
17	10.20000	0.22000
18	15.20000	0.23000
19	20.20000	0.50000
20	27.00000	0.50000

Distance between the emitter plane and mid-plane of the permanent magnet 12.54 cm

R=2 mm

EMITTING RING
Inner radius 0.84 cm
Outer radius 0.85 cm

Fig. 2. Geometry of the electrodes for real magnetic field distribution

Cavity design and output regimes simulation

As initial data for the numerical modeling the beam parameters obtained from simulation of an electron gun with real magnetic field were used. The analysis of modes starting currents predicts strong dependence of minimum starting current value on accelerating voltage, pitch-factor and cavity length. It can be seen that the increase of the harmonic number has two distinct consequences. First, it leads to the growth of minimum starting currents and, second, for higher harmonics the resonant zones become narrower. It is obvious that for the given beam parameters and magnetic field the highest mode which can be excited is $TE_{4,1}$ at forth cyclotron harmonic. Therefore, this mode was selected as operating one in the LOG under consideration. From other hand, in order to reduce the starting current the length of the interaction space ought to be increased, but this results in a significant growth of the ohmic losses. Thus the choice of the cavity length always is a compromise between contradictory requirements. Additionally, there are technological problems to produce permanent magnet with long uniform region (flat-top region) as well as long cavities of precise small radius. Taking into account all these considerations the length of the cavity was chosen to be about 50 mm.

Results of computer simulation of the mode excitation using the self-consistent physical model are presented in Fig. 3 as the LOG output power, efficiency and frequency versus the value of static magnetic field. Although the neighbouring modes were taken into account, this Figure indicates that they are not excited and a single mode operation takes place. At the first stage the electron beam without velocity spread and ripple was assumed. Two maximums at output power corresponds longitudinal RF distribution with one and two maximums (at higher magnetic field the mode with two maximums is excited). At low value of pith-factor, operation zone is very narrow and efficiency is low, but efficiency increases rapidly with pitch-factor growth. Maximum output efficiency is about 1.2% with relatively narrow operating zone. Naturally, important observation concerns the optimum value of the magnetic field in the cavity. It is clear that additional coils for fine adjustment of this field are required. Design cavity additional coil predict magnetic field variation about 0.02 T, that is quite enough to surpass completely the operation zone. As to undesirable excitation of parasitic modes in the output taper after the cavity, for real tube profile the calculated operating mode purity is not less than 95%.
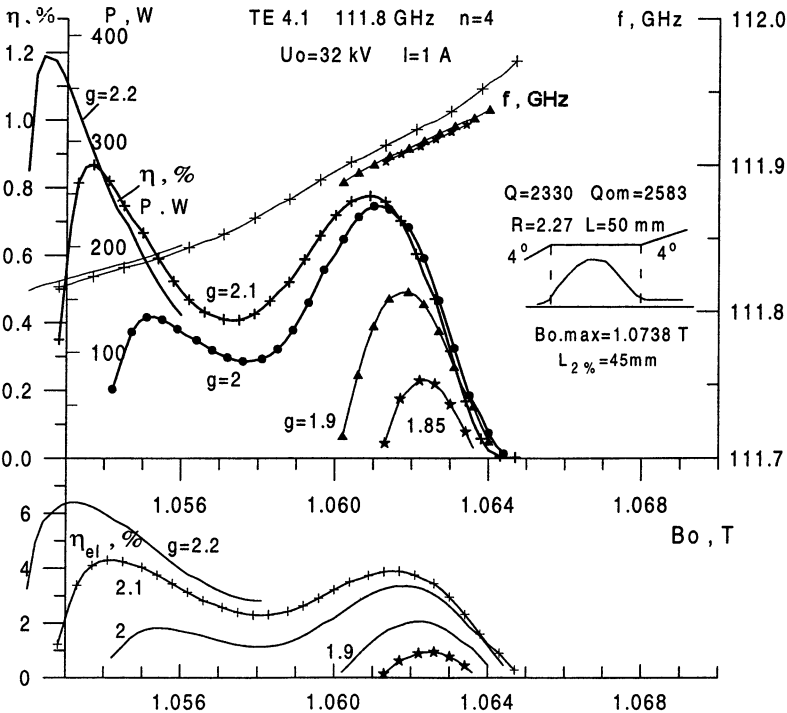
Fig. 3. Output power and efficiency versus magnetic field and pith-factor

133

As calculations shows, small velocity spread does not effect strongly on mode excitation and maximum power. But for velocity spread 20–30% and pitch-factor g~2 efficiency becomes only about 0.5% (in place of 0.8% without velocity spread).

All aforesaid shows a lot of difficulties of effective gyrotron operation at the 4 harmonic. More optimistic result was observed for $TE_{3,1}$ mode at the 3 harmonic of gyrofrequency. Here, for pitch factor g~2 output power was more than 2 kW and output efficiency – of about 6%.

Conclusions

Numerical simulations predict the frequency about 107 GHz, the output power near 1 kW and the efficiency of several percent for LOG tube with axis-encircling electron beam. The experimental test of the tube is planning to the end of 2002. In combination, the predicted output power and frequency of the radiation makes such tube suitable for different applications in the basic research and technology. Additionally, it is hoped that such device will be an excellent tool for accumulating knowledge and experience needed for development of more effective gyro-devices with more powerful axis-encircling beams.

References

1. *McDermott D. B., Luhmann N. C. Jr.*, Pupiszewski A. Phys. Fluids, **26** (7), 1936 (1983).
2. *Lawson W., Latham P. E.*, J. Appl. Physics, **61** (2), 19 (1987).
3. *Bratman V. L., Fedotov A. E., Kalynov Y. K.* et al., IEEE Transactions on Plasma Science, **27** (2), 456 (1999).
4. *Sabchevski S., Idehara T., Glyavin M.* et al., Int. J. Vacuum, **62** (2–3), 133 (2001).

POWERFUL SOURCES OF COHERENT
SUBMILLIMETER-WAVE RADIATION

V. L. Bratman, B. S. Dumesh[1], A. E. Fedotov, V. N. Manuilov,
Yu. K. Kalynov, M. M. Ofitserov, F. S. Rusin[2], S. V. Samsonov

Institute of Applied Physics, Russian Academy of Sciences, Nizhny Novgorod, Russia
[1]Institute of Spectroscopy, Russian Academy of Sciences, Moscow, Russia
[2]Institute of Metrology for Time and Space, Mendeleevo, Moscow region, Russia

The paper describes two types of submillimeter-wave oscillators being developed at IAP: high-harmonic gyrotrons and orotrons. In the gyrotrons, new electron-optical systems that produce thin axially-encircling electron beams are used. A prototype of the submillimeter gyrotron generates 100 kW of output power at the 3rd and 4th cyclotron harmonics at the frequencies of 110 and 130 GHz, respectively. Based on these results, two projects of third-harmonic pulsed gyrotrons with electron energy of 250 and 80 keV have been designed for frequencies of 0.4 and 1.0 THz. The relativistic orotron with electron energy of 200 keV at the frequency of 150 GHz has been designed and fabricated as a prototype of a powerful frequency-tunable submillimeter-wavelength oscillator. A pulsed non-relativistic orotron generating the output power of 50 mW at the frequency up to 380 GHz is also realized.

Introduction

The submillimeter-wave band is one of last weakly-developed electromagnetic ranges. At the same time, this band is very attractive for a number of applications, such as spectroscopy and diagnostics of different media, astrophysics and astronomy, communication systems and environmental quality monitoring. At present, submillimeter-wavelength backward-wave oscillators (BWOs) or free-electron lasers (FELs) are used for most applications. However, for some applications other types of RF oscillators, such as gyrotrons and orotrons, can be more convenient. Subrelativistic gyrotrons with a kilowatt level of output power and higher seem simpler than the expensive FELs and can replace them in some situations. Orotrons can provide a higher output power and a better frequency stability than BWOs. In spite of successful experiments, gyrotrons and orotrons are still seldom used in the submillimeter wavelength range. Further development of these radiation sources can provide new possibilities for many applications.

High-harmonic gyrotrons

First gyrotron operation at submillimeter waves was demonstrated at IAP 30 years ago. At the frequency of 330 GHz their output power amounted up to 1.5 kW in CW regime [1]. In 1980s a gyrotron with a strong pulsed magnetic field provided 40 kW of the output power in single 100 μs pulses at the frequency of 650 GHz [2]. Generation of kW-level power at the frequency of

500 GHz was demonstrated also at MIT [3]. CW gyrotrons with output power of tens of Watts were realized at Sidney University at the frequencies up to 600 GHz [4] and at Fukui University at the frequencies up to 890 GHz [5].

The final purpose of the works started recently at IAP is development of powerful submillimeter-wave gyrotrons with the operating frequency up to 1 THz. Along with traditional gyrotrons, the Large Orbit Gyrotrons that operate at higher cyclotron harmonics are also developed. The operation at cyclotron harmonics allows achievement of higher frequencies with lower magnetic fields as compared with the traditional gyrotron at the fundamental cyclotron reso-nance. Thus, the highest frequency of gyrotron operation was achieved at the second cyclotron harmonic [5]. Unlike the experiments [1–5], the Large-Orbit configuration of Gyrotron (LOG) is chosen in new studies at IAP in order to sim-plify the competition with parasitic modes at the fundamental cyclotron reso-nance. The only principal difference between LOG and traditional gyrotron is the shape of the electron beam. In a traditional gyrotron, the beam consists of con-tinuous totality of Larmor cylinders. In a LOG [6–9], all electrons rotate around the axis of electrodynamics system, so that the beam represents one Larmor cyl-inder or even one Larmor helix. Due to such geometry, a very strong rule of mode selection is realized in LOGs. In the case of an ideally thin and centered beam (so-called axis-encircling beam), only modes with the azimuth index equal to the resonance harmonic number can be excited. Such a method of mode selec-tion was also successfully used in the experimental realization of millimeter-wave CARMs [10], gyro-TWTs and gyro-BWOs [11].

As the first step to submillimeter-wavelength LOGs, the 3rd, 4th and 5th har-monics were selectively excited using a gyrotron with explosive emission gun [9]. This gun produced a 300 keV / 30 A / 20 ns pencil electron beam, which was then pumped by a kicker in order to impart a transverse velocity to electrons. The modes $TE_{3,1}$, $TE_{4,1}$ and $TE_{5,1}$ at the wavelengths of 6.1, 4.8 and 4.0 mm, respec-tively, were used as the operating modes. The output power of about of 600, 200, 120 kW was obtained at the 3rd-5th harmonics, correspondingly.

The results obtained for the short-pulse LOG have been used to design and realise a long-pulse LOG with a thermionic electron gun at the 3rd and 4th cyclo-tron harmonics at the wavelengths of 2.6 and 2.3 mm, respectively. The gun was designed to produce the electron beam with energy of 200–250 keV, current of 10 A and pitch factor $g = 1.2$–1.5 in a resonant magnetic field of 1.6–2.0 T. To produce such a beam, a two-stage electron-optical system was used [12]. First a thin electron beam with its diameter 0.6 mm was formed, and then the electrons acquired the necessary transverse velocity passing through a kicker. Compared to the short-pulse prototype, the use of a thermionic emitter allows using the total emitted current, though complicates the formation of a dense rectilinear beam. For the conventional current density from thermionic cathodes, 5 A/cm^2, the beam cross-section should be compressed by more than 1000 times. To achieve such compression without excitation of large transverse velocities before the

kicker, a system that provided electron trajectories parallel to the guiding magnetic field lines was used. The electron-optical system was designed so that the electron trajectories near the cathode were determined by the electrostatic field of the "Pierce-like" electrodes and the space-charge fields. A system of magnet coils was configured to match the axial magnetic field profile to the particle trajectories. When the electrons achieve the region of a sufficiently strong magnetic field, a conventional adiabatic compression decreases the beam diameter to the required level (Fig. 1). In the area where the magnetic field was of about 0.5 T, the kicker was located. After the kicker, the electron transverse velocity was increased further in the tapered guiding magnetic field.

A traditional axi-symmetrical gyrotron cavity consisting of a cut-off narrowing at the beam injection end, a cylindrical part (6.7 mm in diameter and 22 mm long), and an output taper, was used. The stable selective excitation of the operating modes $TE_{4,2}$ and $TE_{3,2}$ was observed at magnetic fields 1.67–1.75 T and 1.92–1.99 T, respectively. The selective excitation of the proper modes was confirmed by measurement of the wavelength and transverse structure of the output radiation. A maximum efficiency, 4 % for the $TE_{4,2}$ mode and 5 % for the $TE_{3,2}$ mode,
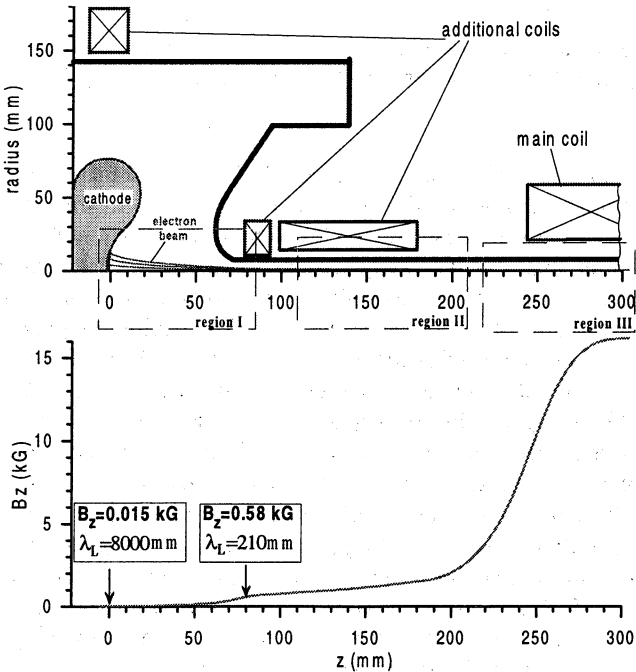
Fig. 1. Electron-optical system, forming the rectilinear beam, and magnetic field profile in the relativistic millimeter-wavelength LOG.

137

was achieved at the current of 4–6 A (Fig. 2). The maximum power of 80–100 kW was measured at the efficiency of 3.5 % for the both modes. The same gyrotron allowed a stable selective generation of the $TE_{4,2}$ operating mode at the 4th cyclotron harmonic for lower electron energies down to 130 keV.
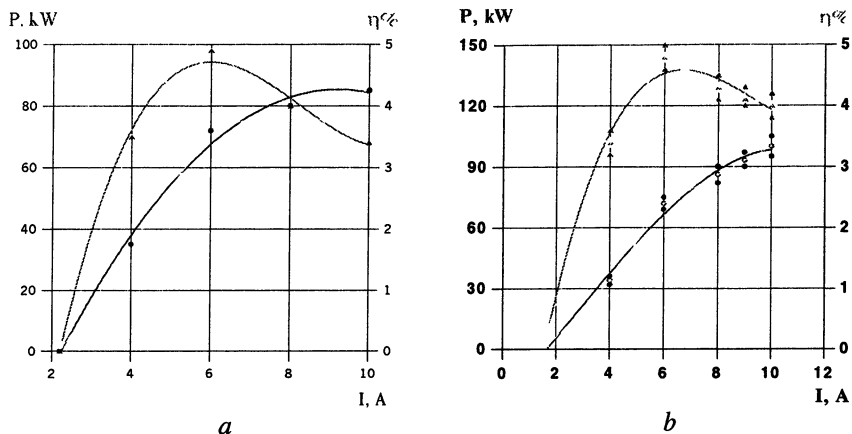
Fig. 2. Dependence of the output power and efficiency on the beam current for modes $TE_{3,2}$ (*a*) and $TE_{4,2}$ (*b*) in the relativistic millimeter-wavelength LOG.

Based on the results for beam formation and for generation of millimeter waves, a submillimeter-wave LOG was designed (Fig. 3a). In this planned experiment, the operating wavelength at the 3rd cyclotron harmonic will be 0.8 mm, i.e. 4 times shorter than in the previous experiment. Almost the same electron optical system with electron energy of 250 keV, but approximately 4 times higher magnetic field in the cavity will be used. The required magnetic field of 6.6 T is typical for modern CW short mm-wave gyrotrons. The value of the magnetic field at the cathode area and in the region of the kicker will not be changed. Correspondingly, a higher ratio of magnetic compression up to 4,000 is needed. In order to achieve the required level of parasitic electron transverse velocity before the kicker, the electron current is decreased down to 3 A. The operating mode $TE_{3,4}$ with high radial index is chosen to decrease Ohmic losses and simplify fabrication of the cavity. According to calculations, this operating mode can be selectively excited in spite of a few close parasitic modes. Calculations show that efficiency of 5 % and output power of tens of kW can be obtained at the 3rd harmonic. In principle, this value can be significantly enhanced using optimization of the cavity shape and magnetic field distribution.

One more challenging LOG project is now under development at IAP (Fig. 3b). The purpose of this project is to achieve the frequency of 1 THz at the kW-level of output power. The project is to be realized at the typical gyrotron
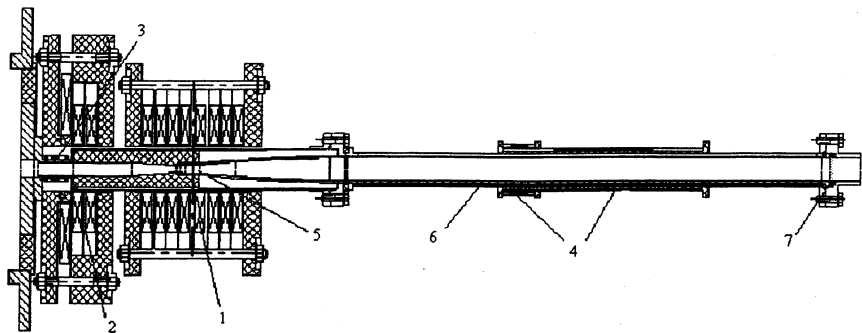
Fig. 3a. Scheme of the relativistic submillimeter-wavelength LOG: *1* – main solenoid, *2* – additional solenoid, *3* – kicker, *4* – collector coil, *5* – cavity, *6* – collector, *7* – output window.
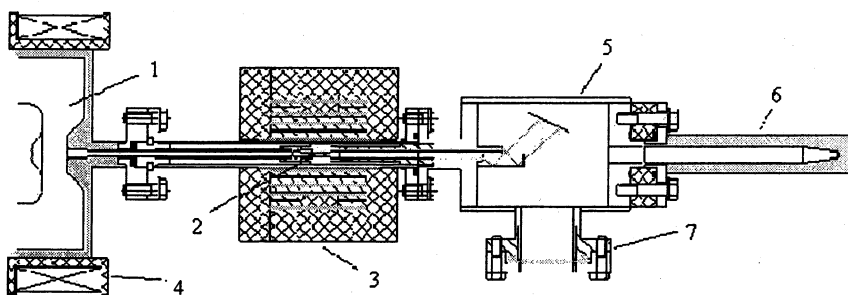
Fig. 3b. Scheme of the subrelativistic terahertz LOG: *1* – cusp gun, *2* – cavity, *3* – main solenoid, *4* – negative cathode coil, *5* – quasi-optical converter, *6* – collector, *7* – output window.

electron energy of 80 keV. Then at the 3rd cyclotron harmonic the operating frequency of 1 THz can be achieved at a relatively moderate magnetic field of about 14 T. According to numerical simulations, the method of two-stage beam formation used earlier is not effective in the situation of a relatively low electron energy and a high magnetic field because of a too large particle spread in velocity and positions of the guiding centers of particles. So, another method using the magnetic cusp near the cathode is considered. In this method, particles are pumped up to some transverse velocity practically from the very beginning, in the region of reverse of magnetic field. After that, transverse velocity increases up to the operating value in tapered magnetic field (the magnetic field increased by 3,000 times). This method was already successfully realized recently with a lower compression in gyro-TWTs and BWOs [13]. According to simulations, the

139

beam with operating current of about 1A and with a rather large electron pitch-factor at a low velocity spread can be obtained in such a system. The calculated efficiency of the gyrotron utilizing such a beam amounts to a few percent at the output power of 1 kW.

Orotrons

For many applications, a significantly lower power is needed as compared to the output power of gyrotrons. Application of submillimeter gyrotrons is compli-cated by the requirement of creation of a strong magnetic field. The magnetic field can be significantly lower in Cherenkov devices based on radiation of elec-trons moving near periodic electrodynamical structures. The magnetic field in these devices is used only for electron beam transportation. However, only BWOs are now used for applications at submillimeter waves. Development of another submillimeter Cherenkov oscillators, namely relativistic and non-relativistic orotrons, is carried out at the Institute of Applied Physics in collabora-tion with the Institute of Metrology for Time and Space, the Institute of Spectros-copy RAS and GYCOM Ltd. The main feature of the orotron [14], or Generators of Diffraction Radiation [15], (unlike other Cherenkov-type devices) is the use of an open cavity providing effective selection of transverse modes. It allows in-creasing the transverse dimensions of interaction region and, therefore, increasing the electron beam current and output RF power. Another advantage of using an open cavity is the high Q-factor that provides high stability of the generation fre-quency. For some applications, it makes it possible to work even without a sys-tem of automatic frequency control. At the same time, the high Q-factor leads to a narrow band of fine (electronic) frequency tuning. One should notice that the open cavities that are used also in gyrotrons, and the methods of feedback reali-zation in gyrotrons and orotrons are very similar.

The purpose of the relativistic orotron project is development of a submilli-meter-wave frequency-tunable oscillator with output power of several tens of kW. To date, the orotron with the operating wavelength of 2 mm has been con-structed and manufactured. The design of this oscillator is based on using a thin rectilinear electron beam with high current density created for the relativistic mm-wave LOG (see above). The small transverse size of the beam (its diameter is 0.6 mm) allows guidance of the electrons close to the periodic structure and, therefore, providing a strong interaction between the electrons and the RF field. In this experiment the flat mirror of the two-mirror open cavity is covered with a comb structure of the 0.7 mm period. The electron beam moves inside the comb in the aperture 1 mm in diameter. The concave mirror is tapered to provide a quasi-optical RF power output from the cavity, similar to the traditional schemes of power output in gyrotrons (Fig. 4). According to the results of numerical simu-lations as well as to the "cold" cavity tests and electron-optical experiments, the output power of 10–30 kW and the step frequency tuning in the 15 % band can

be obtained for such a device. If the experiments with the millimeter-wave orotron are successful, the device with the radiation wavelength of 0.8 mm will be developed.
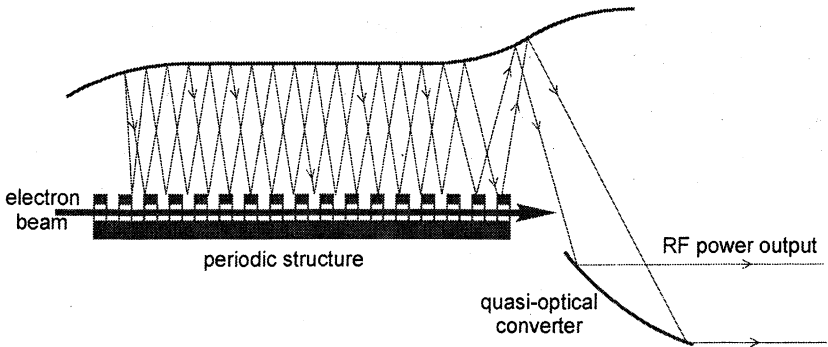

Fig. 4. Scheme of relativistic orotron

The relativistic orotron at short millimeter and submillimeter waves is not realized yet, but non-relativistic low-voltage devices exist already [16]. An orotron with the frequency band of 120–300 GHz was constructed and experimentally tested. In this device (Fig. 5), a multiple-rod periodic structure with the 0.12-mm-period and 0.7-mm-height rods was used. The maximal operating voltage and beam current were 4.5 kV and 250 mA at pulse duration of 3–10 ms. For transportation of the beam inside the structure, the guiding field of 1.25 T (created by a permanent magnet) was used. The weight of the packaged device was 23 kg.
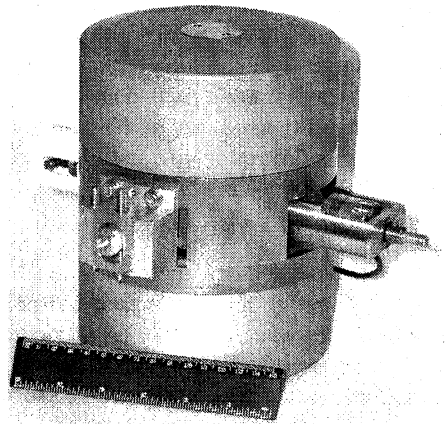
Fig. 5. Non-relativistic orotron of short-millimeter and submillimeter wavelength range.

In the experiment, the output radiation was obtained in the range of accelerating voltages from 0.6 up to 3.7 kV (Fig. 6, *a*). It corresponds to the frequency band of 120–300 GHz. The absence of generation in the middle of this band (at the voltages of 1.7–2.2 kV) can be explained by the competition between operating orotron oscillations and parasitic backward-wave oscillations. The latter were excited at the surface waves of the periodical structure. Measuring the radiation orotron frequency in the long-wave part of the generation band demonstrated a good agreement with theory (Fig. 6, *b*). Discreet electronic and smooth mechanical frequency tuning were also observed. The output power of up to 50–100 mW was measured at the frequency of 140 GHz with a calibrated semiconductor detector.
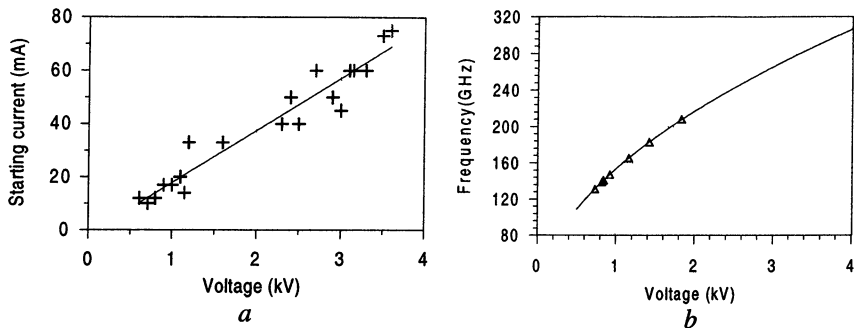
Fig. 6. Millimeter-wave orotron characteristics vs accelerating voltage: *a* – starting current, *b* – calculated and measured frequencies.

A submillimeter orotron at the wavelength of 0.8 mm with the 0.1 mm period of the structure was also manufactured and tested. The output radiation was obtained in the range of accelerating voltages from 1.0 to 4.0 kV, which corresponds to the frequency band of 200–380 GHz. To date, this is the highest frequency obtained for orotrons. The output power measured at the frequency of 370 GHz amounts to 50 mW, which exceeds the power of BWOs in this frequency range. The smooth electronic frequency tuning in the band of 0.02 % (at the single cavity mode) was demonstrated in the experiment. The measured frequency stability amounts to 10^{-7} without any additional systems of frequency control. This orotron is now used as a radiation source in the Free Berlin University ESR spectrometer.

Conclusions

Gyrotrons at high cyclotron harmonics and orotrons allow production of submillimeter-wave radiation using moderate magnetic fields and electron beams with moderate particle energies. The use in the gyrotrons of axis-encircling electron beams produced by original electron-optical systems provides selective excitation of high cyclotron harmonics. It was confirmed in the millimeter-

wavelength range where the output power of 100 kW was generated at the 3rd and 4th cyclotron harmonics at the frequencies of 110 and 130 GHz, respectively. Based on these results, two projects of third-harmonic LOGs with electron energy of 250 and 80 keV and pulsed magnetic field of 6.6 and 13.6 T have been designed for frequencies of 0.4 and 1.0 THz.

According to the theory, similar results can be obtained by using the relativistic orotron. The relativistic orotrons with electron energy of 200 keV and with output power of 30 kW is designed at the frequency of 150 GHz. This oscillator can be used as a prototype of submillimeter-wave relativistic orotron with kilowatt level of output power.

The non-relativistic orotron can generate a submillimeter-wave radiation with output power of several hundreds of milliwatts, which is significantly higher than the output power of existing BWOs being most wide-spread low-power oscillators in this frequency range. To date, a pulsed orotron with the operating voltage of up to 4 kV generating the output power of 50 mW at the frequency up to 380 GHz is realized. This oscillator provides high frequency stability of output radiation and broadband frequency tuning.

References

1. *Zaytsev N. I., Pankratova T. P., Petelin M. I., Flyagin V. A.*, Radio Eng. and Electronics Phys., **19**, 103, (1974).
2. *Flyagin V. A., Luchinin A. G., Nusinovich G. S.*, Int. J. Infrared Millimiter Waves, **4**, 629, (1983).
3. *Spira-Hakkarainen S. E., Kreischer K. E., Temkin R. J.*, IEEE Trans. on Plasma Sci., PS-18, 334, (1990).
4. *Brandt G. F.*, Int. J. Infrared Millimiter Waves, **16**, 879, (1995).
5. *Idehara T., Ogawa I., Mitsudo S., Pereyaslavets M., Nishida N. and Yoshida K.*, IEEE Trans. Plasma Sci., **27**, 340 (1999).
6. *Jory H. R.*, Research and Development Technical Report ECOM-01873-F, Varian Associates (Palo Alto, California, 1968).
7. *McDermott D. B., Luhmann N. C., Kupiszewski A. and Jory H. R.*, Phys. Fluids, **26**, 1936 (1983).
8. *Lawson W., Destler W. W., Striffler C. D.*, IEEE Trans. Plasma Sci., **13**, 444 (1985).
9. *Bratman V. L., Fedotov A. E., Kalynov Yu. K., Manuilov V. N., Ofitserov M. M., Samsonov S. V., Savilov A. V.*, IEEE Trans. on Plasma Sci., **27**, 456 (1999).
10. *Bratman V. L., Denisov G. G., Kol'chugin B. D., Samsonov S. V. and Volkov A. B.*, Phys. Rev. Lett., **75**, 3102 (1995).
11. *Bratman V. L., Cross A. W., Denisov G. G., He W., Phelps A. D. R., Ronald K., Samsonov S. V., Whyte C. G. and Young A. R.*, Phys. Rev. Letts., **84**, 2746 (2000).
12. *Bratman V. L., Kalynov Yu. K., Manuilov V. N., Ofitserov M. M., Samsonov S. V.*, Radioteknika i Electronika, **46**, 744 (2001).
13. *Bratman V. L., Denisov G. G., Kalynova G. I., Manuilov V. N., Ofitserov M. M., Samsonov S. V., Volkov A. B.*, Digest 27th Int. Conf. on Infrared and Millimeter Waves, R. Temkin Ed. (San Diego, USA, 2002), 197.
14. *Rusin F. S., Bogomolov G. D.*, Pis'ma v JhETF, **4**, 236 (1966).
15. *Shestopalov V. P.*, Diffraction Electronics (Kharkov, Vischa shkola, 1976).
16. *Bratman V. L., Dumesh B. S., Fedotov A. E., Grishin Yu. A., Rusin F. S.*, Int. J. Infrared and Millimeter Waves, **23**, 1595 (2002).

EXPERIMENTAL OBSERVATION OF CHAOTIC DYNAMICS IN POWERFUL RELATIVISTIC OSCILLATORS

N. S. Ginzburg, N. I. Zaitsev, E. V. Ilyakov, I. S. Kulagin,
Yu .V. Novozhilova, R. M. Rozental, A. S. Sergeev

Institute of Applied Physics Russian Academy of Sciences, Nizhny Novgorod, Russia

Periodic and chaotic self-modulation regimes were observed in two most studied devices of high power microwave electronics including relativistic BWOs and gyrotrons. For gyrotrons delayed feedback have been used to decrease bifurcation currents. With the current growth the sequence of periodic and chaotic self-modulation patterns took place. At currents of about 100 A the power of X band signals with chaotic self-modulation of envelope amounted to 1–2 MW with 6–10 µs pulse duration.

The investigation of multifrequency processes in powerful microwave relativistic oscillators can be of practical interest for the development of powerful sources of modulated or noise-like signals. In this paper we present the results of an experimental studies of periodic and chaotic self-modulation regimes in two most studied devices of high power electronics as BWOs and gyrotron [2–9]. The experiments were carried out at IAP based on the microsecond accelerator "SATURN" which allowed formation of an electron beam with electron energies $U=150 - 250$ keV, and current up to 300 A. The radiation power in chaotic self-modulation regimes amounted to 1–2 MW at 6–10 µs pulse duration.

1. Observation of chaotic dynamics in a powerful backward wave oscillator

The theoretical study of the multifrequency dynamics of BWOs carried out in [1] showed that as the injection current increases above threshold value, the regime of stationary single-frequency generation is replaced with the regime of periodic self-modulation, first in the sinusoidal form and then acquiring the shape of a sequence of spikes. As the current grows further, the signal modulation becomes chaotic. Up to recently self-modulation regimes were observed experimentally only in non-relativistic BWOs of milliwatt power levels [10]. In the experiments discussed in this paper the first observation of chaotic dynamics in a long pulse BWO at megawatt power levels was carried out.

The configuration of interaction space was in the form of a smoothly corrugated waveguide with a cut-off narrowing at the cathode end and diffraction output of radiation from the collector end, which is typical for a powerful relativistic BWO [2]. The "Saturn" accelerator where experiments were performed, was used in previous experiments to drive a 10 µs relativistic X-band BWO which achieved a steady-state generation with a power level of 5 MW [6].

To observe self-modulation regimes the operating current had to significantly exceed the threshold value. This was achieved by the choice of the TM_{01} operating mode which had a higher coupling impedance with the electron beam (compared to the TE_{11} mode) as well as by substantially increasing the length of the interaction space. At the operating point the group velocity of the TM_{01} mode was high enough (0.4c) to ensure the extraction of radiation energy from the interaction space with a small reflection. It is also important to note that several microwave systems of different length have been investigated. For the shortest BWO of length $l \sim 10\lambda$ (λ – wavelength) only the steady state regime was evident. When the interaction length was increased up to $l \sim 15\lambda$ both the steady state and periodic self-modulation regimes were observed. Further increase of the BWO length up to $l \sim 20\lambda$ in accordance with simulations presented below resulted in a chaotic self-modulation regime.

The simulations were carried out using a time domain approach [1, 9] under the assumption that the electron beam excites a single mode of the corrugated waveguide. The BWO's simulation parameters corresponded to the experiment: length of the slow-wave structure was 62.3 cm, the mean waveguide radius was 1.4 cm, the period and corrugation amplitude were 1.7 cm and 0.25 cm respectively, the electron beam radius was 0.6 cm and the energy of electrons was 150 keV. An impedance of $Z = 0.5\ \Omega$ at an operating frequency of 8.7 GHz and a starting current of 6 A were found based on the results of Ref. [2]. In Fig. 1 the output power temporal dependence, as well as the signal spectra and so-called phase-plane portraits at different values of current are presented. For plotting of phase trajectories the points corresponding to the system states at consecutive moments in time were marked on the plane $\left(\left| A(0,t) \right|, \left| A(0,t - t^*) \right| \right)$, where $A(z,\ t)$ is the normalized field amplitude, t^* is the delay time, chosen to be equal to 1/4 of the self-modulation period. Fig. 1, a corresponds to a steady state operation regime which was established for a current of 7 A. As the current was increased the opera tion regimes became more complicated. Fig. 1, b shows a periodic self-modulation regime for a current of 30 A. As the current increased to 55 A the self-modulation lost its periodicity and became chaotic (Fig. 1, c), as corroborated by the spectra and phase portraits. Due to the space charge effect some simplification of output signal took place at the range of electron current 70–100 A (Fig. 1, d). At these currents the self-modulation became quasi-periodic again. However above a current of 120 A as seen from the spectrum and phase portraits (Fig. 1, e) the self-modulation again acquired chaotic behavior. It should be noted that the period of self-modulation for a current less than 30 A was equal to 7 ns (Fig. 1, b). When the current exceeded 70 A i. e. after passing through the chaotic regime the self-modulation period grew up to 13 ns (Fig. 1, d).
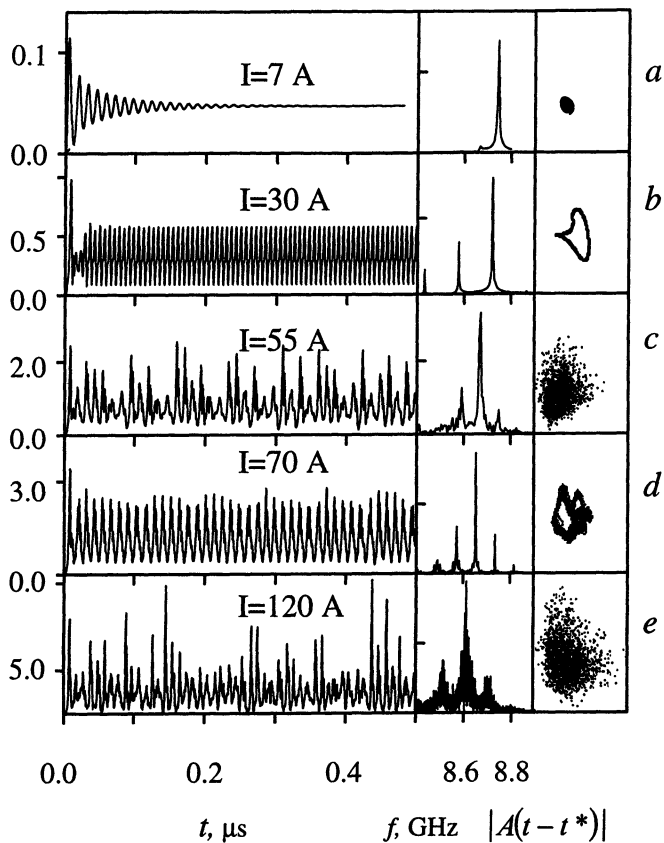
Fig. 1. The simulation of dynamics of the powerful BWO studied experimentally: l=62.3 cm, Z=0.5 Ω, and U=150 kV. The output power temporal dependence (left column), the signal spectra (middle column) and phase-plane portraits (right column) for a different values of beam current.

In experiments at an operating voltage of 150 kV the electron current was changed from 10 A to 140 A. The central parts of the oscillograms with duration ~ 500 ns at the flat top of voltage pulse with fixed value of 150 kV were chosen to study bifurcation currents. These parts of the oscillograms as well as spectra and phase portraits are presented in Fig. 2. At a current of 7 A a steady state regime was established. At a current of 30 A the regime changed to a sinusoidal

146
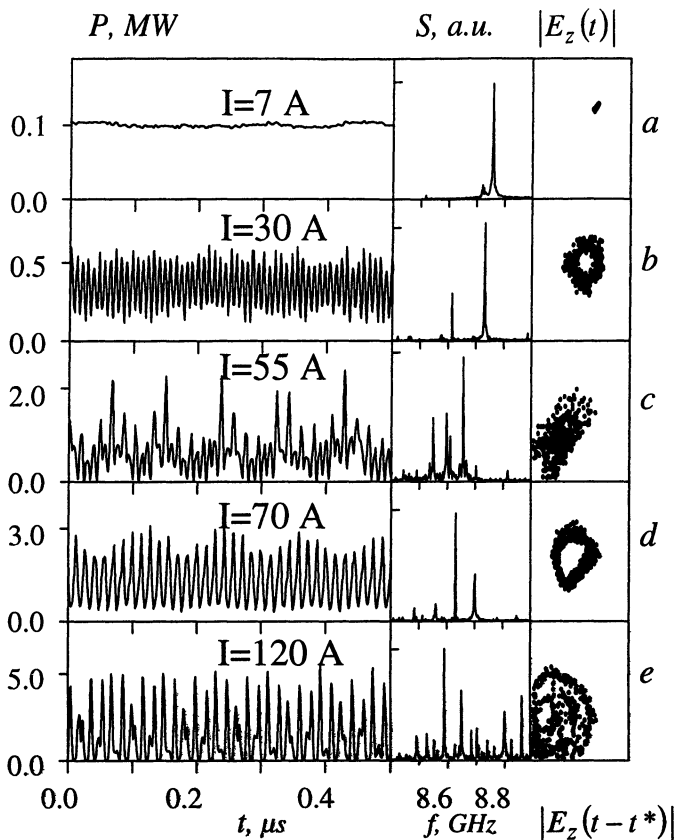
Fig. 2. Experimental oscilloscope traces of output power (left column), radiation spectra (middle column) and phase-plane portraits (right column) for different values of beam current.

self-modulation with a period of about 8 ns, and as the current increased, the time dependence of the output power became more complicated. At a current of about 50 A (Fig. 2, *c*) the self-modulation acquired a chaotic character. For higher currents some simplification of the regime was observed. It is seen from Fig. 2, *d* that under a current of 70 A the self-modulation was quasi-sinusoidal with a period close to 14 ns. Finally for a current greater than 100 A the self-modulation became chaotic again with a relative spectral width of ~ 4% (Fig. 2, *e*). We should emphasize that bifurcation values of currents and the main self-modulation periods were in good agreement with simulations. Based on simulations the simplification of the self-modulation pattern in the current range of 50–100 A could be explained by the influence of space charge. The average radiation

power in the self-modulation regime measured using calorimeter techniques was 1 MW for a current 50 A and 2 MW for a current of 120 A. At an electron accelerating potential of 150 kV this corresponded to an electron efficiency about 10 %.

In conclusion, experiments which observed the transitions from steady state to chaotic self-modulation regime in a powerful BWO were successfully carried out. The observed sequence of operation regimes and corresponding bifurcation currents were in good agreement with the results of simulations.

2. Periodic and chaotic self-modulation regimes in a high-power relativistic gyrotron with a delayed feedback

At present, the sub-relativistic gyrotrons are the most effective sources of high-power radiation in the millimeter wavelength range. Recently it was shown theoretically [11], and experimentally [12] that the efficiency of the gyrotron remains on the sufficiently high level of about 50% at the moderately relativistic energy range. The experiments were performed at the IAP, where the X-band relativistic gyrotron with beam voltage of the 280 kV and current of 40–60 A produced the 7–8 MW microwave pulses. Obviously it is interesting to study the possibility of realisation of self-modulation regimes in such relativistic gyrotrons at high power level.

The theoretical study of the non-stationary processes in gyrotrons with traditional configuration of the interaction space (a weakly irregular waveguide matched with an output section) demonstrates that the self-modulation regimes occur only when the injection current exceeds the threshold magnitude by factor of 10 [13]. (Recently this conclusion was confirmed in the experiment [14] with subrelativistic gyrotron). To reduce the bifurcation currents by several times, the delayed feedback formed by the additional reflections from a collector side of the interaction space has been suggested in [15]. By additional reflection from mismatched output window an expansion of radiation spectrum in non-relativistic tens kilowatts gyrotron was interpreted in [16].
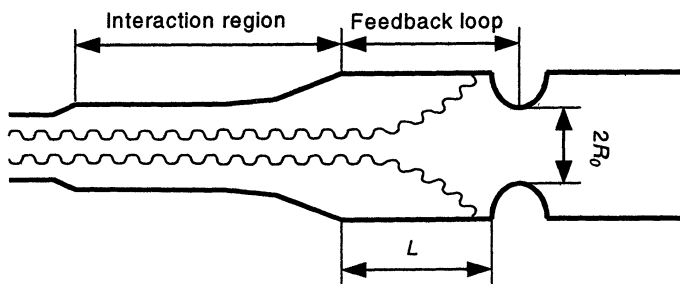
Fig. 3. The layout of the interaction space

In this paper we present the results of an experimental observation of periodic and chaotic self-modulation regimes at megawatt power level in the 3-cm relativistic gyrotron operating at the TE_{01} mode with the delayed feedback formed by a special reflector inserted in output waveguide. The reflector with internal radius $R_0 = 1.9$ cm was spaced on the distances L of 9 cm either 54 cm from a connection of the resonator opening and the output waveguide with radius 2.7 cm (Fig. 3). In experiments for an operating voltage of 230–250 kV the electron beam current changed from 30 to 80 A.

For the configuration with $L \approx 9$ cm only the periodic self-modulation regimes were observed. The typical accelerating voltage and signal oscilloscope trace is presented in Fig. 4. The total duration of a self-modulation in the output signal exceeded 6 µs, that corresponded to the length of a flat-top of the accelerating voltage pulse. In large scale the part of the oscillogram as well as spectrum corresponding to periodical self-modulation regime are presented in Fig 5, a. The self-modulation period and modulation depth was 13.1 ns and 50% correspondingly. The averaged output power achieved 1 MW with the efficiency of about 9% at the injection current of 48 A.
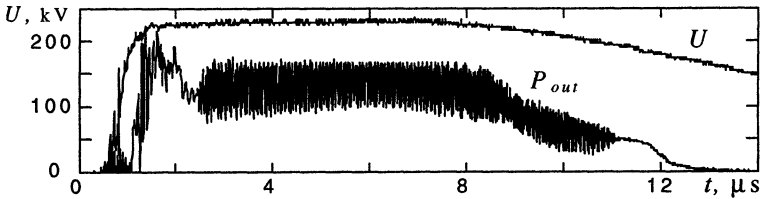
Fig. 4. The typical oscillograms of the accelerated voltage and the output signal in the periodic self-modulation regime.
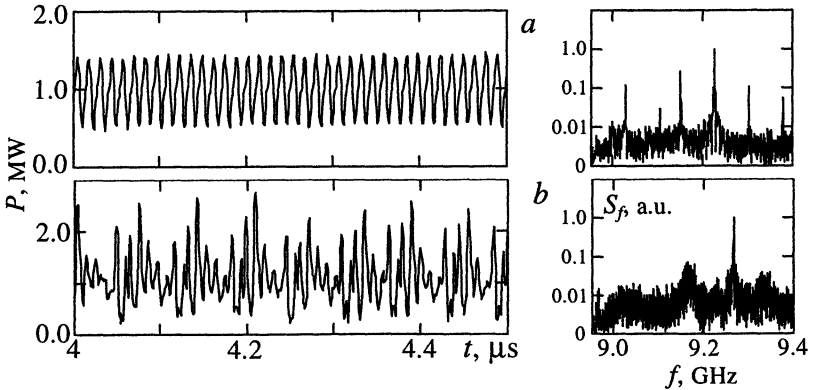
Fig. 5. The typical oscilloscope traces and the corresponding spectra for the periodic – $L = 9$ cm, $I = 48$ A (a) and chaotic – $L = 54$ cm, $I = 78$ A (b) self-modulation regimes.

149

When the distance L was increased up to 54 cm the oscillator behaviour becomes more complicated. Both the periodic and the chaotic self-modulation regimes were observed. In the case of the periodic oscillations the self-modulation period varied from 2.2 to 19 ns depending on the magnetic field value and accelerating voltage. The averaged output power of the chaotic oscillations achieved 1.4 MW with the efficiency of about 7% at the injection current of 78 A and accelerating voltage of about 250 kV. The part of oscillogram and the corresponding spectrum in the chaotic self-modulation regime are presented in Fig. 5, *b*.

In conclusion, experiments which observed the periodic and chaotic self-modulation regime at megawatt power level in relativistic gyrotrons with delayed feedback were successfully carried out. The observed self-modulation patterns were more complex for larger delay time.

3. Summary

In conclusion, experiments which observed the transitions from steady state to chaotic self-modulation regime in a powerful BWO were successfully carried out. The observed sequence of operation regimes and corresponding bifurcation currents were in good agreement with the results of simulations. Experiments on the study of nonstationary regimes at megawatt power level in relativistic gyrotrons with delayed feedback showed the complication of self-modulation patterns with increasing of delay time.

References

1. *Ginzburg N. S., Kuznetsov S. P., and Fedoseeva T. N.*, Sov. Radiophys. Electron., 1978, **21,** 728.
2. *Kovalyov N. F., Petelin M. I., Raizer M.D.* et al., JETP Lett., 1973, **18,** 138.
3. *Carmel Y., Ivers J., Kribel R.E.* et al. Phys. Rev. Lett., 1974, **33,** 1278.
4. *Miller S. M., Antonsen T. M., Levush B.* et al., Phys. Plasmas, 1994, **1,** 730.
5. *Grabowski C., Shamiloglu E., Abdallah C.T.* et al., Phys. Plasmas, 1998, 3490.
6. *Ilyakov E. V., Korablyov G. S., Kulagin I. S.* et al., IEEE Trans. Plasma Sci., 1998, **26,** 332.
7. *Yalandin M. I., Shpak V. G., Shunailov V. G.* et al., Pis'ma Zh. Techn. Fiz., 1999, **25,** 19.
8. *Carmel Y., Lou W. R., Rodgers J.* et al., Phys. Rev. Lett., 1992, **69,** 1652.
9. *Levush B., Antonsen T. M., Bromborsky A.* et al. IEEE Trans. Plasma Sci., 1992, **20,** 263.
10. *Bezruchko B. P., Kuznetsov S. P., and Trubetskov D. I.,* Pis'ma Zh. Exper. Teor. Fiz., 1979, **29,** 180.
11. *Moiseev M. A., Zapevalov V. E., and Zavolsky N. A.,* Int. J. IR & MM Waves, 2001, **22,** 813.
12. *Ginzburg N. S., Zaitsev N. I., Ilyakov E. V.* et al., Tech. Phys. Lett., 2001, **27,** 266.
13. *Ginzburg N. S., Nusinovich G. S., and Zavolsky N. A.,* Int. J. Electron., 1986, **61,** 881.
14. *Chang T. H., Chen S. H., Barnett L. R., and Chu K. R.,* Phys. Rev. Lett., 2001, **87,** 4802.
15. *Ginzburg N. S., Glyavin M. Yu , Zavolsky N. A.* et al., Tech. Phys. Lett., 1998, **24,** 436.
16. *Glyavin M. Yu., Zapevalov V. E., Kuftin A. N., and Luchinin A.G.* Radiophys.& Quant. Electron., 2000, **43,** 369.

A Ka-BAND SECOND HARMONIC GYROKLYSTRON
WITH A PERMANENT MAGNET

I. G. Gachev, I. I. Antakov, V. K. Lygin, M. A. Moiseev,
E. V. Sokolov, and E. V. Zasypkin

Institute of Applied Physics, Russian Academy of Science,
46 Ulyanov Str. 603950 Nizhny Novgorod, Russia

The design and testing results of a powerful Ka-band, TE_{021}, second harmonic gyroklystron amplifier operating with a permanent magnet system are presented. Three-cavity gyroklystron has demonstrated a peak output power of 300 kW at 32.33 GHz with a 3-dB bandwidth of 40 MHz (~0.12 %), efficiency of 22%, and a saturated gain of 22 dB.

Introduction

Gyroklystron amplifiers are currently of interest for millimeter-wave radar due to their capability to provide high peak and average power in the atmospheric propagation windows near 35 and 94 GHz. A Ka-band gyroklystron operating at the fundamental requires an axial magnetic field in the circuit of about 1.4 T that has been provided by a superconducting coil usually. However, superconducting magnet utilization in radar is accompanied by a number of technical problems. Therefore, there is a considerable interest in second harmonic gyroklystron configuration where the required dc magnetic field can be ensured by a conventional coil or a permanent magnet. Proof-in-principle second harmonic gyroklystron experiment was performed in 1994 [1]. Two-cavity Ka-band gyroklystron demonstrated a peak power of 260 kW with an efficiency of 18%, a gain of 17 dB and a bandwidth of 35 MHz.

Over last 15–20 years, an essential progress has been attained in the development of magnetic circuits using Nd-Fe-B permanent magnets those capable to produce magnetic field strength up to 1T in a large volume [2, 3]. Last decade, the successful operation of a gyrotron with permanent magnet system (PMS) were reported by Russian and Japanese researches [4, 5]. In connected with that, during 1998–2002 IAP gyroklystron team efforts were concentrated in the development and testing of a Ka-band second harmonic gyroklystron operating with PMS. In this paper, we describe the PMS and gyroklystron design, and present the results of experimental study.

Permanent magnet system design

The PMS dimensions were simulated using special code in order to satisfy the following requirements:
• axial magnetic field strength in the rf circuit should be 0.7 T;

- flat top region length should be 140 mm, and permissible magnetic field nonuniformity at the flat should be less than 0.5%;
- magnetic field should drop smoothly enough in the region of gyroklystron beam tunnel, gun and collector in order to realize an adiabatic motion of the beam electrons;
- bore diameter in the circuit region should not be less than 60 mm;
- magnetic field gradient at the cathode emitter range should not be larger than 150 Gs/cm;
- total weight of PMS should not be larger than 350–400 kg.

The photograph of the designed PMS is shown in Fig. 1. The bore diameter is varied from 60 mm in the circuit range up to 130 mm at the gun area to accommodate the gyroklystron amplifier. The PMS total length is of 87 cm. The overall weight of the magnet system (including its rigging) is of about 370 kg.
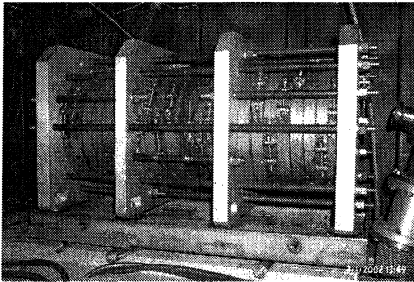
Fig. 1. Permanent magnet system
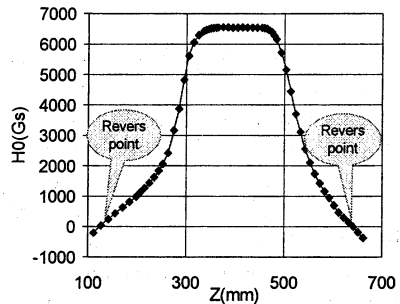
Fig. 2. Magnetic field profile

The measured axial magnetic field profile provided by PMS is presented in Fig. 2. At the flat top region where gyroklystron rf circuit is positioned, a magnetic field strength of 0.656 T with a nonuniformity less than 0.5% has been measured. An actual magnetic field gradient in the cathode region is 130 Gs/cm, its value in the gyroklystron beam tunnel is 950 Gs/cm, and at the collector it is equal to 150 Gs/cm.

Gyroklystron amplifier design

A triode magnetron injection gun was simulated and designed to produce an electron beam with a 70 kV beam voltage, 38 kV mod-anode voltage and a beam current up to 25 A. The mod-anode voltage was provided by a resistive divider network connected between the cathode and ground. The cathode diameter is 32 mm, beam diameter in the circuit is 8.6 mm. Simulations predict at 70 kV beam voltage and 20 A beam current the α-parameter as 1.1, and the perpendicular velocity spread as 23%.

152

As mentioned above, the magnetic field in the gyroklystron has been produced by the PMS. Moreover, three supplementary air-cooled coils are wound directly on the tube body to adjust the magnetic field in the circuit. Each coil generates a magnetic field of about 100–120 Gs in the cavities. Forth coil positioned at the gun area is used to control beam pitch-factor α.

In the simplest gyroklystron version, the RF circuit comprises two oversized cylindrical cavities operating in the TE_{021} mode at the second harmonic of the electron cyclotron frequency. Since the magnetic field in the circuit provided by PMS was 0.656 T only (instead the expected 0.7 T), the rf circuit parameters were chosen to operate the gyroklystron at the frequency of 32.4 GHz. The length and quality factor of the input cavity is 16 mm and 500, respectively. The output cavity length is about 25 mm and its Q-factor is 700. The calculated eighen-frequencies were 32.3 GHz for both drive and output cavities.

To enlarge gain, a three-cavity gyroklystron has also been designed and tested. The input and output cavity parameters of this device are the same as for its two-cavity counterpart. The intermediate cavity is 15 mm long, its Q-factor is 350, and its eighen-frequency is 32.2 GHz.

The drive power is coupled into the circuit through the input circular waveguide inside cathode, then input TE_{01} mode is transformed to the TE_{02} mode by the inner mirror transformer, and then TE_{02} wave excites the operating TE_{021} mode in the drive cavity (Fig. 3). As a driver, a 100 μs, 10 kW mechanically tuneable

Fig. 3. GK in PMS

gyrotron with the operating TE_{011} mode was used in this experiment.
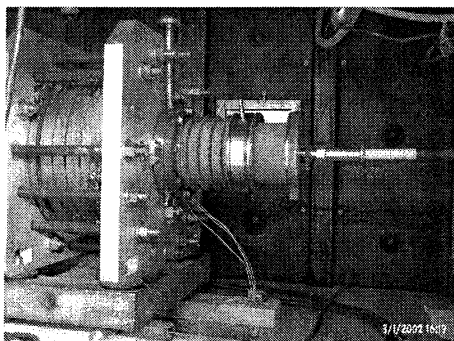
Experimental results

A series of experiments was undertaken to investigate the two-and three-cavity gyroklystron performance. Systematic studies were performed over a wide range of rf circuit parameters, beam current, magnetic field, drive power and drive frequency.

At the beginning, the dependence of the peak output power and efficiency on the beam current for two-cavity tube was measured (Fig. 4). During testing, the beam voltage and mod-anode voltage were fixed while the axial magnetic field in the circuit, drive power and drive frequency were optimized to attain maximum output power at each operating point. As it follows from Fig. 4, the two-cavity gyroklystron is capable to produce a peak output power of 320 kW with an efficiency of 21% using 65-kV, 24-A electron beam. The pulse width was 100 μs,

153

Fig. 4. Peak power and efficiency vs beam current for two-caviy gyroklystron.

and the pulse repetition frequency was 5 Hz. The output power was found to be limited by a self-excitation at the frequency of 32.4 GHz closed to the frequency of the operating TE_{021} mode in the output cavity.

Fig. 5 shows the measured output power versus drive frequency for a 65-kV, 15-A electron beam, and 4 kW drive power. At a central frequency of 32.33 GHz the gyroklystron produced 200 kW peak power, 21% efficiency and 17-dB gain. The measured full width half maximum (FWHM) bandwidth was 45 MHz. A drive curve at the constant beam voltage of 65 kV, beam current of 15 A and input signal frequency of 32.33 GHz was measured. For this case, the output power and gain as a function of drive power are depicted in Fig. 6. A peak power of 200 kW with a saturated gain of 17 dB was achieved with an input power of 3.7 kW. The measured small signal gain was about 19 dB.
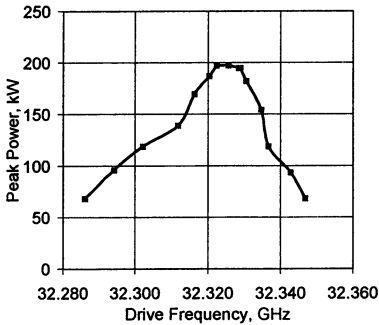
Fig. 5. Peak power vs drive frequency for two-cavity gyroklystron.
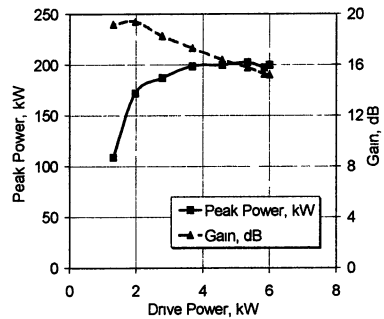
Fig. 6. Peak power and gain vs drive power for two-cavity gyroklystron.

The motivation of the three-cavity gyroklystron development was to demonstrate increased saturated gain, while maintaining comparable peak power and efficiency. Therefore, the intermediate cavity was positioned at the equal distances from both other cavities, and its eighen-frequency was close to the output one. It was expected, the bunching improvement provided by a penultimate cavity should result in the output power saturation at the drive power of 1.5–2 kW that attainable by the ordinary O-type amplifiers (TWT, EIA, klystron etc.).

In Fig. 7–8, the performance characteristics of the three-cavity gyroklystron are presented. This gyroklystron produced 300 kW output power and 22% efficiency using a 65-kV, 21-A electron beam. Fig. 8 presents the drive curve

154

measured at 230-kW power level. The saturated gain of 22 dB was about 3 dB higher than that obtained from the two-cavity experiment with comparable output power and efficiency. For three-cavity tube, the FWHM bandwidth of 40 MHz has been measured.
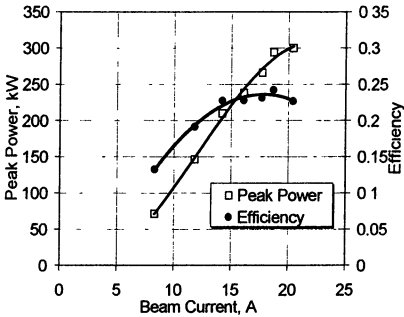
Fig. 7. Peak power and efficiency vs beam current for three-caviy gyroklystron.
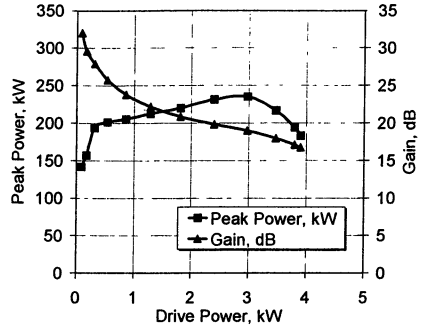
Fig. 8. Peak power and gain vs drive power for three cavity gyroklystron.

Conclusions

In summary, two- and three-cavity, TE_{021}-mode, second harmonic gyroklystron amplifier operating with a permanent magnet system was designed, built and tested successfully. Two-cavity gyroklystron produced 320 kW peak power with 21% efficiency, 19-dB gain and 45 MHz bandwidth. In a three-cavity tube, the output power of 300 kW with 22% efficiency, 22-dB gain, and the similar bandwidth has been demonstrated. To saturate this device, an input power of ~ 1–2 kW is sufficient. It opens the real possibility to develop a "cryogenic-free" amplifier chain for radar transmitter including a solid state driver, ordinary O-type amplifier as a penultimate stage, and a multicavity gyroklystron with PMS as a final stage. Future work will be focused on improving the gyroklystron output power, gain and bandwidth.

References

1. *Zasypkin E. V., Moiseev M. A., Gachev I. G., Antakov I. I.* Study of high-power Ka-band second-harmonic gyroklystron amplifier, IEEE Trans. Plasma Sci., **24** (3), 666–670 (1996).
2. *Clarke J. P., Potenziani E., Leupold H. A.* Permanent-magnet annular, longitudinal field sources, J. Appl. Phys., **61** (8), 3468–3470 (1987).
3. *Takada T., Ohasgi K., Honshima M., Kikunaga T.* Nd-Fe-B permanent magnet circuit for a 28 GHz CW gyrotron, Conf. Digest of the 23rd Int. Conf. IR&MM Waves (Orlando, FL, USA, 1995), 489–490.
4. *Kuftin N., Manuilov V. N., Raiskii B. V., Flyagin V. A., Tsimring Sh. E.* Gyrotron with permanent magnets, Radiophys. Quant. Electron., **35** (6/7), 396–398 (1993).
5. *Kikunaga T., Asano H., Hemmi K., Sato F., Tsukamoto T.* A 28 GHz CW gyrotron with a permanent magnet system, Conf. Digest of the 23rd Int. Conf. IR&MM Waves (Orlando, FL, USA, 1995), 485–486.

A CONTINUOUSLY OPERATING
1300 MHz 100 kW MAGNICON

E. V. Kozyrev, G. I. Kuznetsov, V. V. Tarnetsky, M. A. Tiunov,
I. A. Zapryagaev, O. A. Nezhevenko[1], V. P. Yakovlev[1]

Budker INP, Novosibirsk, Russia
[1]Omega-P, New-Haven, Connecticut, USA

The paper presents a high-efficiency 1300 MHz continuously operating magnicon project with an output power more than 100 kW. The device is designed as an RF power source for industrial accelerator applications. The high efficiency and low operation cost of such facilities mainly depend on RF power source efficiency. The paper represents the structural drawing, dimensions, and the main parameters of the magnicon. The results of the numerical simulation of an electron source, beam dynamics in the RF system and collector are presented. The simulation proved that at a beam current of 2.5 A and electron gun voltage of 65 kV the magnicon output power exceeds 120 kW with a plugin efficiency of 70% and gain of 32 dB.

Introduction

Magnicon is a RF amplifier which consists of the electron gun, RF system, solenoid, and collector. Operation principle of such amplifier is described in detail in [1]. The device schematic layout (Fig. 1) has been chosen on the base of the experience accumulated and previous designs. RF system contains 7 cylindrical cavities, 6 of them are modulating ones, and the seventh (output cavity) serves for converting the beam energy into RF oscillations. In all these cavities circularly-polarized TM_{110} mode oscillations are excited. The power comes out through two waveguide windows in the output cavity sidewall shifted azimuthally by 90 degrees. All the cavities are supplied by tuning units, that provides wide enough frequency range of the device. The RF system, electron gun, and collector form a single bakeable vacuum volume. An electron beam within the modulating and output cavities are guided by a longitudinal magnetic field produce by two solenoids (Fig. 1). Two magnetic lenses are used for beam focusing in the gap between solenoids and to guide the beam into the collector.
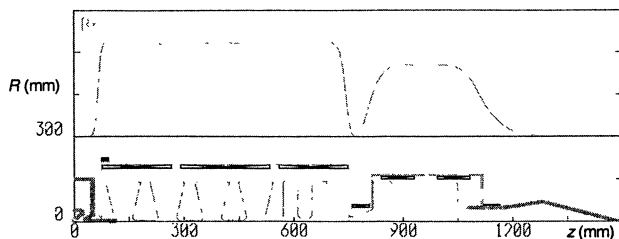
Fig. 1. 1300 MHz magnicon schematic layout.

156

Rf system and beam dynamics

The dominant requirement for the developed device is a high full efficiency. As is known from the magnicon amplifier development experience, high efficiency of such devices is achieved by the use of low-perveance beams (with microperveance less than 0.1). An attempt to develop a magnicon with low power and high efficiency (using low-perveance beam) leads to a sharp drop of the passive cavity gain.

A simplified magnicon deflection system model was numerically studied to determine the conditions with the maximal gain. The model consists of only two cavities: an active and passive one. During this study the following parameters were selected: cavity lengths, gaps between the cavities, cavity detunings considering the beam influence, accompanying magnetic field value, and beam current. Figure 2 shows the dependence between a gain and longitudinal magnetic field value, which is defined by Ω/ω ratio, for 4 beam current values within the limits of the model chosen. Ω is the cyclotron frequency, and ω is the drive signal frequency, with electron energy of 100 kV.

One can see that there is no ampli-
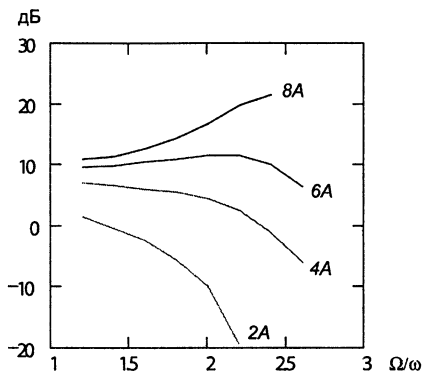
Fig. 2. Gain versus longitudinal magnetic field.

fying for the beam with power less than 200 kW at $\Omega/\omega \geq 1.35$. The gain may be increased by decreasing the accompanying magnetic field and simultaneously increasing the beam current. However, magnetic field decreasing as well as increasing of the perveance leads to the beam cross size increasing which degrades the device efficiency. So there is a need for a compromise between a gain and tolerant efficiency decreasing.

Gain of the passive cavities may be additionally increased (preserving the device efficiency) with optimization of their geometry and so increasing their characteristic impedances and Q-factors. The simplest and most technologically realizable cavity configuration with transformation of parallel end walls into cones with half-angle of 80 degrees (Fig. 1) has been numerically studied. It allowed us to increase the cavity characteristic impedances by 15% and Q-factors – by 23%.

All the magnicon RF system numerical simulations were carried out for the beam with a current of 2.5 A and electron energy of 65 keV. The accompanying magnetic field in the deflecting system has been chosen to be equal to 710 Gs ($\Omega/\omega \approx 1.35$). At these parameters the gain per cavity reaches 6 dB.

The beam modulatuion takes place in six cylindrical cavities placed into an individual solenoid. Drift gaps of the cavities make up ~$\beta\lambda/2$ (β being a relativis-

157

tic factor, and λ is an operating wavelength). The last 3 cavities are specially de-tuned from the central frequency to decrease the total heat losses, and also placed so that to realize a distributed interaction [4]. Here in each of them the total dissi-pation does not exceed 4.3 kW, and the maximal surface electric field strength does not exceed 13 kV/cm.

Cylindrical output cavity is placed into an individual solenoid, which pro-duces a longitudinal magnetic field of 470 Gs that was chosen from criterion to obtain the best interaction between the beam and an output cavity RF field. The output cavity length is almost equal to the operating wavelength to minimize heat losses. The optimal value of the output cavity loaded Q-factor for the length cho-sen is 750 with an unloaded Q-factor value of 4700. At 126 kW output power level the losses in the output cavity walls comprise 2.1 kW with the maximal surface electric field strength of 11.5 kV/cm.

Numerical simulation of a gun, cavity and solenoid fields, as well as beam dynamics in the magnicon has been carried out by special computer programs [5–7]. Figure 3 shows the axial beam dynamics in the magnicon. The main calcu-lated parameters of the device are listed in the Table 1.
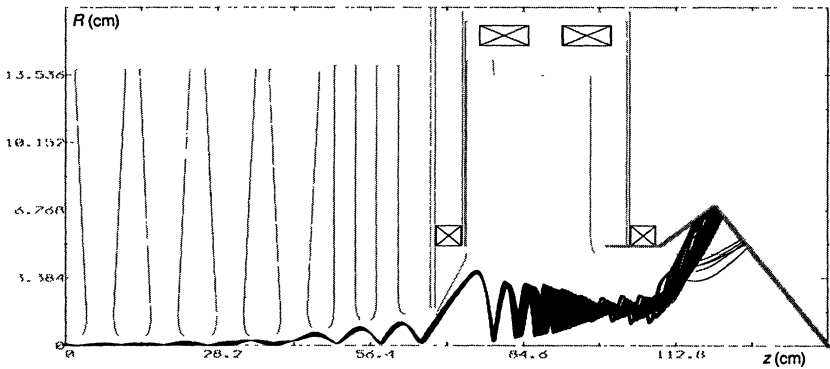
Fig. 3. Beam dynamics in magnicon

<div align="right">

Table 1

</div>

Operating frequency, MHz	1300	E_{Max} in RF system cavities, kV/cm	13
Output power, kW	126	Total losses in modulating cavities, kW	17.7
Input power, W	85	Losses in output cavity, kW	2.1
Electron efficiency, %	78	Supply power for solenoids, kW	6.3
Efficiency, %	70	Supply power for gun and lenses, kW	1.5
Gain, dB	32	Device height including gun and collector, m	1.7
Beam voltage, kV	65	Device external diameter, m	0.42
Beam current, A	2.5	Total device weight including solenoids, tons	0.7

158

Electron source

A diode electron gun with spherical 16.3 mm in diameter LaB_6 cathode has been chosen on the base of magnicon development experience, as well as considering its reliability in continuously operating mode and long lifetime. The gun provides 2.5 A current at a voltage of 65 kV. Figure 4 shows the electron gun geometry.

For bakable device design and cathode beam current of about 1–1.5 A/cm^2 the guaranteed lifetime of such cathode makes up several tens of thousands hours [8]. A beam microperveance of 0.15 lies within a favorable range for obtaining high magnicon efficiency. Numerical simulation of an electron source has been carried out by special-purpose computer code SAM [9]. The main electron gun parameters are listed in the Table 2, simulation results are shown in Fig. 5.

Rc = 8.15 mm   Rbm = 1.5 mm
ϑ = 11.8°   d = 30 mm
α = 67.5°   H = 27 mm
ρ = 8.5 mm   L = 20 mm
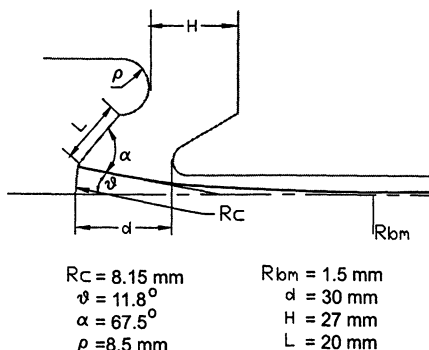
Fig. 4. Electron gun geometry parameters

Table 2

Beam power, kW	160
Gun voltage, kV	65
Beam current, A	2.5
Microperveance	0.15
Electrostatic area compression	46:1
Maximal electric field on focusing electrode, kV/cm	51
Maximal electric field on anode, kV/cm	75
Maximal cathode current density, A/cm^2	1.26
Cathode emission non-uniformity	1.1:1
Distance between cathode center and crossover, mm	82
Beam transverse emittance at gun output, mrad mm	5

Figure 6 shows calculated electric field distributions on the gun electrodes, the maximal electric field strength on the focusing electrode does not exceed 51 kV/cm, and on the anode – 75 kV/cm, that allows us to estimate a reliable operation of the gun in continuous operating regime.

The gun provides an electrostatic beam area compression of 46:1 and beam diameter of 3 mm at the modulator solenoid entrance (95% of the beam current correspond to the 2.4 mm diameter). Matching the electron beam with the magnicon accompanying magnetic field has been carried out by BEAM computer code [10]. Calculated beam envelopes got with account of the transverse electron velocity heat spread on the cathode are shown in Fig. 7.

159
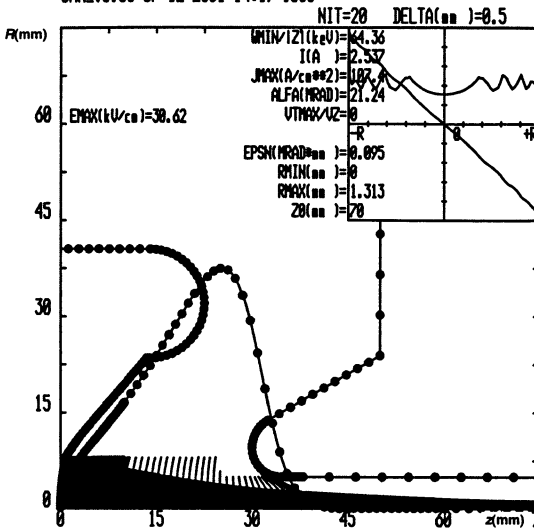
Fig. 5. Gun computer simulation results (SAM code).

Fig. 6. Calculated electric field distributions on the gun electrodes: *a* – on the cathode, *b* – on the anode.

a   *b*
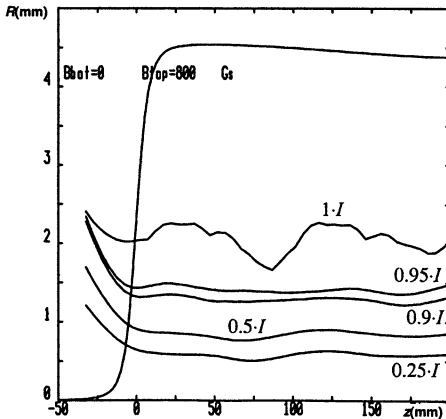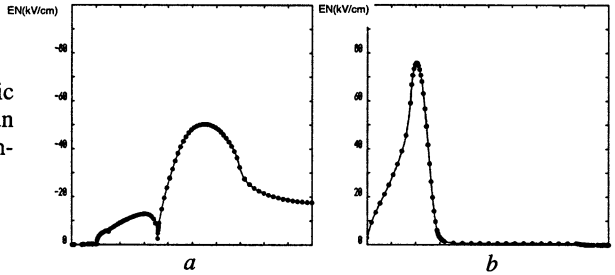
Fig. 7. Calculated beam envelopes paying account of heat spread.

160

Summary

The main difficulty in magnicon development work was connected with the fact that for the given output power and beam microperveance of ~0.1, which is the optimal value for high electron efficiency, the beam current was not enough for effective operation of the passive cavities. Usage of the Ω-like form cavities together with decreasing the accompanying magnetic field value and increasing the microperveance up to 0.15 allowed us to increase the passive cavity gain up to an acceptable value. The two latter actions have leaded to the beam size increasing and hence to the electron efficiency reasonable decreasing, however, the total device efficiency remains at high level. We plan to continue 100 kW magnicon development work on the base of this experience by increasing the beam perveance and decreasing the electron gun voltage.

References

1. *Karliner M. M.* et al., The Magnicon – an Advanced Version of the Gyrocon, NIM-A, V. A269, № 3, 459–473, 1988.
2. *Nezhevenko O.* et al., Magnicon – High Power RF Source for TESLA, Proc. of the Fourth European Part. Accel. Conf. V. 3, 1924–1926, 1994.
3. *Nezhevenko O. A., Kozyrev E. V.*, Proc. of III Russian Workshop on Microwave physics (Nizhny Novgorod, 12–15 February, 2001).
4. *Kozyrev E. V.* et al., Proc. of XVII Workshop on Charged Part. Acc. (Protvino, October 2000), V. 1, 55–58.
5. *Fomel B.* et al., Computer-Aided Electron Gun Design, Proc. of XIII Int. Conf. on High-Energy Accel. V. 1, 353–355, 1987.
6. *Myakishev D. and Yakovlev V.*, The New Possibilities of SuperLANS Code, Proc. of Part. Accel. Conf. (Dallas, 1995), 2348–2350.
7. *Yakovlev V.* et al., Numerical Simulations of Magnicon Amplifier, Proc. of Part. Accel. Conf. (Dallas, 1995), 1569.
8. *Kuznetsov G.*, NIM-A. V. A 340, 204–208, 1994.
9. *Fomel B., Tiunov M., Yakovlev V.* SAM – an interactive code for evaluation of electron guns, Preprint Budker INP 96–11 (1996) (available at www.inp.nsk.su).
10. *Tiunov M.*, BEAM – 2D-code package for simulation of high perveance beam dynamics in long systems, Proc. of International Symp. SCHEF'99 (Dubna, JINR, February 15–17, 1999), 202–208.

LOW-FREQUENCY PARASITIC OSCILLATIONS
IN THE 74.2 GHZ MODERATE-POWER PULSE GYROTRON

D. V. Kas'yanenko[1]*, O. I. Louksha*[1]*, B. Piosczyk*[2]*,*
G. G. Sominski[1]*, M. Thumm*[2]

[1] Saint-Petersburg State Polytechnical University,
29 Polytechnicheskaya St., St. Petersburg 195251, Russia
[2] Forschungszentrum Karlsruhe, Institut für Hochleistungsimpuls- und
Mikrowellentechnik (IHM), D-76021 Karlsruhe, Germany

A 74.2 GHz, 100 kW, $TE_{12,3}$ pulse gyrotron has been designed and manufactured at St. Petersburg State Polytechnical University with a goal to investigate an influence of low-frequency oscillations on gyrotron performance and possible ways of their suppression. In the paper, first results of experiments with this tube are presented.

Introduction

Observed in a number of gyrotron experiments (see, for example, [1, 2]), intense low-frequency oscillations at frequencies < 1000 MHz remain one of the parasitic factors preventing the achievement of high efficiency of gyro-devices. The existing information allows to associate these oscillations with axial motion of space-charge bunches in the trap between cathode and magnetic mirror. Studies of the excitation conditions, some features of development and effective techniques of suppression of low-frequency oscillations were performed at St. Petersburg State Polytechnical University (SPbSPU) using gyrotron models representing the gyrotron-type electron-optical system [3, 4]. To compare the observed phenomena with similar ones developing in operating gyro-devices, an experimental gyrotron including a number of diagnostic elements was designed and manufactured at SPbSPU.

Design overview

For simplification of the diagnostics realization and operation, the tube was designed as a moderate-power gyrotron with comparatively low-level accelerating voltage ~ 30 kV. The main design parameters of the tube are summarized in Table. Calculations of the gyrotron electron-optical and electrodynamic systems were performed at Institute of Applied Physics (IAP), Nizhny Novgorod. The designed values of output power P_0 and efficiency η are $P_0 = 112$ kW, $\eta = 37\%$ (for transverse velocity spread $\delta v_\perp = 0$) and $P_0 = 100$ kW, $\eta = 33\%$ (for $\delta v_\perp = 0.4$).

This gyrotron uses a room-temperature pulse magnetic system and operates in the regime of 10...200 μs single pulses. A schematic drawing of the tube is shown in Fig. 1. A cavity with a length of 28 mm is used as resonator. The

collector serves as a waveguide for output microwave radiation and ends with the 2.312-mm-thick quartz RF-output window. Output microwave power is absorbed in the load which is a part of the thermocouple wattmeter. A part of the power is directed through the 4-mm wavelength waveguide to the spectrum analyzer.

The gyrotron uses a triode-type magnetron injection gun with LaB_6-emitter. In the experiments, the gun has been operated in the diode regime with grounded intermediate anode.

**Main design parameters
of the experimental gyrotron**

Accelerating voltage	$U_0 = 30$ kV
Beam current	$I_b = 10$ A
Cavity magnetic field	$B_0 = 2.75$ T
Cathode magnetic field	$B_c = 0.157$ T
Operating mode	$TE_{12.3}$
Operating frequency	$f_0 = 74.7$ GHz
Cavity radius	$R_0 = 14.45$ mm
Cavity average beam radius	$R_b = 8.53$ mm
Cathode average radius	$R_c = 35$ mm
Cathode angle	$\phi_c = 35°$
Pitch-factor	$\alpha = 1.3$

The magnetic system of the tube was designed as a pulse solenoid that consists of a main, a cathode and a collector coils. Magnetic compression ratio can be adjusted by variation of the cathode coil current. The fourth control coil is used to change spatial distribution of magnetic field in the compression region.
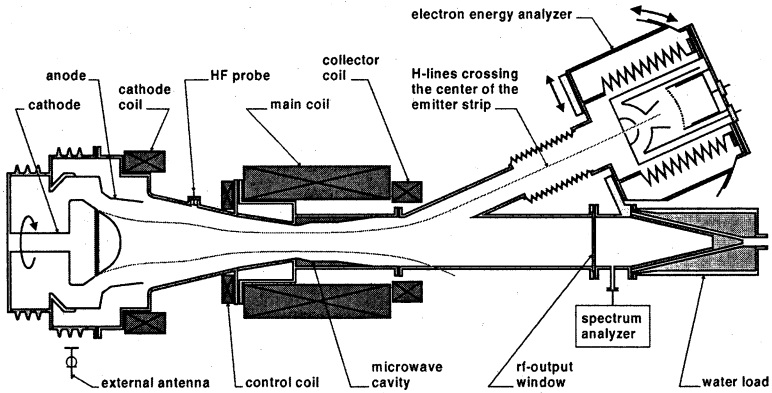
Fig. 1. Drawing of the experimental gyrotron cross-section

For registration of low-frequency instabilities in the helical electron beam and of parasitic low-frequency oscillations outside the tube, probes of two types are used. A HF probe placed in the magnetic compression region measures the induced signal from the electron beam near-zone in the 10…1500 MHz frequency range. An external removable antenna is used for measurement of the radiation penetrating from the gyrotron through both non-metallic details of the tube and external circuits.

6* 163

The electron energy analyzer (Fig. 1) uses the method of retarding field, similar to the analyzers of gyrotrons with higher voltage (see, for example [6]). The analyzer has spherical shape and is placed behind the longitudinal slot of 1 mm width in the gyrotron collector. The input aperture of the analyzer is placed at such distance from the center of the cavity where the magnetic field value is approximately 180 times lower than the maximum value of the magnetic field distribution. A retarding potential is applied to the spherical electrode with cone-shaped insert. For this configuration, the emission of secondary electrons from this electrode is practically eliminated. In the first experiments described below, the longitudinal slot of the collector was closed.

Results

The following experimental results have been obtained in the regime of single pulses with duration of 30–60 μs. Fig. 2 shows the dependence of the output power P_0 on the cavity magnetic field B_0 measured in the operating regime with accelerating voltage $U_0 = 30$ kV, beam current $I_b = 10$ A and magnetic compression ratio $\alpha = 17.5$. Measurements of the frequency of output radiation allowed us to identify the operating $TE_{12.3}$ mode at 74.2 GHz and two neighboring $TE_{11.3}$ and $TE_{13.3}$ modes at the 70.5 GHz and 78.5 GHz, respectively. The maximum output power is equal to 55 kW for $U_0 = 30$ kV, $I_b = 10$ A and 65 kW for $U_0 = 30$ kV, $I_b = 11.5$ A. We don't yet have any clear answer concerning the discrepancy between the experimental and the designed values of output power. One of the possible reasons is the non-uniformities of emission from the surface of the LaB$_6$-cathode. For magnetic field values corresponding to boundary zones between the modes (Fig. 2), the gyrotron operation was unstable. In some cases, signal at frequencies 20...30 MHz was measured with the mixer of the waveguide spectrum analyzer. This signal can appear as a result of either formation of the beat frequency due to interaction of two signals having close frequencies near the cyclotron one, or modulation of the output carrier frequency.
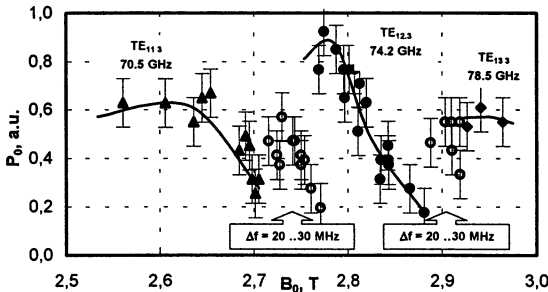
Fig. 2. Output microwave power P_0 as a function of magnetic field B_0 ($U_0 = 30$ kV, $I_b = 10$ A, $\alpha = 17.5$).

164

Low-frequency signals were registered by both the HF probe and the external antenna in the magnetic field range from the lowest values up to the values corresponding to the operating mode excitation. As it follows from our measurements, no essential difference between characteristics of low-frequency oscillations determined by these different techniques was observed. For this reason, we are discussing the results by means of the data obtained using the probe inside the gyrotron only.

The experimental results show that the intensity of oscillations generally increases with increase of the voltage and of the magnetic compression ratio, as well as with decrease of the cavity magnetic field. In the other words, the parasitic oscillations become more intense when the pitch-factor grows. These data agree with results of our simulations and experiments obtained earlier [3–5]. Fig. 3 shows typical plots of the pulse-averaged amplitude of oscillations A_{osc} versus the magnetic field B_0 for different beam currents corresponding to $U_0 = 28$ kV. The $P_0(B_0)$ dependence is shown in this figure as well. Usually, the amplitude of oscillations grows with increase of the beam current.
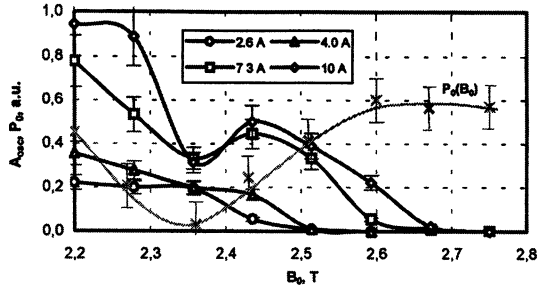
Fig. 3. Average amplitude of low-frequency oscillations A_{osc} ($I_b = 2.6, 4.0, 7.3, 10$ A) and output power P_0 ($I_b = 10$ A) as functions of magnetic field B_0 ($U_0 = 28$ kV, $\alpha = 17.5$).

Simultaneously, the range of magnetic fields providing the conditions for excitation of the oscillations broadens in the direction of stronger fields. The $A_{osc}(B_0)$ dependencies are characterized by a local minimum for the magnetic field value $B_0 \approx 2.35$ T, where the difference between the regime of low current ($I_b = 2.6$ A) without a microwave generation and other regimes with microwave generation ($I_b > 4$ A) is minimum. For this magnetic field value, the output power has also minimum value. Comparison of the $A_{osc}(B_0)$ and $P_0(B_0)$ dependencies allows us to suppose that penetration of microwaves from the cavity into the magnetic compression region and certain effect of these microwaves on the development of the parasitic oscillations may take place. This assumption is confirmed additionally by analysis of the low-frequency oscillation spectra.

Typical "short" waveforms of low-frequency signals and the corresponding spectra are shown in Fig. 4, *a–d*. When magnitude of oscillations is small enough, a waveform usually represents a carrier frequency signal modulated by a much lower (~ 25...30 MHz) frequency. In the case of deeper modulation, two peaks at 125...130 MHz and 150...160 MHz may be seen in the spectra (Fig. 4, *b, c*) where a peak at the modulation frequency is also distinguishable sometimes.

The 125...130 MHz peak is usually the largest. When magnitude of oscillations is huge, the spectra become complicated and noise-like (Fig. 4, *d*). This might be connected with development of non-linear processes in the space charge trapped between the cathode and the magnetic mirror. The modulation frequency is close to the frequency measured with the waveguide spectrum analyzer. Therefore, the influence of microwaves on the space-charge oscillations in the gyrotron trap can be caused by a presence in their spectra the components corresponding to the parasitic oscillations frequency range. Measured values of the carrier frequency of the oscillations are close to predictions based on simulations of the dynamics of the space charge locked between the cathode and magnetic mirror that have been done with the PIC-method described in [5].
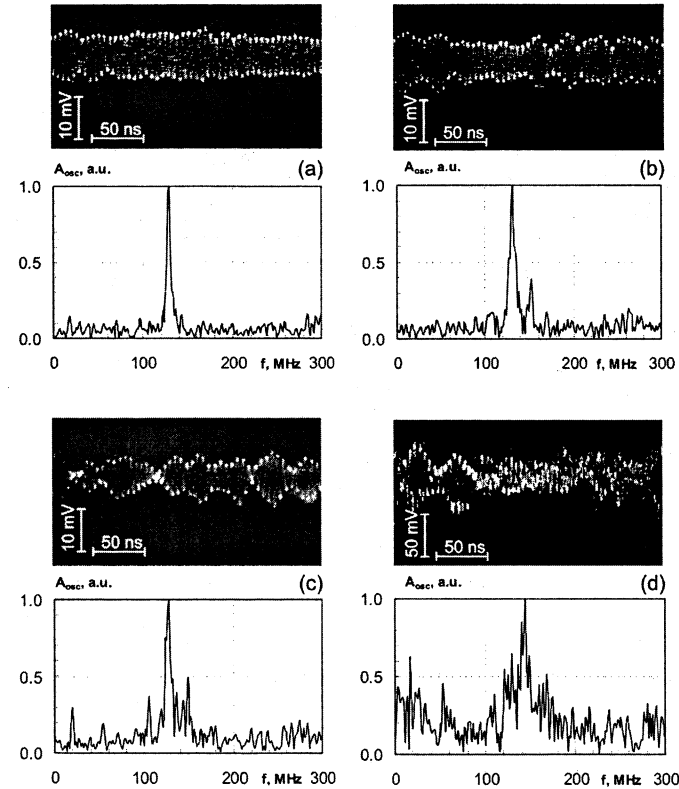
Fig. 4. Typical oscillograms of low-freguency signals and corresponding spectra ($\alpha = 17.5$; $U_0 = 28$ kV (*a*) and 30 kV (*b–d*); $I_b = 4$ A (*a*) and 10 A (*b–d*); $B_0 = 2.51$ T (*a*), 2.62 T (*b*), 2.59 T (*c*) and 2.4 T (*d*)).

According to the experiments performed earlier [1, 2], the complicated electrodynamic structure formed by electrodes of cathode and anode systems, high-voltage feed cable and other wiring connected to the device, may principally have some effect on the low-frequency oscillations in the trapped electron space charge of the gyrotron. To investigate such possible influence of outer circuits on oscillations, we tried to change the electrodynamic structure resonance properties and measured spectral characteristics of low-frequency oscillations. Two parameters were varied in a wide range: the capacitance between the cathode and anode and high-voltage cable length. We have not observed in our experimental conditions any influence of outer circuits onto the low-frequency oscillations. Absence of such influence is confirmed by smooth variation of the oscillation frequency with voltage. That is in good agreement with results of calculations in which the electrostatic approximation was used.

Conclusions and prospects

A 74.2 GHz pulse gyrotron has been manufactured and equipped with a number of diagnostics to investigate an influence of low-frequency oscillations on gyrotron output parameters and electron beam characteristics. First experimental results are in good agreement with numerical simulation data and with results of investigations performed in gyrotron-type electron-optical systems without microwave cavity. As a next step, a study of an influence of axial magnetic field distribution on the parasitic oscillations as well as measurements of the electron energy distribution in the regimes with- and without microwave generation is planned.

References

1. *Tsimring Sh. E.*, Int. J. Infrared Millimeter Waves, **22** (10), 1433 (2001).
2. *Piosczyk B.* et al., 25th Int. Conf. Infrared Millimeter Waves (Beijing, China, 2000).
3. *Louksha O. I., Sominski G G., Kas'yanenko D. V.*, Int. Conf. UHF-99 (St.-Petersburg, Russia, 1999), 130.
4. *Louksha O. I., Sominskii G. G., Kas'yanenko D. V.*, J. Communications Technology and Electronics, **45** (45), suppl. 1, 71 (2000).
5. *Borzenkov D. V., Louksha O. I.*, Zh. Tech. Fiz., **67** (9), 98 (1997).
6. *Glyavin M. Yu.* et al., IEEE Trans. Plasma Sci., **27** (2), 474 (1999).

APPLICATION OF GYROTRON FU SERIES
TO HIGH FIELD ESR MEASUREMENTS

S. Mitsudo, T. Higuchi, T. Idehara, I. Ogawa[1] and M. Chiba[2]

Research Center for Development of Far-Infrared Region, Fukui University
Bunkyo 3-9-1, Fukui 910-8507, Japan
[1]Cryogenic Laboratory, Faculty of Engineering, Fukui University
Bunkyo 3-9-1, Fukui 910-8507, Japan
[2]Depertment applied physics, Faculty of Engineering, Fukui University
Bunkyo 3-9-1, Fukui 910-8507, Japan

The Gyrotron FU series in Fukui University is being developed to provide high frequency source for far-infrared spectroscopy and plasma diagnostics. Submillimeter wave ESR spectrometer using Gyrotron FU series as electromagnetic wave radiation sources and the pulse magnet for high field up to 40 T has been developed. The ESR spectrometer has been successfully applied to several ESR measurements.

Introduction

Electron spin resonance (ESR) spectroscopy in millimeter and submillimeter wave regions using high magnetic fields is one of the most powerful tools for study of the magnetic properties of materials. However, there are many technical problems that we have to overcome, including the following. 1) The power of radiation sources and the sensitivity of available detectors are too low in these frequency regions. 2) High magnetic field is necessary with intensity up to several tens Tesla.

A submillimeter wave gyrotron is used in our ESR spectrometer as a high power radiation source, and an InSb hot electron detector as a high sensitive measurement device. A pulse magnet is useful for generating such a high magnetic field. This high power technique enables us to measure an ESR spectrum during one pulse of magnetic field, instead of the integration technique using a lock-in amplifier.

Medium power, high harmonic gyrotrons in Fukui University (Gyrotron FU Series) have achieved frequency tunability in wide range from 38 GHz to 889 GHz along with high powers in the range from several tens watt to several tens kilowatt [1]. Therefore, the spectrometer has advantages of high power and wide frequency range. We have developed a pulse magnet with the maximum field intensity of 40 T for a submillimeter wave ESR spectrometer.

Gyrotron FU series

Gyrotrons included in Gyrotron FU series are frequency step-tunable sources covering a wide frequency range from millimeter to submillimeter wave region. The output powers are several hundreds watt to several tens kilowatt in fundamental operation and from several tens watt to several kilowatt in second har-

monic operation. This is not so high, compared with the output power of other high power millimeter wave gyrotrons. However, these powers are much higher than other radiation sources employed for ESR experiments in this frequency region. Our gyrotrons are frequency step-tunable sources. As the magnetic field is raised, one resonance after another is excited when adjacent cavity resonances match the electron cyclotron frequencies. Therefore, the resonant cavity is very important part in a gyrotron and should be designed so that suitable frequency steps can be obtained. The range of frequency tunability is determined by the superconducting magnet. For a 17 T superconducting magnet, the frequency is limited below about 440 GHz at fundamental operations of the electron cyclotron resonance, but harmonic operations can extend the range dramatically. However, a harmonic operation is often accompanied by the fundamental operation. The use of the resonant cavity with small diameter removes such mode competition and achieves the single mode operation on high harmonics. For this reason, a resonant cavity of Gyrotron FU IVA was designed with a small radius of 1.615 mm. The operation conditions are as follows. The cathode potential and the beam current are varied from −30 to −40 kV and from 0.1 to 1 A, respectively. The operation is pulsed with the length of 0.1 to 10 ms. Power levels are hundreds of watts at the fundamental and tens of watts at the second harmonic.

Fig. 1. Available magnetic field intensity and frequencies of the Gyrotron FU IV. The thick solid lines shows $g = 2$ ESR resonance condition.

We are improving the operation performances of Gyrotron FU series. Gyrotron FU IV has achieved many advantages as a high quality radiation source, for example, complete cw mode operations, modulations in frequency and amplitude [2], high stabilities of frequency and amplitude, and so on. When the gyrotron is applied to any measurements, these advantages are very convenient. Specially, the complete cw operation with high stabilities of frequency and amplitude is useful for the application to ESR measurement. The operation condition is limited by the heat capacity of the tube. As the consequence, the output power is several tens of watts. Figure 1 shows the available magnetic fields and frequencies of Gyrotron FU IV. The ESR condition for the case of $g = 2$ is also shown by the thick straight line. The completely cw operations were successfully performed up to 301 GHz.

169

ESR system

Figure 2 shows the schematic diagram of our ESR spectrometer. Gyrotron FU IVA is frequency-tunable light source in wide frequency range and has achieved the frequency record of 889 GHz. It consists of a magnetron injection type electron gun, a drift tube, a resonant cavity, an output waveguide and an output window. It is installed in the 70 mm room temperature bore of the 17 T superconducting magnet. The electromagnetic wave from the Gyrotron FU IVA is transmitted by an oversize circular waveguide system with three quasi-optical bends, and fed on a sample located at the center of the pulse magnet. The power transmitted through the sample is measured by an InSb hot electron detector.
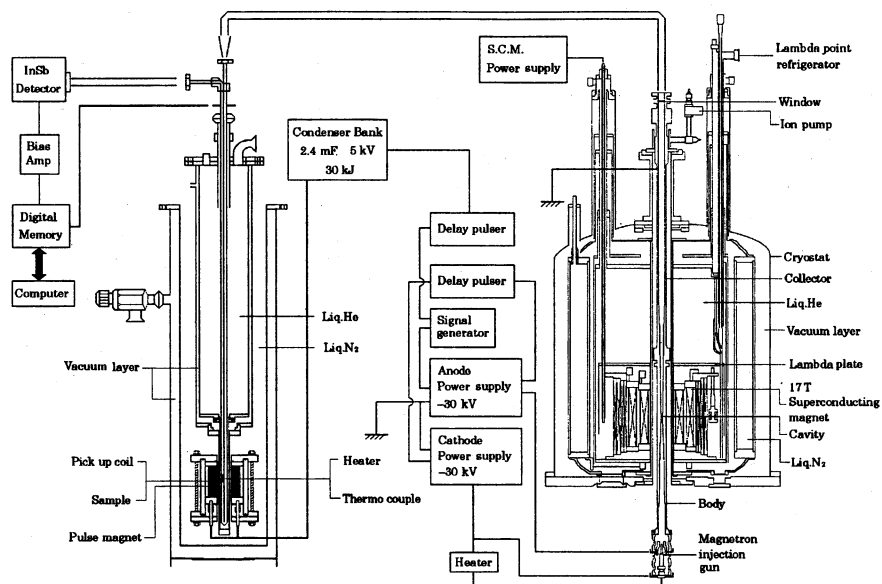
Fig. 2. The schematic diagram of ESR spectrometer using Gyrotron FU IVA as a radiation source and a pulse magnet with the maxmum field intensity of 40 T.

The magnet is fabricated by winding the kapton-coated copper-silver alloy wire on a stainless steel cylinder reel up to eight layers. Each layer is insulated from the next layer and has 25 turns. The length, the inner diameter and the thickness of the stainless steel reel are 80 mm, 12 mm and 0.5 mm, respectively. The cross section of wire is 3 × 2 mm. Both sides of the coil are fixed by FRP flanges. A stainless steel pipe with an inner diameter of 80 mm and a thickness of 10 mm surrounds the coil. The magnet is reinforced by a composite of water and alumina powder impregnated inside the stainless steel pipe. This structure prevents the coil from expanding under Maxwell stress of high magnetic field. The whole

structure of the magnet is immersed in liquid nitrogen. The pulsed magnetic field is produced by discharging a capacitor bank of 30 kJ into the magnet coil. The field intensity pattern is similar to a half sinusoidal one with the width of 2.5 ms.

The signals from the pickup coil for magnetic field and from the InSb detector are measured as functions of time and recorded in a personal computer. Thereafter, the computer arranges automatically both signals for constructing an ESR spectrum as a function of magnetic field intensity. The temperature is measured by the Fe–Au 0.007 at.% – Ag thermocouple.

ESR measurements in $CsFeCl_3$

This ESR spectrometer has been applied to several ESR measurements. One of recent results of ESR measurement will be introduce here.

In the singlet ground-state system $CsFeCl_3$ a large single-ion anisotropy causes a singlet ground state and a doublet as first excited states of Fe^{2+} ion. In addition the magnetic interaction is an isotropic being much lager along crystal c-axis than perpendicular to it. Therefore, a quasi-one-dimensional magnetic model system is ideal to demonstrate.

Many experiments have been done on $CsFeCl_3$. In zero magnetic fields $CsFeCl_3$ shows no long-range order even at very low temperatures. Chiba et al. measured the magnetization in pulsed magnetic field up to 40 T applied parallel to the crystal c-axis. They observed a large liner increasing of magnetization between magnetic field 4 T and 11 T, and a metamagnetic transition around 33 T [4]. In order to clarify the nature of the above-mentioned magnetization process, the ESR measurement is powerful method. ESR measurement has an advantage that a direct observation is possible on the behavior of the electric spin state. ESR measurements were performed under the pulsed magnetic fields up to 40 T at the temperature 4.2 K. Figure 3 shows the observed ESR spectra at the different operating frequencies up to 404 GHz. Several ESR absorptions were observed. Figure 4 shows frequency-field diagram of ESR absorptions (left axis) and the magnetization curve (right axis). The frequency dependence of ESR spectra were observed symmetric with respect to the magnetic fields $B_{c1} = 7.5$ T and $B_{c2} = 33$ T at which magnetization increase rapidly. The symmetric ESR absorptions around magnetic field B_{c1} were explained by the ground-state crossover in framework of fictitious spin $S = 1$ as the same as magnetization process [4]. However, the symmetric absorptions around the magnetic field B_{c2} cannot be explained in the framework of the fictitious spin $S = 1$. One of possible mechanisms of the behavior of the ESR spectra around B_{c2} is the ground-state crossover of the energy level of $S_z = -2$ in framework of fictitious spin $S = 2$. However, at the present we cannot explain how dose the state $S_z = -2$ comes down such a low magnetic field?

171
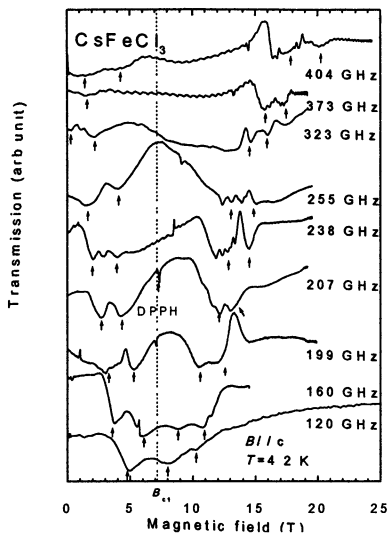
Fig. 3. The observed ESR spectra at the different operating frequencies up to 404 GHz.
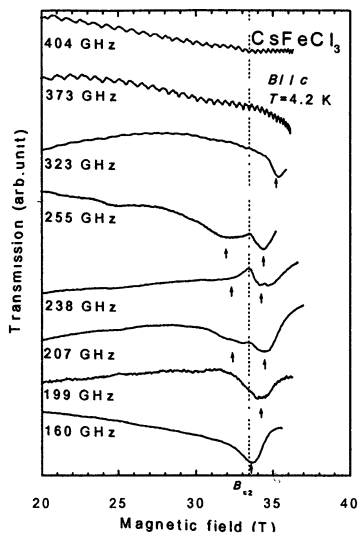
Fig. 4. Frequency-field diagram (left axis) and magnetization process(right axis). Open circles corespond to the magnetic fields of ESR resonances at eache operation frequences. The solid and doted lines are eye guid.
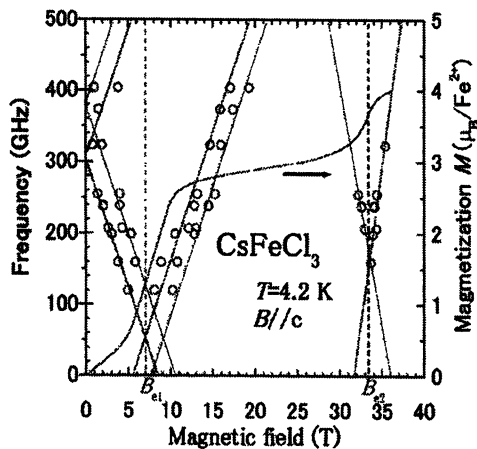
The more details of the analysis of the ESR spectra will be presented in separate paper.

References

1. *Idehara T.* et al., IEEE Trans. Plasma Sci. **27**, 340 (1999).
2. *Ogawa I.* et al., Fusion.Eng. Design **53**, 571, (2001).
3. *Chiba M.* et al., Solid State Commun. **63** (1987) 427.
4. *Tuneto T., Murao T.*, Physica **51**, 186 (1971).

172

MULTIWAVE ANALYSIS OF COAXIAL STRUCTURE WITH CORRUGATED INSERT BASED ON THE SINGULAR INTEGRAL EQUATION METHOD

O. Dumbrajs, Yu. V. Gandel[1], G. I. Zaginaylov[1]

Helsinki University of Technology, Helsinki, Finland
[1]Kharkiv National University, Kharkiv, Ukraine

New generation of gyrotrons based on coaxial cavities is expected to be the most feasible for fusion applications. An advanced coaxial insert has longitudinal corrugations for improvement of mode selective properties. The existing theory of a corrugated insert is valid under the assumption that the width and period of corrugations are smaller than the half wavelength of RF oscillations. As one goes over to higher frequencies, it becomes increasingly difficult to provide validity of this assumption because of the mechanical rigidity of the slots. A new theory based on the full wave analysis and valid for arbitrary size corrugations has bee developed and applied for ITER relevant coaxial gyrotron cavity.

1. Introduction

Design of a gyrotron resonator begins with choosing the geometry of the resonator in such a manner that the cavity supports oscillations of the desired mode at desired frequency. Here as the first step one has to solve the appropriate equation for determining eigenvalues of the modes. Up to date, design criteria for coaxial gyrotrons were worked out on the basis of the simplified surface impedance model [1]. It is rather simple and convenient for optimization of coaxial cavity parameters. However, progress in coaxial cavity gyrotron design is constantly accompanied by increasing azimuthal and radial indexes of the operating and competing modes. It results in increasing a sensitivity of a mode competition scenario to the calculational errors. That is why, the development of more sophisticated methods for analysis of the eigenvalue problem is rather desirable.

2. Equations for determining eigenvalues

A. Old theory. In the case of a coaxial resonator with corrugations on the wall of the insert (Fig. 1) the eigenvalue χ_{mp} of the TE_{mp} mode can be determined by means of the following transcendental equation [1, 2]:

$$J'_m(\chi_{mp})[N'_m(\chi_{mp}/C) + WN_m(\chi_{mp}/C)] -$$

$$- N'_m(\chi_{mp})[J'_m(\chi_{mp}/C) + WJ_m(\chi_{mp}/C)] = 0, \tag{1}$$

where J_m and N_m are the Bessel and Neumann functions respectively, $C=R_{cav}/R_{in}$, R_{cav} is the outer radius of the cavity, R_{in} is the insert radius, and W is the corrugation parameter defined as:
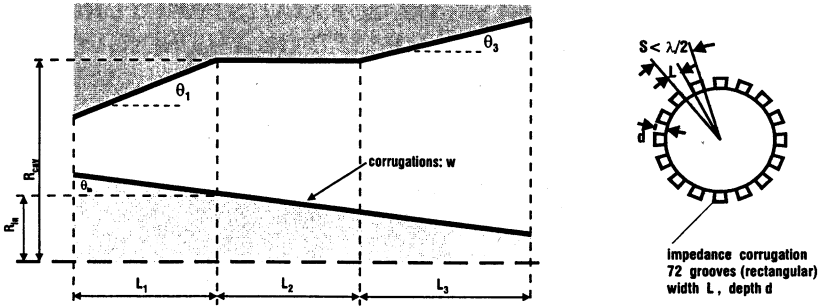
Fig. 1. Coaxial cavity with an insert with longitudinal corrugations (top). Cross section of the insert (bottom).

$$W = (L/S)\tan(2\pi d/\lambda), \qquad (2)$$

where L is the width, S is the period, and d is the depth of corrugations, λ is the wavelength. Eq. (1) is solved numerically for a specific current value of $C(z)$.

B. New theory. The surface impedance model represented by Eqs. (1) and (2) provides rather accurate results for the function $\chi_{mp}(C(z))$ under the condition $S<\pi R_{in}/m$. If this condition is satisfied only marginally, errors for small C might become significant. Close to the surface of gratings, where higher spatial and Fourier harmonics (omitted in (1)) are significant, this model fails.

A more rigorous analysis taking into account all spatial harmonics (full wave analysis) can be based on the integral equation (IE) approach. Usually it leads to the first kind IE with logarithmic singularity. The integration should be accomplished over the surface of the structure. Both of these are not convenient for numerical analysis, since the first kind IE with the logarithmic singularity does not belong to the well-conditioned problems. Meanwhile, surfaces of structures can be rather complex. One modification of the IE approach allowing us to overcome above-mentioned troubles has been suggested in [3, 4]. Instead of first kind IE with logarithmic singularity it has been proposed to use a singular integral equation (SIE) (with the Cauchy-type kernel) with an addition condition. SIE can be derived by differentiation of the initial IE. Whereas, the addition condition can be obtained by integration of the initial IE. Such an approach for a rectangular waveguide grating has been developed in [5, 6].

For coaxial structures with a corrugated insert the SIE approach has been developed in [7]. Since the first kind SIE is equivalent to the second kind Fredholm integral equation, mathematically proved well-conditioned numerical algorithms can be developed for solving SIE. Direct discretization schemes [7] can be used which allows a substantial reduction of analytical and numerical computations. The corresponding exact dispersion relation reads as follows:

174

$$\sum_{n=-\infty}^{\infty} \frac{\Delta_{k_n}(\chi_{mp}, \chi_{mp}/C) 2\sin(k_n\varphi_L/2)}{\Delta'_{k_n}(\chi_{mp}, \chi_{mp}/C) k_n} a_n - \frac{\Delta_0(\chi_{mp}/C', \chi_{mp}/C)}{\Delta'_0(\chi_{mp}/C', \chi_{mp}/C)} = 0. \quad (3)$$

Here $\Delta_\nu(a, b) = J'_\nu(a)N_\nu(b) - J_\nu(a)N'_\nu(b)$, $\Delta'_\nu(a, b) \equiv \partial \Delta_\nu(a, b)/\partial b$, $\varphi_L = 2\pi L/R_{in}$, $k_n = m + nN$, $C' = R_{cav}/(R_{in} - d)$, N is the number of grooves, a_n are normalized amplitudes of spatial harmonics. Retaining only the term with $n=0$ in the sum, assuming that $m\varphi_L/2 << 1$ and the field inside the grooves is uniform, one can reduce (3) to (1). The main difficulty in solving (3) is related to the numerical evaluation of the Bessel and Neumann functions. For $|n| \geq 2$ and typical experimental parameters these functions become very small or very large, beyond the accuracy of ordinary computers. To overcome this difficulty, special new representations were derived which are valid for very large indices and arguments. New representations make it possible to perform calculations with a desired accuracy. The inverse Fourier transform $a_n \sim \int_0^{\varphi_L} e^{-ik_n\varphi} F(\varphi) d\varphi$, where $F(\varphi)$ is the azimuthal electric field E_φ at the aperture of grooves, was used to calculate the normalized amplitudes of spatial harmonics. Here the first kind SIE was derived for $F(\varphi)$. It was solved numerically using two discretization schemes. The first scheme is based on the Gauss quadrature rules for singular integrals similar to those listed in [3, 6]. The second scheme is based on the quadrature rules using the Jacobi polynomials [7]. An excellent agreement is found between the predictions of the two schemes. Also it should be pointed about other schemes of full wave analysis. One of them has been developed in [8] on the basis of a moment method. It is efficient for not too large m and p. Nevertheless, a surprisingly good agreement between the newly developed and this analysis has been also found for the case considered below.

3. Specific example

As an example we consider the ITER relevant 2 MW CW coaxial cavity gyrotron whose design is described in [2]. In this gyrotron the $TE_{34,19}$ mode is supposed to be the working mode at frequency $F = 170$ GHz. The relevant competing modes are shown in the table.

Here Q_{old} and Q_{new} are quality factors obtained by means of the old and new formalisms respectively. The somewhat larger values of Q_{new} can be explained by the fact that in the new theory the absolute values of the derivatives $|d\chi_{mp}(z)/dz|$ are smaller than in the old formalism. In Fig. 2 we illustrate this fact in the case of the $TE_{32,20}$ mode.

Mode	F (GHz)	Q_{old}	Q_{new}
$TE_{34,19}^{-}$	170.02	1643	1659
$TE_{36,19}^{-}$	174.24	1729	1728
$TE_{33,20}^{+}$	173.26	1585	1652
$TE_{35,19}^{-}$	172.13	1689	1697
$TE_{32,20}^{-}$	171.15	1468	1557
$TE_{33,19}^{-}$	167.90	1585	1615
$TE_{32,19}^{-}$	165.79	1507	1557
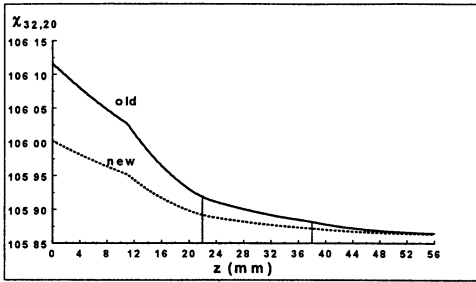
Fig. 2. Eigenvalue of the $TE_{32,20}$ mode as a function of the resonator longitudinal coordinate z. The vertical lines mark the middle section of the cavity.

It can be seen from the table that the relative increase of the quality factor is different for different modes: the smallest ($\sim 0\%$) for the $TE_{36,19}$ mode, the largest ($\sim 7\%$) for the $TE_{32,20}$ mode, and $\sim 1\%$ for the operating $TE_{34,19}$ mode. This means that the mode competition scenario based on the new eigenvalues might be different. Indeed, calculations performed by means of a multimode, self-consistent, time-dependent code show (Fig. 3) that according to the new formalism at low voltages the $TE^-_{33,20}$ mode should oscillate instead of $TE^-_{36,19}$ and $TE^-_{35,19}$ modes.
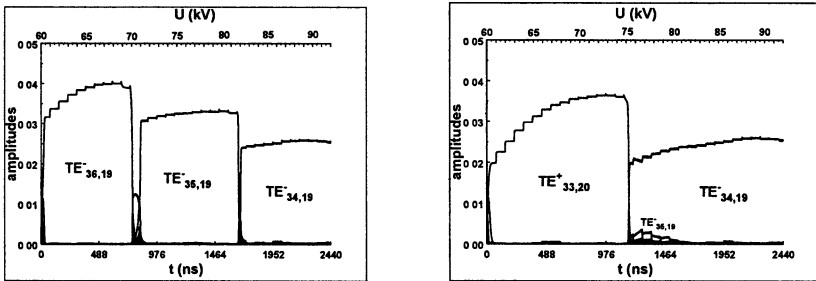
Fig. 3. Mode competition scenarios with old χ (left) and new χ (right). Here the operating current $I = 70$ A, the magnetic field $B = 6.86$ T, the electron beam radius $R_{el} = 10.2$ mm, and the electron pitch factor is 1.30 for $U = 90$ kV.

It is interesting to note that for modes with $m = N/2$ the terms in Eq. (3) corresponding to the fundamental ($n = 0$) and (-1) spatial harmonic ($n = -1$) are the same. As a result, such modes have a structure of a standing wave in the azimuthal direction and will be trapped inside gyrotrons with conventional launchers designed for output of rotating waves. This means that in the particular example N must be larger than 72.

4. Conclusions

A new formalism for calculating eigenvalues of modes in coaxial gyrotron cavities with a corrugated insert has been presented and its impact on the mode competition scenario illustrated. It can be expected that the new formalism will predict smaller thermal wall loading in the inner conductor, because higher spatial and Fourier harmonics neglected in the surface impedance model can lead to extrusion of the total field from the region near the grating. Also it should be noted that the new approach takes into account the coupling between right- and left-rotating modes, appearing due to the azimuthal periodicity. For typical parameters it is usually small. But for modes with $m = N/2$ it is always strong independently from parameters of the periodicity. It leads to formation of a standing wave in the azimuthal direction. Excitation and output of such modes can be rather different from other modes.

References

1. *Iatrou C. T., Kern S., and Pavelyev A. B.*, IEEE Trans., Microwave Theory Tech. **44**, 56 (1996).
2. *Dumbrajs O., Piosczyk B., and Iatrou C. T.*, Proc. 26 th Intern. Conf. on Infrared and Millimeter Waves (France, Toulouse, September 10–14, 2001).
3. *Gandel Yu. V.*, Voprosy kibernetiki (Moscow, AN SSSR, 1986, in Russian) **124**, 166.
4. *Gandel Yu. V.*, Methods of discrete singularities in aerodymamics, electromagnetics and diffraction theory (Feodosia, 1997, in Russian), 176.
5. *Zaginaylov G. I., Hirata A., Shiozawa T., and Ueda T.*, IEEE Trans. Plasma Sci. **28**, 614 (2000).
6. *Zaginaylov G. I., Gandel Yu. V., Kamyshan O. P.* et al., IEEE Trans. Plasma Sci., 2002, **30** (in print).
7. *Gandel Yu. V., Zaginaylov G. I., and Steshenko S. A.*, Radiophysics and electronics **7**, Special Issue, 196 (2002; in Russian).
8. *Raguin J.-Y. and Schuenemann K.*, Proc. Int. Conf. "Electronics and Radiophysics of Ultra-High Frequencies" (St.-Petersburg, Russia, 1999), 403.

FAST COMPUTER ESTIMATION OF BASIC PARAMETERS FOR GYROTRON MAGNETRON INJECTION GUNS

V. K. Lygin, V. N. Manuilov, M. V. Youlpatova

Institute of Applied Physics, RAS, Nizhny Novgorod, Russia

A code for simulation of the gyrotron electron-optical system within the framework of adiabatic theory under the paraxial magnetic field assumption is developed. It allows one to obtain zero order approximation of gyrotron gun basic parameters: magnetic field distribution in any part of the formation system, geometry of electrodes, velocity spread caused by different factors, potential depression and maximum value of perveance and beam current in the cavity and some most important collector parameters.

Introduction

Magnetron injection guns (MIG) are known to be the most efficient formation systems in gyrotron devices. Exact calculation of basic parameters for such systems is a complicated process based on trajectory analysis. Nevertheless, since magnetron injection guns have weakly inhomogeneous electron and magnetic fields along the electron trajectory, it is possible to use adiabatic theory for preliminary estimation of gyrotron MIG parameters and some parameters of gyrotron electron optic system.

The adiabatic theory of magnetron injection gun uses the following assumptions:

- axial symmetry of the system;
- space charge is negligible;
- quaziplane configuration of electrodes;
- magnetic fields are paraxial: $B_z(r, z) \approx B_z(0, z) \equiv B_z$, where r, z are cylindrical coordinates.

Under these assumptions the MIG adiabatic theory was developed in the works [1–4]. It made possible to obtain analytical relation for basic parameters of gyrotron electron optic system.

Calculation of magnetic field distribution

Magnetic field distribution for a magnetic system usually consisting of a number of coils, can be calculated in two ways: using the so-called traditional calculation by coil geometry sizes, described by (1.5) of the work [5], and by using a number of windings of every coil and the value of winding current or winding current density, the relations (1.4), (1.8) in [6]. Calculations allow one to determine the contribution of magnetic field from every coil that may be further used in the trajectory analysis. Based on axial magnetic field distribution we can find approximate cathode location for a given configuration of magnetic system.

BZ

Z(mm)
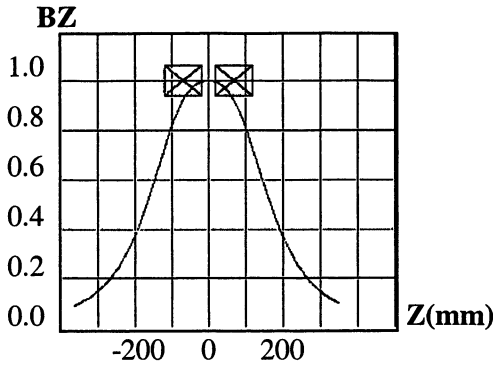
Fig. 1. Example of normalized axial magnetic field distribution for 2 coil magnetic system.

Adiabatic gun parameter calculation

In our code we use the following engineering relations for calculation of basic parameters of the magnetron injection gun [1]:

$$U_a^* = 2.63 \frac{t_\perp^{2/3} U_0^{*2/3} E_k^{2/3}}{B_0^{*2/3} t_h} , \qquad (1)$$

$$d = 2.63 \frac{t_\perp^{2/3} U_0^{*2/3}}{B_0^{*2/3} t_h E_k^{1/3}} , \qquad (2)$$

$$l = 2.63 \frac{t_\perp^{2/3} U_0^{*2/3}}{B_0^{*2/3} t_h E_k^{1/3}} t_l , \qquad (3)$$

$$R_k = 1.23 \frac{t_\perp^{1/6} U_0^{*1/6} B_0^{*1/3}}{E_k^{1/3}} R_0 , \qquad (4)$$

$$\alpha = 1.52 \frac{t_\perp^{1/3} U_0^{*1/3} B_0^{*2/3}}{E_k^{2/3}} , \qquad (5)$$

$$j_k = 4.53 \frac{t_j t_h^{1/2} B_0^{*1/3} E_k^{5/3}}{t_\perp^{1/3} U_0^{*1/3}} , \qquad (6)$$

$$I = 0.93 \frac{t_j E_k R_0 t_l U_0^{*1/2} t_\perp^{1/2}}{t_h^{1/2}} . \qquad (7)$$

The parameters marked by the asterisk are calculated by employing the following substitution:

$$U_0^* = U_0(1 + 0.001lt_\perp),$$ (8)

$$B_0^* = (1 + 0.002U_0)\frac{107}{\lambda \cos \varphi n},$$ (9)

$$U_a^* = \frac{U_a d \cos \psi}{R_k \ln R_a / R_k},$$ (10)

$$R_a = R_k + d \cos \psi.$$ (11)

In this formulae U_0, B_0 are the accelerating voltage and magnetic field in the operating space, U_a is anode voltage, E_k is the electric field on the cathode surface, R_k is the radius of cathode, d is the distance between cathode and anode, l is emitter width, R_0 is the mean beam radius in resonator, α denotes magnetic decompression ratio, $t_\perp$ is the oscillator energy to the full energy ratio, $t_h \approx h/d$, where h is the height of electron above cathode in the first orbit, $t_j = I/I_L -$ beam current to Langmuir current ratio, j_k stands for emission current density, φ is angle between cathode and magnetic field, ψ is cathode angle, λ is wave length and n is operating harmonic number. Figure 2 demonstrates scheme of gyrotron electron optic system.
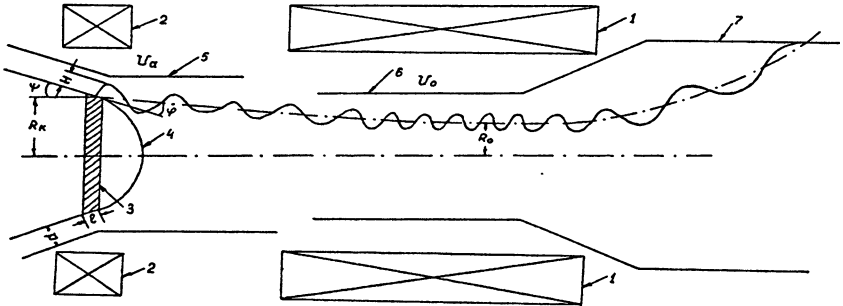
Fig. 2. *1* – main coil, *2* – cathode coil, *3* – emitter, *4* – cathode, *5* – anode, *6* – cavity, *7* – collector.

Velocity spread estimation

Velocity spread depends mainly on thermal electron velocity, the roughness of emitter surface, the electric field of space charge, cathode shift from the axis

180

and position velocity spread [2–3]. The code provides preliminary calculation of velocity spread for every factor in correspondence with the following relations: velocity spread caused by thermal electron velocity:

$$\delta V_\perp \approx 3.6 \sqrt{\frac{E}{U_a t_h}}, \tag{12}$$

velocity spread caused by the roughness of emitter surface:

$$\delta V_\perp \approx 1.5 \sqrt{\frac{r_0}{h}}, \tag{13}$$

velocity spread caused by the cathode shift from axis:

$$\delta V_\perp = \frac{2a\cos\psi}{d}, \tag{14}$$

velocity spread caused by space charge field:

$$\delta V_\perp = \pi \frac{I}{0.5 R_k E_k^2 / B_k}, \tag{15}$$

where E denotes thermal electron energy, r_0 is roughness radius a is the radial shift, B_k is the value of magnetic induction on the cathode surface.

The calculated values allow one to determine the influence of each factor on the value of total velocity spread. The final value of velocity spread is obtained from subsequent trajectory analysis.

Estimation of potential depression, maximum values of perveance and beam current

For every value of resonator potential U_0 there are limit values of beam current, perveance and potential depression relative to a resonator wall. According to [4] for monovelocity electron beam these values can be estimated by the following relations:
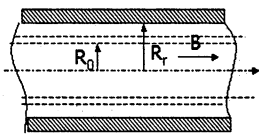
Fig. 3. Electron beam in the cavity.

$$x_{\max} = 2/[3(1 + g_0^2)] \tag{16}$$

$$P_{\max} \approx 13/[(1 + g_0^2)^{2/3} \ln(R_r / R_0)] \tag{17}$$

$$I_{\max} \approx 0.4 U_0^{3/2} /[(1 + g_0^2)^{3/2} \ln(R_r / R_0)] \tag{18}$$

Here x_{max}, P_{max}, I_{max} are maximum potential depression, perveance and beam current, R_0, R_r are the radii of guide center and resonator respectively and g_0 denotes pitch-factor.

181

Account of possible spread velocity can decrease these values. The code provides calculation of the maximum values of perveance, beam current and potential depression for monovelocity electron beam as well as for the electron beam with velocity spread with rectangular distribution function. For example, for 140 GHz gyrotron with resonator potential 80 kV, resonator radius 18 mm, radius of guide center 7.92 mm, pitch-factor 1.4, account for velocity spread of 0.2 decreased maximum value of beam current from 68.5 A for monovelocity electron beam to 55.8 A.

Estimation of main collector parameters

Within the framework of the adiabatic theory we can estimate some collector parameters according to the following relations [7]:

$$B_{col}(z_{ct}) = B_0 / \alpha_{col} \tag{19}$$

$$\alpha_{col} = (R_{col} / R_0)^2 \tag{20}$$

$$l = \begin{cases} \dfrac{\Delta R_{col}}{\mathrm{Sin}\varphi_{col}} + \dfrac{h_k}{(1 + \dfrac{\mathrm{tg}\varphi_{col}}{\mathrm{tg}\gamma})\mathrm{Cos}\varphi_{col}}, & 0 \le \varphi_{col} \le \gamma \\[4mm] \dfrac{\Delta R_{col}}{\mathrm{Sin}\varphi_{col}} + \dfrac{2r_{Lcol}}{\mathrm{Sin}\varphi_{col}}, \gamma \le \varphi_{col} \le \dfrac{\pi}{2} \end{cases} \tag{21}$$

$$\rho_{wm} = \frac{IU_0}{2\pi R_{col}l_{col}} \tag{22}$$

Here z_{ct} is the center of beam trace on collector, B_{col} is magnetic field, α_{col} is magnetic decompression ratio, l denotes beam track length, $\Delta R_0, \Delta R_{col}$ are spread of guiding center radii in resonator and collector respectively, r_{Lcol} is Larmor radius, h_k stands for the step of electron trajectory, φ_{col} is collector angle, γ is angle of approximation line and ρ_{wm} is mean power density.

Maximum pulse duration is estimated from the condition of maximum temperature of resonator wall of 300°.

Code for fast estimation of basic parameters
of gyrotron electron-optic system

The code provides the following possibilities:
- calculation of basic parameters of gyrotron electron-optic system based on the relations given above;

182

- dialog-based and file-based parameters input;
- choosing a calculation method of magnetic field distribution;
- choosing a gun calculation method based on the value of electric field on the cathode surface or on the cathode radius;
- calculation for one and two-potential guns.

Convenient multi-windows interface allows one to consider a few MIG versions simultaneously. It combines high-operating time with graphic data presentation and Web-oriented help system. The code operates in MS Windows 9x and higher.

Conclusions

The proposed code is a useful tool for preliminary analysis of basic parameters for gyrotron electron optic system. Calculated values may be then used as a good approximation for further trajectory analysis. The code may be successfully used for educational purposes.

Acknowledgement. The authors acknowledge M. I. Petelin, A. L. Goldenberg and Sh. E. Tsimring for their great contribution to the theory of gyrotron electron-optic system which was widely used in this work.

References

1. *Karasik V. P.* Physics and Technique of Strong Magnetic Fields. Nauka, Moscow, 1964, 11.
2. *Montgomery D. B.* Solenoid Magnet Design. Mir, Moscow, 1971.
3. *Goldenberg A. L.* et al., Gyrotron, Gorky, 1981, 86.
4. *Tsimring Sh. E.* Izv. Vuzov, Radiofizika, **15** (8), 1247 (1972).
5. *Tsimring Sh. E.* Lectures on microwave electronics. V. 4. Saratov University, Saratov, 1974.
6. *Tsimring Sh. E.* Radio Engineering and Electronics, Moscow, 1990, **35**, 1284.
7. *Goldenberg A. L.* et al., Electronika SVCH, 1973, № 5, 73.

JINR-IAP FEM OSCILLATOR WITH A BRAGG RESONATOR: EXPERIMENTAL INVESTIGATION AND APPLICATION

A. V. Elzhov, N. S. Ginzburg[1], E. V. Ilyakov[1], I. N. Ivanov,
A. K. Kaminsky, V. V. Kosukhin, I. S. Kulagin[1], S. V. Kuzikov[1],
E. A. Perelstein, N. Yu. Peskov[1], M. I. Petelin[1], S. N. Sedykh,
A. P. Sergeev, A. S. Sergeev[1], N. I. Zaitsev[1]

Joint Institute for Nuclear Research, Dubna, Russia
[1]RAS Institute of Applied Physics, Nizhny Novgorod, Russia

The 30 GHz FEM oscillator with Bragg resonator is under development by JINR-IAP co-operation for 10 years. Several types of Bragg resonators have been tested and optimized. The FEM output radiation is used now for experimental investigation of the lifetime of a high Q-factor copper resonator, which simulates the accelerating structure of linear collider CLIC. The report presents one of recent experimental results – precise FEM frequency tuning in the range of 5–6%. The setup and first experiments on test cavity feeding are also described.

Introduction

FEM oscillators with reversed guide magnetic field and Bragg resonator are under investigation at Laboratory of Particle Physics, JINR (Dubna) in collaboration with IAP RAS (Nizhny Novgorod) for last years. It was proved experimentally [1, 2] that for millimeter wavelength range this FEM scheme provides oscillator parameters as follows:
– spectrum width (FWHM) about 0.1%;
– generation efficiency about 20% (with respect to the beam power at the linac output).

Our recent experiments show a possibility of precise tuning of the operating frequency with accuracy about 0.1% in the range of 5–6%, which can be reached by variation of corrugation phase shift between the Bragg reflectors. Figure 1 demonstrates that the central mode (CM) is the only operating mode in wide region of the phase shifts, while near the edge of the region a low-frequency side mode (SM) can be excited as well at the proper choice of experimental conditions.
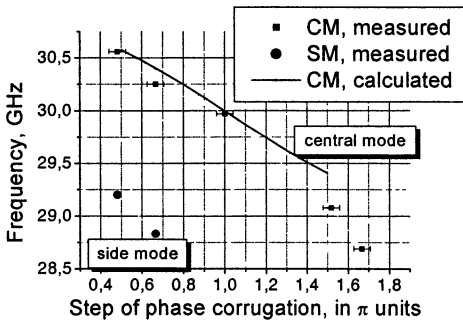
Fig. 1. Dependence of the frequencies of the FEM oscillator modes on the value of the corrugation phase shift between Bragg reflectors.

184

These experiments were carried out on the base of LIU-3000 linac (0,8 MeV, 200 A, 200 ns). Created FEM oscillator with operating frequency f = 30 GHz (i.e. the frequency of the accelerating structures of the CLIC collider, CERN [3]) is suitable for solving some collider-related problems. One of such tasks, which FEL group (JINR) solves with the colleagues from IAP, was declared jointly with CLIC group. The problem is that at frequencies of collider accelerating structures over 10 GHz a new limitation on the operation lifetime of the collider occurs. It is concerned with significant pulsed heating of the components of copper accelerating structures due to the growth of energy absorbed in the structures. The authors of paper [4] consider that the pulsed heating becomes an important impediment to higher gradients at shorter wavelength, and at the frequencies of about 30 GHz and higher this limitation can be even more serious than restrictions because of RF breakdown and dark current trapping.

RF pulsed heating is a process by which a metal is heated from magnetic fields on its surface due to high-power pulsed RF. Since the heating occurs over a short time, the inertia of the material prevents expansion and thermal stresses are induced. If these stresses are larger than the elastic limit, known as the yield strength, then damage in the form of microcracks on the surface may occur after many pulses. This type of damage is known as cyclic fatigue. The extent of metal structures heating by RF pulses may be estimated from paper [5] where the results of similar calculations for electron current pulses are given. Besides, this paper includes comparison of the obtained results with experimental data and their analysis.

The values of the dangerous values of pulsed RF heating at frequencies over 10 GHz are determined very approximately now: from 40 up to 400 °C [4, 6, 7]. We are familiar only with one paper [6] where experimental data on this subject are presented. These data were got at operating frequency of 11.424 GHz. This paper the results on the creation of experimental facility for investigation 30 GHz RF heating are presented.

Test facility scheme and cold measurements results

A characteristic feature of the test facility under design is related to the output RF power of the operating FEM that is only about 10% of power needed for feeding of full-scale accelerating structure of CLIC collider. In order to get the proper data on the influence of RF pulse heating on the accelerating structure material, a special test cavity has been developed and manufactured. It is possible to provide a wide range of heating regimes in this cavity at moderate input power level.

The view of the test facility is presented in Fig. 2. The setup consists of electron linac, FEM oscillator, test cavity, transportation channel of RF beam from FEM to the cavity, and electron-beam/RF/power measuring systems. In order to optimize the test cavity heating and solve electric breakdown problems, a H_{01} mode was chosen as an operating one. The RF beam line contains: forward beam

transformer into Gaussian beam, two confocal mirrors, reverse transformer and wavetype converter (H_{11} to H_{01}). The frequency of RF radiation and spectrum are measured with resonance waveguide filter and heterodyne respectively. To measure spatial distributions of RF power at megawatt level in near-field zone a unique detector based on dielectric waveguide with adjustable attenuation was developed and manufactured.
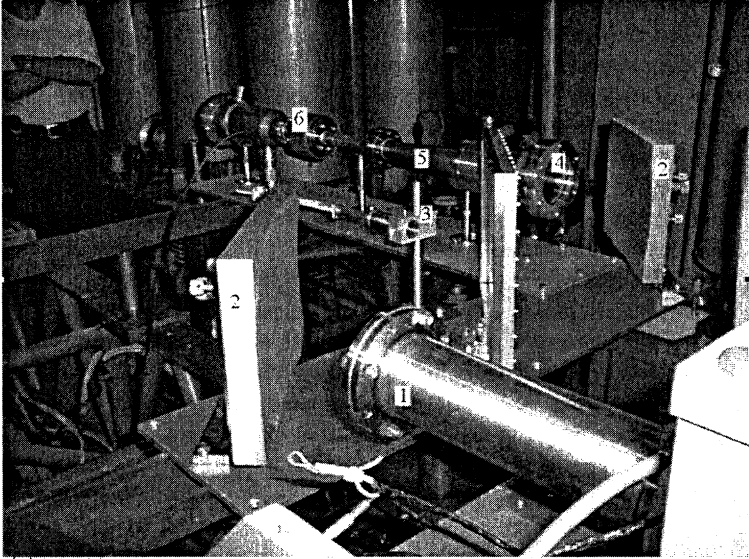
Fig. 2. Overview of the setup for investigating the RF pulse heating: *1* – FEM oscillator output, *2* – mirrors, *3* – detector, *4* – vacuum window, *5* – wavetype converters and mode transformers, *6* – test cavity.

The cold measurements (Fig. 3) demonstrated that the power losses along the RF beam line are low enough in wide frequency range while the test cavity possessed good resonance properties.
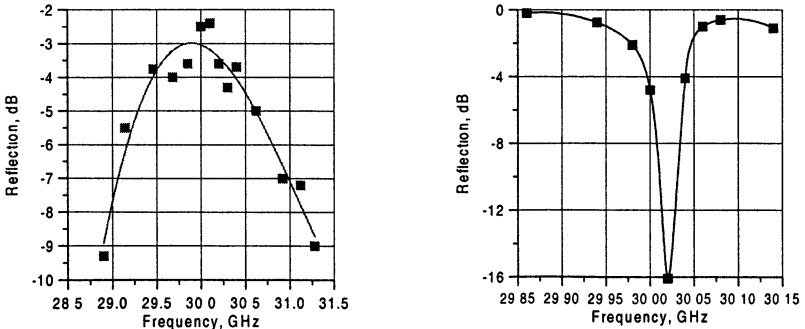
Fig. 3. The results of the cold measurements of the transmission line and test cavity

186

Test cavity feeding: first results

The specific character of the problem imposes additional requirements on the parameters of FEM oscillator, transmission line and measuring systems:

– the FEM oscillator output power must be 20–25 MW at pulse duration of 150–200 ns;

– to reduce the power losses in the cavity it is necessary to match the FEM oscillator spectrum with test cavity band;

– statistics acquisition for chosen regimes of test cavity heating should be amounted to 10^5–10^6 pulses;

– variation of the RF pulse amplitude and duration during investigation of cavity heating should not exceed 10%;

– monitoring RF power and spectrum in each pulse should be provided.

In practice, this set of additional requirements presumes that a full-scale test facility on the base of experimental setup for EFM investigation should be created. The facility is subjected to strong demands on RF oscillator output power and spectrum, stability and lifetime of all systems.

Figure 4 presents a typical oscillogram including an RF radiation pulse at the FEM output (trace 1), a heterodyne signal (trace 2) and corresponding spectral distribution of the radiation (middle trace). The measured power is about 25 MW,
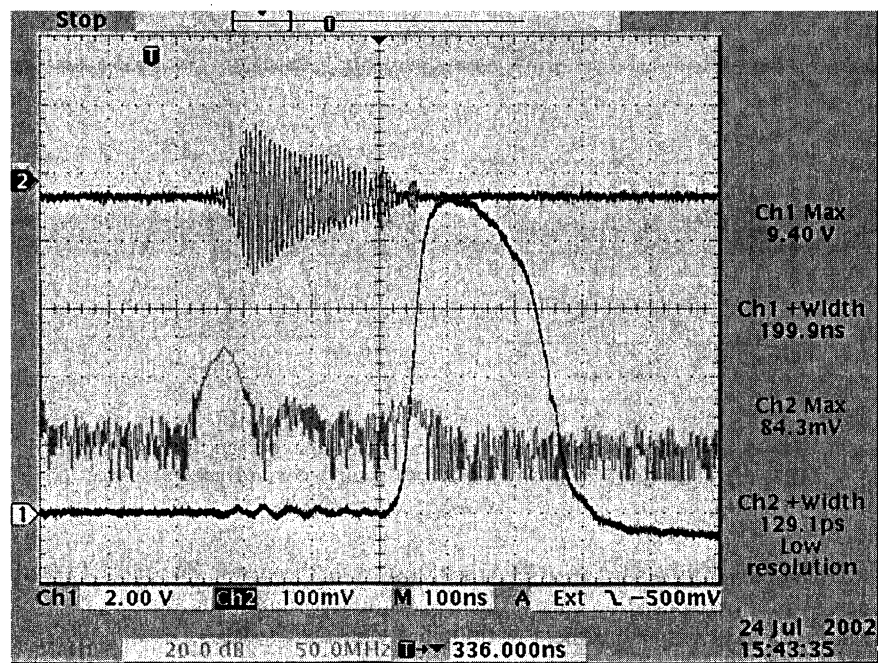
Fig. 4. Typical diagnostic oscillogram

187

pulse duration is about 200 ns and full spectrum width (at 30 dB level) doesn't exceed 50 MHz. So the RF pulse parameters meet the declared requirements. The tests showed that the stability is good enough in short pulse sequences (each of 500 pulses). However the long-term stability is still not satisfactory.

Besides, sufficient RF power losses between FEM output and test cavity exit were revealed in the measurements. Partially they conditioned by difference RF beam line alignment in cold beam-loaded measurements. That is illustrated by Fig. 5 where angular distributions of the RF power measured in various points of transportation channel are shown. One can see clearly from Figs. 5, a–c a RF beam displacement from the system symmetry axis. A satisfactory mode conversion from H_{11} to H_{01} is seen from the measurements at the test cavity output (Fig. 5, d).
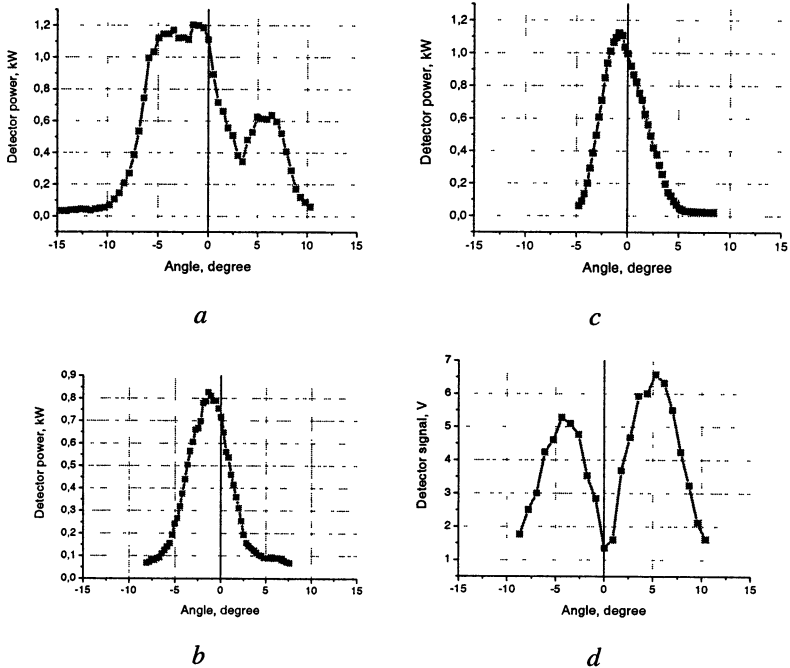
Fig. 5. Angular radiation distributions at the 50 mm behind the FEM window (a), at the first mirror (b), in front of (c) and behind (d) the test cavity.

The power losses between FEM and test cavity input can be reduced significantly after transportation channel modernization. To eliminate the part of losses related to test cavity adjustment additional studies are needed.

Conclusions

All the components of the setup for experiments on RF pulse heating at 30 GHz are created on the base of JINR-IAP FEM. The cold measurements of the transmission line and test cavity have demonstrated good agreement with the simulation data and small RF power losses. RF power detector for hot measurement in the near-field zone and technique for real-time control of the radiation spectrum was put into operation. Preliminary stage of experiment on test cavity feeding has been done. The hot measurements demonstrate some misalignment of the quasioptical system. Permanent spectrum control is required.

References

1. *Ginzburg N. S., Kaminsky A. K., Peskov N. Yu.* et al., Strong Microwaves in Plasmas. Nizhny Novgorod, 2000, **2**, 815.
2. *Ginzburg N. S., Kaminsky A. A., Kaminsky A. K.* et al., Phys. Rev. Let., 2000, **84**, 3574–3577.
3. *Delahaye J.-P.* et al., EPAC'98 (Stockholm, June 1998), 58.
4. *Pritzkau D. P., Bowden G. B., Al. Menegat, Siemann R. H.*, SLAC-PUB-8013 (November 1998).
5. *Kovalenko V. F.*, Thermophysical Processes and Electrovacuum Devices. Moscow, Sovetskoe Radio, 1975, 160–193 (in Russian).
6. *Pritzkau D. P., Siemann R H.*, SLAC-PUB-8554 (August 2000).
7. *Nezhevenko O. A.*, PAC'97 (Vancouver, May 1997), 3013.

POSSIBLE WAYS OF IMPROVEMENT
OF A FEM-OSCILLATOR WITH BRAGG RESONATOR

A. V. Elzhov, A. V .Ganichev[1], N. S. Ginzburg[1],
A. K. Kaminsky, E. A. Perelstein, N. Yu. Peskov[1], S. N. Sedykh,
A. P. Sergeev, A. S. Sergeev[1]

Joint Institute for Nuclear Research, Dubna, Russia
[1]Institute of Applied Physics RAS, Nizhny Novgorod, Russia

Two possible ways of improvement of Bragg FEM-oscillator are discussed. The first way is the use of an additional high-frequency "starting" mode located in the vicinity of the operating mode (so-called "starting mode" regime). In such regime initial conditions can be chosen as more preferable for excitation of the starting mode having large temporal gain. Due to the interaction with this starting mode electron longitudinal velocity decreases and self-excitation condition for operating mode becomes fulfill. Then in the nonlinear competition operating mode suppresses starting mode and a single-frequency regime with rather high electron efficiency establishes. This regime allows excitation of the FEM-oscillator with the initial mismatch greater than the upper limit of self-excitation zone for operating mode increasing efficiency and reducing time of oscillation build-up. Another way is a special profiling of the corrugation depth in Bragg reflectors to optimize the longitudinal distribution of the RF-field. This also can lead to enhance in the oscillator efficiency.

Starting mode regime

High-efficiency narrow-band free electron maser (FEM) can be used as a suitable pulsed microwave power source for testing high-gradient accelerating structures of electron-positron linear colliders. Bragg FEM-oscillator with the operating frequency of 30 GHz (corresponding to CLIC project [1]) is developed in collaboration between JINR (Dubna) and IAP RAS (N. Novgorod). In this paper possible methods of efficiency enhancement of the Bragg FEM are discussed.

It is known that the efficiency for a single-mode oscillator can be increased by operation with the high initial mismatch from the beam-wave synchronism. However, if the mismatch increases then the temporal gain decreases and, therefore, the oscillations build-up time grows. Maximal efficiency is achieved at the boundary of self-excitation zone under high mismatches from the synchronism. When the mismatch for the operating mode is increased further the oscillations are not excited if the initial perturbations are rather small. In practice it means that the oscillator does not start up from a noise level. Nevertheless in certain region of the mismatches if rather large initial (seed) signal is introduced into an oscillator further evolution results in establishment steady-state oscillation regime with rather high efficiency. As it is shown in this paper excitation of an additional mode can be exploited as a source of a seed signal for the operating mode. This additional mode has rather small mismatch from the synchronism that corresponds to high temporal gain but rather small electron efficiency (for this

reason it can be called as "starting" mode). With excitation of the "starting" mode average electron energy and longitudinal velocity falls so, that effective mismatch from the synchronism becomes more favorable for excitation of the operating mode. Afterwards due to nonlinear competition mechanism operating mode suppresses starting mode and single-mode regime of oscillations is realized with rather high efficiency. Note, that similar pattern for a gyrotron was described in [2].

In this paper we study "starting mode" regime in FEM with Bragg resonator of two types: (1) regularly corrugated waveguide section and (2) resonator with a step of phase of corrugation $\Delta\varphi = \pi$. Resonator of the first type has two fundamental eigenmodes positioned at the edges of the Bragg reflection zone: high and low frequency modes (HF and LF). In the resonator of the second type along with HF and LF modes the fundamental mode with maximal Q-factor exists in the centre of the Bragg zone (central frequency mode, CF). Simulations for the single section Bragg resonator were carried in [3] and demonstrated possibility to obtain high efficiency and considerable gain in the "starting mode" regime. In this paper initial energy of the electrons was varied to shift mismatch of the synchronism (in contrast to [3], where the wiggler field amplitude was varied). It allowed us to neglect the influence of the wiggler field on the beam-wave coupling and therefore to compare the oscillator behavior more correctly.

Numerical simulation was carried out for several values of the waves coupling coefficient at the Bragg corrugation α and different lengths of Bragg reflectors. The coupling coefficient defines both the mirrors reflectivity and the width of the effective reflection zone (hence, the frequency difference between the resonator eigenmodes). Besides, the Q-factors of eigenmodes depend on α as well as on lengths of Bragg reflectors, which were also varied in the simulation.

Results of the efficiency optimization for Bragg resonators of both types are presented in Fig. 1. Parameters for the simulations were chosen close to the FEM experiments based on linac LIU-3000 [4]. The coupling factor for the first resonator is chosen twice greater than for the second resonator because the frequency difference between the nearest eigenmodes becomes approximately the same in both cases.

Regions of the parameters corresponding to realization of the "starting mode" regimes are hatched in Fig. 1. They cover rather narrow ranges in energy, not greater than 0.2 in units of γ. It can be seen that the oscillator demonstrates the maximal efficiency just in the starting mode regimes. In the Bragg resonator with a step of phase of corrugation there exist two separated areas corresponding to the jumps from different modes (from HF to CF and from CF to LF).

The maximal efficiency is achieved in the resonator with a step of phase of corrugation when the generation establishes at the central frequency (CF) after the excitation of the higher frequency (HF) as a starting mode. Such a regime is illustrated by Fig. 2 (left column). In the right column for the same resonator different pattern corresponding to transition from CF to LF is shown. In the last case the efficiency is remarkably lower.
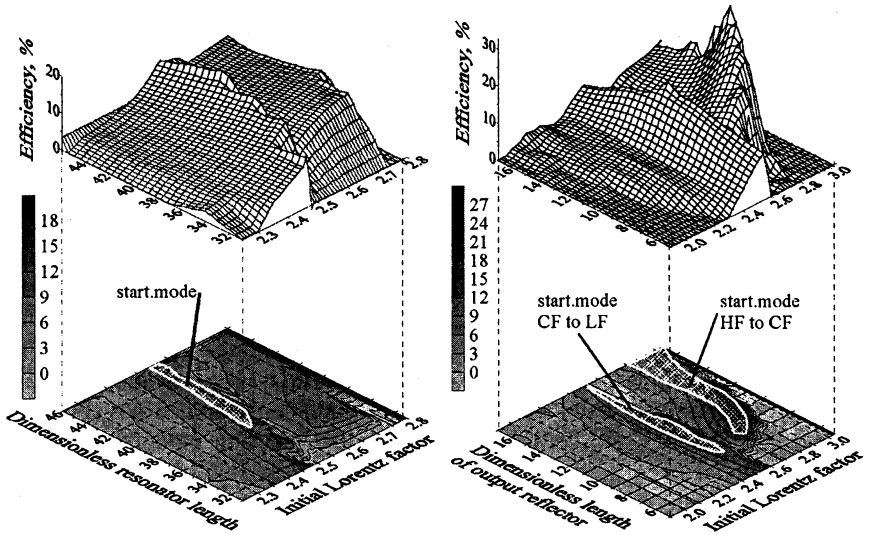
Fig. 1. Efficiency of the FEM versus initial electron beam energy and the resonator length for a single-section regular corrugated Bragg resonator (left) and Bragg resonator with a step of phase of corrugation (right). The waves coupling coefficient (left/right) $\alpha = 0.01/0.02$, guide magnetic field $B_{guide} = -1.2$, wiggler field $b_w = 0.7/0.8$. The input reflector for second-type resonator has fixed length of $L_1 = 19$. All values are in dimensionless units [3].
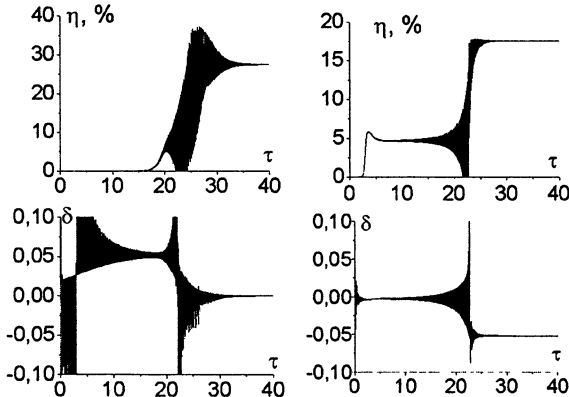
Fig. 2. Time dependence of efficiency η and current radiation frequency $\delta = (f - f_0)/f_0$ in the starting mode regime at two different initial mismatches from synchronism. Resonator parameters: $L_1 = 19$, $L_2 = 11$, $\alpha = 0.02$, $b_g = -1.2$, $b_w = 0.8$. Left column: $\gamma_0 = 2.9$ transition from HF starting mode to CF operating mode: right column $\gamma_0 = 2.54$ – transition from CF starting mode to LF operating mode.

192

Note that a single-frequency regime at the HF mode in the resonator with a step-phase corrugation didn't occur at all. Compared to LF mode having similar Q-factor, for HF mode the beam transverse velocity and wave coupling coefficient is lower that is unfavorable for excitation conditions. This fact is in agreement with the experiments [4].

Results of the simulation demonstrate that realization of the "starting mode" regime in the FEM-oscillator requires an optimal intersection of the self-excitation bands with positions of the resonator eigenmodes. It needs special resonator geometry providing suitable combination of the eigenmodes Q-factors and width of the Bragg reflection zone.

Optimization of the resonator geometry by mirror profiling

Alternative possibility to increase the oscillator efficiency is the optimization of the corrugation profile in the resonator to suppress parasitic LF and HF modes and to improve conditions for excitation and energy extraction for the fundamental mode. To decrease Q-factor for the side modes it seems attractive to introduce a proper variation of the coupling coefficient along the Bragg reflector smoothing the reflectivity spectral characteristic of the resonator.

Simulations were performed to optimize profiled Bragg resonator with the purpose to increase the efficiency of the FEM oscillator in a single-mode regime (generating central frequency). Increase in the efficiency was found in the resonator with linear spatial distributions of the coupling coefficient in each Bragg reflector (Fig. 3, a). Corresponding frequency dependence of the reflection coefficient (Fig. 3, b) demonstrates that the resonator has only single high-Q mode at the frequency of the precise Bragg resonance (fundamental mode for the resonator with a step-phase corrugation).
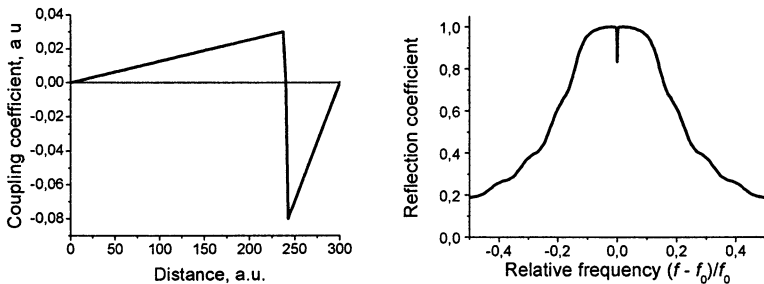
Fig. 3. Optimization of the corrugation in Bragg resonator: spatial distributions of the coupling coefficient in Bragg structures (left) and corresponding frequency dependence of the reflection coefficient (right).

Time dependence of the efficiency and longitudinal distribution of the amplitude for synchronous with the electrons partial wave (forward wave) of the resonator in the stationary regime of the oscillation are presented in Fig. 4. The maximum of electron efficiency in this case was calculated as $\eta = 26.3\%$.
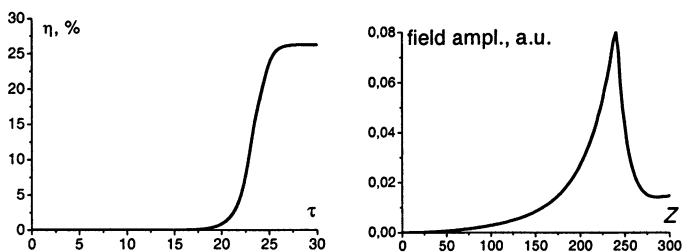
Fig. 4. Time dependences of efficiency η and longitudinal distribution of amplitude of synchronous wave in stationary regime for the FEM-oscillator with profiled Bragg resonator ($L_1 = 24$, $L_2 = 6$, $b_g = -1.2$, $b_w = 0.7$, $\gamma_o = 2.7$).

Summary

– Simulations show possibility to increase the Bragg FEM-oscillator efficiency by realization of the "starting mode" regime.

– The most attractive configuration of Bragg resonator is the resonator with a step of phase of corrugation. High-frequency side mode can be used in this resonator as a "starting" mode. Self-excitation conditions in this regime and possible deviations of the parameters are found.

– Proper variation of the coupling coefficient in Bragg structures can be used for keeping the quality factor of central mode to be high enough even for very short output mirror. This simultaneously depresses parasitic side modes of the Bragg resonator and increase the FEM oscillator efficiency.

References

1. *Delahaye J.-P.* et al., Proc. of EPAC'98, 1998, 58.
2. *Ginzburg N. S., Kovalev N. F., Petelin M. I.*, Oscillators and amplifiers based on relativistic electron beams, Ed. V. M. Lopukhin, Moscow State University, Moscow, 1987, p. 142 (in Russian).
3. *Ginzburg N. S., Elzhov A. V., Kaminsky A. K.* et al., Nuclear Instrum. and Meth., 2002, v. A483, 225.
4. *Elzhov A. V., Ginzburg N. S., Ilyakov E. V.* et al., JINR-IAP FEM Oscillator with Bragg Resonator: Experimental Investigation and Application, these proceedings.

EXPERIMENT TO STUDY EFFECTS
OF MULTI-PULSE HEATING IN A 30 GHz RESONANT CAVITY

*S. V. Kuzikov, A. V. Elzhov[1], N. S. Ginzburg, M. Yu. Golov,
A. K. Kaminsky[1], S. M. Leschinsky, E. A. Perelstein[1], N. Yu. Peskov,
M. I. Petelin, S. N. Sedykh[1], A. P. Sergeev[1], A. S. Sergeev, I. V. Syrachev[2],
N. I. Zaitsev*

Institute of Applied Physics, Russian Academy of Sciences, Nizhny Novgorod, Russia
[1]Joint Institute for Nuclear Research, Dubna, Russia
[2]CERN, Geneva, Switzerland

An experiment to study degradation of copper surface exposed to multi-pulse RF heating
is planned, basing on a 30 GHz free electron maser. Spectral measurements of the FEM
output radiation, low power tests of the mirror line and the cavity have been performed.
Experimental results will be of importance for designing future electron-positron linear
colliders.

Introduction

The new generation of e^+e^- linear colliders is planned to provide 1–5 TeV
energy of the collided particles in the center of masses. Such energy could be
achieved using particle acceleration by very strong microwaves. So the accelerat-
ing structures and other RF components will undergo action of extremely high RF
fields. Except for breakdown threat there is an effect of copper damage due to
multi-pulse mechanical stress caused by Ohmic heating of skin layer [1]. It was
proven that at 11 GHz the heating of a copper surface up to ~120 °C during each
RF pulse leads to essential drop of the conductivity after $5 \cdot 10^6$ pulses [2]. It is
expected that at higher frequencies, which are topics of interest for e^+e^- colliders,
accelerating structures will be heated up even more strongly. Nevertheless, there
is no enough information, neither theoretical nor experimental, about pulse heat-
ing at these frequencies. In order to get new information about the mentioned
effect at 30 GHz, we plan the experiment with the axis-symmetrical cavity fed by
high-power FEM oscillator [3–4].

Experimental set-up

The FEM oscillator elaborated in cooperation of IAP and JINR can produce
30 GHz pulses with parameters: 15–30 MW, 100–200 ns, 0.5–1 Hz. This source
will feed the cavity operating at TE_{01} mode preferable to avoid the RF break-
down. The scheme of the set-up is shown in Fig. 1.

The range of interesting temperatures starts from 50 °C according to the data
obtained at 11 GHz. Nevertheless, we plan to start our experiment with higher

temperatures in order to get more information as faster as possible. It is expected that the temperature rise 400 °C will destroy cavity's Q-factor for 10^5 pulses or faster. In order to provide the temperature of copper 200–400 °C, the TE_{011} mode with Q-factor $\sim 10^3$ is planned to be excited in the cavity. The cavity volume is confined within two diaphragms (Fig. 2). The wall profile is synthesized to provide a sufficiently high temperature at a ridge in the middle of the cavity. The cavity has a special adjustment in order to tune the resonant frequency, which has to be equal the frequency of FEM's oscillations.
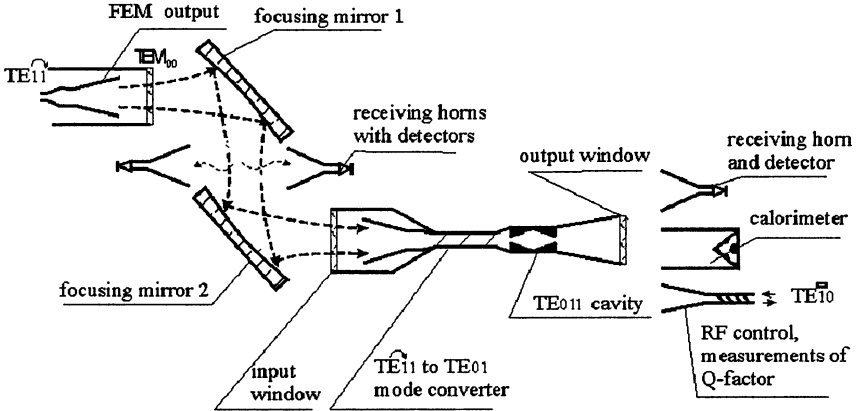
Fig. 1. Scheme of experimental set-up

The temperature rise u at a metallic surface as a function of time t with the effect of the thermal diffusion during RF pulse, taken into account, is given by formula:

$$u(t,0) = \int_0^t \frac{\beta \cdot q(\tau)}{\sqrt{t - \tau}} d\tau, \qquad (1)$$

where q is a flow of the heat inside a metal, and the coefficient β equals for the copper $9.5 \cdot 10^{-6}$ m$^2 \cdot$K/c$^{1/2} \cdot$W. Under the mentioned parameters of the FEM, the maximum temperature at the end of RF pulse should be 370 °C according to calculations based on the formula (1).
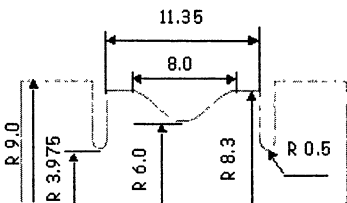
Fig. 2. TE_{011} test cavity.

The FEM output wave is the circular polarized Gaussian beam. This wave-beam is transported to the cavity using a pair of confocal mirrors, the receiving horn, and the TE_{11} (rotating) to TE_{01} mode converter with helical corrugation. All these components are assembled in the vacuum evacuated vessel, separated from the mirror transmission line by the quartz resonant windows. Behind the output window of the system the special equipment (receiving detector, calorimeter, low power Q-meter) can be installed.

Low power & high power tests

The first stage was an investigation of FEM stability in order to prove applicability to goals of our experiment. During tests the FEM oscillator demonstrated ability to be operated continuously at the repetition rate of 0.5–1 Hz for 8–10 hours each day with 15–25 MW output power and 100–200 ns pulse duration. The registration and analysis of more than 10^4 pulses of the microwave radiation of the FEM-oscillator have been carried out. One half of the analyzed oscillator pulses get into 10% spread interval on power, duration and temperature rise. The measured spectrum bandwidth was 20–50 MHz.

The second stage consisted of RF system manufacturing and low power tests. The photograph of the RF system is shown in Fig. 3.
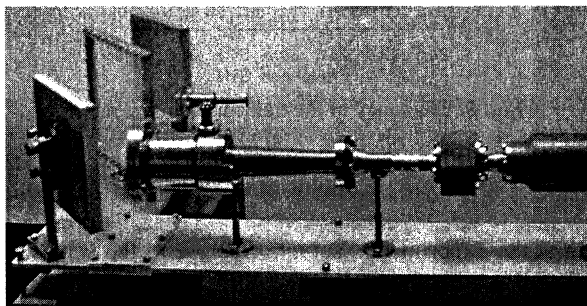
Fig. 3. Photograph of the experimental set-up

All components: horns, windows, mode converter, cavity, and tapers, have been tested at a low power. In particular, the Q-factor of the cavity was 1200 in agreement with calculations. The measured efficiency of the TE_{11} to TE_{01} mode converter was 98±2%.

The power transmission was measured basing on a scheme shown in Fig. 4, where the TE_{01} mode resonant cavity was substituted with a below-cut-off waveguide. The reflected radiation was measured by a network analyzer. Results of the described efficiency measurements are shown in Fig. 5. At central frequency 30 GHz the efficiency reaches ~80%.

197
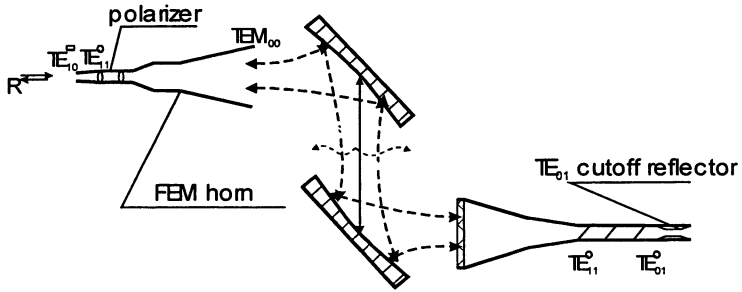
Fig. 4. Scheme of efficiency measurements
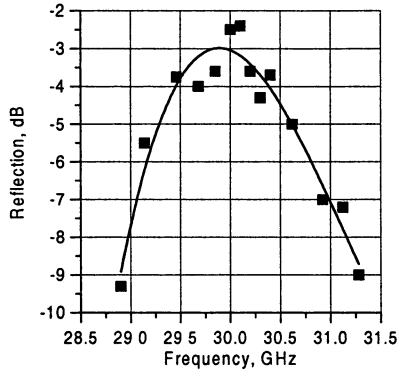
Fig. 5. Efficiency of the transmission system

Conclusions

Preparations of the experimental set-up are close to the state when studies of the pulse-periodic RF heating fatigue of the metal surface can be started.

References

1. *Kovalenko V. F.* Introduction to microwave electronics. M., Sov. Radio, 1971 (in Russian).
2. *Pritzkau D. P.* et al. Experimental Study of Pulsed Heating of Electromagnetic Cavities, PAC97, Vancouver, 1997, p. 3036.
3. *Ginzburg N. S., Kaminsky A. K., Peskov N. Yu.* et al. High-efficiency single-mode FEM-oscillator based on a Bragg resonator with step of phase of corrugation, Phys. Rev. Lett., 2000, vol. 84, p. 3574–3577.
4. *Ginzburg N. S., Kaminsky A. K., Peskov N. Yu.* et al. Theoretical and Experimental Comparison of FEL-Oscillators with Conventional and Reversed Guide Field, IEEE Trans. on Plasma Science, 1998, vol. 26, №3, p. 536–541.

PROJECT OF SUB-MM TWO-WAVE BRAGG FEM

N. Yu. Peskov, A. V. Savilov, A. K. Kaminsky[1], S. N. Sedykh[1], E. A. Perelshtein[1], D. A. Jaroszynski[2]

Institute of Applied Physics RAS, Nizhny Novgorod, Russia
[1]Joint Institute for Nuclear Research, Dubna, Russia
[2]University of Strathclyde, Glasgow, UK

In mm-wavelength Bragg FEM-oscillator driven by a moderately relativistic high-current electron beam the use of a backward feedback wave is proposed as a secondary wiggler wave in order to produce scattered sub-mm radiation at a multiple frequency of mm-wave. Project of 0.8 mm FEM with output power of up to 0.4 MW is considered based on linac LIU-3000 (JINR, Dubna).

Introduction

A Ka-band Bragg FEM-oscillator been developed during the last few years in collaboration between JINR (Dubna) and IAP RAS (N. Novgorod). Stable single-mode operation was obtained at 30 GHz with an output power of ~20 – 30 MW and a high electron efficiency (over 25%) [1, 2]. High electron efficiency and weak sensitivity to the velocity spread were provided by using a reversed guide field regime [3, 4] (in this regime the direction of the electron rotation in the helical wiggler is opposite to the cyclotron rotation in a single guide field). The Bragg mirrors provided selective feedback at a narrow frequency band near 30 GHz.

As a development of these experiments, it seems attractive to use the backward lower-frequency (LF) mm-wave as a secondary wiggler and provide its stimulated scattering into a forward high-frequency (HF) sub-mm wave. Similar regimes were studied theoretically [5] and experimentally in relativistic BWOs when scattering cm operating backward wave into forward mm-wave [6, 7]. To increase efficiency of the HF power extraction from the electron beam bunched at the low frequency we propose operation at a multiple frequency. In this case the backward LF wave and the HF wave are coupled on the same electron beam. A temporal harmonic of the LF modulation of the electron beam can be considered as an initial HF signal. Thus, no feedback (resonator) is required for the HF wave.

In this paper we present results of the simulations for such double-resonance Bragg FEM (ubitron and scattron). It is found that increase in the efficiency of the sub-mm radiation can be achieved when the HF wave is close to the cut-off and the Bragg mirrors change the polarization (rotation) of the LF wave due to approaching this wave to the cyclotron resonance in the reversed guide field. According to the simulation, the proposed scheme can provide the single-mode sum-mm power of hundreds of kW based on a moderately-relativistic electron beam.

Model and main principles of the two-waves FEM

Let us consider a thin axial electron beam oscillating in a helical wiggler (of the period d and the transverse field B_w) and a uniform guide field B_0 inside a circular waveguide (Fig. 1). The traveling circularly polarized LF $TE_{1,1}$ mode (the wave "1") is excited by the beam due to the "ubitron" resonance (Fig. 2)

$$\omega_1 \equiv \omega_{LF} \approx (h_1 + h_w)v_\| , \tag{1}$$

$h_w = 2\pi/d$. The Bragg reflectors provide selective feedback at the low frequency. Let us assume the feedback loop as coupling the forward LF wave "1" of $TE_{1,1}$ type and the backward LF wave (the wave "2") of $TM_{1,1}$ type. Note, that in the experiments [1, 2] the Bragg mirrors were designed for coupling of this pair of waveguide modes.
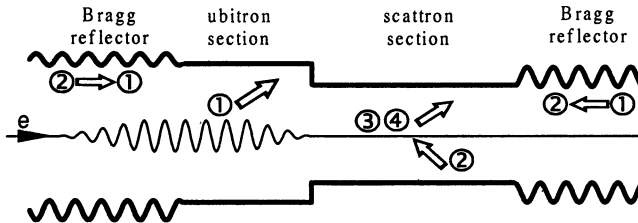
Fig. 1. Schematic of the double-section FEM based on two simultaneous wave/beam resonances
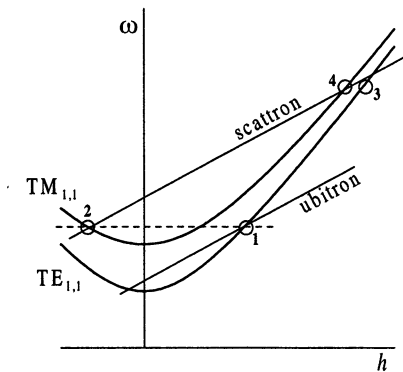
Fig. 2. Dispersion diagram of the double-resonance FEM

To achieve sub-mm radiation the feedback wave "2" can be used as a "secondary wiggler". As a result, this wave can be scattered in the forward $TE_{1,1}$ and $TM_{1,1}$ HF modes (the waves "3" and "4") under the "scattron" resonance condition

$$\omega_3 = \omega_4 \equiv \omega_{HF} \approx \omega_{LF} + (h_{3,4} - h_2)v_\| . \tag{2}$$

200

It is important to note that the FEM possesses the "electron" selectivity: in a circular operating waveguide a helical beam interacts under the resonance conditions (1) and (2) only with the circularly polarized modes having azimuthal index equals to 1.

To increase efficiency of the HF wave excitation we assume also the harmonic condition, i.e. $\omega_{HF} = s\omega_{LF}$ with an integer s. Then the LF wave "1" and the HF waves are coupled on the same electron beam. Namely, the $(s-1)$-th temporal harmonic of the modulation of the electron beam by the LF wave represents a modulation at the frequency of the "scattron" combination wave, i.e. $\omega_{HF} - \omega_{LF}$, which can be considered as an initial HF signal. Therefore a feedback for the HF waves is not necessary.

As it is shown in [8] the intensity of the "scattron" interaction is in reversed dependence of the parameter

$$\omega_{LF} - h_2 v_\parallel \pm \omega_B \ , \tag{3}$$

where $\omega_B = eB_0/\gamma mc$ is the gyro-frequency. This means that in order to increase efficiency of the sub-mm scattering one should increase electron wiggling in the field of the wave "2" due to approaching this wave to the cyclotron resonance. This can be achieved when:
– the wave "2" is close to cutoff, i. e. $|h_2| << \omega_{LF}/c$ and
– a high enough guide magnetic field is used, i. e. $\omega_B \sim \omega_{LF}$.
The sign " $\pm$ " in (3) depends on the rotation of the circularly-polarized "feedback" LF wave "2". Thus, a proper rotation of the wave "2" should be provided. In the case of a reversed guide field, the waves "1" and "2" should be counter-rotated. This can be provided by using the Bragg mirrors, which coupling the forward and backward LF waves of different polarization (rotation).

The proposed two-wave FEM scheme can be realized as a single-section as well as a double-section variant (presented in Fig. 1), in which the resonance conditions (1) and (2) are fulfilled in different sections. Evidently, separation of "ubitron" and "scattron" interaction regions enables a more freedom in the optimization. In this case, a rectilinear electron beam can be used in the "scattron" section.

Results of the simulations

Parameters for the simulations were chosen close to the conditions of the experiments at the linac LIU-3000 (0.7 MeV / 200 A / 200 ns). The electron oscillating velocity in the wiggler of a period of 4.5 cm was taken $\beta_\perp \sim 0.2$. The "ubitron" interaction with a circularly polarized $TE_{1,1}$ mode of a circular waveguide (the wave "1") was considered at 30 GHz. The Bragg mirrors were taken with 85% reflections of this wave into the "feedback" counter-rotating $TM_{1,1}$ mode (the wave "2") and vice versa. Scattering of the backward wave into $TE_{1,1}$ and $TM_{1,1}$ modes (the waves "3" and "4") was calculated to be at 360 GHz

201

(the frequency multiplication is $s = 12$).

In double-section variant (shown in Fig. 1) both "ubitron" and "scattron" interactions were optimised in order to obtain higher output sub-mm power. In particular, a narrower waveguide in the second section results in improvement of the "scattron" interaction (waveguides of radii of 7.8 mm and 6.2 mm were taken for the "ubitron" and the "scattron" sections respectively). In addition, since the wiggler was absent in the "scattron" section, its length can be chosen as long as necessary with no influence on the "ubitron" operation.

As a result of the simulations the output power of the $TM_{1,1}$ wave at a frequency of 360 GHz amounts 300 – 400 kW with practically negligible ($\sim$ 10–20 kW) admixture of the $TE_{1,1}$ wave (compare Fig. 3, b and 3, c). The single-mode structure of the output HF signal was a result of nonlinear competition of the modes.

Fig. 3. Power of (a) the "ubitron" LF wave as well as the "scattron" HF waves (b) $TE_{1,1}$ and (c) $TM_{1,1}$ versus the axial coordinate for the guide magnetic field of 8.6 kG (1), 10.7 kG (2) and 12.8 kG (3).

References

1. *Ginzburg N. S., Kaminsky A. A., Kaminsky A. K., Peskov N. Yu.* et al., Phys. Rev. Lett., 2000, v. 24, p. 3574.
2. *Ginzburg N. S., Kaminsky A. A., Kaminsky A. K., Peskov N. Yu.* et al., IEEE Trans. on Plasma Sci., 1998, v. 26, p. 536.
3. *Kaminsky A. A., Kaminsky A. K., Rubin S. B.*, Particle Accelerators, 1990, v. 33, p. 189.
4. *Conde M. E., Bekefi G.*, Phys. Rev. Lett., 1991, v. 67, p. 3082.
5. *Bratman V. L., Ginzburg N. S., Denisov G. G.*, Radiotechnika i Electronika, 1982, v. 27, p. 1373 (in Russian).
6. *Zhukov P. G., Ivanov V. S., Rabinovich M. S.* et al., ZhETF, 1979, v. 76, p. 2065 (in Russian).
7. *Bratman V. L., Denisov G. G., Ginzburg N. S.* et al., Int. J. of Electron., 1985, v. 59, p. 247.
8. *Savilov A. V., Peskov N. Yu., Kaminsky A. K.*, Proc. of the 24th Int. FEL Conf., Argonne, USA, 2002 (accepted for publication).

202

GENERATION OF POWERFUL COHERENT RADIATION IN SINGLE- AND MULTI-MODULES PLANAR FEMS WITH 2-D DISTRIBUTED FEEDBACK: RESULTS AND PROSPECTS

A. V. Arzhannikov, V. T. Astrelin, V. B. Bobylev, N. S. Ginzburg[1],
P. V. Kalinin, S. A. Kuznetsov, N. Yu. Peskov[1], P. V. Petrov[2],
A. S. Sergeev[1], S. L. Sinitsky, V. D. Stepanov, M. Thumm[3]

Budker Institute of Nuclear Physics RAS, Novosibirsk, Russia
[1]Institute of Applied Physics RAS, N.Novgorod, Russia
[2]RFNC-VNIITF, Snezhinsk, Russia
[3]Forschungszentrum Karlsruhe, Germany

Novel approach to generation of mm-radiation pulses of a gigawatt power by using multi-channel planar FEM-oscillator operated with 2-D distributed feedback is discussed. Project of 4-channel FEM-oscillator of 75-GHz band is considered and based on the ELMI-accelerator (BINP RAS, Novosibirsk).

Introduction

Generation of mm-wave radiation of gigawatt power level at microsecond pulse duration is possible in a planar FEM driven by a sheet electron beam, which is formed at the U-2 accelerator (BINP RAS, Novosibirsk) with the large cross section 3×140 cm [1]. Based on this beam project of a single-module planar FEM has been developed [2]. For synchronisation of radiation from a 140-cm width electron beam the use of two-dimensional (2-D) distributed feedback has been proposed [3]. This approach requires a microwave system having strongly elongated cross-section when operating in the single-module oscillator.

A multi-channel scheme [4] can be considered as an alternative way to achieve a gigawatt power level in mm-radiation. In this case the beam-wave interaction space can be developed in two transverse directions. Such a generator would consist of several connected planar masers (modules) with moderate (~20 cm) width and would represent multilayer microwave system exploiting 2-D Bragg gratings to realise 2-D distributed feedback in each layer. Transverse energy fluxes arising at the 2-D Bragg grating would synchronize each module as well as entire generator via additional waveguides connecting all modules.

Experimental studies of a single-channel 4-mm planar FEM are in progress currently at the "ELMI"-accelerator. For realisation of the multichannel FEM the following key problems should be solved:

– generation of several sheet beams with appropriate parameters,
– design and construction of multilayer magnetic and microwave systems,
– synchronisation of several FEM-modules.

Present paper is devoted to a progress in solutions of above problems.

Scheme of 4-channel FEM

The general arrangement of 4-channel FEM is shown in Fig. 1. The geometry of each single-module was chosen close to the configuration of the current single-channel FEM experiment at the ELMI-accelerator. Each FEM-module is driven by a sheet beam formed in magnetically insulated diode. Transverse velocity of the electrons ($\beta_\perp \approx 0.2$) in each module is pumped in an independent planar undulators made in the form of five parallel planes with coils. Each plane consists of coils connected consequently with alteration of polarity. The number of turns in the coils at the beginning and at the end of each plane is smoothly tapered. Period of the undulators is 4 cm and maximal value of the transverse magnetic field amount 0.2 T. Longitudinal (guide) magnetic field can be varied up to 1.5 T. Difference in the magnetic field strength in different channels was calculated less than 3%. This value seems to be appropriate to provide mutual synchronisation of radiation from different modules. Width of the sheet beams in each channel is 15 cm with the current per unit width (linear current density) ~ 200 A/cm.
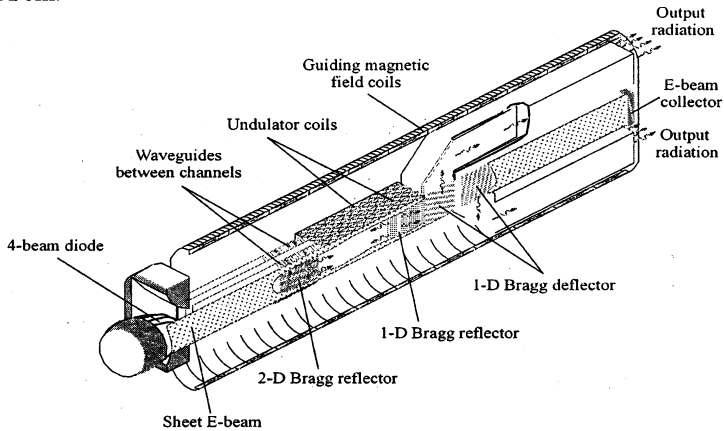
Fig. 1. Scheme of 4-channel FEM-generator

Bragg resonators of different types will be studied in the experiments. Firstly, it is planned to use a hybrid resonator consisting of 2-D and 1-D Bragg reflectors. In such a scheme the up-stream reflector with 2-D corrugation is used for transverse synchronisation of radiation while the down-stream reflector with 1-D corrugation should form the feedback loop and provide self-excitation condition. In practical situation the 1-D Bragg structure is more appropriate as the down-stream reflector for the FEM when the system is closed in transverse direction. The absence of the output for the transverse energy fluxes (which arise in the 2-D structures) results in extremely high amplitude of the electromagnetic field in the case of exploiting down-stream 2-D reflector. The hybrid configura-

tion allows to avoid this problem and to provide a single-mode single-frequency generation in combination with a single directional output of the radiation.

In multimodules FEM synchronisation of different modules is provided bent waveguides which connect up-stream 2-D Bragg structures and transmit transverse energy fluxes from one module to another. The first module should be also connected to the last module by special waveguide to complete the circuit for the transverse flaxes.

After each resonator an additional Bragg deflector is installed to turn output radiation and separate it from the high-current electron beam in the collector section. To prevent the generation process from the influence of the collector plasma the collector is shifted from the resonator output at the distance about 50 cm. The Bragg deflectors are made as sections of a planar waveguide with 1-D corrugation at the angle of 45° to the system axis.

Simulations and experimental testing of FEM components

Synchronisation of the channels. Simulations were carried out for 4-modules FEM with geometry presented in Fig. 1 and parameters close to the experimental conditions at the "ELMI" accelerator. The electron energy was chosen to be 1 MeV, the current per unit width was 200 A/cm. At the operating frequency of 75 GHz the gain (Pierce) parameter was calculated as $C \approx 4 \cdot 10^{-3}$. The interaction space width was $l_x = 20$ cm and length of a regular section of the resonators was $l_z = 35$ cm. The up-stream 2-D Bragg reflector had the length of 16 cm and the down-stream 1-D Bragg reflector had the length of 10 cm. The ohmic losses in the connecting waveguides was taken as 20%.

The simulations show that frequency of the oscillation in a steady-state regime is close to the Bragg frequency of 75 GHz. Stationary regime of the generation is established in all FEM-modules simultaneously. Moreover, amplitudes and phases of the waves in all modules are practically the same (Fig. 3). Temporal dependence of the electron efficiency averaged over 4 modules is shown in Fig. 2.

It should be noted also that syn-

Fig. 2. Simulation of establishment of stationary regime of generation in 4-channel FEM based on "ELMI"-accelerator.

chronisation takes place even under some spread in the resonance conditions for different modules caused, for example, by difference in the electron energies. Situations, when the synchronisation get broken and the separate modules generated at different frequencies, was not observed in the simulations.
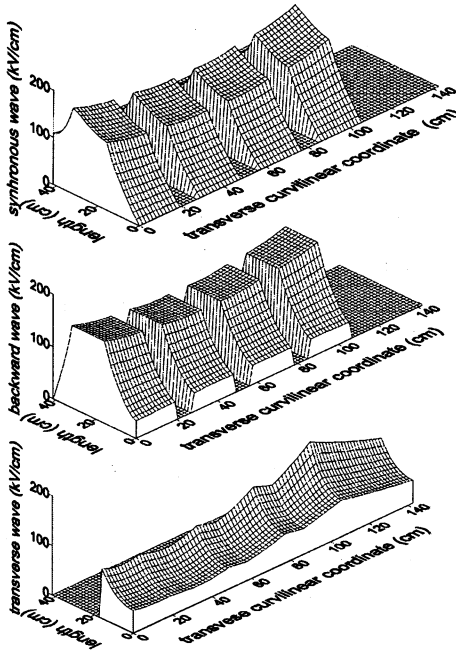
Fig. 3. Structure of the partial waves in the stationary regime of generation in 4-channel FEM.

Generation of the e-beams. Four sheet electron beams are generated by magnetically insulated diode with four parallel strongly elongated cathodes (Fig. 4). Geometry and location of the cathodes and the anode slits were chosen from the self-consistent simulations of the beams generation and propagation to provide similar values of the current density in all channels. Results of the simulations for the current and angle distribution of the beam electrons are shown in Fig. 4. The simulations show that the beams parameters are suitable to drive the FEM-modules. After passing through the anode slits these beams were additionally cut out on the thickness by graphite formers to obtain the required sheet form and the cross sections of 0.4×15 cm.
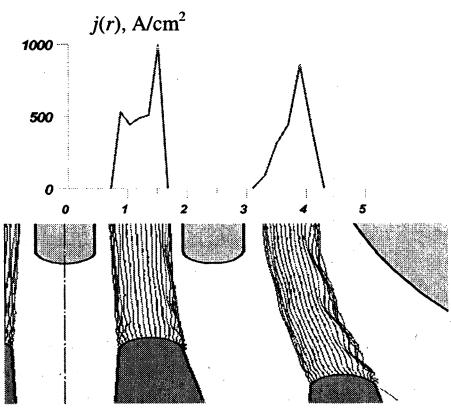
Fig. 4. Results of simulation for current distribution (top graph) and electron trajectories (bottom graph) in 4-beam diode.

Testing of microwave components. Planar resonators composed by Bragg gratings provide possibility to generate single frequency radiation with fixed spatial pattern and then transform this pattern using additional elements like deflectors.

206

Spectral properties of 1-D planar reflectors (Fig. 5) with rectangular grooves were tested. At frequency band of 72–76 GHz the incident wave H_{10} scattered preferentially in backward H_{10} wave and at 76–79 GHz in backward E_{12} wave. In these "cold" experiments only H_{10} wave could be measured and that was the reason for the difference between the experimental data and theoretically predi-cted results.
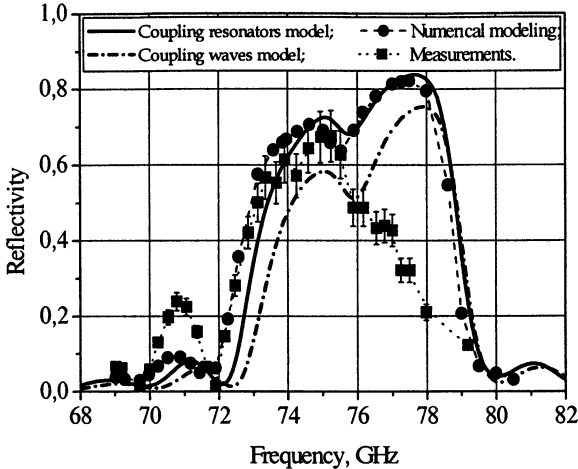
Fig. 5. Spectral properties of 1-D Bragg reflector for corrugation length of 6 cm, width of 19 cm, depth of 0.15 mm and period of 2 mm.

The 2-D reflectors composed by the Bragg gratings with several types of the corrugation profile were studied. It was found that spectral properties of the "chess-board pattern" corrugation are very close to the "ideal" sine corrugation (Fig. 6). Results of "cold" measurements for the reflectors with these two types of corrugation are presented for two resonator configuration: reflectors closed in transverse direc-tion by metal walls (*a*) and reflectors with transverse extraction of energy (*b*). Strong side reflections in the case (*a*) result in the additional bands of reflection near 73.5 and 77 GHz. In the case of open reflectors (*b*) only one reflection zone at 75 GHz is presented.

To separate microwave radiation and sheet electron beam Bragg deflector composed by 1-D Bragg gratings with the corrugation at the angle 45° to the di-rection of the electron beam propagation was designed (Fig. 7). The bandwidth of this deflector (2–2.5 GHz) is sufficient for the radiation output from the resonator (compare Fig. 7 with Fig. 5 and 6). This deflector is used in recent experiments at the "ELMI" accelerator. According to the simulations geometry of the corrugated area at the deflector plates can be optimised for maximum output or for the re-quired distribution of the output radiation.
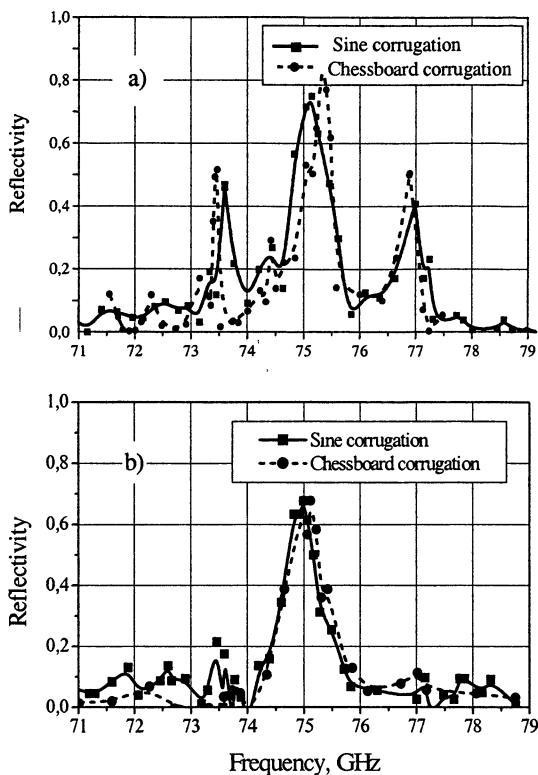
Fig. 6. Spectral properties of 2-D Bragg reflectors: (*a*) closed reflectors and (*b*) opened reflectors for corrugation length of 19 cm, width of 19 cm, depth of 0.15 mm (for "chessboard" grooves) and 0.25 mm (for sine corrugation).
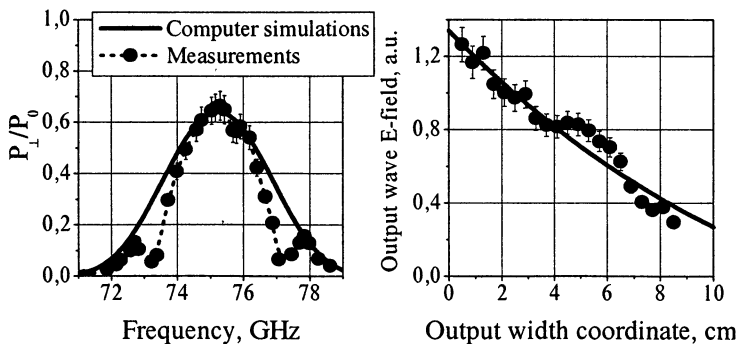
Fig. 7. Properties of the Bragg deflector for corrugation size of 10×10 cm, depth of 0.3 mm, period of 2.82 mm ($P_\perp$ is deflected power, P_0 is incident power).

Experimental investigations of FEM operation

At the present stage of the experiments we studied operation of a single FEM-unit for the future multi-channel FEM. Microwave system of investigated FEM-oscillator was similar to be used as a single channel in the multichannel maser. Operation of the Bragg deflector at the 75 GHz band was preliminary tested in "cold" measurements. Results of these measurements were in good agreement with the simulations. Then this deflector was used in the experiments on generation of 75 GHz radiation at the ELMI-device. In these series of the experiment the amplitude of transverse component of the undulator magnetic field was varied at fixed guide field of 1 T. The typical shot for the undulator field of 0.08 T, when the maximum of the radiation power was obtained, is shown in Fig. 8.
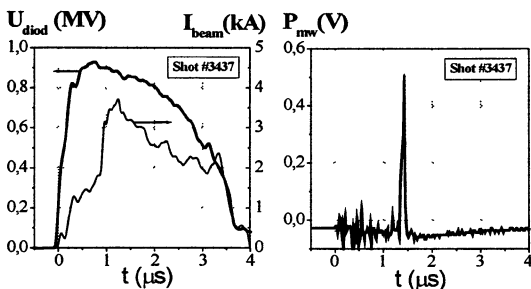
Fig. 8. Signals of the diode voltage, the beam current (left) and the radiation power (right).

The power distribution over the transverse cross section was visualised by lighting of square panel with sizes of 20×20 cm consisting of 100 neon bulbs. The radiation pattern in the case when the panel was located at the distance of 0.5 m from the output window is presented by the right photo in Fig. 9. The left photo shows the geometry of the panel. The distribution of the light intensity in the right photo is qualitatively close to obtained in the "cold" measurements and in numerical simulations for excitation of H_{10} wave in the resonator. Note that for zero undulator field no lighting was registered.
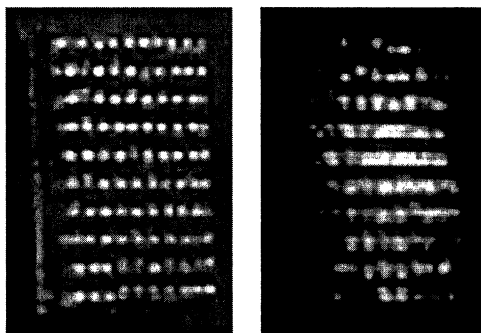
Fig. 9. Geometry (left) and picture of lighting (right) of the neon bulb panel under the microwave radiation pulse.

Conclusions

Theoretical consideration demonstrates that a planar FEM with 2-D distributed feedback can be used as a module for constructing multi-channel devices to produce microwave radiation of a GW-level. Simulations of operation of 4-modules FEM-oscillator prove synchronization of all modules even when the driving beams had some small spread of their parameters. Project for the experimental investigation of 4-channel FEM-oscillator is designed based on the "ELMI"-accelerator.

References

1. *Arzhannikov A. V., Nikolaev V. S., Sinitsky S. L., Yushkov M. V.*, J. Appl. Phys., **72**, 1657 (1992).
2. *Arzhannikov A. V.* et al., Nucl. Instr. and Meth. in Phys. Res. A, **445**, 222 (2000).
3. *Ginzburg N. S., Peskov N. Yu., Sergeev A. S.*, Optics Commun., **96**, 254 (1993).
4. *Ginzburg N. S., Peskov N. Yu., Sergeev A. S., Arzhannikov A. V., Sinitsky S. L.*, Nucl. Instr. and Meth. in Phys. Res. A, **475**, 173 (2001).

FORMATION OF INTENSE ULTRASHORT RELATIVISTIC ELECTRON BEAMS USING MULTI-STAGE AUTOACCELERATION FOR SUPERRADIANCE OBSERVATION

K. Kamada, H. Shirasaka, K. Kurihara, M. Kamada, R. Ando, D. Hasegawa* and N. S. Ginzburg[1]

Department of Phisics, Faculty of Science, Kanazawa University, Kanazawa, Japan
[1]Institute of Applied Physics, Russian Academy of Sciences,
Nizhny Novgorod, Russia

An intense relativistic electron beam with duration of less than 1 ns is obtained by multi-stage autoacceleration. The multi-stage autoacceleration employs coaxial cavities with decreasing lengths. The multi-stage system is also found to be effective to obtain trains of electron bunches from the electron beam with slow rise time. These ultra short electron beams are suitable for observation of superradiance. A single coaxial cavity makes it possible to obtain energy increasing intense electron beams. The energy increasing electron beams are expected to enhance the radiated power of superradiance.

Introduction

We report experiments and simulations to modify the characteristics of intense relativistic electron beams (IREB) using coaxial cavities for specific radiation mechanism called superradiance (SR) [1]. As SR is driven by an electron bunch whose length is shorter or comparable with interaction distance, an IREB with duration of less than 1 ns is requested for millimeter waveband SR. However, it is technically difficult for conventional pulse line system to generate an intense relativistic electron beam with duration less than 10 ns. We propose multi-stage auto-acceleration using a series of passive coaxial cavities with decreasing lengths.

In developing of these experiments we try to obtain a strongly modulated IREB (actually trains of subnanosecond bunches). We applied a series of cavities with decreasing lengths for a long duration IREB with slow rise time. The trains of electron bunches are also expected to apply to SR.

For observation of SR in centimeter waveband rather long nanosecond IREBs are suitable. It was proposed in [2] to use an IREB with increasing energy in time to increase peak power of SR pulse. According to the transmission line theory, the gap voltage of a coaxial cavity, $V_g(t)$, is expressed by the current at the gap, $I(t)$, as below [3],

$$V_g(t) = Z \cdot (I(t) - 2I(t - T) + \ldots) , \tag{1}$$

where Z is the cavity impedance and T is the round trip time of electromagnetic wave in the cavity. The beam is decelerated for the first period T and accelerated

---

* present address: Photon Production Laboratory Ltd., Shiga, 523-0898 Japan.

for the next period. As the initial electron energy and current waveforms are not square shape, we have a possibility to obtain a gradual increasing energy IREB using a cavity with appropriate length.

Multi-cavity multi-stage autoacceleration

Single-stage autoacceleration is an energy transfer process for an IREB, in which kinetic energies of electrons in the first half of the beam pulse are transferred to electrons in the last half by using a passive coaxial cavity. The length of a cavity is set to a quarter of the incident beam length [4, 5, 6]. In the multi-stage autoacceleration, a series of coaxial cavities with decreasing lengths is utilized. The length of the first cavity is set to a quarter of the incident beam length and that of the nth cavity is adjusted to half of that of the $(n-1)$th cavity. The length of the most accelerated part of the IREB after passing through the nth cavity is compressed to $1/2^n$ of its initial length. Only the last 2^nth part of the initial beam pulse is accelerated n times by all cavities. To improve the energy increase of the most accelerated part of the beam, cavities with the same lengths are added. We call it multi-cavity multi-stage autoacceleration.

Schematic of the multi-cavity four-stage autoacceleration is shown in Fig. 1. Pulserad 105A produced by Physics International was utilized to generate a short pulse IREB of 500 keV, 4 kA, 12 ns with rise time of 6 ns. An annular electron beam with a diameter of 1.6 cm and a thickness of 1 mm was injected from a foilless diode into a drift tube with an inner diameter of 3 cm. An axial magnetic field of 0.8 T was applied with solenoid coils. As the pulse length was estimated to be ~3.6 m (12 ns), the first cavity with length of 90 cm (= 3.6/4 m) was connected to the drift tube via a gap at 20 cm downstream from the anode. The lengths of the second, the third and the fourth cavities were 45 cm, 22.5 cm and 11.25 cm, respectively. In the single cavity four-stage experiment [7], one cavity for each stage was mounted. In the multi-cavity four-stage experiment, the numbers of the cavity for the 1st, 2nd, 3rd and 4th stage were 1, 2, 2 and 4, respectively. The impedance of all cavities was 76 Ω. The number of cavities for each stage was decided tentatively by our experimental setup condition. The beam current was measured by a Faraday cup. Aluminum foils of different thickness were placed in front of the Faraday cup to estimate the kinetic energy of the beam electrons.
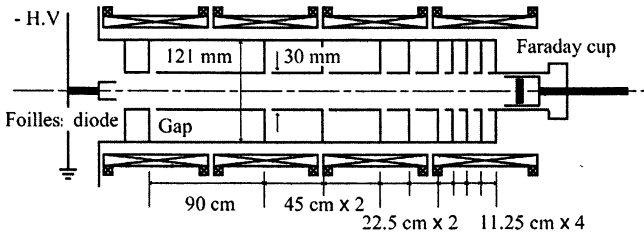
Fig. 1. Experimental apparatus of multi-cavity four-stage autoaccelaration

212

The waveforms of the beam current with and without foils are shown in Fig. 2. The waveforms with aluminum foils in both four-stage autoacceleration clearly show that the most accelerated parts of the beam appear at the end of the beam duration and their widths are about 0.8 ns that is equal to $1/2^4$ of the initial beam duration. These results agree well the principle of the multi-stage autoacceleration. The maximum energies of the beam electrons were estimated to be 0.5, 1.1 and 1.3 MeV, in the control, single-cavity four-stage and multi-cavity four-stage experiments, respectively, so that energy increase was 0.6 MeV in the single-cavity experiment and was 0.8 MeV in the multi-cavity experiment.
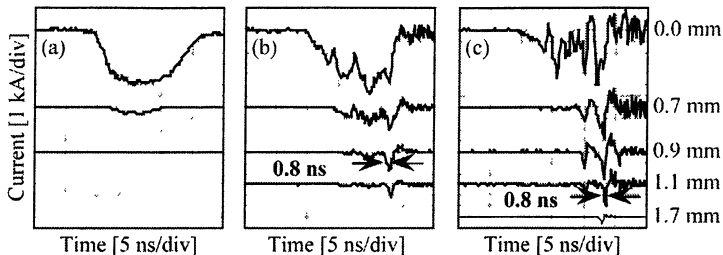
Fig. 2. Faraday cup signals through aluminum foil: a – control experiment, b – single cavity four stage, c – multi-cavity four stage.

Multi-stage automodulation

Pulserad 220G was utilized to generate a long pulse IREB of 500 keV, 4 kA, 175 ns with rise time of 20 ns. When four cavities with the same length of 75 mm were utilized in accordance with the results reported in [8], only a poorly modulated IREB was observed. We noticed that the current rise time of 20 ns was much longer than the round trip time of the cavity. To observe how the relation between the current rise time and the cavity length affected the modulation level, a single cavity whose length was variable was utilized. Pulserad 105A with current rise time of 6 ns was used as a beam source. The beam parameters, magnetic coils, the diameter of drift tube and cavity impedance were also the same as the experiment described above. The lengths of the single cavity were adjusted to 75, 150, 300 and 750 mm. The round trip times for the cavities were 0.5, 1, 2 and 5 ns, respectively.

The beam currents behind the gap are shown in Fig. 3, a. No fluctuation in the beam current was observed, when a smooth drift tube was used. Note that the longer cavity results in the higher current modulation. These waveforms showed the fundamental frequencies corresponded to each cavity lengths. The increases of electron kinetic energy observed behind the cavity with lengths of 75, 150, 300 and 750 mm were 30, 70, 130 and 330 keV, respectively. The increases of electron energy were interpreted to the gap voltages. The induced gap voltage

213

was calculated by eq. (1) for different cavity lengths. The experimental and calculated results show good agreements as shown in Fig. 3, *b*. The gap voltage increases as the cavity length increases and it is saturated with the cavity length of 900 mm. The round trip time of the cavity with length of 900 mm is 6 ns, which is the same as the rise time of the beam current. When the higher gap voltage is obtained, the higher-level current modulation is observed. Therefore, it is concluded that high-level current modulation cannot be expected when the round trip time of the cavity is too much shorter than the current rise time. However, for high-frequency modulation, the cavity must be short, because the duration of the electron bunch by automodulation corresponds to the round trip time of the cavity.
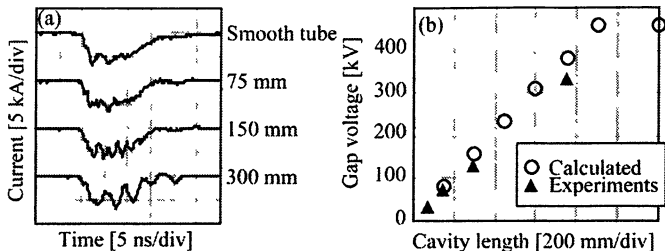
Fig. 3. Faraday cup waveforms behind a single cavity (*a*). Calculated and experimental gap voltage vs cavity length (*b*).

A series of decreasing lengths cavities were utilized to increase the level of modulation. The first cavity should be set to the length appropriate to the rise time of the beam current to obtain highly induced gap voltage. The length of following cavity was decreased to the length corresponded to the requested frequency. We tried the basic experiment of multi-stage automodulation for the IREB with rise time of 20 ns (Pulserad 220G). In Fig. 4, the cavities with lengths of 150 and 150 mm cannot increase the level of modulation. By using decreasing length cavities with lengths of 300, 150 and 150 mm, 0.5 GHz current modulation is obtained. We continue the experiment for higher-level current modulation.
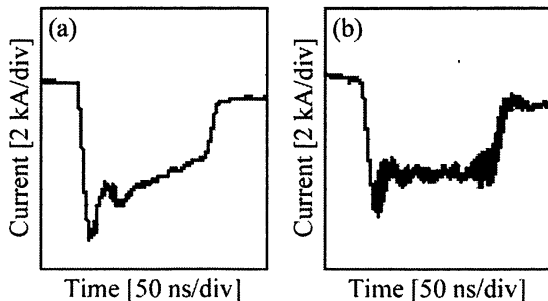
Fig. 4. Faraday cup signals behind the cavities: *a* – 150 and 150 mm cavities; *b* – 300, 150 and 150 mm cavities.

214

Increasing energy IREB

As the calculated gap voltage from the transmission line theory agreed well with the single cavity experimental results, the time evolution of beam electron energy behind the gap was calculated precisely. The induced voltage at the gap was calculated by eq. (1) using the waveforms of the IREB of 500 keV, 4 kA, 12 ns with rise time of 6 ns (Pulserad 105A). The time evolution of electron energies behind the gap is estimated from the sum of the diode and gap voltages. It is calculated for different cavity lengths, L. When the cavity length was set to 60 cm, the gradual increasing energy beam was obtained as shown in Fig. 5 for our current waveforms.
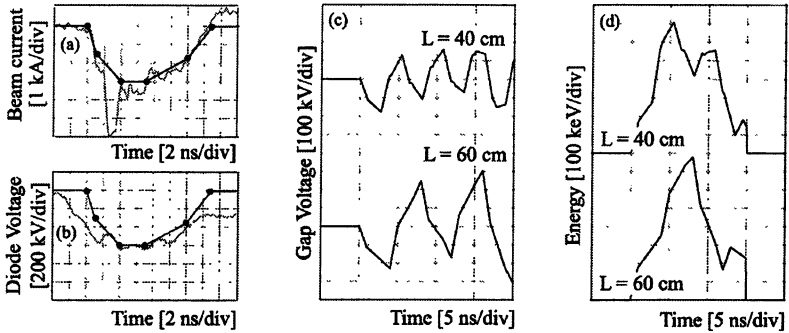
Fig. 5. Beam current (*a*). Diode voltage (*b*). Calculated gap voltage (*c*). Estimated time evolution of beam energy (*d*).

The experiments were carried out with the same beam and apparatus utilized in the automodulation (a single cavity whose length was variable). The time evolution of beam electron energy measured by a Faraday cup with aluminum foils agreed with the calculated results as shown in Fig. 6. The time evolution of electron energy could be changed using a single cavity within the limit of initial diode waveform. It can be estimated for different cavity lengths.
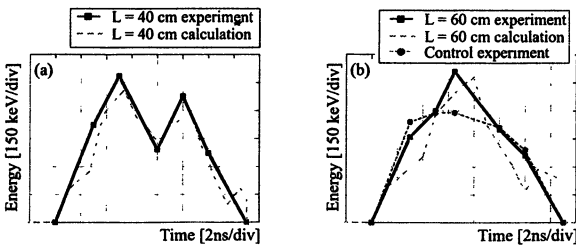
Fig. 6. Experimental (solid line) and calculated (dotted line) time evolution of beam energy: *a* – cavity length is 40 cm; *b* – cavity length is 60 cm.

215

Conclusions

Coaxial cavities are useful to redistribute the electron energy after the IREB is injected from the diode. IREBs with duration less than 1 ns or with increasing energy in time are available using coaxial cavity system. The experiment of trains of electron bunches is now developed. These beams will be applied to superradiance observation.

References

1. *Ginzburg N. S., Zotova I. V.* et al., Phys. Rev. Lett., 1997, **78**, 2365.
2. *Ginzburg N. S.* et al., Proc. of the 14th Int. Conf. on High-Power Particle Beam (to be published).
3. *Friedman M.*, Appl. Phys. Lett., 1982, **41**, 419.
4. *Kazanskii L. N.* et al., At. Energ., 1971, **30**, 30.
5. *Grishaev I. A.* et al., Sov. Phys. Tech. Phys., 1973, **17**, 1871.
6. *Friedman M.*, Phys. Rev. Lett., 1973, **31**, 1107.
7. *Hasegawa D.* et al., IEEE Trans. Plasma Sci., 2000, **28**, 1648.
8. *Friedmn M., Serlin V.* et al., J. Appl. Phys., 1984, **56**, 2459.

DEVELOPMENT OF MICROWAVE SOURCES
OF ULTRASHORT GIGAWATT PULSES
BASED ON SUPERRADIANCE

S. D. Korovin[1], G. A. Mesyats[2],
V. V. Rostov[1], M. I. Yalandin[2]

[1]Institute of High Current Electronics, Siberian Division, RAS, Tomsk, Russia
[2]Institute of Electrophysics, Ural Division, RAS, Ekaterinburg, Russia

This paper presents the theoretical and experimental studies of Superradiance regime of microwave emission in the Cherenkov backward wave oscillator (BWO). The main result obtained in theory and simulations is that, under certain conditions, the peak microwave power can exceed the power of driving electron beam. To realize this regime, the BWO used must possess a respectively broad passband because the group velocity dispersion results in broadening of the microwave pulse. In X-band we obtained a maximal microwave power of 1.2 GW, which is higher than the power of e-beam (320 kV accelerating voltage and 2.8 kA current). Another source operating in the 38 GHz range at repetition rates of 1–3.5 kHz is developed and tested. It is capable of generating stable pulses of 250 ps duration and a peak power of 250 MW.

As it is known [1, 2], the superradiance (SR) can be observed not only for the ensembles of quantum oscillators but also in vacuum electronic devices with different types of induced emission. In both of them the increment of instability should be large enough or in other words the length of an active medium should be significantly higher than that required for steady-state generation regime. As for SR of intense electron beams, practically the maximal peak power of SR is associated with Cherenkov emission from electron beam moving through a periodical slow wave structure (SWS) and interacting with synchronous spatial harmonic of backward wave [3]. In previous experiments the pulses of several hundreds MW's at centimeter and millimeter bands were attained in the SR regime of backward wave oscillators [3–5]. These experiments confirmed backgrounds of the theory [6] and demonstrated that relativistic BWO operating in a significantly nonstationary regime can generate pulses with the duration on the order of ten periods of the RF field with the power, which is essentially higher than observed in the quasi-steady-state cases.

The physical limitations of the level of peak microwave power for the e-beam power being constant were of interest. In this paper, the approach in the development of effective microwave sources of shot microwave pulses with overcoming of e-beam power is proposed. This approach is based on evaluations of characteristic curves for the power conversion coefficient (K) and pulse width of SR depending on the main parameters. We also optimized the geometry of SWS in respect to reduce effect of dispersion of the group velocity and equalize recovery rate of the energy of e-beam along inhomogeneous SWS.

Theory and simulations

Let us find main regularities using the classical model [6]. It may be modified taking into account the moderate electron energy and profiling of the coupling impedance. This model assumes unidirectional motion of electrons and does not include the dispersion of group velocity and non-synchronous interaction. The model contains three (in the case of low field of a space charge and uniform SWS) independent parameters: C – Pierce parameter, γ_0 – relativistic factor and ξ_k – normalized SWS length. The slow variable approximation means the requirement $C \ll 1$ and the following description of synchronous spatial harmonic:

$$E = \text{Re}\left(\hat{E}(r_b) E_{z,-1}(z,t) \exp i\omega_0 (t - z/V_0) \right).$$

Here r_b is the beam radius, ω_0 is the frequency of exact synchronism between the wave and particles having velocity V_0. According to [6], the parameters are defined as

$$\xi_k = \frac{\omega_0 C L}{V_0}, \quad C = \left(\frac{eJ_b \hat{Z}}{2mc^2 \gamma_0^3} \right)^{1/3}, \quad \left(\hat{Z} \equiv 2\left|\hat{E}(r_b)\right|^2 \Big/ k^2 N \right). \tag{1}$$

Here L is the SWS length, J_b is the beam current, N is the wave norm, $k = \omega_0/c$. With no account of space charge field the equations for the phase, wave and boundary conditions can be written as

$$
\begin{cases}
\dfrac{\partial^2 \theta}{\partial \xi^2} = \left\{ \gamma_0^3 \left[\left(1 + C\dfrac{\partial \theta}{\partial \xi} \right)^2 - \left(1 - \gamma_0^{-2} \right) \right]^{3/2} \right\} \text{Re}\left[\chi(\xi) A\ e^{i\theta} \right], \\[4mm]
\dfrac{\partial A}{\partial \tau} - \dfrac{\partial A}{\partial \xi} = \chi(\xi)\ J_1, \\[4mm]
\theta(0) = \theta_0 \in (0, 2\pi), \ \dfrac{\partial \theta}{\partial \xi}\Big|_{\xi=0} = 0, \ A(\tau, \xi_k) = 0 \ , \ A(0, \xi) = A_0(\xi),
\end{cases} \tag{2}
$$

where $\theta = \omega_0(t - z/V_0)$ is the phase of the electron in the wave and

$$\tau = \frac{\omega_0 C(t - z/V_0)}{1 + V_0/V_g}, \ \xi = \frac{\omega_0 C z}{V_0}, \ A = \frac{eE_{z,-1}}{C\gamma_0^3 V_0 m \omega_0}, \ J_1 = \frac{1}{\pi}\int_0^{2\pi} e^{-i\theta} d\theta_0. \tag{3}$$

The function $\chi(\xi)$ describes the distribution of the normalized amplitude of the synchronous harmonic with the following normalizing condition:

$$\frac{1}{L}\int_0^L \chi(z)\, dz = 1. \tag{4}$$

218

In the case of homogeneous SWS we can assume $\chi = 1$. By analogy with the stationary solution for efficiency the power conversion coefficient defining as ratio of microwave peak power to beam pulse power can be described as

$$K = \frac{(\gamma_0 + 1)}{\gamma_0} \frac{v |A(\tau,0)|^2_{max}}{8}, \quad v \equiv 2\gamma_0^2 C. \tag{5}$$

Like in the paper [6], here we use the generalized parameter of nonlinearity v. The use of this parameter is quite clear taking into account that the relativistic factor γ_0 can map out equations in three cases [7]: 1) in the low signal approximation (low efficiency and K) $v \to 0$, 2) in the non-relativistic limit and 3) in the ultra-relativistic limit. It follows from the next reduction:

$$\left\{ \gamma_0^3 \left[\left(1 + C \frac{\partial \theta}{\partial \xi}\right)^2 - \left(1 - \gamma_0^{-2}\right) \right]^{3/2} \right\} = \begin{cases} 1, & v \to 0 \\ \left(1 + \dfrac{v}{2} \dfrac{\partial \theta}{\partial \xi}\right)^3, & \gamma_0 - 1 \ll 1 \\ \left(1 + v \dfrac{\partial \theta}{\partial \xi}\right)^{3/2}, & \gamma_0 \gg 1 \end{cases} \tag{6}$$

It should be stressed on the dimensionless variables (1), (3) in the set of equations (2) with minimal number of independent parameters. In fact, we can import the specific time: $t_S = (1 + V_0/V_g)/\omega_0 C$, where V_g is the group velocity of the wave. This specific time must characterize the order of the pulse width, which is caused by the nonlinearity.

Simulations in the case of homogeneous SWS ($\chi = 1$). A typical time dependence of the wave amplitude and phase at the left (cathode) edge of the SWS is depicted in Fig. 1. In the real device, forward output of the wave is assumed, by using, for example, a broadband reflector [8]. The time $\tau_\Sigma = t_\Sigma/t_S$ marked in Fig. 1 characterizes the normalized pulse delay. If the level of initial noise of e-beam the current is small enough, RF current of the initial fraction of the beam is saturated near the end of SWS even for respectively large length of the device (the condition of extended length of the interaction $\xi_k \gg \xi_{k,st}$, where $\xi_{k,st} \approx 2$ is the BWO starting length, is interested only). In this case the approximate equality $\tau_\Sigma \approx \xi_k$ takes place. It follows that the real molding time of SR pulse is close to the sum of the beam transit time and the wave transit time $t_\Sigma \approx L(1/V_0 + 1/V_g)$. As is seen in Fig. 1, the normalized pulse width ($\Delta \tau = \Delta t/t_S$) is much less than molding time or acquisition interval of the energy in the SR pulse. This fact is just one that can explain the accumulation of the energy and the possibility of the excess of K factor over the unit (Fig. 2, 3).
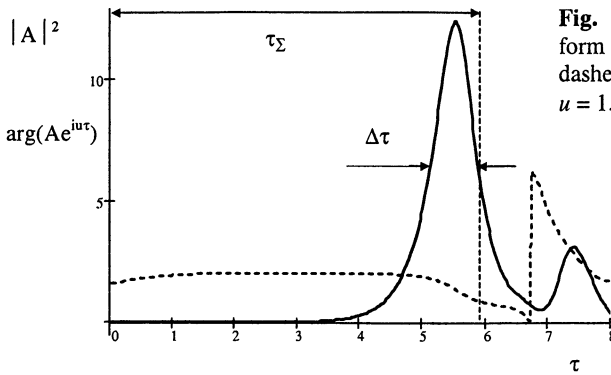
Fig. 1. The typical calculated form of the SR pulse at $z = 0$, dashed line defines the phase, $u = 1.05$, $\xi_k = 6$, $\nu = 0.5$.
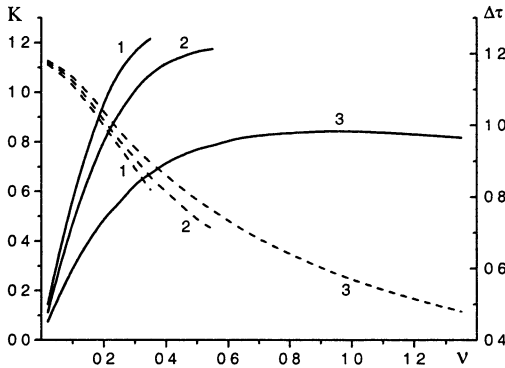
Fig. 2. Conversion coefficient (solid lines) and pulse width (dashed lines) depending on parameter ν: (1) $\gamma_0 - 1 \ll 1$, (2) $\gamma_0 = 1.6$, (3) $\gamma_0 \gg 1$, $\xi_k = 6$.
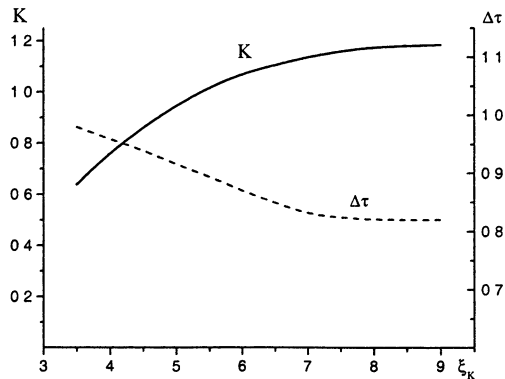
Fig. 3. Simulated conversion coefficient and normalized pulse width depending on normalized SWS length: $\gamma_0 = 1.6$, $\nu = 0.35$.

Conversion of $K > 1$ may be realized only for the moderate electron energy and in the range of parameter $\nu \approx 0.2...0.6$ near the limit where reflection of particles is possible (see Fig. 2). The stop and reflection of particles does not appear in ultra-relativistic approximation (see [7]) and therefore this case was used for

the analysis of inhomogeneous systems (below). The increase of the SWS length for fixed initial condition causes negligible growth of the power conversion, with its saturation (Fig. 3).

Inhomogeneous SWS. Higher power conversion may be achieved in non-uniform SWS where the coupling impedance is profiled rising from the cathode side to collector side, by gradually increase of the SWS corrugation depth. The best type of coupling distribution corresponds to constant amplitude of harmonic (soliton wave) and almost linear rise of the microwave pulse energy. It means that function χ in its asymptotic limit is $\chi(z) \propto (1 - z/L_a)^{-0.5}$, where parameter L_a is closed to L. So, with no account of group velocity dispersion, transverse motion of particles and non-synchronous interaction, the power conversion coefficient may be much more than unit for respectively long SWS with a special profile.

Conceptual experiments

The SWS's used earlier with the diameter of corrugation close to the wave-length had a respectively small pass band (30...40%). Strong frequency dependence of the group velocity over the operating band resulted in broadening of the wave envelope, which essentially (simulations by KARAT code show the factor 2...3 times) decreased the peak power. To reduce this effect SWS's of increased cross size (about 1.5 times [8]) were used. The resonant reflector with low Q-factor can provide the reflection of the pulse instead of a beyond cutoff-neck. To test theoretical prerequisites and main regularities three experiments were realized.

1. The Ka-band experiment [9] was performed with the use a high-current sub-nanosecond electron accelerator based on RADAN-303SNS driver. The pulse power of the 1-ns beam injected by explosive-emission cathode was 600 MW. The microwave pulsed power was determined by integrating of the radiation pattern. Peak powers ranging from 240 to 280 MW ($B \approx 2$ T) and 360...420 MW ($B > 5$ T) were obtained (Fig. 4). The conversion in the strong magnetic field (0.7) was close to simulations, because the length of SWS was not very high ($\xi_k \approx 4.5$).
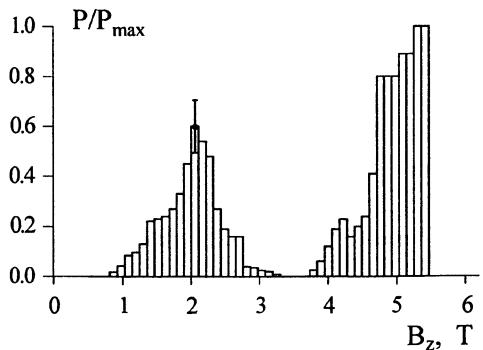
Fig. 4. Experimental dependence of microwave power as a function of magnetic field.

221

2. Above result with magnetic field ranging to the left of the cyclotron resonance stimulated an attempt of realization of pulsed-periodic regime with dc solenoid [10]. The hybrid high-voltage modulator comprised the driver SM-3NS based on semiconductor-opening-switch technology [11] and a hydrogen-filled sharpening spark gap. The SWS was the same. Providing 2 T during 1 s pulses the solenoid was cooled by transformer oil. The bank of "molecular" capacitors with a total capacity of 4.6 F was switched to solenoid in an incomplete discharge regime by a feedback transistor switch, ensuring a 2% current stabilization for a time up to 1 s (with power consumption 50 kJ). The voltage amplitude at the cathode reached 270 kV and the current of 1 ns-width beam was 2 kA. An output signal from the microwave detector was fed to a digital stroboscopic oscilloscope Tektronix TDS-820 with a frequency bandwidth 6 GHz
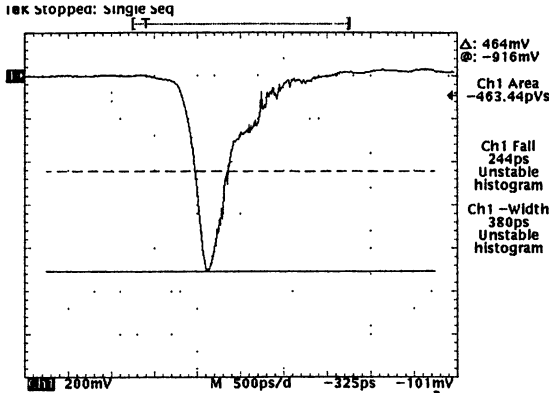
Fig. 5. Microwave signal recorded by stroboscope at PRF of 1 kHz for 512 sequential samples.

and counted at a discretization step of 10 ps. Each oscillogram (Fig. 5) was obtained by accumulating not less than 512 pulses at repetition rates 1...3.5 kHz. As it is seen, the high reproducibility has been achieved. The calorimetric measurements performed under the same conditions gave 65 mJ per pulse. Taking into account the non-linearity of detector we concluded that the typical pulse width was 250 ps. It follows that a peak power was about 250 MW.

3. A BWO with longer SWS length ($\xi_k \approx 6$) was used in the X-band experiment, which was performed on the base of the electron accelerator SINUS-150 [3] in single-shot regime. The guide magnetic field was 2.4 T. The waveform of the e-beam diode voltage and typical microwave detector signal are shown in Fig. 6.
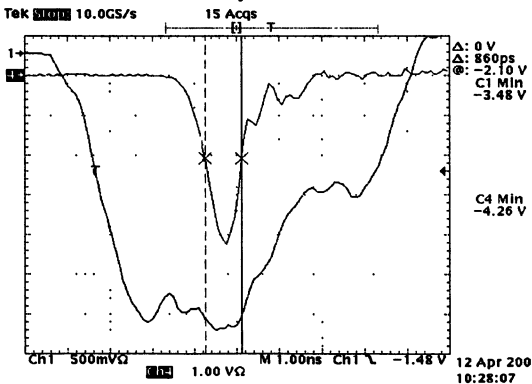
Fig. 6. Pulse of voltage in the diode and microwave signal.

Accounting the nonlinearity of the detector the microwave pulse width was typically of 0.5…0.7 ns. The maximum peak microwave power attained 1.2 GW for the e-beam parameters: 0.9 GW, 320 kV, 2.8 kA (Fig. 7). The central frequency was 9.3…9.4 GHz. According to the heterodyne measurements, about 70% of the spectrum energy is located within 10% band. The pulse energy measured with a calorimeter reached 0.6 J. The power conversion achieved 1.4 and the energy efficiency was ≈ 17% [12].
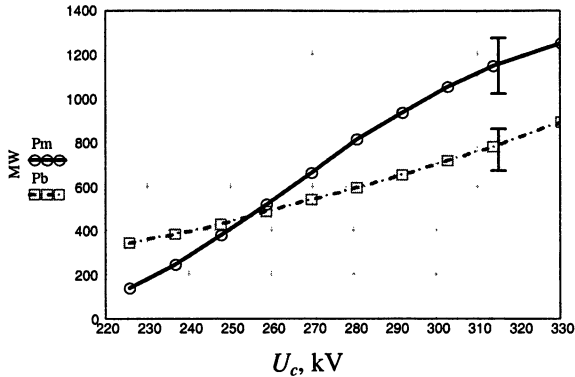
Fig. 7. Microwave power (solid) and beam power vs diode voltage

References

1. *Zheleznyakov V. V.* et al., Izv. Vyssh. Uchebn. Zaved. Radiofiz. **29**, 9, 1095 (1986).
2. *Ginzburg N. S.*, Pis'ma Zh. Tekh. Fiz. **14**, 5, 440 (1988).
3. *Ginzburg N. S.* et al., Physical Review E **60**, 3297 (1999).
4. *Gubanov V. P.* et al., Proc. Of SPIE "Intense Microwave Pulses 4" (Denver, Colorado, 1996), 2843, 228.
5. *Yalandin M. I.* et al., IEEE Trans. Plasma Sci. **28**, 5, 1615 (2000).
6. *Ginzburg N. S.* et al., Izv. Vyssh. Uchebn. Zaved. Radiofiz. **21**, 7, 1037 (1978).
7. *Rostov V. V.* et al., Izv. Vyssh. Uchebn. Zaved. Radiofiz. **46**, 4, 326 (2001).
8. *Rostov V. V.* et al., Pis'ma Zh. Tekh. Fiz. **24**, 10, 43 (1998).
9. *Korovin S. D.* et al., Pis'ma Zh. Tekh. Fiz. **28**, 2, 81 (2002).
10. *Grishin D. M.* et al., Pis'ma Zh. Tekh. Fiz. **28**, 19, 24 (2002).
11. *Lyubutin S. K.* et al., Prib. Tekn. Eksp. 3, 52 (2002).
12. *El'chaninov A. A.* et al., to be published in Proc. of Int. Conf. "Beams 2002".

SECTIONED RELATIVISTIC BACKWARD WAVE OSCILLATOR OPERATING AT LOW MAGNETIC FIELD

E. B. Abubakirov, A. N. Denisenko, N. F. Kovalev, A. V. Palitsin,
E. I. Soluyanov, V. V. Yastrebov

Institute of Applied Physics, Russian Academy of Sciences, Nizhny Novgorod, Russia

A version of the relativistic BWO aimed to provide its efficient operation at low focusing magnetic field was developed and investigated experimentally. The cyclotron absorption in the generator was weakened with a special choice of operating mode and electron beam parameters. To keep efficient operation the BWO had a sectioned design with a built-in Bragg mode converter to provide distributed output of microwave energy and to optimize a longitudinal microwave field structure. An experimental version of the BWO realized in the X-band provided 700 MW 40 ns microwave pulses with about 15% operation efficiency at 0.7 T of guiding magnetic field.

Backward wave oscillators (BWOs) with microwave systems made with slightly corrugated periodic metal waveguides are the simplest and the most spread version of relativistic sources of high power microwaves (HPM). In these devices relativistic electron beam interacts synchronically with the (-1)st spatial harmonics of the operating wave

$$\omega \approx (2\pi/d - h_0)v. \tag{1}$$

Here ω is operating frequency, h_0 is longitudinal wave number of the fundamental harmonics, d is a period of corrugation and v is velocity of electrons. The microwave energy in the BWO is transported mainly by the 0-th spatial harmonics, which intensity usually is much stronger than of other harmonics. As the high-current electron beam is confined with strong static or quasi-static magnetic field so there is possibility of a set of additional cyclotron resonant interactions between electrons and various spatial harmonics of the electromagnetic field

$$\omega - h_n v = p\omega_B. \tag{2}$$

Here $h_n = h_0 + n(2\pi/d)$ is a longitudinal wave number of the n-th spatial harmonic, $\omega_B = eB/(mc\gamma)$ is a cyclotron frequency, B is an induction of the magnetic field, e and m are charge and mass of electron respectively, γ is relativistic mass-factor of electrons, integer p shows the number of resonant cyclotron harmonic. It is essential that for rectilinear electron beams double (Cherenkov and cyclotron) resonance results in absorption of microwaves up to complete suppression of oscillations.

In an experimental design of a microwave source usually several modes are involved into the interaction process, for example in the backward wave oscillator these are an operating wave, propagating toward a cathode and an output wave, propagating in the opposite direction. It results in a very dense "spectrum" of the cyclotron resonances especially in the region of low guiding magnetic fields (Fig. 1).
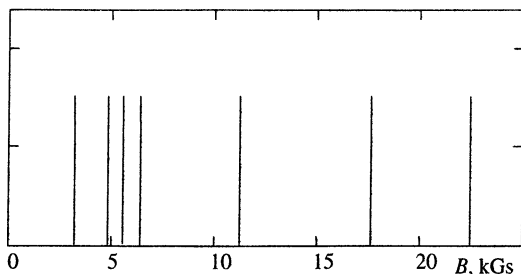
Obviously, the cyclotron interaction is one of serious obstacles, preventing decreasing of focusing magnetic fields in relativistic microwave oscillators. To reduce the intensity of the interaction a special combination of profile of the electron beam and high-frequency field of the operating mode has to be chosen [1, 2]. For a circular waveguide the condition can be expressed as $J_{m\pm1}(k_\perp r_b) = 0$, where J_n is a Bessel function of order n, m and $k_\perp$ are azimuth index and transverse wave number of the operating mode, r_b is a radius of the hollow electron beam (Fig. 2), signs plus or minus correspond to contra directional rotations of the mode structure.
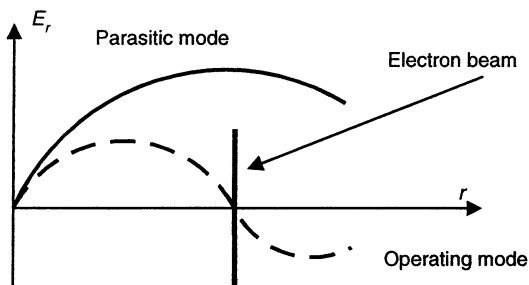
Fig. 2. Transverse distribution of the electric field of operating mode and position of the hollow electron beam minimizing the cyclotron interaction.

The lowest mode of a circular waveguide, which can satisfy the above condition, is TM_{11} with rotating transverse field structure. For this mode the absorption is minimum if the radius of the electron beam is close to the value $r_b = R\,(\kappa_{01}/\kappa_{11}) \approx 0{,}63\,R$, where R is radius of the waveguide, κ_{pq} is q-th zero of a Bessel function J_p.

It should be noted that high operating mode of the relativistic BWO always is transformed partially into some lower one because of Bragg scattering inside the microwave structure of the BWO [3]. So it seems expedient to highlight the mechanism and to use the scattered wave for output of the microwave energy. It is important that the transformation allows making a desired structure of output radiation and, by increasing of group velocity of the wave, shifting its resonant values of magnetic field out from the operating region. For TM_{11} operating mode

it seems convenient to convert it to TE_{11} mode, which forms effectively a Gaussian wave beam by radiation through a simple horn antenna. In this case the microwave system of the generator can be made on a base of periodic waveguide with axis-symmetric corrugation of its walls.

Among various schemes of implementation of the Bragg converter into the relativistic BWO the most prospective is a sectioned design [4], where part of the device with strong Bragg coupling of the waves is situated between two sections providing main wave-electron beam interaction (Fig. 3).

In the scheme microwave energy generated by the main BWO section is mainly reflected by the Bragg mirror. Its small part penetrates to the first BWO section and produces the initial velocity modulation of the electron beam. So now the reflector simultaneously serves as a drift space and the device in a whole gets a longitudinal distribution of high-frequency field, which allows to increase essentially operation efficiency up to 30–40%. The scheme is similar to the BWO with premodulation gap [5], but more reliable for powerful microwaves.

Fig. 3. Sectioned BWO, scheme (top) and microwave field distribution (bottom).

Three sections of the oscillator were made on a base of circular waveguides with an axis-symmetric periodic corrugation of their walls. Edge sections realized backward wave mechanism of interaction of TM_{11} wave with an electron beam, the middle section was the Bragg converter of TM_{11} to TE_{11} mode with about 90% of the transformation efficiency. TE_{11} mode was radiated to atmosphere by a conical horn through oversized vacuum window.

The oscillator was realized in 3-cm wavelength band and was driven with 0.8 MeV, 6 kA tubular electron beam, formed with explosion emission magnetically insulated gun. Electron beam diameter corresponded to the minimum cyclotron absorption for TM_{11} mode with a rotating transverse structure.

Maximum output peak power of the oscillator (up to 700 MW with 15% efficiency) was observed at magnetic fields below the resonance in the interval of 6–8 kGs (Fig. 4). Spectral measurements gave for carrier frequency 10.1 GHz with radiation band of 20–30 MHz. Spatial structure of the radiated wave was close to a Gaussian wave beam with circular polarization (Fig. 4). As microwave system of oscillator was axis symmetric, a direction of the polarization rotation was strictly determined by orientation of focusing magnetic field.

The similar BWO was tested in a pulse repetitive regime of operation with 500 keV, 3 kA, 20 ns electron beam. About 200 MW of microwave peak power was produced in series of pulses with 10 Hz of the repetition rate (Fig. 5).
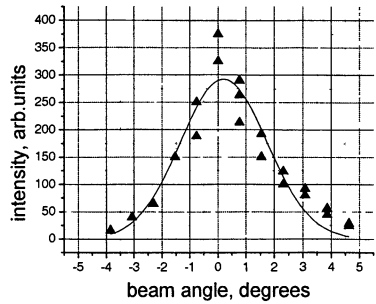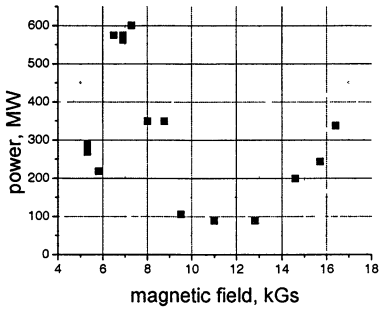
Fig. 4. Dependence of output power of the sectioned BWO on focusing magnetic field (left) and spatial structure of the output wave beam (right).
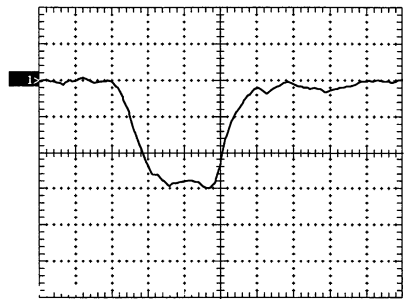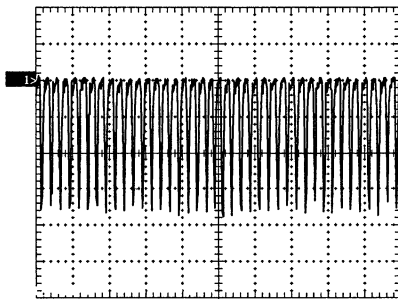

Fig. 5. Microwave pulses generated by the sectioned BWO in the pulse periodic regime: "sliced" pulses from 10 Hz 20 second burst (left) and one pulse from the burst, 5 ns/div (right).

The experimental research demonstrated that the combination of concepts of low cyclotron absorption and sectioned interaction in the BWO made possible to achieve stable and efficient operation of the high-power microwave oscillator at low focusing magnetic fields.

References

1. *Abubakirov E. B., Belousov V. I., Varganov V. N.* et al., Pisma Zh. Tokh. Fiz. **9**(9), 533–536 (1983).
2. *Abubakirov E. B., Belousov V. I., Zaitsev N. I* et al., Proc. of 8th International Conf. on High-Power Electron Beams, World Scientific **2**, 1155–1160 (1991).
3. *Abubakirov E. B., Ginzburg N. S., Sergeev A. S.* Radiotekhnika i electronika **46**(11), 1374–1378 (2001).
4. *Abubakirov E. B., Denisenko A N., Goikhman M. B.* et al., 14th Int. Conf. on High Power Particle Beams (Albuquerque, USA, 2002), Abstracts, 286.
5. *Kurkan I. K., Rostov V. V., Totmeninov E. M.* Pisma Zh. Tokh. Fiz. **24**(10), 43–47 (1998).

A HIGH-POWER VIRCATOR BASED ON AN IRONLESS LINEAR INDUCTION ACCELERATOR OF ELECTRONS

A. V. Yachny[1], V. D. Selemir[2], A. E. Dubinov[1,2], B. G. Ptitsyn[1,2], A. A. Evseyenko[2], V. A. Letyagin[2], R. K. Nurgaliev[2], A. V. Sudovtsov[2]

[1]Sarov Physical & Technical Institute, Sarov, Russia
[2]Russian Federal Nuclear Center, Sarov, Russia

A high-power vircator that is based on the Korvet ironless linear induction electron accelerator built around radial pulse-forming lines is implemented for the first time. Results on the computer simulation and experimental optimization of the vircator are discussed. The experimentally found parameters of the vircator are follows: cathode current 35 kA (at a limit current of 19 kA), microwave pulses base widths 40 and 18 ns, and peak microwave power more than 500 MW.

Introduction

Microwave oscillators with a virtual cathode (VC), including vircators, form a basic class of oscillators in ultra-high-power relativistic high-current microwave electronics [1]. Current vircators are based on high-voltage nanosecond oscillators that are built around single and dual pulse-forming lines [2, 3], inductive energy storage devices with plasma current interrupters [4, 5], or magnetic explosion generators [6, 7].

Ironless linear induction accelerators (LIAs) that exploit radial pulse-forming lines are more promising for feeding the vircators than the above-mentioned sources. The advantage of such LIAs is that they can generate high-voltage pulses of both polarities and operate in the pulse-train mode. Also, in these LIAs, the cathode and the anode can be grounded simultaneously. This enables new types of vircators to be designed that cannot be implemented with conventional feeders, for example, a cyclotron-resonance vircator [8].

Korvet LIA and vircator on its basis

The Korvet ironless LIA, earlier used as an injector for the well-known LIA-10 accelerator [9], consists of four modules, each representing three functionally coupled units: an inductor unit, a GIN-500 pulse voltage generator that charges the capacitor of the inductor unit, and a generator that forms pulses triggering the switches of the inductor. The inductor unit, in its turn, comprises three series-connected sections built on radial lines that are insulated by high-resistivity deionized water. The lines are parallel-connected to GIN-500 through the charge circuit.

Ideally, the unloaded inductor with uniform lines generates rectangular pulses of the accelerating voltage whose amplitude is close to the value of the

228

charging voltage. The base width of the first pulse was 20 ns. The second and third pulses with alternating polarity had 40-ns-wide bases. The parameters of the inductor unit were follows: charging voltage 500 kV, charging pulse with 520 ns, peak amplitude of the accelerating voltage 1.5 MV, and short-circuit current 180 kA.

The vircator was built around one module of the Korvet LIA (Fig. 1). The device integrates coaxial cathode and anode. The cathode represents the cathode holder (thin-walled stainless steel tube), to which a steel substrate was welded on the anode side. Graphite cylinders 20 mm in diameter and 40 mm long acting as emitters were screwed on the substrate. A total of 8 closely spaced emitters were arranged on the substrate, producing a cathode with an outer diameter of 72 mm.
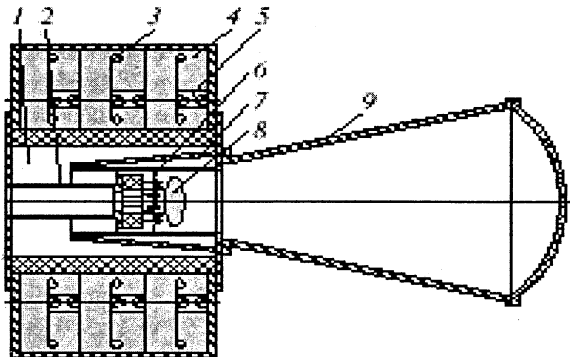
Fig. 1. Vircator based on one module of the Korvet LIA. *1* – vacuum space of the accelerator; *2* – cathode; *3* – high-voltage electrode of the inductor unit; *4* – deionized water; *5* – gas-filled controllable gap; *6* – anode grid; *7* – anode; *8* – virtual cathode; *9* – microwave horn.

The anode was a 380-mm-long hollow cylinder with a diameter of 160 mm. A metallic ring was inserted in the cylinder, and a square-mesh (3 mm on a side) anode grid made of nichrome wire (0.3 mm in diameter) was stretched over it by electric arc welding. Moving the ring with the anode grid along the axis of the vircator, one can vary the anode–cathode spacing. In this work, this spacing was varied between 6 and 19 mm. The anode was terminated by a conical horn antenna.

With the inductor unit charged to the maximal extent, the voltage extracted from the diode of the vircator was 900 kV. In this case, the diode current was 50 kA, which is several times higher than the limit beam current in the anode plane behind the grid (estimated at 15–20 kA).

The currents passing in the vircator were measured with three Rogowski loops.

Computer simulation of the vircator

The computer simulation of the vircator was performed with the software suite based on the Karat 2.5-dimensional PIC code [10]. The geometry of a region being simulated and its dimensions are shown in Fig. 2, a: a tubular cathode with outer and inner diameters of 72 and 32 mm, respectively; an anode with a diameter of 160 mm; and the anode–cathode spacing varying from 7 to 18 mm. Such geometry is roughly identical to the vircator that was based on the Korvet LIA and studied in this work. It was assumed that a 900-kV 40-ns pulse is applied to the diode. Under these conditions, the diode current was as high as ~ 35 kA.

Figure 2, b shows a typical instantaneous phase portrait of a particle ensemble. It is seen that VC is formed in the system and its oscillations generate microwave radiation. Electrons leaving the cathode are reflected from the VC space charge and oscillate in the potential well produced by the cathode, grid, and VC. The simulation showed that the appearance of the VC coincides with the generation of microwave radiation and the time instant the VC collapses, with the instant the generation ceases.
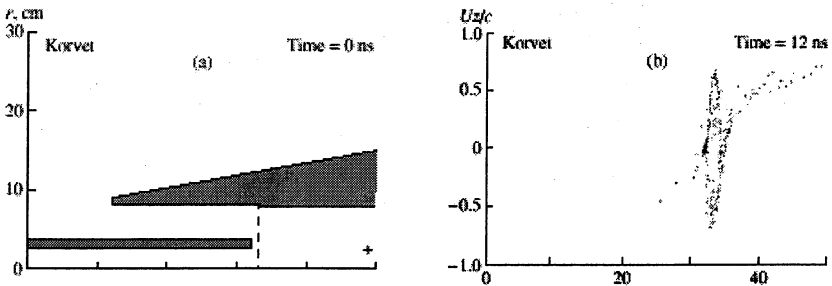
Fig. 2. Computer simulation of the vircator: a) geometry of the region simulated and b) instantaneous phase portrait of the beam.

Figure 3 shows a typical simulated waveform of the extracted power for a cathode – grid spacing of 12 mm. The maximum of the peak power is observed at spacing between 12 and 14 mm, in agreement with experimental data. The values of the peak power, 400–500 MW, are also consistent with experimental findings.
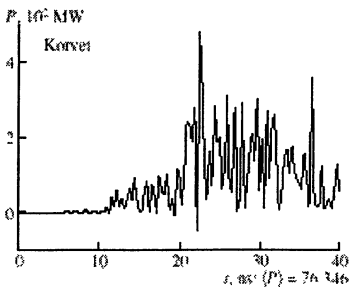
Fig. 3. Simulated waveform of the microwave power.

Thus, the simulation of the vircator based on the Korvet LIA suggests that the device can generate high-power microwave pulses. The agreement between the analytical and experimental results gives promise that the given model can be used to tentatively optimize the system.

230

Experimental study of the vircator

The early experiments were aimed at determining the optimal spacing d between the end face of the cathode and the grid. The spacing was varied between 6 and 14 mm with a step of 1 mm. No radiation was observed for spacing of 6 and 14 mm. For the other spacings, the energy per microwave pulse measured with the calorimeter is listed in Table 1. It follows from Table 1 that the curve $W(d)$ has a narrow peak, which agrees with experimental data obtained elsewhere.

To determine the peak power of a microwave pulse, we recorded pulse envelopes, using the semiconductor detectors, and compared them with the calorimetric data. The peak microwave power obtained at the optimal spacing d = 10 mm was found to be roughly 150 MW.

In another series of experiments, we tried to reduce losses in the waveguide slots where the Rogowski loops were inserted. The cathode length was increased to 130 mm, all other design features being the same. As before, we calorimetrically measured the microwave energy, varying the cathode–grid spacing from 7 to 19 mm. The results are listed in Table 2, where the values of the peak power are also given. Note that the microwave pulses become shorter nearly twice: 20 ns against 40 ns for the shorter cathode).

Table 1. Results of experiments on varying the cathode – grid spacing

d, mm	W, J
7	0.63
8	0.96
9	1.21
10	1.37
11	1.15
12	0.69
13	0.09

Table 2. Results of experiments on varying the cathode – grid spacing

d, mm	W, J	P, MW
7	0.92	180
8	1.45	285
9	1.58	310
10	2.16	425
11	2.50	490
12	2.65	520
13	2.48	485
14	2.44	480
15	2.32	455
16	1.79	350
17	1.64	320
18	1.30	255
19	0.73	145

From Table 2, it is seen that both the energy absorbed by the calorimeter and the peak power of the pulses are maximal when the cathode – grid spacing equal 12 mm. In this case, the peak power reaches 520 MW.
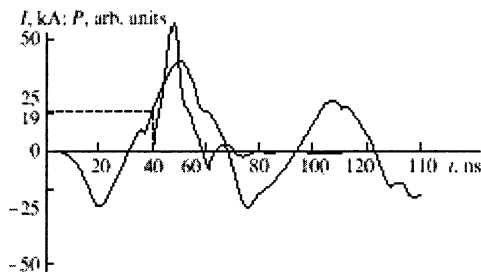
Fig. 4. Synchronized waveforms of the (*1*) cathode current and (*2*) microwave pulse for the longer cathode.

Finally, one more series of experiments were targeted at determining the starting current of microwave generation. To determine the starting current, we synchronized the signals coming from the cathode Rogowski loop and from the semiconductor detectors with regard for the time it takes for the microwave radiation to propagate from the VC to the detector. Superposing the signals, we found that the starting current of microwave generation is I = 19 kA (Fig. 4), which is approximately equal to the flight current.

Conclusions

Thus, we implemented a high-power vircator based on the ironless LIA using radial pulse-forming lines and studied its performance.

The parameters of the vircator are follows: cathode current 35 kA, starting (limit) current 19 kA, base width of microwave pulses 18 ns, and peak power more than 500 MW. The results of simulation using the Karat code are in agreement with experimental data.

References

1. *Dubinov A. E. and Selemir V. D.* Zarubezhn. Radioél., № 4, 54 (1995).
2. *Scarpetti R. D. and Burkhart S. C.* IEEE Trans. Plasma Sci., **13**(6), 506 (1985).
3. *Selemir V. D., Alyokhin B. A., Vatrunin V. E.* et al., Fiz. Plazmy, **20**, 689 (1994), [Plasma Phys. Rep., **20**, 621 (1994)].
4. *Zherlitsyn A. G., Lopatin V. S., and Luk'yanov O. V.* Pis'ma Zh. Tekh. Fiz., **16** (11), 69 (1990) [Sov. Tech. Phys. Lett., **16**, 431 (1990)].
5. *Zhdanov V. S., Babkin A. L., Galkin S. M.* et al., Proceedings of the XXV Zvenigorod Conference on Plasma Physics and Controlled Nuclear Fusion (Zvenigorod, 1998), 169.
6. *Azarkevich E. I., Didenko A. N., Dolgopolov P. V.* et al., Dokl. Akad. Nauk SSSR, 319, 352 (1991), [Sov. Phys. Dokl., **36**, 539 (1991)].
7. *Azarkevich E. I., Didenko A. N., Zherlitsyn A. G.* et al., Teplofiz. Vys. Temp., **32**, 127 (1994).
8. *Pavlovski A. I., Bosamykin V. S., Selemir V. D.* et al., Relativistic High-Frequency Electronics, Inst. Prikl. Fiz. Ross. Akad. Nauk, Gorki, № 7, 81 (1992).
9. *Pavlovski A. I., Bosamykin V. S., Savchenko V A.* et al., Dokl. Akad. Nauk SSSR, 250, 1118 (1980), [Sov. Phys. Dokl., 25, 120 (1980)].
10. *Tarakanov V. P.* User's Manual for Code Karat, Berkley Research Associate Inc. (Springfield, 1992).

EVOLUTION OF THE MICROWAVE SPECTRUM
IN THE COURSE OF A RADIATION PULSE
FROM A RELATIVISTIC CHERENKOV PLASMA MASER

I. L. Bogdankevich, I. E. Ivanov, O. T. Loza, A. A. Rukhadze,
P. S. Strelkov, D. K. Ulyanov, V. P. Tarakanov[1], E. Garate[2]

General Physics Institute, Moscow, Russia
[1]High-Energy Density Research Investigation Center, Moscow, Russia
[2]University of California, Irvine, CA, USA

A new Cherenkov plasma maser driven by a high-current relativistic electron beam (500 kV, 2 kA, 1 μs) was designed. The frequency of microwaves was tuned from 1.5 to 6 GHz with a power output from 50 to 80 MW and pulse duration from 500 to 700 ns. The radiation frequency depends on the plasma density and may be re-established during less than 100 μs. In different operation regimes microwave spectra were obtained with a width from 40 MHz to 1 GHz, and the spectra changed in the course of the pulses. The results of experiments coincide well with that of analytical theory and numerical simulations.

1. Introduction

This work continues our studies, which we have carried out since 1982. The operation of a relativistic Cherenkov plasma maser (CPM) is based on Cherenkov interaction of a relativistic electron beam with plasma [1]. If the speed of electrons coincides with the phase velocity of the wave, an instability arises with a frequency, that depends on the Langmuir plasma frequency. The basic maser has not significantly changed during the past 20 years.

Several years ago we made a plasma maser [2], which operated in the band from 4 to 28 GHz at a power level of 50 MW, and the experimental results coincided with theoretical predictions. Microwave spectra were measured using a calorimetric spectrometer, which consists of a set of cut-off filters, overlapping a significant part of the maser output microwave flux, and calorimeters. After several identical pulses, it was possible to obtain the radiation spectrum of the broad-band source, integrated throughout the pulse duration.

In this research we used another method for measurements of a single microwave pulse spectrum. An oscilloscope with high temporal resolution immediately registered microwave electric field, and then the Fourier-transformation of the obtained waveform was carried out. This approach permits to rise the accuracy and to study the temporal evolution of the spectrum. The range of the available oscilloscope restricted the upper frequency by ≈ 3 GHz, so we designed a new CPM tunable in the band 1.5–6 GHz.

2. Experimental data

Fig. 1 shows the experimental layout, which is the same as in [2], except one feature: in order to generate lower frequencies, the dimensions were increased.

A high-voltage pulse (500 kV, 1 μs) is applied to the explosive-emission cathode *1* of the accelerator. REB *2* with the current 2 kA is injected along the axis of a circular metal waveguide *3* with preformed annular plasma *4*. The plasma density was tuned by the plasma source [3] current. The electron beam and the plasma are in a strong magnetic field with an induction of 0.8 T; the beam electrons have the longitudinal velocity component only. On the right side of the metal waveguide *3*, the electron beam and the plasma are limited by the end of the central conductor *5* of the output coaxial emitter *6*. Microwaves are generated in the plasma waveguide, propagate through a vacuum coaxial waveguide *6*, and are emitted by a horn *7* into the atmosphere through a dielectric window (*8*).

Fig. 1. Schematic of the RCPM: *1* – accelerator cathode, *2* – REB, *3* – metal waveguide, *4* – plasma, *5* – collector, *6* – metal coaxial waveguide, *7* – conical coaxial emitting horn, and *8* – window.

The maser radiation frequency was measured by the calorimetric spectrometer [4], see Fig. 2 (left). An increase of the plasma source current from 18 to 100 A and corresponding increase of the plasma concentration from $5 \cdot 10^{11}$ to $5 \cdot 10^{12}$ cm^{-3} raises the mean radiation frequency from < 2 to ≈ 5.5 GHz. Microwave pulse energy is about 20 J. The waveforms of microwave pulses are also presented in Fig. 2 (right). The measured pulse energy permits to determine the radiation power in absolute units. Fig. 2 shows that the microwave power level is 50 MW, and the pulse duration is about 0.5 μs.

As mentioned above, the comparatively low frequency of the radiation permitted another method of determining the microwave spectrum, namely, a dipole antenna and an oscilloscope with sufficient frequency bandwidth. Measurements of the temporal behavior of the microwave radiation in different regimes revealed a typical situation presented in Fig. 3. At the beginning of the pulse the spectrum is broad and consists of several distinguishable lines, which appear one after the other. Then, for a comparatively long time, the spectrum bandwidth is narrow, although the frequency changes, sometimes discretely. By the end of the pulse the spectrum broadens and finally the radiation terminates, although the electron beam continues its propagation.

If the plasma density is increased the radiation frequencies increase also, but the temporal behavior remains the same: the spectrum narrows down just after the pulse front and broadens after some time. At higher plasma density and for a radiation frequency greater than 3 GHz a narrow spectrum does not appear.

234

Fig. 2. *Left*: spectrum measured by calorimetric spectrometer, plasma source currents are indicated in the upper right corners; *right:* waveforms of microwave pulses in corresponding frequency ranges.
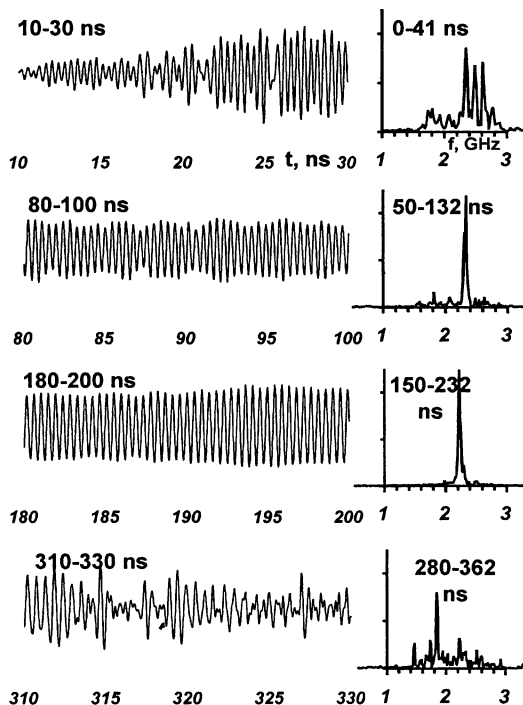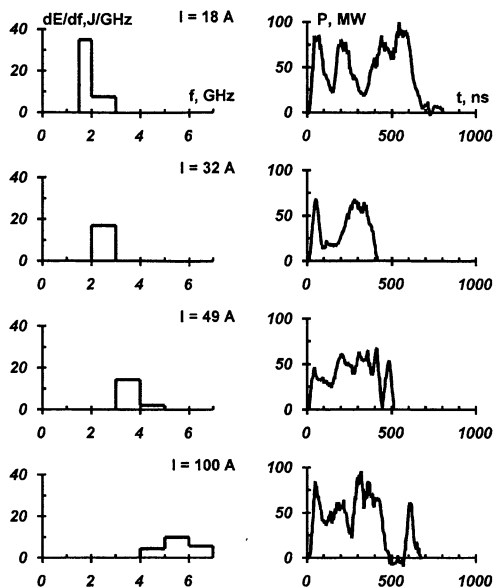
Fig. 3. Fragments of the waveforms of the microwave electric field at different delays from the pulse front (on the left) and the spectra calculated from these waveforms (on the right).

235

Numerical modeling was carried out using the 2-dimensional version of the KARAT code, with the electrons simulated by a PIC-method, and the plasma considered either as a linear medium with invariable properties or it was treated by a PIC-method. The coincidence between experimental data and the results of calculations is demonstrated by Fig. 4. In both the experiments and the calculations the spectrum in the pulse beginning is broad and consists of separate lines, ~ 0.1 GHz one from another. Then the spectrum becomes more narrow, only in the experiment this happens faster. However the further behavior of the calculated spectrum differs qualitatively from the experimental one. In calculations the spectrum remains narrow on the same power level, whereas in the experiment the spectrum broadens and the power drops. The effect of "microwave pulse shortening" is observed: the microwave pulse is less than that of the REB.
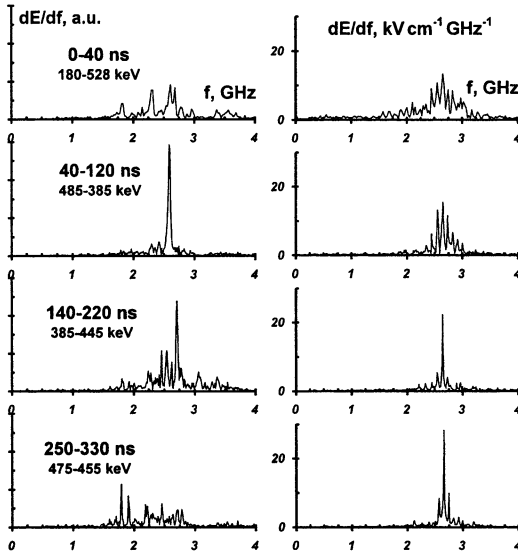
Fig. 4. Microwave spectra for $n_p = 9 \cdot 10^{11}$ cm^{-3}: experiment (on the left) and simulations (on the right). The time intervals in which each spectrum was calculated and the electron energy ranges within this interval are shown.

In simulations with a "linear plasma" the numerical results well coincide with experimental data except the effect of microwave pulse shortening. In tentative simulations with the plasma treated as "particles" the microwave pulse shortening did take place, but only at low plasma densities.

Hence, there are several peculiarities of the maser operation: both the central frequency and the bandwidth depend on the plasma density, both these parameters change in time, and the broad spectrum is actually a set of narrow lines.

3. Discussion

The *dependence of the radiation frequency on plasma density* is straightforward: with an increase in the plasma Langmuir frequency the Cherenkov interaction takes place at a higher frequency.

The *variation of the radiation frequency on the pulse front* is due to the increase of the electron's energy from about 200 to 500 keV during the rise of the beam current (50 ns). As this takes place the frequency drops from 2.6 GHz to 2.4 GHz. The Cherenkov interaction of plasma and electrons takes place at a lower frequency for an increase in the electron's energy.

The *broad radiation spectrum is actually a set of equidistant lines*. This is due to the fact that the maser is an amplifier with feedback. Such a device can work if an integer number, N, of wavelengths coincides with the oscillator length, L as: $\dfrac{L}{\lambda_{dir}} + \dfrac{L}{\lambda_{ref}} = N = 1,\ 2,\ 3,\ ...$ Since the dispersion of the direct wave (which interacts with the electron beam) and the backward wave are different, the wavelengths λ_{dir} for the direct and λ_{ref} for the reflected waves are different. Also different are the group velocities v_{dir}^{gr} and v_{ref}^{gr}. In terms of wavenumbers $k_i = 2\pi/\lambda_i$ the above becomes: $\dfrac{L}{2\pi}(k_{dir} + k_{ref}) = N$. This integer number N might be interpreted as the longitudinal mode number.

If so, the wavenumbers of the waves may change only by a fixed increment. Hence, the radiation frequencies may also be only of a discrete set with the increment δf inversely proportional to the time of complete feedback in the system: $\delta f = \dfrac{<v^{gr}>}{2L}$, where the average group velocity $<v^{gr}> = 2\dfrac{v_{dir}^{gr} \cdot v_{ref}^{gr}}{v_{dir}^{gr} + v_{ref}^{gr}}$.

This was calculated using the linear model of the plasma-beam interaction as $<v^{gr}> = 1.8 \cdot 10^{10}$ cm/s. Taking into account that the length $L = 70$ cm, one may find that the frequency increment has to be 130 MHz which coincides well with the experimental data.

The bandwidth depends on plasma density. As indicated above, the maser is an amplifier with mirrors. The device works if the amplification compensates for the energy losses at the ends of the system: $\kappa_l \cdot \kappa \cdot e^{\delta K L} > 1$, where
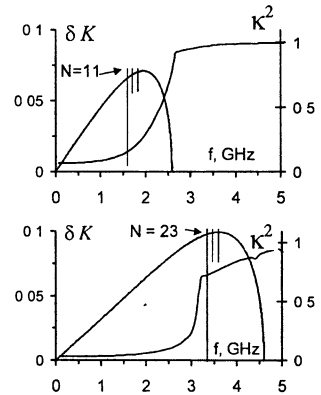
Fig. 5. Frequency dependences of the linear amplification factor δK for and the square of the reflection coefficient κ^2 of the plasma wave from the right end of the plasma waveguide. *Top*: $n_p = 5.25 \cdot 10^{11}$ cm^{-3}; *bottom*: $n_p = 1.25 \cdot 10^{12}$ cm^{-3}.

237

$\kappa_l = 1$ and κ are the reflection coefficients at the entrance and exit of the interaction area, correspondingly, and δK is linear growth rate. Calculations of both κ and δK in the framework of linear theory show that the bandwidth is narrow if the Q-factor is low, and vice versa. For a plasma density $5.25 \cdot 10^{11}$ cm^{-3} ($f \approx 1.6$ GHz, see Fig. 5) $\kappa^2 \approx 0.15$, i.e. $Q \approx 7$, and $\kappa \cdot e^{\delta K \cdot L} \approx 60$, whereas for $1.25 \cdot 10^{12}$ cm^{-3} $\kappa^2 \approx 0.65$, i.e. $Q \approx 30$, and $\kappa \cdot e^{\delta K \cdot L} \approx 1000$.

4. Summary

We designed and operated a relativistic Cherenkov plasma maser which generates microwave pulses with frequency tunable in the band from 1.5 to 6 GHz, and has a pulse duration of 0.5 µs at a power level of 50 MW. In the band between 1.5 and 3 GHz, during the first several hundred nanoseconds the bandwidth is narrow and the frequency corresponds strictly to the energy of the relativistic electrons. Above 3 GHz the spectrum is also tunable, but always broad: see Fig. 6.
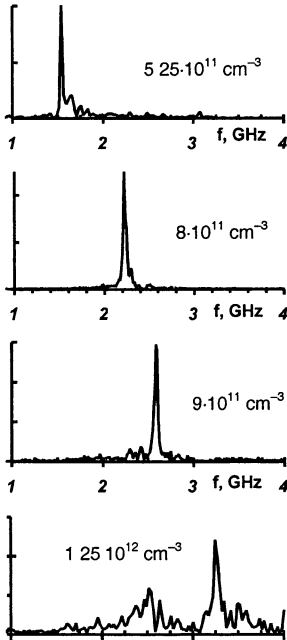
The results of numerical simulations generally coincide with the experimental data. The observed effect of "microwave pulse shortening" may be due to non-linear effects in the plasma: it was not obtained in simulations using a "linear plasma", but was obtained with a PIC-method at low plasma densities. For the higher density plasma the microwave pulse shortening is presumably determined by the comparatively high Q-factor and comparatively strong microwave field in the beam-plasma interaction area.

Fig. 6. Microwave spectra of the maser with invariable energy of driving relativistic electrons for different concentrations of plasma.

References

1. *Kuzelev M. V., Loza O. T., Rukhadze A. A.* et. al., Plasma Phys. Rep., **27**(8), 669–691 (2001).
2. *Strelkov P. S. and Ul'yanov D. K.* Plasma Phys. Rep., **26**(4), 303–307 (2000).
3. *Loza O. T., Ponomarev A. V., Strelkov P. S.* et al , Plasma Phys. Rep., **23**(3), 201–208 (1997).
4. *Bogdankevich I. L., Strelkov P. S , Tarakanov V. P.* et al., Instruments and Experimental Techniques, **43**(1), 82–87 (2000).

MICROWAVE GENERATION BY AN ELECTRON BEAM IN A PLASMA COAXIAL TRANSMISSION LINE

P. I. Markov, E. A. Kornilov, I. N. Onishchenko, G. V. Sotnikov

Kharkov Institute of Physics and Technology, Kharkov, Ukraine

Microwave generation by an electron beam in a coaxial transmission line in which the inner and outer conductors are both corrugated is studied theoretically. An annular electron beam propagates in a transport channel filled entirely with plasma. It is shown that, in the presence of a plasma, the microwaves are amplified to a significantly greater extent and the spectrum of the generated microwaves is broader. The maximum possible amplitude of the longitudinal electric field and the interaction efficiency are determined as functions of the plasma density.

A vacuum slow-wave structure acquires the wellknown hybrid properties when its interaction chamber, where an electron beam propagates, is filled with a plasma. The principles of operation of hybrid plasma-filled slow-wave structures were first reported by Fainberg *et al.* [1]. Filling the transport channel with a plasma makes it possible to substantially enhance the longitudinal electric field, so that the coupling constant increases and, accordingly, the amplification coefficient of the generated microwaves becomes larger. Under proper conditions, the beam interacts with the eighen waves of a vacuum structure, thereby generating intense microwave power fluxes. Carmel *et al.* [2], Zav'yalov *et al.* [3], Antonov *et al.* [4], by experimental investigations confirm that hybrid slow-wave structures provide a basis for the creation of high-power oscillators and amplifiers.

In research on hybrid plasma structures, the first experiments were carried out with vacuum slow-wave structures in the form of a chain of coupled cavity resonators. In such hybrid plasma structures, generation is most efficient when the frequency of the synchronously excited microwaves is equal to the plasma frequency. As a result, in a waveguide with a given plasma density, the spectrum of the excited microwaves is narrow (on the order of the instability growth rate). Kornilov *et al.* [5] suggested that filling a vacuum structure in which a broadband cable wave can propagate with a plasma makes it possible to increase the amplification coefficient, while maintaining the broadband amplification.

Below the results of theoretical investigations of microwave amplifications in a corrugated plasma coaxial transmission line are represented.

Linear regime

The slow-wave structure under consideration is a coaxial transmission line in which the inner and outer cylindrical conductors (of radii ρ and b, respectively) are both corrugated. The transport channel with an inner radius σ and outer ra-

dius a is filled entirely with a plasma of density n_p. The microwaves in the transport channel are generated by a thin annular electron beam with a radius r_b, velocity v_0, and current I_b. The period of the structure is D and the resonators have the same width equal to d. The inner conductor can be displaced with respect to the outer conductor by an arbitrary distance l. In the linear approximation, the dispersion relation describing the generation of a monochromatic wave by an electron beam can be obtained by the method of separate regions. As result we obtain the next complex equation:

$$Y_{12}Y_{32} - Y_{11}Y_{33} = 0, \tag{1}$$

where

$$Y_{12} = \frac{d}{D}\sum_{m=-\infty}^{\infty}\frac{k\varepsilon_3}{k_{\perp m}}\frac{\psi_m^2}{\Delta_m}\left[\frac{F_1\left(k_{\perp m},a,\sigma\right)}{F_0\left(k_{\perp m},a,\sigma\right)} - \frac{\alpha_m^2}{\left(\omega-\beta_m v_0\right)^2}F_1\left(k_{\perp m},a,r_b\right)\frac{F_0\left(k_{\perp m},r_b,\sigma\right)}{F_0\left(k_{\perp m},a,\sigma\right)}\right]$$

$$-\frac{F_1\left(k,a,b\right)}{F_0\left(k,a,b\right)}, \quad Y_{11} = \frac{d}{D}\sum_{m=-\infty}^{\infty}\frac{k\varepsilon_3}{k_{\perp m}}\frac{\psi_m^2}{\Delta_m}e^{im\phi_0}\frac{F_1\left(k_{\perp m},a,a\right)}{F_0\left(k_{\perp m},\sigma,a\right)},$$

$$Y_{32} = \frac{d}{D}\sum_{m=-\infty}^{\infty}\frac{k\varepsilon_3}{k_{\perp m}}\frac{\psi_m^2}{\Delta_m}\left[\frac{F_1\left(k_{\perp m},\sigma,a\right)}{F_0\left(k_{\perp m},\sigma,a\right)} - \frac{\alpha_m^2}{\left(\omega-\beta_m v_0\right)^2}F_1\left(k_{\perp m},\sigma,r_b\right)\frac{F_0\left(k_{\perp m},r_b,a\right)}{F_0\left(k_{\perp m},a,\sigma\right)}\right]$$

$$-\frac{F_1\left(k,\sigma,\rho\right)}{F_0\left(k,\sigma,\rho\right)}, \quad Y_{33} = \frac{d}{D}\sum_{m=-\infty}^{\infty}\frac{k\varepsilon_3}{k_{\perp m}}\frac{\psi_m^2}{\Delta_m}e^{-im\phi_0}\frac{F_1\left(k_{\perp m},\sigma,\sigma\right)}{F_0\left(k_{\perp m},a,\sigma\right)},$$

$$F_n(q,x,y) = J_n(qx)Y_0(qy) - Y_n(qx)J_n(qy), \quad \varepsilon_3 = 1-\omega_p^2/\omega^2, \quad \omega_p^2 = 4\pi e^2 n_p/m,$$

$$k_{\perp m} = \sqrt{(k^2-\beta_m^2)\varepsilon_3}, \quad k = \omega/c, \varphi_0 = 2\pi l/D, \quad \psi_m = \sin(\beta_m d/2)/(\beta_m d/2),$$

$$\Delta_m = 1+\frac{\alpha_m^2 F_0(k_{\perp m},r_b,a)}{(\omega-\beta_m v_0)^2}\cdot\frac{F_0(k_{\perp m},r_b,\sigma)}{F_0(k_{\perp m},a,\sigma)}, \quad \alpha_m^2 = \frac{I_b}{I_A}\frac{\pi c^3(k^2-\beta_m^2)}{\gamma_0^3 v_0}, \quad I_A = 17\text{кA},$$

$\beta_m = \beta_0 + 2\pi m/D$, J_n, Y_n are Bessel and Neumann functions; ω, β_0 are wave frequency and longitudinal wave number.

The results of numerical solution of equation (1) are shown in Figure 1 and Figure 2. For the calculations the parameters experimental setup were taken: $b = 5.3$ cm, $a = 4.0$ cm, $\sigma = 3.5$ cm, $\rho = 1.9$ cm, $D = 0.7$ cm, $d = 0.5$ cm, $r_b = 3.6$ cm, $I_b = 5.0$ A, $W_b = 35$ keV.
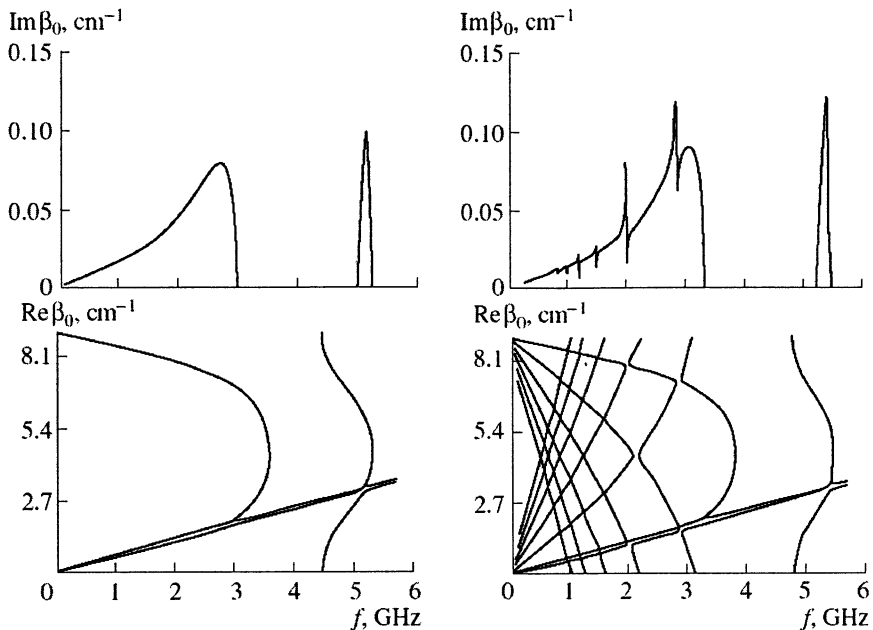
Fig. 1. Real $\text{Re}\,\beta_0$ and imaginary $\text{Im}\,\beta_0$ parts of the longitudinal wavenumber vs frequency for vacuum (at left) and for plasma filled ($n_p = 1.8 \cdot 10^{11} \text{cm}^{-3}$) structures.

As follows from Fig. 1, in addition to the waves that exist in the structure in the absence of plasma, there are many waves associated with the radial modes as well as with the Floquet modes of the natural waves of the coaxial plasma column. If the electron beam velocity is close to the phase velocity of the wave corresponding to the intersection point of the dispersion curves of a pair of eigenmodes of the plasma-filled structure, then a narrow pronounced peak appears in the frequency profile of the imaginary part of the longitudinal wavenumber. A comparison between left and right and pictures on Fig. 1 shows that, in a plasma-filled transport channel, the amplification band broadens by 10% while the amplification coefficient increases simultaneously by the same amount, 10%.

Figure 2 shows the maximum amplification coefficient and the frequency at which the amplification coefficient is maximum as functions of the plasma density. In the frequency band under investigation, the amplification coefficient is almost linearly proportional to the plasma density. Such behavior of the amplification coefficient can be explained by the fact that, as the plasma density increases, the frequency of the wave that resonates with the beam grows linearly and its group velocity decreases.

241
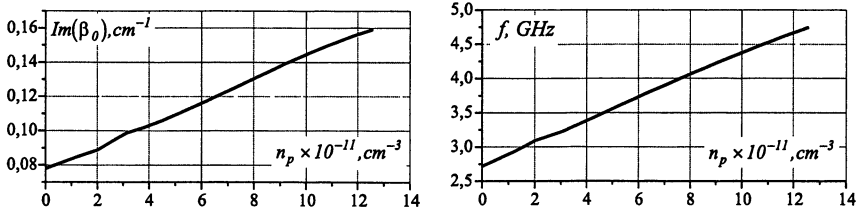
Fig. 2

We also calculate the wave impedance of a coaxial slow-wave structure as a function of frequency for different plasma densities. In the presence of a plasma, the wave impedance changes insignificantly. Hence, plasma-filled slow-wave hybrid transmission lines also provide the possibility of achieving good matching of the slow-wave structure with devices for inputting and extracting microwave power in a broad frequency band.

Nonlinear regime

The nonlinear stage of the interaction between an electron beam and the eigen waves of a coaxial slow-wave transmission line was investigated by using of standard procedure of microwave electronics [6]. The full set of equations for nonlinear analysis is: the equation for the averaged (over the cross section of the transport channel) amplitude E of the longitudinal electric field

$$\frac{dE}{dz} + i(\beta_e - \beta_0^0)E = (\beta_0^0)^2 I_b R_c^0 \frac{1}{2\pi} \int_0^{2\pi} e^{i\theta} d\theta_0 \tag{2}$$

and of the equations of motion of the beam electrons

$$\frac{dv(z)}{dz} = \frac{e}{mv(z)}\left(1 - \frac{v^2(z)}{c^2}\right)^{3/2} \mathrm{Re}\left(Ee^{-i\theta}\right), \qquad \frac{d\theta}{dz} = \beta_e\left(\frac{v_0}{v(z)} - 1\right), \tag{3}$$

where $\beta_e = \omega/v_0$, β_0^0 is the longitudinal wavenumber of the eigenmode of the structure without beam, R_c^0 is the coupling impedance.

Figure 3 shows how the amplitude of the longitudinal electric field depends on the length of the slow-wave structure. Each of the profiles was calculated for the frequency and wave vector corresponding to the maximum amplification coefficient in the linear regime. For a plasma density of $n_p = 1.8 \cdot 10^{11} \, \mathrm{cm}^{-3}$, the longitudinal electric field saturates at 1.42 kV/cm, the optimum length of a hybrid structure being 43.6 cm. For a plasma density of $n_p = 7.2 \cdot 10^{11} \, \mathrm{cm}^{-3}$, the

242

saturation level is 1.93 kV/cm and the optimum length of the structure is 34.8 cm. For the vacuum case, the relevant parameters are equal to 1.3 kV/cm and 48 cm. The profiles of the interaction efficiency indicate that the maximum losses in the energy of the electron beam are nearly the same (about 24–26%) for both vacuum and plasma-filled coaxial slow-wave structures. Hence, our nonlinear analysis confirms the assumption that filling the structure with a plasma results primarily in an

Fig. 3

increase in the frequency at which resonant interaction occurs. Of course, this conclusion refers specifically to the problem as formulated; i. e., in contrast to the analyses carried out Fainberg *et al.* [7], Kornilov *et al.* [5] for other hybrid structures, we don't fix the frequency at which microwaves are. Naturally, in this case, the resonant frequency of interaction increases with the plasma density.
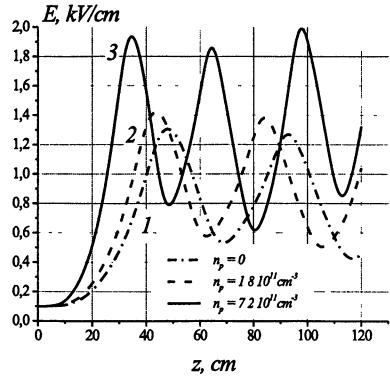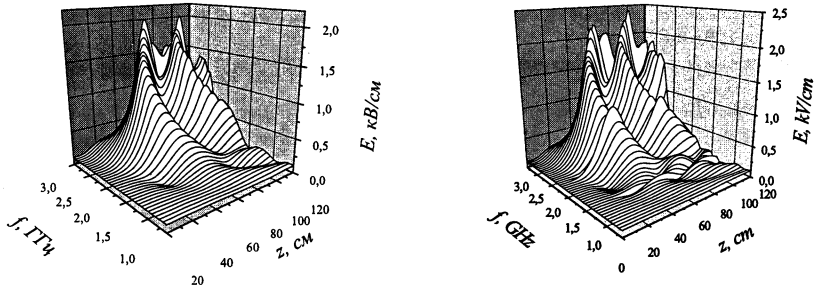
Fig. 4

The amplitude of the longitudinal electric field, calculated as a function of the length of the structure for different eigenfrequencies, is shown in Fig. 4 for a vacuum structure (at the left) and for a structure filled entirely with a plasma of density $n_p = 1.8 \cdot 10^{11} \text{cm}^{-3}$ (at the right). We can see that, over the entire main frequency passband, the optimum length of the structure changes only slightly. The results of nonlinear numerical modeling validate the predictions made in linear theory about the broadening of the frequency band over which microwaves are generated and the increase in the amplification efficiency after the transport channel of a vacuum slow-wave structure is filled with a plasma.

243

Conclusions

Investigations of the electrodynamics parameters of a coaxial plasma-filled slow-wave coaxial transmission line have shown that it holds promise for creating high-power plasma-based microwave devices.

- It is characterized by a broad frequency passband. The amplification efficiency is higher and the frequency amplification band is broader in comparison with the vacuum case.
- In the first passband the amplification coefficient depends linearly on the plasma density; the wave impedance of the slow-wave structure is only weakly dependent on frequency.
- The maximum amplitudes of the saturated microwaves are larger than those in the vacuum case; the optimum length of a plasma-filled SWCTL is significantly shorter than that of a vacuum structure.
- As functions of frequency, the saturation amplitude and the interaction efficiency changes only slightly.

References

1. *Fainberg Ya. B.* et al., Dokl. Akad Nauk Ukr. SSR, Fiz.-Mat. Tekh Nauki, № 11, 55 (1990)
2. *Carmel Y.* et al., Phys. Rev. Lett. **62**, 2389 (1989).
3. *Zav'yalov M. A.* et al., in Proceedings of the IX Symposium on High-Current Electronics, Russia, 1992, p. 132.
4. *Antonov A. N.* et al., Fiz. Plazmy **20**, 777 (1994).
5. *Kornilov E. O.* et al., Ukr. Fiz. Zh. **40**, 312 (1995).
6 *Vainshtein L. A. and Solntsev V. A.* Lectures on Microwave Electronics (Sov. Radio, Moscow, 1973).
7. *Faiberg Ya. B.* et al., Fiz. Plazmy **20**, 757 (1994).

ELECTROMAGNETIC WAVES EXCITATION
IN A SEMI-INFINITE WAVEGUIDE
BY A RELATIVISTIC ELECTRON BUNCH

V. A. Balakirev, I. N. Onishchenko, D. Yu. Sidorenko, G. V. Sotnikov

Kharkov Institute of Physics and Technology, Kharkov, Ukraine

The problem of electromagnetic field excitation in a dielectric-filled metal cylindrical resonator with a hole for a moving bunch of relativistic electrons is considered. The expression for the excited longitudinal electric field is represented. The influence of the boundary at the entrance of the resonator on the field topography of the excited wave is investigated. It is demonstrated that the trailing edge of the excited intense field appears. It is found that due to the presence of the hole for the bunch the field precursor arises, which moves in front of the bunch with the velocity equal to the velocity of light in vacuum.

When a charged bunch moves in a slow-wave medium with a speed, exceeding the speed of propagation of electromagnetic field in this medium, the Cherenkov radiation arises [1]. As this radiation stays behind the particle, it is called "the wake field". If one takes a waveguide filled with dielectric and injects a dense bunch of relativistic electrons along its axis, the intensity of the excited wake field can be high enough for acceleration of charged particles [2, 3] or radiation sources [4].

Usually the simplest model of an infinite waveguide is used for theoretical description of a wake field in a dielectric waveguide [1, 5]. As a real slow-wave structure has finite length, it is necessary to take into account the influence of the longitudinal boundaries of the system.

In an experiment the situation is possible when the entrance of the slow-wave structure is closed by the metal wire mesh, which is transparent for the injected electrons, and the exit is connected to the matched load, which considerably decreases the reflection from the exit. A semi-infinite waveguide is a good approximation for the description of such device. The problem of electromagnetic field excitation during the injection of a charged bunch into a semi-infinite ($z > 0$) waveguide with continuous dielectric filling was solved in [6, 7]. For theoretical description of field excitation in a semi-infinite dielectric waveguide with a vacuum channel by a relativistic electron bunch we used the method, which is different from the one we used in [6, 7].

Consider the resonator, which is a piece of a cylindrical dielectric waveguide of radius b with an external metal jacket and a vacuum axial channel of radius a. The ends of the resonator are closed by metal walls, which are transparent for charged particles. The length of the resonator is L_{sys}. The wake field excitation in the infinite waveguide with such radial structure was considered in [5]. The excitation of the field in the resonator does not differ from that in the semi-infinite waveguide until the reflection from the exit of the resonator takes place

245

or until the charged bunch leaves the resonator. Let the thin annular charged bunch with radius r_b and charge q be injected into the resonator through the entrance $z = 0$ at the moment of time t_b. Assume that the bunch moves uniformly with the velocity v_b. The charge density of such bunch is

$$\rho = \frac{q}{2\pi r_b v_b}\delta(r - r_b)\delta(t - t_b - \frac{z}{v_b}). \tag{1}$$

The longitudinal boundedness of the system allowed us to expand the field components and the current in the Fourier series over the longitudinal wavenumber with taking into account the boundary conditions at the ends of the resonator. After this we applied the expansion of the transversal field components over the eigen radial functions of the waveguide and the Fourier transformations over the time-frequency in order to obtain the radial electric field E_r and the azimuthal magnetic field H_φ. As the eigen functions for the longitudinal electric field E_z are nonorthogonal, we substituted the obtained Fourier transformations for E_r and H_φ to the corresponding Fourier-transformed Maxwell equation and used the boundary conditions at the vacuum-dielectric interface in order to calculate E_z. We omit the cumbersome but simple calculations and below we represent the final expression for the longitudinal electric field excited by thin annular charged bunch (1):

$$E_z^v(r,z,t,r_b,t_b) = -\frac{2qv_b}{L_{sys}}\sum_{m=1}^{\infty}\left\{\frac{I_0(\kappa_{v,m0}r_b)I_0(\kappa_{v,m0}r)}{\omega_{m0}N(\omega_{m0},k_0)}\sin[\omega_{m0}(t-t_b)] \; + \right.$$

$$+\sum_{n=1}^{\infty}\cos(k_n z)\frac{\omega_{mn}^2 I_0(\kappa_{v,mn}r_b)}{\kappa_{v,mn}^2 N(\omega_{mn},k_n)}\left(\frac{2I_0(\kappa_{v,mn}r)}{\omega_{mn}^2-\omega_n^2}\times\right.$$

$$\times\left\{\kappa_{v,mn}^2\frac{\sin[\omega_{mn}(t-t_b)]}{\omega_{mn}}-\left(k_n^2-\frac{\omega_n^2}{c^2}\right)\frac{\sin[\omega_n(t-t_b)]}{\omega_n}\right\} + \tag{2}$$

$$\left.\left.+\frac{2I_0(\kappa_{v,mn}a)k_n^2(\varepsilon-1)}{c^2\kappa_{d,mn}^2}\cdot\frac{\sin[\omega_n(t-t_b)]}{\omega_n}\right)\right\}\times\vartheta(t-t_b),$$

$$N(\omega,k_z) = \frac{\omega^2 a^2}{2c^2\kappa_v^2\kappa_d^2}I_1^2(\kappa_v a)\times$$

$$\times\left[\frac{4}{\pi^2 a^2 A_1^2(\kappa_d a)}-\left(\varepsilon^2\kappa_v^2+\kappa_d^2\right)\frac{I_0^2(\kappa_v a)}{I_1^2(\kappa_v a)}+\frac{2}{\kappa_v a}\left(\varepsilon\kappa_v^2+\kappa_d^2\right)\frac{I_0(\kappa_v a)}{I_1(\kappa_v a)}\right],$$

$k_n = \pi n / L_{sys}$, $\omega_n = k_n v_b$, $n = 0, 1, 2, \ldots$; $D(\omega_{mn}, k_n) = 0$ is the dispersion equation of the waveguide; $\kappa_{d,mn}^2 = \varepsilon \omega_{mn}^2 / c^2 - k_n^2$, $\kappa_{v,mn}^2 = k_n^2 - \omega_{mn}^2 / c^2$, $A_j(x) = N_0(\kappa_d b) J_j(x) - J_0(\kappa_d b) N_j(x)$, N_j, J_j, I_j are the cylindrical functions of j–th order, $j = 0, 1$. In addition, here we introduce the step function $\vartheta(x)$: $\vartheta(x) = 1$ if $x > 0$ and $\vartheta(x) = 0$ if $x \le 0$. We represent the reduced form of the expression (2), which is valid until the moment $t_{out} = t_b + L_{sys} / v_b$ when the bunch will leave the resonator.

For the results of numerical calculations presented below we chose the following parameters of the resonator: $L_{sys} = 100$ cm, $b = 4$ cm, $a = 1$ cm, $\varepsilon = 2$; and of the bunch with rectangular profile of charge distribution: charge 1 nc, length 2 cm, radius 0.5 cm, $v_b = 0.95c$. As the purpose of this work is the investigation of the influence of the entrance boundary, below we considered the moment of time $t < t_b + L_{sys} / c < t_{out}$, hence, the excited field does not reach the exit.
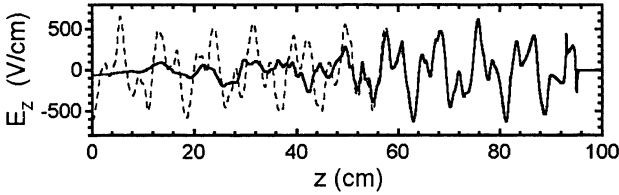
Fig. 1. Field pattern at the waveguide's axis. Continuous line – in the semi-infinite, and dashed line – in the infinite waveguide. $t = 25b / c$.

Taking the entrance boundary into account resulted in the following: in the dielectric waveguide with the hole for the bunch the trailing edge of the intense wake field region appeared, as it was in the waveguide with continuous dielectric filling [6]. This edge (or wave-front) follows the bunch with the velocity smaller than the bunch velocity. As one can see in Fig. 1, there are intense oscillations in the region 60 cm $< z <$ 93 cm behind the bunch (bunch's position is 93 cm $< z <$ 95 cm). One can compare the field in the semi-infinite waveguide with the field in the corresponding piece of the infinite waveguide, which is depicted by the dashed line in Fig. 1. In contrast with the semi-infinite case, there is the intense field in the whole region behind the bunch. Note the coincidence of the field patterns in the region 60 cm $< z <$ 93 cm. The field structure in this region is determined by the multiple reflections of the Cherenkov cone from the metal sidewalls of the waveguide and from the vacuum-dielectric boundary, and by the characteristic "sagging" of the field into the vacuum channel in the reflection points (see Fig. 2, b). The region z $<$ 50 cm in Fig. 1, which borders with the entrance, contains the field of relatively small amplitude. The field topography in

this region, which is represented in Fig. 2, *a*, is qualitatively different from the cone-shaped field structure in the region behind the bunch. It is similar to the structure of transition radiation in the continuous dielectric waveguide [7].
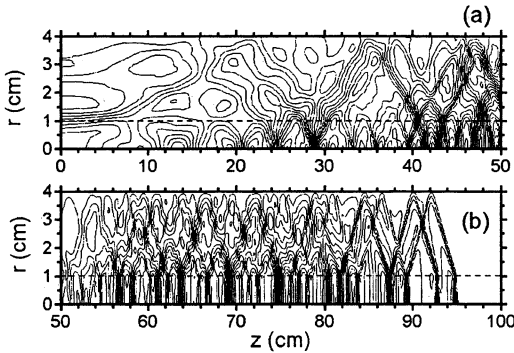
Fig. 2. The topography of the longitudinal electric field: a) the level lines are drawn in the range from −400 V/cm to 400 V/cm with the step of 16 V/cm; b) the level lines are drawn in the range from −800 V/cm to 800 V/cm with the step of 64 V/cm. $t = 25\,b/c$.

In the region 50 cm < z < 60 cm the field amplitude decreases considerably. This is the region of the trailing wave-front. The borders of this region correspond to the value of the wave-front propagation velocity within the range from $0.5c$ to $0.6c$. Note that the group velocities of the first 50 resonance radial modes are within the range from $0.53c$ to $0.55c$. Therefore, in the case of a thin vacuum channel the trailing edge is clearly distinguished and the velocity of its propagation is equal to the group velocity of the resonance wave.

There is one qualitative difference between the semi-infinite waveguides with continuous dielectric filling and with a vacuum channel in the dielectric. In the latter case the field profile in the relativistic bunch region is similar to the profile of the Coulomb field in the motionless or slow bunch. As for the longitudinal field, it has the characteristic peaks of different polarity, which can be clearly seen in Fig. 1 in the region 92 cm < z < 96 cm. At the same time the field profile in the bunch region in the continuous dielectric will have no peaks if the Cherenkov resonance condition is satisfied. This is connected with the fact that under this condition the velocity of electromagnetic field propagation in the continuous dielectric waveguide is smaller than the velocity of the driving bunch. The presence of the vacuum region changes the dispersion picture in such a way that the oscillations appear, which have the group velocity close or equal to the velocity of light in vacuum. The part of the electromagnetic field, which is formed by such eigen waves, outstrips the driving charged particles and forms the profile of the Coulomb field in the bunch region.

The careful investigation of the region in front of the bunch 96 cm < z < < 100 cm showed that there is the precursor of the excited field in this region (see Fig. 3). The amplitude of this precursor is much smaller than that of the Cherenkov field. That in the dielectric the cone-shaped structure is formed, like from the relativistic charged particle, is the characteristic peculiarity of the field

Fig. 3. The precursor: *a* – the level lines are drawn in the range from –0.4 V/cm to 0.4 V/cm with the step of 0.04 V/cm; *b* – the corresponding field profile at the resonator's axis. $t = 25\,b\,/\,c$.
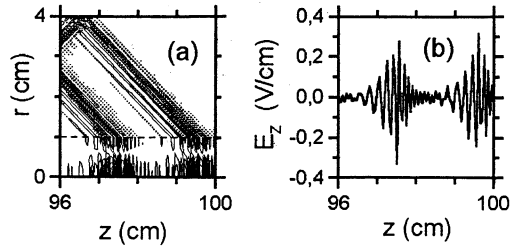
topography in the precursor (see Fig. 3, *a*). We would like to mention that in order to display the field structure in the precursor we had to account 200 members over *m* (radial modes) and 2000 members over *n* (longitudinal wavenumbers) in Eq. (3). At the same time in order to calculate the field pattern, which is represented in Fig. 1, it was enough to take into account only 100 members over *m* and 1000 members over *n*.

Conclusions

Excitation of the wake field by a relativistic electron bunch in a semi-infinite dielectric waveguide with vacuum channel is similar to that in a semi-infinite waveguide with continuous dielectric filling if the radius of vacuum channel is much smaller than the spatial period of excited oscillations.

In this case the bunch leaves behind itself the intense Cherenkov oscillations. The other boundary of the region of the intense field – the trailing wave-front – follows the bunch with the velocity equal to the group velocity of the resonance wave. The amplitude of the transition radiation field is much smaller than the amplitude of the Cherenkov wave.

Contrary to the continuous dielectric waveguide, in the dielectric waveguide with vacuum channel the maximal velocity of propagation of electromagnetic field is equal to the velocity of light in vacuum. That is why the field profile in the region of the relativistic bunch is similar to the Coulomb profile of the motionless bunch. Moreover, even in a thin vacuum channel one can find a weak precursor of the field in front of the driving relativistic bunch.

References

1. *Bolotovskij B. M.*, Usp. Fiz. Nauk, 1961, **75**, 295.
2. *Gai W., Schoessow P., Cole B.* et al., Phys. Rev. Lett., 1988, **61**, 2756.
3. *Onishchenko I. N., Kiseljov V. A., Berezin A. K.* et al., in Proceedings of the Particle Accelerator Conference, New York, 1995 (IEEE, New York, 1995), p. 782.
4. *Zhang T. B., Marshall T. C., Hirshfield J. L.*, IEEE Trans. Plasma Sci., 1998, **26**, 787.
5. *Park S. Y. and Hirshfield J. L.*, Phys. Rev. E, 2000, **62**, 1266.
6. *Balakirev V. A., Onishchenko I. N., Sidorenko D. Yu., Sotnikov G. V.*, Zh. Exp. Teor. Fiz., 2001, **120**, 41.
7. *Balakirev V. A , Onishchenko I. N., Sidorenko D. Yu., Sotnikov G. V.*, Zh. Tekh. Fiz., 2002, **72**, 88.

PROPAGATION AND POST-ACCELERATION OF AN ELECTRON BEAM EXTRACTED FROM A PLASMA IN A PSEUDOSPARK DISCHARGE

A. W. Cross, H. Yin, A. D. R. Phelps, D. Zhu, W. He and K. Ronald

Dept. of Physics, University of Strathclyde, Glasgow G4 0NG, UK

Propagation and post-acceleration of an electron beam extracted from plasma in a three-gap pseudospark discharge were studied in recent experiments. The pseudospark-sourced electron beam has two phases, an initial 22 kv, 50 A hollow cathode phase (HCP) beam of brightness 10^{9-10} Am^{-2} rad^{-2} followed by a 200 V, 200 A conductive phase (CP) beam of brightness 10^{11-12} Am^{-2}rad^{-2}. The aim of these experiments was to post accelerate the lower voltage, higher current CP beam using an acceleration unit driven by a 40 kV, 125 ns voltage pulse generated by a cable Blumlein. The experiments were realized by attaching an acceleration unit to the downstream side of the anode of the discharge chamber. Both the pseudospark discharge and the cable Blumlein were triggered to ensure time correlation between initiation of the pseudospark discharge and post acceleration of the beam.

Introduction

Pseudospark discharge [1–3] experiments to generate a low temperature plasma for use as a copious source of electrons have been carried out at the University of Strathclyde [4, 5]. The plasma can be regarded as a low work function surface that facilitates electron extraction. Electron beam pulses of duration of tens of ns, current density ($>10^8$ Am^{-2}), brightness of up to 10^{12} Am^{-2}rad^{-2} and emittance of tens of mm mrad were measured from a pseudospark discharge. This beam has a higher combined current density and brightness compared to electron beams formed from any other known type of electron source. A pseudospark-based, high-intensity, high-brightness electron beam source was applied for the first time in a free electron maser device at the University of Strathclyde [6, 7].

The experiment reported here was focused on the new study of the propagation and post acceleration of the beam from a three-gap pseudospark discharge chamber. A beam from the pseudospark discharge was transported in a plasma induced ion background and simultaneously accelerated by an accelerating potential. This makes it possible to provide a higher energy electron beam with lower energy spread for future application in a high power free electron maser. This article will present some results from this experiment.

Experimental setup

The experimental setup for the study of the propagation and the post-acceleration of the pseudospark-sourced beam is shown in Fig. 1. The electron

beam was extracted from a three-gap pseudospark discharge chamber. The discharge chamber consisted of a planar anode, a planar cathode with a cylindrical hollow cavity, two intermediate electrodes of 3.25 mm thickness and three Perspex insulators of 3.25 mm thickness. The cylindrical hollow cathode cavity was made of stainless steel having outer and inner diameters of 63 mm and 50 mm respectively, and length 50 mm, in which a trigger electrode made of coaxial cable was inserted. Both the anode and cathode had an on-axis hole of 3 mm diameter. The post-acceleration gap was located 30 mm away from the anode of the pseudospark discharge chamber. The single Perspex disc of inner diameter 5 mm, outer diameter 300 mm and 26 mm thickness was used for acceleration gap insulation. It was made with a recess to achieve a 5 mm acceleration gap separation.
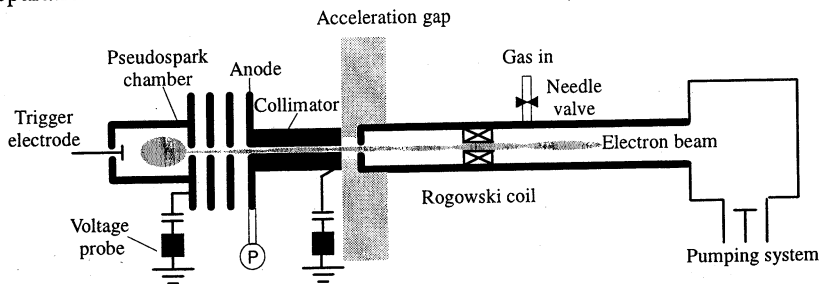
Fig. 1. Schematic diagram for the post-acceleration experiments
of the pseudospark electron beam

A Rogowski coil was located 120 mm downstream of the post-acceleration gap to measure the beam current. The gas inlet was located 30 mm away from the Rogowski coil and was controlled by a very fine mechanical needle valve. The background vacuum requirements were obtained using a two stage pumping system in the form of a rotary pump and an oil-diffusion pump. Air was used throughout the experiments. The pressure was measured by a Baratron type vacuum gauge together with a display meter.

The pseudospark discharge was powered by a dc power supply. The hollow cathode was connected through a 30 MΩ charging resistor to a negative voltage source (–30 kV, 1 mA DC power supply) and the charging voltage was measured by a capacitive voltage probe. The external energy storage capacitance 600 pF was achieved by using three chains of five 1000 pF, 15 kV resin-dipped ceramic capacitors in series across the cathode and anode of the pseudospark discharge chamber. The acceleration unit was driven by a 40 kV, 125 ns voltage pulse produced by a cable Blumlein and the acceleration voltage was measured by another capacitive voltage probe. The cable Blumlein was made by winding in parallel several 50 Ω coaxial cables of 25 m lengths around a spindle to form a Blumlein type of pulse generator. The internal impedance of the cable Blumlein was reduced by increasing the number of the cables used. The pseudospark discharge

251

and the cable Blumlein were triggered by two sets of trigger signals controlled by two delay units and one trigger source. Both trigger signals for the pseudospark and the cable Blumlein were 15 kV pulses. Careful adjustment of the delay units ensured the beam acceleration voltage was applied at the right time.

Experimental results

The propagation of the electron beam from a three-gap pseudospark discharge chamber was studied as a function of the length of a collimator of 3.5 mm internal diameter. In this experiment, the post-acceleration unit was initially disconnected, and only the 3-gap pseudospark discharge chamber was used. The chamber was first evacuated through a small hole in the pseudospark anode by the pumping system typically down to a pressure of 3 mTorr. The desired gas pressure for the pseudospark was reached and balanced by adjusting a very fine mechanical needle valve. The high voltage applied across the pseudospark chamber was then increased slowly until breakdown occurred. To achieve a high current electron beam, it was essential to match the applied discharge voltage and gas pressure in the chamber so that the discharge operated in the pseudospark regime. The beam was measured by a Rogowski coil positioned 150 mm away from the anode of the pseudospark chamber. Rogowski coil beam current measurements 150 mm downstream from the anode showed that with no magnetic guiding field, 70% and 50% of the beam propagated through 30 mm and 60 mm long collimators respectively, as shown in Table. A magnetic field free collimator technique enabled a beam brightness to be measured from a 3-gap pseudospark discharge. The principle of this method is described in reference [8]. At a discharge voltage of 20 kV the measured normalized brightness of CP beam was found to be in the order of $10^{11}Am^{-2}rad^{-2}$.

Propagation of the PS beam through a collimator

Collimator length, mm	Beam measured at 150 mm away from the PS anode	
	Beam current, A	Percentage of beam transported, %
No collimator	240 ± 35	...
30	168 ± 20	70 ± 2
60	118 ± 10	49 ± 3
90	36 ± 5	15 ± 0.1

In the post-acceleration experiment a 30 mm long collimator of 3.5 mm internal diameter was used after the anode of the pseudospark discharge chamber and the acceleration unit was located immediately after the collimator to achieve a gas pressure gradient and to optimize beam current. The acceleration unit was driven by a 40 kV, 125 ns voltage pulse produced by a cable Blumlein. The beam acceleration experiments showed that careful adjustment of the trigger system could ensure successful synchronization between the beam propagation and the application of the acceleration voltage. A 40 kV, 100 A electron beam pulse was measured at a distance of 120 mm from the acceleration gap without a magnetic

guiding field, as shown in Fig. 2. However in Fig. 2 some beam loading effect is evident where it can be seen that as the beam current increases the post acceleration voltage decreases and the flat top of the voltage signal becomes shorter. During the experiments, the beam loading effect was mitigated by reducing the internal impedance of the cable pulser from 50 Ω to 14 Ω. It is possible to further reduce the beam loading effect by continuing to decrease the internal impedance of the cable Blumlein or by using an alternative lower impedance pulse forming line.
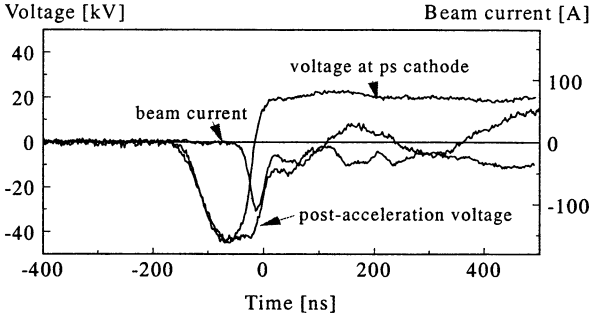
Fig. 2. Typical record of the time-correlated pseudospark discharge voltage, beam current and the acceleration voltage pulse.

Simulations

Beam propagation across the acceleration gap and further along the beam channel was simulated by an electromagnetic particle-in-cell (PIC) code.

The simulations show that a 200 V, 200 A beam in a pseudospark CP phase will propagate across a 40 kV post-acceleration gap of 5 mm separation in a ion background of certain densities. About 10% and 70% of the beam would propagate across the gap when the ion densities are $1 \cdot 10^{12}$ cm^{-3} and $6 \cdot 10^{12}$ cm^{-3}, respectively. Figure 3 shows a simulated beam profile and current variation during its propa-
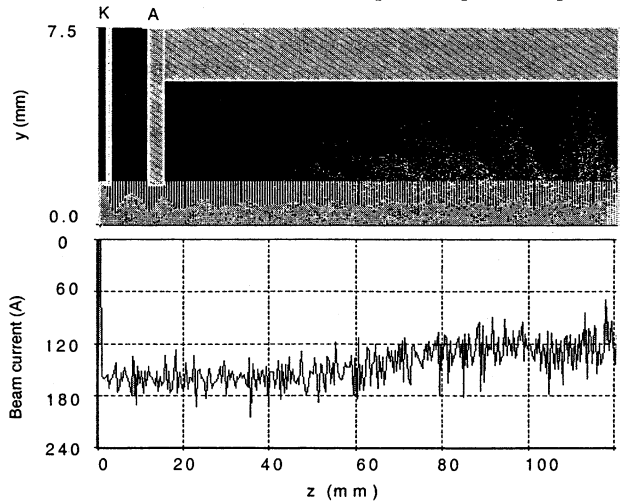
Fig. 3. Simulated beam profile and current variation during propagation across the acceleration gap and further along the beam channel with an ion background of density $6 \cdot 10^{12}$ cm^{-3} (K, cathode; A, anode; z, beam channel axis; vertical dense lines, plasma zone; and cloud, electrons).

253

gation across the acceleration gap in an ion background of density $6 \cdot 10^{12}$ cm^{-3}. It can be seen that for an initial 200 A beam propagating across the acceleration gap and further along the drift tube, a 130 A beam can be obtained at a distance 120 mm away from the acceleration gap. In the experiment, a 100 A beam was measured at a distance about 120 mm away from the acceleration gap. The simulation also shows that with ion background, the shapes of both the cathode and anode of the acceleration gap have little effect on beam propagation.

Discussion and conclusions

The beam in the pseudospark conductive phase was successfully accelerated from about 200 V to more than 40 kV. A 100 A, 40 kV electron beam pulse was measured at a distance of 120 mm from the acceleration gap without a magnetic guiding field. Comparing this with the simulation implies that a favourable ion background exists along the beam channel and the acceleration gap. The ion background can be formed from the background gas ionization by the initial high energy HCP beam during the pseudospark discharge, which also expels electrons in the ionized gas media. Further experiments are planned to investigate this high current electron beam source with respect to triggering accuracy while operating at high pulse repetition frequencies as well as further reduction of the beam loading effect in the post acceleration unit. The ultimate goal of the research is to produce electron beam pulses, which offer very favourable comparison of their brightness with the very brightest available photocathode electron sources and have higher current densities, but at a small fraction of the cost of these systems.

References

1. *Christiansen J. and Schultheiss C.*, Z. Phys., 1979, **A290**, 35.
2. *Gunderson M. A. and Schaefer G.*, Physics and Applications of Pseudosparks. NATO ASI Ser. B, New York: Plenum, 1990.
3. *Frank K. and Christiansen J.*, IEEE Trans. Plasma Sci., 1989, **17**, 748.
4. *Yin H., He W., Cross A. W., Phelps A. D. R., and Ronald K.*, J. Appl. Phys., 2001, **90**, 3212.
5. *Yin H., Phelps A. D. R., He W., Robb G. R. M., Ronald K., Aitken P., McNeil B. W. J., Cross A. W., and Whyte C. G.*, Nucl. Instr. And Meth. in Phys. Res. A, 1998, **407**, 175.
6. *Yin H., He W., Robb G. R. M., Phelps A. D. R., Ronald K., and Cross A. W.*, Phys. Rev. Spec. Topics - Accelerators and Beams, 1999, **2**, 020701(1–5).
7. *Yin H., Robb G. R. M., He W., Phelps A. D. R., Cross A. W., and Ronald K.*, Phys. Plasmas, 2000, **7**, 5195.
8. *Yin H., Cross A. W., Phelps A. D. R., Zhu D., He W., and Ronald K.*, J. Appl. Phys., 2002, **91**, 5419.

STUDY OF KA-BAND COMPONENTS FOR A FUTURE HIGH-GRADIENT ACCELERATOR

S. V. Kuzikov, G. G. Denisov, M. I. Petelin, A. L. Vikharev,
A. A. Bogdashov, A. V. Chirkov, Yu. Yu. Danilov, J. L. Hirshfield[2],
Yu. I. Koshurinov[1], V. I. Malygin, V. G. Paveliev[1], M. Yu. Shmelyov

Institute of Applied Physics, Nizhny Novgorod, 603950, Russia
[1]Nizhny Novgorod State University, Russia
[2]Omega-P, Inc., New Haven, CT 06511, USA

This paper presents a concept of the quasi-optical RF system for future Ka-band electron-positron linear collider. According to this concept two RF feeding systems are considered: the Delay Line Distribution System (DLDS) and the pulse compressor based on a three-mirror traveling-wave resonator. The DLDS is based on oversized waveguides. In such waveguides the so-called image multiplication phenomena are used for power launching, extracting, combining, and splitting of waves. Recent low power tests of mode launchers and other DLDS components are discussed.

The 34 GHz pulse compressor, based on three-mirror resonator, is considered. The results of testing the compressor prototype at a low power level under different modulation methods and different widths of the input pulse are discussed.

Introduction

The known scaling of accelerating gradient with frequency, which is approximately linear, provides strong motivation for developing high-frequency accelerating structures and associated components. The most compelling reason for designing, building and evaluating Ka-band components is to establish this anticipated scaling with solid laboratory evidence; and, of course, to demonstrate the high acceleration gradient.

The DLDS concept is considered as one of perspective solutions for feeding of high-gradient accelerators at 11.424 GHz [1–2]. According to the projected schemes the DLDS is based on relatively oversized delay lines operated with one or several modes and mode launchers completely or partially constructed on the base of single-mode waveguides. Scaling of the mentioned projects to Ka-band seems to be not acceptable because of higher Ohmic attenuation as well as bigger RF power density, which causes a threat of breakdown. More natural way is to use pure quasi-optical solutions in the design of each DLDS component.

Passive pulse compressors, which introduce an alternative method of pulse compression, are based on resonators or delay lines that store the microwave energy [3–4]. Compression is achieved as a result of the transition process, which arises when the resonator is excited with a microwave pulse having an appropriate phase modulation. For higher frequencies, for example, 34 GHz the pulse compressor, based on a three-mirror traveling-wave resonator, seems attractive. It allows operating with moderate microwave fields in the storing

resonator providing an acceptable level of Ohmic losses and acceptable selectivity in terms of spurious oscillations.

Mode launchers

A key component of any DLDS project is a mode launcher, which allows feeding consequently different acceleration sections by means of proper setting the phases of RF pulses from different amplifiers. In the scheme, shown in Fig. 1, the mode launcher has four input channels and the same number of output channels providing four times power gaining. The delay lines behind the mode launcher are assumed to be oversized circular cross-section waveguides operated with axis-symmetrical TE_{01} mode.
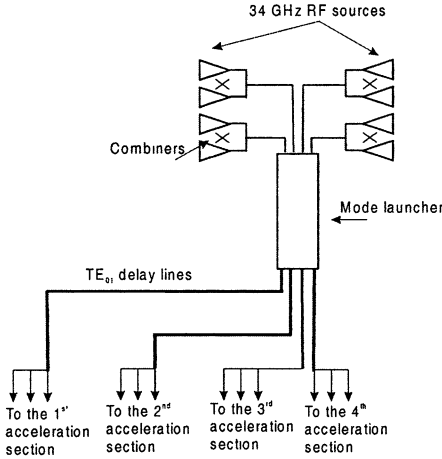
Fig. 1. Scheme of 34 GHz DLDS

We considered two possible versions of the mode launcher both based on image multiplication phenomena in an oversized waveguide [5–6]. In the first version (Fig. 2) the mode launcher is shaped of a smooth oversized (waveguide size is a) rectangular waveguide, where image multiplication occurs at one coordinate only. Four TE_{01} modes at the input of rectangular waveguide are combined into one of four output channels. The position of the resulted channel depends on the mutual phases at the input. The required length of the waveguide equals to a^2/λ.

The mode launcher was calculated using Kirhgof's approach, and results were published in paper [5]. According to these results the wider waveguide the higher efficiency of the launcher. For example, at 34 GHz, width $a = 120$ mm, and length $L = 1600$ mm provide 99% efficiency of the power summarizing.

Preliminary tests were performed with the launcher prototype scaled to 4-times higher frequency in order to minimize launcher sizes and simplify its fabrication. This resulted in higher Ohmic losses (about two times) and more critical alignment of parts. The launcher was fed by one wave and the output

field structure and reflection coefficient from specially shaped mirrors at the launcher output were measured.
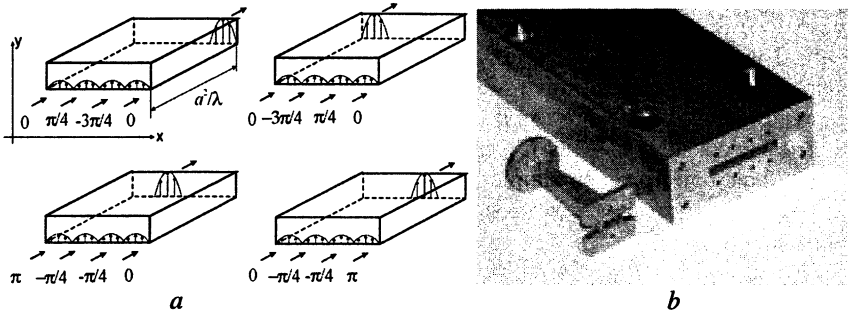
Fig. 2. Mode launcher based on rectangular waveguide:
a – scheme, *b* – photograph of the prototype
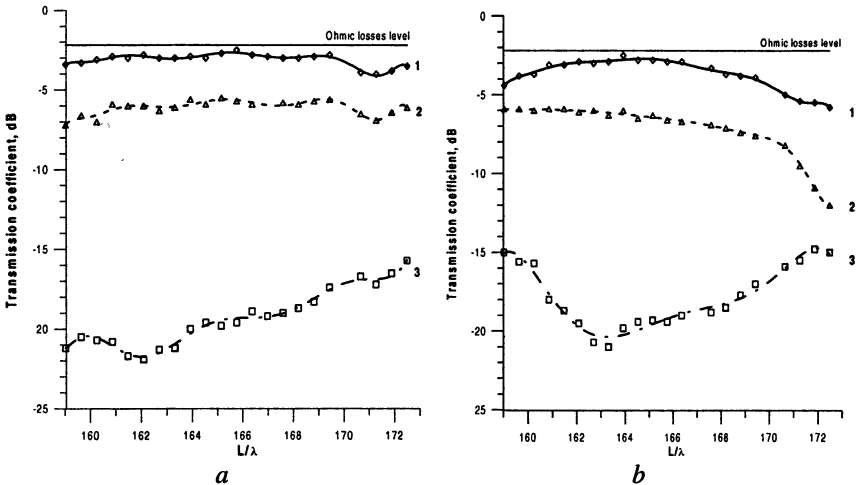
Fig. 3. Measurements of mode launcher efficiency when incident wave is launched into a channel near the wall (*a*), the wave is launched into a channel near the center of waveguide (*b*)

The results of the measurements, carried out for two regimes, are shown in Fig. 3, where reflection is plotted as a function of launcher length normalized on a wavelength. The first used mirror provided phases of four reflected waves at the output end so, that the reflected waves were combined again in the input waveguide where the initial wave was excited. The curves marked by *1* in both Fig. 3, *a* and *b* show the reflection in this case. This reflection was actually the squared efficiency of the launcher, because all other channels were opened and

257

the scattered radiation was free to go away. The measured difference between the reflection and Ohmic losses level is rather small: 0.5 dB.

The curves marked by *2* correspond just to the flat mirror reflectors. In such a case according to image multiplication effect the reflected waves formed two identical waves at input cross-section. One of them came back into the feeding channel, but the second wave was radiated away. So, –3 dB extra losses, measured in this scheme, are agreed well with a theory.

The curves marked with *3* correspond to the case when reflected radiation was combined all power in another channel (not in the feeding channel). In this case we could measure the scattering radiation only. Its level appeared about – 15–20 dB.

The second version of a mode launcher is based on image multiplication in square cross-section waveguide with the impedance corrugation of walls (Fig. 4). The infinite impedance allows combining TE_{01} modes of a circular waveguide, and thus, any mode converters, in order to match such mode launcher with TE_{01} delay lines, are not needed. The length of the launcher equals $2a^2/\lambda$.

a   *b*
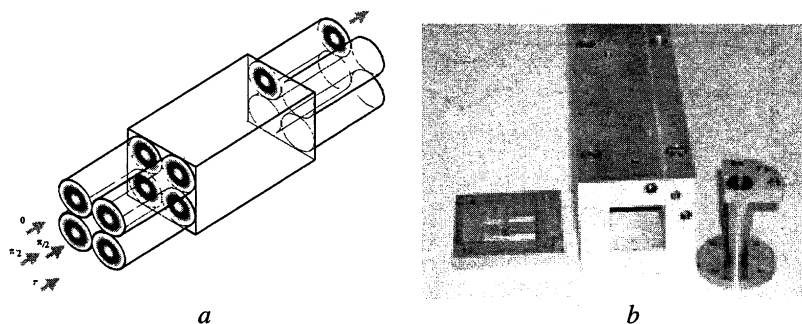
Fig. 4. Mode launcher based on square cross-section waveguide:
a – scheme, *b* – photograph of the tested prototype

For tests we used four-times higher frequency and selected sizes of mode launcher, which provided 93% efficiency. The scheme of efficiency measurements coincides with the scheme chosen for the rectangular mode launcher described above. with mode purity at operating frequency estimated as 96–97%. In our tests we found out that the efficiency of such a mode launcher is very sensible to the accuracy of manufacturing. In particular, difference in sizes of the walls results in an essential drop of the efficiency in comparison with the ideal case. That was the main reason, why we measured rather high power losses (Fig. 5). Nevertheless, taking into account the actual accuracy of fabrication and purity of the incident TE_{01} mode, one concludes that the efficiency of such a component at 34 GHz is able to be high enough.
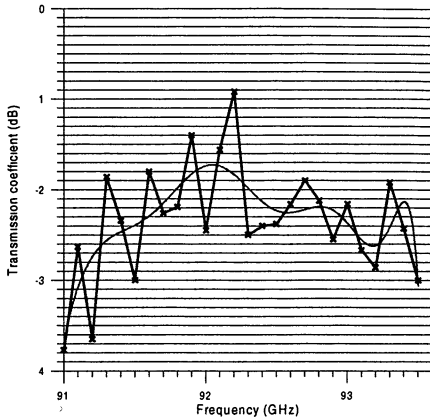
RF components for DLDS

The DLDS system, contained long TE_{01} delay lines, requires a lot of components such as combiner-splitters, windows, miter bends, RF loads and couplers, tapers, and TE_{01} mode converters.

Combiner-splitter is used for combining outputs of RF sources into one waveguide. Comparing different schemes we found that the simplest and most efficient scheme is the wave combining in oversized rectangular waveguide like in the second version of the proposed mode launcher. Dimensions of such a combiner are moderate, and the scheme of the combiner is extremely simple. The opposite dividing scheme can be used for power distribution over different acceleration sections.

Miter bends are used to provide a required trajectory of transmission lines. The component is a very critical point for TE_{01} circular cross-section transmission lines. To make diffraction losses in the miter bend lower a mode combination is prepared in the place of the bend [7]. This mode mixture ($75\%TE_{01}$ + $24\%TE_{02}$ + $1\%TE_{03}$) provides a local decrease of the fields near edges, which inevitably exist in any miter bend. According to this idea the improved miter bend consists of two symmetric mode converters and a plane mirror (Fig. 6, *a*).

Such an improved miter bend was designed, manufactured for the required 34 GHz frequency, and tested at low power level using a special reflection mirror. This mirror provided entire backward reflection of proper TE_{01} mode and small reflection for any other modes because of diffraction. The results of such measurements are shown in Fig. 6, *b*, where the dependence on frequency for the reflection coefficient is plotted. This figure demonstrates that efficiency keeps level of 99% at approximately 3% frequency band.To monitor and to measure the power of microwave such components as bi-directional couplers and vacuum

calorimeters were developed. The components are based on WR28-type waveguide. A spiral stainless steel waveguide channel with rounded surfaces is used for absorption of the waves. The components are intended to operate with high-power microwave and high-vacuum conditions.
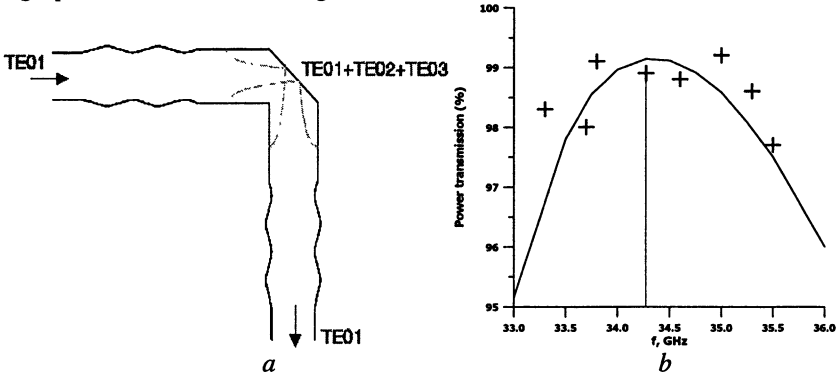
Fig 6. Quasi-optical miter bend: *a* – scheme, *b* - measured efficiency

Three-mirror resonator as a passive compressor

The passive compressor consists of a high-Q-factor three-mirror resonator and an excitation system (Fig. 7).
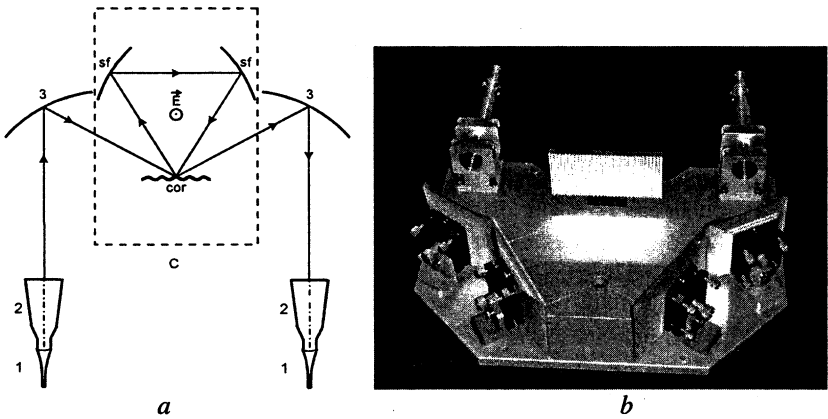
Fig. 7. 34 GHz pulse compressor: *a* – schematic diagram of the pulse compressor with the excitation system (cor – planar corrugated mirror, sf – focusing mirrors, *1* – rectangular to circular cross-section transducer, *2* – horn converting H_{11} mode into Gaussian wavebeam, *3* – feeding mirrors), *b* – photograph

The resonator consists of two focusing mirrors that provide a high-Q-factor operating eigenmode of the running-wave type, and the third mirror with fine

corrugation on its surface. The corrugation provides coupling of the eigen mode in the resonator with the wave beam formed by the excitation system. The coupling with the resonator is provided by using the -1st diffraction maximum of the grating. The corrugation amplitude is selected to provide the required Q-factor. The resonator does not require an additional -3dB coupler, since it is ring-shaped and the reflection from the resonator is negligibly small.

In order to have the highest resistance to RF breakdown, the polarization of the electric field in the resonator is chosen such as to make the component normal to the surfaces of all the mirrors small and tending to zero within the approximation of the infinite mirror apertures.

The excitation system includes a horn that converts the main mode of the standard rectangular waveguide into a Gaussian beam, and a pair of matching mirrors. These mirrors provide a distribution of the field, which is close to the transverse distribution of the field of the operating mode (the lowest TEM_{00n} mode) over the corrugated mirror of the resonator. The radiation at the compressor output is focused again into the receiving horn.

Let us consider a linear frequency modulation of the input pulse, as compared to the step-wise modulation used in SLED and SLED-II, in order to reduce the bandwidth requirement for the high-power amplifier that generates the input signal to the compressor.

Let us determine compression efficiency η as the ratio of the output pulse energy stored in the accelerating section to the pulse energy at the compressor input. Let us define also the pulse compression ratio s as the ratio of durations of the input T and output τ pulses. The power amplification ratio P_g is given by a multiplication of the compression ratio on the efficiency.

The results of optimization are shown in Fig. 8 where the efficiency and power amplification coefficient are plotted as functions of the compression ratio s. The optimized parameters that correspond to point A in Fig. 8 are $f_0 =$ $= 34.272$ GHz, $s = 4$, $\eta = 65.89\%$, $P_g = 2.64$.
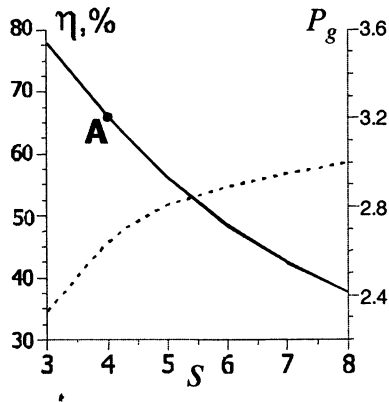
Fig. 8. Characteristics of compressor: efficiency η (solid lines) and P_g (dashed lines). The input pulse is frequency-modulated linearly.

261

Testing the compressor at a low power level

We used a high-stability ($\Delta f/f = 10^{-5} - 10^{-6}$) klystron-type pulse generator as a source of input microwave pulses. The source worked in the regime of generation of rectangular pulses $\tau = 80\text{–}120$ ns. The measured loaded Q-factor of the resonator proved to be slightly lower than the calculated value and was $Q_{ext} = 3500\text{–}3700$, which did not make it possible to achieve the maximum possible compression.

The manufactured prototype of the compressor was tested both in the scheme with step-wise frequency modulation, and that with linear frequency modulation. In the first case we used an electrically controlled phase rotator based on a p-i-n diode with its phase switching time $\tau_s \sim 1$ ns to switch the phase from 0 to 180°. At the length of the input pulse 80 ns, $s = 4$, and $P_g = 3$, efficiency of compression was 75%, which corresponds totally to efficiency of the SLED compressor at the same compression coefficient.

In order to obtain the linear frequency modulation of the microwave pulse we used the sawtooth generator. Samples of the oscillograms of the output pulses obtained in this variant of compressor operation are shown in Fig. 9.

a b
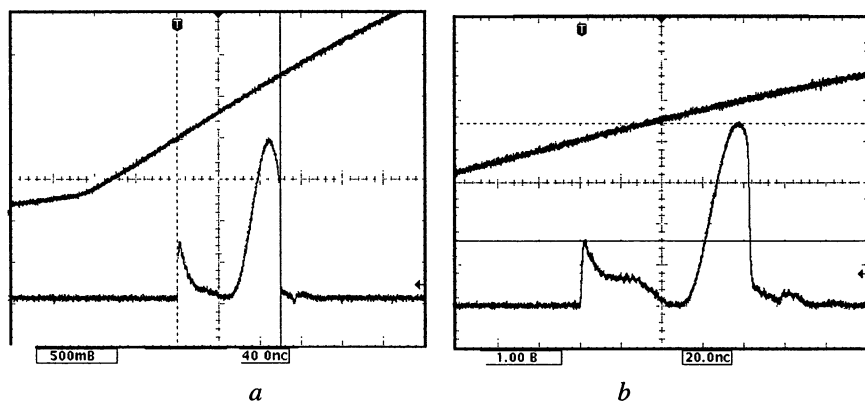
Fig. 9. Oscillograms of the output pulse in the case of linear frequency modulation:

$a - T = 100$ ns, $\Delta f_g = 39.3$ MHz, $s = 3.6$, $\eta = 65\%$, $P_g = 2.34$;
$b - T = 80$ ns, $\Delta f_g = 51$ MHz, $s = 4$, $\eta = 59\%$, $P_g = 2.36$

Experimental characteristics of compressed pulses and parameters of compressor operation are listed in Table.

Compression with linear frequency modulation: experimental data

T, ns	Δf_g, MHz	S	η, %	P_g
120	19.4	3	58	1.74
120	28.6	3	71	2.13
110	33.2	3.5	62	2.17
100	39.3	3.6	65	2.34
90	45.4	3.7	65	2.41
80	51.0	4	59	2.36

Summary

The main components of Ka-band transmission line for future accelerator system were designed, fabricated and tested in low power experiments. The test results agree well with the design parameters. Therefore, Ka-band DLDS seems to be feasible.

A passive quasi-optical compressor with linear frequency modulation on the bases of the three-mirror resonator was demonstrated. The results of the studies show that the developed version provides good compression parameters.

Therefore, the competition between a DLDS and pulse compressor will be continued at high power experiments planned for 2002-2003 with 34 GHz magnicon.

References

1. *Mizuno H.* et al., A new RF power distribution system for X band linac equivalent to an RF pulse compression scheme of factor 2^N, 17th International Linac Conference (Tsukuba, Japan, 1994).

2. *Tantawi S.* Active and Passive Multimoded Components for High Power RF Systems, 9th International Workshop on linear colliders LC2002 (California, SLAC, February 4–8, 2002).

3. *Farkas Z. D.* et al., SLED: A Method of Doubling SLAC's Energy, Proc. 9th Conf. On High Energy Accelerator (SLAC, Stanford, CA, USA, May 2–7, 1974), p. 576, SLAC-PUB-1453.

4. *Balakin V. E., Syrachev I. V.* VLEPP RF Power Multiplier, Proc. 3rd Int. Workshop on Next Generation Linear Collider, Branch INP (Protvino, Russia, 1991), p. 1990.

5. *Kuzikov S. V.* Wavebeam Multiplication Phenomena to RF Power Distribution Systems of High-Energy Linear Accelerators, International Journal of Infrared and Millimeter Waves, **19**(11), pp. 1523–1539 (1998).

6. *Denisov G. G., Kuzikov S. V.* Microwave systems based on controllable interference of paraxial wavebeams in oversized waveguides, Proceedings of the International Workshop Strong Microwaves in Plasmas (Nizhny Novgorod, August 2–9, 1999), Vol. 2, pp. 955–960 (2000).

7. *Denisov G. G.* et al., New Components for TE01 Transmission Lines, Proceedings of the International Workshop Strong Microwaves in Plasmas (Nizhny Novgorod, August 2–9, 1999), Vol. 2, pp. 943–948 (2000).

IMPROVED MULTI-FUNCTION MITER BENDS
FOR CORRUGATED WAVEGUIDES OF HIGH-POWER
MILLIMETER-WAVE TRANSMISSION LINES

V. I. Belousov, A. V. Chirkov, G. G. Denisov, V. I. Malygin

Institute of Applied Physics Russian Academy of Sciences, Nizhny Novgorod, Russia

Oversized corrugated waveguides are widely used in transmission lines of ECW systems at fusion plasma installations. The lines typically include waveguide sections and miter bends to provide a required trajectory of the line and quasi-optical components for control and measurement of microwave radiation parameters. This paper presents our approaches for the component improvements and some design details of improved multi-function miter bends, which include: elements which make diffraction losses in miter bends small enough (shaped mirrors and special up-tapers of the waveguide ends in the bends); bi-directional couplers for measuring the power and the energy in pulse for transmitted and reflected radiation; corrugated mirrors for the polarization control.

Introduction

The miter bend is a very critical component of oversized corrugated waveguide transmission lines (with the HE_{11} mode) and diffraction losses in it should be strongly reduced because of two reasons:

- Diffraction losses, which occur at each miter bend, are multiplied to the number of miter bends in the line. This number may be up to 10–15 and this means that losses in each bend should be very small (less than 1%),
- The radiation scattered in the bends propagates partly in the backward direction in the form of high-order modes which are trapped between bends and may cause arcing.

The mode conversion losses in the traditional design version with a plane mirror of a 90° HE_{11} miter bend are [1]:

$$P_c / P = 0.29 \, (\lambda / a)^{3/2}. \tag{1}$$

At 70 GHz and D = 27.79 mm the losses calculated with this formula are approximately 5% and the results of the measurements are about 5.4% [2]. The Gaussian beam approximation for the radiation from an open-ended HE_{11} waveguide is very convenient to design of a curved (ellipsoidal) mirror, which partially compensates the phase distortions caused by diffraction on the mirror aperture. The measured levels of parasitic modes for this case are about 4.3% [2]. These diffraction losses are approximately 25% lower as compared to those of the plane mirror. The shape of the optimum curved HE_{11} mirror is determined from the requirement of minimum diffraction [1]. The measured losses are about 2.7% [2]. These diffraction losses are approximately 50% lower as compared to those of the plane mirror.

This paper presents our approaches for the component improvements and some design details of improved multi-function miter bends, which include:

- Elements which make diffraction losses in miter bends small enough: shaped mirrors and special up-tapers of the waveguide ends in the bends;
- Bi-directional couplers for measuring the power and energy in pulse for transmitted and reflected radiation, mounted in a bend;
- Corrugated mirrors for the polarization control in a bend.

Quasi-optical miter bend with low losses

If the phase corrected mirror of a miter bend is shifted from the ends of the corrugated waveguides to distance "L" of about one diameter and its size is increased, than it is possible to decrease dramatically the diffraction losses. We calculated the field distribution at the position of the phase correcting mirror directly, using the Kirchoff integral. The optimal mirror reverse the phase front of the incident beam [3, 4]:

$$\Psi(x, y) = -2 \cdot \arg\left[\int_S K(x, y, \xi, \gamma) F_{init}(\xi, \gamma) d\xi d\gamma \right], \tag{2}$$

$$K(x, y, \xi, \gamma) = \frac{k}{2\pi j} \frac{L}{r} \frac{\exp\{jkr\}}{r}, \tag{3}$$

$$r = \sqrt{L^2 + (x - \xi)^2 + (y - \gamma)^2}, \tag{4}$$

where $K(x, y, \xi, \gamma)$ is Green's function of Helmholtz's equation, $F_{init}(\xi, \gamma)$ is the initial field at the miter bend input. This phase corrector provides the conjugated phase $F^{*}_{init}(\xi, \gamma)$ at the output of the miter bend. So the distribution of the field at the output of the miter bend corresponds to the HE_{11} mode. The size of the mirror is defined by the minimum diffraction losses and is bigger than a mirror in a conventional miter bend. This is a quasi-optical miter bend with a shaped mirror. The calculated losses of a quasi-optical miter bend with the synthesized mirror at 70 GHz and $D = 27.79$ mm are about 0.7% ($L_1 = 50$ mm, $\Delta = 5$ mm), which means that the diffraction losses are approximately 8 times lower as compared with a flat mirror or 4 times lower, as compared with the mirror optimized by Vaganov [1]. For testing in experiment quasi-optical miter bend ($f = 82.7$ GHz and $D = 88.9$ mm), the same construction like using in the transmission lines at LHD installation (Japan) (Fig. 1, a) was fabricated. The theoretical calculations of diffraction losses with a plane mirror are 1.86% and with a shaped mirror are 0.3%. The measured amplitude distribution and reconstructed phase front at the output of the quasi-optical miter bend are in good agreement with theoretical calculations: $\eta_a(\eta_{a,\varphi})_{HE11} = 99.7\%$ (99.1%) (Fig. 1, b).
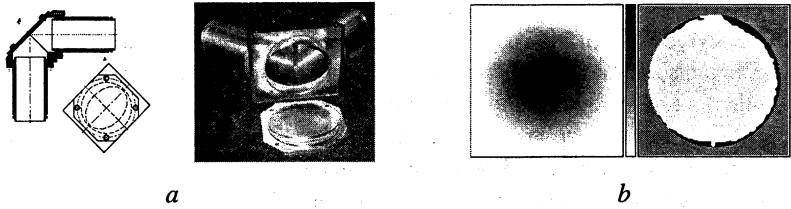
Fig. 1. Quasi-optical miter bend with low losses

To simplify the profile of the phase corrected mirror in the miter bend, it is necessary to convert the HE_{11} mode to a Gaussian beam, using a non-linear up-taper [5, 6]. The length of this converter is rather short and the profile of this up-taper is described by the formula:

$$r(z) = r_0 \left(1 + (z / \alpha\, k\, r_0^2)^2\right) + d\, (1 + \sin(2\pi z/T)), \tag{5}$$

where r_0 – initial radius, $k = 2\pi/\lambda$, $\alpha \cong 0.2$, $d = \lambda/8$, $T = \lambda/3$. At $f = 82.7$ GHz, $D_{in} = 63.5$ mm, $D_{out} = 85.7$ mm and the length of the up-taper is 206.2 mm (Fig. 2, b). The measured amplitude distribution and reconstructed phase front at the output of the converter are in a good agreement with theoretical calculations $\eta_a(\eta_{a,\varphi})_{Gauss} = 99.8\%$ (99.3%) (Fig. 2, c).

The construction of a quasi-optical miter bend is very convenient for use as a polarizer or a meter of transmitted and reflected power (MTRP).
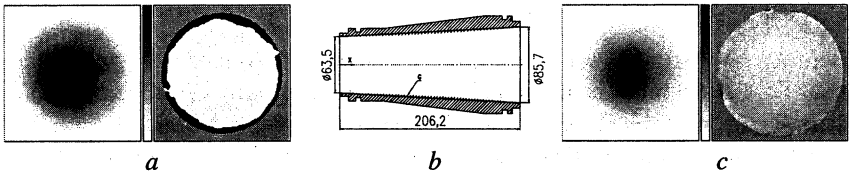
Fig. 2. Converter of HE_{11} mode to a Gaussian beam: a – input HE_{11} mode; b – non-linear up-taper; c – output gaussian beam.

Polarizer in a quasi-optical miter bend

A polarizer is needed to control the polarization of radiation in the transmission line which is very important for experiments at fusion plasma installations. The polarizer in a quasi-optical miter bend with two up-tapers consists of two corrugated mirrors and one shaped mirror (Fig. 3, a). The calculated diffraction losses are 0.95%. The value of losses is a bit higher than in a quasi-optical miter bend, because we tried to minimize in parallel the size of the polarizer. This polarizer can operate at broadband frequency range (30÷40%).

266

The measured amplitude distribution and reconstructed phase front at the output of the polarizer are in good agreement with theoretical calculations $\eta_a(\eta_{a,\varphi})_{HE11} =$ = 99.4% (98.8%) (Fig. 3, b).

a   *b*
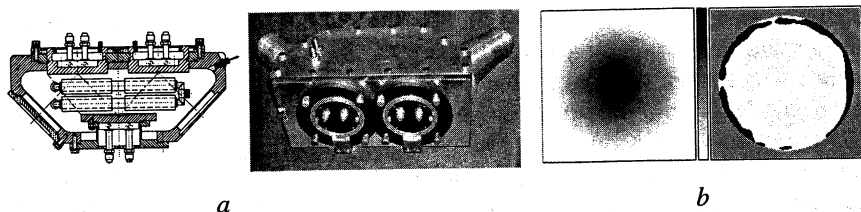
Fig. 3. Polarizer in a quasi-optical miter bend

MTRP in a quasi-optical miter bend

The measurement of megawatt microwave power is a very complicated problem, especially in the CW regime of operation. To split and measure a small part of a wave beam it is possible to use a corrugated mirror [7]. If the corrugation has the angle of 45° to the incident plane of the wave beam, then the coupling wave beam propagates in the direction under the angle of 45° to the incident plane. The transmitted and reflected wave beams propagate in different directions relatively to the incident plane. The value of the splitting power (P^r_{-1}) depends on the depth (l_0) of the corrugation and incident power (P^i):

$$P^r_{-1} \sim (k\,l_0)^2 P^i. \tag{6}$$

The MTRP in a quasi-optical miter bend with two up-tapers is presented in Fig. 4, *a*. The first corrugated mirror splits about 1% of the input power and this wave beam propagates to the second semitransparent mirror and to the small calorimetric load. This mirror transmits about 1% of the power to the detector channel. So, the small calorimetric load measures the transmitted power and the microwave detector measures dependence of the power on time. The reflected channel has a detector but no calorimetric load.

The calculated diffraction losses in the bend are very small, 0.1%. The measured mode purity at the output of the MTRP is $\eta_a(\eta_{a,\varphi})_{HE11} = 98.9\%$ (98.3%) (Fig. 4, *b*).

a   *b*
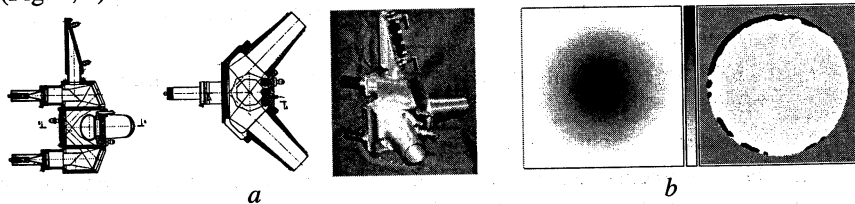
Fig. 4. MTRP in a quasi-optical miter bend

267

High purity HE$_{11}$ mode exciter

A special mode exciter was designed and fabricated for measurements of very small losses in the waveguide components. The high purity HE$_{11}$ mode exciter consists of a HE$_{11}$ mode exciter (purity 95–97%, pre-exciter), two shaped mirrors and a two-mirror cavity (Fig. 5, a). Two shaped mirrors convert the output radiation of the pre-exciter to the optimum microwave distribution to excite the two-mirror cavity. The two-mirror cavity consists of a shaped mirror and a flat semitransparent mirror, which is placed directly at the entrance of the corrugated waveguide. The shaped mirror of the two-mirror cavity has a non-quadratic profile, so that the field of the cavity eigenmode at the second flat (semitransparent) mirror corresponds to the HE$_{11}$ mode [8]. The measured amplitude distribution and reconstructed phase front at the output of the high purity HE$_{11}$ mode exciter are in good agreement with theoretical calculations. The purity of HE$_{11}$ mode for waveguides $D_1 = 63.5$ mm ($\eta_a(\eta_{a,\varphi})_{\text{HE}11} = 99.8\%$ (99.1%)) and $D_2 = 88.9$ mm ($\eta_a(\eta_{a,\varphi})_{\text{HE}11} = 99.6\%$ (99.0%)) is more thfn 99% (Fig. 5, b).

a $\qquad\qquad\qquad\qquad\qquad\qquad\qquad\qquad\qquad\qquad$ b
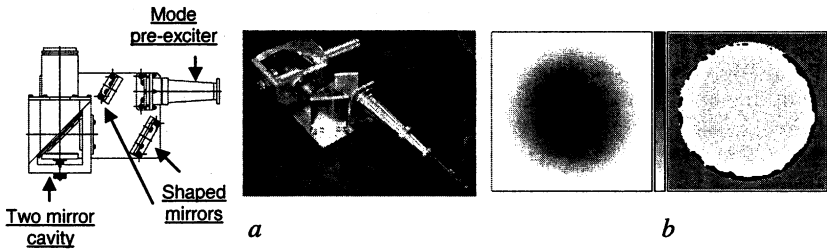
Fig. 5. High purity HE$_{11}$ mode exciter

Conclusions

☐ The new designs of low-loss multi-function miter bends were developed. They include:

- Shaped mirror which make diffraction losses in miter bends very small (< 0.5%);

- Non-linear up-taper that simplify the profile of a shaped mirror in a miter bend;

- MTRP for monitoring of power and energy in pulse for transmitted and reflected radiation;

- Polarizer for the polarization control.

☐ All these elements are compact and have a water-cooling systems for operation in the CW megawatt power level regime.

The design of these units gives a possibility to use them in evacuated or pressurized transmission line.

For testing these waveguide components a high purity HE_{11} mode exciter (> 99%) was developed.

References

Vaganov R. B., Radio Eng. Electron. Phys., 1990, **17**, 76.

Thumm M., Conf. Digest 14th Int. Conf. IR and MM Waves (Orlando, Dec. 10–14, 1990), 437.

Bogdashov A. A., Chirkov A. V., Denisov G. G., Vinogradov D. V. and Kuftin A. N., Malygin V. I., Zapevalov V. E. International Journal of Infrared and Millimeter Waves, **16**(4), 1995, 735–744.

Chirkov A. V., Bogdashov A. A., Denisov G. G. Proceedings of the XXVIII Moscow International Conference on Antenna Theory and Technology (Moscow, 1998), 551–553.

Belousov V. I., Piskunova L. V., Vlasov S. N., Izv. VUZ. Radiofizika, **27**(3), 1984, 1214–1217.

Malygin V. I., Vlasov S. N., Izv. VUZ Radiofizika, **32**, 1989, 657–660.

Belousov V. I. et al., Coll. Pap. "Gyrotron", Ed. Flyagin V. A., Inst. Appl. Phys. (USSR, Gorky, 1989), 155–160.

Belousov V. I., Denisov G. G., Chirkov A. V. Methods of calculation and parameter control of the eigenmodes of a simple two-mirror cavity. Radiophysics and Quantum electronics, **43**(8), 2000, 663–670.

DEVELOPMENT AND RESEARCH OF PLASMA SWITCHES OF HIGH POWER MICROWAVES

A. L. Vikharev, A. M. Gorbachev, O. A. Ivanov, V. A. Isaev, S. V. Kuzikov, V. A. Koldanov, and J. L. Hirshfield[1]

Institute of Applied Physics RAS, Nizhny Novgorod, Russia,
[1]Omega-P, Inc., New Haven, USA

The paper considers several types of electrically controlled plasma switches, which can be used in the active compressor operating at the low-loss TE_{on} mode. Results of numerical modelling and experimental investigation of such switches at a low power level are presented.

Introduction

One of the main problems that arise in creation of high-power active microwave pulse compressors is development of a switch capable of efficiently switching between the energy storage regime and the regime of energy extraction [1–4]. Such a switch should provide a short switching time (~10 ns) and have high electric reliability. The output reflector should be designed in such a way as to make intensity of the electric fields in the neighborhood of the gas-discharge tubes as low as possible and to provide wave switching simultaneously. The principal limitations to the output power above the level of about 100 MW in the existing compressors arise from the strong electromagnetic fields in the output reflector that lead to self-breakdowns in the plasma switch. For example, when the power of the output pulse is ~100 MW, the intensity of the mean-square electric field reaches the values of $E = 25$ kV/cm. For operation in the X-band, the Omega-P, Inc. and Institute of Applied Physics teams developed a novel active microwave compressor [3–4]. This is a version of a microwave compressor operating at the TE_{01} mode of a circular waveguide, which can produce 100 MW of the output power at the frequency of 11.4 GHz.

In compressors with plasma switches based on gas-discharge tubes there are two ways to prevent self-breakdown and thus increase the output power. Therefore, in order to increase electric reliability of the switch, one has to decrease the gas pressure in the tubes (one way) or increase it (another way). On the other hand, it is necessary to weaken the electric fields in the switch down to the level that does not exceed the threshold of the gas self-breakdown in the tubes. Hence, the design of switches has to be different. Therefore, we manufactured and tested experimentally two different types of electrically controlled plasma switches with low and high pressure in the tubes. The experiments were performed at a low power level in two stages. At the first stage we checked the coefficient and speed of switching for each of the switches. Then the switch was built into a compressor and we studied the possibility of obtaining compressed pulses using this switch.

Low-pressure plasma switch at the TE₀₃ active mode

In this switch plasma appears at low gas pressure in the tubes. The switch has inherent resonator properties and a significantly lower Q-factor, as compared to the storing resonator, and is "brightened" of plasma at the operating frequency of 11.4 GHz. The scheme of the switch is shown in Fig. 1. It is formed by a section of a circular cylindrical waveguide, which is limited with diaphragms at the both ends and comprises a resonator exited at TE_{03} mode. Two gas-discharge quartz tubes shaped as rings were placed into the reflector. Each of the tubes had electrodes that fed in high-voltage pulses that formed plasma in the tubes. Operation of the switch was measured in a compressor prototype [3–4], which operated on the TE_{01} mode. The principle of operation of the switch is as follows. In the regime of energy storage in the compressor the length of the reflector is set to such a value as to make its resonance frequency, 0.7 GHz, lower than the active frequency of the compressor, f_0. This provides a close-to-unity coefficient of reflection from the reflector. At the same time, a significant initial drift of the output reflector away from the active frequency of the compressor makes it possible to reduce electric fields in the gas-discharge tubes in the regime of energy storage significantly, as compared to other types of switches. When plasma with density N_e exceeding critical density N_c is produced in the tubes, the efficient length of the reflector becomes equal to the resonance length for the active frequency of the compressor, f_0. As a result, the transmission coefficient of the output reflector grows sharply.

Thus, the output reflector becomes brighter at the resonance frequency. Figure 2 shows distribution of the electric field in the switch with no plasma and with plasma in the gas-discharge tubes. Note that the requirement for the value of electron density, at which resonance brightening of the reflector is observed, is not too strict, since the band of its transparency is 50–80 MHz.
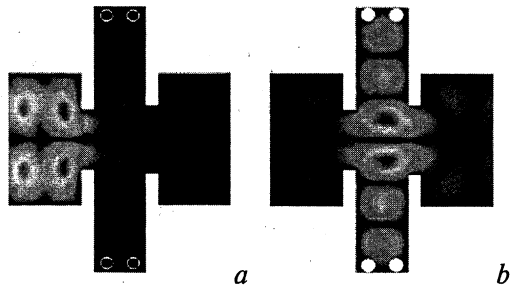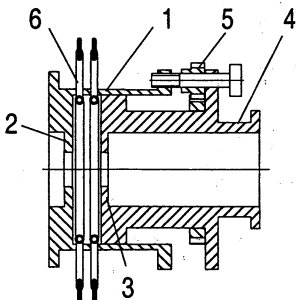
Fig. 1. Low-pressure plasma switch: _1_ – circular waveguide; _2, 3_ – diaphragms, _4_ – stepped widening, _5_ – adjustment device, _6_ – gas-discharge tube.

Fig. 2. Instantaneous distribution of the electric field in the switch: _a_ – in the regime of energy storage; _b_ – in the regime of output of the compressed pulse.

At the same time, resonance tuning of the reflector leads to more intense fields at the tubes; hence, to prevent higher Ohmic losses at the stage of power output the pressure in the tubes should be sufficiently low. Operation of the low-pressure plasma switch was modeled numerically by means of the FDTD method and was tested experimentally at a low power level. The results of investigation are presented in Table 1.

Table 1. Numerical and experimental results for the compressor with a modified output reflector

Frequency	11.42 GHz
Pressure	0.01–0.5 Torr
Operating mode	TE_{03}
Output pulse power	100 MW
Electric field near the tubes	10 kV/cm
Power gain	9–10
Output pulse duration	80–90 ns

Calculations show that in this type of the plasma switch the root-mean-square electric field near the tubes will be 10 kV/cm at the output power of 100 MW. The coefficient of transmission through the reflector at the active frequency, f_0, was –35 dB. The pressure of nitrogen in the tubes was varying in the range of $p = 0.01$–0.5 Torr. The duration of the output pulse was $\tau_{0.5} = 80$–90 ns (depending on reflector settings), and the maximum compression coefficient was $k \approx 9$–10.

High-pressure plasma switch based on mode conversion

In these switches plasma is created at a high gas pressure inside the tubes and operation of switches is based on conversion of the TE_{02} mode into the TE_{01} mode. The field can be weakened by decreasing the coupling between the main volume of the storing resonator and the switch volume. A simplified scheme of such a switch is shown in Fig. 3.
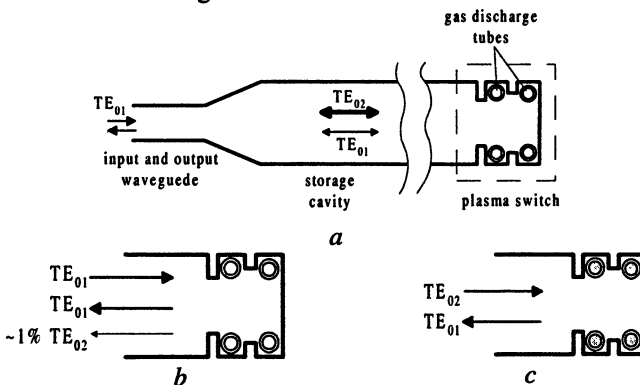
Fig. 3. Schematic diagram of compressor with the switch based on conversion of the TE_{02} mode into the TE_{01} mode (a); mode conversion during energy storage (b); and during energy extraction (c)

In the regime of power storage the resonator is fed by the TE_{01} mode of a circular waveguide, where the switch provides weak coupling of the feeding mode into the TE_{02} mode, which is cut off at the entrance due to over-critical narrowing. Thus, the microwave power is stored in the TE_{02} mode. A schematic drawing of the switch is shown in Fig. 4.
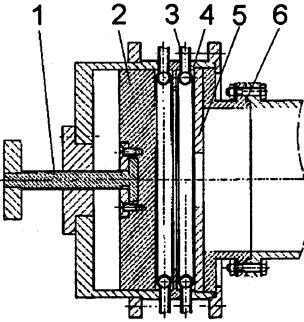
Fig. 4. Plasma switch based on mode conversion: *1* – mechanical adjustment, *2* – sliding short, *3* – gas discharge tubes, *4* – stepped widening, *5* – diaphragm, *6* – circular waveguide.

The switch is based on a reflector made as a widening of the cylindrical waveguide hooded with a small-diameter diaphragm. The axially symmetric TE_{023} mode is excited in the reflector. Two gas-discharge quartz tubes were placed into the reflector.

The principle of operation of the switch is as follows. In the energy storage regime the power is stored at the TE_{02} mode, which is reflected from the switch completely without scattering into the TE_{01} mode. The latter is achieved by mutual compensation of radiation flows, which are formed by scattering at the diaphragm and radiation from the waveguide widening that acts as a resonator.

The coefficients of conversion into the TE_{01} mode and of reflection of the TE_{02} mode into itself for the switch with and without plasma in the gas-discharge tubes are shown in Fig. 5. It is seen that in the regime of storage at the resonant frequency 11.424 GHz the $TE_{01} \rightarrow TE_{02}$ conversion is negligibly small. At this frequency the working electric field in the discharge tubes is 22 kV/cm.
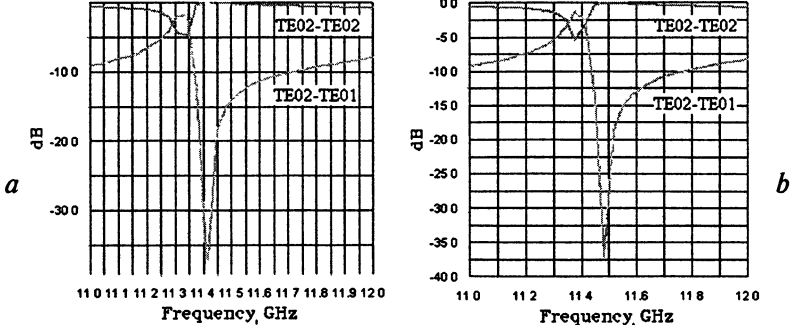
Fig. 5. Coefficients of reflection of TE_{02} mode into itself and of conversion into TE_{01} mode during the storage regime (*a*), and during the extraction of energy (*b*)

273

Operation of the switch was measured in a compressor prototype, which operated on the TE_{02} mode. When a high-voltage pulse was fed in and the plasma appeared in the reflector, the resonance frequency of the latter changes and the coefficient of TE_{02}-to-TE_{01} conversion during the reflection from the reflector increased up to 15–20%. The microwave energy stored in the resonator was emitted through the output horn on the TE_{01} mode. In this case a compressed pulse was detected in the branch of the signal reflected from the compressor; the duration of this pulse was determined by the TE_{02}-to-TE_{01} conversion coefficient. The compression ratio obtained in the experiments was 8–9 with duration of the compressed pulse 100 ns. The amplitude of the output pulse and, correspondingly, the compression ratio depended strongly on the pressure of nitrogen in the gas-discharge tubes. This makes it possible to optimize parameters of the output pulse. The results of investigation are presented in Table 2.

Table 2. Numerical and experimental results (low-power test) for the plasma switch based on mode conversion (TE_{02}–TE_{01})

Frequency	11.42 GHz
Pressure	300–500 Torr
Operating mode	TE_{02}
Output pulse power	100 MW
Electric field near the tubes	22 kV/cm
Power gain	8–9
Output pulse duration	80 ns

Conclusions

The use of plasma switches with resonance properties makes it possible to reduce intensity of the electric field at the gas-discharge tubes in the regime of energy storage in the compressor significantly. Besides, the use of low gas pressure in the tubes of such switches provides high electric reliability of switches and a low level of Ohmic losses in plasma at the stage of microwave power output from the compressor.

Design of the plasma switches based on mode conversion developed by us makes it possible to: make the design of the active compressor significantly simpler; and obtain compressed pulses with higher power than those in the existing compressors by raising the gas pressure in the switch up to 500–600 Torr.

References

1. *Alvarez R. A.*, Rev. Sci. Instrum., 1986, **57**, 2481.
2. *Yushkov Yu. G., Avgustinovich V. A., Artemenko S. N.* et al., Proc. of the Intern. Workshop "Strong microwaves in plasmas", IAP, Nizhny Novgorod, 1996, **2**, 911.
3. *Vikharev A. L., Gorbachev A. M., Ivanov O. A.* et al., JTP Letters, 1998, **24** (20), 6.
4. *Vikharev A. L., Gorbachev A. M., Ivanov O. A.* et al., Proc. of 8th Workshop "Advanced Accelerator Concepts", Baltimore, Maryland, 1998.

A FREE ELECTRON MASER AMPLIFIER – ENERGY RECOVERY EXPERIMENTS

C. G. Whyte, A. W. Cross, D. A. Jaroszynski, W. He,
K. Ronald & A. D. R. Phelps

University of Strathclyde, Glasgow, Scotland, UK

We present results from a reversed guide magnetic field Raman Free Electron Maser (FEM) amplifier experiment at Strathclyde University. The FEM has been designed for zero slippage to achieve maximum instantaneous bandwidth. Results show an instantaneous −3 dB bandwidth of 30% for fixed cathode voltage and magnetic field. The device can be tuned over a range of 65% of the centre frequency by adjusting the cathode voltage. Amplifier saturated gain was measured at 23 dB giving a peak output power of over 1 MW. Broadband unsaturated gains of over 35 dB have been measured. Energy recovery experiments have also been conducted. Results show the potential to increase the FEM amplifier efficiency from 5–6% to nearly 40%.

Introduction

FEM's with an axial guide magnetic field are one of the promising sources of powerful coherent radiation in the microwave, millimetre and sub-millimetre wavelength range. High efficiency (35%) operation of such devicies was achieved by [1, 2, 3] in regimes with a reversed guide field when the cyclotron rotation of the beam electrons and their rotation imposed by the helical wiggler have opposite directions. Prior to reversed guide field operation it was observed that when these rotations were co-directed, i.e. forward guide field regime, the efficiency was limited to ~12%. Theoretical interest [3] and evidence presented by [4, 5] shows that for an FEM driven by an ideal (without any spread of parameters) electron beam of the same energy and operating transverse velocity the efficiency will be approximately the same in both guide field regimes. Recent simulations by [6] demonstrate a strong dependence of FEM efficiency on the spread of beam parameters and this dependence is different for different guide field configurations. It has been shown that for reversed guide field regimes (more general, for regimes far from the cyclotron resonance) the quality of the electron beam formed in the slowly up-tapered wiggler entrance is better than in regimes close to cyclotron resonance. As a result, FEMs operating in the reversed guide field regime possess a rather small sensitivity to the initial spread of beam parameters. In contrast, the conventional guide field regime close to cyclotron resonance is more sensitive to beam quality and the presence of initial parasitic transverse velocity, present in all real electron beams, leads to a significant drop in efficiency. The highest efficiencies achieved to date have been for oscillators using cavities defined by Bragg reflectors. This approach allows the maximisation of the cavity Q-factor to maximise the saturated output power. This is not

possible in an amplifier, however the interaction efficiency of an amplifier can be improved by the recovery of energy from the electrons in the spent beam. This can be achieved by the use of a depressed collector.

Method

A reverse guide field FEM amplifier operating in the Raman regime with energy recovery has been designed and constructed at Strathclyde. The FEM amplifier is designed for a near grazing intersection of the beam line and waveguide mode to maximise the frequency tuning range. The maser may be tuned either by varying the beam voltage or by varying the undulator and guide magnetic field strengths.

A bifilar helical undulator of 40 periods has been constructed to give a maximum on axis field of 0.12 T. The undulator magnetic field was tapered at the input by current return loops which were used to create a stepped reduction the total current flowing in the first two periods of the undulator. The output taper was formed using a one-half period section of undulator; this section had half the period of the main undulator. The undulator current was provided by an critically damped capacitor discharge circuit which produced a maximum peak current in excess of 7 kA. A maximum axial guide field of 0.3 T was produced by a water-cooled DC solenoid.

Two separate quasi-resonant input couplers were designed and cold tested in the laboratory, one for each of the waveguide bands over which the FEM can be tuned. These devices use a simple stub tuned right angled rectangular to circular waveguide transition with the stub placed close to the end of the rectangular waveguide section. The optimal stub position was determined experimentally for each coupler. These couplers showed a bandwidth of approximately 4 GHz in each case.

A velvet cathode in a Pierce configuration gives a maximum beam current of 50 A, representing 100% of the diode current. The electron gun diode has been modelled using a fully relativistic 2.5 D code, including space-charge effects, developed at Strathclyde.

A two electrode depressed collector provides an axi-symetric decelerating electric field at the output end of the axial guide field. Electrons are collected on only one of these electrodes, the other being used purely for field shaping. The voltage on the collecting electrode can be varied between 50% and 100% of the voltage on the field-shaping electrode. The total voltage applied to the depressed collector can also be varied between zero and the cathode voltage.

The high voltage power supply for the FEM consists of two four cable stacked Blumlein circuits which provide a maximum voltage of 350 kV with a flat top pulse length of 60–80 ns. The depressed collector power supply consists of a seven stage Marx bank with an output inductor and a low impedance resistive divider with variable division ratio. Time correlation between the power

276

supplies was achieved using thyratron triggers firing field distortion spark gaps for both power supplies. The thyratron for the blumlein supply was triggered from the output of the Marx bank to eliminate the Marx bank spark gaps as a source of timing jitter. This system achieved a timing jitter of approximately 10 ns.

Three input power sources were used in this experiment, two 1μs pulse length, 25 kW peak power magnetrons operating at 9.1 and 9.5 GHz were used for high output power measurements. A 1-kW TWTA driven by digital synthesiser was used to evaluate the broadband frequency performance of the system at lower input powers. The FEM output power was sampled using a crystal detector mounted in a screened enclosure, the crystal was connected to a 500 MHz bandwidth digitising oscilloscope in a screened room using double screened cables.

Results

Figure 1 shows the voltage pulse shape and output radiation pulse shape for the Raman FEL amplifier operating with approximately 5 kW input power from the 9.5 GHz magnetron. The amplifier gain for this measurement was 23 dB with a corresponding peak output power of 1 MW ± 20%. This represents an efficiency of over 5%. The FEM amplifier gain as measured using the 1 kW nominal output TWTA is presented in Fig. 2. The input power with the correct polarisation for these measurements was a maximum of 300 W ± 10%.
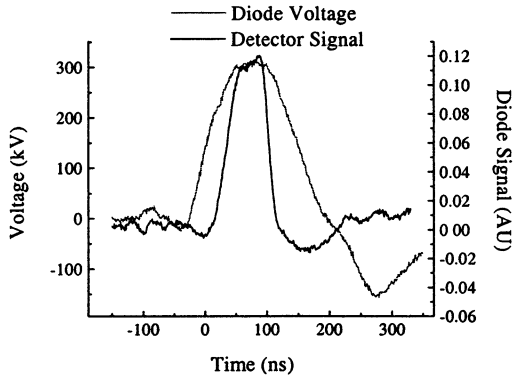
Fig. 1. Cathode voltage and microwave output signal waveforms.

The two sets of curves represent measurements performed using the two input couplers. During these experiments the FEM amplifier magnetic fields were not varied, only the cathode voltage was adjusted. The gain was reduced in the experiments in the higher frequency range due to decreased beam current. This was due to beam scraping in the cut-off section of the waveguide input coupler. Future experiments are planned using a broadband input coupler, which does not have this restriction. Cold test measurements of the new coupler have confirmed the modeled performance of less than 20 dB return loss over 10 GHz bandwidth. Figure 3 shows the percentage of beam current collected as a function of voltage on the collecting electrode. These experiments were performed at the normal FEM amplifier operating condition for 10 GHz amplification, except that a radiation output horn was not included due to space limitations.

277
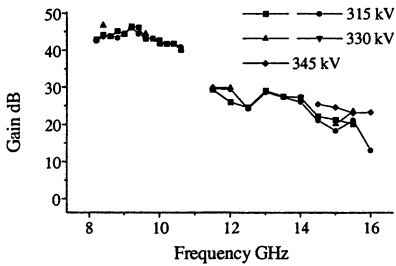
Fig. 2. FEM Amplifier gain as a function of frequency.
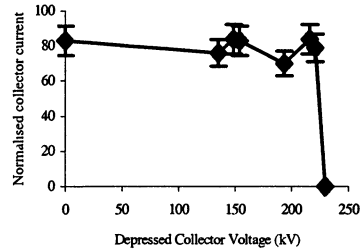
Fig. 3. Collector current as a function of voltage.

The amplifier would oscillate and give saturated output power in these conditions, these are therefore the least favorable conditions in which to attempt energy recovery and give an indication of the worst-case scenario. The maximum collected current was approximately 85%; this was due to a small misalignment of the interaction region with respect to the electron gun and can be corrected. The percentage of beam current collected was constant with collector voltage up to 76% of the cathode voltage; this indicates a recovery of 11 MW from the spent electron beam and an increase of efficiency from less than 6% to 40%.
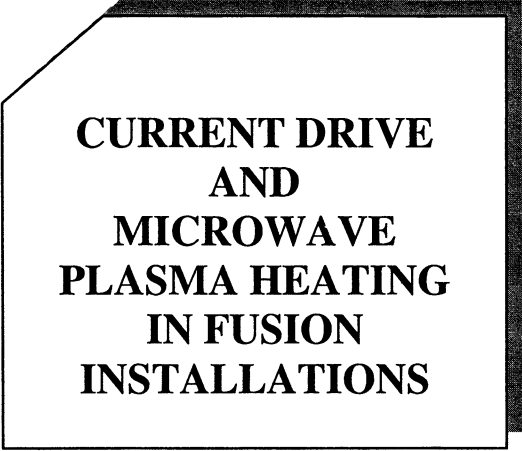
A thermionic cathode system, which will be used to investigate long pulse stability, is currently being constructed.

Conclusions

The Raman FEL amplifier has shown a gain of over 35 dB over a 30% frequency band. The frequency range of operation can be extended to 65% of centre frequency by adjustment of the cathode voltage. Saturated gain of 23 dB with an output power of 1 MW and efficiency of 5% has been measured. Depressed collector experiments have shown that the efficiency of the FEM Amplifier can be increased from 5–6% to 40%.

References

1. *Kaminsky A. A., Kaminsky A. K., Rubin S. B.* Particle Accelerators, 1990, **33**, 189.
2. *Conde M. E., Bekefi G.*, Phys. Rev. Lett. 1991, **67**(22), 3082.
3. *Ginzburg N. S., Kaminsky A. K., Kaminsky A. A., Peskov N. Y., Sedykh S. N., Sergeev A. P., Sergeev A. S.* High-Efficiency Single-Mode Free-Electron Maser Oscillator Based on a Bragg Resonator with Step of Phase Corrugation. Phys. Rev. Lett. 2000, **84**(16), 3574–7.
4. *Zhang S. C. and Elgin J.*, Phys. Rev. E, 1997, **55**, 4684–4693.
5. *Freund H. P., Antonsen T. M.* Principles of free electron lasers. Second Edition (1996). ISBN 0 412 72540 1.
6. *Ginzburg N. S., Kaminsky A. K., Kaminsky A. A., Peskov N. Y., Sedykh S. N., Sergeev A. P., Sergeev A. S.* International Workshop on High Power Microwave Generation and Pulse Shortening (Edinburgh, 10–12 June 1997).
7. *Peskov N. Yu., Ginzburg N. S., Samsonov S. V., Bratman V. L.* Proc. of 19th Int. FEL Conf. Beijing (1997).

CURRENT DRIVE AND MICROWAVE PLASMA HEATING IN FUSION INSTALLATIONS

20 YEARS OF ECRH AT W7-A AND W7-AS

V. Erckmann, U. Gasparino, H. P. Laqua, H. Maassberg,
N. B. Marushchenko, H. Renner, M. Rome', W7-AS Team,
W. Kasparek[1], G. A. Müller[1]

Max-Planck-Institut für Plasmaphysik, EURATOM Ass.,
Teilinstitut Greifswald, D-17491 Greifswald, Germany
[1]Institut für Plasmaforschung, Universität Stuttgart, Germany

Basic research on high power ECRH started 20 years ago at IPP using 28 GHz pulses with 200 kW for 40 ms at the W7-A stellarator. These pilot experiments triggered a strong activity to explore the unique capability of localized heating and current drive. The physics achievements were strongly linked to the progress in source and transmission line technology. The capability and versatility of ECRH is reviewed using W7-A and W7-AS, which was shut down in July 31, 2002, as example experiments. Milestone achievements are discussed. Standard heating scenarios such as O-mode, X-mode as well as advanced scenarios like mode-conversion heating via the O-X-B process at different harmonics were investigated and selected results are presented. First experiments with current drive by Bernstein-waves are reported. The results from W7-A and W7-AS establish the experimental and technological basis for the 10 MW, CW ECRH-system at W7-X, which aims at demonstrating the inherent steady state capability of stellarators.

1. Introduction

The operation of the W7-AS stellarator was terminated on July 31, 2002 and the experimental stellarator research at IPP is now focussed on the construction and operation of the W7-X stellarator [1]. The scientific investigation of the IPP stellarators W7-A and W7-AS was strongly supported by a powerful and flexible ECRH system. The ECRH-activities started 20 years ago with 28 GHz at 200 kW output power for 40 ms pulses. Net current free plasma build-up and heating was achieved at W7-A for the first time in July 1983 [2]. All previous investigations were performed with ohmic plasma start-up as the only available method. W7-A operation had to be restricted, however, to a magnetic induction of 1 T (machine capability 3.5 T) and a plasma density below the cut-off density of $1.0 \cdot 10^{19}$ m^{-3} for 1st harmonic O-mode (O1). First milestone achievements with this system are reviewed in Sec. 2. It became clear immediately, that further progress in ECRH would be closely linked to the technological development of sources operating at higher frequency (to match the resonance condition for higher magnetic induction), and higher microwave power (to compete with other heating methods). The basic advantages of ECRH, i.e. easy coupling to the plasma without antenna structures close to the plasma boundary, strongly localized power deposition near the resonance layer, complete power absorption at electron temperatures, which are easily present in fusion bulk-plasmas, were demonstrated in an early state of the experiments. The development of high-power, low-loss microwave transmis-

sion systems and lauchers with high flexibilty and mode purity thus became a key issue for ECRH and ECCD. Following these guidelines IPP initiated the industrial development of gyrotrons operating at 70 GHz, which corresponds to a resonant magnetic induction of 2.5 T and a cut-off density of $n_{e,crit} = 6.2 \cdot 10^{19}$ m^{-3} (O1). This frequency allowed also to operate at 1.25 T with $n_{e,crit} = 3.1 \cdot 10^{19}$ m^{-3} for 2nd harmonic X-mode (X2) operation. The 28 GHz system at W7-A was replaced by the 70 GHz system and first plasma operation with 70 GHz started already in 1984 with a 200 kW, 100 ms source. Large progress in the transmission technology was made with respect to pure mode irradiation, allowing detailed investigations of microwave propagation and absorption. In particular experiments on 'stimulated heat wave propagation' were proposed and executed for the first time in 1984 at W7-A and became a powerful method for heat transport analysis in all ECRH-equipped fusion devices later on. W7-A operation was terminated in Nov. 1985. Port access at W7-A was very restricted and thus the first flexible in-vessel launcher with steerable launching mirrors, which was invented by the IPF-Stuttgart group [3], was installed in W7-AS, which started operation in Oct. 1988. This key technology allowed detailed investigation of phase-space wave-particle interaction physics (ECCD, ECRH) in a wide range from perpendicular to oblique launch ($< 40°$) at on- and off-axis deposition. The ECRH system was upgraded to 1 MW microwave power at 70 GHz consisting of 5 gyrotrons with 200 kW each for 3 s pulses. The density restictions, however, remained, although stellarator confinement did not show a density limit in the range available with ECRH. To overcome this limit, IPP strongly encouraged the development of 140 GHz gyrotrons and a first prototype from the development line at Forschungszentrum Karlsruhe with 100 kW for 400 ms pulse duration became operational at W7-AS in 1991 [4]. Basic investigations were performed in an extended density regime with a cut-off density of $n_{e,crit} = 1.25 \cdot 10^{20}$ m^{-3} at a resonant magnetic induction of 2.5 T, for X2-mode. Within the frame of an intense collaboration with the russian research laboratories IAP Nizhny Novgorod and Kurtchatov Inst. Moscow the first 140 GHz, 0.8 MW, 0.5 s gyrotron was developed and provided by the russian partners for W7-AS in 1993, marking a milestone in gyrotron and ECRH technology [5, 6]. The 70 GHz gyrotrons and transmission lines were step by step replaced by 140 GHz units, resulting in a final installation of 4 units at 140 GHz with a total power of 2.3 MW and one unit at 70 GHz with 0.5 MW. The latter was maintained to keep the option of 1.25 T operation open. The high available ECRH-power led to the discovery of new confinement regimes such as H-mode and "electron-root" confinement. The experiments in the last period of the W7-AS lifetime were focussing on the β-limit and island-divertor operation. Both requires high density operation, which is even beyond the X2 density cut-off. Efficient Bernstein-wave heating via the O-X-B mode conversion process was demonstrated at W7-AS for the first time [7] and recently extended towards a plasma density off $3.5 \cdot 10^{20}$ m^{-3}. Here O, X, and B are the ordinary, extraordinary and electron Bernstein mode. Instead of an

upper density limit, as for the standard ECRH-scenarios, a lower density limit exists for this scenario at $n_{e,crit} = 2.5 \cdot 10^{20}$ m^{-3} for the O2-mode at 140 GHz. Current drive with Bernstein waves was demonstrated in high density plasmas. The experimental investigations were closely followed by the development of 3D ray-tracing codes and Fokker – Planck calculations taking into account the stellarator specific trapped particle physics.

Some example experiments on power deposition and the theoretical modeling are presented in Sec. 2. Selected experiments on plasma confinement with ECRH are shown in Sec. 3 and current drive experiments are discussed in Sec. 4. Some results on mode conversion heating and current drive are presented in Sec. 5.

2. Modes, propagation and absorption

ECRH-experiments started at W7-A with 28 GHz, 200 kW with a maximum pulse duration of 40 ms. The first shot with a pulse duration of 5 ms is seen in Fig. 1, showing the plasma start-up from the neutral gas with a small delay after turn on of rf. The plasma develops a net-current (top left), stored plasma energy (top right), plasma density (bottom left), the rf-signal is also shown (bottom middle). The microwaves were launched from an open ended waveguide perpendicular to the magnetic axis. The launched waveguide mode TE$_{02}$ contained 50% O- and 50% X-mode polarization, i.e. the X-mode fraction is absorbed only after multiple reflections from the torus walls ("dirty coupling").
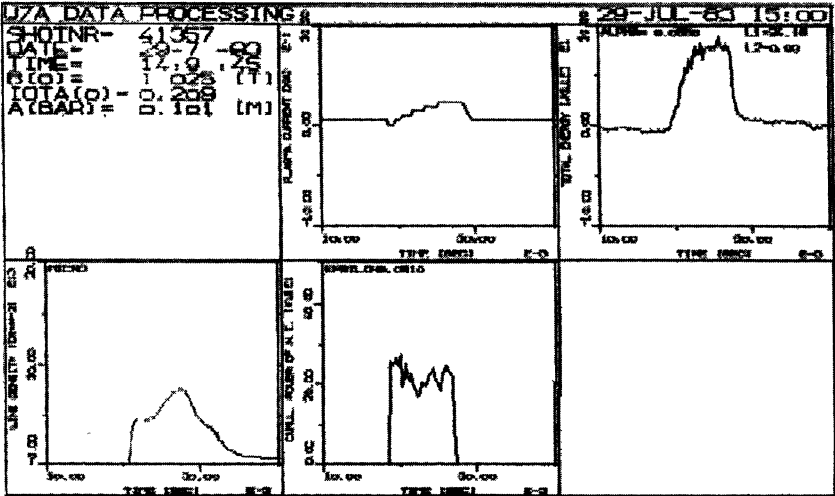
Fig. 1. The first ECRH shot at W7-A with 28 GHz, 200 kW showing plasma start up from the neutral gas.

On- and off-axis heating was shown already at W7-A [8] while tuning the magnetic field and thus the resonance layer. With the improved launcher at W7-AS with in-vessel steerable launching mirrors [3] each microwave beam could be steered to arbitrary poloidal and toroidal launch angles. An example for off-axis heating with two microwave beams of 0.2 MW each in X2 mode ($B_0 = 1.25$ T) and resonance on-axis is shown in Fig. 2 together with the ray-tracing calculations in the 3-D stellarator geometry. The profiles of n_e and T_e for off-axis heating are compared to on-axis heating. Whereas the T_e-profile changes from peaked (on-axis deposition) to hollow (off-axis deposition), the n_e-profile shows only a small change from slightly hollow (on-axis) to flat (off-axis). The discusssion of the density profile effect is beyond the scope of this paper.
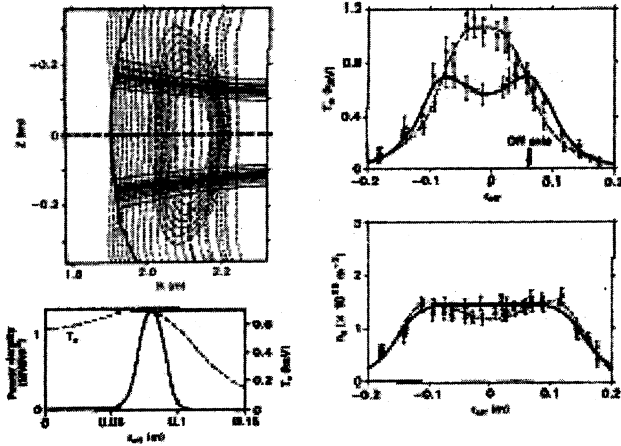
Fig. 2. Ray-tracing calculations for off-axis heating with two rf-beams at W7-AS (left) and related profiles of the electron temperature T_e and density ne (right). W7-AS flux-surfaces are shown together with contours of $|B| = $ const. (almost vertical dashed lines with the resonance layer on axis) and the microwave rays (top, left), the off-axis power deposition profile is shown on left, bottom. The n_e (right, bottom) and T_e-profiles (right, top) for off-axis heating (solid line) are compared to on axis heating (dashed line).

The very narrow power deposition of ECRH can be used to stimulate a localized periodic perturbation of the electron temperature by ECRH power modulation. This perturbation propagates outward from the deposition region in the plasma thus driving a heat wave. From the local measurement of the phase and amplitude of this heat wave both, the heat transport coefficient of the plasma and the power deposition profile can be determined locally [9, 10]. First experiments on the propagation of a heat pulse induced by switching ECRH on/off were performed at the Spherator FM-1 [11]. The improved technique with periodically modulated ECRH allows to track a heat wave rather than a heat pulse and was applied for the first time at W7-A [12].

284

In the experiment described here the deposition profile was derived from the analysis of stimulated heat waves in ECRH power modulation experiments, with the time dependent electron temperatures from ECE measurements (see Fig. 3).
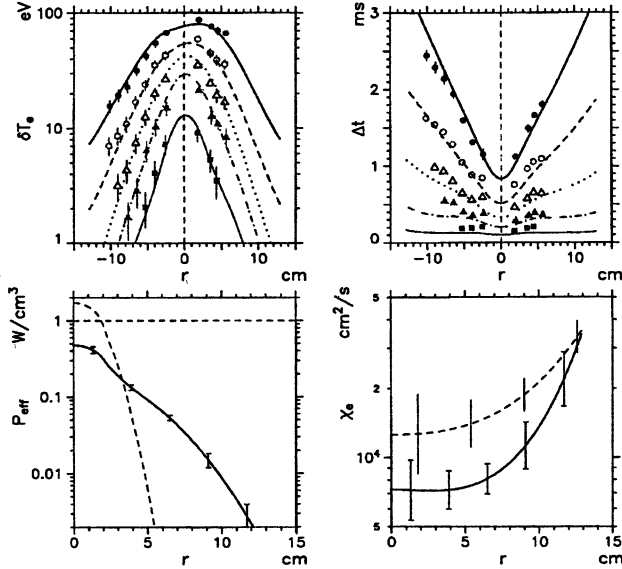
Fig. 3. The temperature modulation amplitudes δT_e and the time delays Δt versus radius r, for different modulation frequencies, $f_{mod} = 92$, 200, 400, 800 and 2000 Hz (upper left and right plots) from ECRH power modulation experiments at $B_0 = 2.5$ T (O1-mode, 70 GHz) with on-axis deposition. The power deposition profile (lower left, solid line) is compared to the "ray-tracing profile" shape (dashed line). The plot on the right gives the "effective" heat conductivity $\chi_e(r)$ (solid line). For comparison, the $\chi_e(r)$-profile from the stationary power balance analysis with the power deposition profile from ray-tracing is also shown (dashed line).

The ECRH-power was modulated with an amplitude of 10–30% and different frequencies from 0.05–5 kHz. This kind of analysis requires a proper modelling of the transport effects in the transient energy balance. The heat transport was described by a purely diffusive model. No evidence for a significant convective contribution was found. Peaked deposition profiles are usually obtained for both O- and X-mode heating from a 3D Hamiltonian ray-tracing code based on the assumption of a Maxwellian electron distribution function (single pass absorption). From the heat transport analysis of modulation experiments we obtain similarly peaked absorption profiles, but additionally a much broader contribution is present (see Fig. 3), whose width and relative integral contribution with respect to the "thermal" peaked part depends on the particular heating scenario, collisionality regime and magnetic configuration. The measured broadening of

the deposition profile is attributed to the fast transport via the drift orbits of trapped electrons in the long mean free path regime. Taking the broader component of the power deposition profile into account, the input power is recovered by the heat transport analysis within the errors.

3. Improved confinement modes with ECRH

3.1. The "electron root". Experiments with strong X2-mode heating from the low field side in the equatorial plane were performed in a wide density and power range. The central electron temperatures range from 5.7 keV at $1.7 \cdot 10^{19}$ m^{-3} to 3 keV at $7.5 \cdot 10^{19}$ m^{-3} at constant input power of 1.2 MW. A pronounced steepening of the temperature gradients is seen in the centre of the plasma [12] at densities below $4 \cdot 10^{19}$ m^{-3}. A similar behaviour was measured during a power scan at constant density of $0.2 \cdot 10^{20}$ m^{-3}, where the steepening occurred between 0.2 and 0.4 MW. Radial profiles of T_e and n_e are shown in Fig. 4 for discharges with different heating power at constant density. The stationary transport analysis of these discharges results in a central ($r/a < 0.3$) electron heat diffusivity, which is well below the neoclassical heat diffusivity, once electric fields are neglected. Strongly positive radial electric fields up to 50 kV/m were measured in the plasma centre, which lead to good agreement with neoclassical theory including electric fields (electron root "solution"). It is worth noting, that the ions are energetically decoupled from the electrons under these conditions and the energy balance is dominated by the electrons. The appearance of the electric fields and the corresponding steep temperature gradients shows
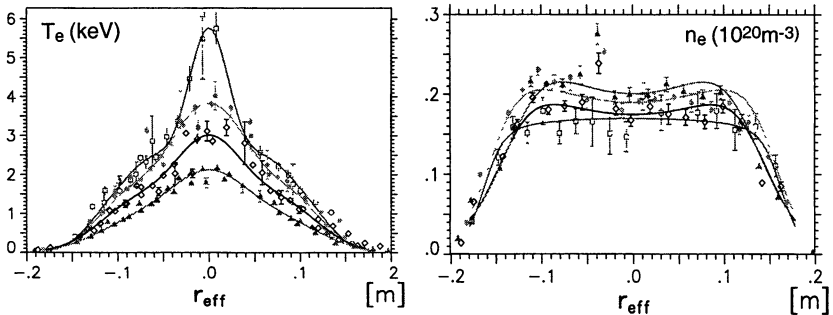
Fig. 4. Radial profiles of the electron temperature (left) and density (right) at different heating power of 0.2 (triangles), 0.4 (open circles), 0.8 (dots) and 1.2 MW (squares).

a threshold behaviour at a density around $(0.2–0.4) \cdot 10^{20}$ m^{-3} for 1.2 MW heating power and a power threshold around 0.2–0.4 MW for constant density of $0.2 \cdot 10^{20}$ m^{-3} (see Fig. 4). The discharge could be placed at the threshold by careful adjustment of the heating power density while tuning the deposition region. The

central electron temperature then is jumping iteratively between two states of low (say 4 keV) and high (5 keV) temperature during one discharge with some hysteresis between rise- and fall-time constants. The experiments are explained by a substantial loss of fast trapped particles driven by ECRH itself, which in turn generates a positive electric field with its beneficial effect on the bulk electrons. This picture is consistent with the results of switching experiments, where the central confinement is lost on a fast timescale (< 0.3 ms), whereas the remaining profile relaxes on the diffusion timescale. Also these switching experiments display a threshold nature while switching from 1.2 to 0.8 (0.4) MW.

3.2. The stellarator H-mode. The phenomenon of spontaneous abrupt transitions from low (L-mode) to high (H-mode) confinement properties of both energy and particle transport was first observed at ASDEX in 1982 [14] and later on confirmed in other tokamak experiments [e. g. 15, 16]. The first stellarator H-mode [17] was observed in 1992 under high density ECRH conditions at 140 GHz in W7-AS with $B_0 = 2.5$ T, ι around 0.5 and $I_p = 0$ to control the edge rotational transform. The first results were obtained with a new 140 GHz ECRH system operating at 0.5 MW for 0.5 s pulse duration in X2-mode. The cut-off density for the 140 GHz system is $1.2 \cdot 10^{20}$ m^{-3} which is a factor of two higher as compared to the previously available 70 GHz ECRH system.

In the high density flat top phase a transition to a plasma state with better global confinement occurs. The density starts to increase further after the transition, although the external gas feed is turned off by the feedback system, which indicates an improved particle confinement. The most pronounced signatures of the transition is a drop of the D_a line emission signals from both limiters indicating a reduced particle recycling. Edge localized modes (ELMs) as a significant fingerprint of H-mode discharges as well as quiescent ELM-free H-mode phases of over 100 ms were observed.

The electron temperature profile as a whole increases after the transition and, in particular, a pronounced steepening of the edge temperature gradient is observed. The edge ion temperature measured by impurity line broadening increases also after the transition, which, together with the measured steepening of the edge density gradients gives clear evidence for the development of a transport barrier close to the plasma edge. An enhanced poloidal plasma rotation velocity of up to 3.5 km/s was measured in the H-mode like phase by B-IV impurity line doppler measurements and indicates an increase of the radial electric fields from typically 30 to 100 V/cm. The rotational transform, the density and the edge condition (limiter position) are leading parameters for the achievement of the H-mode. Below a central density of about $(4-5) \cdot 10^{19}$ m^{-3} no transitions were observed, which explains a posteriori, that no clear H-mode was found in previous ECR-heated discharges, because of the density limitations from the cut off condition for 70 GHz heating. The H-mode was observed in the vicinity of major resonances of $\iota = 1/2$ or 1/3, in optimum confinement regimes.

The improvement of the energy confinement by typically a factor of two as compared to the L-mode is the most important figure of merit of the H-mode in divertor tokamaks. The confinement improvement in the H-mode of W7-AS is 50% in the best cases and comparable to the H-factor in limiter tokamaks. With the experience from these experiments H-modes were found also later on with NBI heating.

4. Electron cyclotron current drive

Stellarators are well suited for the investigation of ECCD, because the sensitivity limitations for the measurement of small currents are much lower in stellarators as compared to tokamaks, where the EC-driven currents have to be discriminated against large inductively driven currents. Furthermore the flexibility in the magnetic configuration allows to investigate the current drive physics and the related wave particle interaction in phase space with high accuracy.
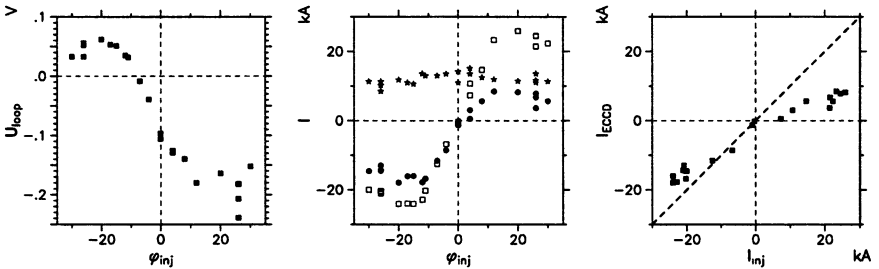
Fig. 5. Left: Loop voltage vs. toroidal angle of injection in net current free discharges. Perpendicular injection corresponds to $\varphi_{inj} = 0°$. Centre: Theoretical (open squares) and data from current balance of the EC-driven current (dots) together with the bootstrap current (stars) as a function of the launch angle. Right: EC-driven current from current balance versus linear prediction.

A toroidal launch angle scan is shown in Fig. 5 with 1.2 MW power in X2-mode [18] from low field side at a density of $2.5 \cdot 10^{19}$ m^{-3}. Net current free conditions with $I_{ind} + I_{boot} + I_{ECCD} = 0$ (I_{ind} is the inductive component, I_{boot} and I_{ECCD} are the bootstrap and the EC-driven components, respectively) were maintained with inductive current compensation. During the scan the toroidal magnetic field was adjusted to keep the Doppler shifted deposition profile close to the plasma axis ($\Delta B/B \cong 5\%$ for $|\varphi_{inj}| = 30°$). Under these conditions, ray-tracing calculations predict a peaked deposition profile with flux surface averaged power densities of up to 50 MW/m^3. The required inductive loop voltage for current compensation is shown in Fig. 6 (left) as a function of the launch angle φ_{inj} ($\varphi_{inj} = 0°$ corresponds to perpendicular injection, $I_{ECCD} = 0$). For a quantitative comparison of the measured data with theory we assume a linear superposition of the three cur-

rent contributions. The bootstrap current is calculated by the DKES code taking into account the ambipolar radial electric field and the inductive current is calculated assuming neoclassical resistivity (effective charge ranges from $Z_{eff} = 3$–6 for the different discharges). The calculations are performed for each discharge using the measured profiles of n_e and T_e. The different current contributions are plotted in Fig. 5 (middle). The EC-driven current is derived from the current balance $I_{ECCD} = -I_{ind} - I_{boot}$ and is plotted in Fig. 5 (right) versus the linear theoretical ECCD current, I_{inj} from ray-tracing (adjoint approach with trapped particles included). Fairly good agreement with linear theory is observed even at these extremely high power densities except for launch angles in co-direction. This may be a hint for a degradation of the CD-efficiency at high power density.
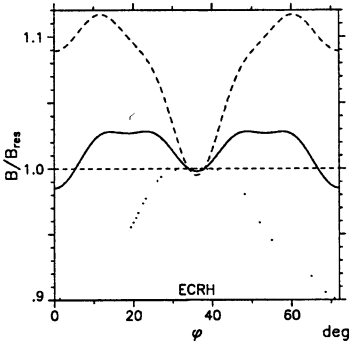
Fig. 6. Magnetic field strength on-axis, normalized to the resonant field at the ECRH launching position, versus the toroidal angle within one field period for $i_a \sim 0.345$. The solid line refers to the "standard" configuration of W7-AS, the dashed and the dotted lines correspond to the "minimum B" and the "maximum B" launching scenarios, respectively.

The EC-wave absorption increases the perpendicular energy of electrons and thus particles, which are trapped in magnetic mirror fields have significant influence on the CD-efficiency. Current drive modeling [19] tends to overestimate the CD-efficiency by a factor of 2–3 if trapped particle effects are neglected. The role of trapped particles in the ECCD physics was investigated by making use of the unique W7-AS flexibility to operate at different magnetic mirror configurations [20].

A launch angle scan was performed with inductive compensation of the EC-driven current ($I_p = 0$) for two magnetic configurations with a similar toroidal magnetic mirror ratio as shown in Fig. 6. The fraction of trapped particles, however, was changed by changing the toroidal ripple on the magnetic axis in the toroidal position of power launching at $\varphi = 36°$. For case 1 the magnetic mirror maximum was placed in the ECRH plane, i. e. mainly passing particles are directly heated and the impact on the driven current is mainly by the friction with the background trapped particles (dotted line in Fig. 6). For case 2 the minimum of the magnetic mirror was placed in the ECRH plane and, following ray-tracing predictions, the power is mainly absorbed by trapped and barely passing particles (dashed line in Fig. 6).

As seen from Fig. 7, the loop voltage at perpendicular launch ($\varphi = 0$) with no ECCD is non-zero for both cases and represents the voltage for bootstrap current compensation. The loop voltage and thus the driven current is much larger in case 1 (Fig. 7, top, left, note the different scales) as compared to case 2 (Fig. 7, top, right). A large fraction of ECCD power is absorbed in this case directly by trapped particles, which do not contribute to current drive. The ECCD efficiency even changes sign in case 2, which is a consequence of the ECRH induced trapping of otherwise barely passing particles. As shown in Fig. 7 (bottom), the experimental agree well with the calculated CD-efficiency from linear theory [21, 22].
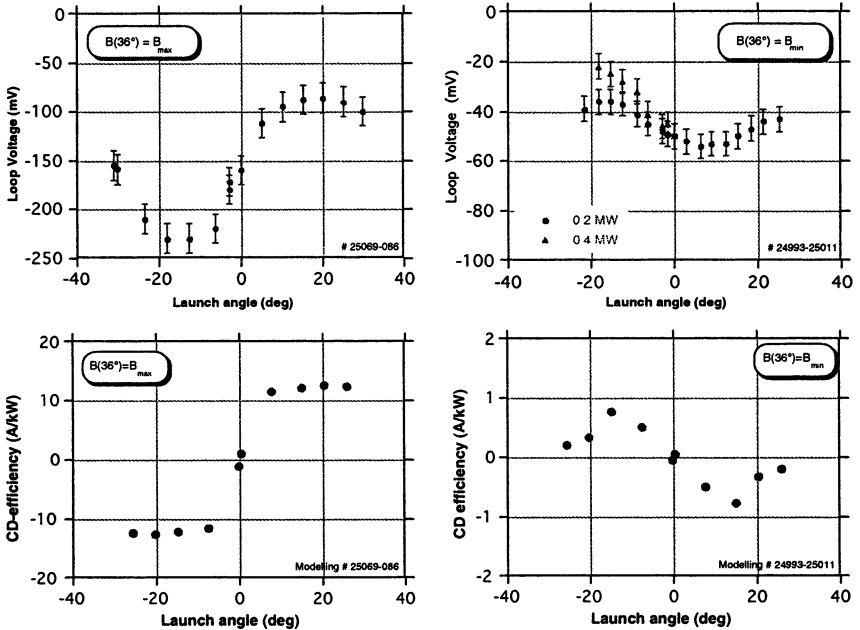
Fig. 7. Effect of trapped particles on ECCD. Top: Loop voltage response on a launch angle scan with plasma net current $I_p = 0$ for two magnetic field configurations in W7-AS. The ECCD power is 0.4 (triangles) and 0.2 MW (dots). Bottom: Current drive efficiency from linear theoretical modelling based on the experimental profiles of density and temperature.

5. Mode conversion heating via the O-X-B process

The standard ECRH scenarios have intrinsic density limitations by the cut-off condition. In view of reactor relevant conditions it may be desirable to have ECRH-access to even higher densities. This is provided by O2-mode launch,

which has a weak absorption at W7-AS parameters, but is a promising candidate at W7-X [23]. Another candidate is the O-X-B mode conversion process [24] as a possibility to overcome density limitations. The essential part of this scheme is the conversion of an O-wave at oblique launch from the low field side into an X-wave at the O-wave cut-off layer.

As shown in Fig. 8 the transverse refractive indices N_x of the O-wave and X-wave are connected at the optimal launch angle with a corresponding longitudinal (parallel B) index $N_{z,\mathrm{opt}}^2 = Y(Y+1)$ with $Y = \omega_{ce}/\omega$ (ω is the wave frequency, ω_{ce} is the electron cyclotron frequency) without passing a region of evanescence ($N_x^2 < 0$). For optimal launch an evanescent region always exists near the cut-off surface whose geometrical size depends on the density scale length $L = n_e/(dn_e/dx)$. A considerable fraction of the energy flux, however, can be transmitted

Fig. 8. Refractive index N_x versus $(\omega_p/\omega)^2$ for the O-X-B conversion process at optimum launch angle.

through this region, if L becomes small [25]. Density fluctuations generally lead to a reduced O-X conversion efficiency and are taken into account in the modeling. A significant heating efficiency is obtained only at a very small density scale length (i.e. steep gradients) or a very low fluctuation amplitude. After the O-X-conversion the X-wave propagates back to the upper hybrid resonance (UHR) layer where the refractive index of the X-wave is connected to that of the electron Bernstein waves (EBW) as shown in Fig. 8 and conversion into EBWs may take place. The EBWs propagate then towards the plasma centre where they are absorbed by electron cyclotron damping. Efficient OXB-heating with 70 GHz 1st harmonic EBWs was already successfully demonstrated at W7-AS [7] but the higher harmonic OXB heating with 140 GHz EBWs remained unexplored until improved performance by divertor operation above the critical density of $2.4\cdot10^{20}$ m^{-3} was achieved recently. For RF-heating with 140 GHz electron Bernstein waves, this requires an interaction with at the third or higher harmonic. Note, that the cyclotron absorption is still high enough for efficient heating.

Three 140 GHz beams with a total power of 1.5 MW were launched at the optimum launch angle into an NBI sustained (up to 4 MW) high-density plasma (up to $3.5\cdot10^{20}$ m^{-3}). Here the optimisation criterion was the increase of plasma energy shown in Fig. 9 during the heating pulse and the related reduction of the non-absorbed ECRH stray radiation. A magnetic field scan was performed to achieve central power deposition. 4th harmonic heating with central power deposition is not accessible since the next harmonic appears at the edge. For the 2nd

harmonic we have achieved power deposition at an normalized effective radius of r/a = 0.3 cm. The central plasma temperature rises from about 270 eV to 310 eV during the EBW-heating and the temperature profile broadenes. The plasma energy content is increased during EBW-heating by about 40% and about half of this energy increase is due to the profile change. The EBW-heating efficiency was comparable with NBI despite the slight off-axis power deposition with 140 GHz 2nd harmonic EBW-heating. Since the plasma is optically thick for higher harmonic EBW, also third and fourth harmonic heating could be succesfully demonstrated with 140 GHz at 1.5 T and 1.1 T, respectively. The maximum achievable density is limited so far by the heating power, which has to balance thermal losses. By additional EBW-heating this density limit could be-significantly increased.
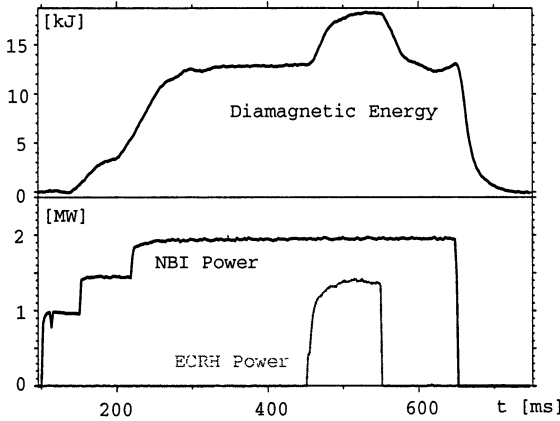
Fig. 9. Total stored plasma energy (top) and heating power(bottom) as a function of time during electron Bernstein wave heating (140 GHz) at a density of $3.5 \cdot 10^{20}$ m^{-3} and a magnetic field of 2.12 T.

Recently we have performed first experiments on current drive by EBWs. Due to their electrostatic character the parallel component of the refractive index can become of the order of unity implying a high EBW current drive (EBCD) efficiency [26]. Since the CD efficiency scales like T_e/n_e the experiment were performed with 70 GHz first harmonic EBW-heating at a density of $1.05 \cdot 10^{20}$ m^{-3}. An ECRH beam with 0.45 MW power was launched to a net-current free NBI (0.5–1 MW) sustained target plasma. The magnetic field was adjusted to 2.15 T for central power deposition. Here the large $N_\parallel$ (≈ 1) component of the EBWs requires a stronger reduction of the resonant magnetic field than for standard ECCD with electromagnetic waves. Since O-X-B mode conversion requires a fixed optimal launch angle no angular scan is possible to investigate the driven current. However the $N_\parallel$ component of the EBWs was varied by both, the magnetic field reversal and the change of the magnetic configuration (see Fig. 6).

The loop voltage represents a measure for the driven current in net current free discharges. The highest CD efficiency was achieved in the case of co-EBCD (see Fig. 10, left). Here with 450 kW a current of 1.85 (+1, −0.5) kA was driven. In a similar discharge, but with zero loop voltage, the plasma current rises to about 1.2 kA during the EBW-heating (Fig. 10, right).

292
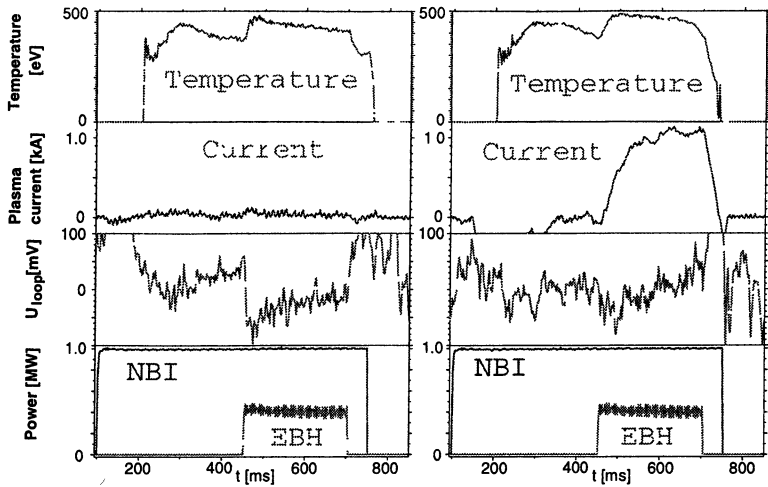
Fig. 10. EBW-current drive at a plasma density of $1.1 \cdot 10^{20}$ m^{-3}. Net current free discharge with inductive compensation of the EBCD current (left) and with free running plasma current (right).

Fokker – Planck calculations were performed for the experimental plasma parameters to estimate the distortion of the electron distribution function and the resulting current. Due to a large $N_{\parallel}$ value and to the associated strong Doppler shift, the EC-interaction takes place at more than two times the thermal velocity. Thus the quasi-linear diffusion is situated far away from the trapped electron loss cone, as illustrated in Fig. 11. Further, the resonance curve is no longer an ellipse as for $|N_{\parallel}| < 1$, but become a parabola for $|N_{\parallel}| = 1$ and a hyperbola for $|N_{\parallel}| > 1$. The perpendicular refractive index $N_{\perp}$ is about 40, which means that the wave length is of the order of the gyro radius. In that case the quasi-linear diffusion operator splits into many maxima (see Fig. 11). The calculated current was within the error bars in agreement with the experimental results.
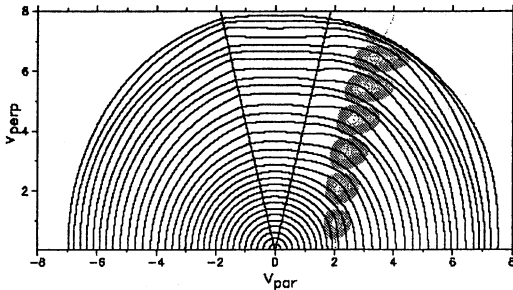
Fig. 11. Contours of the electron distribution function in a logarithmic scale as a function of the parallel velocity V_{par} and the perpendicular velocity V_{perp}. Both are normalised to the thermal velocity. The grey structure is the quasi-linear diffusion operator for EBWs with $N_{\parallel} = 1.0$. The calculation was limited to $|V| < 8 V_{thermal}$.

293

6. Conclusions

ECRH and ECCD was investigated in the IPP stellarators W7-A and W7-AS with strong effort to improve both, the experimental and theoretical tools. Significant contributions to the physics understanding of the wave-particle interaction in complex stellarator magnetic configurations were made. The deposition profile as well as the wave propagation physics was studied in quantitative detail. The deposition profiles in the long mean free path regime is affected by the wave interaction with trapped particles. The measured profiles consist of a very narrow peaked component, which contains the main power fraction (70–100%) and is consistent with the ray-tracing results representing absorption by the thermal bulk of the electron distribution function. A second component contains up to 30% of the total power and is much broader. This part depends on the number and distribution of trapped particles It is worth noting, that taking into account this effect results in a full power accountability of the launched power. The direct and indirect (friction of passing particles with background trapped electrons) interaction of trapped particles with EC-waves affects the current drive efficiency as measured in experiments with different magnetic mirror configurations and verified by CD-theory. Improved confinement modes were discovered which are related to strong ECRH. The rapid loss of trapped particles, which are pushed into the loss-cone by ECRH generates strong positive electric fields ("electron root") in the plasma centre, which in turn improves the central bulk confinement

Mode conversion heating and current drive via the O-X-B process was investigated experimentally. This heating scheme extends the ECRH application towards high densities beyond the cut-off density of the O-mode. Efficient O-X-B heating was demonstrated for the first time up to the fourth harmonic resonance at W7-AS. The efficiency of the process is determined by the density gradient scale length as well as density fluctuations at the O-X-conversion layer. The experiments benefit from the steep density gradients, which are typical for W7-AS. First EBW current drive experiments in overdense plamas were investigated and good agreement with Fokker – Planck modelling is obtained.

References

1. *Erckmann V., Hartfuß H. J., Kick M., Renner H., Sapper J., Schauer F., Speth E., Wesner F., Wagner F., Wanner M., Weller A., Wobig H.,* The W7-AS team and the W7-X teams, Proc. of the 17th IEEE/NPSS Symposium Fusion Engineering (San Diego, 1997), v. 1, p. 40.
2. *Wilhelm R., Janzen G., Müller G.,* et al., Plasma Phys. and Contolled Fusion, **26**, 259 (1984).
3. *Erckmann V.,* W7-AS Team, *Kasparek W., Müller G. A., Schüller P. G. and Thumm M.:* Electron Cyclotron Resonance Heating Transmission Line and Launching System for the W7-AS Stellarator. Fusion Technology, **17**, 76 (1990).
4. *Erckmann V., Gasparino U., Giannone L., Hartfuß H. J., Maaßberg H., Tutter M.,* W7-AS Team, *Kaparek W., Müller G. A., Schüller P. G., Dammertz G., Gantenbein G, Geist T., Kuntze M., Nickel H. U., Pioczyk B. and Thumm M.,* Int. School of Plasma Physics (ISPP-10), High Power Microwave Generation and Application (Varenna, Italy, 1991), p. 511

5. *Erckmann V., Alexandrov N., Il'in V. I., Kurbatov V. I., Malygin S. A., Malygin V. I.,* W7-AS Team and ECRH Group, Proc. 20th EPS Conference on Controlled Fusion and Plasma Physics, Lisboa, Poland, Eds.: J. A. Costa Cabral, M. E. Manso, F. M. Serra, F. C. Schüller, **17C**, 345 (1993).

6. *Erckmann V., Burhenn R., Geist T., Hartfuss H. J., Kick M., Maassberg H.,* W7-AS Team, *Kasparek W., Müller G. A., Schüller P. G., Il'in V. I., Kurbatov V. I., Malygin S., Malygin V. I.,* Radio Frequency Power in Plasmas, Ed. M. Porkolab, J. Hosea, (New York, USA, 1993), AIP Conf. Proc., **289**, 137.

7. *Laqua H. P., Erckmann V., Hartfuß H. J., Laqua H.,* W7-AS Team, and ECRH Group, Phys. Rev. Lett., **78**, 3467 (1997).

8. *Erckmann V.,* W7-A Team, NI-Team (W7-A5) and ECRH Group (IPF Stuttgart), Plasma Physics and Controlled Fusion, **28** (9A), 1277 (1986).

9. *Hartfuß H. J., Maaßberg H., Tutter M.,* W7-A Team, ECRH Group, Nuclear Fusion, **26**, 678 (1986).

10. *Gasparino U., Erckmann V., Hartfuß H. J., Maaßberg H., Rome' M.,* Plasma Phys. Control. Fusion, **40**, pp. 233–244 (1998).

11. *Ejima S., Okabayashi M., Schmidt J.,* Phys. Rev. Lett., **32** (16), 872 (1974).

12. *Erckmann V.,* ECRH-Team (IPF Stuttgart) and W7-A Team: Proc. 10th Int. Conf. on Plasma Physics and Controlled Nucl. Fusion Research (London, 1984), IAEA Vienna, v. 2, p. 419.

13. *Maaßberg H., Beidler C. D., Erckmann V., Gasparino U., Geiger J., Laqua H., Marushchenko N., Murakami S.* and the W7-AS Team, Strong Microwaves in Plasmas, Editor A. G. Litvak (Inst. of. Appl. Physics, Nizhny Novgorod, Russia, 2000), v. 1, p. 7–26.

14. *Wagner F.* et al., Phys. Rev. Lett., **42**, 1408 (1982).

15. *Odajima K.* et al., Plasma Physics and Contr. Nucl. Fusion Research (1986), IAEA, Vienna (1987), v. 1, p. 151.

16. *Kaye S. M., Bell M. G., Bol K.,* Nucl J. Mat., **121**, 115 (1984).

17. *Erckmann V., Bogdanov S. D., Borschegovsky A. A., Hiznyak V. I., Il'in V. I., Kasparek W., Kubo S., Kuftin A. N., Kurbatov V. I., Malygin S. A., Malygin V. I., Orlov V. B., Pech P., Roi I. N., Schüller P. G. and Wagner F.,* Phys. Rev. Lett., **70** (14), 2086 (1993).

18. *Erckmann V., Laqua H. P., Maassberg H., Geiger J., Dammertz G., Kasparek W., Thumm M.,* W7-X and W7-AS teams IPP, W7-X team FZK, W7-X team IPF Stuttgart, Fusion Engineering and Design, **53**, 365–375 (2001).

19. *Gasparino U.,* Theory of Fusion Plasmas, Varenna, 195 (1990).

20. *Erckmann V., Gasparino U., Hartfuß H.-J.,* W7-AS Team, NBI Team, *Kasparek W., Müller G. A., Schüller P. G., Borschegovsky A., Il'in V. I., Kurbatov V. I., Malygin S., Malygin V. I.,* Fusion Engineering and Design, **26**, 141 (1995).

21. *Rome' M., Erckmann V., Gasparino U. and Karulin N.,* Plasma Phys. Control. Fusion, **40**, 511–530 (1998).

22. *Gasparino U., Idei H., Kubo S., Marushchenko N., Rome' M.,* Nucl. Fusion, **38** (2), 223 (1998).

23. *Erckmann V., Karulin N. and Wobig H.,* Proc. 21st EPS Conference on Controlled Fusion and Plasma Physics, v. 18B, Part II, p. 1008 (1994).

24. *Preinhaelter J. and Kopecky V.,* J. Plasma Phys., **10**, 1 (1973).

25. *Mjølhus E.,* J. Plasma Phys., **31**, 7 (1984).

26. *Litvak A. G.* et al., Phys. Letters A., **188**, 64 (1994).

CONFINEMENT AND STABILITY STUDIES
WITH ECRH IN ASDEX UPGRADE

H. Zohm, G. Gantenbein[1], A. Keller, F. Leuterer,
M. Maraschek, A. Mück, R. Neu, F. Ryter, J. Stober,
W. Suttrop and the ASDEX Upgrade Team

MPI für Plasmaphysik, Garching, Germany, EURATOM Association
[1]Institut für Plasmaforschung, Stuttgart University, Stuttgart, Germany

Recent results regarding confinement and stability studies using ECRH in the ASDEX Up-
grade tokamak are reported. Progress has been made in understanding heat and particle
transport in terms of a "stiff" temperature profile model together with the assumption that
particle transport is closely coupled to the energy transport, but includes an inward pinch of
the order of the neoclassical Ware pinch. Regarding stability, it has been possible to sig-
nificantly increase β during NTM stabilization by ECCD. Finally, sawtooth control by
small amounts of ECRH/ECCD power in a dominantly NBI heated discharge was demon-
strated.

1. Introduction

The research program of the ASDEX Upgrade tokamak [1] (R_0 = 1,65 m,
a = 0,5 m, a cross-section is shown in the left part of Fig. 1) is oriented towards
the preparation of ITER. This includes physics studies in all three major areas of
interest, i.e. transport, stability and exhaust as well as technical issues related to
heating, fuelling and exhaust systems. In the areas of confinement and stability,
recent experimental success has been achieved by the use of ECRH and ECCD
due the unique flexibility of this heating scheme, both in deposition as well as in
temporal variation. This paper summarizes the results achieved in 2001 and
2002.

2. The ASDEX upgrade ECRH system

ASDEX Upgrade is at present equipped with 4 GYCOM gyrotrons (see
Fig. 1, right part) operating at 140 GHz corresponding to absorption at the second
harmonic of the electron cyclotron frequency at 2,5 T [2, 3]. The gyrotrons can
deliver 500 kW each in normal operation for 2 s and 700 kW for 1 s in the so-
called "optional regime". The microwaves are injected from 4 independently
steerable launchers, allowing the poloidal and toroidal injection angles to be
changed on a shot-to-shot basis.

This setup allows for a great flexibility in deposition. The position and width
of the deposition have been measured from modulated ECRH and power switch-
on experiments and are in good agreement with TORBEAM modeling [4], pro-

viding a firm basis for experimental studies in which narrow and precise localization of the power deposition is used as a tool.
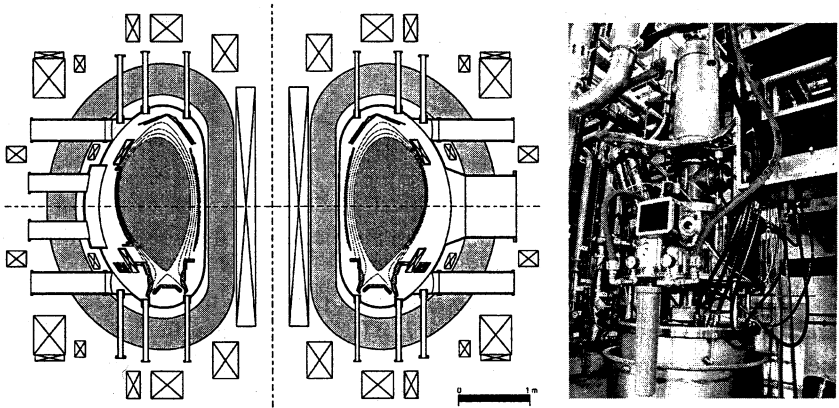
Fig. 1. Cross-section of the ASDEX Upgrade tokamak (left) and assembly of one of the 140 GHz GYCOM gyrotrons (right).

3. Electron heat transport

On ASDEX Upgrade, both electron temperature T_e [5] as well as ion temperature T_i [6] profiles usually show a "stiff" behavior in the sense that, for a given boundary condition (i.e. edge temperature), the profile in the confinement region exhibits a relation $1/L_T = \nabla T/T \approx$ const. This behavior is also seen in other tokamaks [7]. This can be motivated with the theoretically expected onset of temperature gradient driven turbulence such as ITG/TEM or ETG modes below a certain value of the gradient length. As a consequence, one expects a fixed ratio of temperatures at two radii, which is indeed found to be true for $T(\rho = 0,4)/T(\rho = 0,8)$, where sawteeth usually do not strongly influence the transport.

Based on these considerations an empirical model has been developed and successfully tested on ASDEX Upgrade [8]. It assumes a generic dependence of the electron heat diffusivity as a function of the critical gradient length of the form

$$\chi_e = \chi_{e0} + \lambda q T^{3/2} \left(\frac{1}{L_{Te}} - \left(\frac{1}{L_{Te}} \right)_{crit} \right) H \left(\frac{1}{L_{Te}} - \left(\frac{1}{L_{Te}} \right)_{crit} \right), \tag{1}$$

where H is the Heaviside function, λ a free parameter and χ_{e0} describes the (small) residual transport in the absence of turbulence. In particular, this model

predicts a different behavior of the heat diffusivity when the power flux is modulated around a certain value: it has been shown before that, in this case, which applies for heat wave propagation experiments, the heat pulse diffusivity χ_{HP} can be derived from the steady state power balance heat diffusivity $\chi_{PB} = -q/n\nabla T$ by $\chi_{HP} = (\partial\chi_{PB}/\partial\nabla T)\,\nabla T$ [9] if the dominant variation is due to the temperature gradient. For the specific form of Eqn. (1), this gives

$$\chi_{HP} = \chi_0 + 2\lambda q T^{3/2}\left(\frac{1}{L_{Te}} - \left(\frac{1}{L_{Te}}\right)_{crit}\right)H\left(\frac{1}{L_{Te}} - \left(\frac{1}{L_{Te}}\right)_{crit}\right), \qquad (2)$$

i. e. χ_{HP} is expected to jump at the critical gradient and then to have a higher value than χ_{PB}. Note that, for conditions in the vicinity of the threshold, this leads to substantial differences between χ_{HP} and χ_{PB}.

Experiments were carried out in ASDEX Upgrade to test this behavior. In a series of discharges with plasma current $I_p = 0,8$ MA, toroidal field $B_t = 2,3$ T and line averaged electron density $n_e = 2 \cdot 10^{19}$ m^{-3}, the total ECRH power was kept constant, but the power was deposited in two different locations with different respective power levels that were varied from discharge to discharge [10]. The experimental values of χ_{HP} are deduced from the Fourier transform of T_e by the usual methods [9].

The results are shown in Fig. 2. On the left side, the T_e profiles for these cases are shown. It can be seen that due to the constant total heating power and therefore the constant power flux through the edge, the edge conditions stayed basically the same throughout this series of experiments. Conversely, in the plasma core, the power flux was varied by up to a factor of 10. In response to this, also the core T_e profiles show a variation in ∇T_e and $\nabla T_e/T_e$. Clearly, the case with the strongest central heating shows the highest temperatures. In addition, the gyrotron power was partially with a modulation amplitude of 20 % in order to probe the heat pulse diffusivity.

On the right side of Fig. 2, the analysis of the experimental data in terms of heat diffusivity is shown [7]. All evaluations were done at fixed radius $\rho = 0,5$. The full circles show the results from power balance analysis. The full red line is a fit to the experimental points using Eq. (1). The fit parameters are $q\lambda$ and $\kappa = (1/L_{Te})_{crit}$ (note that χ_{e0} in Eq. (1) is so small that we have neglected it in the fit). With these parameters, we then calculate the heat pulse diffusivity from Eq. (2). This is shown on the right hand side of Fig. 2 by the dashed line. Also shown are the experimental values for the modulated ECRH, i. e. the heat pulse diffusivities (open circles). A very good agreement is obtained, giving strong evidence for the underlying physics picture of a critical gradient for onset of turbulence. It should also be noted that a more sophisticated model, namely the Weiland ITG/TEM model gives an equally good description of similar experiments [11].

298
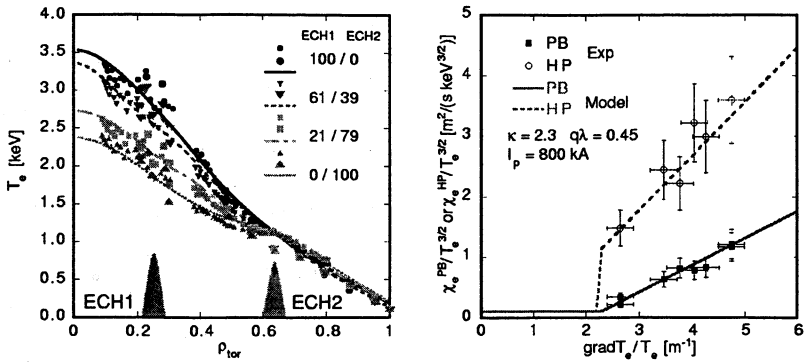
Fig. 2. Electron temperature profiles from a series of experiments in which the ECRH power was varied between two different locations, but kept constant in total (left). The right figure shows the evaluated heat diffusivities from power balance and for modulated ECRH, i. e. the heat pulse diffusivity.

In Fig. 2, it can also be seen that with the lowest heat flux in the center, we come close to the marginal point at which turbulence sets in. This marginal point agrees well with that predicted from TEM turbulence, but does not agree with that ETG turbulence which is too high by a factor of about 2. Also, Fig. 2 demonstrates that there is a certain variation in L_{Te}, pointing towards the fact that, as can also be seen from the analysis of the heat diffusivities, the usual operating point is not situated at the marginal point of turbulence onset, but somewhat above. The profiles are only "moderately stiff", but the model of a critical gradient for turbulence onset still presents the correct physics picture.

Finally, it should be noted that in experiments with internal transport barriers (ITBs), the critical gradient can by far be exceeded locally within the ITB because turbulence is suppressed. By using 1,6 MW of ctr-ECCD in a low density discharge, electron temperatures in excess of 20 keV could thus be reached [12].

4. Particle transport

In addition to energy transport, it is also of major interest to understand the transport of particles in a magnetically confined fusion plasma. Density profiles are usually not "stiff" in the sense that a fixed ratio of density values at different radii is observed. Instead, the degree of peaking is found to vary, depending on the experimental conditions [13]. One common observation is the fact that with central heating, a reduction of density peaking is observed, whereas off-axis heating favors peaking. This may be most pronounced with ECRH, which provides strong local heating, and has been called "ECRH pump-out" of particles [14].

299

On ASDEX Upgrade, a heuristic model has been successfully applied to model this behavior [15]. It is based on the assumption of a close coupling between heat diffusivity χ and the particle diffusion coefficient D, i. e. $D \propto \chi$. In addition, an inward pinch for the particles of the order of the neoclassical Ware pinch is taken into account. These assumptions, together with the spatial decoupling of the source for the turbulence (the heating power) and the source for the particles (usually the ionization of neutral particles introduced via gas puff in the edge) can describe the non-stiff behavior of the density profiles and, in particular, the dependence of density peaking on the central heating.

Fig. 3 shows an example from an L-mode discharge in ASDEX Upgrade in which 1.6 MW of central ECRH power was applied and the density profile responded with a flattening. Due to the nonlinear dependence of χ_e, a sharp increase in heat diffusivity occurs in the center. This in turn leads to an increase of D in our model and thus, the enhanced particle transport dominates the inward pinch and the density profile flattens, as can be seen in the right part of Fig. 3.
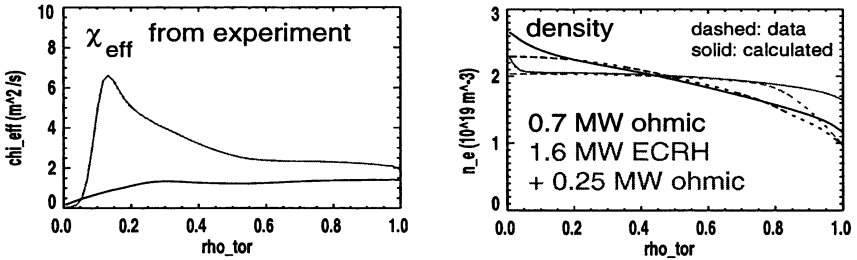
Fig. 3. Heat diffusivity (left) and modeled density profile (right) for a discharge with central ECRH power. Density profile flattening occurs as a consequence of coupled particle and heat diffusivities.

These findings also have a consequence for impurity transport. Under circumstances with strong density peaking, a tendency for accumulation of impurities in the plasma center is observed. This can be understood by neoclassical transport that predicts a much stronger accumulation for high Z impurities than for hydrogen. In ASDEX Upgrade, where the inner wall is partly covered by W, an accumulation of W can be observed when strong density peaking occurs (under usual circumstances, W does not accumulate in ASDEX Upgrade discharges) [16].

Figure 4 shows an example for such a discharge (#14225) in which off-axis heating was supplied by 3.4 MW of NBI heating with a reduced acceleration voltage (38 keV instead of the usual 65 keV). It can be clearly seen that the slow density rise is accompanied by a large increase of the central W-concentration c_W. Also shown is a discharge in which 1,2 MW of central ECRH is added. A dramatic decrease of the W-concentration results; after switch-off of the ECRH, c_W

starts to rise again. The electron density profiles shown in the right part of Fig. 4 show that indeed the profiles are peaked when W accumulates and that ECRH flattens the density profile; thereby strongly reducing the neoclassical inward drift for high Z impurities [17].
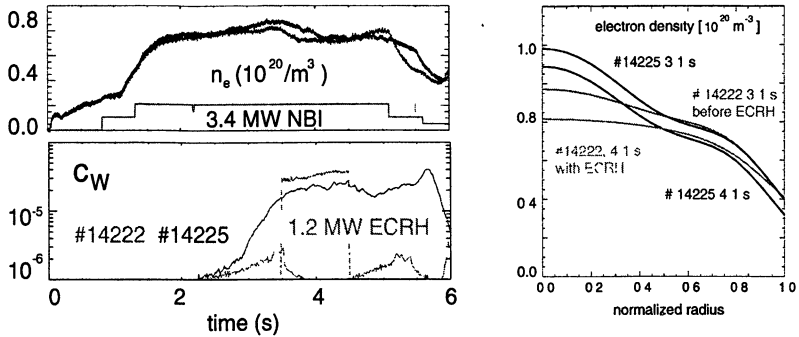
Fig. 4. *W*-accumulation in a discharge with off-axis heating and density profile peaking. The addition of central ECRH dramatically reduces the tendency for *W*-accumulation.

5. Neoclassical tearing mode (NTM) stabilization

A main objective of ECRH experiments on ASDEX Upgrade is to study the effect on MHD stability. In particular, it was shown that NTMs, that give rise to concerns for ITER since their onset β_N has been found to scale unfavorably with normalized ion gyro radius, can be stabilized by ECCD at the rational surface. In previous experiments, it had been found that, although the mode could be completely suppressed, the discharge did not completely recover its confinement properties at NTM onset [18]. This was attributed to the effect of ECCD on the discharge, namely the flattening of the density profile.

Recent experiments have therefore focused on the increase of β by adding more NBI power while the NTM is stabilized by ECCD [19]. Figure 5 shows an example where β_N is increased above the onset value, but the mode then reappears.

Figure 6 shows the position of the rational surface indicated by the red trace, deduced from the phase jump of the ECE modulation due to the island. Note that there is a slow inward motion of the surface and an additional outward motion proportional to b due to the Shafranov shift. At the mode reappearance, the surface has moved by more than 3 cm. It had been shown before that the deposition must be precise within 2 cm of the rational surface to obtain optimum stabilization [18]. Thus, the reappearance of the mode cannot actually be attributed to a lack of ECRH power, but rather to a mismatch in positioning.

301
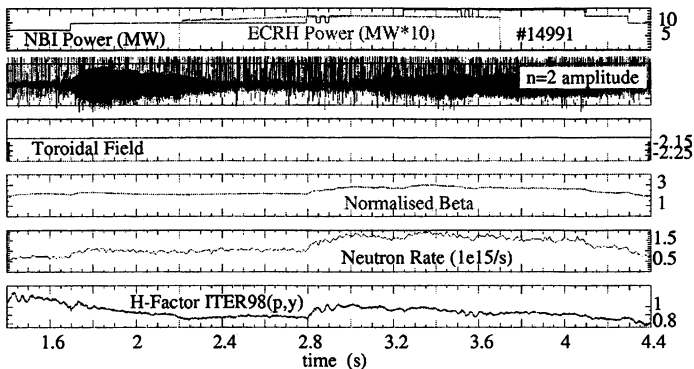
Fig. 5. NTM stabilization experiment with increase in total heating power during the phase in which ECCD stabilizes the mode. β_N can be increased above the onset value but then the mode reappears.
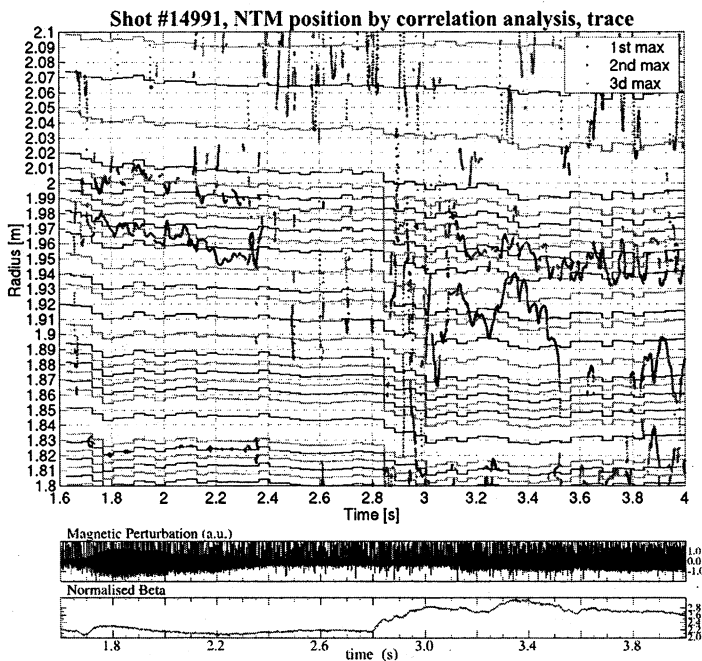
Fig. 6. Position of the (3, 2) surface derived from the phase jump of the modulation in ECE signals induced by the island (the darkest lines). The position can only be inferred when the island is present. The surface moves in time due to a slow global change an the effect of the Shafranov shift.

302
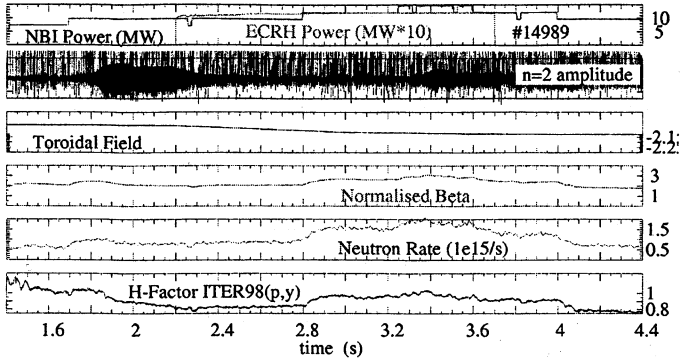
Fig. 7. NTM stabilization experiment with increase in total heating power similar to Fig. 5. Here, a feed-forward ramp in B_t is applied in order to better match the ECRH deposition to the mode rational surface and higher β_N is achieved.

Figure 7 shows an NTM stabilization experiment similar to the one shown in Fig. 5, but this time with a feed-forward ramp in B_t to account for the mismatch in deposition. Under these circumstances, β_N achieves a stationary value of 2,7, i. e. well above the onset level of 2,4. With even more NBI power, β_N exceeds 3 and the mode reappears. Again, ECE analysis of the mode rational surface and the ECCD deposition indicates a mismatch in this phase, so it is not clear if this value of β_N already represents the ultimate limit of the method or if even higher β_N is possible. This will be addressed in future experiments where the position of the mode and the deposition can be detected on-line from ECE measurements and the deposition is feedback controlled by a radial shift of the plasma, or, at an even later stage, by feedback control of the poloidal launch angle.

It should be noted that in the examples shown above, the confinement time expressed by the ITER98(p,y) scaling recovers to good H-mode confinement. However, this may also be linked to the fact that the NBI sources used here to increase β, deposit the heating power more off-axis and thus have a tendency to produce density peaking and better confinement [20]. In fact, the recovery of confinement in these discharges is also accompanied by a slight increase in density peaking, whereas the first reduction in confinement due to ECRH goes together with density flattening. Further experiments will also aim at sorting out these subtle details in the heating profile and their effect on confinement.

6. Tailoring of sawteeth with ECRH/ECCD

Another aspect of tokamak MHD stability that can be controlled by ECRH is the sawtooth instability. This central relaxation phenomenon leads to a repetitive mixing of the hot plasma core with the outer region, thereby reducing the energy

confinement time, but on the other hand also providing an effective means to get particles, such as the He ash in a fusion reactor, out of the center of the discharge. It has been found before that fast particles, such as those created by ICRH, tend to stabilize sawteeth [21], but may lead to so-called "monster" sawteeth that lead to huge crashes of the stored energy after long sawtooth-free periods. Thus, it is clearly desirable to have a method that not only suppresses sawteeth, but can actually be used to tailor period and amplitude. In addition, sawtooth crashes can lead to the triggering of NTMs by generating seed islands at rational surfaces prone to neoclassical tearing, an effect that may also be influenced by sawtooth tailoring [22].

Experiments were performed on ASDEX Upgrade to investigate the possibilities of tailoring sawteeth by ECRH and ECCD [23]. The target plasma was an ELMy H-mode discharge with line averaged electron density $n_e \approx 6 \cdot 10^{19}$ m^{-3}, heated with 5 MW of NBI power. An example is shown in Fig. 8, where central ctr-ECCD removes the sawteeth at a power level of 800 kW. In order to study the dependence of the sawtooth period on the ECRH / ECCD deposition, the toroidal magnetic field was slowly varied during some discharges. This was done for pure ECRH heating, for co-ECCD and for ctr-ECCD at a fixed microwave power of 800 kW.
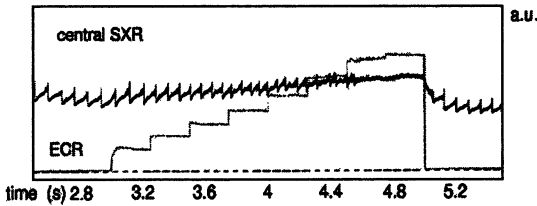
Fig. 8. Sawtooth stabilization by central counter-ECCD: at a power level of 800 kW, sawteeth are completely stabilized in a discharge with 5 MW of NBI heating.

Figure 9 shows the results of these scans for co- and ctr-ECCD. For reference, the sawtooth period in discharges without ECRH is also shown. Note that the jump in sawtooth period without ECRH at $\rho = -0,25$ comes from the use of different NBI sources (in ASDEX Upgrade, the amount of trapped particles, as well as the heating profile, are different for different NBI sources, leading to different sawtooth periods). For co-ECCD, stabilization of the sawteeth occurs when ECCD is done outside the sawtooth inversion radius (the precise location of the $q = 1$ surface is not clear in these experiments). This is consistent with a decrease of the local current density gradient there, which removes some of the drive for the sawtooth. Conversely, with ctr-ECCD we observe stabilization when the deposition is central, again consistent with a decrease in current density gradients around $q = 1$. Precise analysis of the MHD stability under these circumstances will be done in future work.
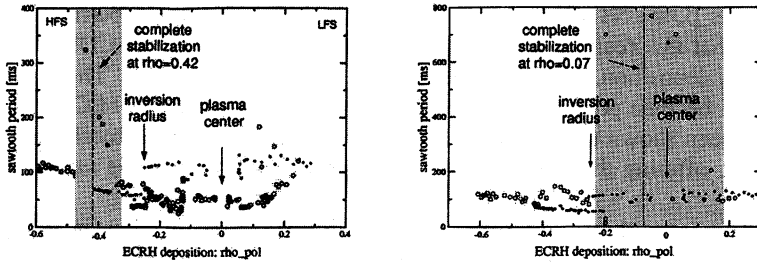
Fig. 9. Sawtooth period as a function of the ECCD deposition radius obtained from slow ramps of the toroidal field. Negative values of ρ indicate deposition on the high field side. Complete stabilization occurs for co-ECCD outside the sawtooth inversion radius (left) and for central ctr-ECCD (right).

The results for pure ECRH (not shown in Fig. 9) are similar to those obtained with co-ECCD. This can be explained by the fact that pure ECRH, due to its local heating, has a tendency to increase the current density around the deposition due to the lower resistivity; this effect adds up with the effect of co-ECCD, but subtracts from the current driven by ctr-ECCD. Thus, co-ECCD and ECRH should lead to qualitatively similar results, whereas the fact that ctr-ECCD produces the inverse trend, points towards a significant amount of current directly generated by ECCD, similar to previous findings in the analysis of NTM stabilization experiments [16].

An interesting point to note is that with central co-ECCD it is possible to decrease the sawtooth period, pointing towards a possible avoidance scheme of fast particle stabilized monster sawteeth by ECRH. In this sense, ECRH provides real tailoring of sawteeth rather than avoidance.

7. Summary and conclusions

ECRH has been used in ASDEX Upgrade to experimentally investigate heat and particle transport. It is found that a model based on the onset of turbulence above a critical temperature gradient length very well describes the experimental results, both in power balance as well as in heat pulse analysis. Coupling the particle diffusion coefficient to the heat pulse diffusivity and allowing for an inward pinch velocity of the order of the Ware pinch leads to an equally good description of particle transport. In particular the tendency of the density profiles to become flat under the application of ECRH is reproduced well. This effect has also been used to avoid central impurity accumulation, which can occur with peaked density profiles.

Concerning stability, ECCD has successfully been used to stabilize NTMs and operation above the usual onset β_N for NTMs has been demonstrated. At

even higher β, the NTM was found to reappear. Analysis of the experimental data suggests that this reappearance is due to a mismatch between ECCD deposition and mode deposition, calling for feedback-controlled deposition. These experiments will become possible in the near future in ASDEX Upgrade. ECCD/ECRH has also been shown to be a suitable tool for tailoring of the sawtooth repetition frequency, offering the possibility to either prolong or shorten the sawtooth period.

It is foreseen that in the future, the ASDEX Upgrade ECRH system will be extended to give more power and longer pulse length by adding gyrotrons with 1 MW and 10 s capability. These tubes are also designed to operate at different frequencies. In addition, the poloidal launch angle of the new launchers will be steerable in real time, allowing for an even more flexible use of ECRH in ASDEX Upgrade.

References

1. *Gruber O.* et al., Nucl. Fusion, **41**, 1369 (2001).
2. *Leuterer F.* et al., Fus. Eng. Design, **53**, 277 (2001).
3. *Leuterer F.* et al., Fus. Eng. Design, **56/57**, 615 (2001).
4. *Kirov K.* et al., "ECRH power deposition studies in ASDEX Upgrade", submitted to Plasma Phys. Contr. Fusion.
5. *Ryter F.* et al., Phys. Rev. Lett, **86**, 2325 (2001).
6. *Tardini G.* et al., Nucl. Fusion, **42**, 258 (2002).
7. *Ryter F.* et al., Plasma Phys. Contr. Fusion, **43**, A323 (2001).
8. *Imbeaux F.* et al., Plasma Phys. Contr. Fusion, **43**, 1503 (2001).
9. *Lopez-Cardoso N.* et al., Plasma Phys. Contr. Fusion, **37**, 799 (1995).
10. *Ryter F.* et al., 19th IAEA Fusion Energy Conference (2002) IAEA-CN-94 EX/C4-2Ra.
11. *Tardini G.* et al., Nucl. Fusion, **42**, L11 (2002).
12. *Peeters A. G.* et al., 19th IAEA Fusion Energy Conference (2002) IAEA-CN-94 EX/P4-03.
13. *Stober J.* et al., Plasma Phys. Contr. Fusion, **43**, A39 (2001).
14. *Erckmann V.* et al., Plasma Phys. Contr. Fusion, **36**, 1869 (1994).
15. *Stober J.* et al., Nucl. Fusion, **41**, 1535 (2001).
16. *Neu R.* et al., Plasma Phys. Contr. Fusion, **44**, 811 (2002).
17. *Dux R.* et al., "Accumulation of impurities in Advanced Scenarios", accepted for publication in Journal of Nucl. Materials.
18. *Zohm H.* et al., Phys. Plasmas, **8**, 2009 (2001).
19. *Gantenbein G.* et al., 29th Conference on Plasma Phys. and Contr. Fusion (Montreux, Switzerland, ECA, 2002), **26B**, P-1.036.
20. *Stäbler A.* et al., 29th Conference on Plasma Phys. and Contr. Fusion (Montreux, Switzerland, ECA, 2002), **26B**, O-5.03.
21. *Campbell D.* et al., Phys. Rev. Lett., **60**, 2148 (1988).
22. *Sauter O.* et al., Phys. Rev. Lett., **88**, 105001 (2002).
23. *Mück A.* et al., 29th Conference on Plasma Phys. and Contr. Fusion (Montreux, Switzerland, ECA, 2002), **26B**, P-1.037.

RECENT RESULTS OF ECH EXPERIMENT
BY AN UPGRADED HEATING SYSTEM IN LHD

T. Shimozuma, S. Kubo, H. Idei, Y. Yoshimura, T. Notake[1],
T. Watari, Y. Mizuno, S. Ito, S. Kobayashi, Y. Takita, M. Sato,
K. Ohkubo, K. Ida, N. Ohyabu, I. Yamada, K. Narihara,
S. Inagaki, Y. Nagayama, Y. Takeiri, H. Funaba, M. Yokoyama,
S. Murakami and the LHD Experimental Group

National Institute for Fusion Science,
322-6 Oroshi-Cho, Toki-City, Gifu, 509-5292 Japan
[1]Nagoya University, Graduate School of Energy Engineering and Science,
Furoh-Cho, Chikusa-Ku, Nagoya, 464-8601 Japan

Continuous improvements on the Electron Cyclotron resonance Heating (ECH) system
have realized over 1,8 MW injection power on the Large Helical Device at the 5th experi-
mental campaign. The improvements are not only installation of new gyrotrons, but also
improvement of transmission efficiency by means of realignment of the waveguides. Those
hard-working efforts to establish the high power and reliable system enabled to achieve
some epochal results such as over 10 keV electron temperature, over 150 kJ stored energy
plasmas and the formation of a internal transport barrier, proving that ECH is an effective
heating method in a large heliotron-type machine.

1. Introduction

The experiment on the Large Helical Device (LHD) has been extensively
proceeding since 1998 in the National Institute for Fusion Science (NIFS) [1, 2].
The Electron Cyclotron Heating (ECH) is one of the effective methods to pro-
duce and heat plasmas in LHD. Its high power density and localization of the
deposition can be used for the controls of plasma pressure and current profiles,
which lead to the stabilization and/or destabilization of some instabilities in high
temperature plasmas.

In the last experimental campaign, some upgrades of the ECH system were
undertaken. These efforts contributed to the over 1,8 MW injection into the LHD
vacuum vessel, and opened the new regime of high temperature and low colli-
sional plasma.

In this report, the ECH system on the LHD will be described in detail, in-
cluding upgrades executed in the system. Furthermore new experimental results
obtained in the latest campaign will be overviewed.

2. LHD project

The LHD is the largest heliotron-type device ($l = 2$, $m = 10$) with two helical coils and three pairs of poloidal coils which are all superconducting magnets for steady state operations. The maximum magnetic field reaches 3 T on the magnetic axis of 3,5 m. Major and minor radii of the produced plasmas are typically 3,6 m and 0,6 m, respectively.

Objectives of the LHD project are the production of currentless plasmas in high temperature and low collisionality regime on the heliotron-type magnetic field configuration and the elucidation of the important research issues in physics and engineering for the heliotron-type plasma reactors.

Following main targets are given. 1) Confinement study of high performance plasmas, i. e. high fusion triple products and high β plasmas, which can be extrapolated to the fusion-relevant plasma researches. 2) Divertor study and quasi-steady state plasma sustainment over 30 minutes. 3) Researches of high energy particles. 4) Total understanding of toroidal plasma physics by complementary approach to tokamaks.

Obtained plasma parameters so far are summarized in Table 1.

Table 1. **Main plasma parameters obtained in LHD**

Max. electron temperature	10 keV	Max. β value	3,2% at 0,5 T
Max. ion temperature	5 keV	Max. density	$1,6 \cdot 10^{20}$ m^{-3}
Max. confinement time	0,36 s	$n\tau Ti$	$2,2 \cdot 10^{19}$ keVm^{-3}s
Max. stored energy	1,16 MJ	Plasma sustainment	2 min by ICRF

3. Features of recent ECH system

The ECH system for LHD has been improved step by step. The ECH experiments on LHD started with the three-gyrotron system (one 84 GHz, one 82,7 GHz and one 168 GHz gyrotrons) at first cycle campaign of 1998. At the second cycle campaign one more 84 GHz gyrotron could be operated. In 1999 (third cycle) the ECH system was upgraded to six-gyrotron system, which consisted of one 84 GHz, two 82,7 GHz and three 168 GHz gyrotrons. The 84 GHz gyrotron allowed plasma productions in two minutes at low injection power level of 50 kW [3]. The fourth experimental campaign in 2000 proceeded with five gyrotrons (two 82,7 GHz and three 168 GHz gyrotrons). The reconsideration of transmission paths, the replacement of phase correcting mirror in the MOUs and the realignment of the corrugated waveguide improved the transmission efficiency by 10% on the average.

At the last experimental campaign (fifth cycle) in 2001, two more 84 GHz gyrotrons (0,8 MW/3 s) have been installed. The seven-gyrotron system realized over 1,8 MW injection power into LHD. Beside one new evacuated transmission line was prepared for one 84 GHz line to transmit higher power. For LHD high reliability of ECH system operation is required. For this purpose, the multi-optical arc detectors were equipped on the miterbends to protect gyrotrons from dangerous arcing in the waveguides and windows. Real time power monitors set on the miterbends helped to detect reflected millimeter waves and spurious oscillation in the gyrotrons. Big brick or stainless steel dummy loads were installed in the transmission lines near LHD to accelerate long pulse conditioning including gyrotrons and transmission lines. According to the inward sift of LHD plasma configuration, the scanning range of the antenna focal point was modified. One newly installed antenna had a larger scanning area in both poloidal and toroidal directions.

LHD Main Hall   **Heating Device Room**

Three 168GHz Gyrotrons

Dummy loads

Two 84GHz Gyrotrons

Two 82.7GHz Gyrotrons

Six φ88.9mm corrugated WG Lines

One evacuated φ31.75mm corrugated WG line
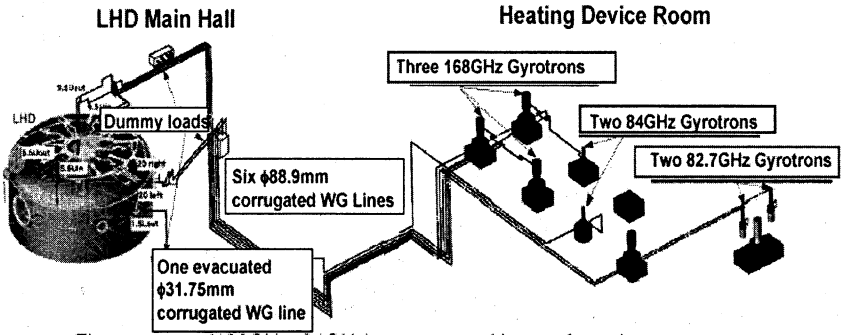
Fig. 1. Schematic view of the ECH system at the fifth experimental campaign

Figure 1 shows the schematic view of the ECH system. The gyrotrons and high voltage power supplies are installed in the neighboring heating device room to the LHD main hall. The 84 GHz and 168 GHz gyrotrons are operated by the semi-conductor power supplies. Two 82,7 GHz gyrotrons are connected to the conventional regulator tube driven power supply.

Table 2 summarizes the whole ECH system such as gyrotrons, high voltage power supplies and transmission lines. Each component will be described in detail in the next subsections.

Table 2. Summary of ECH system

GYROTRONS	Number	Max. Power	Max. Pulse	Electron Gun	Collector Type
82,7 GHz (GYCOM)	2	0,45 MW	2 s	Diode	–
84 GHz (GYCOM)	2	0,8 MW	3 s	Diode	Depressed Collector
168 GHz (TOSHIBA)	3	0,5 MW	1 s	Triode	Depressed Collector

POWER SUPPLIES	Number	Collector PS	Body PS	Anode PS
Solid-state Type	5	< 65 kV, 42 A	< 90 kV, 100 mA	< 50 kV, 50 mA (Modulation)
Regulator Tube Type	1	< 81 kV, 50 A (Modulation)	–	< 40 kV (Modulation)

TRANSMISSION LINES						
Lines	Length	MOU	Miter Bend	Window	Other Components	Antenna
6	Corrugated WG 88,9 mm in dia. < 130 m	4–5 mirrors	< 17	BN SiN	Polarizer, WG Switch, Dummy Load, Arc Detector, Power Monitor	Upper and Outer Antenna
1	Corrugated WG 31,75 mm in dia. < 75 m	2 mirrors	9	Diamond	Polarizer, WG Switch, Dummy Load, Arc Detector,	Lower Antenna

3.1. Gyrotrons and power supplies. Many types of the gyrotrons have been operated in the ECH experiments. The 82,7 GHz gyrotrons (GYCOM) have a diode-type magnetron injection gun without a depressed collector. The 84 GHz gyrotrons (GYCOM) have also a diode–type gun with a depressed collector. These frequency rage gyrotrons are capable of the fundamental ordinary mode heating at 3 T. On the other hand, the 168 GHz gyrotrons (TOSHIBA) have a triode-type electron gun with a depressed collector. These are used for the second harmonic extraordinary mode heating at 3 T magnetic field. The specifications of these gyrotrons are summarized in Table 3.

The total output efficiency of the 84 GHz gyrotrons reaches 50% by means of the collector potential depression. Its pulse width achieved 3 seconds and it was limited by the output window of the boron nitride.

Frequency spectrum of the gyrotrons is one of the most important indicators of the high power stable operation with wide dynamic range. A frequency measuring system, which consisted of a high frequency spectrum analyzer and millimeter wave range mixers, was prepared. The measurable frequency ranges cover from 60 GHz to 170 GHz in the millimeter wave range. Fig. 2, *a* shows a frequency spectrum of the 84 GHz gyrotron. The width of the spectrum is below 100 kHz. A single mode oscillation was observed. The central frequency gradually decreased from 84,07 GHz to 83,87 GHz ($\Delta f = 200$ MHz) during 2 s pulse in Fig. 2, *b*. This is due to the thermal expansion of the interaction cavity of the gyrotron.

310

Table 3. **Specification of gyrotrons**

Frequency	82,7 GHz	84 GHz	168 GHz
Collector Voltage	<70 kV	<65 kV / <90 kV	<65 kV / <85 kV
Beam Current	<22 A	<30 A	<35 A
Output Power	0,5 MW	0,8 MW	0,5 MW
Pulse Length	<2 s	<3 s	<1 s
Output Efficiency	32%	50%	30%
Oscillation Mode	TE10,4	TE12,5	TE31,8
Output Mode / Purity	Gaussian (MOU out) 95%	Gaussian (MOU out) >95%	Gaussian (MOU out) >95% (design)
Duty Factor	0,01	0,01	0,01
Electron Gun Type	Diode	Diode	Triodes
Depressed Collector	None	Single	Single
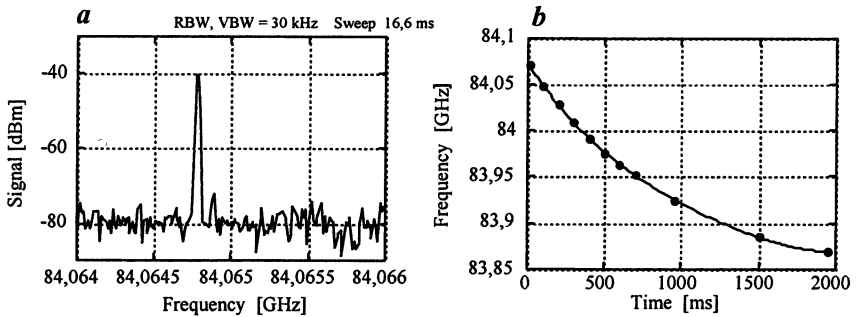
Fig. 2. Frequency spectrum of the 84 GHz gyrotrons (*a*) and oscillation frequency change during 2 second pulse (*b*).

The frequency spectrum of a 168 GHz gyrotrons was also measured. In Fig. 3, *a* two oscillation frequencies are shown. The higher frequency mode with 168,27 GHz is the $TE_{31,8}$ mode, which is the main one of this gyrotron, and high output power comes out from the gyrotron window. On the other hand, the lower frequency mode with 167,62 GHz could be identified as a competing mode of $TE_{28,9}$. The width of the spectrum was below 500 kHz as shown in Fig. 3, *b*. A single mode oscillation could not be observed in a short pulse operation of 10ms. This phenomena lead to the degradation of the oscillation efficiency.
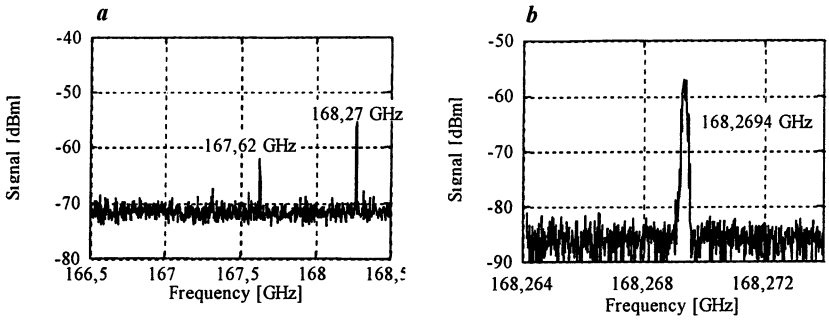
Fig. 3. Oscillation spectrum of a 168 GHz gyrotron (*a*). Two frequencies are observed in a 10 ms pulse. The frequency span is expanded for the main oscillation mode in *b*.

3.2. Transmission system including power monitors and arc detectors.

In LHD, each transmission line consists of matching optics units (MOUs), corrugated waveguides, miterbends, polarizers, arc detectors, power monitors, dummy loads and injection windows. The details are summarized in Table 2. The MOU includes 4 mirrors, two are phase correcting mirrors and two are mirrors for beam alignment. High power millimeter waves are transmitted through the corrugated waveguides with diameters of 88,9 mm and 31,75 mm over 100 m distance. The narrow waveguide is evacuated for higher power transmission capability.

Arc detector is one of the most important components to avoid dangerous damage of gyrotrons and transmission components. Our system realizes not only fast detection of arcings, but identification of arc position. Arcings in the waveguide lines and MOUs are detected optically via optical fibers. In the waveguide, the fiber heads are installed in the miterbends' reflectors. Those are monitoring two different directions inde-
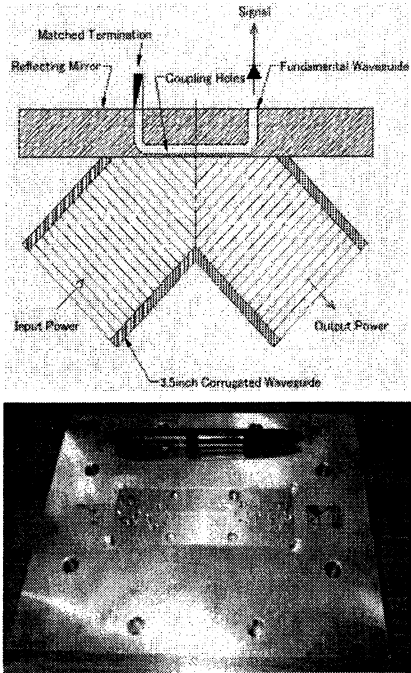
Fig. 4. Structure of the power monitor, which is installed in the miterbend (above). Photograph shows a miterbend back plate in which two standard waveguides are machined for picking up two electric field components.

312

pendently. Identification of the arc position is based on the difference of arrival time of arc light. Minimum distance to be discriminated is 10 m (30 ns).

The reliable real time monitors of gyrotron oscillation and transmission power are required for the safe operation as well as experimental data analysis. The arrays of small holes are drilled on the miterbend back plate, and leaking RF through the holes is coupled to the standard waveguide manufactured in the back plate (Fig. 4). Two components of electric field direction (parallel and perpendicular to the back plate surface) are independently monitored. The coupling coefficient is measured to be about --70 dB in the cold test stand.

In the non-evacuated transmission line, dry air is normally forced to flow from the LHD injection window to the MOU in order to remove   ozone which can be a seed for a big arcing. Nevertheless arcings sometimes occur when operation reaches new regime of power level and pulse length and when polarizer mirrors are rotated. To accelerate the conditioning of the transmission lines, including miterbends and polarizers, brick dummy loads were installed near LHD. One load can deal with the power of 2–4 lines (Fig. 5). Microwave power entered in the dummy load is scattered by a reflector mirror and absorbed in the brick. Air in the load is exhausted for cooling. For power estimation a Teflon tubing load is also installed in the each line.
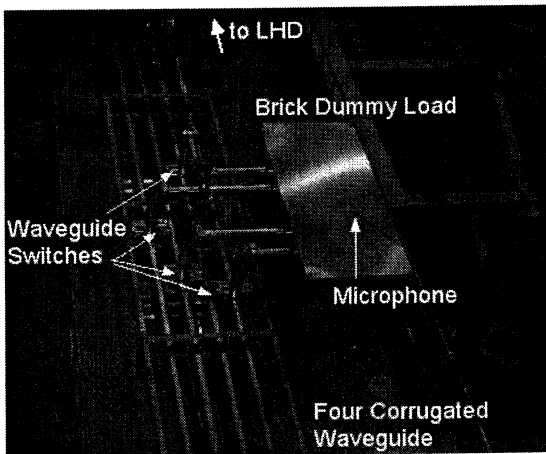
Fig. 5. Brick dummy load which can handles power from four lines. Main transmission lines are swiched to the dummy load during line conditioning. Audio microphone can pick up sound in the dummy load.

Transmission efficiency for each line is evaluated by comparing with the measured powers at the gyrotrons window, at the MOU output position and at the corrugated waveguide near LHD.

Table 4 summarizes the transmission efficiency for each line together with constituent elements such as corrugated waveguides, the number of mirrors and miterbends, and the length of the transmission line. Though the optimization of beam alignment is not complete, the general aspects of the transmission efficiency can be deduced from the results as follows.

Table 4. **Summary of the transmission efficiency for each line**

No	Frequency	Transmission Lines	Mirrors & Polarizers	Number of Miterbends	Length	Transmission efficiency
1	168 GHz	Corrugated WG φ88 8mm Atmosphere	4,2	17	110 m	61 %
2	168 GHz	Corrugated WG φ88 8mm Atmosphere	4,2	11	85 m	67 %
3	168 GHz	Corrugated WG φ88 8mm Atmosphere	4,2	14	90 m	65 %
4	84 GHz	Corrugated WG φ31 75mm Evacuated	2,2	9	75 m	(77 %) w/o coupling effi in MOU
5	84 GHz	Corrugated WG φ88 8mm Atmosphere	5,2	15	95 m	(89 %) w/o coupling effi in MOU
11	82.7 GHz	Corrugated WG φ88 8mm Atmosphere	4,2	13	120 m	(77 %) w/o coupling effi in MOU
12	82.7 GHz	Corrugated WG φ88 8mm Atmosphere	4,2	12	130m	75 %

1) Transmission efficiencies for the higher frequency lines (168 GHz) are lower than those for the low frequency 84 GHz lines. 2) More miterbends and longer length of the lines degrade the efficiency. 3) The narrow evacuated line does not have so good efficiency, though fewer miterbends and shorter length. 4) The coupling efficiency from gyrotrons to the corrugated waveguide is almost 80%, and the loss at one miterbend is estimated to be 1,5% on the average.

3.3. Injection antennas. Millimeter waves led into the LHD port are focused on the equatorial plane by some quasi-optical mirrors. There are three types of antennas in the LHD ECH system. The first type is a topside injection antenna, so called U-port antenna, which is connected to 82,7 GHz or 168 GHz lines. The second type is an outside injection antenna (O-port antenna), which is installed on the horizontally elongated cross-section of the LHD plasma, and which has a wide scanning range in poloidal and toroidal directions. The third type of the antenna is a newly installed one, which launches millimeter wave power from a lower port on the vertically elongated cross-section (L-port antenna).

Figure 6 illustrates the L-port antenna, which consists of two mirrors, one is a fixed focusing mirror and another is a movable flat mirror. This antenna is connected to the evacuated waveguide and is steerable in wide range both poloidally and toroidally.
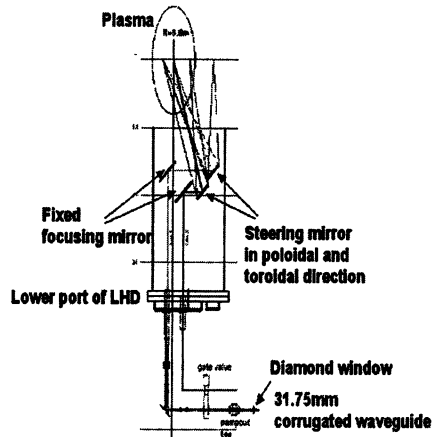
Fig. 6. New antenna system installed in the lower port of LHD.

4. Recent ECH experimental results

The fifth experimental campaign on LHD had been proceeding from September 18th, 2001 to February 14th, 2002. With the upgraded ECH system described above, many epochal results were obtained, such as the achievement of high electron temperature over 10 keV, 150 kJ plasma stored energy by only ECH power and the observation of an internal transport barrier by centrally localized ECH. These results could be realized due to the accordance of the electron cyclotron resonance (ECR), magnetic axis and millimeter wave focal position.

4.1. Configuration of the experiments.

Figure 7 shows the configuration of the ECH experiments, i.e. the magnetic configuration of mod-B lines and magnetic surfaces, and the millimeter wave injection condition. The ECR for fundamental and second harmonic resonance located at major radius of around 3,5 m and the magnetic axis was adjusted to be on it by the external coils. Then all ECH powers were concentrated on the magnetic axis. The power of 82,7 GHz and 168 GHz were injected from U-port antennas and 84 GHz power was launched from the L-port antenna. The injection power was over 1,8 MW.
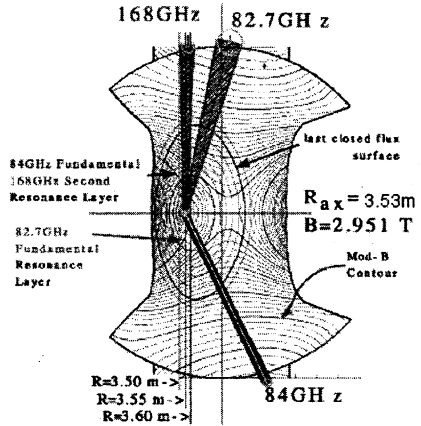
Fig. 7. Configuration of magnetic field and millimeter beam injection. The magnetic axis locates at a major axis of 3,5 m on which ECR exists.

4.2. Achievement of high electron temperature and high plasma stored energy.

The attainment of over 10 keV electron temperature was one of the most important milestones in the experimental campaign on LHD. For ECH physics, such extremely low collisionality regime is especially interesting for the plasma confinement of the stellarators [4].

Figure 8 shows the time evolution of the plasma parameters for the shot where the highest central electron temperature was achieved. The line-averaged electron density reached $0{,}6\cdot10^{19}$ m^{-3}, when Te reached 10 keV. The electron temperature profiles are plotted in Fig. 8, *d* for two time slices shown in *a*.

The region of 10 keV exists just on the magnetic axis at $t = 0{,}44$ s. The high temperature region expanded outward after more ECH power was injected. This could be due to the high field side shift of the ECR layer by relativistic effect.

When the ECH power of 1,8 MW was injected and gas puffing was gradually increased, the electron density also increased gradually and the total stored energy reached 150 kJ at the end of ECH pulse shown in Fig. 9. The electron temperature of the plasma at $t = 0,7$ s is shown in Fig. 9, e. The central value is about 3 keV, while the ion temperature reached 1,5 keV (Fig. 9, d).
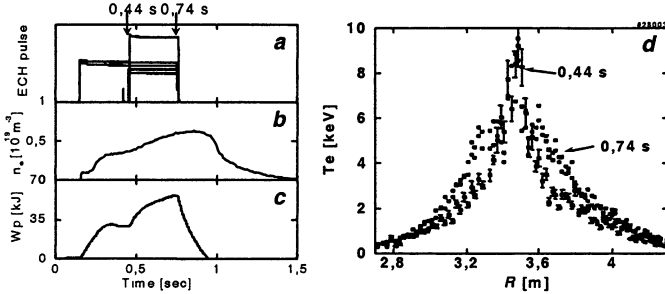
Fig. 8. Time evolution of some plasma parameters. a – ECH-pulse waveform; b – Line–averaged electron density; c – Plasma stored energy. Electron temperature profiles measured by Thomason scattering are plotted at $t = 0,44$ and 0,74 s in d.
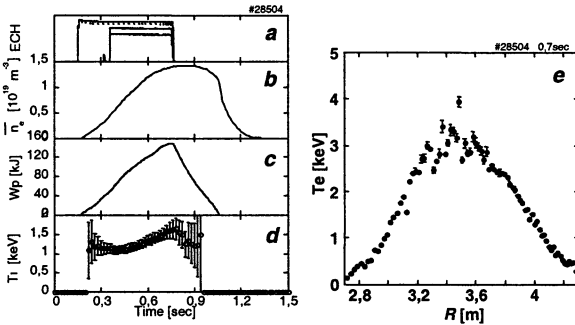
Fig. 9. Time evolutions and Te profile of the high plasma stored energy shot. a – ECH-pulse; b – plasma stored energy; c – line-averaged density; d – ion temperature. The electron temperature profile at $t = 0,7$ s is plotted in e.

4.3. Observation of an internal transport barrier. Recently the confinement improvements on the plasma core have been observed in tokamaks and stellarators by means of centrally localized ECH. Such phenomena are observed mainly on the electron thermal transport only in the low collisional state. In a low collisional regime of stellarators, the improvement of plasma confinement is a critical issue in relation to the production of the radial electric field induced by the loss of the high-energy electrons (so called an electron root).

316

In LHD, highly focused ECH on the plasma center induced the transport barrier (ITB) formation in the core region. A steep gradient of the electron temperature as high as 55 keV/m was observed with the central temperature of 8 keV [5].

The experiments were performed with the magnetic field strength of 2,854 T at the magnetic axis of 3,5 m. The plasmas were produced and heated by a counter neutral beam injection (NBI) with injection energy of 120–150 keV and power of about 4 MW. The obtained plasmas have electron and ion temperatures that are almost equivalent with a value of 2 keV. For these experiments the plasma density was kept at a low-density level of $0,3-1,0\cdot10^{19}$ m^{-3}. An NBI driven plasma current reached about 30 kA at the timing of ECH injection.

The 82,7 GHz and 84 GHz ECH beams with the ordinary mode polarization were perpendicularly injected and strongly focused near the magnetic axis at which the fundamental electron cyclotron resonance (ECR) was present.

The 84 GHz ECH power of 288 kW was injected into the NBI sustained plasma from $t = 1,0$ s as shown in Fig. 10, a. Then 82.7 GHz power of 250 kW was added from $t = 1,2$ s. The plasma stored energy increased slightly by the ECH power. The clamping of the electron density was observed at the beginning of the ECH pulse. The central electron temperature increased stepwise with the addition of the ECH power. By the first ECH injection the electron temperature increased about 1 keV in the core region. After the second ECH pulse the central temperature built up to over 8 keV. The high temperature region was limited within $\rho < 0,2$ in Fig. 10, b.
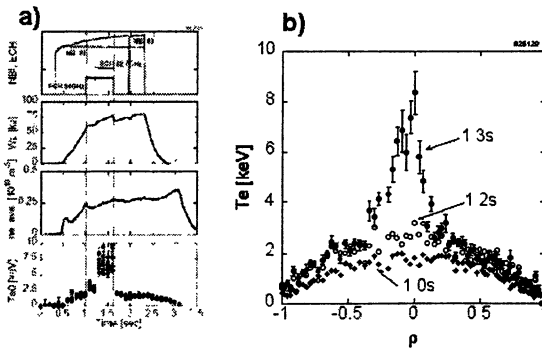
Fig. 10. a) Time evolution of ECH-pulse, plasma stored energy, electron density and electron temperature of central part. b) Electron temperature profiles at $t = 1,0$ s (NBI plasma), $t = 1,2$ s (only 84 GHz injection) and $t = 1,3$ s (84 and 82,7 GHz injection).

The central electron temperature T_{e0} (averaged over ±80 mm around the plasma center) is plotted as a function of ECH injection power in Fig. 11. The data are given for two different line-averaged densities of 0,3 and $0,5\cdot10^{19}$m^{-3}. The formation of the transport barrier has an obvious ECH power threshold,

which increases with the density. Changes in the barrier width that is the distance between the foot positions are also shown in the figure. The width is found to be constant above the threshold power and independent of the ECH power and electron density in these operational ranges.
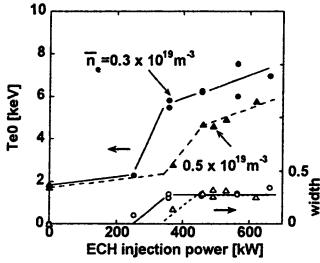
Fig. 11. The central electron temperature is plotted as a function of the ECH injection power for two different electron densities. The width of ITB is also plotted in the unit of ρ.

The evaluation of the electron thermal diffusivity profile was performed by transport analyses for the cases of 282 kW and 177 kW injections. In Fig. 12, a the analyzed electron temperature profiles are plotted together with the absorbed ECH power density profiles, p_{ECH}, estimated by ray tracing calculations. For the low injection power of 177 kW (dashed line in Fig. 12, b), χ_e once increases within $\rho \approx 0{,}4$. When the ITB was formed for the 282 kW injection (solid line), the value of χ_e decreased obviously to one order of magnitude of the 177 kW injection case without ITB.
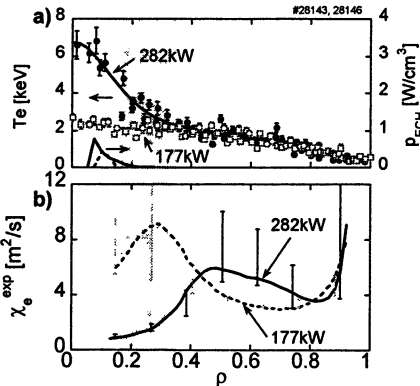
Fig. 12. a) Electron temperature profile for transport analyses with absorbed ECH power density estimated by a ray tracing calculations. b) χ_e profiles for the injection powers of 282 kW and 177 kW.

Since the ambipolarity condition of the electron and ion particle fluxes predicts a production of a radial electric field within the transport barrier region, a transition to the electron root is expected by the central ECH, and the produced radial electric field E_r improves the electron thermal transport in the core region as the neoclassical theory predicts. The electric field shear at the ITB could contribute to the suppression of the anomalous transport.

318

5. Summary

In the 5th experimental campaign (2001), seven-gyrotron system was operable. One transmission line, which was evacuated in whole system, was installed in addition to the six existed 88,9 mm lines in atmospheric pressure. This line allows transmitting over 500 kW power. Flexible experiments could be performed by the inward shift of a scanning range of the existed antennas and by an installation of a new lower port antenna.

Such improvement enabled the experiments in an extended power regime (injection power of over 1,8 MW) of LHD. Especially on-axis heating opened new regime such as a high electron temperature state of over 10 keV and a formation of a transport barrier in the core. Such high temperature plasmas with the ITB are characterized by a high central temperature with its steep gradient around $\rho = 0,2$–$0,3$. The formation of the ITB has a clear power threshold, which increases with the electron density. The mechanism of the ITB formation is not still clear. The ambipolar condition of electron and ion fluxes predicts a strong positive radial electric field in the core (the electron root). This electric field can reduce the electron thermal diffusivity. This neoclassical depiction is not sufficient to explain the amount of χ_e reduction completely. A sheared electric field may play an important role to suppress the anomalous transport. Direct measurement of E_r and turbulence behavior is the subjects of future work.

References

1. *Motojima O., Yamada H.,* et al., Phys. Plasmas, **6**, 1843 (1999).
2. *Fujiwara M., Kawahata K., Ohyabu N.,* et al., Nuclear Fusion, **41**, 1355 (2001).
3. *Shimozuma T., Kubo S.,* et al., Fusion Engineering and Design, **53**, 525 (2001).
4. *Kubo S., Shimozuma T., Idei H.,* et al., Journal of Plasma and Fusion Research, **78**, 99 (2002).
5. *Shimozuma T.* 12th Joint Workshop on ECE and ECRH, Paper № 056 (2002).

ELECTRON CYCLOTRON RESONANCE HEATING WITH THE PRELIMINARY 110 GHz SYSTEM ON TEXTOR

E. Westerhof[1], *G. M. D. Hogeweij*[1], *J. A. Hoekzema*[2], *F. C. Schüller*[1], *C. J. Barth*[1], *H. Bindslev*[1,4], *A. J. H. Donné*[1], *P. Dumortier*[3], *J. C. van Gorkom*[1], *R. J. E. Jaspers*[1], *D. Kalupin*[3], *H. R. Koslowski*[2], *A. Krämer-Flecken*[2], *N. J. Lopes Cardozo*[1], *H. J. van der Meiden*[1], *A. Messiaen*[3], *T. Oyevaar*[1], *R. W. Polman*[1], *L. Porte*[5], *V. S. Udintsev*[1], *B. Unterberg*[2], *M. Vervier*[3], *D. van Eester*[3], *G. van Wassenhove*[3]* and TEC Team*

Partners in the Trilateral Euregio Cluster (TEC):
[1]FOM-Rijnhuizen, Ass. Euratom-FOM, Postbus 1207,
NL-3430 BE Nieuwegein, Netherlands
[2]Institut für Plasmaphysik, FZJ, Euratom Association, D-52425 Jülich, Germany
[3]Laboratoire de Physique des Plasmas-Laboratorium voor Plasmafysica, Association Euratom-Belgian State, ERM/KMS, Brussels, Belgium
[4]Optics and Fluid Dynamics Department, Ass. Euratom-National Laboratory Risø, DK-4000 Roskilde, Denmark
[5]MIT Plasma Science and Fusion Center, Cambridge, MA, USA

A 110 GHz, 400 kW, 200 ms gyrotron has been employed on TEXTOR for ECRH. The highly localised electron heating allowed the identification of (multiple) electron transport barriers. The RTP q-comb model for the electron heat conductivity gives a good description of TEXTOR results with ECRH in Ohmic discharges. Central ECRH in the current ramp phase speeds up central current penetration due to the highly peaked T_e profile. A stable evolution of these discharges with early heating required the combination of counter-NBI with central ECRH. In RI-mode, central ECRH resulted in an increase of the confined energy in proportion to the ECRH power, without signs of power degradation as is usual in RI-mode with NBI and ICRH. Efficient ECRH is observed up to the X-mode cut-off density. The gyrotron has also been successfully used for diagnosis of energetic ions by means of Collective Thomson Scattering.

1. Introduction

After closure of the Rijnhuizen Tokamak Project (RTP) in 1998, the high temperature plasma physics research of the FOM-Instituut voor Plasmafysica "Rijnhuizen" has been concentrated on the TEXTOR tokamak at the Forschungszentrum Jülich, in the framework of the Trilateral Euregio Cluster (TEC) agreement. One of the major contributions of the FOM team is a > 800 kW, 140 GHz > 3 s, Electron Cyclotron Resonance Heating (ECRH) system [1], that is currently being installed. In preparation of experiments with this new ECRH system, the 400 kW, 110 GHz, 200 ms gyrotron, which had been in operation on the RTP tokamak since 1994, was installed on TEXTOR. A quasi-optical trans-

mission line is used for transport of the microwaves from gyrotron to the toka-
mak. The beam is launched from a movable mirror that allows covering most of
the poloidal cross-section and variation of the toroidal injection angle from $-45°$
up to $+45°$. ECRH localisation is optimised by injection of a focussed Gaussian
beam with a waist in vacuum of 3 cm (1/e width of the E-field amplitude) located
for perpendicular injection at $R = 1.60$ m, i. e. 15 cm on the high field side from
the centre of the machine. The power injected into the plasma is estimated at
270 ± 30 kW. Linear, vertical or horizontal polarisation has been used to couple
mostly to X- or O-mode, respectively. In most cases reported here the waves
have been injected perpendicular to the toroidal field.

In this paper the main physics results are reported that have been obtained
with the preliminary ECRH system. These include measurement of electron
transport barriers in the various regimes of ECRH + Ω and ECRH + RI-mode
(Radiatively Improved mode [2]), and of heating during the current ramp phase
(Section 2). The results of ECRH in the current ramp phase and in the RI-mode
are presented in more detail in Sections 3 and 4. The final Section provides a
summary and outlook of the research programme with the new, high power, long
pulse length ECRH system.

2. Electron transport barriers

The dominance of ECRH power in RTP led to a highly non-linear response
of the plasma profiles to changes in ECRH localisation. This suggested the pres-
ence of multiple electron transport barriers located near low rational values of the
safety factor q [3]. To explain these results, the so-called q-comb model for elec-
tron heat conductivity, χ, has been developed in which χ is supposed to be a
function of q only with a constant high value interspersed with narrow regions of
low conductivity located near the low rational values of q: 1, 4/3, 3/2, 2, 5/2, 3,
7/2 ... [4]. When the absolute values of the heat conductivity are scaled by a fac-
tor of 0.83 consistent with L-mode scaling [5] between RTP and TEXTOR, the
same model also describes well TEXTOR discharges with central ECRH [6]. In
fact, the inner most barrier near $q = 1$ is clearly visible in the electron temperature
profile, shown in Fig. 1, as measured with a high resolution TV Thomson
Scattering system [7].

The central barrier near $q = 1$, is confirmed by scanning the ECRH deposi-
tion through the plasma: the barrier is seen in the data of either $T_e(0)$ or the total
plasma energy. This applies to Ohmic discharges with ECRH (Fig. 2), as well as
to RI-mode discharges (Fig. 3). The relation between the barrier and $q = 1$ is con-
firmed by the sawtooth behaviour. The sawtooth inversion radius is close to the
barrier and, for Ohmic discharges, the sawtooth period has a maximum when
ECRH is deposited close to the barrier/sawtooth inversion radius (Fig. 2 bottom).
For $I_p = 255$ kA, sawteeth are stabilised during the 200 ms ECRH pulse when the

power is deposited in a broad region outside the inversion radius. Once sawteeth are stabilised by off-axis ECRH, the discharge remains non-sawtoothing after switch-off of ECRH. For RI-mode discharges, the sawtooth period is reduced for heating inside the barrier/inversion radius, whereas it is almost unaffected otherwise (Fig. 3 bottom).
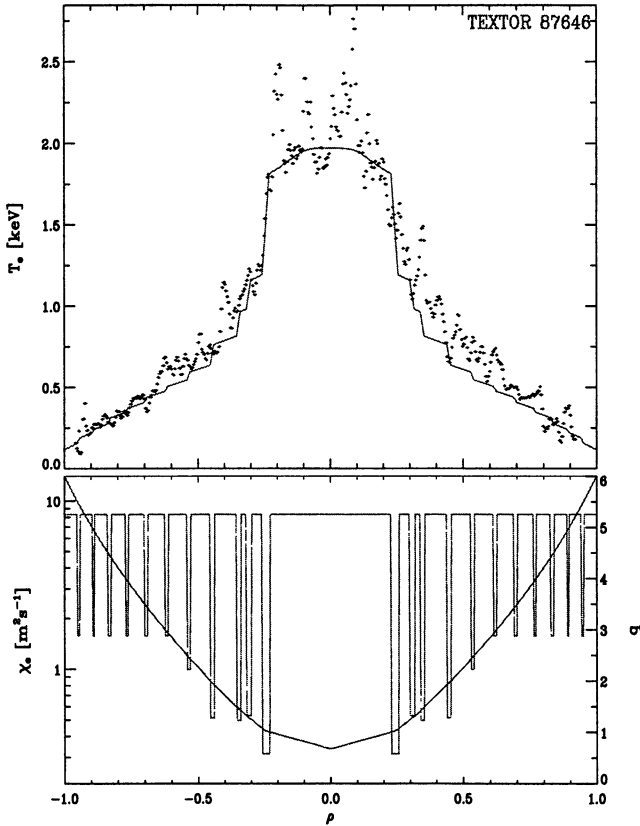
Fig. 1. The T_e profile in a typical TEXTOR discharge with central ECRH simulated with the RTP q-comb model for the heat conductivity [3]. $P_{ECRH} = 250$ kW. The dots shown in the top panel represent T_e measured by Thomson scattering; the solid curve gives the result of the simulation. The bottom panel shows the q profile and the corresponding profile of the electron heat conductivity (the curve with peaks).
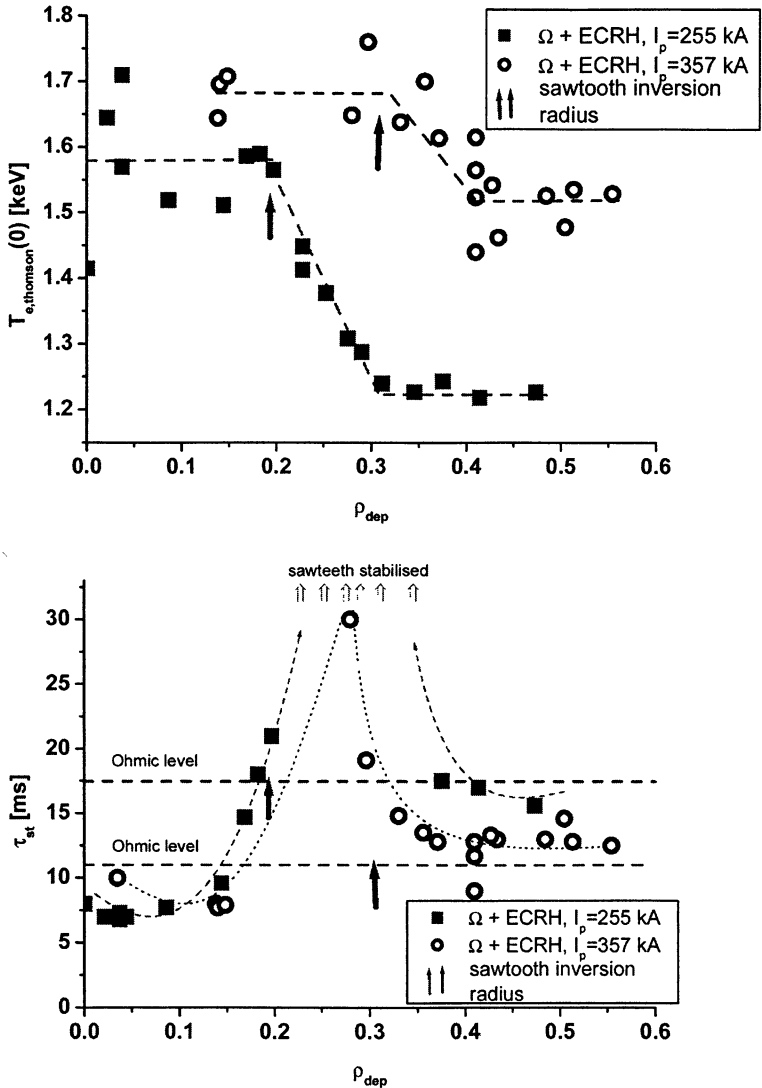
Fig. 2. The central T_e from Thomson scattering (top) and the corresponding sawtooth period (bottom) achieved in Ohmic discharges with ECRH (270 kW) as a function of the ECRH deposition radius. The ECRH deposition radius is varied by changing the toroidal field. Two datasets are shown for different plasma currents: squares for 255 kA and circles for 357 kA. In the lower current case sawteeth are stabilised, when ECRH is deposited within a region just outside the sawtooth inversion radius ranging from $\rho_{dep} = 0.23$ to 0.35.
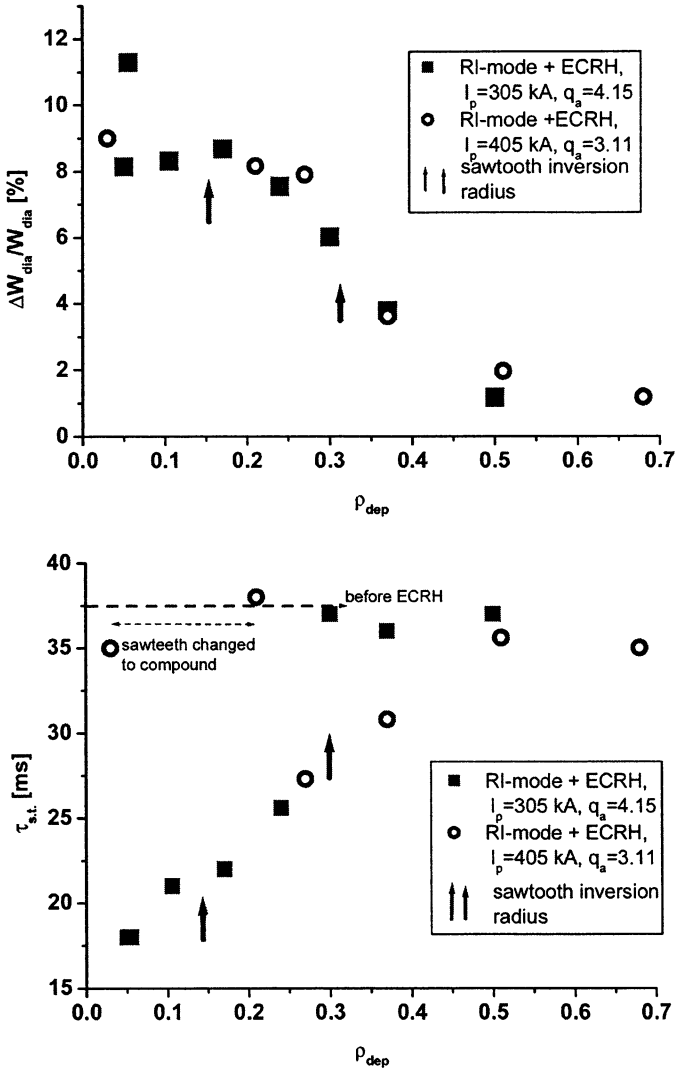
Fig. 3. The normalised change in confined energy $\Delta W_{dia}/W_{dia}$ from diamagnetic measurements (top) and the corresponding sawtooth period (bottom) achieved in RI-mode discharges as a function of ECRH deposition radius. The ECRH (270 kW) deposition radius is varied by changing the poloidal injection angle. The datasets shown are for plasma currents of 305 kA (■) and 405 kA (○). In both cases a barrier is seen close to the inversion radius and the sawtooth period is found to drop for deposition inside the inversion radius. In the high current case (405 kA) the sawteeth are seen to change character from normal to compound or humpback like when the deposition is inside $\rho = 0.20$.

3. ECRH during the current ramp phase

Given that the electron heat conductivity displays barriers near rational values of q, it will be attractive to control the current density profile in such a way as to make optimal use of these barriers. One way to optimise the q profile is by creating negative central shear (NCS), i.e. a hollow current density profile. Both in ASDEX-Upgrade as well as in TCV a strong electron transport barrier and high $T_e(0)$ have been obtained in discharges with central counter-ECCD [8, 9]. In those experiments, the counter-ECCD is instrumental both for sustaining or achieving NCS as well as for supplying the central electron heating.

A generally used technique to create a hollow current density profile is by means of early heating during the current rise phase of the discharge: an increased temperature slows down current penetration, resulting in a hollow current profile. This method has been employed in a series of TEXTOR discharges with the aim of exploring a possible NCS regime [10]. In the experiments, a fast initial ramp (100 ms) up to $I_p = 200$ kA is followed by a slower ramp up to 350 kA at $t = 600$ ms. Early heating is provided by 1 MW of counter-NBI from $t = 200$ ms. In addition to providing plasma heating a central counter driven current is expected to assist in attainment of NCS. Somewhat later ECRH (270 kW, $t = 250$–450 ms) is applied for additional electron heating to establish the presence of electron transport barriers. At $t = 350$ ms, the electron temperature profile is measured by Thomson Scattering. T_e profiles as obtained for different positions of ECRH deposition are shown in Fig. 4. Two electron transport barriers are identified in these profiles at normalised minor radii of $\rho = 0.13$ and 0.35. The inner barrier is much wider than the width of the ECRH deposition profile (typically $\Delta\rho = 0.05$).

At the beginning of the ECRH pulse the q-profile as measured by polarimetry is slightly reversed or flat with a central value of about 2 to 2.5. Polarimetry is perturbed by ECRH and no measurements of the q-profile are available during ECRH. With central ECRH, regular sawteeth appear close to the end or shortly after ECRH. In normal discharges without early heating, sawteeth generally appear only much later. This indicates a strong evolution of the current density profile in the phase with central ECRH: in spite of the higher temperature, the strong central peaking of the T_e profile leads to a faster central current penetration, because of the reduced gradient length. This is confirmed by calculations of the current penetration using the experimental T_e profile with neoclassical conductivity and an estimate of the beam driven current (see Fig. 5).
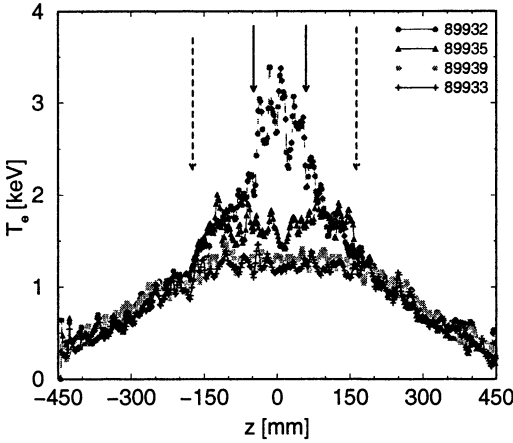
Fig. 4. T_e profiles from Thomson scattering at $t = 350$ ms for different positions of ECRH deposition: 89932 $\rho_{dep} = r_{dep}/a = 0.06$; 89935 $\rho_{dep} = 0.23$; 89939 $\rho_{dep} = 0.50$; 89933 NBI-only.
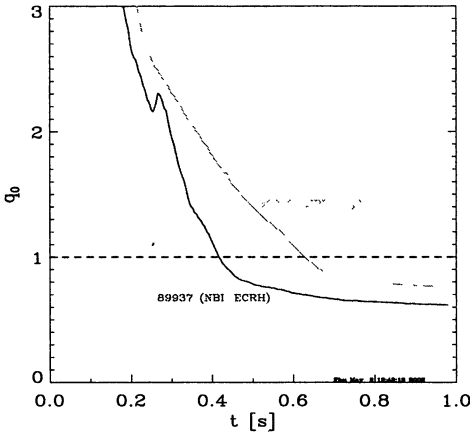
Fig. 5. The evolution of the central safety factor for a discharge with central heating (89937) compared with a NBI-only case (89933). In 89937 q_0 drops below 1 at $t = 0.42$ s, consistent with appearance of sawteeth.

Apart from providing the necessary pre-heating, counter-NBI also proved essential for stability during central ECRH. Without NBI, ECRH in the current ramp phase is accompanied by one or more strong core collapses. Core collapses are also observed with off-axis ECRH as seen in the central T_e evolution (Fig. 6). A particularly strong core collapse is observed in the case where EC deposition coincides with the inner barrier (discharge #89940).

Replacing part or all of counter-NBI by co-NBI leads to increased MHD activity during ECRH as shown in Fig. 7. Even when only part of the counter-NBI is replaced by co, the discharge evolution is strongly affected: increased MHD activity appears to prevent central current penetration, such that central $q = 1$ and sawteeth are never attained. Instead, the discharge typically ends in a disruption some time after ECRH. Only the combination of early heating with counter-NBI plus a subsequent pulse of central ECRH is seen to result in an evolution towards

326

a stable sawtoothing discharge. Further analysis is required to determine whether differences in wall stabilisation due to rotation or the effects of the different beam driven currents are responsible for the increased susceptibility of the discharge to MHD instabilities as the amount of co-NBI is increased.

Fig. 6. The evolution of $T_e(0)$ from ECE for different positions of the ECRH deposition: 89937 $\rho_{EC} = 0.00$; 89940 $\rho_{EC} = 0.13$; 89935 $\rho_{EC} = 0.23$; 89939 $\rho_{EC} = 0.50$.
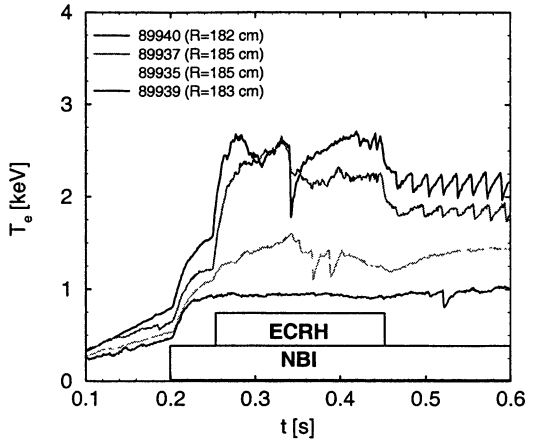
Fig. 7. The evolution of $T_e(0)$ from ECE for different ratios of counter- and co-NBI: 91356 counter-NBI; 91358 balanced NBI; 91355 co-NBI.
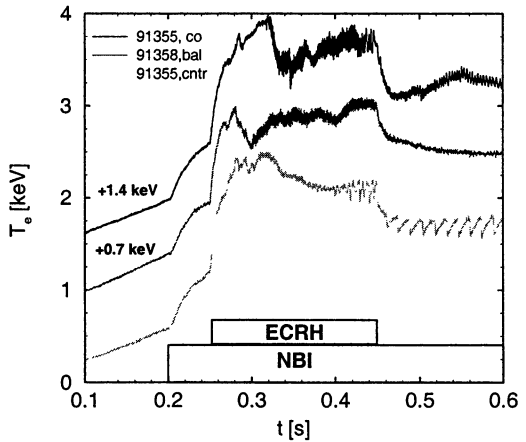
4. ECRH in the radiatively improved mode

On TEXTOR a regime with improved confinement, Radiatively Improved mode or RI-mode, has been established by injection of radiating species in the plasma edge (typically Ne or Ar) [2]. Apart from a radiating mantle, this regime is characterised by establishment of a peaked density profile with a possible suppression of ion temperature gradient (ITG) turbulence as a consequence. The

energy confinement in RI-mode scales with line averaged density $<n_e>$ as in the linear Ohmic confinement regime, but the general degradation of confinement with total heating power remains [2]:

$$\tau_{RI} \propto <n_e> P_{tot}^{2/3} I_p. \tag{1}$$

The improvement of confinement is attributed to the suppression of the ITG turbulence, which is a major cause of anomalous ion heat conductivity. The electron heat conductivity and its improvement in RI-mode are less well known. It is thus of particular interest to study pure electron heating as provided by ECRH. However, the 200 ms pulse length and 270 kW injected power of the preliminary 110 GHz system are limited when compared to confinement times of about 50 ms and the total heating power of about 2.7 MW of typical RI-mode discharges. Still, interesting results have been obtained on ECRH in RI-mode [11].
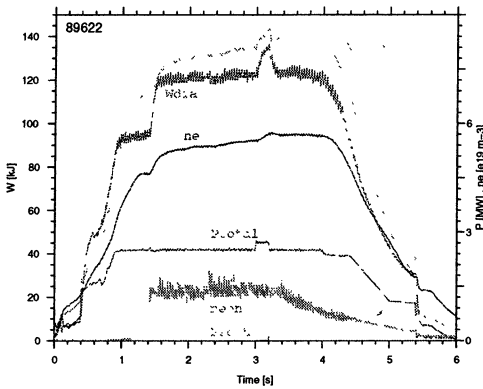
Fig. 8. Evolution of a typical RI-mode discharge. The increase of W_{dia} with the injection of Ne signifies the transition to RI-mode. The curve labelled $W_{dia,RI}$ signifies the expected W from RI-mode scaling [2].

Results for a typical RI-mode discharge with central ECRH are shown in Fig. 8, which gives the time evolution of the total heating power and the diamagnetic energy W_{dia}. Also shown is the energy content $W_{dia,RI}$ expected on the basis of RI-mode confinement scaling. During ECRH the density continues to rise: no density pump-out is observed during ECRH in RI-mode. Given that $P_{ECRH}/P_{tot} \approx$ $\approx 0.27/2.7$ [MW] ≈ 10 %, an increase in stored energy during ECRH of typically 3 % is expected on the basis of the RI-mode scaling. However, in many cases $\delta W_{dia}/W_{dia} \approx 9$ % is observed, i.e. the confinement degradation with total power appears not to apply to ECRH. Fig. 9 shows $\delta W_{dia}/W_{dia}$ normalised to $\delta P/P_{tot}$ for a number of discharges as a function of the line average density $<n_e>$. In comparable L-mode discharges (also shown in Fig. 9) the normalised efficacy $(\delta W_{dia}/W_{dia})/(\delta P/P_{tot})$ is close to the expected value of 0.3. The effectiveness of ECRH is seen to hold up to $<n_e> \approx 5.5 \cdot 10^{19}$ m^{-3}. Abel inversion of the interferometry data shows that this corresponds to $n_e(0) \approx 7.5 \cdot 10^{19}$ m^{-3}, coinciding within measurement accuracy with the 110 GHz X-mode cut-off density. The central

ECE channels start decreasing when $\langle n_e \rangle \geq 4.3 \cdot 10^{19}$ m^{-3}. That the effectiveness of ECRH is much less affected by the approach of the density cut-off than ECE can be understood by the differences in antenna patterns of the ECE and ECRH systems: whereas the ECRH wave beam is well focused inside the plasma, the ECE antenna pattern has a divergence of 12.5° (1/e half width of the intensity). Ray tracing calculations confirm that the ECRH power deposition profile is practically constant up to the cut-off density, while the radiation temperature in the 109 and 112 GHz central ECE channels starts decreasing already at $n_e(0) \geq$ $\geq 6.5 \cdot 10^{19}$ m^{-3}. Above X-mode cut-off the efficiency of ECRH is decreased below the 20 % level. At these high densities, injecting O-mode yields $(\delta W_{dia}/W_{dia}) / (\delta P/P_{tot}) \approx 0.6$, in reasonable agreement with an estimated first pass absorption of 2nd harmonic O-mode at the prevailing density and temperature of 45 %.

Fig. 9. The normalised efficacy of ECRH in RI-mode discharges (circles). The colours indicate the plasma current. Also L-mode discharges are given (diamonds) and two discharges with O-mode ECRH at high density (squares).
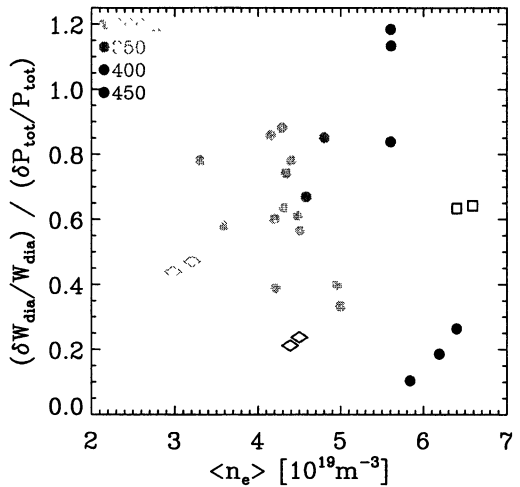
With increasing density in the RI-mode, the sawtooth behaviour changes from normal to humpback like. This changeover to hump-back like sawteeth in a standard RI-mode discharge is shown in Fig. 10, which displays central ECE in 3rd harmonic X-mode (for these higher densities 2nd harmonic ECE is affected by cut-off) together with the increasing line averaged density. Interestingly, with central ECRH the transition occurs at a slightly lower density. Fig. 11 shows the central 3rd harmonic ECE during ECRH in three different discharges: from bottom to top, a discharge at moderate density showing normal sawteeth with shorter period during central ECRH, a discharge close to cut-off showing first the short period normal sawteeth changing into humpback like towards the end of the ECRH pulse, and finally a discharge just above cut-off in which no effect of ECRH can be seen.

329
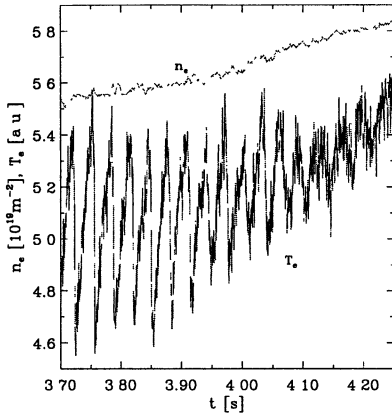
Fig. 10. The sawtooth behaviour in a standard RI-mode discharge measured with 3rd harmonic X-mode ECE. With increasing density, the sawtooth behaviour changes from normal to humpback like. Note that the changeover occurs at a density just above the 110 GHz X-mode cut-off.
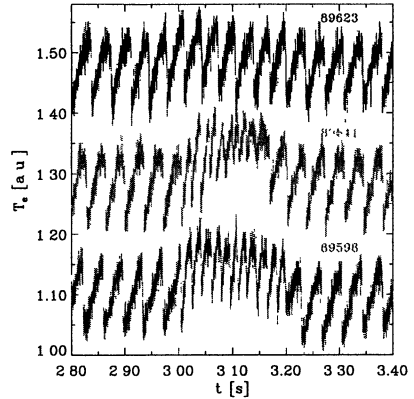
Fig. 11. The sawtooth behaviour during central ECRH in RI-mode at different densities. The density increases from well below for discharge 89598 (bottom trace) to above cut-off for 89623 (top trace). The middle trace showing a transition to humpback like sawteeth during ECRH is for a case close to cut-off, 89641.

5. Collective Thomson scattering

The 110 GHz system has also been used as source for a fast ion collective Thomson scattering (CTS) diagnostic, which became operational August 2000. A number of dedicated experiments have been performed in pursuit of both generic fast ion physics such as fast ion sawtooth sensitivity and confinement time, and specific Ion Cyclotron Resonance Heating (ICRH) physics issues intended to challenge and benchmark model calculations. The diagnostic measures the fast ionpopulation density as a function of a selected velocity component. The signal to noise ratio and other constraints permit a velocity space resolution on the order of 10^5 m/s with typically a total of 15 points in the velocity distribution recorded. The spatial resolution is 10 cm radially while the temporal resolution is 4 ms at up to 100 time slices. The spatial location of the measurement and the direction of the resolved velocity component were varied between shots. While data have been recorded to investigate a broad range of phenomena, initial analysis has concentrated on the behaviour of fast ions at sawteeth. An example of a measured ion phase space distribution is shown in Fig. 12, where both contours of the logarithm of the phase space density and time traces for selected velocities are plotted. The plots show the effects of the switch off of the ion heating at 2.2 s after

330

which the velocity distribution contracts; the energetic ion population decaying in approximately 50 ms. Also evident is the effect of sawteeth. Comparing measurements from like discharges, in which the orientation of the resolved velocity component and the location of the measurement volume were varied independently, both inhomogeneity and anisotropy in the fast ion dynamics at sawteeth were observed. More detailed physics results are reported elsewhere [12].
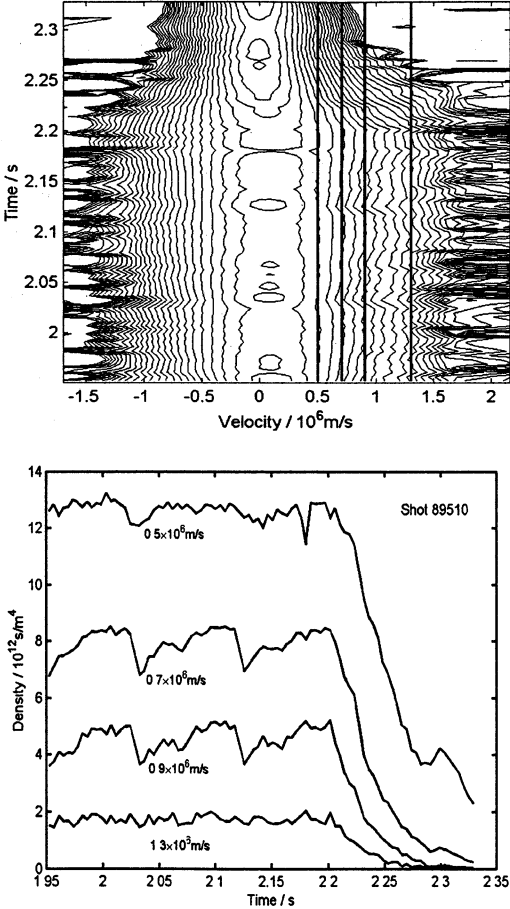
Fig. 12. Both plots show the phase space density; number of ions per unit volume and unit velocity. In this shot (89510) the resolved velocity component makes an angle of 65.7° with the static magnetic field. The measurement volume is just to the high field side of the plasma centre, near the electron density inversion radius. Auxiliary heating (ICRH and NBI) is switched off at 2.2 seconds. **Top**: Contours of the logarithm of the ion phase space density. **Bottom**: Time traces of the phase space density for selected velocities.

331

6. Summary and perspective

Extensive physics studies have been performed with the preliminary 110 GHz, 270 kW (injected power), 200 ms gyrotron on TEXTOR. Results provide further confirmation for the RTP q-comb model for electron heat conductivity [4]. Electron transport barriers are identified in various plasma regimes. The association of the central barrier in Ohmic and RI-mode discharges with central ECRH is corroborated by the closeness of the barrier to the sawtooth inversion radius, and by the change in sawtooth behaviour with the crossing of the barrier.

Currently TEXTOR is in shutdown for installation of the Dynamic Ergodic Divertor (DED) [12]. At the same time, a new high power (> 800 kW), long pulse length (> 3 s), 140 GHz gyrotron is being installed, which will become operational at the restart of TEXTOR. With the higher power and longer pulse length it is expected that major progress will be made in the study of electron transport barriers. In particular, the higher power will allow to sustain and to heat discharges with optimised shear conditions. Also electron heating in RI-mode is improved. Detailed studies are planned on the interaction of localised ECRH/ECCD and various MHD modes including NTM. The combination with the DED should allow studies of the interaction of ECRH with externally created and controlled magnetic islands, and analysis of ergodic field regions through localised electron heating.

References

1. *Hoekzema J. A.* et al., this workshop.
2. *Weynants R. R.* et al., Nucl. Fusion, **39**, 1637 (1999).
3. *Lopes Cardozo N. J.* et al., Plasma Phys. Control. Fusion, **39**, B303 (1997).
4. *Hogeweij G. M. D., Lopes Cardozo N. J., de Baar M. R., Schilham A. M. R.* Nucl. Fusion, **38**, 1881 (1998).
5. *Kaye S. M.* Nucl. Fusion, **37**, 1301 (Eq. 6) (1997).
6. *Schüller F. C.* et al., 27th EPS Conf. on Contr. Fusion and Plasma Physics, Budapest, Hungary, 12–16 June 200, http://epsppd.epfl.ch/Buda/pdf/d1_002.pdf.
7. *Barth C. J.* et al., Rev. Sci. Intrum., **72**, 1138 (2001).
8. *Günter S.* et al., Phys. Rev. Lett., **84**, 3097 (2000).
9. *Pietrzyk Z. A.* et al. Phys. Rev. Lett., **86**, 1530 (2001).
10. *Westerhof E.* et al., 28th EPS Conf. on Contr. Fusion and Plasma Physics, Madeira, Portugal, 18–22 June 2001, http://epsppd.epfl.ch/Madeira/html/pdf/P1.014.pdf.
11. *Hogeweij G. M. D.* et al., 28th EPS Conf. on Contr. Fusion and Plasma Physics, Madeira, Portugal, 18–22 June 2001, http://epsppd.epfl.ch/Madeira/html/pdf/P4.013.pdf.
12. *Bindslev H.* et al., Proc. 10th Int. Symp. On Laser-Aided Plasma Diagnostics, Fukuoka, Japan, 2001) pp. 97–108, http://www.risoe.dk/euratom/cts.
13. *Finken K. H.* et al., Nucl. Fusion, **39**, 637 (1999).

THE TRANSMISSION SYSTEM
FOR ECRH ON THE STELLARATOR W7-X:
DESIGN ISSUES AND TESTS OF PROTOTYPE COMPONENTS

W. Kasparek, G. Dammertz[1], V. Erckmann[2], G. Gantenbein, H. Hailer,
F. Hollmann[2], L. Jonitz[2], H. P. Laqua[2], W. Leonhardt[1], G. Michel[2],
M. Schmid[1], P. G. Schüller, K. Schwörer, R. Wacker, M. Weissgerber[2]

Institut für Plasmaforschung, Universität Stuttgart, Pfaffenwaldring 31,
D-70569 Stuttgart, Germany
[2]Max-Planck-Institut für Plasmaphysik (IPP), EURATOM-Association,
Wendelsteinstraße 1, D-17491 Greifswald, Germany
[1]Forschungszentrum Karlsruhe, Association Euratom-FZK, IHM,
Postfach 3640, D-76021 Karlsruhe, Germany

For the fusion plasma experiment Wendelstein 7-X which is built up at the Max-Planck-Institut
für Plasmaphysik (IPP) at Greifswald, a powerful heating system using millimetre waves is
under construction. The system is designed to heat the plasma at the second harmonic
frequency of the electron cyclotron resonance and will include 10 gyrotrons at 140 GHz,
generating 1 MW of CW power each. The millimetre wave power will be transmitted via two
multi-beam waveguides (MBWG) over a distance of about 60 m.
The design of the complete system is discussed. Measurements on various components as
well as on a prototype system are presented. For the prototype system, calorimetric
measurements show a transmission efficiency of about 90% in good agreement with theory,
and low-power measurements of radiation patterns yield a high mode purity for the
millimetre wave beams.
The design of the mirrors and thermo-mechanical calculations are discussed. The calculations
are confirmed by investigations of the mirror surfaces under application of a heat load
equivalent to the absorbed power from a 1 MW mm-wave beam. High-power tests (e.g.
890 kW/180 s) of the mirrors in the test stand of a prototype gyrotron for W7-X show no
problems and are used to develop calorimetric loads, directional couplers, and other beam
diagnostics.

Introduction

For the stellarator W7-X, currently under construction at Max-Planck-Institut
für Plasmaphysik (IPP) in Greifswald, Germany, a 140 GHz, 10 MW CW Elec-
tron Cyclotron Resonance Heating (ECRH) system is built up [1, 2]. The RF
power will be delivered by 10 gyrotrons presently being developed [3], and fed
from the source to the plasma via quasi-optical transmission lines [4, 5]. All
transmission components are placed in an underground duct connecting the gyro-
tron building with the experimental hall. The design of the transmission system is
illustrated by the CAD drawing in Fig. 1.

The set-up consists of single-beam and multi-beam elements. For each gyro-
tron, a matching assembly of five single-beam mirrors is used. Two of these mir-
rors match the gyrotron output to a Gaussian beam with the correct beam parame-

333

ters, two others are used to set the appropriate polarisation needed for optimum absorption of the radiation in the plasma. A fifth mirror directs the beam to a plane mirror array, which is situated at the input plane of a multiple-beam wave guide (MBWG) [5]. This MBWG is designed to transmit up to seven beams (five 140 GHz beams, one 70 GHz beam plus an additional spare channel) from the gyrotron area (input plane) to the stellarator hall (output plane). It consists of 4 focusing mirrors in a confocal arrangement plus additional plane mirrors to fit the transmission lines into the building. At the output plane of the MBWG, a mirror array separates the beams again and directs them via vacuum barrier windows to individually movable antennas in the torus. To transmit the power of all gyrotrons, two symmetrically arranged MBWGs will be built. The total length of the transmission is about 60 m.
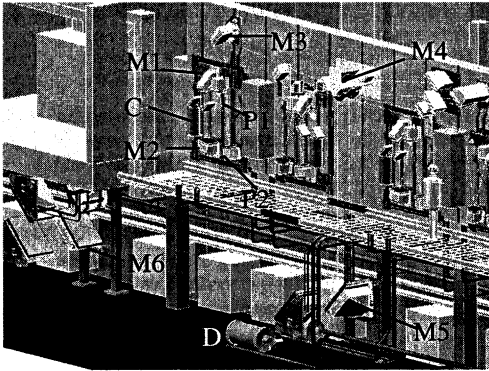
Fig. 1. View into the gyrotron hall with the under-ground duct and the transmission system. On top one can see 3 matching and polarizer mirror assemblies (M1, M2, P1, P2, M3) with calorimetric loads (C) and the plane mirror array (M4) injecting the individual beams into the MBWG system (M5, M6, ...). At the bottom, two dummy loads (D) are installed.

The mirrors of the MBWG feature optimized surfaces with respect to low mode conversion [2, 6] of the on-axis as well as off-axis TEM_{00} beams using physical optics and analytic calculations. Furthermore, the configuration of the mirrors is such that mode conversion which is a general feature of curved surfaces cancels at the end of the MBWG. A detailed discussion of the concepts is found in [6]. Additionally, distances and focal lengths for each beam path are chosen such that a geometric-optical imaging from the gyrotron output to the torus windows occurs [4]. This feature makes the system less sensitive to misalignment especially for the case that the gyrotron output beam changes slightly its direction during the pulse due to thermal expansion of the internal gyrotron optics.

Transmission characteristics of a prototype system

The ECRH system for W7-X will finally comprise more than 160 water-cooled mirrors for beam matching and polarisation adjustment, transmission, switching of beams, and for the launchers. Due to the complexity of the system and to test its performance and stability, a full-scale prototype has been built, which consists of a lens horn with beam parameters corresponding to the W7-X gyrotrons,

a 5-mirror matching assembly and one MBWG system. In the first instance, non-cooled reflectors are installed in the test line. Instead of the input reflector array M4 to be used in the real system, a motorized 2-mirror beam shifting system allows to inject the probing beam at arbitrary positions into the MBWG, thus a low-power test of all transmission channels is possible.

Amplitude and phase measurements of the beams have been performed at the characteristic planes using various field scanning devices together with a vector network analyser. As an example, Fig. 2 gives the beam power and phase distributions for all transmission channels at the output plane of the MBWG. The results show an almost rotationally symmetric amplitude distribution and only small variations of the phase and thus demonstrate the good imaging characteristics of confocal systems even for off-axis beams. Within the experimental uncertainties the results are in good agreement with the calculations: the mode purity of the gaussian beams – as obtained from matching of the design gaussian beam to the measured amplitude and phase profiles – is typically 99% with a maximum deviation of the beam centers from the design value of 8 mm, and a beam squint with respect to the optical axis of < 2.6 mrad. These small displacements can be easily compensated by the beam distribution mirror array which will be placed at this position.
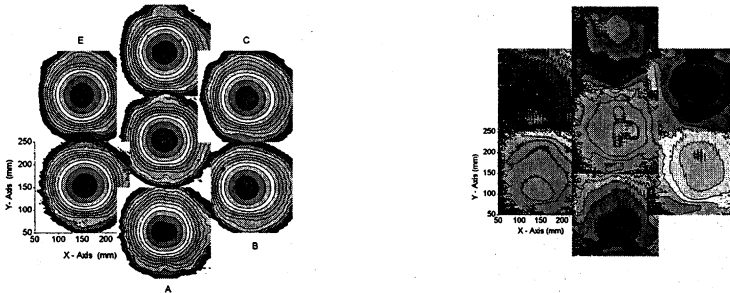
Fig. 2. Measurements of amplitude and phase distributions for seven 140 GHz beams at the output plane of the MBWG. Scale: 3 dB/colour step, 20°/colour step.

The total transmission efficiency of the prototype system including diffraction due to imperfect surfaces, ohmic loss, typical misalignment, and atmospheric absorption was checked by calorimetric methods and yielded 90±2%, which is in good agreement with the theoretical value of 92%.

Mirror design and thermal properties of the mirror surface

To reach high transmission efficiency, the design of the mirrors must guarantee a mechanically stable surface under the heat load imposed by the ohmic loss of the millimetre waves. The construction consists of a 60–70 mm thick honeycomb structure from stainless steel and a thin (2 mm) sheath of electro-formed copper on the mirror surface. Optimised cooling channels are milled directly be-

low the copper layer into the stainless steel structure and form one or several spirals going from the centre to the edge of the mirror. An example for a multi-beam mirror (surface 1.1×0.74 m) prior to electro-forming of the surface is shown in Fig. 3 (left). A complete single-beam mirror (0.33×0.33 m) fixed to his mounting, consisting of a spring-loaded central ball in a cone and two motor driven micrometers for remote adjustment is depicted in Fig. 3 (right).
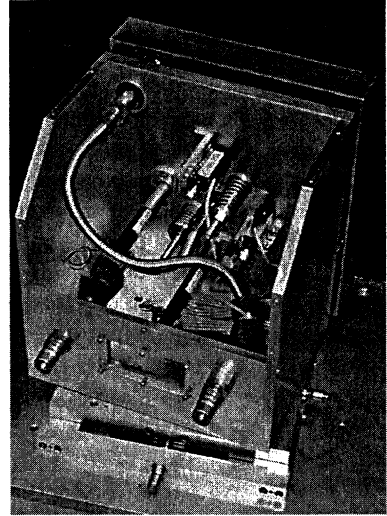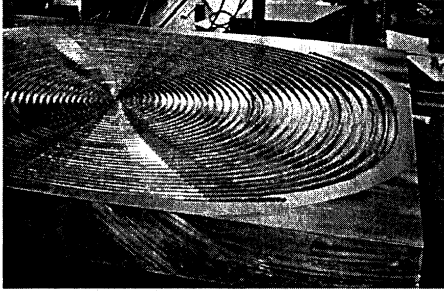
Fig. 3. Stainless-steel body of a multi-beam mirror with 4 cooling channels prior to electro-forming of the mirror surface (left). Single-beam mirror (0.33×0.33 m) fixed to the mount, which consists of a spring-loaded central ball in a cone and two motor driven micrometers for remote adjustment (right).
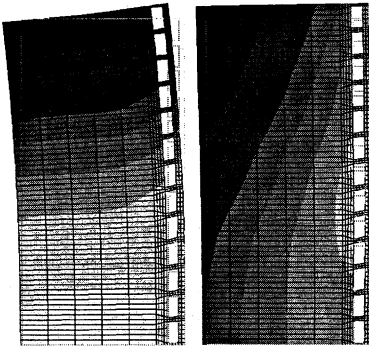
Fig. 4. Calculation of the deformation for a (axially symmetric) plane mirror model with a radius of 117 mm under a thermal load of 2 kW. Deformation is multiplied by a factor of 1000. Left: at 32 s after start of microwaves, Right: in steady state of irradiation.

According to thermo-mechanical calculations, a very low thermal deformation is obtained with this design, even during the transient phase in the first minute after power switch-on.

Figure 4 shows a calculation for a rotationally symmetric mirror model which includes the 58 mm thick mirror body with the frame structure, optimised cooling channels with a flow of 8 L/min and a thermal load of 2 kW with a distribution corresponding to a gaussian microwave beam with a radius $w = 50$ mm. The maximum displacement of the initially plane mirror surface at the edge of the mirror ($R = 117$ mm) is 6.1 μm at 32 s after switch-on, while deformation is essentially spherical, corresponding to a defocusing mirror

336

with a focal length of $f = -934$ m. Further calculations show, that the main cause of the deformation is the thermal gradient in the mirror body due to an increase of the cooling water temperature by microwave absorption. A summary of essential data for this mirror under microwave irradiation is given in Table 1.

Table 1. **Summary of calculated data
for a single-beam mirror under microwave irradiation**

	At $t = 32$ s	Stationary
Max. Surface temperature in °C	20 + 9.8	20 + 9.8
v. Mises Stress in N/mm^2	22	21
Deformation at $R = 117$ mm in μm	6.1	0.76
Focal length at $R = 54$ mm in m	−934	−3600

To confirm these results experimentally, two measurements have been performed. In a first experiment, the mirror was kept at a temperature of 20 °C and suddenly, the water flow with a temperature of 40 °C was started. The deformation was measured with a scanning millimetre wave reflectometer at a frequency of 150 GHz. In Fig. 5 one can see, that the deformation reaches its maximum after about 30 s. The resulting curvature corresponds to a focal length of −75 m which agrees well with the calculated value of −69 m

Fig. 5. Deformation of a mirror by a sudden increase of the cooling water temperature. Measurements are done by scanning reflectometry at different times after start of water flow.

for these extreme conditions. A second effect is the slight angular misalignment (indicated by the tilted curves in Fig. 5) due to the asymmetric mount of the mirror. If the results are downscaled to the conditions at W7-X (i.e. max. rise of cooling water temperature of 3 °C), a negligible deformation ($f > -500$ m) and mis-alignment ($\Delta\alpha < 0.002$ deg.) can be expected.

In the second experiment, the millimetre waves were simulated by focussed infrared radiation with a power of 3.6 kW, where 1.23 kW were absorbed by the (for this case blackened) mirror. Here, a minimum focal length of −675 m was measured, which agrees within 35% with the calculated values.

Similar experiments with comparable results were also performed with a plane and a focussing multi-beam mirror.

337

Modification of transmission properties by mirror deformation

The deformation measurements confirm the calculations and show especially, that the mirror deformation is mainly spherical, resulting in spherical modifications of the phase-fronts of the reflected beams, which leads only to a modification of the parameters of the gaussian beam, but not to a conversion to high-order modes. To get an estimate for the variation of the beam parameters at the torus windows of W7-X due to simultaneous deformation of all mirrors in the transmission line, calculations using gaussian beam propagation [4] have been performed. The results are given in Table 2 for a typical and the worst-case deformation, and are compared to the reference case, where no deformation exists. It is shown, that even in worst case, only a change of the beam waist radius of 4% is expected; the beam diameter at the window remains practically constant.

Table 2. **Parameters of the 140 GHz beam**
at the vacuum barrier window after transmission via 16 mirror surfaces
as a result of deformation due to mm-wave heating,
R_{beam}: **Radius of beam at torus window,**
W_0: **Radius of beam waist,**
Z_0: **Position of beam waist behind the window**

	R_{beam} (mm)	W_0 (mm)	Z_0 (mm)
Reference case: No deformation	22.9	22.3	164
Typ. deformation, $f = -1000$ m	22.7	21.8	201
Max. deformation, $f = -500$ m	22.7	21.4	235

This small variation corresponds to a coupling of 99.6% to the designed antenna beam [7]. The angular misalignment of the whole system due to the deformation of the mirrors is also negligible, especially as the positioning of the mirrors will be made such that the misalignment of adjacent mirrors cancels each other.

High-power test of the mirrors

At the Forschungszentrum Karlsruhe (FZK), the development of the 140 GHz/1 MW CW-gyrotron for the ECRH system on W7-X is in progress [3]. In the test stand, the output beam of the prototype gyrotron is guided via two matching mirrors (M1, M2) and two polarising mirrors to the dummy load. During high-power tests with a power of up to 890 kW (500 kW) and a pulse length of 3 (25) minutes all mirrors perform well and no serious problems were observed; especially on the corrugated surfaces of the polarisers, no arcing was seen provided that they were clean.

For power monitoring, three different systems have been integrated into the mirrors. In M1, a grating coupler consisting of a holographic grating with a groove depth of about 20 μm is used, which deflects about 10^{-3} of the incident power into a matched scalar horn. In M2, a waveguide coupler [8] is integrated into the mirror surface. To get high performance also for CW operation, the coupling waveguide is embedded into the copper surface by electro-forming techniques without any discontinuities. Additionally, thermocouples in the copper surface as well as in the cooling channels allow in-situ calorimetry of the power lost on the mirror surface with a time resolution of about 1 s.

Conclusions and outlook

The multi-beam transmission concept for the ECRH system on W7-X promises efficient power transmission with imaging from gyrotron to the torus windows. Low power measurements confirm the expected high mode purity and yield a transmission coefficient of about 90%.

The tests of the mirrors confirm the thermo-mechanical calculations and show, that the mirror design with optimized cooling channels lead to very small distortions of the surface under the expected thermal loads. The resulting change of the transmission properties of the complete lines are negligible. The application of these mirrors in a gyrotron test stand under real conditions (890 kW, 180 s) shows no problems and allows to optimise the beam diagnostics and power monitors for CW applications.

At present, the majority of the mirror mounts is installed at IPP Greifswald, and the mirrors are under fabrication. First high-power tests of the system are planned for 2003.

References

1. *Erckmann V.* et al., The W7-X project: Scientific Basis and Technical Realization. Proc. 17th IEEE/NPSS Symposium on Fusion Engineering (San Diego, USA, 1997), Ed. IEEE, Piscataway, NJ 1998, 40–48.
2. *Kasparek W.* et al., ECRH and ECCD for the stellarator W7-X. In "Strong Microwaves in Plasmas 1999", ed. A. G. Litvak (Inst. of Applied Physics, Nizhny Novgorod, 1999), 185–204.
3. *Dammertz G.* et al., Frequenz, **55**, 270–275 (2001).
4. *Goldsmith P. F.* Quasi-optical Systems. IEEE Press, Chapman and Hall, Publishers, New York (1998) ISBN 0-7803-3439-6.
5. *Empacher L.* et al., Design of the 140 GHz/10 MW CW ECRH System for the Stellarator W7-X. In Fusion Technology 1996, Elsevier Science B. V. Amsterdam (1997), 541–544.
6. *Empacher L., Kasparek W.,* IEEE Trans. Antennas Propagat. **AP-49**, 483–493 (2001).
7. *Joyce W. B. and DeLoach B. C.,* Appl. Optics, **23**, 4187–4196 (1984).
8. *Empacher L.* et al., Proc. 20th Int. Conf. on Infrared and Millimeter Waves (Lake Buena Vista Orlando, 1995), 473–474.

THE DESIGN OF THE JET-ECRH SYSTEM
AND DESIGN CONSIDERATIONS FOR ITER

A. G. A. Verhoeven, W. A. Bongers, B. S. Q. Elzendoorn,
M. Graswinckel, P. Hellingman, W. Kooijman, O. G. Kruijt,
J. Maagdenberg, D. Ronden, J. Stakenborg, A. B. Sterk, J. Tichler,
S. Alberti[1], M. Henderson[1], J. A. Hoekzema[2], A. Fernandez[3], K. Likin[3],
A. Bruschi[4], S. Cirant[4], S. Novak[4], B. Piosczyk[5], M. Thumm[5], A. Guigon[6],
C. Damiani[6], J. Pamela[6], A. Kaye[7], C. Fleming[7], H. Zohm[8]

FOM-Instituut voor Plasmafysica 'Rijnhuizen', Association EURATOM-FOM;
verhoeven@rijnh.nl; P.O. Box 1207, 3430 BE Nieuwegein, the Netherlands
[1]Euratom/CRPP-Lausanne; [2]Euratom/FZJ-Julich; [3]Euratom/CIEMAT, Madrid;
[4]Euratom/CNR-Milano; [5]Euratom/FZK-Karlsruhe; [6]Euratom/CSU Culham;
[7]Euratom-JET/UKAEA Culham; [8]Euratom/IPP-Garching

Abstract-An ECRH (Electron Cyclotron Resonance Heating) system has been designed for
JET in the framework of the JET Enhanced-Performance project (JET-EP) under the Euro-
pean Fusion Development Agreement (EFDA). Due to financial constraints it has recently
been decided not to implement this project. Nevertheless, the design work conducted from
April 2000 to January 2002 shows a number of features that can be relevant in preparation
of future ECRH systems, e. g., for ITER.

1. Introduction

The ECRH system was designed to comprise 6 gyrotrons, 1 MW each, in or-
der to deliver 5 MW into the plasma [1]. The main aim was to enable the control
of neo-classical tearing modes (NTM). One of the major items was the plug-in
launcher, steerable in both toroidal and poloidal angle, and able to handle 8 sepa-
rate mm-wave beams. Water cooling of all the mirrors was a particularly ITER
relevant feature. Another important issue was the power-supply and modulation
system, including series IGBT switches, to enable independent control of each
gyrotron and all-solid-state body power supplies to enable fast modulations up to
10 kHz.

2. Physics background

The frequency of 113.3 GHz is chosen for reasons of compatibility with the
envisaged 170 GHz at ITER. ECRH and ECCD are possible both in the X2 (cold
resonance at 2 T) and O1 (cold resonance at 4 T) mode.

Since JET-EP will probably not operate at $Bt > 3.5$ T for a significant num-
ber of pulses, the situation is similar to that envisaged in ITER, where the
170 GHz cold resonance is at 6 T, but the central field is 5.3 T at maximum. The

whole exercise of discussing ECRH physics in JET-EP and the implications for the system design (such as launcher geometry, installed power, modulation frequencies, etc.) can therefore be thought of as prototypical for ITER itself. In order to assess the possibilities for physics studies, a series of reference equilibria is constructed based on existing JET discharges that are scaled by simple physics rules to JET-EP parameters [2]. Then, ray or beam tracing techniques coupled with an absorption model are used to infer the deposited-power and driven-current profile [3].

The modelling uses the exact geometry of the launcher, including the different launching positions of different beams and the Gaussian optics of the focused beams. In addition to central heating and current drive, the following ECRH specific tasks are discussed:

- NTM stabilisation, where, based on the modelling of successful experiments in ASDEX Upgrade, power and modulation requirements are assessed;
- $j(r)$ control in advanced scenarios, where either central counter-CD or off-axis co-CD are envisaged as a tool to control reversed-shear profiles;
- transport studies using modulated ECRH to infer the electron heat transport without directly heating ions or inputting particles or momentum;
- exploration of scenario with $Te \geq Ti$, which will be dominant in ITER under α-heating, but are not accessed in present day low-density, ion-heated discharges.

These applications and their implications on the system design are studied in detail [2]. It is shown that with the envisaged 5 MW in the plasma, many of the goals are achievable and significant contributions to the understanding of reactor-grade plasmas can be expected.

3. The transmission-line system

The system includes 6 over-moded evacuated, corrugated waveguide lines of 63.5 mm diameter for transmitting the 6 MW (10 s) at 113.3 GHz from the gyrotrons to the launching antenna in the fundamental HE_{11} mode [4]. The lines will be on average 72 m in length and have each 9 miter bends for an estimated transmission efficiency of 91%. The last leg of the waveguide leading to the torus will be designed to accommodate for the torus movement during disruptions and thermal cycles. The exhaust of the pumping system will be fed to the tritium exhaust stack, see Fig. 1.

All lines will also be designed to be compatible for 170 GHz operation. Tritium safety aspects have played an important role in the design of the transmission-line system. At JET the safety rules require 2 windows for tritium containment, with vacuum inner space monitoring for leak detection. Furthermore, fast valves will be installed to enhance the safety of the system.
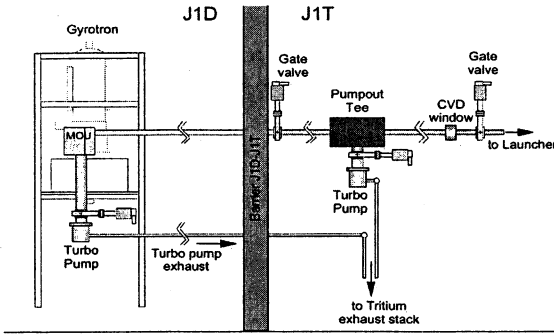
4. The launcher

The launcher is designed to inject a maximum of 8 beams, each 1 MW into the JET plasma [5]. It is designed as a plug-in module, in order to minimise the installation time, see Fig. 2.
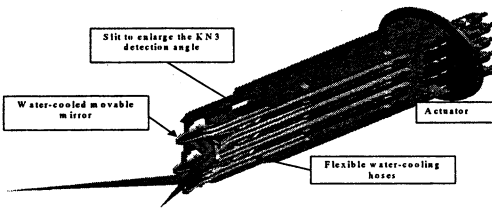
Fig. 2. Launcher assembly

The last mirrors of the system are steerable in order to have the maximum flexibility in the orientation of each beam. Double wall hoses will supply the cooling water. The hoses consist of two coaxial "bellows", each one is reinforced with stainless-steel weaving, see Fig. 3.
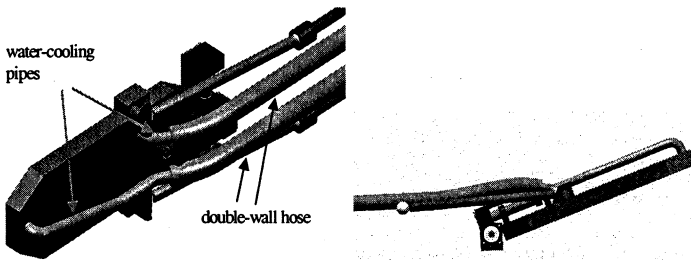
Fig. 3. Steerable mirror with water cooling

342
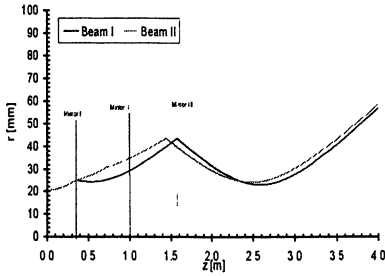
Fig. 4. Beam radius (w) as a function of position along the beam lines.

For the JET-EP-ECRH system, a mm-wave beam from a wave-guide output is launched into the plasma after reflecting on several curved mirrors and a movable flat mirror. The flat mirror reflects two incoming beams into the plasma.

The mirror can be moved using two steering rods, whose combined strokes determine the orientation of the mirror surface. The input of the launcher is a waveguide of 63.5 mm diameter. This corresponds to a beam waist (w_0) of 20.4 mm at the waveguide output. The main criterion used for assessing the performance of the launcher is the energy density at the resonance plane. See for the beam radius in the optimised set-up Fig. 4.

5. Testing of launcher sub-systems

Tests on launcher sub-systems are required in order to decrease the fail-rate of the ECRH launcher during its lifetime. The tests will be done under JET operation conditions as much as possible. Operation temperature of the launcher itself as well as the mirror system will be the same as during JET operation. Movements of the vessel caused by disruptions will be simulated in a later stage, at a different location.
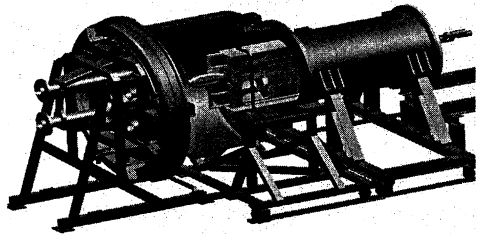
Fig. 5. Launcher test facility

Also thermal effects caused by plasma radiation are not included in these tests. The tests that will be done are mainly life cycle tests. Double bellow cooling hoses are the most critical parts in the system. A breakdown of this system will have major effects on JET operation schedule. Also the mirror speed will be measured. Another important issue is the reliability of the linear bearings to guide the steering rods. The new ideas implemented in the design have to prove their reliability; linear bearings based on a different principle were often not well performing in former JET designs. General view of the test facility is presented in Fig. 5.

343

6. The double disk window unit

In the novel design for the double-disk window unit, direct contact between the coolant and the CVD-diamond disk is avoided [6]. The cooling of the CVD disk is provided indirectly by heat conduction through a copper tube which is brazed directly to the CVD disk, as shown schematically in Fig. 6.
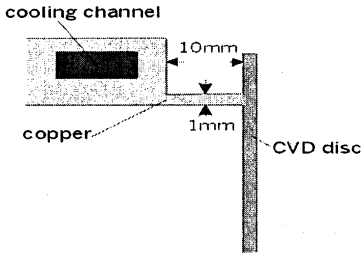
Fig. 6. Schematic arrangement of the brazing geometry as performed at TED.

Such a design becomes possible with a new brazing technique developed at Thales Electron Devices (TED), France. For reasons of thermo-mechanical stresses during brazing, the thickness of the copper tube must be 1 mm over a length of about 10 mm before it can be increased to a larger value for the enclosure of a cooling channel. A schematic design of such a double disk window unit is shown in Fig. 7. The dimensions are in agreement with the requirements of a WG63 transmission line. The thickness d_{disk} of the CVD disks and the distance d_{gap} between the disks determine the microwave transmission characteristic. As is evident from Fig. 6, the mechanical design of the double disk window becomes very simple if only one cooling channel on one side of the CVD disk is needed. An advantage of this design is that there is no direct contact between the CVD disk and the coolant, there is no risk of water (coolant) leakage in case of cracks inside a CVD disk. This practically eliminates the risk of tritium contamination of the coolant. Consequently, it is not necessary anymore to cover the rim of the CVD disk with a copper sheath as was foreseen in the ITER window design with direct cooling of the CVD disk. Further on there is no risk of trapped mm-waves inside the disk. In addition, there are no problems with corrosion. By using a brazing of the copper tube on one side only, the distance between the disks can be made as small as desired. This improves the transmission characteristic and reduces the sensitivity to mechanical tolerances.

344
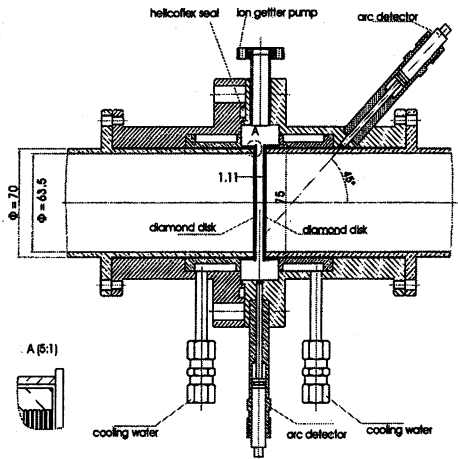
7. The gyrotron power supplies

The configuration of the gyrotron power supply is described by [7]. The gyrotron is very sensitive to internal arcs. Energy deposition must be limited to as low as 10 J. To limit the energy, fast IGBT switches are connected in series with the gyrotrons. These switches can disconnect the gyrotron from the power supply within a few μs. Such switches based on IGBT technology are already designed and commercial available for moderate repetition rates. The mm-wave output power of the gyrotron can be modulated either by the body voltage or the collector voltage. A disadvantage of modulation by the body power-supply only, is the higher heat load on the collector. For large power modulation, simultaneous modulation of the collector voltage is to be considered. This can be achieved by switching on and off the collector voltage completely by means of the series IGBT switch at the required switching frequency of 10 kHz. A test of such an IGBT switch from the Japanese IDX company was very successfully executed at the Japan Atomic Energy Research Institute [8]. See test set-up in Fig. 8. This switch has been developed under the direction of JAERI and build by IDX. The switch consists of an array of 100 water-cooled IGBTs and is rated for 100 kV DC, 100 A continuous. At a voltage level of 70 kV, a 10 kHz square-wave modulation was achieved during a pulse train of 1 ms. The test results are given in Fig. 9.
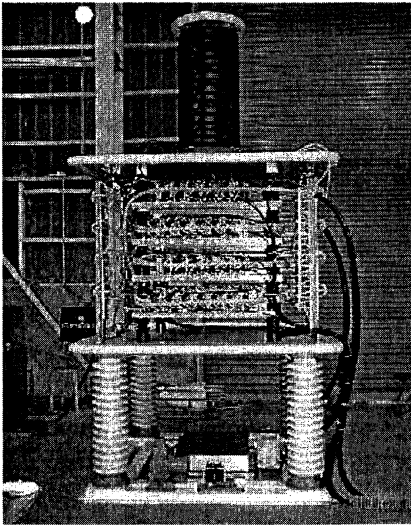
Fig. 8. Test-circuit for
10 kHz modulation test.
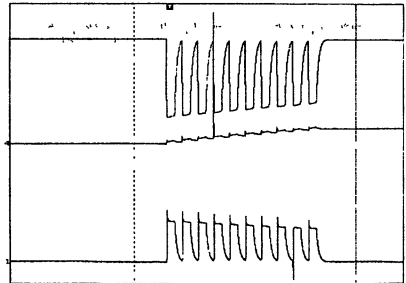
Fig. 9. Top: voltage across load
resistor with 70 kV amplitude
bottom: load current, 35 A max.

8. Conclusions

A conceptual design of an ECRH system for JET was undertaken. A technically feasible design was developed, which could meet the physics objectives. Amongst others, the value of the system for extrapolation to ITER of NTM stabilisation techniques was demonstrated. Unfortunately, due to budgetary constraints, it was decided not to implement the project.

References

1. *Verhoeven A. G. A.* et al., The ECRH system for JET, 26th Int. Conf. on Infrared and Millimeter Waves (Toulouse, September 10–14, 2001), p. 83. http://www.rijnh.nl/n7/d_EP/d_ECH/d_GEN/d_J/EP-ECH-GEN-J-H-006.pdf; *Verhoeven A. G. A.* et al., The 113 GHz ECRH system for JET, EC12 (Aix-en-Provence, France, May 13–16, 2002), http://wshop.free.fr/ec12/PAPERS/058-Verhoeven.pdf.
2. *Zohm H.,* private communication.
3. *Nowak S.* et al., Impact of ECRH Launcher Flexibility on NTM Stabilization and Advanced Scenarios in JET-EP, EC12 (Aix-en-Provence, France, May 13–16, 2002), http://wshop.free.fr/ec12/.
4. *Henderson M.* et al., Design of the evacuated waveguide transmission lines for JET-EP ECRH project, ibid.
5. *Elzendoorn B. S. Q.* et al., 22nd SOFT (Helsinki, September 9–13, 2002).
6. Piosczyk 2001 FZK Final Order Report http://www.rijnh.nl/n7/d_EP/d_ECH/d_GEN/d_E/EP-ECH-GEN-E-R-016.doc.
7. *Sterk A. B., Verhoeven A. G. A.,* 22nd SOFT (Helsinki, September 9–13, 2002).
8. IDX. www.idx-net.co.jp/whats/katarogu/index.html.

THE LHCD SYSTEM FOR ITER

F. Mirizzi, Ph. Bibet[1], P. Bosia[1], L. Doceul[1], S. Kuzikov[2], K. Rantamaki[3], A. A. Tuccillo, F. Wasterjna[3]

Associazione EURATOM–ENEA sulla Fusione, C. R Frascati,
P.O. Box 65, 00044 Frascati, Rome, Italy
[1]Centre d'Etude de Cadarache, 13108, St Paul lez Durance France
[2]Institute of Applied Physics, Nizhny Novgorod, Russia
[3]VTT Energy, Finland

LH waves have demonstrated the highest far off-axis current drive efficiency as compared with other systems. A powerful LHCD system has been proposed for ITER and a preliminary design of this system has been presented during the EDA. The total radiofrequency (RF) power coupled to the plasma is set to 20 MW at a frequency of 5 GHz. This last value is a compromise between technical constraints on the available RF power sources and physics limits determined by wave coupling to alpha particles. The paper reviews the system and its main microwave components.

Introduction

The Lower Hybrid Current Drive (LHCD) system for ITER is designed to inject into the plasma a total radiofrequency power of 20 MW (CW) at a frequency of 5 GHz. It provides two essential functions: off-axis current drive and plasma heating, and several auxiliary functions as plasma and burn control, help in plasma shut-down, wall conditioning at full field, plasma breakdown, MHD control and assisted current rise. A detailed report on the analysis and design of the system is given in [1].

The following description gives the actual situation of the design of the system, which general schematic is given in Fig. 1. Some further optimisation of its main components could eventually improve the performances of the whole system.
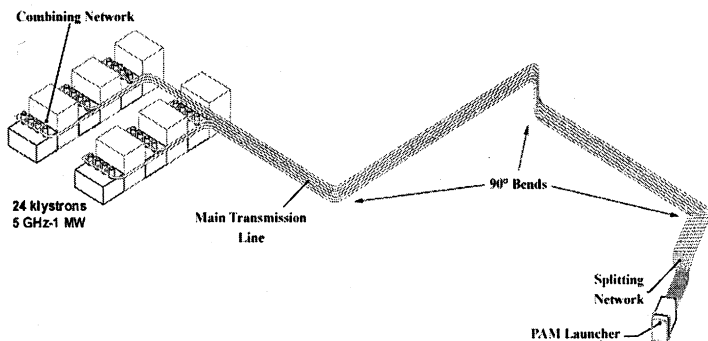
Fig. 1. Schematic layout of the system

347

System overview

The system is based on 24 klystrons, grouped four by four in six identical subsystems. Each klystron delivers an output power of 1 MW (CW) at a frequency of 5 GHz through a rectangular WR 229 waveguide (cross section 58.17×29.08 mm). The attenuation of this waveguide (0.025 dB/m at 5 GHz in the fundamental mode TE_{10}) is too large owing to the length (~ 60 m) of the Main Transmission Line (MTL). To reduce the transmission losses, the MTL is made of oversized circular standard waveguide C–10 (inner radius 105.57 mm), that carries the combined power of a whole subsystem (4 MW) in the TE_{01} mode. At the end of the MTL, the RF power is split in four rectangular waveguides, again the WR 229, to conveniently feed the launcher. A detailed description of the transmission line is given in [2, 3].

The combining/splitting network

The Combining Network (CN) is the transition between the 4 rectangular waveguides of a generic LHCD subsystem and the circular waveguide of one out of the 6 MTLs; the Splitting Network (SN) is the inverse transition. A possible configuration of the CN (Fig. 2) has been analysed and optimised using the High Frequency Structure Simulator (HFSS), a computer code developed by ANSOFT, based on the Finite Elements Method (FEM), used also for the analysis of many others microwave devices of the system. The device is composed of 4 rectangular to circular sector transitions (sector angle = 90°) coupled to a single circular waveguide. It also converts the TE_{10} mode of the rectangular waveguides to the TE_{01} mode of the circular waveguide.

By appropriate choice of the radius, the TE_{01} mode is the fundamental one in a sector waveguide with sector angle of 90° [4], so that the conversion efficiency of this transition is very close to 1. The optimised transition has a return loss lower than 30 dB at 5 GHz.
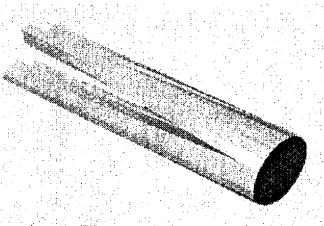
Fig. 2. The combining network   Fig. 3. E-field in the transition
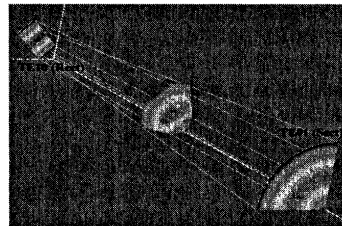
The E-field configuration at the input, output and at an intermediate section of this transition, as given by HFSS, is shown in Fig. 3. The analysis shows that the component is bi-directional, so that it could be also used as Splitting Network.

348

The 90° bends

Bends in oversized circular waveguide are critical components. Two particular types of bends have been investigated using analytic models based on the generalised telegraphist equation: the bend with constant curvature radius, optimised with a waveguide radius of 108 mm and a curvature radius of 4154 mm, and the improved quasi-optical mitre bend. The second one, composed by an ordinary mitre bend, connected to the transmission line through two straight sections of corrugated waveguide, has a total length of about 3.3 m. For both curves the calculated efficiency is better than 99%.

The launcher

A launcher based on the concept of the Passive Active Multijunction (PAM) antenna [5] has the potentiality to face the considerable heat flux (heat load 0.5 MW/m^2, neutron flux 0.5 MW/m^2) and the extreme electromechanical torques (8.7 MNm) determined by the harsh plasma environment of ITER. The massive walls between its active waveguides give mechanical stiffness to the structure and permit its effective water cooling through longitudinal pipes drilled into them. The coupling characteristics of the launcher, also depending on the distance between adjacent radiating waveguides on the same row, are improved by means of passive waveguides located between the active ones.

The launcher, which main characteristics are reported in Table 1, is divided into 4 identical and independent blocks disposed on two rows. Each block is composed by 6 PAM modules.

Table 1. Main characteristics of the launcher

PAM modules per block	3 × 2
Rows per block	12
Active/Passive wgs per row in a block	24/25
Row height	56 mm
Width of active wgs	9.25 mm
Wall thickness between active wgs	13.25 mm
Width of passive wgs	7.25 mm
Depth of passive wg (optimised)	15 mm
RF power density (active wgs)	33 MW/m^2
Corresponding electric field	≤ 6.2 kV/cm
Phase Pitch between active wgs	270°
$N_\parallel$ peak (at $\Phi = 180°$ between modules)	2
$N_\parallel$ ($\Phi = -90° \div 90°$ between modules)	$1.9 \div 2.1$
Directivity (at $N_\parallel = 2$)	~ 70%

349

The RF power distribution network

This network distributes the RF power of each single output waveguide of the SN (1 MW) into the 48 active waveguides of a PAM module disposed on 6 rows and 8 columns.
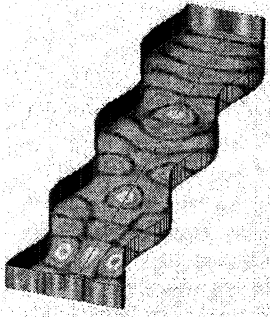
Fig. 4. TE_{10}/TE_{30} Mode converter.

The RF power is first divided by two through a conventional 3 dB hybrid coupler located in the cryostat region of the machine. Three ceramic, double disk, windows, one at its input and two at the outputs, separate the coupler from the atmospheric pressure and from the vacuum. A TE_{10}/TE_{30} mode converter on each output branch of the coupler, followed by a 4.77 dB, H-plane, power splitter, distributes the RF power into the three upper, respectively lower, rows of a PAM module. The power distribution in the 8 waveguides of a generic column is obtained through 3 consecutive groups of E-plane bijunctions.

The TE_{10}/TE_{30} mode converter is based on periodic variation of the width of a rectangular waveguide, with period equal to the beat wavelength between the two modes. A preliminary analysis with HFSS gives a conversion efficiency better than 97%. The E-field configuration in the converter is shown in Fig. 4.

The multi-junction

In Fig. 5 is shown the HFSS model of a generic row of a PAM module; only the active waveguides, assuming perfect radiating conditions, have been considered. It does not include the phase shifters that have been independently optimised.

The cross section of the waveguides has been dimensioned to have a width lower than 30 mm (to avoid TE_{01} mode) and a height lower than 60 mm (to avoid TE_{20} mode). The power density is limited to 34 MW/m^2 in the mouth region, and kept "as low as possible" elsewhere.

The computed reflection losses of the whole row are lower than 35 dB over a bandwidth of 100 MHz,

Fig. 5. HFSS model of a row of a PAM module (top view).

while the average output power per waveguide is about 9 dB over a 300 MHz bandwidth.

Conclusions

A preliminary design of the LHCD system for ITER has been completed. Some components need more accurate analysis and optimisation. The computation must be followed by the realisation of the mock-up of the critical components to check their real performances. In particular the coupling property of the PAM is going to be evaluated on FTU [6]. A new experiment is in preparation to test all the technical aspects of the launcher on Tore Supra (use of special materials at the mouth, cooling feasibility, etc.) [7].

References

1. *Bibet Ph.* et al., Detailed Design Description (DDD) of the LHCD system; ITER EDA document (Garching, Germany, 2000).
2. *Bibet Ph.* et al., Report on the transmission line of the LH system on ITER–FEAT Contract FU05 - CT 2001-00019 (EFDA/00-553) (Garching, Germany, 2001).
3. *Mirizzi F., Bibet Ph.* Appendix to the Reports on ITER–FEAT LHCD Transmission Line and Launcher. Design of the Main Microwave Components. Part 1 – The transmission line. Part 2 – The Launcher. Contract FU05 - CT 2001-00020 (ENEA: EFDA/00–554, CEA: EFDA/00-553) (Garching, Germany, 2001).
4. *Spordler F., Hunger H. G.* Waveguide tapers, transitions and couplers., P. Peregrinus LTD, IEE Electromagnetic Waves Series 6 (1979).
5. *Bibet Ph., Litaudon X., Moreau D.* Principle of a retroreflecting LH antenna., Conference IAEA 1994: LHCD in ITER (IVA-LH).
6. *Mirizzi F.* et al., Preliminary test on the Passive Active Multijunction launcher for FTU; this workshop.
7. *Bibet Ph.* et al., Coupling and power handling of the new Tore Supra LHCD launcher, Proceeding of the 21st SOFT (Madrid, Spain, 2000), p. 679–684.

THEORETICAL ANALYSIS
OF A REMOTE STEERING ANTENNA
AND COMPARISON WITH EXPERIMENTS

K. Ohkubo, S. Kubo, T. Shimozuma, H. Idei, Y. Yoshimura,
T. Notake[1], W. Kasparek[2]

National Institute for Fusion Science,
322-6, Oroshi-Cho, Toki, Gifu, 509-5292, Japan
[1]Nagoya University, Graduate School of Energy Engineering and Science,
Furo-Cho, Chikusaku, Nagoya, 464-8601, Japan
[2]Universitaet Stuttgart, Institut fuer Plasmaforschung,
Pfaffenwaldring 31, D-70569, Stuttgart, Germany

A theoretical study of the square waveguide antenna with corrugated walls was carried out
with reference to experimental results. When the length of the waveguide to which the
Gaussian beam is injected obliquely is changed, a recursive Gaussian beam with high effi-
ciency radiates from the waveguide exit in the asymmetric or symmetric direction with re-
spect to a waveguide axis at the almost same interval. Because the optimum waveguide
length for the maximum efficiency decreases stepwise with increasing the injection angle,
adjustment of the waveguide length is not continuous but discrete. This method enables the
injection angle which was limited to 10 degrees in the fixed waveguide length to be in-
creased by about two times.

1. Introduction

In recent years, a great deal of interest has been shown in a remote steering
antenna for electron cyclotron heating (ECH) and current drive (ECCD) of plas-
mas for the international thermonuclear experimental reactor (ITER). The simple
mechanism makes this a promising alternative antenna design. The structure,
which avoids the use of fast movable mirrors in a vacuum vessel, is advantageous
from the point of view of maitenance which has to be done in an environment
that is evacuated, neutron-irradiated and has a strong magnetic field. Since the
method of launching millimeter wave beam from a corrugated waveguide to re-
motely control the angle was first proposed [1], experimental tests have been
carried out at both low and high power levels using two types of square
waveguides, one with corrugated walls on two sides and one with four walls cor-
rugated [2, 3]. In the theoretical investigation on the antenna with corrugated
walls on two sides only, an analysis of the mode content based on a mode match-
ing method shows that an input Gaussian-like beam [4] or a Gaussian beam [2, 5]
can be represented approximately by the composition of five hybrid modes. Field
analysis at the boundary walls shows that two smooth walls in a square corru-
gated waveguide could be replaced by corrugated walls if the waveguide is

352

highly oversized [6, 8]. In this paper, an analysis based on mode matching, summing of the propagating hybrid modes and taking the Fourier transform with phase factor is carried out. The comparison is carried out for parallel, perpendicular and 45 degrees polarizations with respect to scanning plane along the wall. By analyzing the system for different lengths of waveguide and various injection angles, we found out that in addition to the well-known fundamental branch, many branches with high efficiency more than 94 % exist. This method can extend the scanning angle of the ITER alternative antenna to as large as 25 degrees. It is pointed out that launching waves in both directions by one-sided injection with respect to the waveguide axis is also possible.

2. Radiation from the remote steering antenna

The Gaussian beam with $f = 158$ GHz, $w_0 = 22$ mm and the waist point at the entrance is injected into the square waveguide with all the walls corrugated (60.08×60.08 mm) and scanned along the direction perpendicular to E_{gy}, where E_{gy} is the electric field along the y-direction of the Gaussian beam. In the numerical calculation, 30×30 modes for mode number m_p and n_p with field data of 128×128 points was used. The power efficiency $|B_0|^2$ of radiation with the same waist size as the injected Gaussian beam of which waist point is at the waveguide exit is calculated as functions of waveguide length L and injection angle β. The receiving angle corresponding to the asymmetric direction is $-\beta$ and that to the symmetric direction is β.

In Fig. 1 numerical results are shown. A number of "rib-shaped" traces showing higher efficiency are found corresponding to the waveguide length vs. the injection angle plane in both the asymmetric and symmetric directions. In the asymmetric direction, a fundamental branch stating from $L \sim 7.8$ m which is equal to $4a^2/\lambda$ has efficiency $|B_0|^2 \sim 0.97$ for small angle, where this includes the power truncated at the entrance to the waveguide. With increasing β, power and the corresponding waveguide length gradually decreases. At $\beta > 5$ degrees, the second branch with a slightly shorter length than the fundamental branch appears with high $|B_0|^2$ in the asymmetric direction. At the same time, fundamental branch in the symmetric direction with $|B_0|^2 \sim 0.97$ appears between fundamental and second branches in the asymmetric direction. At $\beta > 15$ degrees, a third branch appears in the asymmetric direction. With increasing β, a series of branches appears in both the asymmetric and symmetric directions. As shown in Fig. 2, (c) the optimized L, (a) its maximum $|B_0|^2$ and (b) the windows for the waveguide length Δ_{90} for which efficiency is larger than 90% are plotted for the asymmetric and symmetric directions. The optimized L for the angle larger than 10 degrees shows a stepwise variation due to the branch structure and Δ_{90} is around 4 ~ 2 cm.
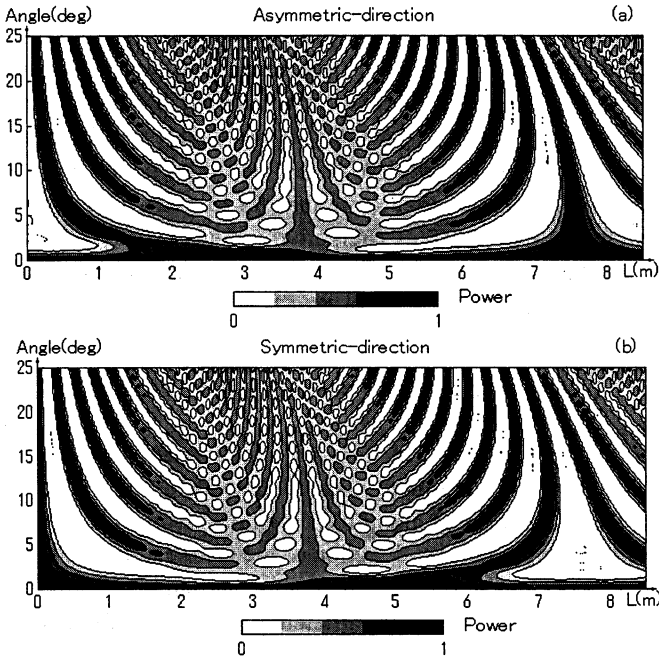
Fig. 1. Contour plots of radiation efficiency $|B_0|^2$ in scanning perpendicular to E_{gy} with waist point at $z = 0$ mm where $f = 158$ GHz, $w_0 = 22$ mm and $a = 60.08$ mm. (a) – asymmetric direction, (b) – symmetric direction.
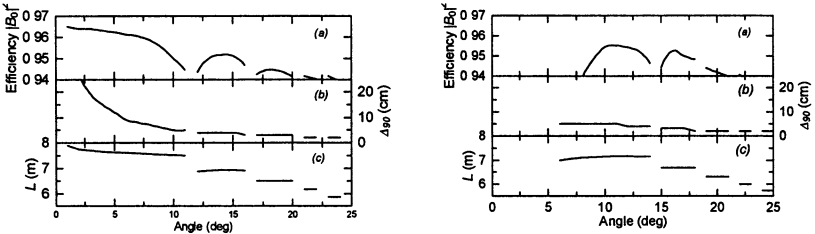
Fig. 2. The scanning perpendicular to E_{gy}(a) theoretical maximum $|B_0|^2$, and (b) the window Δ_{90} for waveguide length with an efficiency more than 90%, and (c) the optimum L are plotted as a function of injection angle. Here, $f = 158$ GHz, $w_0 = 22$ mm, waist point at $z = 0$ mm and $a = 60.08$ mm. Left figure: asymmetric direction; right figure: symmetric direction.

Thus for the waveguide length in the real antenna it is not necessary for the length to decrease continuously, but discrete changes are sufficient. Thus the length-control method can be used to increase an injection angle and maintain high radiation efficiency (> 94%). This alternative antenna is available for such

as the ITER-ECH. The branch structure results from composition between excited modes with large coupling coefficients. In order to obtain highest efficiency, the optimized L is necessary. For angles larger than 10 degrees, the width of various branches does not change considerably. In the region between branches, recurrence of beam pattern degrades. In some cases, millimeter wave power radiates on both sides of the waveguide axis. Except the symmetric direction, the radiation using branches with length more than $4a^2/\lambda$ has no high efficiency The same branch structure is obtained also in the phase rotation of 45 degrees and in the parallel scanning. This results from the similar mode coupling data obtained at the entrance to the waveguide when scanned in x- and y-axis.

When $L = 7.5$ m, $|B_0|^2$ in Fig. 3 is calculated as a function of injection angle with the perpendicular scanning to E_{gy}. This graph corresponds to the vertical cut of Fig. 1, a and b. Because the truncated power at the entrance is included in the calculation, $|B_0|^2$ at $\beta = 0$ is 0.97. With increasing β, peaks with rather low transmission efficiency appear. The coupling efficiency is smaller than for the Gaussian beam coupled with fundamental branch due to the fixed L. As for the parallel scanning, the same graph as Fig. 3 is obtained. Coupling near 0 degrees in the symmetric direction is due to the finite waist size of the beam. In Fig. 4, experimental power transmission normalized to the transmitted power for $\beta = 0$ is shown for both scans [7]. The difference between the parallel and perpendicular scans is very small. However, no dip near 5 degrees and no complete vanishing near 16 degrees as shown in calculation are seen. This is due to the fact that the detection system used for the measurements includes an angular range of 4 degrees and thus also detects side lobes near the main beam. It is noted that the radiation from the symmetric direction at 17 degrees with 77 % efficiency was observed. The experimentally observed efficiency agrees well with theoretical analysis in Fig. 3.
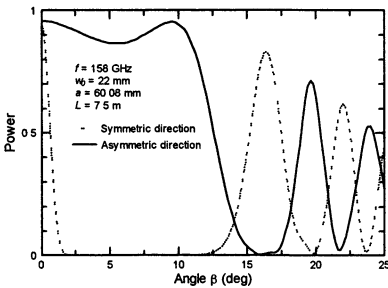
Fig. 3. Theoretical radiation efficiency $|B_0|^2$ in perpendicular scanning, where $f = 158$ GHz, $w_0 = 22$ mm, $a = 60.08$ mm and $L = 7.5$ m.
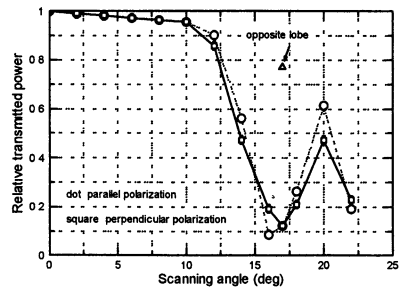
Fig. 4. Experimental relative transmission power for parallel and perpendicular scannings, where $f = 158$ GHz, $w_0 = 22$ mm, $a = 60.08$ mm and $L = 7.5$ m.

The branch structure is explained as follows. The waveguide wavenumber β_g is written by

$$\beta_g = \left[1 - (m_p\lambda/2a)^2 - (n_q\lambda/2a)^2\right]^{1/2} 2\pi/\lambda \,. \tag{1}$$

For x-axis scanning, phase difference $L\Delta\beta_g$ between modes with index (m_2, n_q) and (m_1, n_q) is approximately written by

$$L\Delta\beta_g \approx \frac{L\lambda}{4a^2}\pi(m_1 - m_2)(m_1 + m_2)(1 + \frac{\sin^2\beta}{2}) \,. \tag{2}$$

Here, β is the injection angle and $m_2 = [2a\sin\beta/\lambda]$ is substituted. The operator $[u]$ takes only the integer part of the argument u. The correction term of Eq. 2 is the phase error from the normal incidence between two modes [2]. For the adjacent mode and main mode with $m_1 - m_2 = 1$, the optimum lengths for the asymmetric image with $L\Delta\beta_g = (2s + 1)\pi$ and the symmetric image with $L\Delta\beta_g = 2s\pi$ are given by

$$L = \frac{2s+1}{2m_2+1}\frac{4a^2}{\lambda}\frac{1}{1 + (\sin^2\beta)/2} \,, \tag{3}$$

$$L = \frac{2s}{2m_2+1}\frac{4a^2}{\lambda}\frac{1}{1 + (\sin^2\beta)/2} \,, \tag{4}$$

respectively. When the integer s is equal to m_2, the fundamental branch for the asymmetric direction is formed and a value for s different from m_2 creates higher branches on each side of the fundamental branch. With increasing injection angle, m_2 and s in the fundamental branch increase and the number of branches with $s < m_2$ increases.

3. Summary

The oblique coupling of Gaussian beam in a square corrugated waveguide and radiation from the waveguide exit are studied theoretically and experimentally. The experimental results are explained well by numerical calculations. Radiation with high efficiency for the symmetric and asymmetric directions is obtained. An adjustment of the waveguide length enables high efficiency ($> 94\%$) with the angle larger than 10 degrees to be obtained. This method is recommended for the ITER-ECH antenna and also for a launcher in small devices with a narrow port where it is not possible to install a mirror.

References

1. *Prater R., Grunloh H. J., Moeller C. P., Doane J. L., Olstad R. A., Makowski M. and Harvey R. W.* Proc. of 10th Joint Workshop on ECE and ECRH, World Scientific, p. 531 (1997).

2. *Chirkov A. V., Denisov G. G., Kasparek W., Wagner D., Gantenbein G., Haug M. and Hollmann F.* Fusion Engineering and Design, **53**, 465 (2001).

3. *Takahashi K., Sakamoto K., Hayashi K. and Imai T.* Joint Meeting of US-Japan RF Heating Technology Workshop and EU-Japan RF Antenna and the Related Technology Workshop Inuyama (2002).

4. *Moeller C. P.* Proc. 23rd International Conference on Infrared and Millimeter Waves, p. 116 (1998).

5. *Denisov G. G., Kuzikov S. V. and Kobayashi N.* International J. Infrared and Millimeter Waves, **22**, 1735 (2001).

6. *Ohkubo K.* International J. Infrared and Millimeter Waves, **22**, 1709 (2001).

7. *Kasparek W., Gantenbein G., Plaum B., Wacker R., Filipovic E., Chirkov A. V., Denisov G. G., Kuzikov S. V., Ohkubo K., Hollmann F., Wagner D.* Proc. 12th Workshop on ECE and ECRH (Aix-en-Provence, 2002, to be published).

8. *Ohkubo K., Kubo S., Shimozuma T., Yoshimura Y., Idei H., Sato M. and Kasparek W.* Joint Meeting of US-Japan RF Heating Technology Workshop and EU-Japan RF Antenna and the Related Technology Workshop (Inuyama, 2002).

PRELIMINARY TESTS ON THE PASSIVE ACTIVE MULTI-JUNCTION LAUNCHER FOR FTU

F. Mirizzi, Ph. Bibet[1], A. Marra, P. Petrolini, A. A. Tuccillo

Associazione EURATOM–ENEA sulla Fusione, C. R Frascati, P.O. Box 65,
00044 Frascati, Rome, Italy
[1]Centre d'Etude de Cadarache, St Paul lez Durance, France

The Passive Active Multi–junction launcher (PAM) is a robust coupling structure, able to withstand the strong thermal loads and the electromechanical stresses of ITER. A collaboration between CEA-Cadarache and ENEA-Frascati has started to test on relevant plasmas this still conceptual launcher. In the frame of this collaboration the first step has been the realisation of a PAM for the LHCD system of the Frascati Tokamak Upgrade (FTU), where the coupling characteristics of the launcher will be assessed. All the technical aspects of the PAM will be later tested in a full rated experiment on Tore Supra. This paper reports the results of the low power measurements of the microwave characteristics of the PAM for FTU.

Introduction

During the last few years the need for robust Lower Hybrid (LH) coupling structures, able to withstand the strong thermal loads (heat load 0.5 MW/m^2, neutron flux 0.5 MW/m^2) and the electromechanical stresses foreseen for the next generation of tokamaks has became compelling. In this respect the PAM concept, proposed by CEA (Cadarache) [1], seems a good solution, combining optimum coupling properties with relevant robustness and effective cooling through ducts drilled in the thick vertical walls between active waveguides.

The validation of the PAM concept with the test on FTU is generally considered a "priority action" to validate the possibility of using a PAM as a LH launcher on ITER. The decision to continue the validation of the PAM concept with a full-scale test of an efficiently water-cooled ITER like launcher is likely to take place after positive results of the test on FTU.

The decision to verify the coupling characteristics of a PAM on FTU arose from the similarity between high plasma density and high magnetic field of FTU and ITER.

Lay-out of the launcher

The overall mechanical configuration of the PAM launcher for FTU is mainly determined by the lay-out of the actual LHCD system [2] and by the dimension of the FTU ports.

The launcher consists of 12 PAM modules, arranged three by three in 4 rows. The 12 modules are fed by a 12 rectangular waveguides system coupled to the main (circular waveguide) transmission line of one out of the six LH sub-system

of FTU. Each module has 2 active and 2 passive waveguides at the mouth (Fig. 1); the cross section of each of them is 28×5 mm^2. The thickness of the vertical walls is 0.8 mm and the depth of the passive waveguides is 0.25 λ_g. The built-in phase shift between the two active waveguides of a generic module is set to 270°.

With these parameters, according to the analysis done using the computer code Slow Wave Antenna (SWAN), the $N_{\parallel\,peak}$ of the structure is 2.42. The power directivity is close to 70% for electron density at grill mouth near cut-off. The $N_{\parallel}$ can be varied between 1.6 and 2.9 when the feeding phase between the three modules in the same row is varied in the range ±180° degrees.

Fig. 1. The launcher mouth

The wall thickness does not allow for a water cooling system, but the overall energy delivered to the launcher during the RF pulses (maximum pulse length 1 s) leads to a temperature increase of only a few degrees.

The launcher has an optimised length of 660 mm; for convenience it has been split in 2 sections (Fig. 2). The input section (rigth) includes the primary bi-junctions (the septa of the three bi-junctions in the upper row are visible in the figure) and, in the alternate waveguides on the same row, 90° phase shifters. In the output section (left), the vertical walls between adjacent waveguides in the same row are thickened through "ad hoc" tapers. 180° phase shifters are built in every second waveguide of each PAM module to realise the required phase shift of 270° at the mouth.
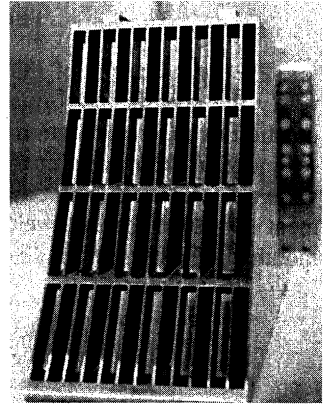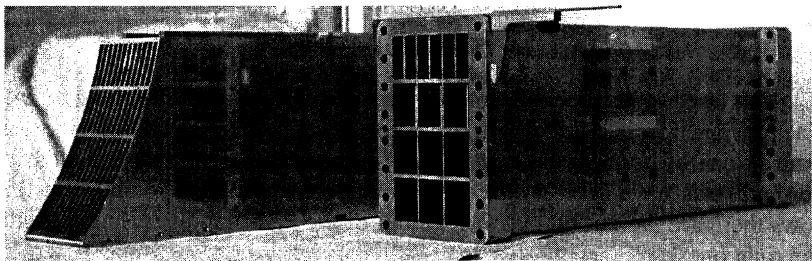
Fig. 2. The two sections of the PAM

Due to the complexity of their inner structure and to the stringent tolerances on the dimensions, both the two sections have been obtained by electrical erosion in stainless steel, a material that is easy to machine and assures a relevant mechanical stiffness to the structure.

More detailed information on this launcher are given in [3].

The measurement procedure

The two sections of the launcher have been characterised independently to verify the specific performances, in term of scattering parameters, of each bi-junction in the input section and of the active waveguides in the output one. In a second phase the two sections have been connected together to verify the micro-wave performances of the whole structure. A complete set of "ad hoc" measurement tools has been developed for this purpose; for example, the "counter–mouth" in Fig. 3, permits the use of standard, flat flanged, waveguides transitions at the mouth of the launcher, properly shaped to match the average profile of the plasma.
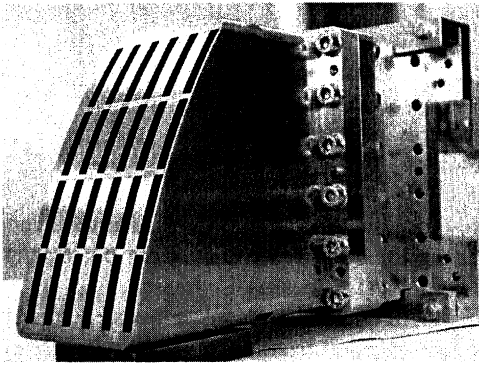
Fig. 3. The PAM counter-mouth

All the diagrams in this paper report the values of the scattering parameters at f_0 = 8.015 GHz, the design frequency of the launcher, but all the measurements have been made over a frequency band of ±20 MHz around f_0. The figures at the top of the diagrams indicate the phase shift in the related waveguides. For a direct comparison to the theory, the values obtained by the computer code "High Frequency Structures Simulator" (HFSS), based on the "finite elements method", developed by ANSOFT, are reported on the same diagram. Straight lines link the values pertaining to waveguides belonging to the same horizontal row to give more evidence to the diagram.

The input section

This section includes the primary E-plane bi-junctions of the 12 modules. Each bi-junction is a three-port, asymmetric device due to the 90° phase shifter built in one of its two output waveguides. Looking from the top side, the output vertical rows have been progressively numbered (1÷6) left to right; in the odd rows there are the left output waveguides of the PAM modules, in the even rows the right ones.

The diagram in Fig. 4 reports the amplitude of the transmission parameters for the primary bi-junction of each PAM module (S12 for the odd output waveguides, S13 for the even ones).

The asymmetry of the E-plane bi-junctions is pointed out by the different amplitudes of related S12 and S13.

The differences between measured and computed (HFSS) values (~ 6.7%) are due to the RF losses on the real walls (in the HFSS model perfectly conduct-

360

ing walls have been considered), and also to the not perfectly matched load on the third port, that introduces a non zero reflection.
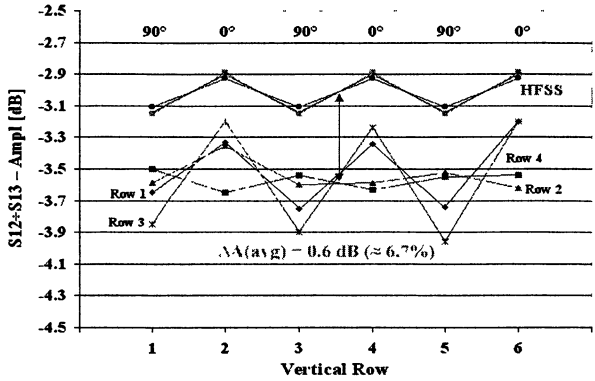
Fig. 4. Input bi-junctions: S12÷S13 amplitude [dB]
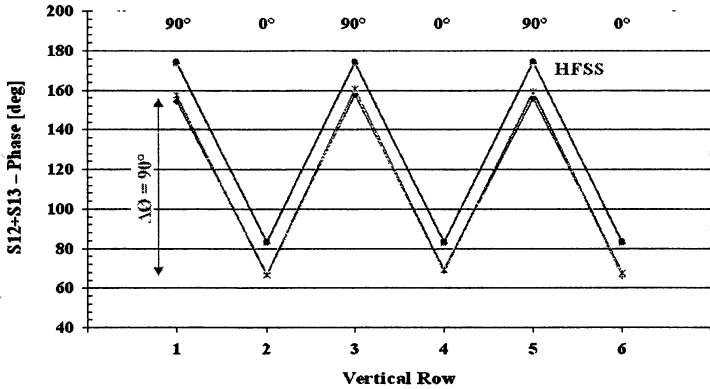
Fig. 5. Input bi-junctions: S12÷S13 phase [deg]

The phases of the same parameters are given in Fig. 5. It is evident the perfect correlation between the computed and the measured values. The average reflection losses of this section are lower than 30 dB.

The output section

The amplitude of the transmission characteristics (S12) of this unit (substantially made of two ports devices) is summarised in the diagram in Fig. 6.

The difference between computed and measured values (about 10% in amplitude), as for the previous section, is determined by the imperfect dummy loads and the simplified computation hypothesis. The measured phases, instead, are in total agreement with the design values (Fig. 7).

361
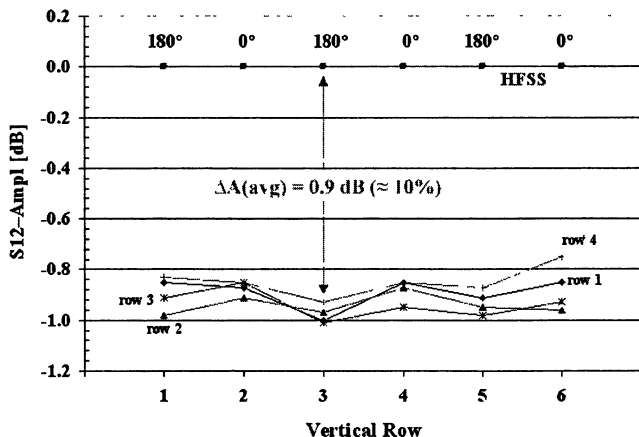
Fig. 6. Output section: S12 amplitude [dB]
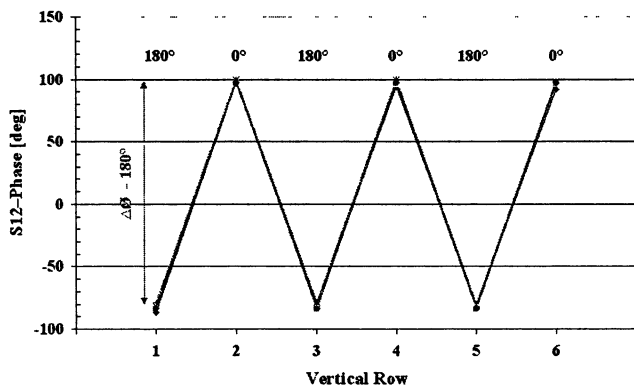
Fig. 7. Output section: S12 phase [deg]

The whole launcher

To complete the definition of the RF characteristics of the launcher, the two sections have been connected together. The results of the specific measurements are summarised in the diagrams given in the following. Due to the bi-junctions in the first section, each complete PAM module is a three-port device.

The diagram in Fig. 8 gives the amplitude of the transmission parameters (S12÷S13) compared to the computed values. The average difference between the two sets of values (about 1.3 dB, 14% in amplitude), is lower than the sum of the distinct differences pointed out for the two composing sections.

As for the two composing sections, the phases correspond to the design value (Fig. 9); this assess the accuracy of the design and of the realisation of the launcher.

362

Fig. 8. Whole launcher: S12÷S13 amplitude [dB]
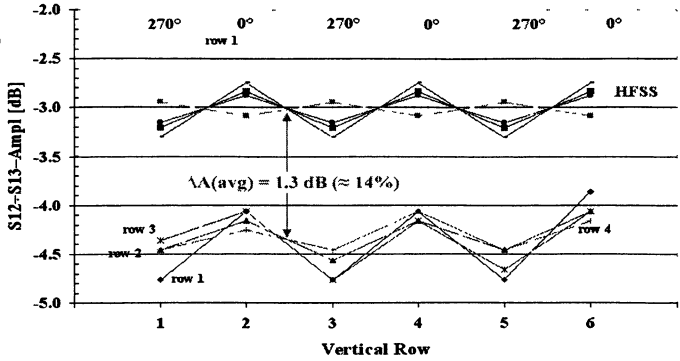
Fig. 9. Launcher: S12÷S13 phase [deg]
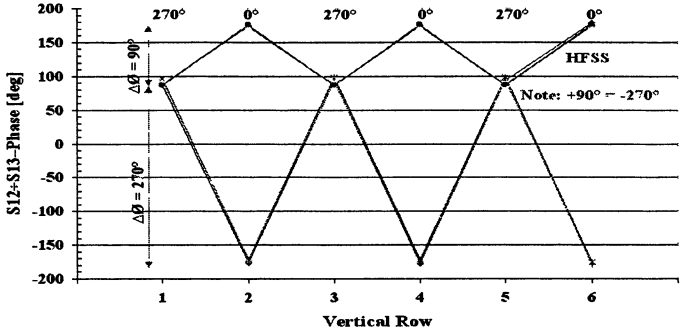
Conclusions

The test of a PAM on FTU is considered to be a fundamental step towards the realisation of an LHCD system for ITER. It is an essential "proof of principle" test before a successive technical test on Tore Supra of an ITER type launcher.

The measurements of the RF characteristics of the PAM for FTU have been completed. The results, especially from the point of view of phases, agree with the design values. The observed average difference in amplitude between measured and computed values could be ascribed to the measurement set-up (bad mechanical matching between flanges, not perfectly matched dummy loads, etc.) and to some simplified computing hypothesis. The full power test of the launcher is now in preparation; the test on plasma is foreseen for the beginning of the next year.

References

1. *Bibet Ph., Litaudon X., Moreau D.,* Principle of a retroreflecting LH antenna. Conf. IAEA (1994): LHCD in ITER (IVA-LH).
2. *Mirizzi F.* et al., A 8 GHz, high power, microwave system for the heating of thermunuclear plasmas. Proc. of the 23rd European Microwave Conference (Madrid, 1993).
3. *Mirizzi F., Bibet Ph.* et al., Toward an active-passive waveguide array for Lower Hybrid application on ITER. Proc. of the 20th SOFT (Marseille, France, 1998).

363

TESTS AND PERFORMANCE OF THE SIX-GYROTRON SYSTEM ON THE DIII–D TOKAMAK

John Lohr, Y. A. Gorelov, K. Kajiwara, Dan Ponce, R. W. Callis, J. R. Ferron, C. M. Greenfield, R. J. LaHaye, R. I. Pinsker, R. Prater, M. R. Wade[1], R. A. Ellis[2]

General Atomics, P.O. Box 85608, San Diego, California, 92186-5608. USA
[1]Lawrence Livermore National Laboratory, Livermore California, 94551, USA
[2]Princeton Plasma Physics Laboratory, Princeton New Jersey, USA

The DIII–D gyrotron complex for electron cyclotron heating (ECH) and electron cyclotron current drive (ECCD) has been expanded to include five operational gyrotrons with a sixth being commissioned. The generated rf power exceeds 4.0 MW and the transmission lines deliver about 80% of this power to the tokamak. Among the experiments performed during the most recent campaign, the installation has been used to achieve stabilization of the $m/n = 2/1$ and 3/2 neoclassical tearing modes, to control the rate of current penetration early in the discharge, and to study ECCD contributions to advanced tokamak discharges with high bootstrap fractions. Observations of the thermal performance of CVD diamond output windows have shown good agreement with theoretical predictions, but have revealed a number of interesting phenomena connected with impurities, including points of visible light emission at hot spots identified by infrared measurements. One window was cleaned *in situ* by alumina grit blasting and Raman spectra verified the removal of some surface contamination. A significant new capability is the simultaneous control of the output power of the entire array of gyrotrons by the DIII–D plasma control system. This allows a predetermined electron temperature evolution to be followed at a specific location in the plasma and opens a new group of experimental possibilities leading to the achievement of higher levels of tokamak performance.

1. DIII–D ECH installation

The DIII–D 110 GHz ECH installation comprises three Gycom[*] gyrotrons with 750 kW nominal output power and two second pulse length and two CPI[**] gyrotrons generating 1.0 MW for 5.0 s pulse length. A third CPI gyrotron opened a small leak through the copper of the collector and is currently being repaired. This tube has generated 550 kW for 10.0 s pulses and 800 kW for 0.7 s pulses. The power and pulse length performance of the system is summarized in Table 1.

The transmission lines are windowless and up to 100 m in length with up to 14 miter bends. In the worst case, the transmission efficiency is 80%, that is, the attenuation, measured in cold test, is –1 dB from the output of the matching optics unit (MOU) to beyond the final miter bend. The lines consist of evacuated 31.75 mm diameter circular corrugated waveguide and incorporate pairs of

---

[*] Gycom, Nizhny Novgorod, Russia.
[**] Communications and Power Industries, Palo Alto, California, USA.

grooved mirrors providing flexible control of the elliptical polarization of the injected rf power. Monitors of the forward and reflected power, vacuum isolation and dummy load power measurements are also provided. Results of a cold test of line transmission are presented in Fig. 1. The source was swept over a 1% range to ensure that no resonances were present to bias the measurement. Transmission of the entire line was compared with short path transmission using the same hardware and a calibrated attenuator to provide the reference signal levels.

Table 1. **Power and pulse length parameters for the DIII–D ECH system**

Gyrotron	Parameters			
	Current Best		Normal Operation	
	P_{GEN} (kW)	Length (s)	Power (kW)	Length (s)
Gycom 1 (Katya)	850	2.1	750	2.0
Gycom 2 (Boris)	750	2.1	750	2.0
Gycom 3 (Natasha)	650	2.1	650	2.0
CPI 1 (Scarecrow)	1000	0.8	in repair	at CPI
CPI 2 (Tin Man)	1000	5.0	800	5.0
CPI 3 (Lion)	1000	5.0	800	5.0

The polarization of the injected rf was measured by selecting linear polarization in two orthogonal directions at the final miter bend in the system and then making power measurements using orthogonal orientations of a fundamental rectangular horn and square law detector for signal picked off from the main beam with a –80 dB coupler. In all cases at least 95% of the rf power was in the desired polarization.

Coupling to the waveguide is performed for the Gycom gyrotrons using a two mirror phase correcting relay located in an evacuated MOU. This system has typi-

Fig. 1. Cold test measurements of the efficiency of a DIII-D transmission line 93 m in length having 14 miter bends, including two polarizing miters. The measured loss is –1 dB.

cally yielded 83–85% efficiency. The two mirror system is necessary for these tubes to correct the intentionally broadened rf output beam to a free space Gaussian which couples well to the HE1,1 waveguide mode for low loss transmission. The development of artificially grown diamond gyrotron output windows with $\tan(\delta) < 1 \cdot 10^{-4}$ and thermal conductivity > 1.2 kW/(m·K), has permitted gyrotrons to be designed which produce Gaussian rf beams directly without exceeding the maximum allowable power density in the center of the window. For these gyrotrons, a single ellipsoidal mirror can be used for coupling. This arrangement, which has about 95% efficiency, reduces the cost of the coupling system. A comparison between the MOU power loading for the non-Gaussian two mirror system and the single mirror Gaussian system is shown in Fig. 2. The data are for

the normal operating regimes of the gyrotrons and, although not normalized for the total power on any specific shot, the general increase in efficiency for the Gaussian beams is clear.
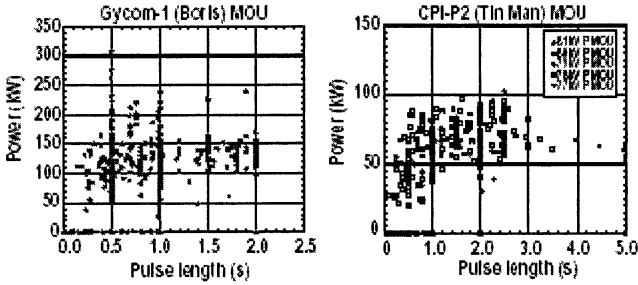
Fig. 2. MOU power loading for a two mirror phase correcting mirror system and a single mirror system coupling a Gaussian rf beam generated by a gyrotron with CVD diamond window to waveguide. The single mirror Gaussian coupler is nearly a factor of 3 more efficient than reconstruction of the Gaussian beam and coupling to waveguide with the two mirror system.

Each transmission line includes a combination dummy load which can be switched in remotely and used to absorb the rf power for tuning and monitoring. The first section of the combination is essentially a bad piece of waveguide in which a smooth wall section followed by tapered corrugations generates surface modes which are then damped evenly over a 1.5 m water cooled section. This portion of the load absorbs about 75% of the incident power and is cooled by water flow of about 4 L/s. The remaining 25% of the power is absorbed by an inconel can load. The combination can handle 1 MW cw. Any power reflected from the inconel section is damped in the mode conversion section, therefore the two sections present an extremely black load for gyrotron testing. The loads are indistinguishable from the plasma from the standpoint of reflected rf power.

The rf beams are injected into the DIII–D tokamak from three articulating launcher assemblies, each of which can accommodate two rf beams. The launchers can scan over 40° in both the toroidal and poloidal directions and two of the launchers can scan at 10°/s in both directions. This range covers the maximum in co- and counter-current drive efficiency and the tokamak upper half plane poloidally.

The launchers are equipped with radiatively cooled mirrors having different designs for evaluation. The simplest have thin Glidcop mirrors held in an inconel frame. A modification to this design has a thicker region (boss) in the center at the point of maximum power loading to provide thermal inertia. This mirror is grooved and oxidized on the back surface to enhance radiation to the water cooled shroud. For the launcher with the most delicate mirror drives, the mirrors are molybdenum brazed to graphite, minimizing the torque loading during dis-

366

ruptions. A fourth design uses a Glidcop mirror surface supported by a brazed multi-layer laminate of copper and inconel. This design has good thermal transfer away from the mirror surface with low eddy currents during disruptions. The bossed and laminated mirrors are designed for 1 MW 10-second pulses.

2. CVD diamond windows

The CVD diamond windows on the DIII–D CPI gyrotrons have been characterized. For about 800 kW passing through the windows, the peak central temperatures on two of the windows, measured using an infrared camera, plateau after about 3 s at values consistent with ANSYS modeling which maintains a factor of about three below the yield stress of 350 MPa. The third window, installed on the CPI-P1 (Scarecrow) gyrotron, has a time dependence of temperature after a 700 ms pulse indicating that its peak temperature could equilibrate after reaching a dangerously high value in excess of 200 °C. These results are summarized in Fig. 3. In order to perform the measurements, the emissivity of the diamond was measured in a test setup simulating the actual installation. The camera can see the inside of the gyrotron through the window, which makes a measured 10% maximum contribution to the window measurement. Typically the effective emissivity is found to be about 0.1 for clean diamond viewed through a room temperature sapphire window in the test setup. But any contamination on the window surface could invalidate the calibration and the modeling by increasing the absorbed power for a given tan(δ) of the bulk material or by increasing the emissivity or both. Once the window is installed on the gyrotron, contamination on the inside surface is inaccessible for evaluation or cleaning. The CPI-P1 gyrotron developed a small vacuum leak through the copper of the collector, which is being repaired. The cleanliness of the window will be evaluated during the course of the repair.

Fig. 3. Peak central temperature of the CVD diamond windows on the three CPI gyrotrons. Two of the windows have performance consistent with the modeling calculations, while one has abnormally high apparent temperature for 700 ms pulses. This could be due to a coating resulting in unexpectedly high microwave absorption, to emissivity higher than the calibrated value or both.

The window on the CPI-P2 (Tin Man) gyrotron was suspected to have been coated during the braze and bakeout processes and the outer surface was cleaned by blasting with 3 μm diameter alumina grit. Raman scattering measurements performed *in situ* before and after the cleaning indicated that outer surface contamination was removed by this process.

On all the diamond windows bright spots are observed both in the visible and infrared during high power operation. These are assumed to be small particulate

contamination on the window surface which is heated by the beam. Infrared hot spots which are not seen in the visible view could be impurities, probably graphite, in the bulk of the window lattices. Because the DIII–D system operates in vacuum, there is no tendency for the surface particulates to be burned away during high power operation. The very high thermal conductivity of the diamond appears to obviate excessive stress buildup from these local hot spots. As with the bulk measurements of window temperature, it is difficult to differentiate between areas of higher than ambient temperature and areas with higher emissivity. The apparent temperatures measured by infrared techniques therefore represent the upper bound on the inferred temperatures.

3. Feedback control of the generated rf power

The DIII–D Plasma Control System (PCS) has been used to modulate the total rf power generated by the gyrotrons in response to a pre-programmed requirement. Although this new capability is still in the demonstration stage, no difficulties or instabilities in the control process have been identified.

In the first tests of the capability, a desired time evolution of the electron temperature at an intermediate radius in the plasma was programmed into the PCS. The electron temperature measured by the ECE diagnostic was compared with the pre-programmed waveform and an error signal was generated, which was converted to a command to the ECH complex to generate higher or lower power as required to zero the error signal. The gyrotrons can be modulated from 100% to about 10% of maximum output by changing the applied high voltage from the nominal operating value to about 80% of nominal, the exact range having been determined by the operators so that the output remains a monotonic function of applied high voltage. In Fig. 4, *a* the results of a test are presented in which a sawtooth time dependence of the electron temperature at a normalized radius $\rho = 0.4$ was commanded. The actual temperature was measured by the ECE diagnostic and the gyrotron complex was modulated accordingly to bring the command and the measurement together.

Limitations on the fidelity with which the temperature tracks the command arise due to the finite injected rf power, the inability to decrease the temperature faster than about an energy confinement time and the necessity of maintaining some minimum rf output to ensure clean response when a power increase is required. The capability was then used to demonstrate that the flux penetration early in a plasma discharge could be controlled by controlling the electron temperature. In Fig. 4, *b* the central current density measured by the MSE diagnostic is plotted as a function of time for a series of four discharges in which different time evolutions of the electron temperature at $\rho = 0.4$ were commanded. The lowest temperature case was for no rf injection and the electron temperature evolved normally. The two intermediate temperature cases had a preprogrammed temperature evolution and indicate the excellent reproducibility. The highest
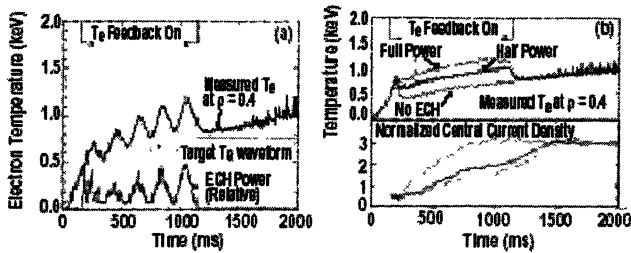
Fig. 4. Test of PCS feedback control of the ECH system power. The target temperature was preprogrammed and compared with ECE measurements (*a*). The difference signal then determined the modulator output. The PCS feedback control was then used to control Te and determine the rate of flux penetration early in the discharge (*b*).

temperature case used nearly the maximum available rf output power. At the highest electron temperature, the flux penetration is slowed and the central current density increases more slowly. The case without rf has the most rapid flux penetration and the two cases with intermediate power lie in between the extremes. In the future, active control of both the steering and the power of the injected rf will be used to facilitate other experiments with demanding requirements for reproducibility and profile control.

4. Experimental results

4.1. Neoclassical tearing mode suppression. The neoclassical tearing mode (NTM) manifests itself as a helical tube following a low order rational magnetic field line which has less than the ambient current density. The mode typically is triggered by a transient MHD event, for example a sawtooth crash, which forms an island in the normally concentric flux surfaces responsible for good tokamak confinement. Within the island, once it forms, the electron temperature is nearly constant as a function of plasma radius, with the result that the pressure gradient driven bootstrap current within the island drops to zero. The island is a stable structure, which can lock to the vessel wall stopping plasma rotation and precipitating a disruptive termination. Across the width of the island transport is rapid, so even if the island does not precede a disruption, confinement is degraded and the plasma beta decreases. The instability can be stabilized by electron cyclotron current drive which is applied to the interior of the island structure. The island width is typically about 8 cm in DIII–D and the DIII–D ECH system, which can drive current in a region extending about 6 cm radially and 8–10 cm poloidally and toroidally is well suited to generate current within the necessary localized volume. The current required for stabilization is moderate, about the value of the absent bootstrap current in the island, 100–200 kA.
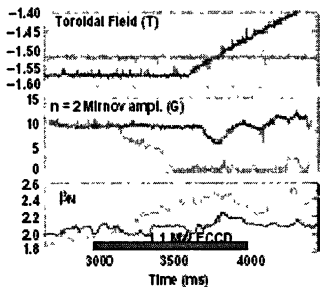
Fig. 5. Suppression of the *m/n* = = 3/2 tearing mode by ECCD. The ECCD location was determined by sweeping the resonance past the islands by varying B_T.

The ECH system has been able to stabilize both the *m/n* = 3/2 and 2/1 tearing modes on DIII–D. The ECCD must be located to within about 2 cm of the island center to achieve stabilization. The exact location at which to drive current can be determined empirically by scanning the ECCD region across the island. In Fig. 5 two discharges are shown in which the *m/n* = 3/2 NTM was targeted. In the first, the toroidal magnetic field was scanned under control of the PCS and the amplitude of the NTM was measured by magnetic probes connected to observe even n modes. As the field changed, the $2\omega_{ce}$ resonance and ECCD location was swept across the pre-existing island structure. At a particular value of B_T, a decrease in the mode amplitude was noted. On a subsequent discharge, the toroidal field was maintained at that value and the mode was stabilized. Following stabilization, in the absence of a seed island, it was possible to increase β above the previous value at which the NTM had occurred.

The *m/n* = 2/1 NTM is more difficult to stabilize, since it lies at a larger radius than the 3/2 mode and has a smaller width. This mode often precedes a disruption, so for large future devices like ITER, which could suffer damage in a major disruption, its stabilization is of some importance. Stabilization of this mode has also been demonstrated, as shown in Fig. 6. The PCS commanded a decrease in β once the mode had been started to make it easier to stabilize with the limited rf power, about 2.2 MW, available. The control system then varied B_T by moving the resonance ≈ 2 cm to achieve stabilization. Although a direct

Fig. 6. Suppression of the *m/n* = 2/1 tearing mode by ECCD. For the comparison without suppression, the ECCD was applied away from the islands.

on/off comparison was not performed, on a comparison shot with the same β program, for which the ECCD was not at the island location, the mode persisted.

4.2. ECCD efficiency. It is critical, both for NTM suppression and for advanced tokamak operation with non-monotonic j(r) profiles, that the efficiency of ECCD not decrease as the ECCD location is moved. The efficiency is expected to decrease as the local electron temperature decreases, that is, as the current drive is moved out from the plasma center. It also is expected that increasing the perpendicular component (to the magnetic field) of the electron velocity
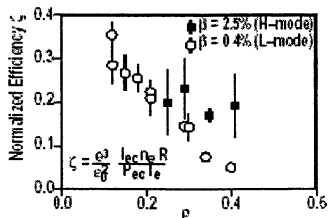
Fig. 7. The ECCD efficiency remains high for off-axis absorption if β remains high.

increases trapping of the heated electrons, removing a fraction of the population from the role of current carrier and decreasing the current drive efficiency. It was found through detailed efficiency measure-ments that, for high enough values of β, the current drive efficiency remained high even if the resonance were moved outside the magnetic axis to the banana region as shown in Fig. 7.

This observation, which makes ECCD even more attractive for MHD suppression and advanced tokamak operation, can be explained by a shift of the resonant electrons away from the trapping boundary as β increases.

Up to 140 kA of EC driven current has been observed in DIII–D for injected rf power to about 2 MW. This efficiency is sufficient both for advanced tokamak scenarios currently under consideration and for MHD mode suppression, as described above.

5. Conclusions

The 110 GHz ECH/ECCD system on the DIII–D tokamak generates in excess of 4 MW for pulse lengths greater than 2 s, with about 1.6 MW available for 5 s pulses. Experiments have been performed on MHD suppression, feedback control of the output power and ECH and ECCD efficiency.

NBI-DRIVEN ION CYCLOTRON INSTABILITY
IN THE LOWER HYBRID FREQUENCY RANGE
IN THE W7-AS EXPERIMENT

A. G. Shalashov, H. Maassberg[1], E. Hoszhauer[2], W. Kasparek[2],
L. V. Lubyako, E. V. Suvorov, W7-AS Team[1]

Institute of Applied Physics, RAS, Nizhny Novgorod, Russia
[1]Max-Plank-Institut für Plasmaphysik, EURATOM-Association, Germany
[2]Institut für Plasmaforschung, Universität Stuttgart, Stuttgart, Germany

The lower hybrid plasma turbulence triggered by injection of hydrogen beams at the W7-AS stellarator is investigated by the collective Thomson scattering technique and by measurement of ion cyclotron emission of a plasma column. Theoretical interpretation of the observations based on numerical simulations of fast ion distribution functions caused by injection of different neutral beams is proposed.

Introduction and experimental conditions

The lower hybrid (LH) plasma turbulence driven by a rather weak diagnostic hydrogen beam was initially detected at the W7-AS stellarator by the collective Thomson scattering (CTS) of powerful microwave radiation [1]. The detected turbulence was characterized by very narrow frequency and angular spectra, which allowed a straightforward theoretical interpretation [2]. In the present paper this experiment is the starting point for further, more detailed investigations, both experimental and theoretical. A special attention is paid to the short-wave activity triggered by launching of intense neutral beams used for plasma heating. A new interest to the ion-beam-driven plasma micro-instabilities at W7-AS arose due to the recent start-up of a new NBI heating system with a transverse to magnetic field launch [3], for which formation of unstable ion distributions was expected from theoretical considerations.

The experiment was performed in a hydrogen plasma ($N_e = (2 \div 6) \cdot 10^{13}$ cm^{-3}, $T_e = 1 \div 1.2$ keV, $T_i = 600 \div 900$ eV) supported by electron cyclotron resonance heating (ECRH) at the second harmonic of the X-mode (0.5 MW, 140 GHz). Slightly off-axis ECRH shifted to the high-field side was used to improve the CTS conditions. At the developed phase of the discharge, an additional NBI heating was applied using the tangential NBI (≈ 55 keV, up to 0.5 MW, launch angle $\approx 40°$ with respect to magnetic field), or the quasi-transverse radial NBI (≈ 55 keV, 0.6 MW, launch angle $\approx 70°$), or their combination. The CX diagnostics neutral beam (≈ 35 keV, ≈ 20 kW, launch angle $\approx 90°$) periodically launched into the plasma was also used as a driver of enhanced LH turbulence. All neutral beams were hydrogen and were injected in toroidal positions with strong vertical elongation of the plasma column (elliptical plane).

372

The CTS measurements were performed using one of the 140 GHz gyrotron of the ECRH system as a source of probing radiation in nearly back-scattering geometry (scattering angle ≈160°) with the scattering volume located in the equatorial plane. With the fixed scattering angle the wave vector of the detected electron density fluctuations was also fixed and corresponded to the approximately doubled vacuum wavenumber of the probing radiation ($\lambda_p \approx 1$ mm and transverse propagation). Used scattering geometry had practically no radial spatial resolution within the plasma diameter (about 20 cm in the equatorial plane). Most of the CTS spectra have been registered with a 40-channel spectrum analyzer covering 200 MHz frequency range in the vicinity of the LH frequency with frequency resolution about 5 MHz and temporal resolution about 1 ms. In addition to the CTS system, the broad-band loop antenna was installed near the plasma column for the registration of ion cyclotron emission (ICE) in the frequency range 20÷1200 MHz with time resolution 20 ms.

Experimental results

The detailed studies of conditions for LH turbulence excitation and for enhanced ICE level were performed depending on the magnetic configuration, plasma parameters and NBI launching scenarios (tangential NBI, nearly radial NBI, diagnostic beam, and various combinations).

With injection of the radial heating beam or of the diagnostic beam, CTS diagnostics revealed a sharp increase of the scattered signal corresponded to turbulent activity of LH waves propagating transverse to the magnetic field in a very narrow frequency range ($\Delta f / f_{LH} \leq 2\%$). With injection of the longitudinal neutral beam this signal was strongly suppressed. An example of temporal evolution of the CTS signal in a frequency channel corresponding to the LH frequency is shown in Fig. 1 together with the NBI and ECRH power monitors output. Here the developed LH turbulence is found to be quasi-stationary during diagnostic and radial heating NBIs. The enhanced CTS signal disappeared with injection of the longitudinal beam while either of two transverse NBI systems continued operation. In other experimental conditions radial NBI provided the enhanced turbulence only at the switching-on phase during the beam collisional slowing
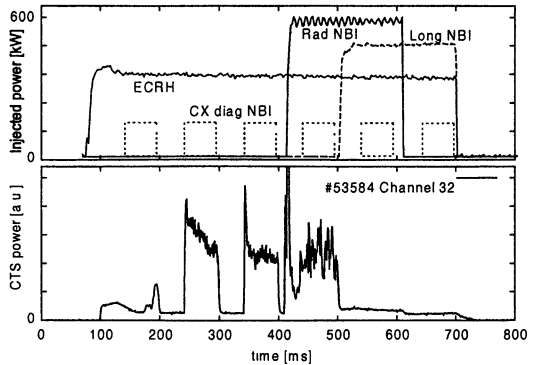
Fig. 1. Shot story and evolution of the CTS signal

373

down time, which was well resolved by the detection system. In such shots further injection of the diagnostic beam after the collisional relaxation of the heating beam did not trigger the LH turbulence.

To check the influence of fast ion confinement the scan over the magnetic configurations was performed, in which the depth of local magnetic well in the launching plane was reduced up to the formation of the B-field hump. In the latter case, the minimum of B was shifted from the elliptical plane to the triangular plane, the fraction of ripple-trapped fast ions was diminished, and the rate of their convective losses was also diminished because of a strongly reduced toroidal curvature corresponding to the triangular cross-section. The configuration scan revealed that the LH turbulence triggered by the diagnostic NBI and by the radial heating NBI demonstrated the opposite behavior. The diagnostic beam excited a turbulence when there was a local minimum of B in the launching plane and ceased to trigger it when this minimum was decreased or became a local maximum (in the latter case, convective losses of ripple-trapped fast ions were significantly lower). The radial beam being far enough from trapping, nevertheless, also reacted to the local magnetic configuration: it generated LH turbulence in the initial stage (during a slowing-down time) in the presence of a local minimum of B in the launching plane and supported stationary LH activity in configurations with the local maximum of B. No explanation for this effect is found from theoretical modeling.

It was observed experimentally that conditions for excitation of LH turbulence are essentially different for opposite directions of magnetic fields in the whole magnetic structure of the stellarator: more effective excitation by the diagnostic neutral beam and by the radial heating neutral beam take place for opposite directions of $\mathbf{B}$. This result is understandable for the diagnostic beam which possesses up-down asymmetry (being vertically injected) and, there-fore, may react to the change of the vertical drift direction, and less understandable for the heating beam with radial injection, in which there is no well pronounced up-down asymmetry.

Fairly good correlation of the ICE and CTS data was found in the radial NBI. Typically, rather broad-band activity at ion cyclotron harmonics adjacent to the LH frequency from below was registered with the loop antenna unlike the CTS measurements, which were always characterized by a pronounced narrow line in the spectrum. An example of the ICE response with radial NBI is shown in Fig. 2. ICE activity related to the diagnostic NBI was never registered unlike the previous experiments [2].
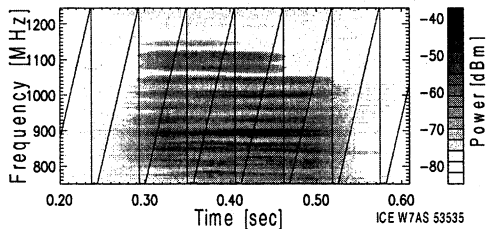
Fig. 2. Dynamical ICE spectrum near the LH frequency (1150 GHz). Radial NBI: 300–500 ms

Stability analysis for ion distributions caused by different NBIs

The NBI-driven distribution functions of fast ions have been numerically calculated both at the transient and stationary stages using a time-dependent bounce-averaged Fokker–Planck code (based on [4]) for modeling the collisional slowing-down of the beam ions taking into account the ripple-trapped ion losses. Unlike the diagnostic neutral beam, for which the collisional slowing-down is negligible as compared to convective losses, ion distributions for the heating NBIs are governed mainly by collisions except for the short phase after switching-on (typically of few ms). With these ion distributions calculated for different NBI scenarios, instability conditions in the vicinity of ion cyclotron harmonics following from the solution of the electrostatic dispersion relation are investigated.

The most unstable modes are found under the double-resonance condition when the LH frequency is close to a high ion cyclotron harmonic. Dispersion relation for these modes can be obtained using the inequalities $|\omega - n\omega_{ci}| << \omega_{ci} << \omega << \omega_{ce}$, $k_{\parallel}\upsilon_e << \omega$ and $k_{\parallel} << k_{\perp}$:

$$1 + \frac{\omega_{pe}^2}{\omega_{ce}^2}\left(1 - \frac{3}{8}\frac{k_{\perp}^2\upsilon_e^2}{\omega_{ce}^2}\right) - \frac{\omega_{pe}^2}{\omega^2}\frac{k_{\parallel}^2}{k^2} - \frac{\omega_{pi}^2}{\omega^2}\left(1 + \frac{3}{2}\frac{k_{\perp}^2\upsilon_i^2}{\omega^2}\right) - H_n\frac{\omega_{ci}}{\omega - n\omega_{ci}} = 0 \, ,$$

where $k_{\parallel}$ and $k_{\perp}$ are parallel and transverse wave numbers; ω_{ci}, ω_{ce}, ω_{pi} and ω_{pe} are cyclotron and plasma frequencies, $\upsilon_{i,e} = \sqrt{T_{i,e}/m_{i,e}}$ are thermal velocities of ions and electrons correspondingly;

$$H_n = -\left(2n\omega_{pi}^2/k^2\right) \cdot \int J_n^2\left(k_{\perp}\upsilon_{\perp}/\omega_{ci}\right)\partial f_i/\partial\upsilon_{\perp}^2 \, d^3\mathbf{v} \, ,$$

where f_i is ion distribution function including both thermal and beam components. An approximate solution of the dispersion relation is

$$\omega \approx \omega_{LH} - \Delta/2 \pm \sqrt{\Delta^2/4 - \gamma_m^2} \, , \quad \gamma_m = \sqrt{-\omega_{LH}^2 H_n \Big/ \left[2n\left(1 + \omega_{pe}^2/\omega_{ce}^2\right)\right]} \, ,$$

where ω_{LH} is the solution of the dispersion relation with $H_n = 0$ and $\Delta = \omega_{LH} - n\omega_{ci}$. One can see that an absolute instability of hydrodynamic type arises provided that two instability condition are satisfied: "free energy" is negative, $H_n < 0$, and double-resonance condition is met, $|\Delta| < 2\gamma_m$. The latter condition is easily realized in the experiment due to the radial variation of the stellarator magnetic field. Some examples of quantity H_n as a function of wavenumber are presented in Fig. 3 for various ion distributions calculated for the standard magnetic configuration.

Simulations show that unstable distributions providing $H_n < 0$ in a range of wave numbers registered by the CTS may be generated with injection of the radial heating or diagnostic beams. Both beams provides growth rates of the same order (up to $0.1\omega_{ci}$), although the densities of the diagnostic beam, which with poor confinement possesses a

Fig. 3. Evolution of H_n ($k_\perp v_i / \omega_{ci}$) resulting from the radial and longitudinal NBIs (solid lines) and from the thermal plasma with different ion temperatures (dashed lines). Time step in sets of curves is 0.7 ms.

strongly peaked ion distribution, and of the heating beam with the distribution function resulting from the slowing-down process differ by two orders of magnitude. For the heating NBI, the instability is strongly pronounced in the switching-on phase (with maximum growth rates $\sim 0.3\omega_{ci}$), while for a steady-state phase the instability condition is very sensitive to the injected beam energy composition and to the fast ion loss rate. In particular, we model a series of ion distributions corresponding to the magnetic configuration scan described above. According to this modeling, instability would vanish with reducing the fraction of the ripple-trapped ions in both cases of diagnostic and of heating beams. For the heating beam, however, these results contradict the experiment, for which maximum LH activity was registered when magnetic configuration deviated from the standard configuration with maximum losses.

Ion distributions resulting from the longitudinal NBI never provide the hydrodynamic instability (negative contribution to H_n). Moreover, they reduce the growth rates or even stabilize the LH activity driven by other (transverse) beams. This provides more efficient stabilization than the bulk ion heating until the ion temperature is not extremely high (< 1.5 keV). It was fairly well resolved in the experiment: the longitudinal NBI led to decay of the LH signal on a faster time-scale than the ion temperature increase. From the results of modeling it follows that radial NBI can also stabilize LH instability triggered by the diagnostic beam if the steady-state distribution resulting from the heating beam provides positive contribution into H_n. This was also confirmed experimentally.

The origin of the harmonic structure in the observed ICE spectra may be attributed to kinetic instabilities of ion Bernstein waves. The convective type instabilities in the vicinity of ion-cyclotron harmonics are found even for steady-state distributions resulting from both longitudinal and radial NBIs. These instabilities are realized in a wide range of cyclotron harmonics due to corresponding contribution of the beam-driven ion distributions to the anti-Hermitian part of dielectric tensor. These results demonstrate the principal possibility to detect an enhanced
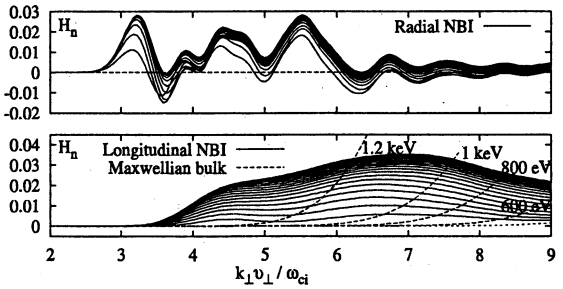
small-scale activity at ion-cyclotron harmonics inside the plasma volume; however, further analysis of wave propagation in nonuniform plasma towards the plasma edge is needed in order to interpret the results of ICE measurements by a system located outside the plasma volume.

Conclusions

The numerical modeling of ion distributions resulting from different NBI scenarios at W7-AS shows that these distributions can trigger a strong instability of the hydrodynamic type close to the LH frequency the growth-rate being roughly proportional to the square-root of the beam density. Such a situation is realized with the injection of the strictly trans-verse diagnostic beam or of the quasi-transverse heating beam and corresponds to the experimental observations. The analysis of the ion distribution function driven by the diagnostic NBI shows that the hydrodynamic instability is realized only when fast ions are trapped in the local minimum of B. This means that the unstable ion distribution is localized in the launching plane, while the LH turbulence is measured in the toroidally separated CTS section. Therefore, the excited small-scale LH waves can either propagate around the torus, or they possess a global structure.

References

1. *Suvorov E. V.* et al., Plasma Phys. Control. Fusion, **37**, 1207 (1995).
2. *Suvorov E. V.* et al., Nucl. Fusion, **38**, 661 (1998).
3. *Rust N.* et al., 29th EPS Conference on CFPP (Montreux, 2002), P-4.045.
4. *Marushchenko N.* et al., Comp. Phys. Comm., **103**, 145 (1997).

ESTIMATIONS OF ELECTRON BERNSTEIN CURRENT DRIVE EFFICIENCY ON THE W7-AS STELLARATOR

N. B. Marushchenko, F. Volpe, V. Erckmann, H. P. Laqua, H. Maassberg and the W7-AS Team

Max–Planck–Institut für Plasmaphysik, EURATOM Association,
Greifswald and Garching, Germany

Introduction

The "standard" ECR methods of heating are subject to a density cut-off (see, for example, [1]). For W7-AS stellarator with $B_0 = 2.5$ T these limits are $n_e < 0.6 \cdot 10^{20}$ m^{-3} for the O1-mode and $n_e < 1.2 \cdot 10^{20}$ m^{-3} for the X2-mode. At the same time the electron Bernstein waves (EBW) do not have any upper limit for propagation, but it can be excited only within the warm and dense ($\omega_{pe} > \Omega_e$) plasma. A method with this purpose was proposed in [2]. It consists in oblique launch of the O-mode, followed by mode conversion in the X-mode and finally in EBW. Below this method will be referred as OXB-scheme. Experimentally OXB-scheme of heating was performed only few years ago [3], and the results were very optimistic.

The idea of the OXB-scheme is based on the existance on the cut-off layer ($\omega_{pe} = \Omega_e$) of an "angular window" $N_\parallel = N_{\parallel,opt}$, where the oblique launched O-mode converts into the slow X-mode, and, further, after turn back to the upper hybrid resonance layer, into the Bernstein electron wave (EBW), which penetrates into the dense plasma up to complete dissipation. In the region of intensive resonant interaction the longitudinal refractive index of EBW reaches values $|N_\parallel| \gtrsim 1$. Consequently, as estimated in [4], the current drive efficiency can exceed that for O1- or X2-modes. In contrast to usual ECCD, where the main mechanism for current generation is an anisotropy of the distribution function created by heating, EBW can also directly transfer appreciable momentum to the electrons.

The main goal of this work is to compare the experimental results, obtained for current drive generating by OXB-scheme at W7-AS stellarator for two different configurations, with predictions of the ray-tracing and Fokker–Planck simulations.

Numerical simulations

Despite the request of fixed launch angle for efficient OXB conversion, the value of $N_\parallel$ can be varied by reversing the magnetic field and by changing

the configuration. The axial dependence of B over the toroidal angle is shown on the Fig. 1. For the "standard" configuration (solid line) minimum of B corresponds to the elliptical plane (36°), while for the "max B" case (dotted line) minimum of B situated on the triangular plane (0°). The deposition profiles and the final values of $N_{\parallel,\perp}$ for both these cases were obtained by ray-tracing calculations with the ART code [5]. While the initial conditions for the rays are the same for the two configurations, the

subsequent behaviour of the rays is quite different. Plasma parameters used for simulations ($n_e \approx 10^{20}$ m^{-3}, $T_e \approx 0.7$ keV, $P_{EC} \approx 450$ kW, $Z_{eff} \approx 1.5$) are typical for the experiments. The results for "standard" configuration are shown in Fig. 2. Starting with $N_{\parallel} = -0.6$, the ray, converted into EBW, changes the direction and near the peak of deposition ($r_{eff} \approx 2$ cm) has already $N_{\parallel} \simeq 1$. The behaviour of the ray for the "max B" configuration (Fig. 3) is the opposite:
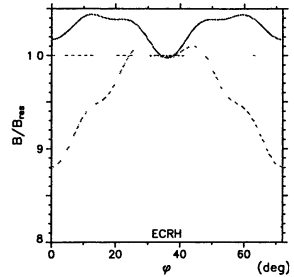
Fig. 1. $|B|$ along the axis for "standard" (line) and "max B" (dots) configurations.

the sign of $N_{\parallel}$ has no changes, and near the peak of deposition ($r_{eff} \approx 4$ cm) are reached a more big values, $N_{\parallel} \simeq -1.4$. This difference is similar to the asimmetry numerically found in tokamaks between EBW injection from above and below the equatorial plane [6].
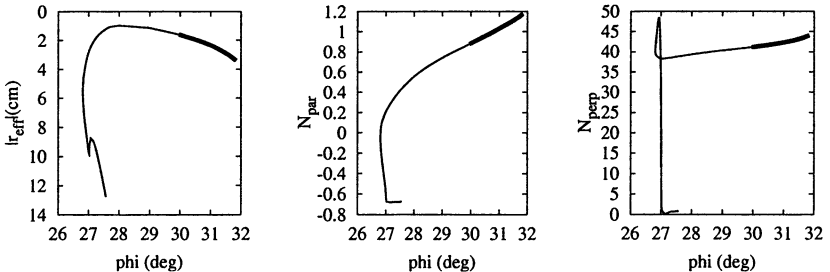
Fig. 2. "Standard" configuration: evolution along the ray of r_{eff} (*left*), $N_{\parallel}$ (*middle*) and $N_{\perp}$ (*right*). Deposition region shown by thick line.

Since EBWs have $k_{\perp}\rho_e \sim 1$, transversal refractive index after conversion to the values $N_{\perp} \sim c/v_{th}$ changes rather slightly, being defined predominantly by B and T_e, and evolution of $N_{\perp}$ for EBW-part seems very similiar for both looked configurations (Fig. 2 and 3, *rights*). Furthermore, the ap-

pearence of big $|N_\parallel|$ values is a mere geometrical consequence of the big values of $N_\perp$ (see, e.g. [6]).
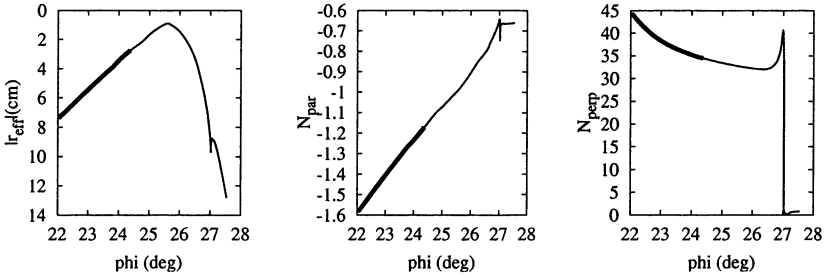
Fig. 3. "Max B" configuration: notation the same as in Fig. 2

In order to calculate EBCD efficiency also Fokker–Planck simulations were done by the FPTM code [7] for both the "standard" and "max B" configurations. The input parameters were taken from the results of ray-tracing calculations in the deposition region.

Because plasma parameters used for simulations give $\nu_* \sim 0.1$ (here ν_* is the ratio of the poloidal precession time to the collisional time for thermal electrons), one has to conclude that only the tail electrons surely are in long-mean-free-path regime. This means that the bounce-averaging is not strictly correct for all electrons taken into account ($\nu_* \ll 1$ approach is violated for the barely trapped electrons), and, as consequence, the calculated EBCD efficiency tends to be underestimated. Since only the estimation of EBCD efficiency is the goal of FP-simulation, the linearised collisional operator is used, which is quite accurate for this case.

The model of quasilinear diffusion is also quite standard and based on the assumption of linear behaviour of $|B|$ along $\mathbf{B}$ within the resonant inter-action zone. For simplicity the EBW-beam is assumed to be Gaussian. This assumption has to be not so far from reality, because the rate of dissipation along the ray, obtained by ray-tracing calculations (not shown here), has clearly peaked form. The electrostatic nature of EBWs enables to approximate the polarization with $\mathbf{E} \simeq (E_x, 0, 0)$ in the frame where $\mathbf{k} = (k_\perp, 0, k_\parallel)$. This value was used in the quasilinear diffusion coefficient.

On the left of Fig. 4 the distribution function for the "standard" configuration is shown. The value of $N_\parallel = 0.99$ corresponds to the peak of dissipation. The density of absorbed power, $p_{ECH} \approx 20$ W/cm^3, was estimated through the position and width of the deposition region as calculated by the ray-tracing. The fraction of trapped electrons estimated for this configuration at $r_{eff} \simeq 2$ cm (maximum of dissipation) is about $f_{tr} \simeq 0.24$.

380

Trapped electrons do not participate in resonant interaction, and the main mechanism of driving the current is the same like in traditional ECCD methods, i.e. inducing an anisotropy in the collisionality. The obtained value of an efficiency is $\eta \equiv I_{CD} n_e R_0 / P_{ECH} \simeq 1.2 \cdot 10^{18}$ A/Wm^2, and, respectively, a driven current $I_{CD} \simeq -2.5$ kA for $P_{ECH} \simeq 450$ kW is predicted.
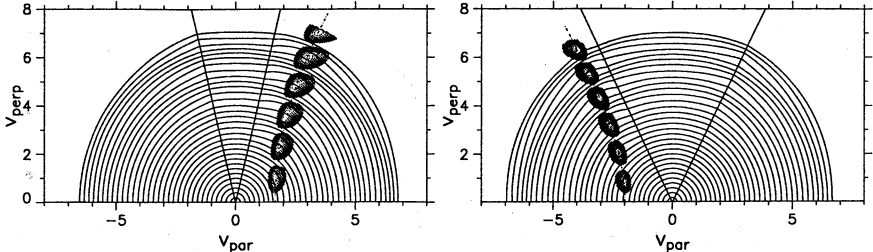
Fig. 4. *Left:* "Standard" configuration, $N_{\parallel} = 0.99$ (co-EBCD), $p_{ECH} = 20$ W/cm^3, $j_{CD} = -145$ A/cm^2; *right:* "max B" configuration, $N_{\parallel} = -1.4$ (counter-EBCD), $p_{ECH} = 12$ W/cm^3, $j_{CD} = 150$ A/cm^2.

Other case, obtained for the "max B" configuration, is shown on the Fig. 4 (*right*). In spite of the bigger fraction of trapped electrons ($f_{tr} \simeq 0.475$ at $r_{eff} \simeq 4$ cm), the predicted current for the same launched power is higher, $I_{CD} \simeq 3.7$ kA, and the efficiency $\eta \simeq 1.9 \cdot 10^{18}$ A/Wm^2 is about 50% higher than for the "standard" configuration. This is due to the higher values $|N_{\parallel}| > 1$ and to the consequent increased parallel component of quasilinear diffusion. In other words, in addition to the heating anisotropy effect, the electrons receive also direct momentum from EBW.

The $N_{\parallel} \simeq 1$ case seems formally similar to the autoresonant ECCD regime, where the diffusive line coincides with the resonant line, (see, for example, [8]). However for EBWs, as consequence of $N_{\perp} \sim c/v_{te} \gg 1$, the diffusive line is broken in smaller domaines (visible in Fig. 4) in correspondence of the zeroth of $J_n(k_{\perp}\rho_e)$. Consequently, the idea of a long autoresonant interaction fails.

Experimental results

A microwave beam ($f = 70$ GHz, $P = 0.45$ MW) launched into a current-free plasma ($n_e \simeq 10^{20}$ m^{-3}, $T_e \simeq 0.7$ keV, $Z_{eff} \simeq 1.5$), prepared by NB injection with $P_{NBI} \simeq 1.0$ MW. OXB-conversion was optimised with respect to the angular window in order to minimise the non-absorbed radiation. In order to have central deposition, the magnetic field was adjusted

to 2.15 T on axis. The time-behaviour of the feed-back controlled loop-voltage U_{loop} used for compensation of the plasma current, indicates the appearance of a driven current: $U_{loop} = R_{pl}(I_b + I_{NBI} \pm I_{CD})$, where I_b, I_{NBI} and I_{CD} are the bootstrap, NBI driven and EBW driven currents, respectively.
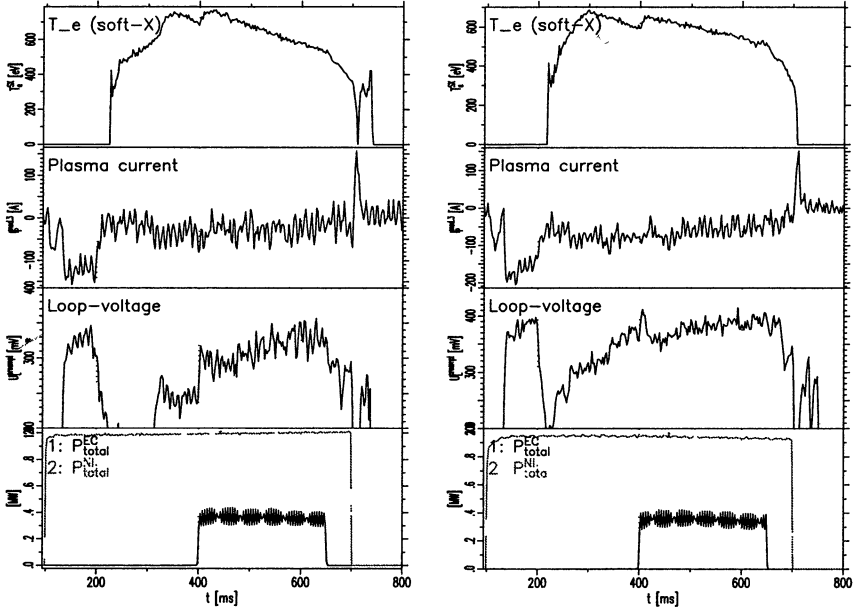
Fig. 5. *Left:* #54087, "standard", $I_{CD} \approx -(1.8 \pm 0.5)$kA (co-EBCD); *right:* #54100, "max B", $I_{cd} \approx (2.0 \pm 0.5)$kA (counter-EBCD).

An example of EBCD for the "standard" configuration is shown on the Fig. 5 (*left*). In the first part of the discharge (before the power from gyrotron launch) the ohmic current compensates the sum of bootstrap and NBI driven current. After switching on the power for EBW the reaction of loop-voltage evidently indicates an appearance of EBCD, and the value of driven current can be estimated as $I_{cd} \approx \Delta U_{loop}/R_{pl} \approx -(1.8 \pm 0.5)$ kA, with efficiency $\eta_{exp} \simeq (1.1 \pm 0.3) \cdot 10^{18}$ A/Wm^2, in good agreement with the theoretical expectations ($\eta_{theo} \simeq 1.2 \cdot 10^{18}$ A/Wm^2). The bootstrap current I_b and the plasma resistance R_{pl} were calculated with help of the DKES code.

The other case, performed for the "max B" configuration (Fig. 5, *left*), is more complicated to interpret. First, the discharge is not stationary because

382

of impurity accumulation. Secondly, there is also EBW heating of electrons, and changes of the loop-voltage reflect also changes of I_b and conductivity, associated with the temperature increase. Nevertheless, current drive was calculated by 3D least square fitting of n_e, T_e and Z_{eff} for a large parameter range [9] as $I_{CD} \approx (2.0 \pm 0.5)$ kA, with efficiency $\eta_{exp} \simeq (1.3 \pm 0.3) \times \times 10^{18}$ A/Wm^2. This result is also not so far from the theoretical predictions, especially if to remember about some inaccuracies of the used model and that the experimental estimation of I_{CD} is not so precise.

Conclusions

Numerical and experimental results confirm the possibility to use the OXB heating scheme also for noninductive current generation at the W7-AS stellarator. Experiments show a high efficiency, $\eta_{EBCD} \simeq 10^{18}$ A/Wm^2, in agreement with numerical predictions. This is of the same order of the EBCD efficiency for low-field-side launch of the X2-mode at W7-AS [1]: $\eta_{ECCD} \sim 10^{18}$ A/Wm^2 for the "standard" configuration (with the power $P_{EC} \simeq 1.2$ MW launched in plasma of $n_e \simeq 2.5 \cdot 10^{19}$m^{-3} and $T_e \simeq 5$ keV the current drive $I_{ECCD} \simeq 20$ kA was obtained), but EBCD has the advantage of being not subject to upper density limit.

References

1. *Erckmann V. and Gasparino U.,* Plasma Phys. Control. Fusion **36**, 1869 (1993).
2. *Preinhaelter J. and Kopecký V.,* J. Plasma Phys. **10**, 1 (1973).
3. *Laqua H. P.* et al., Phys. Rev. Lett. **78**, 3467 (1997).
4. *Litvak A. G.* et al., Phys. Lett. A **188**, 64 (1994).
5. *Volpe F.,* PhD Thesis, Univ. Greifswald (Germany, 2002).
6. *Forest C. B.* et al., Phys. Plasmas **7**, 1352 (2000).
7. *Marushchenko N.* et al., Comput. Phys. Comm. **103**, 145 (1997).
8. *Zvonkov A. V.* et al., Plasma Phys. Rep. **24**, 379 (1998).
9. *Laqua H. P.* et al., Phys. Rev. Lett. **90**, 075003 (2002).

RAY TRACING FOR ECR HEATING
IN THE MIRROR TRAP WITH LONGITUDINAL LAUNCH

O. B. Smolyakova, E. V. Suvorov

Institute of Applied Physics, RAS, Nizhny Novgorod, Russia

The ray-tracing procedure has been applied for calculating the ray trajectories and the power deposition along them for the situations modelling the longitudinal launch of microwave power into axially symmetric magnetic trap. Two installations are modelled: the large-scale plasma source with low electron temperature where collisional absorption is dominating and moderate-size ECR source of multi-charged ions (MCI) with high electron temperature which provides cyclotron resonant (noncollisional) absorption.

Introduction

Ray tracing technique is the reliable tool to study electromagnetic wave propagation and absorption in a weakly inhomogeneous magnetized plasma. We present here results of modelling performed for the longitudinal launch of microwave power into the plasma of axially symmetric magnetic traps. Specific features related to physics and to modelling are marked for large-scale plasma source with low electron temperature and dominating collisional absorption and for moderate-size ECR source of multi-charged ions with high electron temperature.

Numerical modelling

Within 3D geometrical optics approximation ray trajectories and can be calculated according to the usual geometrical optics approximation:

$$d\xi_i / ds = \partial G / \partial \eta_i, \quad d\eta_i / ds = -\partial G / \partial \xi_i, \tag{1}$$

here ξ_i, η_i, are generalized co-ordinates and momenta, τ is optical depth along the ray, and $G = 0$ is the dispersion relation

$$G = (n^2 - n_{o,e}^2), \tag{2}$$

in which refractive indices of normal waves $n_{0,e}$ are defined by well-known Appleton – Hartree formulas [1] and are dependent on the angle ϑ between magnetic field B and wave vector k, and parameters $u = \omega_{ce}^2 / \omega^2$ and $\upsilon = \omega_{pe}^2 / \omega^2$ (ω_{ce}, ω_{pe} are the electron gyrofrequency and plasma frequency, respectively and ω is the microwave frequency).

Power deposition into the plasma is defined by optical depth calculated along ray trajectories:

$$\tau = \int_0^l 2\,\mathrm{Im}\,k\,dl. \tag{3}$$

To simplify ray tracing procedure the distribution of plasma parameters within the trap is approximated by a number of analytical expressions. The magnetic field distribution is modelled as the magnetic field of two identical circular current turns, their planes being perpendicular to the axis of the installation (z) and their centers placed at the trap axis z $(r_\perp = 0, z = \pm L)$. The radius of the turns is taken to provide mirror ratio at the axis $r \approx 4$. The latter may be changed (if necessary) by adding of homogeneous magnetic field parallel to the axis of the system.

The plasma density distribution in the mirror trap is approximated by the following:

$$N_e = \left(1 - \frac{r_\perp^2}{a^2}\right)^\kappa \cdot \left[N_0 + \left(N_{max} - N_0\right)\left(1 - \frac{z^2}{L^2}\right)\right], \tag{4}$$

where L is the half-length of the installation, a is the plasma radius, N_{max} is the maximum electron density achieved in the center of the chamber $(z = 0, r_\perp = 0)$, N_0 is the density "jump" at the axis in the beginning of plasma column $(r_\perp = 0, z = \pm L)$, κ is the factor defining the "flatness" of density radial profile.

For the case of density "jump" at the beginning of plasma column Booker equation is solved to determine wave vector component parallel to axis to find boundary condition for the ray tracing inside the plasma.

Large-scale plasma source

The first set of parameters corresponds to the installation proposed for separation of heavy fraction from Hanford waste (see D10 this item): plasma half-length is $L = 2$ m, plasma radius is $a = 0.4$ m; magnetic field in the center is $B_0 = 1.5 \div 3$ kG; maximum plasma density for the steady state is $N_{max} = 2 \cdot 10^{13}$ cm^{-3}, electron temperature is $T_e = 2$ eV.

Collisional absorption is governed by electron-ion collisions with the collision frequency defined determined by plasma density and electron temperature (see e.g. [1]):

$$\nu = 5.5 N / T_e^{3/2} \ln(220 T_e / N^{1/3}). \tag{5}$$

The collisional absorption of normal waves in a magnetized plasma is determined as

$$\operatorname{Im} k_j = \omega/c \operatorname{Im} n_j^2 / 2n_j, \ \operatorname{Im} n^2 = \left[2\upsilon s P + 2\upsilon(1-\upsilon)Q\right]/\left(P^2 + Q^2\right),$$

$$P = 2(1-\upsilon) - 2s^2 - u \sin^2 \alpha \pm \operatorname{Re}\sqrt{u^2 \sin^4 \alpha + 4(1 - is - \upsilon)^2 u \cos^2 \alpha}, \qquad (6)$$

$$Q = -2s(2-\upsilon) \pm \operatorname{Im}\sqrt{u^2 \sin^4 \alpha + 4(1 - is - \upsilon)^2 u \cos^2 \alpha}, \ s = \nu/\omega.$$
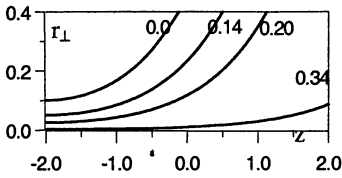
Fig. 1. Ray trajectories and optical depths for frequency radiation $f = 100$ GHz. $N_{max} = 2 \cdot 10^{13}$ cm^{-3}.

The aim of modelling is to find the possibility to provide efficient power deposition into the plasma with the density varying in a wide range beginning from end of pre-ionization stage up to steady-state value. An example of ray tracing calculations for the high frequency range ($\omega \gg \omega_{ce}$) is presented in Fig. 1 for steady-state parameters together with the single-pass optical depth. The microwave beam is launched along the axis with the beam waist about 20 cm in the beginning of plasma column; microwave frequency is 100 GHz, plasma density independent of z has parabolic radial distribution with $N_{max} = 2 \cdot 10^{13}$ cm^{-3}. The results are not much sensitive to the longitudinal and radial density profiles and demonstrate that it is possible to support steady-state discharge with efficient utilization of 100 GHz microwave power with if chamber walls possess high enough reflectivity (full absorption of microwave power can be achieved in 5–10 passes).
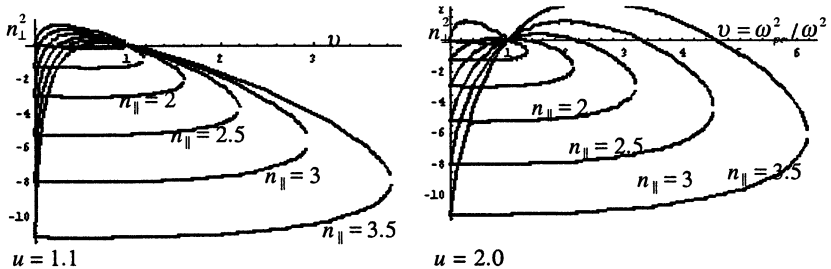
Fig. 2. Function $n_\perp^2(\upsilon)$ for several u and parallel refractive indices

For essentially lower densities typical of pre-ionization stage more realistic is to provide electron heating by the microwave radiation in the vicinity of the electron cyclotron frequency range ($\omega \approx \omega_{ce}$). Simple diagrams in Fig. 2 demonstrate specific features of wave propagation in a simple 1D geometry with the uniform magnetic field and density gradient transverse to it; for microwave radiation with the frequency below ω_{ce} central parts of the plasma column are separated from the vacuum by the evanescent regions. So, there is a number of possibilities for

trapping the radiation in radial direction making use of cut-offs at various densities (low-density cut-offs, high density cut-offs, cut-offs at critical density).

Fig. 3 demonstrates the trapping of ray trajectories in the vicinity of critical plasma density which corresponds to a rather low absolute value ($\approx 10^{12}$ cm^{-3}), typical of the final stage of the break-down; optical depth in a single pass is rather small but this is not very important at the break-down stage which is governed by the microwave field intensity. Three rays presented are incident from the vacuum in the same radial point with incidence angles 0 and $\pm$ 10 deg.

Fig. 3. Rays trapped between critical surface and cut-off surface for $B = 2$ kGs, $\omega_c = 2.5\omega$, $N_{max} = 1.2 N_c$.

The more efficient absorption can be rea- ched in the same frequency range for higher densities. Fig. 4 presents ray trajectories resulting from the microwave beam with the aperture radius 8 cm and divergence $\pm 30°$ incident to the plasma with the magnetic field $B_0 = 1.5$ kG. The radial distribution of plasma in (3) is taken to be parabolic, $N_0 = N_{max} / 3$; the microwave frequency is $\omega \approx \omega_{ce}/1.5$. The low plasma density under consideration ($5 \cdot 10^{11}$ cm^{-3}) is, nevertheless, above critical density for a specified microwave radiation frequency. The density jump at the plasma input provides transformation of the diverging beam into converging one because components transverse to the magnetic field of k-vector and of group velocity are in opposite directions. Optical depth which is of order of few tenth grows uniformly along the ray path.
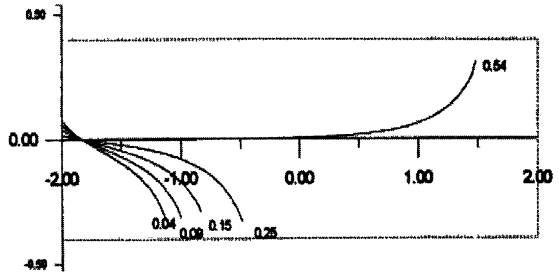
Fig. 4. Ray beam for $N_{max} = 5 \cdot 10^{11}$ cm^{-3}, $N_{min} = N_{max}/3$, $\kappa = 1$, $B_0 = 1.5$ KGs, $B_{max} = 1.5 B_0$, $\omega_c = 1.2\omega$.

In Fig. 5 ray trajectories are presented for high density typical of the steady-state stage of discharge. Here the single-pass optical depth is very high even in the case when rays are not penetrating far into the plasma in z direction. Crosses at the ray trajectories denote points where optical depth reaches the value 1. It should be noted that rays are trapped only in the case of large enough density "jump" at the

Fig. 5. Ray trajectories for density distribution (3), $N_{max} = 2 \cdot 10^{13}$ cm^{-3}, $N_{min} = N_{max}/3$, $\kappa = 1$, $B_0 = 2$ kGs, $B_{max} = 1.5 B_0$, $\omega_c = 1.2\omega$.

387

plasma boundary; similar effect can be also achieved without density "jump" in the case of very flat radial density profiles.

Moderate-size multi-charge ion source

Plasma and microwave beam parameters (according to experimental conditions) are the following: magnetic configuration corresponds to mirror ratio around 3–4, magnetic plugs are spaced by 20 cm (half-length of plasma column is $L = 10$ cm), plasma radius a is within 0.5÷5 cm. Converging microwave beam (convergence angle about ± 15 deg.) at the frequency $F = 37.5$ GHz with the aperture diameter 8 cm in the beginning of plasma column enters the vacuum chamber close to the magnetic plug. Cyclotron resonance ($B \approx 9$ kG) takes place in region where $B \approx 1.5B_{min}$, plasma density is slightly below critical (corresponds to plasma parameter $\upsilon = 0.9$); high electron temperature (of order 500 eV) provides resonant cyclotron absorption.
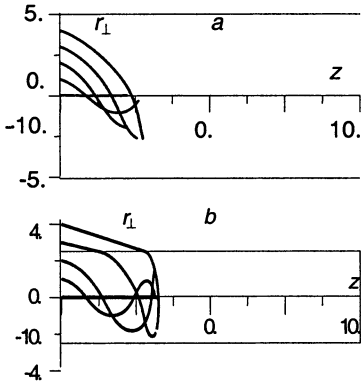
Fig. 6. Ray beam trajectories in trap for MCI production for various plasma radii: $a = 5$ cm (a); $a = 2.5$ cm (b).

Examples of ray trajectories are presented in Fig. 6, a, b for two values of plasma radius $a = 5$ cm (a) and $a = 2.5$ cm (b) for parabolic radial density profile homogeneous over z ($\kappa = 1$ and $N_0 = N_{max}$ in Eq. (3)). The main difference for these two radii is that the main part of rf beam enters plasma cylinder through the end or through the side surface.

Ray trajectories tend to the resonant point $\omega \rightarrow \omega_{ce}$ where $\vartheta \cong 0$, $k \rightarrow \infty$. The optical depth was calculated along quasi-optical beam ray trajectories, where the difficulty arises from the fact that cyclotron resonance absorption calculated by perturbation theory in the resonance region possesses a divergence $1/\vartheta^4$ with $\vartheta \rightarrow 0$ (see e.g. [2]). To eliminate this, additional condition

$$\text{Im } k < (1/2)\text{Re } k \tag{7}$$

is imposed providing the validity of geometrical optics approximation. Further calculation of resonance absorption is performed using numerical solution of the complex dispersion equation for longitudinal propagation (see e.g. [1])

$$\frac{i\pi}{(n^2-1)}W(z) = \sqrt{\pi}n\beta_T, \quad z = (1-\sqrt{u})/(n_\parallel \beta_T), \tag{8}$$

with $W(z)$ being the plasma dispersion function and $\beta_T = V_{Te}/c$. This solution is used only in the case of negligibly small longitudinal component of electric field in corresponding normal wave when the propagation angle satisfies the condition [3]:

$$\vartheta \ll \vartheta_1^2 = 2(1-\upsilon)/[1-(\upsilon/(1-\sqrt{u}))]. \tag{9}$$

The procedure mentioned above can't be applied in the case when both conditions (8) and (9) are invalid. In this case the resonant total power absorption can be estimate within phase integral method [1], and the determination of full absorption along the ray trajectory needs more sophisticated investigation.

Calculation of ray trajectories presented in Fig. 6 is stopped when the optical depth calculated using mentioned above procedure reaches the value about 1.5. It should be noted that for the model and set of parameters under consideration for the main part of rays modelling the quasi-optical beam the optical depth calculated using mentioned above procedure reaches the value 1.5 before the violation the geometrical optics approach.

References

1. *Ginzburg V. L.* Propagation of Electromagnetic Waves in Plasma (in Russian), Nauka, Moscow, 1967.
2. *Akhiezer A. I.* et al., Plasma elecrodynamics (in Russian), Nauka, Moscow, 1974.
3. *Timofeev A. V.* Fizika plasmy (in Russian), v. 18, pp. 407–410 (1992).

MICROWAVE FLUCTUATION REFLECTOMETRY

E. Z. Gusakov, A. Yu. Popov, B. O. Yakovlev

Ioffe Institute, St.-Petersburg, Russia

Fluctuation reflectometry is widely used technique providing information on the plasma low frequency turbulence. It is often used for monitoring the density fluctuations behavior in the tokamak discharge, in particular, for indication of the transition to improved confinement regimes. The plasma probing by ordinary or extraordinary microwave is used in this diagnostics and the reflected wave spectral broadening is usually measured. Technical simplicity and operation at a single access to plasma are among its merits, which however cause interpretation problems related to localization of measurements and wave number resolution. In order to improve the fluctuation reflectometry wave number selectivity a more sophisticated correlative technique, using simultaneously different frequencies for probing was proposed [1, 2]. The data interpretation in this technique is based on the hypothesis that the wave backscattered off long wavelength fluctuations dominating in the turbulence spectra comes from the cut-off layer. Therefore, the turbulence correlation length is often determined from the shift between two cut-offs at which the coherence of two reflectometry signals at different frequencies vanishes [1]. In contradiction to the above approach, the numerical analysis performed in [3] in one dimensional model, in the framework of Born approximation, had shown slow decay of coherence with increasing frequency difference of reflectometer channels. According to [3], poor localised small angle scattering responsible for this effect plays a significant role in producing the fluctuation reflectometry signal.

Linear 2D model

The rigorous theoretical analysis of fluctuation reflectometry carried out in this Section in the frame of linear 2D model, applicable in the case of low turbulence level, when the probing line is observable in the spectrum of reflected wave, had shown that the scattering efficiency is maximal for poorly localised small angle scattering along the incident wave ray trajectory as well. However unlike the 1D model, in 2D one it is produced by fluctuations running in poloidal direction and possessing finite wave number. Thus it is not possible, even in a stationary model, to rule this effect out by re-normalization of the density profile. As in 1D model, small angle scattering results in slow decay of the correlation function of two signals and, consequently, makes estimation of the turbulence correlation scale in linear regime of scattering questionable.

Our analyses is based upon the reciprocity theorem in the form introduced by Piliya [4] which gives the scattering signal received by the antenna

$$A_s(\omega - \Omega) = \frac{i\omega\sqrt{P_i}}{16\pi} \int \frac{\tilde{n}_\Omega(\vec{r})}{n_c} E_{za}^2(\vec{r}) d^3\vec{r} \,, \tag{1}$$

where $A_s(\omega - \Omega)$ is the signal amplitude in the waveguide, normalised so that $|A_s(\omega - \Omega)|^2$ gives the spectral power density of the scattering signal received by

antenna and a single antenna operation is assumed; $\tilde{n}_\Omega(\vec{r})$ is a spectral harmonic of density perturbation at frequency Ω ; P_i is the probing power and E_{za} gives the distribution of the probing wave electric field in plasma in the case of unit incident power. In the case of slab linear background density profile $n = n_c x / L$ the probing electric field can be represented as

$$^\backprime E_{za}(x,y) = \int \frac{dk_y}{2\pi} W(x,k_y) f\left(k_y\right) e^{ik_y y}, \tag{2}$$

where $\left|f\left(k_y\right)\right|^2$ is the antenna diagram in the poloidal direction and the field spatial distribution for each poloidal harmonic is expressed in terms of integral representation for the Airy function

$$W(x,k_y) = \sqrt{\frac{8\omega l}{c^2}} \exp\left\{i \int_0^{x_c(k_y)} k_x(x',k_y)dx' - i\frac{\pi}{4}\right\} \int_{-\infty}^{\infty} \exp\left\{i\left(\frac{p^3}{3} + \alpha p + \xi p\right)\right\} dp, \tag{3}$$

where $l = (Lc^2/\omega^2)^{1/3}$ is the Airy length; $\xi = (x-L)/l$; $\alpha = -k_y^2 l^2$; $k_x\left(x_c,k_y\right) = 0$ and $k_x\left(x,k_y\right) = \sqrt{\frac{\omega^2}{c^2}\left(1-\frac{x}{L}\right) - k_y^2}$. Following the approach of [5] we represent density fluctuations as a Fourier integral

$$\tilde{n}_\Omega(x,y) = \int \frac{d\kappa dq}{(2\pi)^2} e^{-i\kappa(x-L)-iqy} \delta n_\Omega(q,\kappa), \tag{4}$$

where κ and q are correspondingly "radial" and "poloidal" components of the fluctuation wave vector and finally obtain the fluctuation reflectometry signal as a superposition of signals, produced by density spectral harmonics

$$A_S(\omega-\Omega) = \frac{e^2 \ell^2}{\sqrt{\pi} mc^2} \sqrt{P_i} \int \frac{dq dk_y d\kappa}{(2\pi)^3} f\left(k_y\right) f\left(q-k_y\right) C\left(\kappa,q,k_y\right) e^{i\Psi} \delta n_\Omega(q,\kappa), \tag{5}$$

where Ψ is the phase of scattered wave, which in paraxial case, $\left|k_y\right| \ll \omega/c$ and $\left|k_y - q\right| \ll \omega/c$, takes the form

$$\Psi \simeq \frac{4}{3}\frac{L\omega}{c} - \frac{Lc}{\omega}\left[k_y^2 + \left(q-k_y\right)^2\right] + \frac{1}{2}\left(\frac{c}{\omega}\right)^3 L\left[k_y^4 + \left(q-k_y\right)^4\right].$$

The factor $C\left(\kappa,q,k_y\right)$ in (5) is the scattering efficiency introduced in [5] as the integral

391

$$C(\kappa,q,k_y) = \sqrt{\frac{i\pi}{\beta}} \int_{-\infty}^{\infty} \frac{\exp\left\{i\left(\frac{\beta^3}{12}\xi^3 - \frac{\beta\sigma}{2}\xi - \frac{\delta}{4\beta}\xi^{-1} - (\xi-1)s\right)\right\}}{(\xi-1+i\varepsilon)\sqrt{\xi+i\varepsilon}}\,d\xi, \qquad (6)$$

where $\beta = \kappa\ell$; $s = \kappa L$; $\delta = \ell^4 q^2 \left(q - 2k_y\right)^2$; $\sigma = \ell^2\left[-k_y^2 - \left(q - k_y\right)^2\right]$.

The realistic assumption that the long scale component satisfying the condition $\beta \ll 1$ dominates in the turbulence spectrum as well as modeling of the antenna diagram by the Gaussian dependence

$$f\left(k_y\right) = \sqrt{2\sqrt{\pi}\rho}\,\exp\left[-k_y^2\rho^2/2\right] \qquad (7)$$

allows one after averaging to obtain the following expression for the CCS of two scattering signals at frequencies ω_0 and ω in terms of the turbulence spectrum

$$\left\langle A_s(\omega_0)A_0^*(\omega)\right\rangle_\Omega = 4\pi\left(\frac{e^2}{mc^2}\right)^2 P_i l^3 \rho^2 \exp\left\{-i\frac{4L\Delta\omega}{c}\right\} J(\Delta\omega), \qquad (8)$$

where $\Delta\omega = \omega - \omega_0$,

$$J(\Delta\omega) = \iint dq\,d\kappa\,\frac{\exp\left\{-q^2\rho^2/2 + i\Delta\omega/\omega(q^2 Lc/\omega + 2kL)\right\}\left|\delta n_{\Omega,\kappa,q}\right|^2}{\sqrt{\kappa^2\rho^4 + \left[2Lc/\omega\kappa + L(cq/\omega)^2\right]^2}} \qquad (9)$$

and the turbulence is supposed to be statistically homogeneous and stationary, so that the following relation holds for the average cross-correlation spectrum

$$\left\langle \delta n_\Omega(q,\kappa)\delta n_{\Omega'}^*(q',\kappa')\right\rangle = (2\pi)^2 \left|\delta n\right|_{\Omega,q,\kappa}^2 \delta(q-q')\delta(\kappa-\kappa')\delta(\Omega-\Omega'). \qquad (10)$$

In the case $\rho^2 \ll 2Lc/\omega$, when the cut off is situated in the wave zone of the antenna, the main contribution in (9) is provided by fluctuations satisfying condition $\kappa = -cq^2/2\omega$. These fluctuations are responsible for small angle scattering of the probing beam all over the plasma. The slow logarithmic kind of coherence dependence of CCS on normalized frequency shift has been computed also for more realistic isotropic spectrum $\left|\delta n\right|_{\Omega,\kappa,q}^2 / n_c^2 \sim Q^3/(q^2 + \kappa^2 + Q^2)^{3/2}$. It is shown in Fig. 1, a, b. The decay of coherence here is very slow, which provides no possibility for the turbulence correlation lengths determination.

In the above treatment no exact dispersion relation was supposed for the density fluctuations, which is realistic in the case of high turbulence level, however in the case of weak turbulence one can expect a drift wave type of dispersion

$\Omega = Q_d v_d$, where v_d is the electron diamagnetic drift velocity. Modeling this kind of dispersion by a spectrum $|\delta n|^2_{\Omega,q,\kappa} \sim \exp\left[-\left(\kappa^2/K^2 + (q-Q_d)^2/Q^2\right)\right]$, we get the coherence dependence shown in Fig. 2, a, b for $L = [100;20]c/2\pi\omega$; $K = 0.3\omega/c$, $Q = 0.3Q_d$, $Q_d = [0.4;0.2;0.1]\omega/c$. The coherence decrease is also slow here, which complicates the turbulence coherence length estimation.
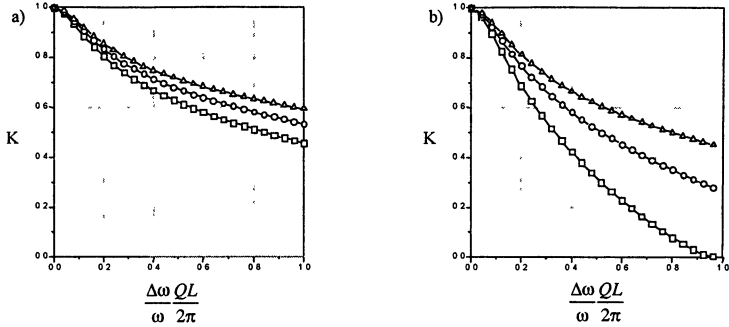
Fig. 1. Dependence of coherence on normalized cut-offs separation. $a)$ $L = 50c/\pi\omega$, $b)$ $L = 10c/\pi\omega$, where $\triangle$ – $Q = 0.4\omega/c$; $\circ$ – $Q = 0.2\omega/c$, $\square$ – $Q = 0.1\omega/c$.
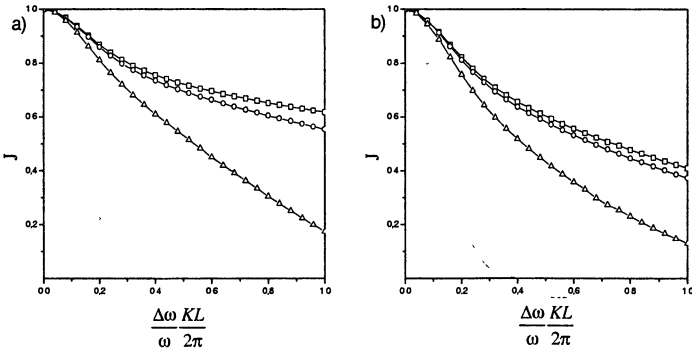
Fig. 2. Dependence of coherence on normalized cut-offs separation. $a)$ $L = 50c/\pi\omega$, $b)$ $L = 10c/\pi\omega$, where $\triangle$ – $Q_d = 0.4\omega/c$; $\circ$ – $Q_d = 0.2\omega/c$; $\square$ – $Q_d = 0.1\omega/c$.

In contradiction to above predictions a quick decay of coherence is often observed in experiment [1, 2]. In some cases the coherence is suppressed at cut off separation comparable to the vacuum wavelength [1]. A linear theory is unable to explain these results, moreover one should not expect it to account for these observations made under conditions when no probing line was observable in the reflected spectrum [2]. Nevertheless the linear theory elucidates the way in which a non-linear

approach should be developed. Taking into account that according to [5] the scattering efficiency is maximal for fluctuations possessing small radial component of wave vector, comparable to the density scale length, and making use of the fact that long scales are dominant in the tokamak turbulence one can conclude that the transition to nonlinear regime occurs via small angle multi-scattering.

Non-linear 1D model

In this Section we focus on investigation within 1D model, which, as it will be shown below, has a potential to describe the main features of fluctuation reflectometry both in linear and non-linear regime. We obtain the amplitude of the wave reflected from the cut off in the framework of WKB approximation as

$$E_{zs}(\omega,t) = E_{zi} \exp(i\phi_r), \tag{11}$$

where E_{zi} is the incident wave amplitude; its phase, ϕ_r, consists of two parts $\phi_r = \phi_0 + \delta\varphi$; the unperturbed part of the phase is given by $\phi_0 = 2\int_0^{x_c} k_0(x,\omega)dx - \pi/2$, where $k_0(x,\omega)$ is the O-mode wave number given by

$$k_0(x,\omega) = \sqrt{\frac{\omega^2}{c^2} - \frac{4\pi e^2 n(x)}{m_e c^2}} \tag{12}$$

and x_c is a cut-off point so that $k_0^2(x_c,\omega) = 0$ and $n(x_c) = n_c$.

The fluctuating part of the reflected signal phase is given by the first order expression

$$\delta\varphi(t,\omega) = -\frac{\omega^2}{c^2} \int_0^{x_c} \frac{\delta n(x,t)}{n_c} \frac{dx}{k_0(x,\omega)} . \tag{13}$$

Supposing the density fluctuation correlation length, l_c, to be much smaller than the system size $l_c \ll x_c$. It is easy to calculate the average reflected field

$$\langle E_{zs}(\omega_k,t_k)\rangle = E_{zi} \exp\left(i\phi_0(\omega_k) - \frac{\sigma_{kk}}{2}\right) \tag{14}$$

and the cross-correlation function of signals in two frequency channels ($j \neq k$)

$$K_{jk} = E_{zi}(\omega_j) E_{zi}^*(\omega_k)\{\exp[\sigma_{jk}] - 1\} \times$$
$$\times \exp\left\{i[\phi_0(\omega_j) - \phi_0(\omega_k)] - \frac{\sigma_{kk} + \sigma_{jj}}{2}\right\}, \tag{15}$$

where subscript "j" stands for (t_j, ω_j) and the matrix $\sigma_{jk} = \langle \delta\varphi_j, \delta\varphi_k \rangle$ is a phase perturbation correlation function ($\langle ... \rangle$ is the statistical averaging)

$$\sigma_{jk} = \frac{\omega_j^2 \omega_k^2}{c^4} \int_0^{x_c(\omega_j)} dx' \int_0^{x_c(\omega_k)} \frac{\langle \delta n(x',t_j)\delta n(x'',t_k) \rangle}{n_c^2} \frac{dx''}{k_0(x',\omega_j)k_0(x'',\omega_k)}. \qquad (16)$$

Formulas (14), (15) describe extinction of the probing line in the non-linear regime, when $\sigma_{kk}/2 \geq 1$ and decay of the coherence both in linear and non-linear regimes.

The behavior of the cross-correlation function at the transition from linear to non-linear regime is shown in Fig. 3, where it is plotted against normalized cut off separation Δ/l_c for different level of turbulence possessing Gaussian spectrum. As it is seen for small density perturbations $\delta n/n_c < 10^{-3}$ the decay of coherence is slow independently of the turbulence level, however at the larger perturbations $\delta n/n_c > 2\cdot10^{-3}$ the situation is different. The high coherence region is narrower and its width decreases with growing turbulence level. At $\delta n/n_c > 2\cdot10^{-2}$ it is already much smaller then the turbulence correlation length.
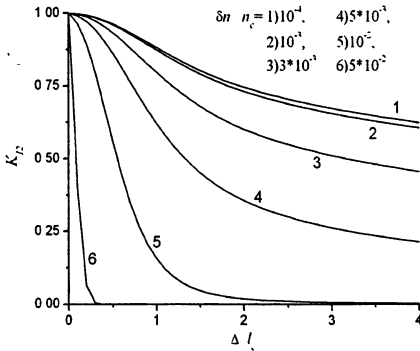
Fig. 3. Dependence of the normalized cross-correlation function on cut-off separation for different turbulence levels. $2\pi c/\omega = 0.52\,\text{cm}$, $l_c = 2\,\text{cm}$, $x_c = 60\,\text{cm}$.

Coming to analysis of a spatially inhomogeneous turbulence case, let us assume, for the sake of simplicity, that only the level of density perturbations is variable

$$\langle \delta n(x',t_j)\delta n(x'',t_k) \rangle = \delta n^2\left(\frac{x'+x''}{2}\right)K_n\left(x'-x'',t_j-t_k\right). \qquad (17)$$

We suppose below that the turbulence inhomogeneity scale, a, is smaller than the distance between the plasma edge and cut-off, but larger than the turbulence correlation length so that an equality $x_c(\omega_1) \gg a \gg l_c$ holds. After substituting the above expression into (21) we obtain the following expression for the phase correlation function:

$$\sigma_{12} = 4\frac{\omega^2 x_c(\omega_1)}{c^2}\int_0^\infty d\xi \frac{\delta n^2\left(\dfrac{x_c(\omega_1)+x_c(\omega_2)}{2}-\xi\right)}{n_c^2} S(\xi,\Delta,\tau), \tag{18}$$

where the kernel S is determined by the turbulence spectrum

$$S(\xi,\Delta,\tau) = \int_0^{\pi/2} K_n(\Delta - 2\xi\cos 2\varphi,\tau)\,d\varphi. \tag{19}$$

The localization of fluctuation reflectometry is prescribed by asymptotic behavior of the form-factor S at large $\xi \gg l_c$, which in the case of large cut-offs separation $\Delta \gg l_c$, $\xi - 2\Delta \gg l_c$ takes the following form:

$$S(\xi,\Delta,\tau) \simeq \bar{K}_n(\tau)l_c / \left(2\sqrt{4\xi^2 - \Delta^2}\right), \tag{20}$$

where $\bar{K}_n(\tau) = l_c^{-1}\int_{-\infty}^{\infty} K_n(\varsigma,\tau)d\varsigma$. For growing distance from the cut-off the form–factor S decreases, however not fast enough to guarantee the dominant contribution of the cut-off in the signal. The value of the phase correlation function is very sensitive to behavior of the turbulence level far from cut-off and is determined by it in the case of density perturbations growing towards the edge.

The situation is different in the case of small cut-off separation important for high turbulence level. Under condition $\Delta \ll l_c$ and $\xi \gg l_c$ the kernel S takes the following asymptotic form:

$$S(\xi,\Delta,\tau) \simeq \frac{\bar{K}_n(\tau)l_c}{4\xi}\left(1+\frac{\Delta^2}{8\xi^2}\right). \tag{21}$$

As it is seen, the first term in the right hand side of (21), being responsible for frequency broadening at high turbulence level, is only slowly decreasing with coordinate, in agreement with (20). On the contrary, the second term proportional to the quantity Δ^2, which describes the coherence suppression at growing cut-off separation, is a stronger function of ξ. The dependence of $S(\xi,\Delta,\tau) -$

$-\dfrac{\bar{K}_n(\tau)l_c}{4\xi} \sim \bar{K}_n(\tau)l_c \dfrac{\Delta^2}{32\xi^3}$ guarantees the dominant input of the nearest vicinity of cut-off into the correlation decay at high turbulence amplitude.

Conclusions

According to the above analysis the volume small angle scattering from long radial scale component of density turbulence plays an important and in some

cases dominant role in formation of fluctuation reflectometry signal. For low level density perturbations, when the linear approach is valid and, from experimental viewpoint, the probing line is observable in the reflected spectrum, it cause the slow decrease of the coherence, shown above for different fluctuation spectra and complicates interpretation of fluctuation reflectometry data, leading to degradation of wave number resolution. Backscattering in the cut-off plays dominant role in radial correlation reflectometry signal only if the long radial scales satisfying condition $\kappa = -q^2 c / 2\omega$ are suppressed in the spectrum or in the case of small density scale length $L \ll 2\omega / Q^2 c$ leading to saturation of the scattering efficiency at large radial scales. Only under these conditions the wave number resolution with radial correlation reflectometry appears to be possible at low turbulence level. The transition of the fluctuation reflectometry from linear to non-linear scattering regime has been followed in the present study. In non-linear regime the reflected signal spectrum broadening is also not localized to the cut-off and determined by the wide region of plasma in which the turbulence is situated. In spite of this, the coherence decay in radial correlation reflectometry deep in non-linear regime is only sensitive to the turbulence level in the cut-off. The role of poor localized small angle scattering in coherence decay is not so strong there. As it was shown it is rather enhancing coherence than suppressing it. In non-linear regime another effect, negligible at small density perturbation level comes into play. Namely, it is phase mismatch produced by the part of plasma between cut-offs evanescent for a smaller frequency of the probing wave. The coherence decays quickly if this phase mismatch's average absolute value, produced by smaller scales, exceeds π, thus making two signals statistically independent. Based on this mechanism we can foresee that such a localization improvement persists in the 2D model under development now. However it should be stressed that in this non-linear regime the cut-off separation at which the coherence of two signals is suppressed provide us with information not on correlation length but on the ratio of its square root and the density perturbation amplitude.

References

1. *Costley A., Cripwell P., Prentice R., Sips A. C.,* Rev. Sci. Instrum. **61**, 2823 (1990).
2. *Mazzucato E., Nazikian R.,* Phys. Rev. Lett. **71**, 1840 (1993).
3. *Hutchinson I.,* Plasma Phys. Control Fusion **34**, 1225 (1992).
4. *Novik K. M., Piliya A. D.,* Plasma Phys. Control. Fusion **36**, 357 (1994).
5. *Gusakov E. Z., Tyntarev M. A.,* Fusion Engineering and Design **34–35**, 501 (1997).

STUDY OF TOKAMAK TUBULENCE VIA DOPPLER REFLECTOMETRY DURING RF PLASMA HEATING

V. V. Bulanin, V. V. Dyachenko[1], L. A. Esipov[1], E. R. Its[1], S. I. Lashkul[1], S. V. Lebedev[1], A. V. Petrov, O. N. Shcherbinin[1]

State Polytechnical University, St.-Petersburg, Russia
[1] Ioffe Institute, St.-Petersburg, Russia

The present report is devoted to investigation of plasma turbulence behaviour during a transition to the improved confinement triggered by RF power launching in the limiter discharges of the TUMAN-3M and the FT-2 tokamaks. The experiments have been carried out with using of the Doppler reflectometry based on backscattering with oblique incidence of probing microwave beam, for which in plasma there is a cutoff. The observation of Doppler frequency shift of scattering spectra in such an experiment allows to estimate the plasma fluctuation poloidal velocity in tokamak. A specific transition to improved confinement initiated by RF pulse was revealed in the TUMAN-3M tokamak during ICR heating. The drastic narrowing of backscattering spectra associated with the transport suppression has been observed. The experiment in the FT-2 tokamak has been performed during the transition to H-mode triggered by RF pulse of lower-hybrid frequency region. The strong shear of plasma rotation observed via Doppler reflectometry strictly corresponded to appearance of the improved confinement. The common and specific features of turbulence suppression in the TUMAN-3M and FT-2 devices during L-H transitions triggered by RF power launch are summarized and compared. The possible mechanisms of plasma rotation shear are discussed in conclusion.

Introduction

It is well known that the experiments on powerful ICR heating of plasma have given in discovery of transition to the improved confinement (H-mode) in the diverter discharge of tokamak [1]. The theory predicts the following sequence of events leading to the H-mode during the RF ion heating [2]. The peripheral loss of fast ion generated by RF power results in negative radial electric field occurrence [3]. The sheared E×B rotation suppresses plasma fluctuations [4] that is the reason of abnormal transport reduction. As a result sharp profile of plasma pressure appears and sustains the negative electric field. The key factors of the transition such as the shear of rotation and the plasma turbulence suppression are just the subjects of the presented experiments. The investigations have been performed in the limiter discharges of the TUMAN-3M and the FT-2 tokamaks with the using of novel approach based on the Doppler reflectometry method. In the paper the experimental data obtained during the L-H transitions triggered by ICR and lower-hybrid (LH) heating are presented and compered to find out the common and specific features of plasma rotation and turbulence suppression in these two devices.

Method of diagnostics

The Doppler reflectometry employed to study of the L-H transition is based on backscattering with oblique incidence of probing microwave beam, for which in plasma there is a cutoff [5, 6]. The monostatic antenna scheme is used that is the same antenna is arranged to launch the probing beam and to receive the backscattered radiation. According Bragg condition the wave vector of scattering fluctuations in a vicinity of probing beam reflection is to be along the poloidal direction. So the observation of Doppler frequency shift of scattering spectra in such an experiment allows to estimate the plasma fluctuation poloidal velocity. Reflectometry system in the TUMAN-3M tokamak ($a = 0.22$ m, $R = 0.53$ m, $I_p = 160$ kA and $B_T = 1.2$ T) makes it possible to probe plasma by either O- and X-mode over frequency band $F = 17$–25 GHz. A specially designed monostatic antenna scheme allowed to change the incidence angle in the range $\varphi = \pm 30°$ with respect to last closed flux surface (LCFS). The single antenna tilted at fixed angle $\varphi = 16°$ with respect to LCFS was used in the FT-2 tokamak ($I_p = 22$ kA, $B_T =$

Fig. 1. 2D plot of weighting function – W: a) TUMAN-3M, $F = 25$ GHz, $\varphi = 20°$; b) FT-2, $F = 37$ GHz, $\varphi = 16°$. Arrows show antenna direction.

$= 2.2$ T, $R = 0.55$ m, $a = 0.08$ m) to probe plasma by O-mode radiation over frequency band $F = 26$–37 GHz. On the both tokamak schemes the quadrature detection of backscattering signal was employed to evaluate scattering spectra in the blue and red spectral regions. The 2D weighting function in real space has been proposed to realize spatial and k-resolution of the Doppler reflectometry [6, 7]. The weighting function $W(\mathbf{r})$ is introduced to compute in Born approximation the microwave mixer response by integrating the product of $W(\mathbf{r})$ by plasma density fluctuations over spatial co-ordinates. In Fig. 1 the weighting functions concerning the tokamak FT-2 and TUMAN-3M experimental conditions are shown in actual cylindrical geometry of minor cross-sections. Based on this kind of $W(\mathbf{r})$ simulations the spatial and wavenumber resolutions have been estimated as $\Delta r/a = 0.06$, $\Delta k/k = 0.3$ for the FT-2 and $\Delta r/a = 0.04$, and $\Delta k/k = 0.12$ for the TUMAN-3M tokamak.

Fig. 2. Envelopes of monitoring diagnostics signals and spectrum width δf for discharge with ICRH in TUMAN-3M.

A specific transition to improved confinement triggered by RF pulse was revealed in the TUMAN-3M tokamak during ICR heating experiment. The RF pulse with 100 kW power and 12 MHz frequency was launched from the low-field side with the use of a single-loop antenna. The L-H transition was characterized by steep increase of plasma density accompanied by D_α emission decrease just at the moment of the RF pulse switching on (see Fig. 2). The transition is not related to heating of main ion component because the transition occurs immediately after the RF pulse switching on and its occurrence is weakly depended on the concentration of resonant hydrogen minority. In a run of reflectometry experiment it was found that scattering spectrum width δf always strongly correlated with changing of abnormal transport at the

plasma edge. As one can see in Fig. 2, *d* the drastic narrowing of scattering spectra is observed just at the moment of the transition to the improved confinement. So it is believed that spectrum broadening is mainly determined by chaotic displacement of scattering fluctuations which are assumed to be responsible for abnormal transport. In Fig. 3 the temporal dependence of the Doppler frequency shift Δf is shown for two different cutoff positions. The data have been obtained in two discharges with the identical parameters shown by monitoring diagnostics. As one can see in

Fig. 3. Temporal dependencies of Doppler frequency shifts Δf during ICRH in TUMAN-3M for various frequencies of probing radiation.
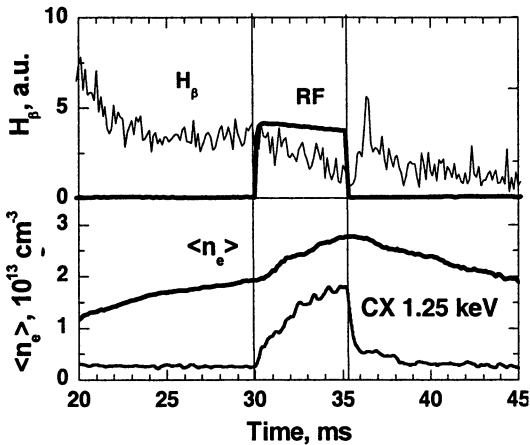
Fig. 4. Temporal variations of the main plasma parameters in the FT-2 LH-heating experiment. I_p = 22 kA, B_T = 2.2 T, RF power is 100 kW.

Fig. 3 the difference between Doppler frequency shifts occurs just after RF pulse switching on that could be treated as the onset of plasma rotation shear. The frequency shifts are essentially decreased during RF pulse. However the difference between the shifts still remains even after RF pulse switching off.

The detail investigation of poloidal rotation via the Doppler reflectometry has been performed in the FT-2 tokamak during a transition to improved confinement triggered by LH heating. The RF power at 920 MHz frequency was launched into plasma with a two-waveguide grill. Some reduction of H_β emission accompanied by plasma density increase (see Fig. 4) could be treated as a transition to the improved confinement. Typical scattering spectra are shown in Fig. 5 for the 26 GHz probing frequency with a cutoff near limiter. As is expected the antenna inclination results in a shift of scattering spectra. The positive frequency shift in the picture means the ExB drift under the negative radial electric field. The frequency shift is changed in a time during the RF power launching. Moreover the inversion of frequency shift is clearly observed. Simultaneously some reduction of
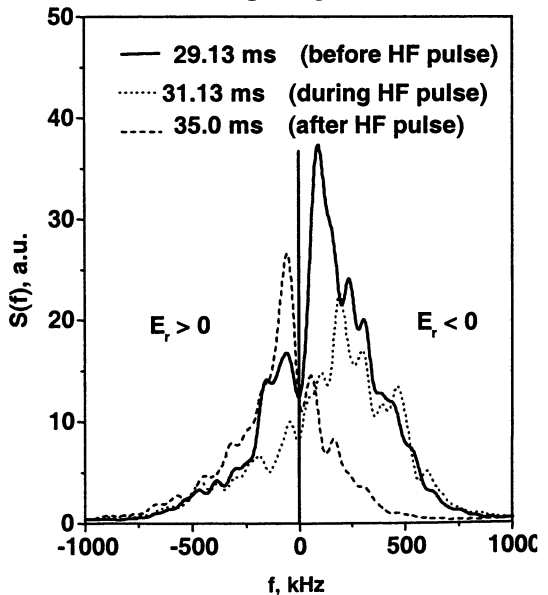
Fig. 5. The backscattering spectra obtained in the FT-2 LH-heating experiment. F = 25.9 GHz, φ = 16°.

Fig. 6. Temporal variations of the normalized Doppler frequency shifts (*a*) and of the estimated cutoff radial positions r_c (*b*) in the FT-2 LH-heating experiment.

the scattering is appeared. However, the narrowing of spectra is not pronounced. In Fig. 6 the temporal behavior of the Doppler shifts are summarized and compared between at various probing frequencies that is for various cutoff radial positions. The frequency shifts are here normalized to *k*-poloidal value to estimate the poloidal velocities of plasma fluctuations. The poloidal velocities are approximately the same for different cutoff positions in the OH stage of a discharge. So the shear of rotation is of a moderate value. The RF pulse switching on results in the negative electric field increase near the limiter.

Then the negative field increasing is observed following deeper cutoff position. In opposite, the electric field at the plasma edge is decreased and even changes a sign. As a result, a strong shear of rotation is appeared (see Fig. 6).

Discussion

The common origin of the transition to the improved confinement in the both tokamaks is probably a fast ion generation. The generation of fast ions just after RF pulse switching on is confirmed by the CX diagnostics on the both devices (see Fig. 2, *c* and Fig. 4, *b*). The onset of negative radial electric field due to the loss of these ions is indirectly supported by the Doppler reflectometry data. Some increase of the negative electric field in the inner region of the TUMAN-3M discharge could be a reason of different changing of the Doppler frequency shift for different radial positions of cutoffs (see Fig. 3). In the FT-2 tokamak the negative electric field onset results in some increase of poloidal rotation evidently seen during RF pulse (see Fig. 6). For both experiments the decrease of the Doppler frequency and even the changing of shift sign are detected after the RF pulse switching off. In the TUMAN-3M conditions it may be resulted from the weighting function displacement outward in SOL where the sign of electric field has to

402

be changed. The frequency shift decrease in the FT-2 tokamak may be of the same reason. However, in this device more plausible cause is an occurrence of powerful mechanism of electron loss. Such loss could be resulted from some electromagnetic instability development. A number of experimental data prove support for this view. The MHD activity is always observed just in the moment of the velocity inversion. The hard X-ray signal burst is happened just at the same moment indicating loss of super thermal electrons due to magnetic flattering. At last some reduction of electron temperature has been observed with Thomson scattering diagnostics near plasma edge just before the RF pulse switching off. The occurrence of positive electric field near the limiter and the increase of negative electric field in deeper region result in formation of strong shear of rotation. Such shear of rotation could be a reason of transport barrier shifted towards inner region of a discharge.

References

1. *Steinmetz K.* et al., Phys. Rev. Lett., **58**, 124 (1987).
2. *Burrell K. L.*, Phys. Plasmas, **4**, 1499 (1998).
3. *Itoh S.-I., Itoh K.*, Phys. Rev. Lett., **60**, 2276 (1988).
4. *Biglari H., Dimond P. H., Terry P. W.*, Phys. of Fluids, B 21 (1990).
5. *Bulanin V. V.* et al., Plasma Physics Reports, **26**, 813 (2000).
6. *Hirsch M.* et al., Plasma Phys. Control. Fusion, **43**, 1641 (2001).
7. *Bulanin V. V.* et al., 29th EPS Conf. on Plasma Phys. and Contr. Fusion (2002), ECA 26B, P.-2.121.

STUDY OF ELECTRON HEAT PULSE PROPAGATION WITH A TWO-FREQUENCY SET OF GYROTRONS ON T-10 TOKAMAK

S. V. Neudatchin, A. Ya. Kislov, V. A. Krupin, S. E. Lysenko,
Yu. D. Pavlov, K. A. Razumova, A. V. Syshkov, A. A. Borshagovskii,
V. V. Chistyakov, V. I. Ilin, I. N. Roi

Nuclear Fusion Institute, RRC "Kurchatov Institute", Moscow, Russia

The 130 GHz gyrotron was recently installed on T-10 in addition to the set of 4 gyrotrons with 140 GHz frequencies. Sawteeth-free plasma was created either by high-field-side off-axis ECRH (140 GHz) or by low-field-side off-axis ECRH (130 GHz) at $r/a \sim \pm 0.45$. Outward heat pulse propagation (HPP) with dynamic electron heat diffusivity $\chi_e^{HP} \approx 0.2 \div 0.3$ m^2/s (at $0.2 < r/a < 0.37$) and R/L_{Te} up to 23) was created by switching-on the on-axis ECRH (130 or 140 GGz) imposed on the background created by off-axis ECRH. Inward cold HPP with $\chi_e^{HP} \sim 0.1$ m^2/s (at $r/a < 0.3$ and R/L_{Te} up to 17) was created by cutting-off the off-axis ECRH. Off-axis ECRH forms the region of the improved transport in low-shear zone near $q \sim 1$ and q reduces during HPP.

Slow inward electron heat pulse propagation (HPP) induced by off-axis ECRH switching-on at T-10 was reported in [1]. The value measured by various analytical and numerical methods of HPP analysis is not power balance electron heat diffusivity χ_e^{PB} value but $\chi_e^{HP} = \delta\Gamma_e/(n_e\delta\nabla T_e)$, where χ_e^{HP} is dynamic electron heat diffusivity, $\delta\Gamma_e$ is electron thermal flux perturbation and $\delta\nabla T_e$ is ∇T_e perturbation. For L-modes with Ohmic or central ECRH on T-10, the χ_e^{HP} values (with typical values of order of a 1–3 m^2/s) are usually few times greater than χ_e^{PB} values [2–3] (so called "enhanced HPP"). This difference can be explained by dependence of χ_e on ∇T_e [2–3]. The χ_e^{HP} dependence on ∇T_e, however, does not affect the diffusive picture of HPP since it can be written as $\chi_e^{HP} = \chi_e^{PB} + (\partial\chi_e^{PB}/\partial\nabla T_e)\nabla T_e$ (shown analytically and with transport code calculations in [2–3], see also [4] for wider references).

In order to investigate the sensitivity of electron transport in sawteeth-free plasmas to the normalized inversed electron temperature gradient length $R/L_{Te} = R\nabla T_e/T_e$, the new set of experiments has been performed in T-10 tokamak plasmas. In the experiments described below, sawteeth oscillations were suppressed either by high-field-side off-axis ECRH with 140 GHz (see Fig. 1, *a*) or by low-field-side off-axis ECRH with 130 GHz (see Fig. 1, *b*). T_e was measured by two 12-channels ECE heterodyne radiometers with 17 μs sampling rate. The data presented below were averaged in 0.42 ms time interval.

Fig. 1. Scheme of on-axis ECRH imposed on background created by off-axis ECRH.
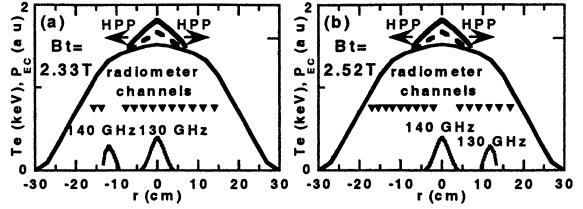
Fig. 2 shows the evolution of T_e measured by the radiometer (low-field-side data) during nearly on-axis (shifted by ~ 3cm from plasma centre) ECRH imposed on the sawteeth-free plasma created by off-axis ECRH (see Fig. 1, a). Central line averaged density $\bar{n}$ (0) is equal to $1.4 \cdot 10^{19}/m^3$, $R = = 150$ cm, $r = 29$ cm, $I_p = 0.18$ MA, $B_t = 2.3$ T. Fig. 3, a presents HPP in detail. Fig. 3, b shows the evolution of heat wave sharpness Sh = $(\delta \nabla T_e/\delta T_e)/(\nabla T_{eOH}/T_{eOH})$ [4–5] (normalized to OH level) and $(\nabla T_e/T_e)/(\nabla T_{eOH}/T_{eOH})$ which reaches 2.3. The value of R/L_{Te} reaches 23 on the heat wave front. High values of Sh represents low sensitivity of HPP to convective and convective-like terms.
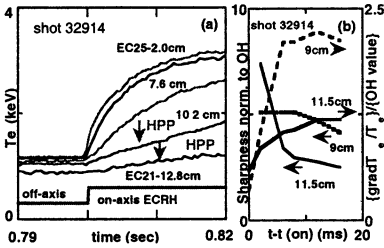
Fig. 3. a) HPP in detail with the positions given from camera centre; b) Evolution of heat wave sharpness Sh = $(\delta \nabla T_e/\delta T_e) \times \times (\nabla T_{eOH}/T_{eOH})^{-1}$ and $(\nabla T_e/T_e)/(\nabla T_{eOH}/T_{eOH})$.
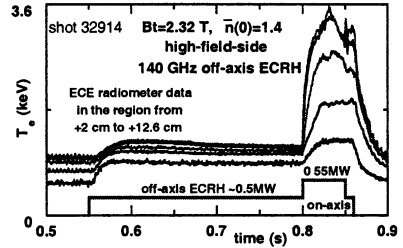
Fig. 2. Timetraces of T_e at off-axis 140 GHz and on-axis 130 GHz ECRH.

Numerical analysis of HPP (e.g. see method in [4] or [5], with the experimental boundary condition for δT_e at 7.6 cm) gives the value of $\chi_e^{HP} \approx 0.2 \div 0.3$ m^2/s in the region $0.2 < r/a < 0.37$. Timetraces of experimental and calculated values of $\delta T_e(r, t)$ are shown in Fig. 4. The χ_e^{HP} values are close to those of χ_e^{PB} obtained with ASTRA transport code [6] in the same region before HPP. The small shear zone with $q(0) \approx 1.1$ is observed in calculations due to broadened T_e profile and peaked Z_{eff} profile. Later, q values decrease at $r/a < 0.4$ during HPP. The analysis of HPP induced by smaller ~ 0.06 MW on-axis ECRH shows similar values of χ_e^{HP} under small variation of
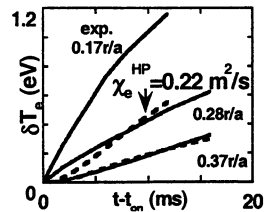
Fig. 4. HHP (see Fig. 3, a) dashed lines-calculations.
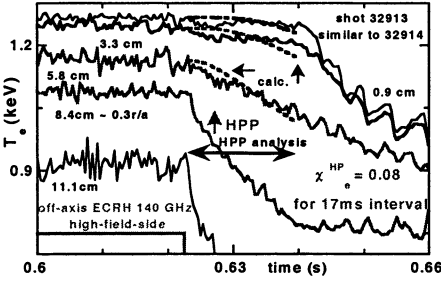
Fig. 5. Cold inward HHP from off-axis ECRH cut-off, dashed lines–calculations.

$\nabla T_e/T_e$ and demonstrates the validity of the HPP analysis at large δT_e values observed at 0.5 MW heating.

The inward cool wave was induced by cut-off of the off-axis ECRH. Figure 5 displays the timetraces of T_e in shot 32913 (all parameters are the same as in Fig. 2 besides the time of off-axis ECRH and the absence of central ECRH). The central T_e responds with significant delay ($\sim$ 20 ms and up to $\sim$ 30 ms in some pulses) to ECRH cut-off. The dotted lines on Fig. 5 represents calculated δT_e values imposed on the nearly steady-state background. Slow inward cold pulse propagation with $\chi_e^{PB} = 0.08$ m^2/s inside $r/a < 0.27$ is found for 17 ms time interval (0.1 m^2/s for 12 ms). Power balance analysis performed with ASTRA transport code gives $\chi_e^{PB} \approx 0.1$ m^2/s at $r/a = 0.22$ just before destruction of the improved confinement due to current redistribution and, later, the start of sawteeth oscillations. The value of R/L_{Te} reaches 17 on the cool wave front with the value of $\nabla T_e/T_e$ exceeds 1.7 times the OH level. The Sh exceeds 5 during HPP.

Figure 6 displays the evolution of T_e measured at the high-field-side in shot 34493 (0.17 MA/2.52 T, $\bar{n}(0) = 2.1 \cdot 10^{19}$/m^3) with low-field-side off-axis 130 GGz ECRH and nearly on-axis 140 GHz ECRH (see Fig. 1, *b*). The analysis of HPP was done for both low and high-field sides radiometers data. For HPP induced by on-axis ECRH, the analysis gives $\chi_e^{HP} \approx 0.18 \div 0.33$ m^2/s in the region $0.18 < |r/a| < 0.36$ from both sides. The χ_e^{HP} values are

Fig. 6. Timetraces of T_e at on-axis 140 GHz and off-axis 130 GHz ECRH.

20–30% less for the high-field-side. This asymmetry is probably created by plasma motion. The values of χ_e^{HP} rise up to $\sim$ 1 m^2/s and higher with the increase of $|r/a|$.

The evolution of T_e shown on Fig. 6 responds without significant delay to ECRH cut-off. Sawteeth oscillations start earlier in comparison with that shown on Figs. 2, 5. The analysis of the inward cool wave in 12 ms time interval gives $\chi_e^{HP} \approx 0.2$ m^2/s inside $\pm$ 0.27 r/a region with the similar 20–30% asymmetry of the χ_e^{HP} values.

In our old single result [7] obtained by the similar scheme of experiments on T-10 (0.38MA/3T, $\bar{n} = 3 \cdot 10^{19}$/m^3), HPP with $\chi_e^{HP} \approx 0.14$ m^2/s at $r/a \approx 0.45$ was induced by 0.4 MW on-axis heating imposed on 0.9 MW off-axis heated sawteeth-free plasmas. This result was fully confirmed in the present paper. Typical critical values of $R/L_{Te} \approx 4$–6 were reported at ASDEX-U and FT-U earlier. Recent analysis of HPP created by off-axis modulated ECRH shows slow HPP under R/L_{Te} up to ~ 10 [8–9]. The hypothesis of the jumps in transport coefficients at the time of ECRH switching-on and turning-off in T-10 is considered in [10].

a) The target sawteeth-free background was created by high-field side off-axis 140 GGz ECRH at $r/a \sim -0.45$ (0.5 MW, 180 kA/2.32 T, $\bar{n} = 1.4 \cdot 10^{19}$/m^3). Power balance analysis performed with ASTRA transport code [6] shows $\chi_e^{PB} \approx$ $\approx 0.2 \div 0.4$ m^2/s inside $r/a \approx 0.35$. Slow outward HPP ($\chi_e^{HP} \approx 0.2 \div 0.3$ m^2/s in the zone $0.2 < r/a < 0.37$) was induced by nearly on-axis 130 GHz ECRH with 0.55 MW input power. The value of R/L_{Te} reaches 23 on the heat wave front with the value of $\nabla T_e/T_e$ exceeds 2.3 times the Ohmic level (in a contrast, $\chi_{eOH}^{HP} \approx$ ≈ 0.6–1 m^2/s). Numerical analysis of HPP created by smaller ~ 0.06 MW on-axis ECRH shows similar values of χ_e^{HP}.

Another perturbation of T_e (inward cool wave) was induced by cut-off of the off-axis ECRH. The central T_e responds with significant delay (up to ~ 30 ms in some pulses) to ECRH cut-off. Slow inward cold HPP with $\chi_e^{HP} \approx 0.1$ m^2/s inside $r/a < 0.27$ was found. The value of R/L_{Te} reaches 17. The power balance analysis gives $\chi_e^{PB} \approx 0.1$ m^2/s at $r/a = 0.23$ in the end of the slow inward HPP. The similar values of $\chi_{e,i}^{HP} \approx 0.1$ m^2/s were observed for ITB-event-induced HPP throughout strong ITB at JT-60U [4].

b) The target sawteeth-free background was created by low-field side off-axis ($r/a \sim +0.45$) 130 GHz ECRH (0.5 MW, 170 kA/2.52 T, $\bar{n} = 2.1 \cdot 10^{19}$/m^3). For HPP induced by nearly on-axis 140 GHz ECRH, the analysis shows $\chi_e^{HP} \approx$ $\approx 0.18 \div 0.33$ m^2/s in the region $0.18 < |r/a| < 0.36$ and $\chi_e^{HP} \approx 1$ m^2/s and increases with the rise of $|r/a|$. The analysis of the inward cool wave created by off-axis ECRH switching-off gives $\chi_e^{HP} \approx 0.2$ m^2/s inside $\pm$ (0.27 r/a). The analysis of the radiometers data measured at both sides of plasma column gives 20–30% asymmetry of χ_e^{HP} values. We should reduce χ_e^{HP} values obtained from low-field-side data by ~ 10–15%.

Before HPP, q profile calculated with ASTRA shows small shear zone at $r/a \leq 0.35$ and $q(0) \approx 1.1$. The Z_{eff} profile peaks at sawteeth-free phase. During HPP, q reduces due to peaking of T_e and unmeasurable variation of Z_{eff} profile. The evolution of the current (calculated with constant in time Z_{eff}) represents well the time and the region covered by first sawteeth which was appeared after slow inward cold HPP. Nevertheless, the accuracy of calculations does not allow us to clarify the exact role of $q = 1$ and shear. The improved version of present paper should be submitted in Nuclear Fusion special ECCD/ECRH issue.

References

1. *Alikaev V. V.* et al., 1987 Plasma Physics and Controlled Nuclear Fusion Research (Proc. 11th Int. Conf., Kyoto, 1986), v. 1 (IAEA: Vienna), p. 111.

2. *Neudatchin S. V.* 1986 Influence of Electron Temperature Perturbations on Electron Heat Diffusivity in a Tokamak, in: Voprosy Atomnoi Nauki i Tekniki, Questions of Atomic Science and Engineering, Thermonuclear Fusion Series, **3**, p. 39.

3. *Bagdasarov A. A., Vasin N. L., Esipchyk Yu. V., Neudatchin S. V., Razumova K. A., Savrukhin P. V. and Tarasyan K. N.* Soviet J. Plasma Phys., **13**, 517 (1987).

4. *Neudatchin S. V., Takizuka T.* et al., Pl. Phys. Control. Fus., **43**, 661 (2001).

5. *Neudatchin S. V., Cordey J. G. and Muir D. G.* Proc. 20th EPS Conf. on Control. Fus. and Pl. Ph. (Lisboa, 1993), v. 1 (EPS), p. 83 and JET rep. JET-P(93)27.

6. *Pereversev G. and Yushmanov P. N.* 2002 IPP-Report 5/98.

7. *Bagdasarov A. A., Vasin N. L., Neudatchin S. V., Savrukhin P. V.* Proc. 15th Int. IAEA Conf., (Washington, 1990), v. 1 (IAEA: Vienna, 1991) 253.

8. *Tardini G., Peeters A. G., Pereversev G. V.* et al., Nuclear Fusion, **42**, L11 (2002).

9. *Jacchia A.* et al., Nuclear Fusion, **42**, 1116 (2002).

10. *Andreev V. F.* et al., Plasma Physics Reports, **28**, 367 (2002).

FIRST ECRH EXPERIMENTS ON TORE SUPRA

*M. Lennholm, G. Agarici, G. Berger-By, P. Bosia, F. Bouquey, J. Clary,
C. Darbos, G. Giruzzi, M. Jung, R. Magne, D. Roux, J. L. Segui, X. Zou*

Association EURATOM/CEA, Département de Recherches sur la Fusion Contrôlée,
CEA/Cadarache, F-13108 Saint-Paul-Lez-Durance, France

The Tore Supra Electron Cyclotron Resonance Heating (ECRH) and Electron Cyclotron
Current Drive (ECCD) system has been put into operation over the last few years. The very
first limited experiments were carried out in 1999. More extensive, though still rather pre-
liminary, experiments followed in the brief Tore Supra campaign of 2001. Recently ex-
periments have resumed on Tore Supra and the ECRH plant has been brought back into
operation. This paper is divided in two parts. The first part gives a brief overview of the
technical aspects of the system, while the second presents the experimental results and as-
sociated analysis.

1. Technical description

This section describes technical aspects of the 118 GHz Tore Supra ECRH
system, dividing the presentation into Power Generation, Transmission and
Launching.

Power generation. The ECRH system will, by 2006, be able to couple
2.4 MW for up to 600 s to the Tore Supra plasma. The power will be provided by
6 gyrotrons supplied by Thales Electron Devices (TED) (Fig. 1). At present two
gyrotrons are available for plasma experiments. The first of these – the prototype
– was delivered in 1999, while the first series tube was delivered in 2000. Prior to
delivery, the series tube passed the factory acceptance tests at the TED test stand,
supplying 500 kW for 5 s. Long pulse acceptance testing followed at CEA Cada-
rache. The maximum pulse length achieved was 110 s with a power of 300 kW [1].

Frequency	117.7 GHz
Output power / pulse length [+]	500 kW / 5 s,
	400 kW / up to 600 s
Cathode Voltage	81.5 kV
Anode Voltage	24.8 kV
Beam Current	22 A
Operating Mode	TE 22,6
Electronic Efficiency	33
Mode Purity at Window	95.8 %
Window Material	Sapphire
Output	Gaussian Beam
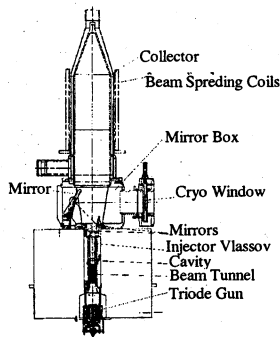
Fig. 1. Gyrotron specifications
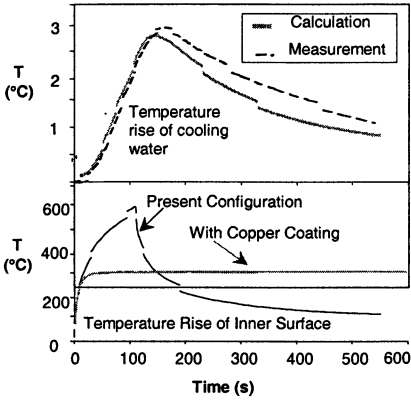
Fig. 2. Heating of mirror box

The pulse length limitation manifested itself by a strong degassing inside the gyrotron. This result, though a world record at the time, falls well short of the specifications, which requires 400 kW for 210 s.

Detailed calorimetric measurements indicated that 10 kW was deposited in the mirror box inside the gyrotron. Figure 2 shows the results of a simulation of the thermal behaviour of the mirror box, assuming a power of 10 kW deposited on its inner surface. In the top traces, the predicted temperature rise of the cooling water is compared to the measured value. The bottom traces show the predicted temperature of the inner wall in the present configuration and with the inner wall covered by copper everywhere except in front of the cooling channels. The temperature predicted following a 110 s pulse is seen to increase to approximately 600 °C for the present configuration. This is well in excess of the temperature at which the gyrotron was baked, explaining the strong degassing. Covering the inner walls of the gyrotron with copper as described would keep the temperature below the baking temperature, thus avoiding excessive outgassing [4, 7].

The spectrum of the power emitted from the gyrotron contains, in addition to the peak at the desired frequency, spurious peaks at 116.7 GHz and 119.8 GHz. While the frequency of the main peak decreases, as expected, by approximately 300 MHz in the first 500 ms due to the heating of the gyrotron cavity, the frequency of the spurious oscillations stays virtually constant indicating that these oscillations do not originate in the gyrotron cavity. RF calculations shows that a TE 20, 8, 4 mode at 119.7 GHz can be generated in the injector inside the gyrotron (Fig. 3). This mode would cause

Fig. 3. Electric field of TE 20, 8, 4 mode and injector radius

a power deposition in the mirror box of approximately 8 kW, which could be the explanation of the observed heating [4, 7].

Re-optimising the gyrotron for short pulse operation, following the long pulse tests, the maximum power was found to be only slightly more than 300 kW, showing that the first series gyrotron had been degraded since its delivery from TED. Thermal simulations of the injector heating, taking into account the additional 20 kW deposited due to the spurious oscillations, do not indicate excessive heating and hence the gyrotron degradation still remains unexplained.

New upgraded gyrotrons, the first of which is due for delivery in Autumn 2003, are being designed by TED, taking into account the above observations. The specifications for these gyrotrons require pulse length up to 600 s at 400 kW, while retaining the capability of producing 500 kW for 5 s.

Transmission. The microwave power is transmitted from the gyrotron via evacuated corrugated cylindrical 64 mm diameter waveguides operating in HE11 mode. The power is coupled from the gyrotron to the waveguide via a matching optics unit (MOU), which uses an elliptical mirror to focus the gaussian beam emerging from the gyrotron onto the aperture of the waveguide. The MOU in addition contains two mobile corrugated mirrors allowing complete control of the wave polarization. The following components are situated in each transmission line: 2 pumping sections, 1 power monitor miter bend, 1 DC-break and a vacuum valve allowing the torus vacuum to be isolated from the transmission line vacuum. During operation this valve is opened, bringing the torus vacuum up to the gyrotron window. The line contains 4 additional miter bends and the length of each waveguide section between bends can be adjusted using flexible elements. The only elements in the line that are actively cooled are the miter bends and the power monitor miter bends.

In the experiments carried out till date no polarising mirrors were installed in one of the MOUs. As a result the power injected into Tore Supra in the 1999 campaign was mainly in mode-X, which used at the Toroidal Field of 4 T, entails that only a small fraction of the injected power was absorbed by the plasma. Prior to the 2001 campaign an additional miter bend was introduced in the line, modifying the polarisation of the wave, thereby achieving almost pure mode-O injection. Recently a new MOU with corrugated mirrors has been installed, allowing complete control of the polarisation from all gyrotrons [6, 7].

Launching. The ECRH power is launched into the plasma, using an antenna situated in a main horizontal port of Tore Supra. The principal components of this antenna are: Six stainless steel corrugated waveguides, radiating gaussian beams with a waist diameter of 26.7 mm, six spherical focusing mirrors, used to assure the maximum power density at the plasma centre and three flat mobile mirrors, allowing the direction of the gaussian beam entering the plasma to be controlled. Using two stepper motors for each mobile mirror, the injection angles can be varied from −30° to 30° toroidally and from −25° to 25° poloidally [6, 7].

411
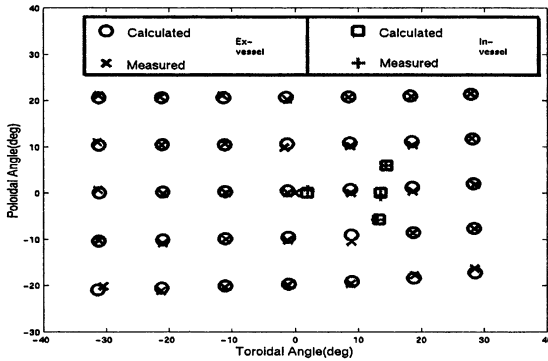
Fig. 4. Antenna calibration

Fig. 5. Remote steering antenna

The mirrors in the antenna are cooled with water at 30 bar 150 deg. The water connections to the mobile mirrors, which consist of armoured bellows, are probably the most fragile elements in the antenna.

Figure 4 shows a comparison between calculated injection angles and the achieved angles measured with a laser. The measurements have been performed with the antenna on a test stand and subsequently with the antenna installed on Tore Supra.

In order to make the experiments on Tore Supra as relevant as possible in relation to the design of an ECRH system for ITER, a modification of the antenna, replacing two of the existing cylindrical stainless steel waveguides with square "remote steering" waveguides [8, 6] is planned (Fig. 5). This modification will allow the steering mirrors to be situated outside the vacuum vessel. The remote steering on Tore Supra will be implemented for poloidal angle variation only while the existing in-vessel mobile mirror will be used for toroidal steering. As a result a wide flexibility in steering angles is retained, at the same time as the feasibility of remote steering in long pulse plasma operations is tested. Although it is not needed on Tore Supra, a "dogleg" in the middle of the square waveguide, which would be necessary for neutron shielding in ITER, is included in the design. The proof that such a "dogleg" can be used, remains a critical issue for the design of "remote steering" ECRH antennas for ITER.

412
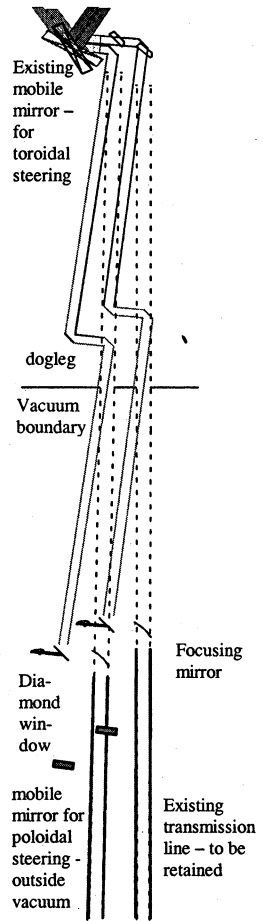
2. Experiments

This section contains a brief summary of the preliminary experiments carried out with the prototype gyrotron in 1999, followed by a description and analysis of the more extensive series of experiments of the 2001 campaign. It finishes with a single – raw – result of the present campaign and a view towards the near and medium term future.

1999 – First experiments. As mentioned, the few shots of the 1999 campaign were performed with the prototype gyrotron, using a MOU without polarising mirrors[2, 3]. For linearly polarised waves, the polarisation of the wave entering the plasma can be defined via the angle β between the electric field vector and the plane defined by the wave propagation vector and the total magnetic field. From the following simple transport equation:

$$\partial T_e / \partial t = (2/3)\chi^{ANA}(\partial^2 T_e / \partial r^2 + (1/r)\partial T_e / \partial r) - T_e / \tau_d + S(r, t) \qquad (1)$$

(T_e – electron temperature, t – time, χ^{ANA} – heat diffusivity, r – normalized minor radius, τ_d – damping time) and using a ray-tracing code to find the power deposition $S(r, t)$, the expected steady state central electron temperature as a function β can be computed. The computed temperatures for 3 shots, with different toroidal injection angles have been compared to the observed central electron temperatures. For each value of β the calculations have been normalised to give agreement with the steady state value of the measurements for the shot with the largest

negative toroidal injection angle. Fig. 6 shows the results for 3 values of β with good agreement observed for $\beta = 70°$, in excellent agreement with the value of $\beta = 72°$ found assuming horizontal polarisation at the output of the gyrotron and taking into account the mitre bends, antenna mirrors and toroidal and poloidal magnetic fields. The good agreement observed for $\beta = 70°$ confirms the calculated polarization angle, and justifies the modification of the line layout carried out prior to the 2001 campaign [7].
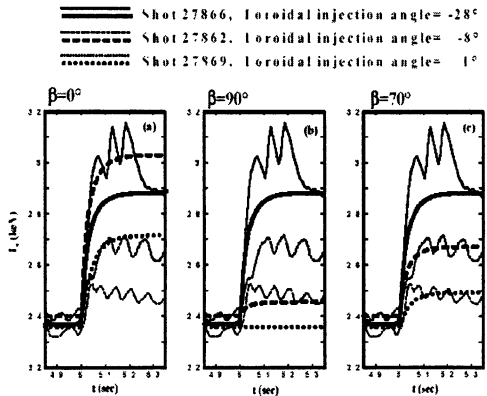
Fig. 6. Calculated and measured central electron temperatures for 3 shots

2001 – Results and analysis. In the 2001 campaign, the prototype gyrotron, now injecting O-mode, was used for plasma operation together with the first se-

ries gyrotron. The two gyrotrons were operated separately and simultaneously with a variety of polarisations and injection angles. Most experiments were performed with 100 % power modulation with modulation frequencies up to 25 Hz, allowing determination of the power deposition and analyses of the heat diffusion. Fig. 7 shows the ECRH power and the Electron Temperature at different radii as measured by the ECE diagnostic for one such pulse. The results of a Fourier transform of the ECE signals given as the amplitude and phase of the 1st, 2nd and 4th harmonics are plotted as a function of normalised minor radius in Fig. 8. The power deposition radius can be easily determined as the radius at which the phase is at a minimum and the amplitude is at a maximum. Figure 9 shows the measured deposition radius as a function of the predicted value for all modulated pulses from the 2001 campaign. Good agreement is observed, confirming that polarizations and injection angles were as expected. The slight discrepancy near the plasma centre is probably due to inaccuracies in the plasma equilibrium reconstruction [5].
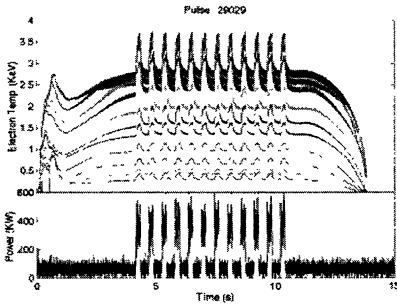
Fig. 7. Typical modulated pulse
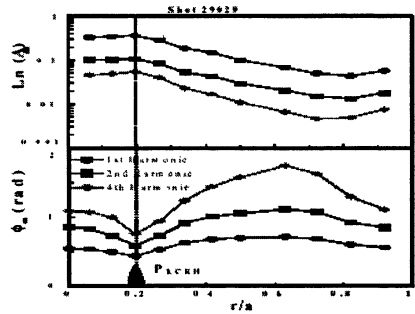
Fig. 8. Fourier transform of ECE signals – amplitude and phase

For shot 29029 a transport analysis has been performed employing two different methods. In the first method – the heat pulse diffusivity method – the heat diffusion coefficient is determined as,

$$\chi^{HP} = -\frac{3}{4} \frac{\omega}{\phi'_\omega (A'_\omega / A_\omega)},$$

where A_ω, ϕ_ω are the amplitude and phase of the Fourier coefficients as shown in Fig. 8, prime refers to the radial derivative and $2\pi\omega$ is the modulation frequency. In the second method – the analytical method – the transport equation (1) is solved analytically. Inserting the power source $S(r, t)$ as a narrow gaussian centred at the deposition radius found above, the values of χ^{ANA} and τ_d can be adapted to get the best fit between calculated and measured electron temperatures at different radii.

414

Figure 10 shows the heat diffusivity resulting from the two methods as a function of minor radius. The ECE channels measuring the edge temperature are affected by emission from relativistic electrons near the plasma centre and these measurements therefore cannot be trusted for transport analysis. In addition, the central ECE measurements were heavily affected by sawteeth, with a sawtooth period similar to the modulation period, resulting in some uncertainty on the determination of the central transport coefficients. In the rest of the plasma it is seen that the analytical heat diffusivity remains below the heat pulse heat diffusivity and that their values agree well. This analysis shows that modulated ECRH is a powerful tool for determining transport coefficient throughout most of the plasma radius [5].
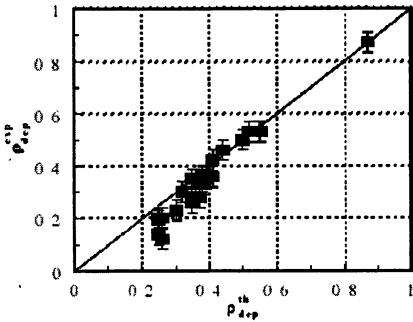
Fig. 9. Measured versus calculated deposition radius
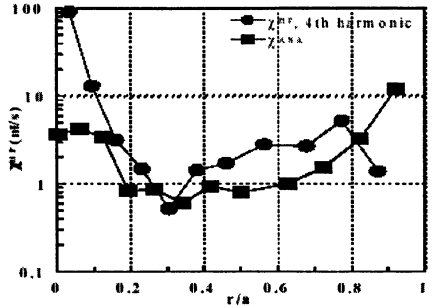
Fig. 10. Transport coefficients calculated for pulse 29029 using 2 methods

2002 – and beyond. The main aim for Tore Supra in the present campaign is to exploit the long pulse capability resulting from the installation of an actively cooled pumped limiter and from actively cooling the whole of the Tore Supra vessel. A record pulse with duration of 213 s has been achieved, at a plasma current of 0.7 MA driven mainly by 3 MW of Lower Hybrid power. The total energy of this pulse was a new world record of 0.61 GJ. In the operation leading up to the long pulses, 300 kW ECRH power was injected for 20 s together with 3 MW of LH power. The ECRH power was modulated 100% at 1 Hz (Fig. 11). The influence of the ECRH power on the electron temperature and on the density is clearly seen. In addition it is seen how an MHD
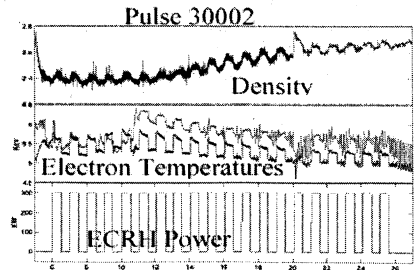
Fig. 11. 20 second pulse modulated at 1 Hz

415

mode, which appears in the second half of the pulse, is suppressed or reduced by the application of ECRH. In the continuation of the 2002 campaign the ECRH system will be operated with up to 800 kW of power, with the emphasis on a complete characterization of the antenna and the polarisers followed by long pulse plasma operation in conjunction with attempts at further increasing the Tore Supra pulse duration and injected energy [9]. For subsequent experimental campaigns attempts will be made to control – in real time – the power deposition and wave polarisation, in order to enable feedback control of various plasma parameters. The capability to carry out such real time control becomes ever more important as ECRH power increases towards 2.4 MW and as the Tore Supra pulse duration increases.

Conclusions

The Tore Supra ECRH system has been used to inject up to 800 kW into plasma, while one gyrotron has produced 300 kW for 110 s into a CW test load. The pulse duration is limited by excessive degassing, due to spurious microwave oscillations inside the gyrotron. Six upgraded 400 kW up to 600 s tubes will be available by 2006, with the first due for delivery in 2003. In plasma experiments the power deposition has been varied over a wide range by varying injection angles, polarisation and magnetic field, showing good agreement between predicted and observed deposition radius. Initial analysis has proven that modulated ECRH injection is a powerful tool to determine transport coefficients as a function of the plasma minor radius.

References

1. *Darbos C.* et al., Fusion Engineering and Design, Vol. 56–57, p. 605–609.
2. Girruzi, Proc.18th IAEA (Sorrento, 2000).
3. *Zou X.* et al., Proc. 27th EPS (Budapest, 2000).
4. *Darbos C.* et al., Proc. EC12 (Aix-en-Provence, 2002).
5. *Zou X.* et al., Proc. EC12 (Aix-en-Provence, 2002).
6. *Lennholm M.* et al., Proc. EC12 (Aix-en-Provence, 2002).
7. *Lennholm M.* et al., 19th SOFE (Atlantic City, 2002).
8. *Kuzikov S. V.* Simulation of Remote Steering System for ITER ECRH/ECCD, ITER Scientific Report, IdoMS No. G52 RE 500-11-10W0.1,2000.
9. *Darbos C.* et al., (Proc. 22st SOFT, Helsinki, 2002) Submitted for publication in Fusion Engineering and Design.

GEOMETRO-OPTICAL CODE
FOR RAY TRACING IN WARM PLASMAS

M. A. Balakina, O. B. Smolyakova, M. D. Tokman

Institute of Applied Physics RAS, Nizhny Novgorod, Russia

Geometro-optical code for ray tracing in warm (subrelativistic) plasmas is under considera-
tion. Principal possibilities of this code are being demonstrated on the analyses of the
scheme of tangent injection of microwave radiation. This scheme provides the minimal
width of the power deposition layer.

For the present time it is evident (see [1]) that relativistic modelling is re-
quired for a range of microwave applications on large magnetically confined fu-
sion plasmas today and should be the norm for such applications on next step
devices such as ITER [2]. So, the efficient and sufficiently accurate codes are
required for computing the refractive index and susceptibility of the plasmas.
More over, using of the "cold" dielectrical permitivity tensor $\hat{\varepsilon}$ or neglecting of
the antihermitian part of $\hat{\varepsilon}$ may lead to erroneous result [3].

Basing on this reasons the original ray-tracing code has been developed pro-
viding in particular for the correct account of the antihermitian part of $\hat{\varepsilon}$, calcula-
tion of the warm (subrelativistic) plasmas dielectric permitivity tensor and suit-
ability (after some modification) for different types of magnetically confined
fusion plasmas installations. In present work we shall consider some features of
this code in application to typical tokamak parameters (ITER like, see [2]) – the
corresponding equilibrium configuration for the toroidal (i.e. magnetic field flux
through the circular contour perpendicular to the symmetry axis of the torus)
magnetic flux ψ and dependencies for electron temperature and concentration.
Further we shall use the effective radius $\rho = 1 - \psi/\psi_c$ as the "label" of the surface
of constant flux ψ; on magnetic axis $\psi_c = 9.62$.

An important aspect of the ray tracing code in warm plasmas is the descrip-
tion of electron cyclotron wave dispersion and absorption. The major difficulty in
applying the geometrical optics (GO) here consists of the fact that despite the
existence of a weakly damping solution[1] of the dispersion equation

$$D = \det\left\| k^2 \delta_{ij} - k_j k_i - \omega^2 / c^2 \varepsilon_{ij} \right\| = 0 \tag{1}$$

with $|\mathrm{Re}\, k| \gg |\mathrm{Im}\, k|$, the imaginary and real parts of the dispersion equation (and
its derivatives with respect to k, ω) are of the same order. In [4] it is shown that
the influence of the thermal effects on beams propagation can be taken into ac-
count correctly by using the "effective" real Hamiltonian $H(r, k)$ if the corre-
sponding solution $k(r)$ for $H = 0$ coincides with the dependence $\mathrm{Re}\, k(r)$ taken
from the solution of the dispersion equation (1). It is essential (for details, see [4,

---

[1] This is connected with the properties of polarization of normal electromagnetic waves at non-
longitudinal propagation relatively magnetic field [3].

5]) that such effective Hamiltonian, in general, can not be derived correctly by neglecting the antihermitian components of the dielectrical permitivity tensor $\hat{\varepsilon}$ in the dispersion equation (1).

To construct real Hamiltonian in our code we use the next procedure. Let's rewrite dispersion equation (1) like the biquadratic equation for the perpendicular to the field B component of refraction index $N_{\perp} = k_{\perp} c / \omega$:

$$D = A(N_{\perp})N_{\perp}^4 + B(N_{\perp})N_{\perp}^2 + C(N_{\perp}) = 0.$$

Note that coefficients A, B, C are complex in the region of absorption. Then from two normal modes

$$D = A(N_{\perp}^2 - X_1(N_{\perp}))(N_{\perp}^2 - X_2(N_{\perp})) = 0$$

one choose the only:

$$D = N_{\perp}^2 - X_i(N_{\perp}) \approx N_{\perp}^2 - X_i(\text{Re } N_{\perp}) = 0. \tag{2}$$

At last, taking the real and imaginary parts of (2) and equate them with zero we have expressions for real ray Hamiltonian and absorption coefficient (more details in [6]):

$$H = (\text{Re } N_{\perp}^2) - \text{Re } X_i, \tag{3a}$$

$$\text{Im } N_{\perp} \approx \text{Im } X_i(\text{Re } N_{\perp}) / 2\text{Re } N_{\perp}. \tag{3b}$$

Such form of the ray Hamiltonian is equivalent to the one proposed in [4]. Analyses undertaking in [4] (on the basis of the expansion of the field on WKB modes) demonstrated numerically, that trajectories of beams in slab geometry can really be described by ray tracing with Hamiltonian in the form (3a) and the direction of the corresponding trajectories coincides with the modified energy flux propagation. (Note that in case of media with dissipation and dispersion one should consider the modified expression for the wave energy flux [5]).

In order to characterize the absorbed power spatial distribution, it is useful to introduce the quantity

$$U(\rho) = \partial \exp(-\tau) / \partial \rho, \quad \tau = \int 2\text{Im } k ds,$$

where τ is the plasmas optical width from the entry point to the plasmas volume till the current point (s is the coordinate along the ray trajectory). We will determine the characteristic half-width of the function $U(\rho)$ in the ordinary way:

$$\Delta = \left(\overline{(\rho - \bar{\rho})^2} \right)^{1/2} = \sqrt{\bar{\rho^2} - (\bar{\rho})^2}, \quad \bar{\rho^k} = \int \rho^k U(\rho) d\rho / \int U(\rho) d\rho.$$

Tensor of the dielectrical permitivity $\hat{\varepsilon}$ in this code can be calculated both in cold plasmas approximation and weakly relativistic Shkarofsky formulation [7, 8] (for resonances up to the third harmonics).

To demonstrate our code on the concrete example, let's consider well-known problem concerning tearing mode stabilization (see [9] and the literature cited therein). For both traditional methods of stabilization (temperature profile modification with additional local heating and current profile modification with non-inductive current drive) there is a permanent difficulty to provide as narrow spatial size of the energy release zone as possible. Perhaps, a possible way to solve

this problem consists of using the scheme of the tangent injection of RF radiation, where the beam propagates at a tangent to the chosen magnetic surface in the EC absorption region.

We considered the efficiency of the proposed scheme of radiation launch for the magnetic surface with a safety factor $q = 2$, in the vicinity of which the tearing mode playing a critical role in disruption may be localized.

The optimization of the ray entrance direction aimed to minimize the heated plasmas slab volume is done in the following way. The first stage is to choose the point of the relativistic "cut-off" of the cyclotron resonance r_0 inside the plasmas volume (which is also the point where the ray is tangent to the chosen magnetic surface). At this point, one finds the initial values of the wave vector k_0 by solving the set of nonlinear equations:

$$H\left(r_0, k_0\right) = 0, \tag{4}$$

$$\left(\partial H / \partial k_0 \cdot N_\psi\right) = 0, \tag{5}$$

$$N_\parallel^2 / 2 = 1 - n\Omega_c / \omega. \tag{6}$$

The equation (4) means that its solution $k(r)$ coincides with dependence $\operatorname{Re} k(r)$ at dispersion equation (1) solving. The relation (5) states that the ray propagates at a tangent to the chosen magnetic surface at the point r_0 (N_ψ is perpendicular to the chosen magnetic surface in r_0). The equation (6) is the condition of the relativistic resonance cut off in warm approximation.

It must be emphasized that the cut off condition sets the connection between ω and $N_\parallel$. So, there are two variants of the scheme with tangent injection realization. First, choosing of the initial point r_0 one can alter the radiation frequency ω so that cut off condition to be satisfied for the value $N_\parallel$ determined beforehand, and, second, initially unknown value $N_\parallel$ (now determined by the choice of the point r_0 and the value of k_0) corresponds to a given frequency $\omega = \omega_0$. Further we will term the first variant as "the scheme with frequency adjustment" and the second one as "the scheme with a given frequency".

We shall use a kind of criteria (upper limit) for Δ values. At exceeding of this limit one can consider the corresponding energy release half-width like "wide". Value $\Delta_{crit} = 0.005$ corresponds to determined in [9] maximum of half-width of energy release profile at which the tearing mode stabilization by temperature profile modification using additional local EC heating of surfaces with $q = 2$ is yet possible.

Let us consider how parameter Δ depends on the choice of the "touch point" r_0. One can use the angle $\theta = \arccos\left(k_z / |k|\right)$ between axis OZ and ray trajectory in r_0 as characteristic of where r_0 is chosen (see Fig. 1, b). So, $\theta = 90°$ means that ray trajectory in r_0 is close to horizontal line; $\theta = 0°$ corresponds to merely vertical line. Results of this calculation for the single ray is presented on Fig. 1, a both for "the scheme with frequency adjustment" (full line) and "the scheme with a given frequency" (dashed line). Calculations showed that Δ is minimal on "horizontal" trajectories (with $\theta \to 90°$).

Let us now pass on from the modeling case of the single ray to more actual case of the beam with the finite aperture. The beam is modeling by the system of initially parallel rays with gaussian power distribution in dependence on the distance from the beam axis. Note, that in real experiment one should consider a broad beam focused in vicinity of the "touch point" (see Fig. 2).
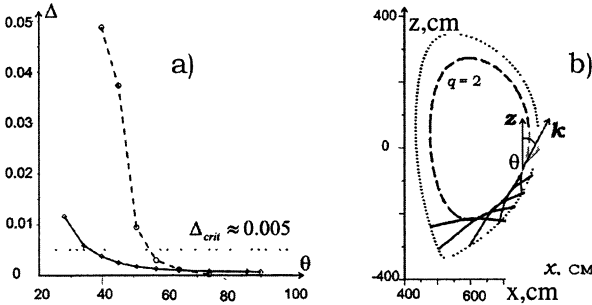
Fig. 1. The dependence of the energy release half-width Δ from angle θ for single ray for "the scheme with frequency adjustment" (solid line) and "the scheme with a given frequency" (dashed line). Here $N_\parallel \approx v_T / c \approx 0.1$ in r_0.

Let us use "vacuum" relations for the evolution of the gaussian beam width $d(z) = d_0 \sqrt{1 + 4z^2 / k^2 d_0^4}$. To estimate the effect let us limit ourselves by approximation of flat-parallel GO beam with relatively small diameter in resonance region. Such beam will correspond to behaviour of the real focused beam (on Fig. 2 it is the region inside the oval contour). In this case the condition of applicability of GO description consists in that the beam should not diverge sufficiently at least on length of absorption ($z \approx \Delta l_r$), i. e. $\Delta l_r \leq k d_0^2 / 2$. According to our

Fig. 2. To estimation of the role of diffraction: real focused beam (left) and "modeling" beam (right).

evaluations the absorption length Δl_r is 5 ... 8.5 cm, so for wave number $k \approx \approx 30$ cm^{-1} and beam of diameter in the narrowest place about $d_0 \approx 1$ cm condition $\Delta l_r \leq 15$ cm is quite appropriate.

Results of comparison of the tangent and horizontal injection are presented on Fig. 3. It is clearly seen that the tangent injection provides more efficient localization of the energy release zone even for the beam with 10 cm in diameter. The cause of this is the additional "focusing" of the beam in resonance zone. This caused by the formation of the caustics (see Fig. 4) due to refraction of the beam from the central plasmas regions with higher density. Such "additional focusing" makes it possible to use rather wide (more usual for experiment) beams without special focusing of them to the absorption region[2], that may be difficult for technical realization.

---

[2] Since the energy release width at a tangent injection is determined by the beam aperture, then to keep any effect from the tangent injection (in comparison with the horizontal injection where the energy release width is determined by the absorption length) we should provide the beam width lesser than the absorption length.
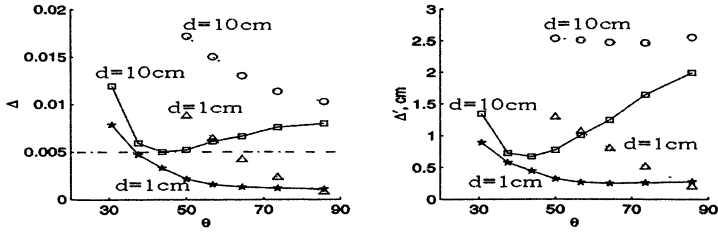
Fig. 3. Half-width Δ in ρ – units (left) for the case of tangent injection (solid lines) and horizontal injection (dotted lines) for two beams: 1 cm and 10 cm in diameter. On right is the corresponding dimensional estimations: $\Delta' = \Delta/|\nabla\rho|$.
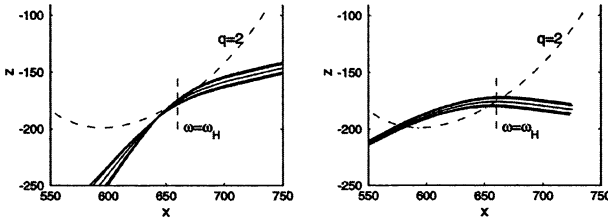
Fig. 4. Tangent injection of the beam of 10 cm in diameter (left) and corresponding beam at the horizontal injection (right).

On the basis of numerical simulation of the energy release width minimization in the scheme with tangent injection of radiation the possibilities of our geometrical optical code are demonstrated. Calculations showed that for parameters of large scale toroidal installation (case of warm plasmas) at such radiation launch one can provide quite localized energy release, which is appropriate both for possible experiments on tearing mode stabilization by non-inductive current generation and for even more hard requirements of the tearing mode stabilization using EC heating of chosen region of plasmas volume. Naturally, this derivation may be fulfilled with far more precision after successive account of diffraction and fluctuations of plasma's parameters.

References

1. *Bindslev H.*, Relativistic effects in millimeter wave applications on magnetically confined plasmas. Proceedings of the 9th Joint Workshop on ECE and ACH (Borrego Springs, Calofornia, 23–26.01.1995), p. 585.
2. International Atomic Energy Agency, Vienna, 1999. Preprinted from: Nuclear Fusion, **39** (12), (1999).
3. *Alikaev V. V., Litvak A. G., Suvorov E. V., Fraiman A. A.* High-Frequency Plasma Heating. Ed. by A. G. Litvak (New York: Amer. Inst. of Phys., 1992).
4. *Westerhof E.* Plasma Phys. Contr. Fusion, **39**, 1015 (1997).
5. *Tokman M. D., Westerhof E., Gavrilova M. A.* Plasma Phys. Contr. Fusion, **42**, 91 (2000).
6. *Balakina M. A., Smolyakova O. B., Tokman M. D.* Plasma Physics, **29** (1), 72 (2003).
7. *Shkarofsky I. P.* Phys. Fluids, **9**, 561 (1986).
8. *Westerhof E.* Transactions of the 3rd Carolus Magnus Summer School on Plasma Physics, (Spa, Belgium, 8–19.09.1997), p. 139.
9. *Westerhof E.* Nuclear Fusion, **27** (11), 1929 (1987); E. Westerhof. Nuclear Fusion, **30** (6), 1143 (1990).

EFFECTIVE LOWER HYBRID HEATING
AND TRANSPORT BARRIER FORMATION
IN THE FT-2 EXPERIMENT

S. I. Lashkul, A. B. Altukhov, V. N. Budnikov, A. D. Gurchenko,
E. Z. Gusakov, V. V. Dyachenko, L. A. Esipov, E. R. Its, M. Yu. Kantor,
D. V. Kouprienko, T. Kurki-Suonio[2], K. M. Novik, A. Yu. Popov,
S. V. Shatalin[1], V. L. Selenin, A. Yu. Stepanov, E. O. Vekshina[1],
V. B. Yermolajev

A. F. Ioffe Physico-Technical Institute, St.-Petersburg, Russia
[1]St.-Petersburg State Technical University, St.-Petersburg, Russia
[2]Assn Euratom-Tekes, Helsinki Univ. of Tech, Finland

1. Introduction

One of the main goals of the FT-2 experiments is to understand the plasma Lower Hybrid (LH) wave interaction to obtain effective plasma heating [1, 2]. The LH power of 100 kW at 920 MHz is launched by a two-waveguide grill from the low field side, with a refractive index in the range $N_{||} \cong 2 \ldots \cong 3$ [1]. The conditions for LH resonance at $f = 920$ MHz and $B_\Phi = 2.2$ T are realised at electron density of $n_e(0) \sim 3 \div 3.3 \cdot 10^{13}$ cm^{-3} , which is sufficiently high to disable any current drive. The effective ion heating caused by a transition from parametric to classic absorption of the launched LH wave has been established during a long period of the experiments in the FT-2 tokamak. The experiments have demonstrated effective plasma LH heating LHH, resulting from both direct absorption of RF power and plasma transport suppression [2]. This paper gives a brief description of the new experimental and simulated data of the LHH experiment.

2. Mechanism of the LH wave energy transport and absorption

The complicated character of the physical processes for LH wave propagation and absorption in plasma core are due to the fact that, in the inner plasma region, the experiments demonstrate the excitation of daughter waves corresponding to a decay of an electron plasma wave into an LH wave and a quasi-mode: LH $\rightarrow$ LH$'$ + QM, or into an LH wave and ion-cyclotron harmonics: LH $\rightarrow$ LH$'$ + IC [1]. These phenomena have been observed in the experimental campaign in FT-2 since 1990.

Both types of instabilities have been predicted by Porkolab [3] and, apparently, they represent the main channels for the development of parametric instabilities in a tokamak plasma. When the initial Ohmic electron temperature T_e is sufficiently high to make the threshold power for parametric instabilities

$(P^{th} \propto T_e^{\alpha}/n_e^{\beta})$ large enough to prevent the instabilities from absorbing the LH-power in the edge region the wave at frequency f_0 penetrates directly into the inner region without the parametric decay and is absorbed at its resonance density. Experimentally it has been shown, that the optimal central absorption is obtained only at high electron temperatures, $T_e \geq 400$ eV.

The new phase of the investigations is related to the development of the time of flight modification of Enhanced Scattering (ES) technique. Recently, the RADAR probing set was installed at FT-2 [4]. The dependence of the frequency spectrum of the scattering signal as well as its power and time delay averaged in the receiver pass band on the scattering point position were studied by the ES technique. The parallel refractive index N_z was calculated from the radial wave number of the LH wave extracted from the delay time. The first measurements at lower density shows that in the case of low RF power level (< 40 kW; $N_{||}{}^{grill} \cong$ $\cong 2 \div 3$), the resonance cone of the LH wave can be seen. In the vicinity of the resonance cone, which was theoretically simulated using ray tracing, the scattered power of the LH wave propagating into the plasma grows, and the role of the LH waves originally excited by the grill is enhanced [4]. For this case $N_{||} \cong$ $\cong 5$ was measured, which indicates a slowed-down component of the pumping wave. At higher density and RF power the predictions of the linear theory for the propagation of the LH wave in tokamak plasma were no longer confirmed. In this case the LH wave pattern was very different from predicted by theory. In addition to the line corresponding to LH frequency, lines shifted by ion cyclotron harmonics had appeared in the spectrum, indicating the excitation of parametric decay instabilities. The physical picture of LH wave propagation and the problem of the LH wave number spectrum formation are under further investigation.

One of the main achievements of the plasma LH wave interaction study at FT-2 is the realisation of effective ion heating when parametric processes are suppressed [1]. A central ion heating from $T_i(0) = 90$ up to 300–350 eV by LHH is observed at high electron temperatures ($T_e \geq 400$ eV). The ion temperature measurements by the CX analyser are supported by spectral data [5].

3. Conditions for the confinement of high-energy ions

The observed effective heating requires not only the high energy ions created by the LH waves but also a good confinement in the plasma core needed for their thermolisation. At first sight, it seems that the high energy ions created by the LH waves are necessarily ill-confined in the FT-2 tokamak: FT-2 is small ($R = 55$ cm, $a = 8$ cm) with somewhat exceptional features: due to the small plasma current ($I_p = 22$ kA) the poloidal magnetic field is small compared to the toroidal field ($B_T = 2.2$ T, $q = 5$–6). This leads to poloidal Larmor radii that can be several centimetres, of the order of the minor radius. Furthermore, FT-2 also has a large toroidal ripple with the ripple-loss region extending deep into the bulk plasma.

With this wide ripple-loss region, a large number of trapped particles generated during LH heating can suffer a prompt loss even at half minor radius. Consequently, the high energy ions born on trapped orbits are expected to easily escape the plasma. The observed high efficiency of ion heating points out at additional mechanism that can result in an increase in the confinement time of the high energy ions.

In this paper the high efficiency of the LH heating is analysed using the Monte-Carlo code ASCOT [6]. ASCOT follows the guiding center trajectories of test particles in a tokamak magnetic geometry with a toroidal ripple. Collisions with stationary background plasma are simulated using binomially distributed Monte-Carlo operators derived from the Fokker – Planck equation. The effect of LH wave are included using Monte-Carlo [7] operators that give the change in the particle perpendicular energy $W_\perp$, the magnetic surface coordinate ρ, and the toroidal momentum p_Φ due to the LH heating The net effect is that ions are moved across the trapped-passing boundary in the velocity space, thereby producing very wide drift orbits and increasing the direct orbit loss probability.

In the simulations, the evolution of the radial electric field is based on the fact that, neoclassically, any non-ambipolar particle fluxes lead to the appearance of an ambipolar electric field which sustains the charge neutrality through the polarisation drift

$$v_{pr} = (1/\Omega B)\, \partial E_r/\partial t. \tag{1}$$

Evaluating the non-ambipolar flux across a flux surface as a function of time, one can obtain the radial electric field from the radial current balance as $\partial E_r/\partial t = (1/\alpha)\,(j_{NC} + j_{visc})$ on flux surface ρ at time t. Here j_{NC} is the neoclassical radial ion current arising from standard guiding-center drifts (excluding the polarisation drift) and ion-ion collisions, and j_{visc} is the gyroviscosity current [6].

In the simulations the plasma current density is given by a parabolic profile. The stationary hydrogen background plasma is modelled by

$$n, T = n_0, T_0\, (1 - \rho^2)^\alpha{}_{n,T} + n_{sep}, T_{sep},$$

where $n_0(T_0)$ is the central density (temperature) and n_{sep}, T_{sep} is the value of plasma density (temperature) at the separatrix. $\alpha_{n,T}$ are chosen to approximate the density and temperature profiles. The profiles correspond to the well-developed phase of the mode to find the steady-state solutions.

The radial electric field is initialized to its neoclassical, ambipolar value with vanishing parallel flow, given by Hinton and Hazeltine [8]. In ASCOT simulations, Eq. (1) was then solved until a steady-state E_r profile was obtained. The E_r profile obtained from the simulation with central heating [6] assumes larger values than the standard ambipolar E_r^{STAND} field profile calculated from [8]. The plausible explanation (within neoclassical physics) for the radial electric field significantly larger than the standard neoclassical one is provided by the presence
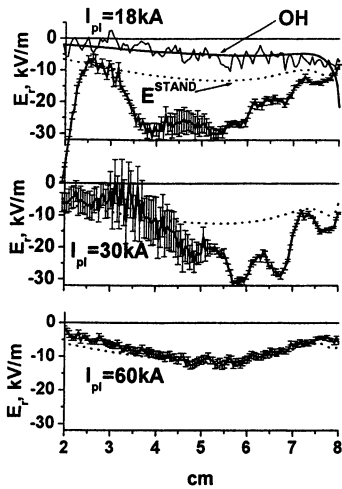
Fig. 1. The E_r field profiles obtained from the simulation for three different plasma currents: 18 kA, 30 kA and 60 kA. Otherwise all the main plasma parameters have been taken identical. The standard neoclassical ambipolar field for OH and LHH conditions E_r^{STAND} is also shown.

of steep density and ion temperature gradients when the banana width of the high energy ions, $r_B = \rho_p\sqrt{\varepsilon}$, is larger then the density scale length $n/\nabla n$. Here $\rho_p = (\sqrt{2m_iT_i})/ZeB_\vartheta$ is the poloidal gyroradius. This conjecture is supported by E_r modelling at different plasma currents. Figure 1 gives the E_r field profiles obtained from the simulation for three different plasma currents: 18 kA, 30 kA and 60 kA. In the simulations, all other parameters were left unchanged. The higher the plasma current, the smaller the banana width and the smaller the discrepancy between the ASCOT simulation and the standard formula.

It is important to notice, that in FT-2, with its small ratio $B_p = 0.02B_T$, the Mach number $M_p = v_\vartheta B_\Phi/v_{thermal}B_\Phi$ of the poloidal rotation easily exceeds unity even for a relatively small E_r. At high M_p the number of trapped (resonant) ions is strongly reduced, leading to a situation in which the bulk ions (instead of the resonant ones) become the main carriers of the E_r-driven radial flux. At the same time practically all orbits are transformed into passing ones, and the orbit widths are strongly reduced. The orbit widths are efficiently "squeezed" [6]. Because a large enough radial electric field thus confines both the banana and ripple blocked ions, this mechanism could facilitate an efficient thermalization of fast ions generated by LW wave.

This conjecture was verified by experiments with two different plasma currents: 18 and 30 kA, corresponding to $M_p = 1.4$ and 0.8, respectively. The time history of the central ion temperature during RF pulse for two discharges with the same initial density $n^{OH}(r = 0$ cm$) = 3\cdot10^{13}$ cm^{-3} but with different plasma current (18 and 30 kA) is shown in Fig. 2. The evolution of the high energy CX neutral particle fluxes ($E_{CX} = 1343$ eV and 1875 eV) along central chord, which views the plasma wave interaction region, are also shown. The higher the plasma current, the lower M_p value and the poorer the confinement of the high energy resonant ions and the poorer the LHH efficiency. The ASCOT simulations also show a decrease of the CX neutral particle fluxes with reducing M_p values, consistent with the experimental data shown in Fig. 2.

425
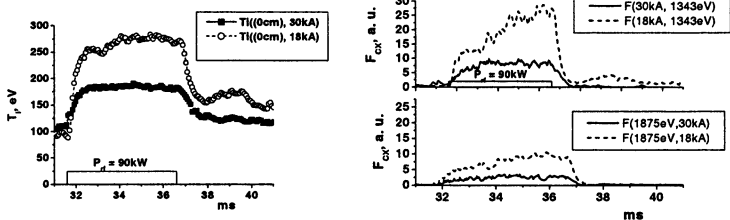
Fig. 2. The time history of the central ion temperature during RF pulse for two discharges with the same initial density $n^{OH}(r = 0 \text{ cm}) = 3 \cdot 10^{13} \text{ cm}^{-3}$ but with different plasma current (18 and 30 kA). The high energy CX neutral particle fluxes ($E_{CX} = 1343$ eV and 1875 eV) along central chord are shown also.

4. Transition into improved confinement mode

In these experiments the effective ion heating results in the Improved Core Confinement (ICC) mode accompanied by the formation of an Internal Transport Barrier (ITB) [2]. The ICC accompanied by Internal Transport Barrier (ITB) formation was confirmed by measuring the peculiarities of the density and the electron and ion temperature profiles, as well as by the diamagnetic, spectroscopic, bolometric, reflectometry and Mirnov probes diagnostics data. The energy confinement time during the RF pulse increases from ~ 0.8 ms to ~ 1 ms. After switching off of the RF heating pulse it further increases up to 2.3÷3.5 ms when an L–H transition has occurred [2, 6].

A comparative study of plasma confinement for two typical RF heating scenarios, on-axis and off-axis, was performed in FT-2 [2]. It should be kept in mind that, during LHH, the ion temperature and density transport barriers are formed at around $r = 5 \div 7$ cm for both central and non-central ion absorption of RF power. It has also been shown that the RF pulse switch-off is followed by an L–H transition and formation of an External Transport Barrier (ETB) near the Last Closed Flux Surface (LCFS) [2, 10].

The new experimental data were obtained by the spatial spectroscopic technique, retooled with additional pulsed helium puffing in hydrogen plasma at the plasma region ($r = 5$–7 cm) where an ITB is formed [10]. The high-resolution spectroscopy of the HeII-line provides a local measurement of $T_{i,\text{opt}}$ and poloidal velocity v_θ of He$^+$ ions at the plasma periphery. According to the radial force balance equation, the measured change in the ion poloidal velocity is $v_\theta = \nabla_r P_{iz}/Zen_{iz}B_\Phi - E_r/B_\Phi + v_\Phi B_\theta/B_\Phi$, where $B_\Phi >> B_\theta$. In the absence of a toroidal momentum source, we assumed that the toroidal velocity v_Φ of the He$^+$ is smaller than v_Φ and, being weighted with $B_\theta/B_\Phi \approx 0.04$, can be taken negligible.

The change in the poloidal rotation of helium ions results from a strong radial variation of the plasma radial electric field E_r and $\nabla_r P_{iz}$ of the helium ions.

426

The measurements of these give the variation of the E_r in the region $r = 5$–6 cm from -10 kV/m at $t = 30$ ms up to -20 kV/m at 31–32 ms when the ITB is formed. These values are in good agreement with the E_r-values calculated from the neoclassical theory and ASCOT code simulation shown in Fig. 1 for $I_{pl} = 18$ kA. The observed increase of ion temperature and plasma pressure lead to a rise in E_r and, consequently, in the poloidal ExB rotation shear $\omega_{E \times B}$. Accordingly [9], when $\omega_{E \times B}$ increases to $\omega_{E \times B} > \gamma_{lin}^{max}$, where γ_{lin}^{max} is the maximum linear growth rate of the dominant instability, the microscale plasma turbulence responsible for anomalous transport is suppressed.

The end of RF pulse was followed by an L–H transition, characterized by an abrupt decrease of the H_β line emission and additional gradual rise of $|\Delta T_i|$ at $r = 7$ cm [10]. This could be explained by the appearance of an additional E_r and its increased shear near LCFS ($r = 7.8$ cm, also observed by Langmuir probes [2]). The X-mode fluctuation reflectometry measurements demonstrate a sharp decrease in the reflectometry BS signal P_s in the frequency band ΔF from 0.2 to 1.0 MHz during and after the RF pulse. Experiments demonstrate that the improved confinement is associated with a modification of microscale turbulence by the shear of the poloidal velocity [10].

It thus appears that both the L–H transition as well as the fast decrease of the transport near $r = 5$–6 cm is due to the generation of a strong negative E_r caused by LH heating. This is also confirmed by spectral measurements. Furthermore it is found that, in the SOL region, the L–H transition is accompanied by significant modifications in the distribution of the poloidal and radial plasma parameters [10]. The plasma periphery data near LCFS are still under further analysis.

References

1. *Budnikov V. N., Irzak M. A.*, Plasma Physics and Controlled Fusion 12A, A135 (1996).
2. *Lashkul S. I., Budnikov V. N., Vekshina E. O.* et al., Plasma Physics Reports, **27**(12), 1001–1010 (2001).
3. *Porkolab M.*, Physics of Fluids, **20**(9), 2058 (1977).
4. *Altukhov A. B.* et al., 29th Europ. Conf. on Contr. Fus. and Pl. Phys. (2002), P4.072.
5. *Budnikov V. N., Chaschina G. I., Dyachenko V. V.* et al., 22[d] Europ. Conf. on Contr. Fus. and Pl. Phys. (1995), II-085.
6. *Kurki-Suonio T.* et al., Plasma Physics and Controlled Fusion, **44**, 331 (2002).
7. *Heikkinen J. A.* et al., Physics of Plasmas, **2**, 3724 (1995).
8. *Hinton F. L. and Hazeltine R. D.*, Rev. Mod. Phys., **48**, 239 (1976).
9. *Waltz R. E., Kerbel G. D. and Milovich J.*, Phys. Plasmas, **1**, 2229 (1994).
10. *Lashkul S. I., Budnikov V. N.* et al., 29th Europ. Conf. on Contr. Fus. and Pl. Phys. (2002), P4.090.

CONTENTS OF VOLUME 1

CURRENT DRIVE AND MICROWAVE PLASMA HEATING
IN FUSION INSTALLATIONS

431

STRONG
MICROWAVES
IN PLASMAS

PROCEEDINGS
OF THE INTERNATIONAL WORKSHOP

In two volumes

Volume 1